N-Heterocyclic Tetrylenes: Potential Platforms for Multidimensional Applications

विद्या वाचस्पति की उपाधि की अपेक्षाओं की आंशिक पूर्ति में प्रस्तुत शोध प्रबंध

A thesis submitted in the partial fulfilment of the requirements of the degree of Doctor of Philosophy

द्वारा / By

मौशाखी घोष / Moushakhi Ghosh
पंजीकरण सं. २०१६२०१७ / Registration No.: 20162017

शोध प्रबंध पर्यवेक्षक / Thesis Supervisor:
डॉ. शबाना खान / Dr. Shabana Khan

भारतीय विज्ञान शिक्षा एवं अनुसंधान संस्थान पुणे
INDIAN INSTITUTE OF SCIENCE EDUCATION AND RESEARCH PUNE
(2024)

Dedicated to My parents

&

In Loving Memory of My Baba and Pishi

INDIAN INSTITUTE OF SCIENCE EDUCATION AND RESEARCH PUNE
भारतीय विज्ञान शिक्षा एवं अनुसंधान संस्थान पुणे
(An Autonomous Institution, Ministry of Education, Govt. of India) Dr. Homi Bhabha Road, Pashan, Pune – 411008

Declaration

Name of student: Moushakhi Ghosh

Registration No.: 20162017

Thesis Supervisor: Prof. Shabana Khan

Department: Chemistry

Date of joining program: August 1, 2016

Date of Pre-synopsis seminar: October 19, 2023

Title of Thesis: N-Heterocyclic Tetrylenes: Potential Platforms for Multidimensional Applications

I declare that this written submission represents my ideas in my own words and where others' ideas have been included; I have adequately cited and referenced the original sources. I declare that I have acknowledged collaborative work and discussions wherever such work has been included. I also declare that I have adhered to all principles of academic honesty and integrity and have not misrepresented or fabricated or falsified any idea/data/fact/source in my submission. I understand that violation of the above will be cause of disciplinary action by the institute and can also evoke penal action from the sources which have thus not been properly cited or from whom proper permission has not been taken when needed.

The work reported in this Thesis is the original work done by me under the guidance of Dr. Shabana Khan.

Moushakhi Ghosh.

Ms. Moushakhi Ghosh

Date: May 17, 2024

INDIAN INSTITUTE OF SCIENCE EDUCATION AND RESEARCH PUNE
भारतीय विज्ञान शिक्षा एवं अनुसंधान संस्थान पुणे
(An Autonomous Institution, Ministry of Education, Govt. of India) Dr. Homi Bhabha Road, Pashan Pune – 411008

Certificate

Certified that the work incorporated in this thesis entitled "***N-Heterocyclic Tetrylenes: Potential Platforms for Multidimensional Applications***," submitted by Ms. Moushakhi Ghosh was carried out by the candidate, under my supervision. The work presented here or any part of it has not been included in any other thesis submitted previously for the award of any degree or diploma from any other University or Institution.

shabanakhan

Date: May 17, 2024

Dr. Shabana Khan

Acknowledgments

"At times, our own light goes out and is rekindled by a spark from another person. Each of us has cause to think with deep gratitude of those who have lighted the flame within us."

– Albert Schweitzer

First and foremost, I thank God for giving me the strength, resilience, and guidance to pursue this doctoral degree. The blessings have been my source of inspiration and motivation throughout this journey.

I owe a debt of gratitude to ***Dr. Shabana Khan***, my thesis supervisor, for her insightful advice and tremendous support during my Ph.D. Her expertise, patience, and encouragement have been instrumental in shaping the direction and quality of this research. I am truly grateful for her mentorship and dedication to my academic and personal growth. I thank her for believing in me and motivating me, mostly when I felt lost. I am fortunate to be pursuing my doctoral degree under her mentorship. After numerous highs and lows during the last few years, I came to realize that I had the privilege of doing my Ph.D. under a truly remarkable human being.

I also want to express my heartfelt gratitude to my research advisory committee (RAC) members, ***Dr. Pramod Pillai*** and ***Dr. Sakya S. Sen***, for their valuable feedback and constructive criticism, enriching this work and strengthening its merit. I sincerely thank former directors ***Prof. Krishna N. Ganesh***, ***Prof. Jayant B. Udgaonkar***, and present director ***Prof. Sunil S. Bhagwat***.

I sincerely thank ***Dr. Pramod Pillai***, ***Prof. Abhishek Dey***, and their research group (especially ***Sumit Da*** and ***Paramita Di***), whose collaboration and expertise have been invaluable throughout this journey. I wholeheartedly thank my friend-turned-collaborator ***Joy***. Their contributions have greatly enriched the research conducted for this thesis. Special thanks to (present and past lab members of ***Dr. Sakya S. Sen***, especially ***Dr. Milan K. Bisai*** and ***Dr. Gargi Kundu***), whose timely assistance has significantly helped me during this journey.

I sincerely thank ***Dr. Sandeep Mishra***, ***Dr. Srinu Tothadi***, and ***Parveen Nasa*** for their continuous support with NMR and single crystal X-ray diffraction data analysis. Financial support for this research was generously provided by the ***Trimurti Research Grant***, ***SERB International Travel Grant***, and ***Infosys Travel Grant***. I also thank ***IISER Pune*** for providing

state-of-art research facilities and fellowship during this tenure. For this, I could attend the International Conference on Phosphorus, Boron, and Silicon (PBSi 2023), Berlin, Germany.

I am incredibly grateful to my school teachers (particularly ***Rijula Gupta***, ***Sister Nisha***, ***Nirmal Dutta***, ***Nishith Sen***, and ***Subrata Saha***) and professors (***Dr. Amrit Mitra***, ***Dr. Nabanita Kundu***, ***Dr. Papia Ganguly***, ***Dr. Nupur Basu***, and ***Dr. Haimanti Mallik***), whose guidance, teachings, and mentorship laid the groundwork for my academic journey. I am grateful to them for instilling in me a love of learning and a dedication to pursue this doctoral journey.

I am grateful to my parents for believing in my choices and granting me the freedom to pursue my career path independently, without ever questioning me. I am deeply grateful to my father, ***Late Shri Dhiresh Ghosh***, ***Baba***, whose belief in my potential inspires me every day. Though he is no longer with me, his spirit lives on in my determination to shine brightly in the future, just as he always wanted. His love, guidance, and sacrifices have shaped the person I am today, and I carry his values with me at every step of my academic journey. I am profoundly grateful to my mother, ***Smt. Rekha Ghosh Biswas***, ***Ma***, whose presence and support during my secondary and graduation exam days have been a source of strength and inspiration. Her love, encouragement, and sacrifices have driven my academic achievements, and her belief in my abilities has enabled me to move forward during the most challenging times. I am forever indebted to her for her selflessness in my success. I would like to express my heartfelt gratitude to my late aunt, ***Late Namita Ghosh***, ***Pishi***, whose love and support left an indelible mark on my life. Her presence continues to inspire and uplift me every day. Her belief in my potential and her encouragement to pursue my academic aspirations have strengthened me throughout this journey. I thank my sister, ***Smt. Baishakhi Sarkar***, ***Didi***, for all the sacrifices she had made for me as my elder sister over the years.

I wanted to take a moment to express my deepest gratitude for my friend, ***Dr. Prakash Panwaria***. His presence has been a source of comfort, strength, and encouragement. He has been a constant source of reassurance and positivity in moments of doubt and difficulty. His belief in me and words of encouragement have uplifted me when I needed them the most. I owe a part of my success to his steadfast support. My doctoral journey would likely have been incomplete without his support. During this period, I am reminded of how fortunate I am to have him as a friend.

My heartfelt gratitude to each one of the C-127A lab members (***Dr. Jabed***, ***Dr. Nilanjana***, ***Ruksana***, ***Sandeep***, ***Brij***, ***Prachi***, ***Vijay***, and ***Kumar Gaurav***) for their contributions and support during our time together in the lab. I appreciate and thank ***Ruksana*** for taking the extra effort, always listening to my problems, and helping me with probable solutions during this journey. I thank my senior lab members, ***Dr. Nasrina Parvin***, ***Dr. Shiv Pal***, and ***Dr. Neha Kathewad***, for the initial days of my Ph.D. I thank my MS mentor, ***Mr. Rajarshi Dasgupta***, for the experimental learnings he lent me to survive in the organometallic laboratory. During this tenure, I could share what I had learned while monitoring a few MS students, ***Arshad***, ***Nehali***, and ***Aswini***. I thank them for allowing me to help them in their respective work.

A few friends (***Sampreeti***, ***Sushmita***, ***Sakshi***, ***Indra***, and ***Joy***) are treasures that I hold. I want to thank them for the countless conversations, shared moments, and memories we have created together. Whether it is a random chat or a spontaneous catch-up call, every interaction with them brings warmth to my heart and a smile to my face. ***Dr. Indra N. Chakraborty*** has always been my go-to person in IISER, consistently offering solutions to all my problems and never failing to be there whenever I needed him. I cannot thank him enough for that. I thank my childhood friend ***Dr. Pranjal Dutta*** for his awesome advice regarding my career opportunities. Whether it was Lady Brabourne College or IISER Pune, he helped me out when I was indecisive. I could not have made a better decision without his input. Thanks a lot, man! A shout-out to my integrated Ph.D. batchmates—***Prakash, Indra***, ***Joy***, ***Suman***, ***Ateek***, ***Abhishek***, ***Saikat***, ***Pulak***, ***Debanjan***, and ***Markose***. We embarked on this journey together, all of us novices in the research world. Now, as I stand on the brink of completion, it is satisfying to see how much we have grown and gained together.

I am grateful for the countless individuals who have crossed my path and left a positive imprint on my life during this journey. Their willingness to lend a helping hand has not gone unnoticed, and I am immensely thankful for their presence in my life's journey. As I reflect on the many blessings in my life, I am reminded of the collective impact of all those who have touched my life in meaningful ways. Their contributions may not have been recognized individually, but they have shaped the person I am today, and for that, I am grateful. This thesis is dedicated to the memory of my beloved father and aunt, whose light continues to illuminate my path. This thesis would not have been possible without the efforts and support of all those mentioned above. Thank you for being part of this remarkable journey.

Moushakhi Ghosh

Content

Synopsis

The main objective of this thesis, entitled "***N-Heterocyclic Tetrylenes: Potential Platforms for Multidimensional Applications***" is to improve our knowledge of the structure and bonding characteristics of mainly silylene-stabilized coinage metal complexes and their use in photophysics and as surface ligands on nanoparticles. We have also explored this ligand for small molecule activation and stabilization of reactive cationic species of heavier group 13 elements. We aimed to use NHTs in various domains, including small molecule activation, homogeneous catalysis, photophysics, and surface modifications of nanoparticles. The following chapters are divided according to the categorization of their uses in different fields.

Chapter 1: Introduction

"They're very flexible. They don't solidify. They're stable, non-flammable, non-toxic, and they pose no threat to the environment."

-Robert West

As said by the pioneer Prof. Robert West, silicon is the second most earth-abundant element, and the use of it as a semiconductor material is extensive, unlike its low valent counterpart, which is typically in a +2-oxidation state. The group 14 elements, called N-heterocyclic tetrylenes (NHTs), typically possess six electrons in their valence shell. They are one of the most extensively researched ancillary ligands in contemporary main-group chemistry, having previously been viewed as rare and transient laboratory curiosities. NHCs have demonstrated greater promise than their heavier counterparts since their first isolation by Arduengo and co-workers in 1991. The early uses of carbenes as ancillary ligands have been enriched by the fundamental work of the Nobel laureate Ernst Otto Fischer in 1973. However, the chemistry of its heavier analog, silylenes, is restricted in small molecule activations and recently in transition metal-mediated homogeneous catalysis. Thus, remembering the saying by Kipping,

"You want to get up in the morning and think out ten times as much as it's possible to do, and then come down and do it."

- Organosilicon pioneer Frederic S. Kipping, 1934, Bakerian Lecture Royal Society.

We tried to broaden our comprehension of NHTs' adaptability in transition metal chemistry, catalysis, photophysical properties, and surface capping ligands.

Chapter 2: Functionalized N-Heterocyclic Silylenes (NHSis) for Small Molecule Activation and Reactivities

In this chapter, we looked into how bis-silylene reacted with chalcogens, which resulted in the isolation of Si=Ch (Ch= S, Se, and Te). Higher homologs of ketones are oligomeric or polymeric due to an unfavorable overlap between the $p\pi$(Si)- and $p\pi$(Ch)-orbitals and a significant variation in electronegativity between Si(II) and Ch atoms. As a result, one of the ongoing challenges facing synthetic chemists is the separation of these compounds. Additionally, our research reveals novel C-H···Ch interactions made possible by the bis-silylene ligand backbone. Moreover, we showed that bis-silylenes may stabilize Lewis acid cations of reactive group 13. Therefore, this portion of the thesis aims to understand how bis-silylenes behave when reactive species are stabilized and small molecules are activated. We have also isolated several hetero atom functionalized coinage metal complexes using different NHSis, investigated their distinct bonding patterns and reactivity, and finally used them in homogeneous catalysis. This work is not only limited to the access of NHSi-metal- complexes. However, it also reports several unique compounds *via* homolytic and heterolytic bond cleavage of N-H, B-B, and Se-Se bonds and a unique and superior approach toward C-C coupling.

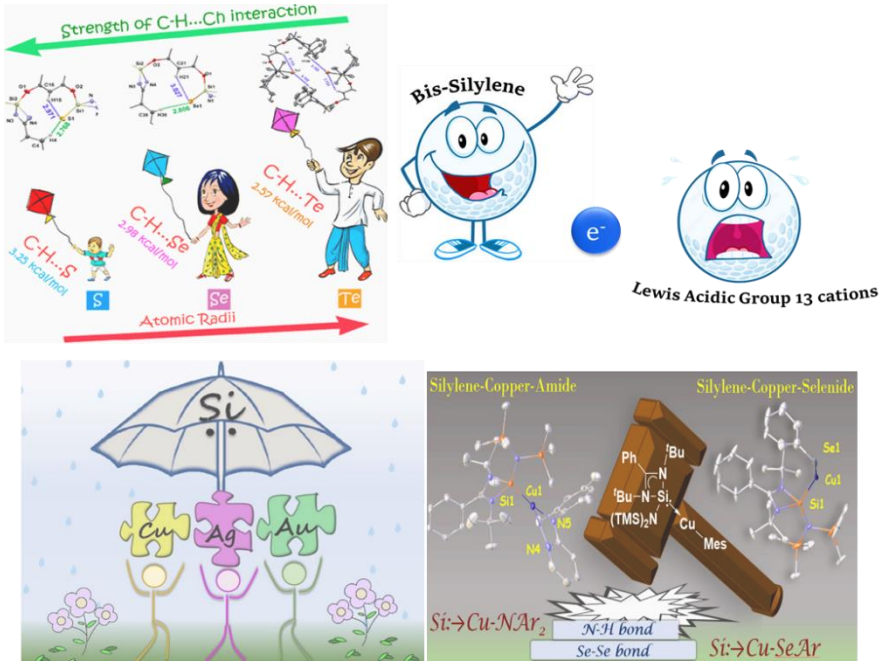

Small molecule activation and stabilization of reactive species

Chapter 3: NHSis Coordinated Copper(I) Complexes as Potential Luminogens

Recent years have witnessed a sudden growth in the area of carbene (N-heterocyclic carbene (NHC)/ cyclic alkyl amino carbene (CAAC)) coordinated coinage metal amide complexes due

to their facile synthesis and distinctive photophysical properties. They have shown remarkable ligand effects on the properties of the derived metal amide complexes. However, the chemistry of NHSis with coinage metals is still elusive. In this chapter, we have synthesized a series of luminescent NHSi coordinated Cu amide complexes. Depending upon the substituent attached to the amide moiety, the origin of emission changes. With this work, we have synthesized NHSi-based luminescent compounds for the first time featuring thermally activated delayed fluorescence and dual emission.

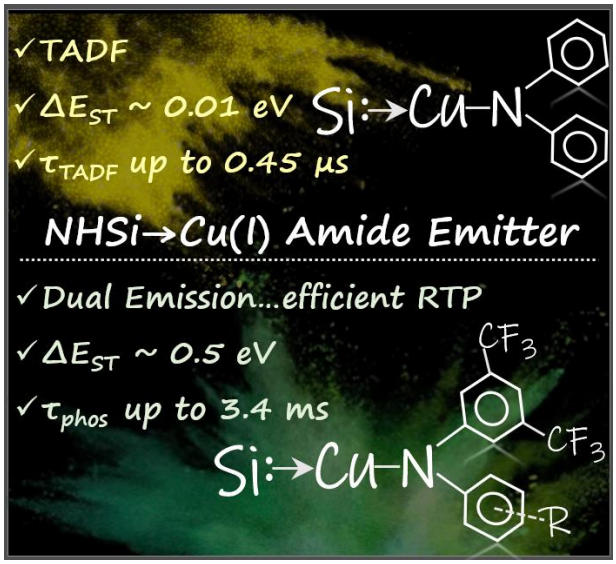

Photophysical properties of Silylene Copper Emitters

Chapter 4: NHT-Capped Nanoparticle Synthesis and Their Catalytic Applications

Recently, there has been a surge in utilizing NHCs as surface-capping ligands for metal/metalloid nanoparticles, providing remarkable stability to the ligand-capped nanoparticles in solution. Focusing on this, we explored the potential of the strong σ donor CAAC as a capping agent for gold nanoparticles (AuNPs) alongside NHSis. The final part of the thesis focused on these newly synthesized carbene and silylene-functionalized AuNPs, characterized using various spectroscopic techniques. Furthermore, we investigated their catalytic performance as catalysts for the electrochemical reduction of carbon dioxide and formic acid oxidation (FAO). Beyond their electrocatalytic activities, we explored their catalytic potential in organic transformations such as nitroarene reduction. We aim to provide new insights into the unforeseen capabilities of NHTs as surface-capping ligands, offering valuable perspectives for main-group chemists. Ultimately, this thesis endeavors to shed light on the unique potential applications of NHTs, particularly NHSis, in various real-world scenarios, thus contributing to a deeper understanding of fundamental main group chemistry.

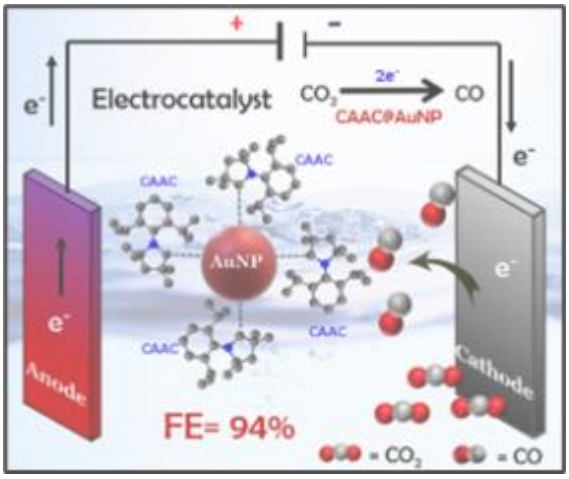

Surface modification of AuNPs with NHTs and their catalytic utilities

List of Abbreviations

$AlCl_3$	Aluminum trichloride
B_2cat_2	Bis(catecholato)diboron
B_2pin_2	Bis(pinacolato)diboron
IPr	1,3-bis(2,6-diisopropylphenyl)imidazol-2-ylidene
IDip	1,3-bis(2,6-diisopropylphenyl) imidazol-2-ylidene
CAAC	Cyclic alkyl amino carbene
Cbz	Carbazole
CCDC	Cambridge crystallographic data centre
DCM	Dichloromethane
DFT	Density Functional Theory
DDT	Dodecanethiol
py_2BMe_2	Di(2-pyridyl)dimethylborate
C_6D_6	Deuterated benzene
$CDCl_3$	Deuterated chloroform
DFAFC	Direct formic acid fuel cell
SIMES	1,3-dimesitylimidazolin-2-ylidene
$EtAlCl_2$	Ethyl aluminium dichloride
ESP	Electrostatic potential surface
$GaCl_3$	Gallium trichloride
$GaBr_3$	Gallium tribromide
GaI_3	Gallium iodide
Hz	Herz
HOMO	Highest occupied molecular orbital
XLCT	Halogen-to-ligand-centered charge transfer
$InCl_3$	Indium trichloride
$InBr_3$	Indium tribromide
InI_3	Indium triiodide
LUMO	Lowest unoccupied molecular orbital
LSPR	Localized surface plasmonic resonance
mmol	Millimole
MNDO	Modified neglect of diatomic overlap
MNPs	Metal nanoparticles

MLCT	Metal-to-ligand-centered charge transfer
TMEDA	N,N,N,N-tetramethylethylenediamine
ICy	N,N′-bis(cyclohexylimidazol)-2-ylidene
IMES	N,N′-bis(2,4,6-trimethylphenyl)imidazol)-2-ylidene
NHTs	N-heterocyclic tetrylenes
NHCs	N-heterocylic carbene
NHSis	N-heterocyclic silylenes
NTO	Natural transition orbital analysis
NLMO	Natural localized molecular orbital analysis
NBO	Natural bond order analysis
NRT	Natural resonance theory
NCI	Non-covalent interaction index
NHE	Normal hydrogen electrode
Bpin-Bdan	Pinacolato-1,8-diaminonaphthalenato diboron
ppm	parts per million
PAAH	Polyallyl amine hydrochloride
PNP	p-nitrophenol
QTAIM	Quantum theory of atoms-in-molecules
RTP	Room temperature phosphorescence
RISC	Reverse intersystem crossing
TADF	Thermally activated delayed fluorescence
RHE	Reference Hydrogen Electrode
SPR	Surface plasmon resonance
SQUID	Superconducting quantum interference device magnetometry
Mes	2,4,6-trimethyl
Trip	2,4,6-triisopropyl
THF	Tetrahydrofuran
TEM	Transmission electron microscopy
TON	Turn over number
TGA	Thermogravimetric analysis
XPS	X-ray photoelectron spectroscopy
WBI	Wiberg bond index
ZFC	Zero-field-cooled

List of Publications

15. ***Moushakhi Ghosh***, Joy Chatterjee, Prakash Panwaria, and Shabana Khan,* N-heterocyclic silylenes coordinated zinc (II) complexes: Synthesis, characterization, and investigation of their optical properties, (*Manuscript under preparation*).

14. ***Moushakhi Ghosh***, Paramita Saha, Abhishek Dey*, and Shabana Khan*, N-heterocyclic silylene capped gold nanoparticles for CO_2 functionalization (*Manuscript under preparation*).

13. ***Moushakhi Ghosh***, Ruksana Akhtar, Sumit Roy, Ajmal Pandikassala, Mayur P. Sangole, Kirandeep Singh*, Sreekumar Kurungot*, Pramod Pillai*, Shabana Khan*, Exploration of Magnetism and Catalytic Properties of Cyclic (Alkyl)(Amino)Carbene (CAAC) Stabilized Gold Nanoparticles, (*Manuscript under preparation*).

12. ***Moushakhi Ghosh***, Prakash Panwaria, Srinu Tothadi, and Shabana Khan*, Facile Access to SiNSi Pincer Based Bis-silylene Co-ordinated Group 13 Cations, (*Manuscript under revision*).

11. ***Moushakhi Ghosh***, Joy Chatterjee, Prakash Panwaria, Ashwath Kudlu, Srinu Tothadi, and Shabana Khan*, Silylene-Copper-Amide Emitters: From Thermally Activated Delayed Fluorescence to Dual Emission, *Angew. Chem. Int. Ed.* **2024**, e202410792.

10. ***Moushakhi Ghosh***, Kumar Gaurav, Prakash Panwaria, Srinu Tothadi, and Shabana Khan*, N-Heterocyclic Silylene Supported Copper(I) Aryl Complexes: Multitasking Cu(I) Synthon. *(Manuscript under revision)*; available at ChemRxiv **2024**.

9. ***Moushakhi Ghosh***, Paramita Saha, Sumit Roy, Sudip Barman, Pramod P. Pillai*, Abhishek Dey*, and Shabana Khan*, Cyclic(Alkyl)(Amino)Carbene Stabilized Gold Nanoparticles for Selective CO_2 Reduction. *ACS Catal.* **2024**, *14*, 7011-7019 (*Published at Front Cover*); also available at ChemRxiv 2023.

8. ***Moushakhi Ghosh***, Nasrina Parvin, Prakash Panwaria, Srinu Tothadi, Rangarajan Bakthavatsalam, Arshad Therambram, and Shabana Khan*, Diverse Structural Reactivity Pattern of a POCOP Ligand with Coinage Metals. *Dalton Trans.* **2024**, *53*, 7763-7774.

7. ***Moushakhi Ghosh*** and Shabana Khan*, N-Heterocyclic Carbenes Capped Metal Nanoparticles: An Overview of Their Catalytic Scope. *ACS Catal.* **2023**, *13*, 9313-9325.

6. ***Moushakhi Ghosh*** and Shabana Khan*, Silylene coordinated coinage metal complexes: An itinerary of their utilities; Book Chapter in Advances in Inorganic Chemistry, *Academic Press*, **2023**, *81*, 279-303 [ISSN 0898-8838].

5. ***Moushakhi Ghosh***, Nilanjana Sen, and Shabana Khan, Coinage Metal Complexes of Germylene and Stannylene. *ACS Omega* **2022**, *7*, 6449-6454.

4. ***Moushakhi Ghosh***, Srinu Tothadi, and Shabana Khan*, Carbazole Substituted Amidinato Silylene: Synthesis, Bonding, and Coordination Behavior with Coinage Metals. *Organometallics* **2021**, *40*, 3201-3210.

3. ***Moushakhi Ghosh*** and Shabana Khan*, N-Heterocyclic Silylenes in Coinage Metal Chemistry: An Account of Recent Advances. *Dalton Trans.* **2021**, *50*, 10674-10688.

2. ***Moushakhi Ghosh***, Prakash Panwaria, Srinu Tothadi, Aloke Das* and Shabana Khan*, Bis (silanetellurone) with C–H···Te interaction. *Inorg. Chem.* **2020**, *59*, 17811-17821.

1. Neha Kathewad, Nandha Kumar, Rajarshi Dasgupta, ***Moushakhi Ghosh***, Shiv Pal and Shabana Khan*, Synthesis and Photophysical Properties of PNP Based Au(I) Complexes with Strong Intramolecular Au···Au Interaction. *Dalton Trans.* **2019**, *48*, 7274-7280.

Chapter 1: Introduction

Partly adapted from: a) ***M. Ghosh*** and S. Khan*, N-Heterocyclic Silylenes in Coinage Metal Chemistry: An Account of Recent Advances. *Dalton Trans.* **2021**, *50*, 10674-10688 and **b)** ***M. Ghosh*** and S. Khan*, N-Heterocyclic Carbenes Capped Metal Nanoparticles: An Overview of Their Catalytic Scope. *ACS Catal.* **2023**, *13*, 9313-9325.

"*Nothing in life is to be feared, it is only to be understood.*" **-Marie Curie**

1.1 Introduction.

1A.1 Understanding of N-heterocyclic tetrylenes (NHTs).

Our fundamental approach to understanding the main group elements has been thoroughly changed over the years due to the ground-breaking discoveries in this field.[1, 2] Initializing out of curiosity and spearheading work with N-heterocyclic carbenes (NHCs) have performed a significant task in the main group chemistry.[3-5] The ligands play a vital role in stabilizing main group compounds in their sub-valencies. Carbenes are a fascinating family of compounds defined as neutral donors with a divalent carbon atom with a six-electron valence shell. However, because of their coordinative unsaturation and incomplete electron octets, which make them intrinsically unstable, they have only ever been regarded as very reactive intermediates in the early days before their isolation. The isolation of a free, uncoordinated carbene remained elusive until groundbreaking investigations in the late 1980s and early 1990s, despite attempts at syntheses dating back to 1835. Bertrand and co-workers reported the synthesis of the first isolable carbene in 1988.[6] However, Arduengo and co-workers first isolated "bottleable" carbene, 1,3-di(adamantyl)imidazol-2-ylidene in 1994.[7] In this context, NHCs have proved their wealth as spectator ligands in numerous fields like organometallic chemistry, homogenous catalysis, medicinal chemistry, and materials chemistry (Chart 1A.1).[8]

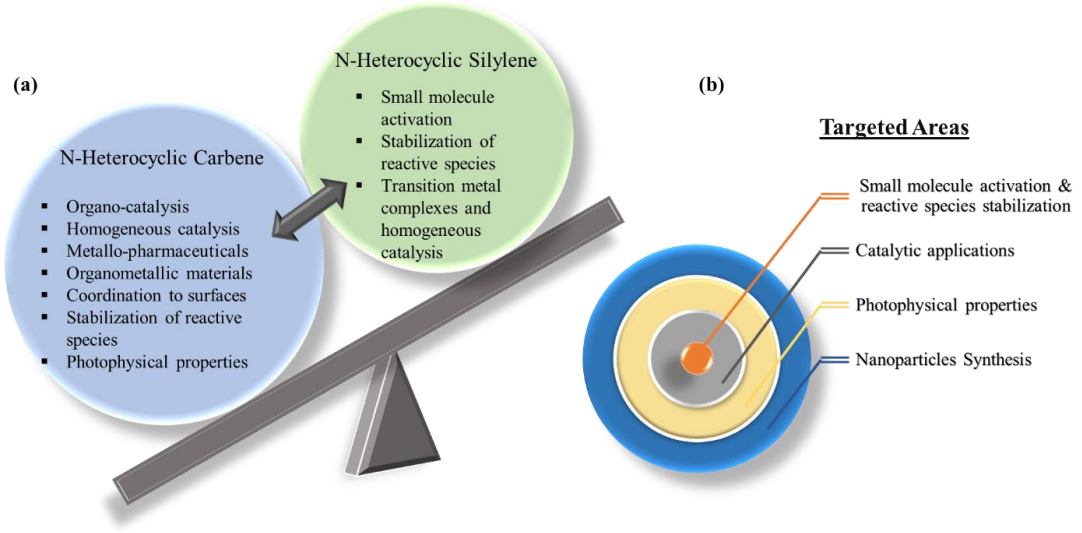

Chart 1A.1 (a) Schematic diagram of broad applications of NHCs and NHSis; (b) Targeted areas covered in this thesis.

It is nothing but an embellishment to state that the concept of NHCs is now well researched, and they are indeed more than mere "phosphine mimics".[9-12] Conversely, the

chemistry of low-valent compounds of higher group 14 elements (Si, Ge, Sn, and Pb) is still at infancy. However, their different physical and chemical properties are expected to possess brighter prospects in novel applications.[13-16] Among the heavier tetrylenes, silylenes are explored widely to activate small molecules and make transition metal complexes. Many of these transition metal complexes have found their potential use in several catalytic organic transformations.[17-21] Nevertheless, the chemistry of silylene with coinage metals (Cu, Ag, and Au) was not well explored until recently.[22]

1A.2 Silylenes: fundamental electronic and bonding properties.

The silicon analog of carbene, namely silylene, generally possesses a singlet ground state with a vacant *p*-orbital and a lone-pair, which possesses a high *s*-character. This peculiar characteristic of silylenes arises from their less inclination towards hybridization because of the larger atomic radius and minimal *s*- and *p*-orbital overlapping,[20,21] resulting in a relatively large ΔE_{S-T} energy gap (Chart 1A.2). Hence, the paired electrons of silylene occupy the low-lying HOMO orbital, and the energetically higher *p*-orbital remains vacant. Therefore, they can act as Lewis base as well as Lewis acid and display very high reactivity. The stabilization of such reactive species generally requires thermodynamic and kinetic protection, usually provided in the form of the heteroatom-based ligand with sterically hindered substituents.[23] Although recent studies have enabled us to discuss more about singlet silylenes, unfolding the possible syntheses of "triplet silylene" is difficult to tame.[24-26]

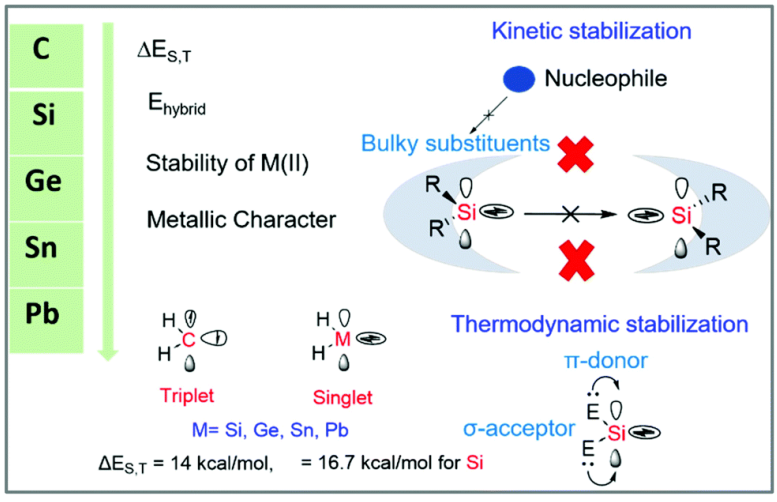

Chart 1A.2. General trends of group 14 elements, thermodynamic (π-donor and σ-acceptor), and kinetic (bulky substituents) stabilization.

To this end, all thanks to the group of Schulz,[27] Inoue,[28] Aldrige, Jones,[29, 30] and Rivard.[31] for isolating several promising silylenes with relatively low HOMO-LUMO gap, and

thus have lower singlet to triplet promotional energy, which enables dihydrogen activation.[32-34] The silylenes have traveled quite a long way in main group chemistry, and many variations are reported now (Chart 1A.3).[34-40] Their journey has also been timely documented in many elegant reviews.[17, 19-21, 34, 41-45]

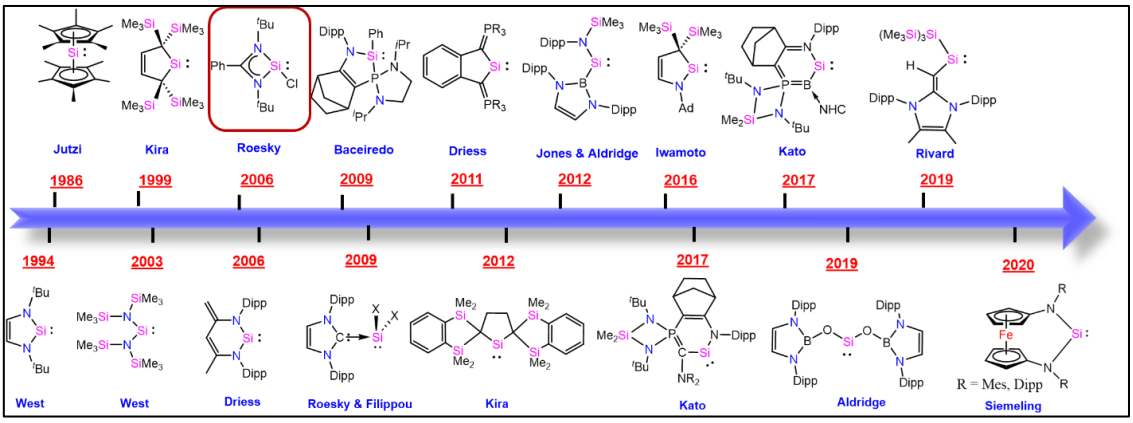

Chart 1A.3. Selected examples of reported monomeric silylenes.

1A.3 Motivation of the thesis.

The chemistry of transition-metal complexes bearing isolable N-heterocyclic silylenes (NHSis) ligands has recently developed appealing and new synthetic methods with a wide range of properties that have significantly influenced organic methodologies, particularly small-molecule activations and a very small number of organic transformation reactions. We have expanded our understanding of NHTs' adaptability in transition metal chemistry, catalysis, photophysical properties, and surface modification of nanocomposite by introducing the additional facets through this thesis. The first section of the thesis demonstrated how bis-silylene reacts with chalcogens to generate the Si=Ch (Ch= S, Se, and Te) bond. Due to an unfavorable overlap between the *pπ*(Si)- and *pπ*(Ch)-orbitals and a significant variation in electronegativity between the Si(II) and Ch atoms, higher homologs of ketones are oligomeric or polymeric. So, isolating such molecules has always been challenging for synthetic chemists. With this work, we also establish unique C-H···Ch interactions due to the polar nature of Si=Ch bonds. The bis-silylene ligand backbone also helped to stabilize reactive group 13 Lewis acid cations. Thus, in this part of the thesis, we aimed to show how bis-silylenes behave in small molecule activation and stabilizing reactive species. Utilizing various NHSis, we have also isolated several coinage metal complexes, explored their unique reactivity and bonding patterns, and ultimately used them in homogeneous catalysis. The literature reports and motivation of our thesis is further elaborated in Section 1B. These complexes could be of great interest for their photophysical properties. By finetuning the electronic and steric properties,

we explored their optoelectronic properties. The concept and literature reports have been documented in Section 1C.

Recently, NHCs have been utilized as surface-capping ligands for metal/metalloid nanoparticles. The wingtip functionalized NHC offers exclusive stability to the ligand-capped nanoparticles in the solution. This prompted us to explore the strong sigma donor cyclic alkyl amino carbene (CAAC) as a capping agent onto the surface of gold nanoparticles (AuNPs), which was also expanded with NHSis. The last part of the thesis dealt with these newly synthesized carbene functionalized AuNPs, which were well characterized using several spectroscopic techniques and utilized these AuNPs as catalysts for the electrochemical reduction of carbon dioxide and formic acid oxidation (FAO). Our thesis aims to pledge new insight for the main group chemist about the unforeseen potentials of NHTs as a surface capping ligand. Overall, given that main group ligands are unquestionably crucial in contemporary synthetic chemistry, this thesis attempted to highlight the unique potentials of NHTs, particularly NHSis, towards a few real-time applications. We hope, perhaps, this will accelerate the process of comprehending the fundamental main group chemistry.

1A.4 Synthesis and functionalization of four-membered benzamidinato silylene.

A significant advancement in silylene chemistry was made in 2006 when Roesky and co-workers isolated the four-membered NHSi (**1A.2**). This compound is widely used as a ligand or functional group in small molecule activation and catalytic or stoichiometric transformations with transition metals. First, a very low isolated yield (only 10%) of **1A.2** was obtained when the corresponding trichlorosilane precursor (**1A.1**) was treated with metallic K (Scheme 1A.1).

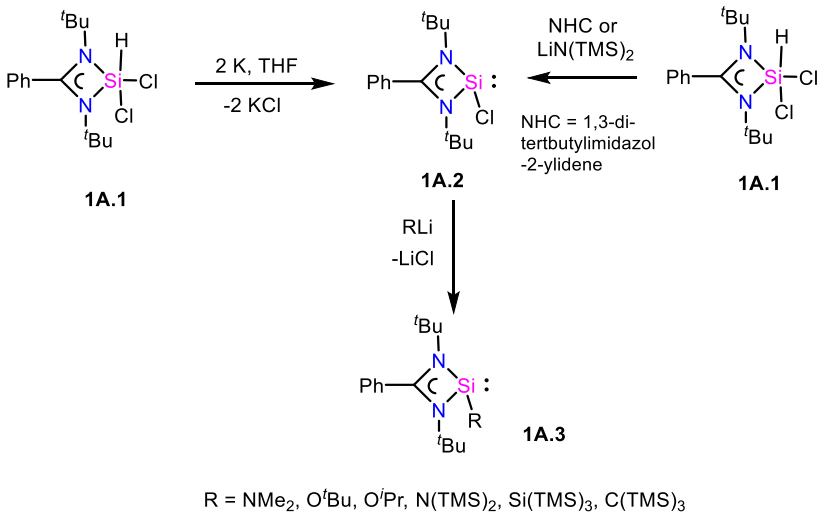

Scheme 1A.1. Synthesis of functionalized benzamidinato silylenes (**1A.2** and **1A.3**): a four-membered NHSi.

Later, in 2009, the same group modulated the process to enhance the yield of the **1A.2** employing $LiN(SiMe_3)_2$ as the reducing agent, conversion by base-induced elimination of HCl from its corresponding chlorohydridosilane (**1A.1**) was observed, yielding 90% with $LiN(SiMe_3)_2$. The high yield access of **1A.2** greatly boosted the further functionalization of NHSi in different scaffolds. In a chelating scaffold using the salt elimination approach, **1A.1** has recently been used as the precursor for several functionalized monosilylenes (**1A.3)** (Scheme 1A.1) and bis-silylenes.

1B Isolation of NHSi coordinated heavier ketones and group 13 elements.

1B.1 Isolation of NHSi coordinated heavier ketones.

Significant progress in silylene chemistry has been made in the past several decades in terms of easily activating small compounds by using the ambiphilic character of divalent Si centers and the narrow HOMO–LUMO energy gap, which mimics transition-metal complexes. Various small molecules like P_4, CO_2, CO, NH_3, and O_2 have been activated using functionalized NHSi.[44] In this section, we will discuss the NHSi ligated heavier ketones. Up until three decades ago, it was thought that the heavier double-bonded compounds between silicon and chalcogens (Si=S/Se/Te) were elusive species because of their enhanced reactivity and very weak *pπ-pπ* overlap between silicon and chalcogens atoms. Corriu *et al.* first reported stable diaryl-Si-thiones and diaryl-Si-selones (**1B.4**) in 1989 (Chart 1B.1).[46]

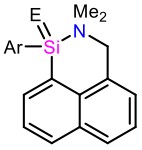

E = S, Ar = Phenyl; **1B.4A**
E = S, Ar = Napthyl; **1B.4B**
E = Se, Ar = Phenyl; **1B.4C**

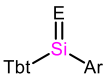

E = S, Ar = 2,4,6-$^{i}Pr_3C_6H_2$; **1B.5A**
E = Se, Ar = 2,6-$^{i}Pr_2C_6H_3$; **1B.5B**
E = Te, Ar = 2,6-$^{i}Pr_2C_6H_3$; **1B.5C**
Tbt = 2,4,6-$[(Me_3Si)_2CH]_3C_6H_2$; **1B.5D**

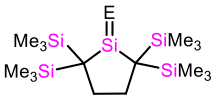

E = S; **1B.6A**
Se; **1B.6B**
Te; **1B.6C**

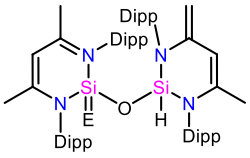

Dipp = 2,6-$^{i}Pr_2C_6H_3$

E = O; **1B.7A**
S; **1B.7B**
Se; **1B.7C**
Te; **1B.7D**

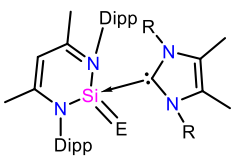

Dipp = 2,6-$^{i}Pr_2C_6H_3$

E = O, R= Me; **1B.8A**
S, R= Me; **1B.8B**
Se, R= Me; **1B.8C**
Te, R= Me; **1B.8D**
E = O, R = ^{i}Pr; **1B.8E**
E = S, R = ^{i}Pr; **1B.8F**
E = Se, R = ^{i}Pr; **1B.8G**
E = Te,R = ^{i}Pr; **1B.8H**

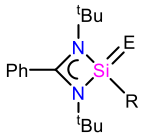

E = S, R= $N(TMS)_2$; **1B.9A**
E = Se, R= $N(TMS)_2$; **1B.9B**
E = Te, R= $N(TMS)_2$; **1B.9C**
E = S, R= $Si(TMS)_3$; **1B.9D**
E = Se, R= $N(TMS)_2$; **1B.9E**
E = Te, R= $N(TMS)_2$; **1B.9F**

Chart 1B.1. Reported monomeric Si=E (E = S, Se, and Te) complexes.

Later, employing sterically hindered aromatic groups, Tokitoh, Okazaki, and co-workers synthesized and characterized a series of heavier diaryl Si chalcogenones (**1B.5**) (Chart 1B.1).[47-49] Followed by this, Kira, West, Driess, So, and co-workers have further reported the series of monomeric silachalcogenones (**1B.6-1B.9**) (Chart 1B.1).[50-56]

1B.2 Isolation of 4-membered NHSi coordinated group 13 complexes.

1B.2.1 4-membered benzamidinato silylene-based aluminum (III) complexes.

The first five coordinated NHSi aluminum adducts were isolated by Tacke and co-workers (Scheme 1B.1). When dissolved in toluene, compound **1B.10C** dissociates in free NHSi and $AlPh_3$, whereas complex **1B.11B** remains stable in solution.[57] It was obtained by reacting disilylene LSi–SiL (L = $PhC(N^tBu)_2$) with $AlH_3.NEtMe_2$ in a ratio of 3:2 in toluene. This compound was serendipitously isolated by Roesky and co-workers (Scheme 1B.1). Following that, they treated LSi–SiL with $AlMe_3$ in toluene to examine the bonding pattern, and isolated the Lewis-acid base adduct, **1B.14**. Synthesis of compound **1B.14** validated complex **1B.13** adduct formation, followed by the Si atom's insertion into the Al-H bonds. They further reacted mesitylsilylene, LSiMes (Mes = 2,4,6-trimethylphenyl) with alane $AlH_3.NEtMe_2$ in the ratio to isolate the intermediate state to produce complex **1B.16**.[58]

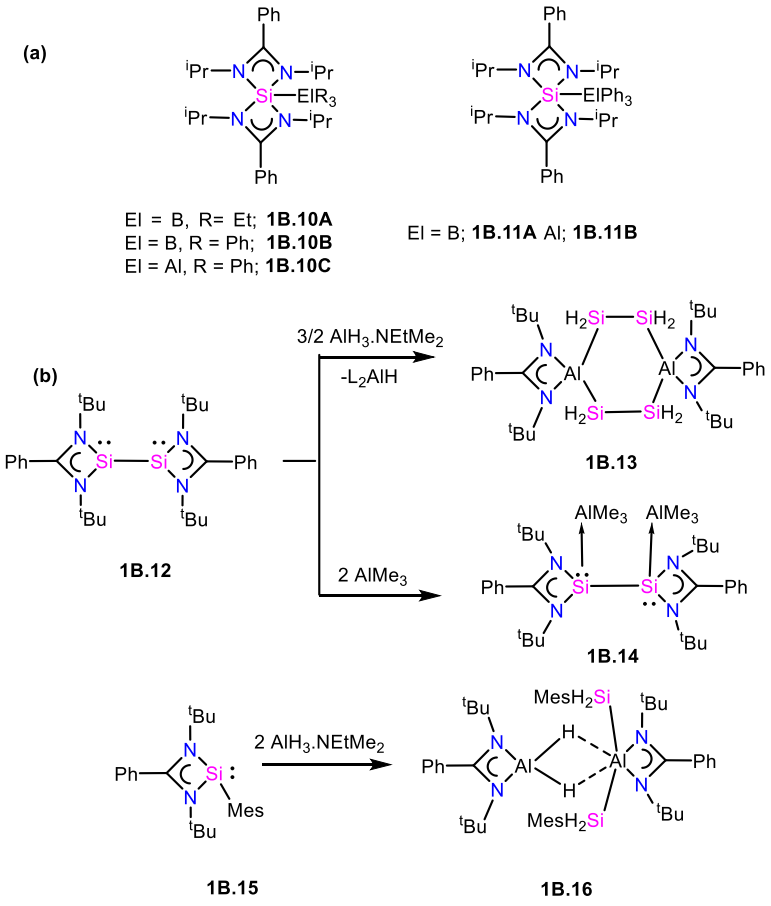

Scheme 1B.1. (a) Synthesis of five-coordinate NHSi-based alkyl borane and alane complexes; (b) Reactivities of NHSi with alane and trimethyl alane.

The same group reported the silylene-aluminum adduct using hybrid silylene based on phosphine (**1B.17**). The treatment of **1B.17** with $AlCl_3$ and $EtAlCl_2$ in diethyl ether afforded the complexes **1B.18** and **1B.19** are reported (Scheme 1B.2). The molecular structure of **1B.18** and **1B.19** shows that only the NHSi moiety is coordinated with the aluminum precursor, while phosphorus is tilted towards it but does not coordinate.[59] Roesky and co-workers employed the benzamidinato chlorosilylene (**1B.20**), ^{t}Bu group substituted cyclopentadienyl aluminum chloride (**1B.21**), and the equivalent of KC_8 to form the bis-silylene supported Al(III) complex (**1B.22**) in which one silylene forms an aluminum adduct while the other silylene remains uncoordinated. They also treated their interconnected bis-silylene (**1B.23**) with **1B.21** and **1B.24** to form the identical compounds (**1B.25-1B.26**).

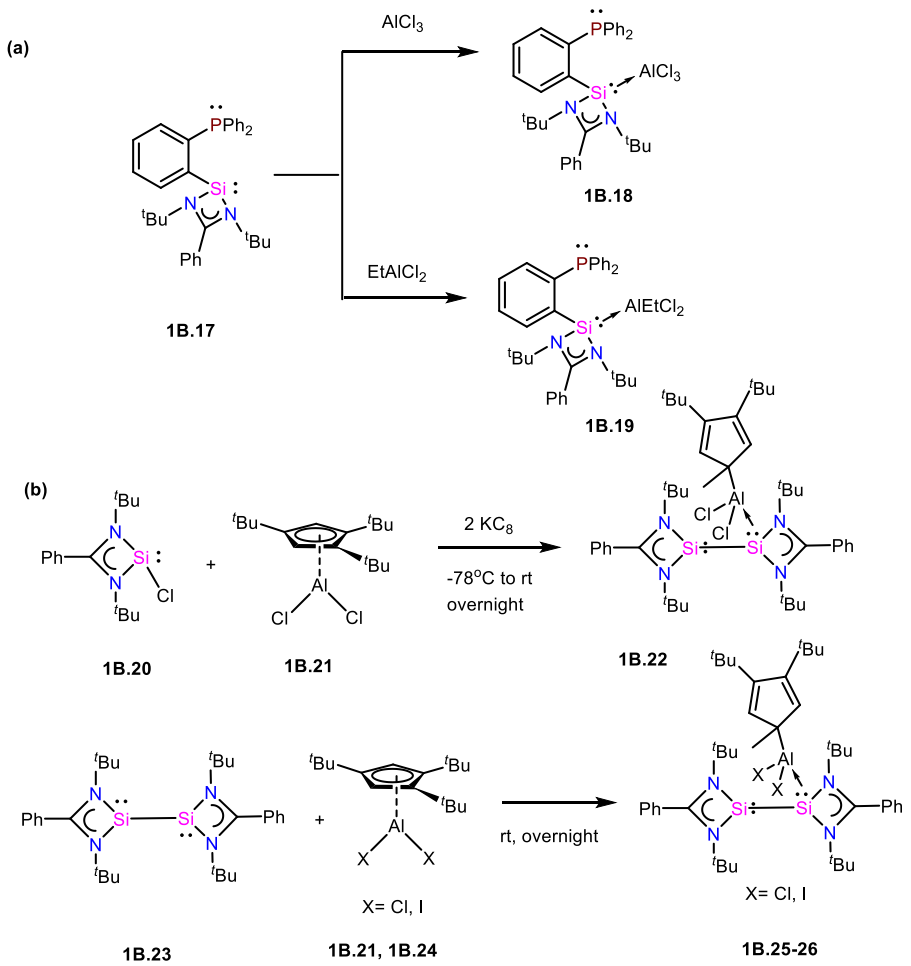

Scheme 1B.2. (a) The reaction of **1B.17** with aluminum trichloride ($AlCl_3$) and ethyl aluminum dichloride ($EtAlCl_2$); (b) Reactivities of NHSi and bidentate NHSi with aluminum halide (AlX_3) under reducing condition (KC_8).

1B.2.2 4-membered benzamidinato silylene-based gallium (III) complexes.

Driess and co-workers isolated Lewis acidic boranyl functionalized silylene in a 9,9-dimethylxanthine ligand framework (**1B.27**). **1B.27** was treated with one molar equivalent of $GaCl_3$ in toluene, forming the complex **1B.28** as a yellow solid.[60] To isolate the NHSi stabilized gallium (III) complex, Roesky and co-workers treated **1B.17** with $GaCl_3$ to afford **1B.27** (Scheme 1B.3). The silylene moiety coordinates in a monodentate form, whereas the phosphine remains uncoordinated but leans in the direction of the gallium center, suggesting a weak interaction.[59] In the presence of two equivalents of LSiCl (**1B.20**), GaI_3 reacts with two equivalents of potassium graphite to afford **1B.30**, which can also be generated by the direct substitution of one chloride group by elusive GaI_2 species.[61]

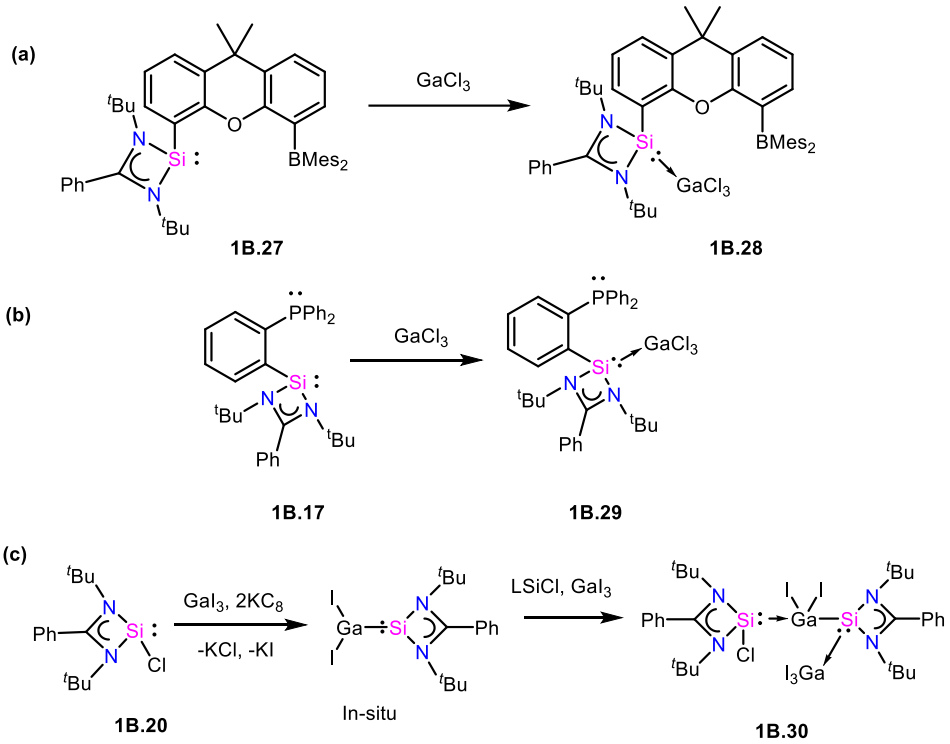

Scheme 1B.3. (a) Reaction of xanthine substituted NHSi (**1B.27**) with gallium trichloride ($GaCl_3$); (b) Reaction of NHSi and phosphine-based hybrid ligand with $GaCl_3$; (c) Reactivities of NHSi with gallium iodide (GaI_3) under reducing condition (KC_8).

1B.2.3 4-membered benzamidinato silylene-based indium (III) complexes.

Jutzi and co-workers first isolated the disilyl indium compound, $[Cp^*_2Si(Me)]_2InMe$ (**1B.32**). During the synthesis of complex **1B.32 (**Scheme 1B.4**)**, one methyl group migrates from In to Si center, and the Cp* moieties get rearranged from $\eta^{2/3}$ to η^1, contributing to the formation of an intermediate monosilyl substituted indium compound (**1B.32**). The NHSi→In(III) precursor is then isolated by Sen and co-workers using **1B.33**. Treatment of **1B.33** with an equimolar

amount of $InCl_3$ or $InBr_3$ in toluene form monomeric compounds $[PhC(N^tBu)_2SiN(SiMe_3)_2InCl_3]$ (**1B.34**) and $[PhC(N^tBu)_2SiN(SiMe_3)2InBr_3]$ (**1B.35**), respectively.[62]

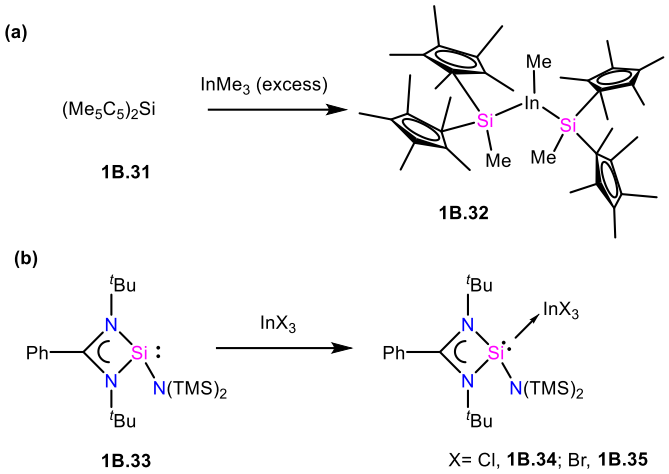

Scheme 1B.4. (a) Reaction of decamethyl silicocene $[(Me_5C_5)_2Si]$ with trimethyl indium ($InMe_3$); (b) Reaction of NHSi with indium halides ($InCl_3$ and $InBr_3$).

1B.3 Motivation and objectives.

The synthesis and isolation of NHSi coordinated heavier ketones, and the coordination of group 13 Lewis acid elements was restricted with monomeric silylenes. Bidentate silylenes remain largely unexplored in this context. Bidentate silylenes are a class of silylenes attached to the functionalized framework of various ligand backbones (**Scheme 1B.5**). Due to the enhanced electronic effect, this class of NHSis is a stronger σ-donor ligand than the monomeric one.

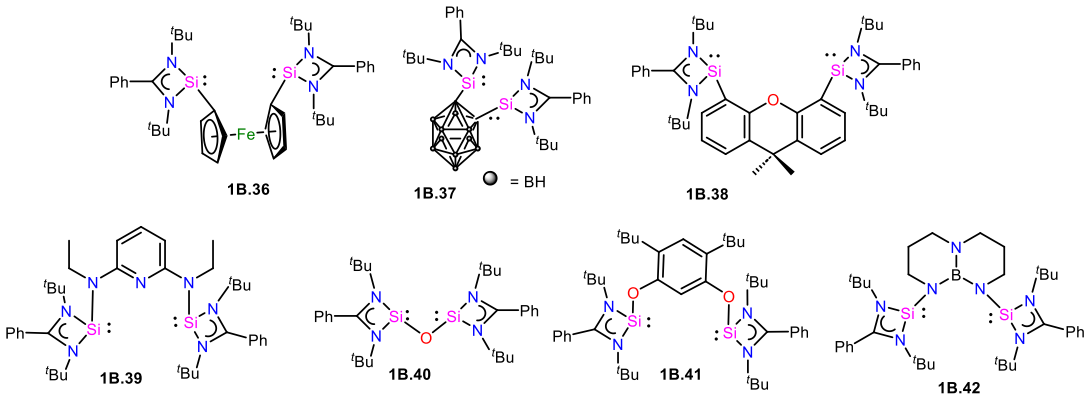

Scheme 1B.5. Few isolated bis-silylene motifs.[21, 63]

With the use of these bis(NHSi)s, Driess and co-workers were able to separate a variety of unique transition-metal complexes for catalysis as well as low-valent main group compounds, such as mono-valent group 15 and zero-valent group 14 complexes with

interesting chemical reactivities and electronic structures. Thus, reactivity patterns of such bidentate NHSis are of particular interest. Driess and co-workers[64] recently stated, *"…it would be interesting to extend this investigation to other main group elements such as groups 2, 12, 13, and heavier group 15."* This motivated us to explore the bidentate silylene for stabilizing heavier ketones and coordinating group 13 elements, which were hitherto unknown.

1C Background of the application of carbene-coinage metal complexes and prelude of NHSi-coinage metal complexes.

The synthesis of NHC-coinage metal complexes has received much attention due to the ease of trans-metallation of NHC-Ag(I) complexes prepared from Ag_2O and NHC precursors.[65] The diverse application of NHC-coinage metal complexes in various fields like medicine, photophysics, and organic transformations have dominated NHC-coinage metal chemistry for several years.[66-69] Very recently, another class of carbene, cyclic alkyl/aryl amino carbene (CAAC or CArAC), reached a milestone as their coinage metal complexes showed up to 100% quantum yield efficiency and were utilized for OLED fabrication.[69-71] Similarly, the gold complexes of carbenes have been proven to be very efficient catalysts in several catalytic transformations and their application in excellent potential chemotherapeutics.[72] In a nutshell, carbene-group 11 complexes have now attained a new height in terms of their applications. Unlike its lighter congener, silylene-coinage metal complexes are in their infancy. The majority of the work with transition metals is done on NHSis, which have been proven to be efficient ligands and are well documented in a few recent reviews by Driess and co-workers.[12, 17, 19-21] These reviews summarize the catalytic performances and selectivity of electronically fine-tuned NHSis supported transition metal complexes. But their potentialities with group 11 metals remained underdeveloped despite the fact that these metals are proven to be very efficient in the current trend in catalysis.[4, 73-76] This is particularly surprising that the progress in the field was kept slowly rising even after the revelations of the promising results with its most praised lighter analogue, NHCs. Hence, there is an utmost need to investigate the coinage metal (Cu(I)/Ag(I)/Au(I)) chemistry of the silylenes thoroughly, as the uniqueness of their tuneable electron donation and acceptor properties certainly guarantees pervasive applications in the coming time.

1C.1 Silylene-coinage metal complexes.

Before isolating any structurally characterized silylene-M (M = Cu, Ag, and Au) complexes, Frenking *et al.* in 1998 showed a theoretical model of tetrylene-Cu, Ag, and Au complexes.[77]

For the comparison, Frenking referred to 5-membered N-heterocyclic tetrylene-coinage metal complexes. He suggested that NHSi-M bonds are expected to be ionic with negligible covalent contribution, displaying Si-Au > Si-Cu > Si-Ag bond stability order. While explaining the NHC-bonding scenario, Frenking discussed the structural factors and stability of NHSi/NHGe-M complexes in more detail. Considering the electronic configuration of M as s^0d^{10}, this study further showed that the tetrylene s donate to the *s*-orbital of the metal. A slight decrease of the electronic population occurs at the d_z^2-orbital of the metal, attributing a small back donation from M to the ligand. The predicted bond lengths reveal a shortening of the M-Cl bond for Cu and Ag but elongation for Au compared to the free M-Cl bond (Chart 1C.1). The reason can be attributed to the pronounced relativistic effect in the latter. These quantum chemical findings are indeed essential to understanding the bonding pattern and electronic distribution in 5-membered NHSi-coinage metal complexes, which afterward become more relevant with the successful isolation of such complexes.

1C.A

Atoms	Bond length (Å)
Cu-Cl	2.061
Si-Cu	2.137
Ag-Cl	2.314
Si-Ag	2.338
Au-Cl	2.308
Si-Au	2.227

1C.B

Chart 1C.1. Calculated bond lengths of M-NHSi complexes (**1C.A**) and bond lengths of free M-Cl (**1C.B**) as predicted by Frenking *et al.*[77]

1C.2 Pentamenthylcyclopentadienyl silylene gold(I) complexes.

The first silylene coinage metal complex was reported by Jutzi *et al.* in 1990, where they utilized decamethylsilicocene (**1C.1**) as the Si(II) source.[78] They obtained **1C.1**→AuCl (**1C.2**) by performing the reaction of **1C.1** with carbonylgold(I)chloride, which was proceeded with the loss of a CO molecule (Scheme 1C.1). Spectroscopic studies and elemental analysis established the composition of **1C.2**, but X-ray structure could not be obtained. The temperature-dependent ^{1}H NMR of **1C.2** revealed that one Cp* ring is σ-bonded to silicon, and the other is π-bonded. The significantly less π-bonding stabilization in **1C.2** than in **1C.1** can be attributed to the electron withdrawal from Au by $d\pi$-$p\pi$ back-bonding. They also reacted **1C.2** with tert-butyl cyanide and pyridine, resulting in **1C.3** and **1C.4**, respectively. These

compounds showed that both Cp* rings are σ-bonded to the silicon, implying the electrophilic silicon in them. It was concluded that the ring slippage ($\eta^5 \rightarrow \eta^1$) of the Cp* group is essential in stabilizing the low valent Si(II)-Au complex (**1C.2**) along with the kinetic protection provided by the bulky Cp* group.

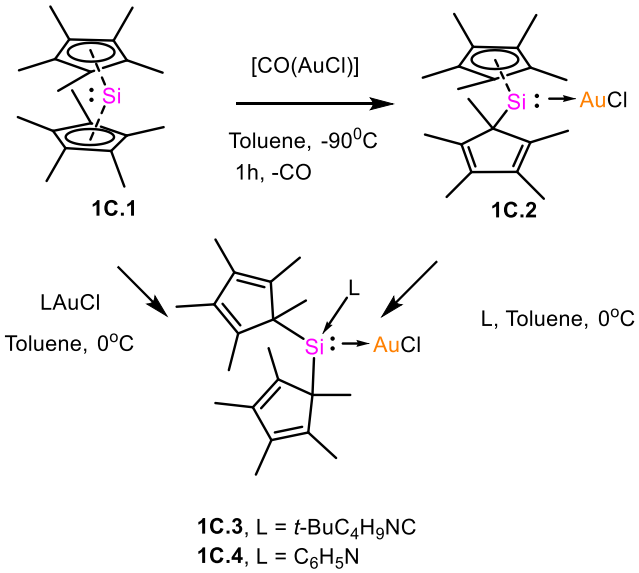

Scheme 1C.1. Synthesis of decamethylsilicocene (**1C.1**) supported gold (I) complexes **1C.2**, **1C.3**, and **1C.4**, respectively.

1C.3 4-membered benzamidinato silylene based coinage metal (Metal = Cu(I), Ag(I), and Au(I)) complexes.

A close look at the literature on the isolable silylenes reveals that the 4-membered NHSi, benzamidinato silylene, by Roesky and co-workers, has enjoyed stupendous attention due to the ease of its synthesis, thermodynamic stability, and tunability.[43, 79, 80] Hence, a large number of reports prevail on the chemistry of this system.[21, 42-44] This section will cover all the coinage metal complexes supported by benzamidinato silylene and other modified derivatives. Utilizing the benzamidinato chlorosilylene (**1C.5**) Driess and co-workers prepared a copper(I) complex (**1C.8**) with [Cu(tmeda)(CH_3CN)][OTf] (tmeda=N,N,N,N-tetramethylethylenediamine) (Scheme 1C.2).[81] Similarly, the reaction of [Cu(tmeda)(CH_3CN)][OTf] with PhC(N^{t}Bu)$_2$XSi:, **1C.6-1C.7** afforded **1C.9-1C.10**, respectively. All three complexes (**1C.8-1C.10**) display a distorted tetrahedral geometry around the four-coordinate Si(II) atom. Driess and co-workers further prompted to check the structural features of a spacer-separated bis-NHSi (**1C.11**) supported cationic copper(I) complex **1C.12** (Scheme 1C.3).[81] This dinuclear copper-based cyclo-octane type complex (**1C.12**) is unique due to the simultaneous presence of silicon, copper, and oxygen.

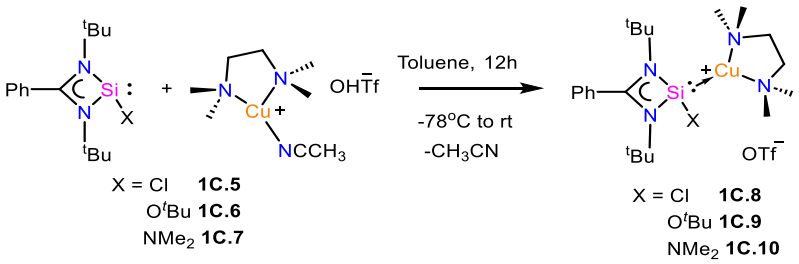

Scheme 1C.2. Synthesis of heteroleptic NHSi Cu(I) ion pair **1C.8-1C.10**.

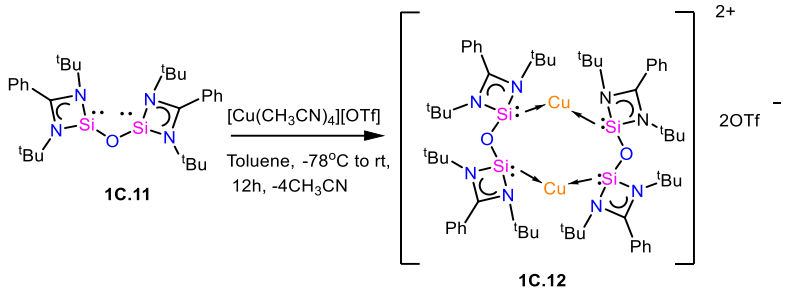

Scheme 1C.3. Synthesis of complex **1C.12**.

Our group, in recent developments, has utilized a sterically demanding trimethylsilylamide substituted benzamidinato silylene (**1C.13**) and isolated several Cu(I), Ag(I), and Au(I) complexes (**1C.14-20)** (Scheme 1C.4).[82, 83] A straight forward reaction of **1C.46** and metal halide precursors provided the desired complexes in good yield.[83, 84]

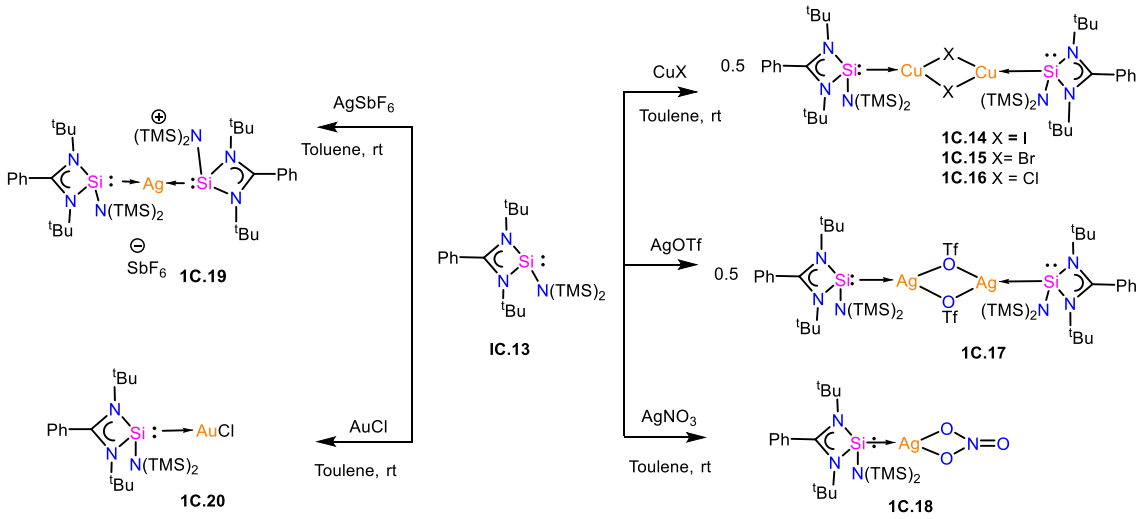

Scheme 1C.4. Reactivity of sterically demanding NHSi (**1C.13**) to various coinage metal salts.

Similarly, the reaction of **1C.13** with AgOTf and $AgNO_3$ afforded complexes **1C.17** and **1C.18**, respectively. Further, a dimeric cationic complex **1C.19** was obtained upon treatment of **1C.13** with $AgSbF_6$, where two silylene molecules are coordinating to an $Ag(I)^+$.[83] Subsequently, the reaction of $AuCl.SMe_2$ with **1C.13** afforded a monomeric complex **1C.20**

displaying a linear Si-Au-Cl bond with Si-Au bond distance of 2.265(1) Å and bond angle of 179.47(3)°, as predicted by Frenking *et al.*[77] It is important to note that **1C.20** is the first example of structurally characterized silylene-Au(I) complex, which possesses a donor-acceptor Si→Au bond unlike **1C.2**.

1C.4 N-aryl phosphine substituted 4-membered NHSi-gold (I) complexes.

Continuing our previous work, we functionalized **1C.5** with the (2,6-*i*Pr$_2$C$_6$H$_3$NPPh$_2$) group to obtain a hybrid bidentate silylene **1C.21**.[85] Upon reaction of **1C.21** with one equivalent of AuCl(SMe$_2$), a monocoordinate Au(I) complex **1C.22** was obtained. Interestingly, **1C.22** does not show any coordination from the PPh$_2$ group; only the silylene is coordinated (Scheme 1C.5). This implies that the silylene is a stronger *σ*-donor ligand than phosphine. Further, treatment of **1C.22** with halogen abstracting reagent AgSbF$_6$ produced a dimeric dinuclear Au(I) complex **1C.23** (Figure 1C.1). This is the first silylene Au(I) complex, which features an aurophilic interaction between two Au supported by Si(II) and P(III) atoms. The phosphine and NHC ligands are well known to make such complexes as they display interesting photophysical properties due to the presence of the Au···Au interaction.[86, 87] However, there was no precedence of such complex with silylene.

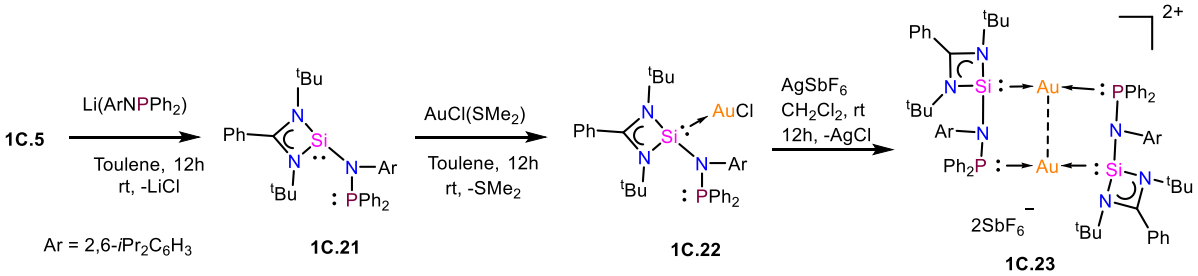

Scheme 1C.5. Syntheses of **1C.21-1C.23.**

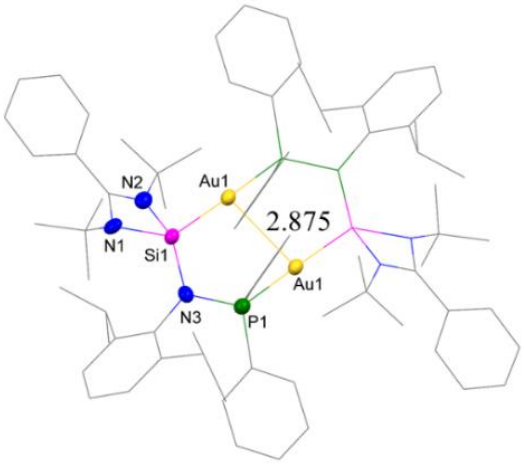

Figure 1C.1. Molecular structure of compound **1C.23** displaying aurophilic interaction (Å).

Roesky and co-workers recently reported a benzamidinato silylene-based bidentate ligand with an additional phosphine donor arm installed on a phenyl backbone (**1C.24**).[59] Since PPh_2 and Si(II) groups are installed on a phenyl backbone, this modified ligand system is expected to be rigid. Hence, the reaction of **1C.24** with CuCl produced a complex **1C.25** (Scheme 1C.6) with a distorted tetrahedral copper(I) and $CuCl_2^-$ counter anion. This reaction underwent differently as compared to the previously reported reactions of Si(II) with CuCl.[83] The central Cu(I) was described to be diamagnetic Cu(I) as their analysis for a hypothetic combination of Cu(0)-Cu(II) gave no EPR signal for paramagnetic Cu(II) .

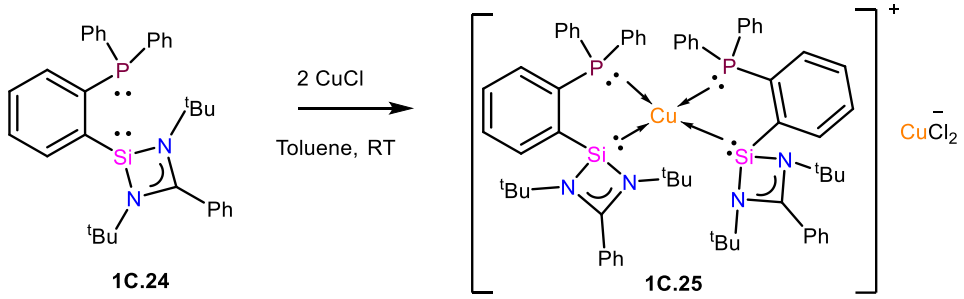

Scheme 1C.6. Reaction of bidentate ligand **1C.25** with CuCl.

1C.5 4-membered NHSi-chalcogenone-copper (I) complexes.

The silanechalcogenones could be utilized as ligands to stabilize the transition metal complexes.[56] They are expected to be a better match for the coinage(I) metals due to the soft-soft interactions.[88] Therefore, we were curious to explore the silanethione/silaneselenone (**1C.26** and **1C.27**) as ligands for preparing copper(I) complexes and studying their bonding situation. Thus, the silanechalcogenones (**1C.26** and **1C.27**), upon reaction with copper(I) halides, produced a series of copper(I) complexes, **1C.28-1C.31** (Scheme 1C.7).[84] The silanechalcogenones were found to be better donors and afforded monomeric Cu(I) complexes **1C.28-1C.31**, whereas the parent silylene (**1C.13**) gave dimeric Cu(I) complexes (**1C.47-1C.49**). It is important to note that **1C.28-1C.31** can also be prepared by the reaction of **1C.14-1C.16** and elemental sulfur/selenium. The DFT calculations revealed that the Si→CuBr bond (WBI = 0.68) is much weaker than the Si=S bond (WBI = 1.55). Hence, it was proposed that the reaction proceeds *via* the insertion of S or Se into the Si→Cu bond. Interestingly, a sterically demanding NHC (1,3-bis(2,6-bis-(diphenylmethyl)-4-methylphenyl)imidazol-2-ylidene) copper(I) bromide complex upon reaction with elemental sulfur/selenium did not afford similar product, indicating that NHC forms stronger bonds with CuX. This fact was also supported by theoretical calculations, which reveal that carbene-S→CuBr formation is 51.6 kcal/mol more endergonic than silylene-S→CuBr formation.

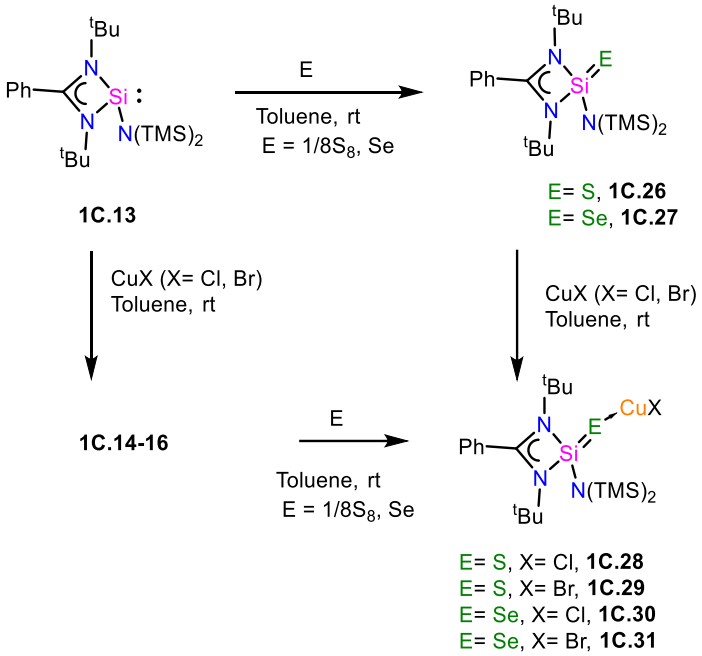

Scheme 1C.7. Synthesis of benzamidinato-silylene chalcogenones supported copper(I) halide complexes (**1C.28-1C.31**).

1C.6 4-membered NHSi with pyridyl substituent, its copper(I) complexes, and CuAAC reaction.

The benzamidinato chlorosilylene (**1C.5**) has been proven to be an excellent precursor for preparing various silicon(II) frameworks, which were further used in transition metal chemistry.[21] Accordingly, Stalke *et al.* functionalized **1C.5** with a pyridyl substituent to have an additional N-coordination site.[89] Synthetically, they applied a new strategy by seizing the lone-pair of silylene first with a metal and then performing the functionalization (Scheme 1C.8). The reaction of **1C.5** with various copper(I) precursors produced a series of tetrameric Cu(I) clusters **1C.32-1C.34**, which upon further reaction with four equivalents of MesNHPy and lithium hexamethyldisilazane afforded the trimeric complexes **1C.35-1C.37**. No ^{29}Si NMR spectrum was obtained for these complexes presumably due to rapid dissociative equilibrium on the NMR time scale. The authors further utilized these complexes (**1C.33** and **1C.36**) as catalysts for the copper-catalyzed alkyne azide cycloaddition (CuAAC) reaction (Scheme 1C.9).[90-92] The NHC-copper(I) complexes have already been well explored for the CuAAC reaction,[93] but this is the first report of the NHSi-Cu(I) complex in CuAAC catalysis. Although both complexes were found to catalyze the CuAAC reaction, the efficiency of **1C.36** was better than **1C.33**, mirroring the utility of N-donor pyridyl moiety, which apprehended the catalytic potential of **1C.36** (Scheme 1C.9). This report opened the door for the silylene-supported coinage(I) metal complexes to be utilized in many more important catalytic reactions.

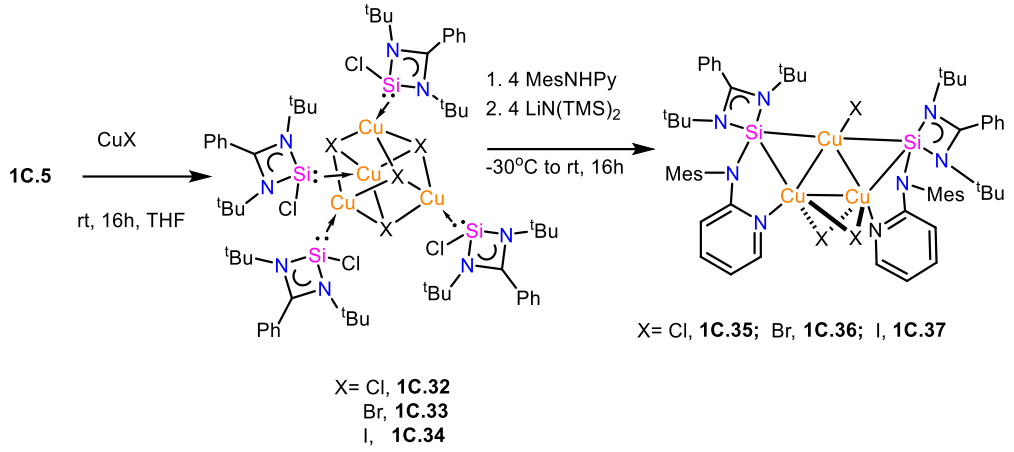

Scheme 1C.8. Syntheses of **1C.32-1C.37**.

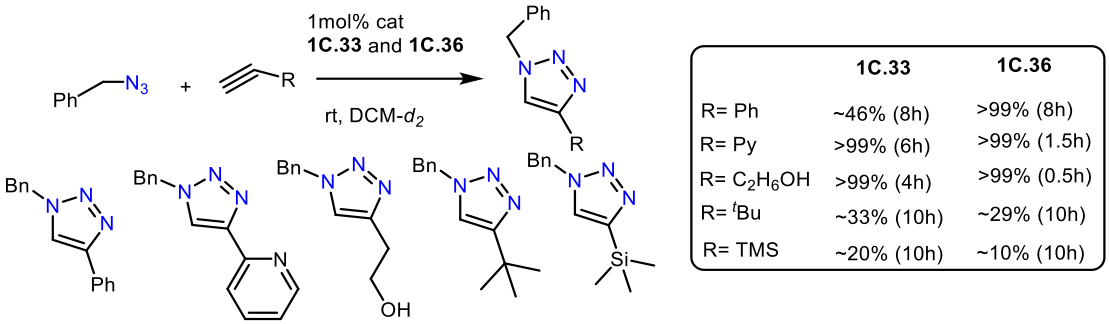

Scheme 1C.9. Catalytic CuAAC reaction using **1C.33** and **1C.36** as catalysts.

1C.7 4-membered NHSi-copper(I)-arene complexes and their catalytic application.

The π-complexes of coinage metals are of great interest as they are considered to be generated *in situ* during the catalytic reactions.[94-100] Among the different types of π-coordinating substrates (alkene, alkyne, and arene), arene forms the weakest bond with coinage metals.[101-105] Hence, they are highly reactive and very challenging to isolate with low coordination numbers. Upon comparing the first-row transition metals, it can be figured out that the group-11 metals have a very low affinity towards the η^6 binding mode with an arene.[106] The explanation lies in the filled d^{10} configuration, which causes the repulsion of the π-electron cloud of arene, as mentioned by Armentrout and co-workers.[106] Similar predictions were made by Guo and co-workers, who proposed the formation of η^6 type bonding of benzene with $Cu(I)^+$ in the gas phase but η^2 in the condensed phase.[107] That explains the less occurrence of Cu(I)-η^6-arene complexes very well (Chart 1C.2).[108, 109] The most significant report in this connection is from Hayton and co-workers, who isolated two half sandwich complexes [(η^6-C_6Me_6)Cu(PR_3)][PF_6] (R=Ph and OPh) (**1C.C**) where C_6Me_6 ring is bound to the Cu(I) ion in η^6 coordination mode.[110] They deduced that the preference for η^6 mode over η^2 mode is exclusively due to the steric repulsion between the Me-group and PR_3 unit.

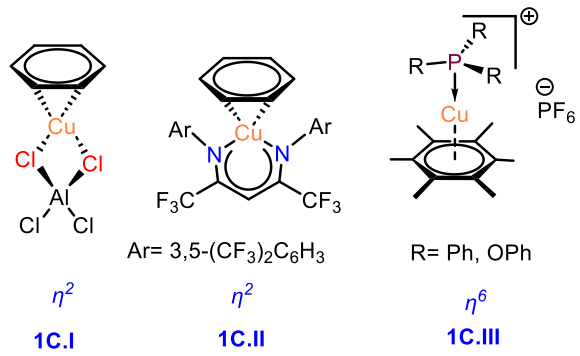

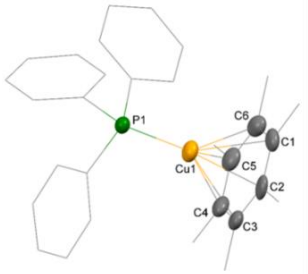

Atoms	Bond length (Å)
Cu-C1	2.291(4)
Cu-C2	2.284(5)
Cu-C3	2.283(5)
Cu-C4	2.292(5)
Cu-C5	2.286(5)
Cu-C6	2.289(4)

Chart 1C.2. Reported examples of Cu-η^2-C_6H_6 and Cu-η^6-C_6Me_6. The molecular structure of Hayton's phosphine stabilized Cu-η^6-C_6Me_6 (**1C.C**) and selected Cu···C bond lengths.

However, they also theoretically showed that when benzene is employed instead of hexamethylbenzene, η^2 mode is preferred. The notable observation was made by our group when we treated **1C.15** with an equivalent amount of $AgSbF_6$ in the presence of hexamethylbenzene and benzene (Scheme 1C.10), which afforded the monomeric complexes of the composition, $[\{PhC(N^tBu)_2SiN(SiMe_3)_2\}Cu(\eta^6\text{-arene})]^+[SbF_6]^-$ (**1C.37** and **1C.38**).[111] The distance between the Cu atom and the centroid of the benzene ring ($Cu–C_{centroid}$ 1.960 Å) in **1C.37** is slightly longer than those in Hayton's $[Cu(\eta^6\text{-}C_6Me_6)]^+$ complexes (1.800(3) and 1.775(6) Å).[111] Analogous reaction with NHC (IPr, IPr = 1,3-bis(2,6-diisopropylphenyl)imidazole-2-ylidene) led to the corresponding complexes with η^2 binding mode $[Cu(\eta^2\text{-arene})]^+$.

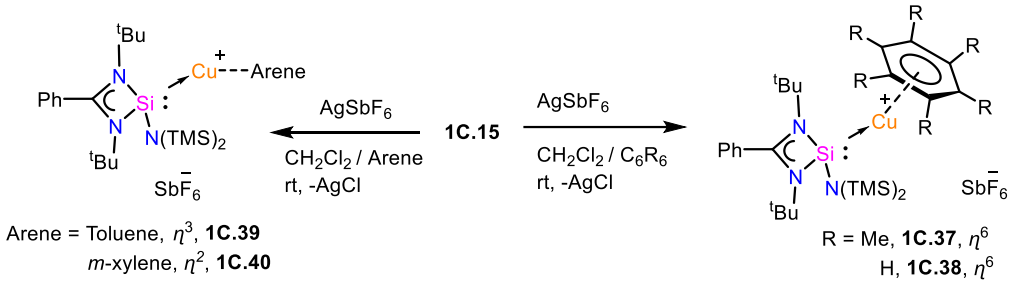

Scheme 1C.10. Syntheses of monomeric copper-arene complexes **1C.37-1C.40**.

Energy decomposition analysis (EDA) for **1C.37** shows electrostatic repulsion between arene moiety and silylene fragment, which can be relieved by the ring slippage from η^6 to η^2. The dispersion interaction contributes to the bonding between the C_6H_6 ring and the Cu-silylene fragments and outweighs the benzene-silylene steric repulsions. Furthermore, extension towards unsymmetrical arenes (toluene and xylene) afforded $[\{PhC(N^tBu)_2SiN(SiMe_3)_2\}Cu(\eta^3\text{-}C_7H_8)]^+[SbF_6]^-$ (**1C.39**) and $[\{PhC(N^tBu)_2SiN(SiMe_3)_2\}Cu(\eta^2\text{-}Me_2C_6H_4)]^+[SbF_6]^-$ (**1C.40**) (Scheme 1C.10).[112] As σ-

donating ligands bind more strongly than π-donating ligands, displacement reactions of the arene with different σ-donor ligands were carried out. Upon reaction of **1C.39** with MeCN, a dimeric cationic copper(I) complex (**1C.41**) along with $Cu(CH_3CN)_4SbF_6$ salt was formed (Scheme 1C.11). On the other hand, treatment of IPr produced a complex **1C.42**, where NHC and NHSi are both coordinating to the Cu(I) center.

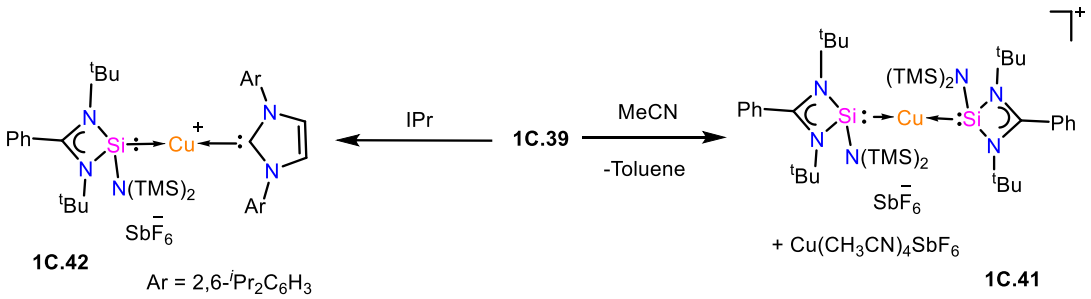

Scheme 1C.11. Syntheses of compounds **1C.41** and **1C.42**.

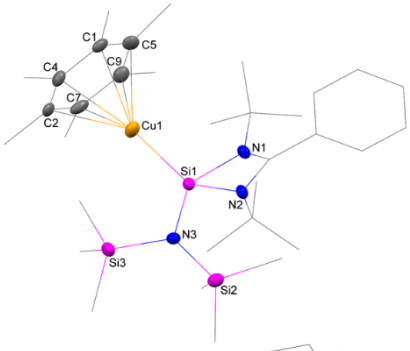

Atoms	Bond length (Å)
Cu1-C1	2.449(5)
Cu1-C2	2.372(4)
Cu1-C4	2.443(5)
Cu1-C5	2.407(4)
Cu1-C7	2.318(4)
Cu1-C9	2.310(4)

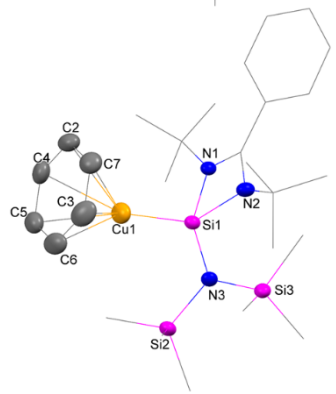

Atoms	Bond length (Å)
Cu1-C2	2.454(7)
Cu1-C3	2.477(8)
Cu1-C4	2.413(9)
Cu1-C5	2.359(9)
Cu1-C6	2.342(9)
Cu1-C7	2.379(8)

Figure 1C.2. Molecule structures of complex **1C.37** and **1C.38**. Metrical parameters of **1C.37** and **1C.38** reveal a η^6 mode coordination of benzene/hexamethylbenzene with $Cu(I)^+$.

The catalytic activity of **1C.39** has also been studied for CuAAC reaction to synthesize 1,2,3-triazoles. A series of aryl azides and alkynes were scrutinized to check the substrate scope. The reaction of aromatic azides with electron-donating groups and aromatic alkynes was found to be very efficiently catalyzed by **1C.39** with a low catalyst loading (0.5 mol %) (Scheme 1C.12). Upon comparison, **1C.39** was found to be better performing than **1C.36**.

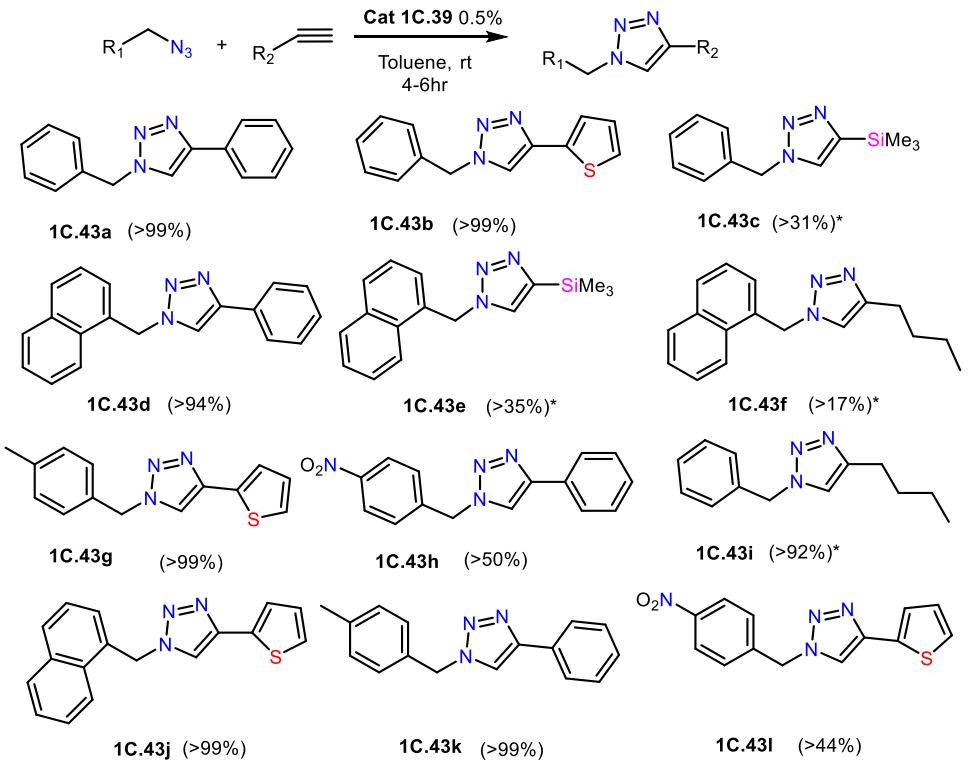

Scheme 1C.12. General scheme and substrate scope for the Click reaction using **1C.39**. Reaction conditions: azide (0.2 mmol), alkyne (0.2 mmol), and toluene (2 mL) at room temperature. *Heating at 50°C.

1C.8 4-membered NHSi-gold(I)-arene complexes and their catalytic application.

Au(I) complexes are very popular among the coinage metal complexes for catalytic C-C bond formation.[113] In most of the gold(I) catalyzed reactions, *in situ* generated cationic Au(I) species [LAu$^+$] [L = Ligand) is the actual catalyst, which further activates the alkyne/alkene bonds.[114, 115] However, due to very high Lewis acidity, they have not been isolated till date. Hence, there are only a few well-defined [Au(I)-arene]$^+$ (arene = xylene and toluene) complexes reported till date (Chart 1C.3),[115-117] and among them, only CAAC supported η^2-gold(I) complex (**1C.V**) is known to be utilized in hydroamination reaction.[118]

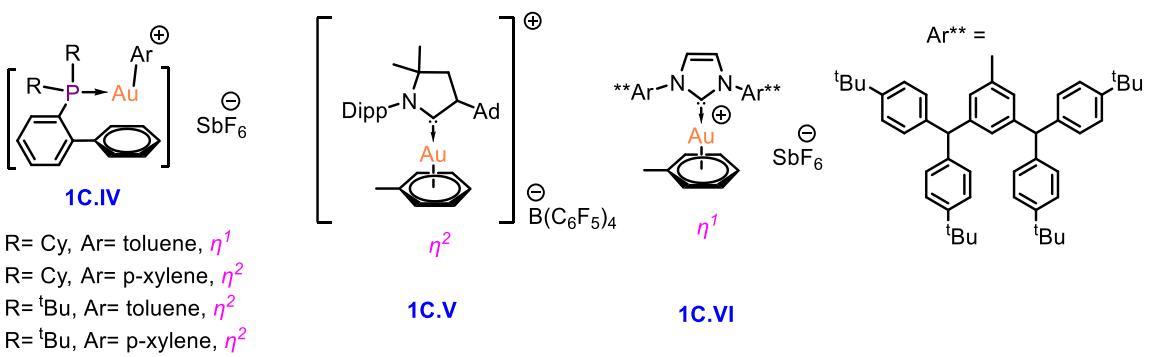

Chart 1C.3. Reported examples of [Au-arene]$^+$ cationic complexes.

Consequently, we synthesized NHSi stabilized cationic Au(I)-arene complexes, **1C.44** and **1C.45** (Scheme 1C.13). To execute and compare the catalytic attempts, we also prepared the NHC analog, **1C.47**. To estimate the donor strength of the ligands involved in these complexes, we prepared LCpCo(CO) complexes (L = $[(^tBu)_2C_6H_3O)]_3P$ (**1C.48**), NHSi], and from the stretching frequency (ν) of CO, the electron-donating strength was observed as NHSi> NHC> $[((^tBu)_2C_6H_3O)]_3P$. The $\%V_{bur}$ was also calculated, revealing the highest for **1C.20** (54%) [**1C.46** = 45.5% and **1C.43** = 37.8%].[119] We chose a glycosidation reaction for the catalytic trails, which are fundamental reactions that facilitate the synthesis of glycoconjugates and oligosaccharides.[120-122] Mannopyranosyl carbonate donor and a model glycosyl acceptor were chosen for initial screening, and as a result, 1,2-*trans*-isomer was found to be the major product. The efficiency of **1C.44** and **1C.47** was found satisfactory for a wide range of glycosyl donors (Scheme 1C.14). The NHC-supported complex **1C.47** performed better than NHSi-Au(I) complex **1C.44**. The reason was validated by the mechanistic investigation, which revealed that the NHC supported Au(I)-alkyne complex is more activated by the donation of π electrons from an alkyne to Au and also by a greater back donation from Au→alkyne in comparison with Au(I)-alkyne complex supported by silylene.

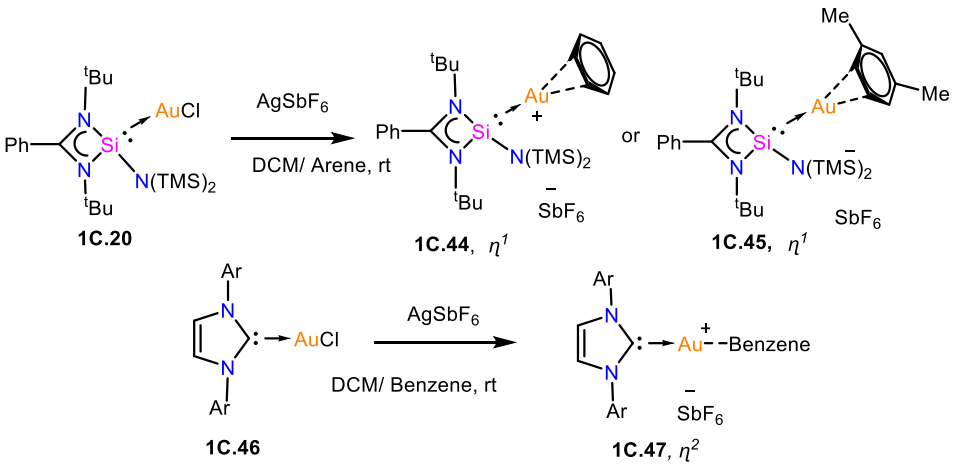

Scheme 1C.13. Syntheses of complexes **1C.44-1C.47**.

The efficiencies of catalysts **1C.44** were also exploited to synthesize the pentamanann core of HIV1-gp12052 (Scheme 1C.15), and the expected product was obtained in good yield under mild conditions. Further, the catalytic reaction of propargyl 1,2-O-orthoester with glycosyl acceptor afforded almost full conversation by **1C.44** and was found superior over other catalysts. The use of Au(III) salts always resulted in a significant amount of the side product,[123] which was diminished in this case. Overall, Au(I)-arene complexes were proved to be efficient catalysts in glycoside synthesis.

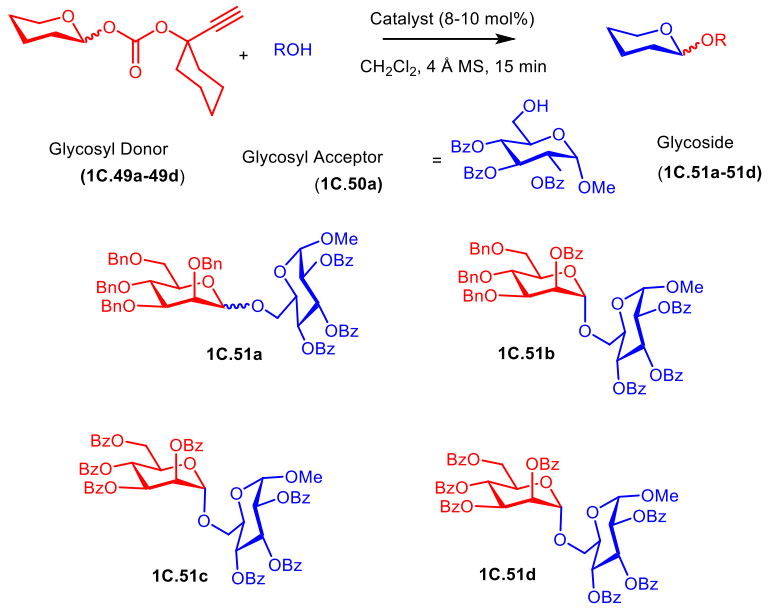

Scheme 1C.14. Activation of glycoside donors using catalysts **1C.44**, **1C.47**, **1C.48.** [a]using catalyst **1C.44**, [b]using catalyst **1C.47**, and [c]using catalyst **1C.48**.

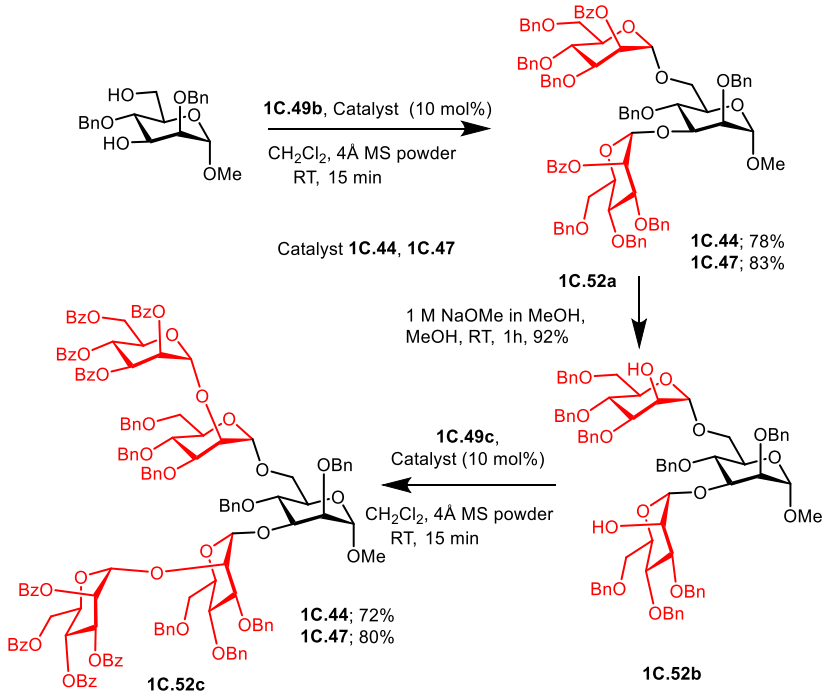

Scheme 1C.15. Synthesis of pentamanann core of HIV1-gp120 by using catalysts **1C.44** and **1C.47**.

1C.9 4-membered NHSi-silver(I)-arene complexes and their catalytic application.

Very recently, we have reported the benzamidinato-silylene supported silver(I)···arene complexes (**1C.53**-**1C.55**).[122] All these complexes displayed η^2- coordination mode with various arenes (benzene, toluene, and hexamethyl benzene). Subsequently, **1C.53** was utilized

towards A^3 coupling (generally a three-component coupling which includes alkene, aldehyde, and amine) afforded various propargyl amines (**1C.90I-1C.90XIX**) in good to excellent yield. Interestingly, **1C.53** showed a high efficacy even with a very low catalyst loading (0.05 mol%) (Scheme 1C.16) under solvent-free conditions.

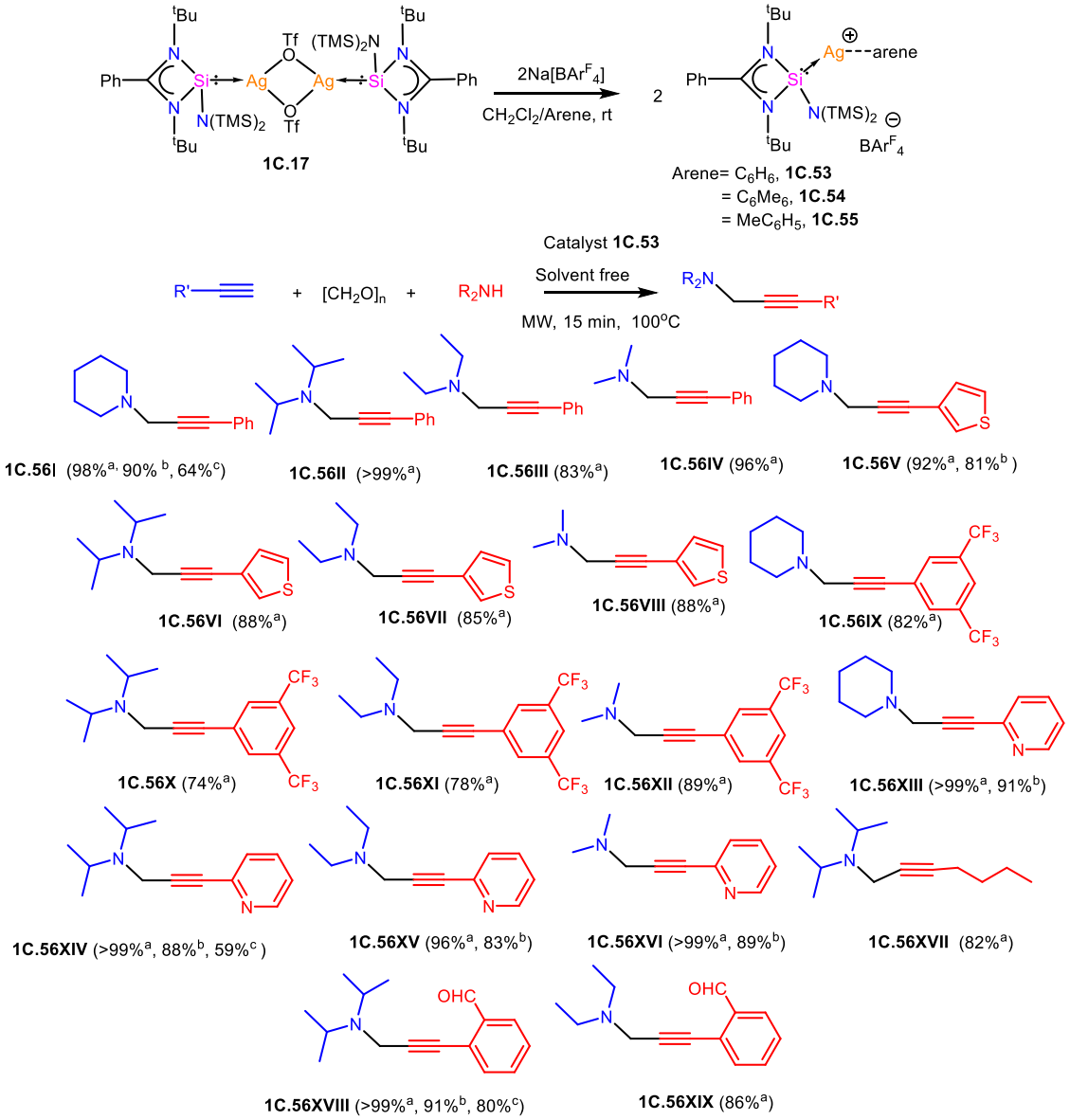

Scheme 1C.16. Syntheses of **1C.53-1C.55**. Catalytic application of **1C.53** in A^3 coupling reaction. [a]1 mol% of **1C.53**. [b]0.1 mol% of **1C.53**. [c]0.05 mol% **1C.53** (stock solution in dichloromethane, DCM), 5 min, 150°C.

1C.10 Motivation and objectives.

Silylene chemistry has traveled a long way since its isolation in 1993. A humongous amount of work has been done on low-valent silicon compounds and their application in activating small molecules. Moreover, many silylene-supported transition metal complexes have also

been isolated, and their bonding properties have been studied. Now, NHSis are gradually taking their infant strides in the area of homogenous catalysis. While silylene and bis-silylene-based transition metal complexes of groups 8-10 are emerging in homogeneous catalysis, there is a drained extension for group 11 complexes. On the contrary, the coinage metal chemistry supported by carbenes and phosphines has shown tremendous results till date, covering their structural, photophysical, medicinal, and catalytic activities. All these aspects with the NHSis are still open and expected to give rise to new and interesting developments.

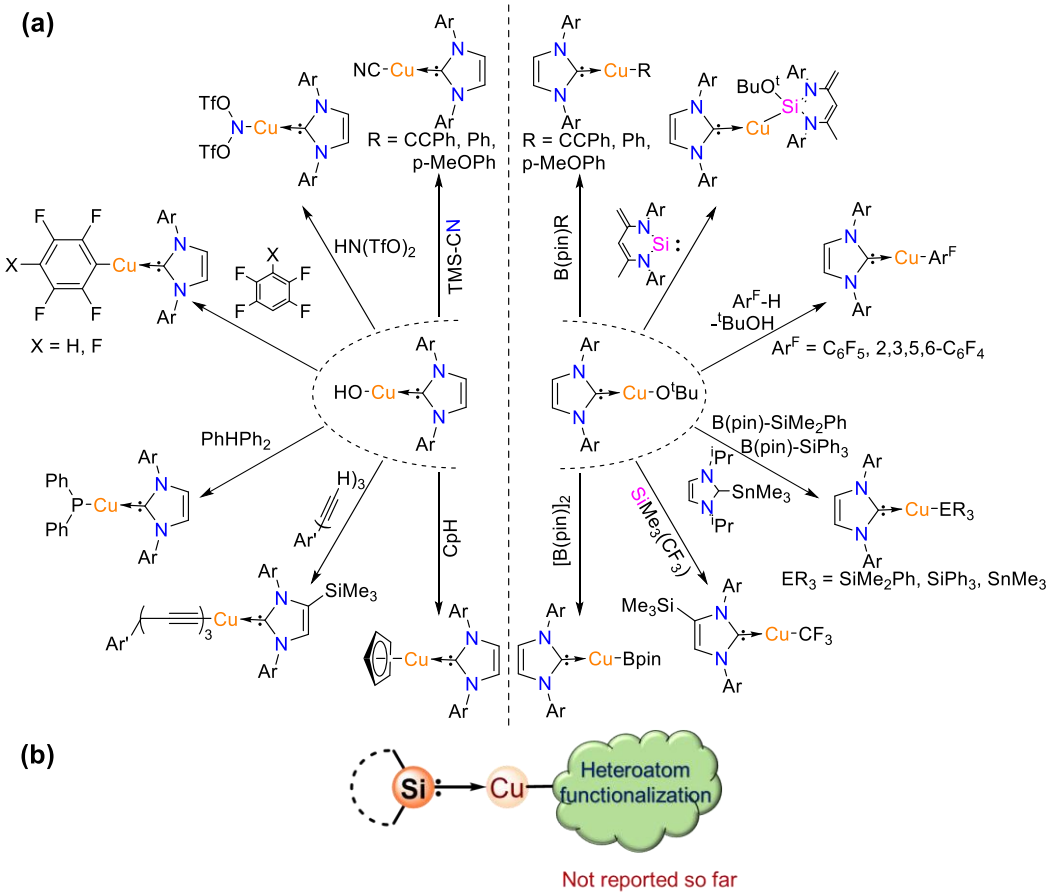

Chart 1C.4. Various reported heteroatom functionalized NHC→Cu(I) based complex documented by Braunstein and co-workers;[124] (b) Context and aim of our study.

With the past and present precedence of NHC coinage metal chemistry (**Chart 1C.4a**), it can be predicted that many new vistas can be opened up for the NHSis in the near future. The isolation of NHSi-CuX (X = Halide) complexes was challenging, as observed by other researchers and us. Similarly, Iwamoto and Radius groups also reported the rearrangements.[125, 126] That is the most probable reason for the unknown NHSi-coinage metal functionalization chemistry (**Chart 1C.4b**). All the NHSi-coinage metal complexes known to date are mostly cationic or halides.[22] Therefore, no NHSi-Cu-BR_2/NR_2/SeR complexes were isolated before

our work, as described in Chapter 2D. Hence, the isolation of NHSi-copper(I)-BR_2/NR_2/SeR complexes is unique and first in this area, unlike the carbene analogs, as documented by Braunstein and co-workers.[124]

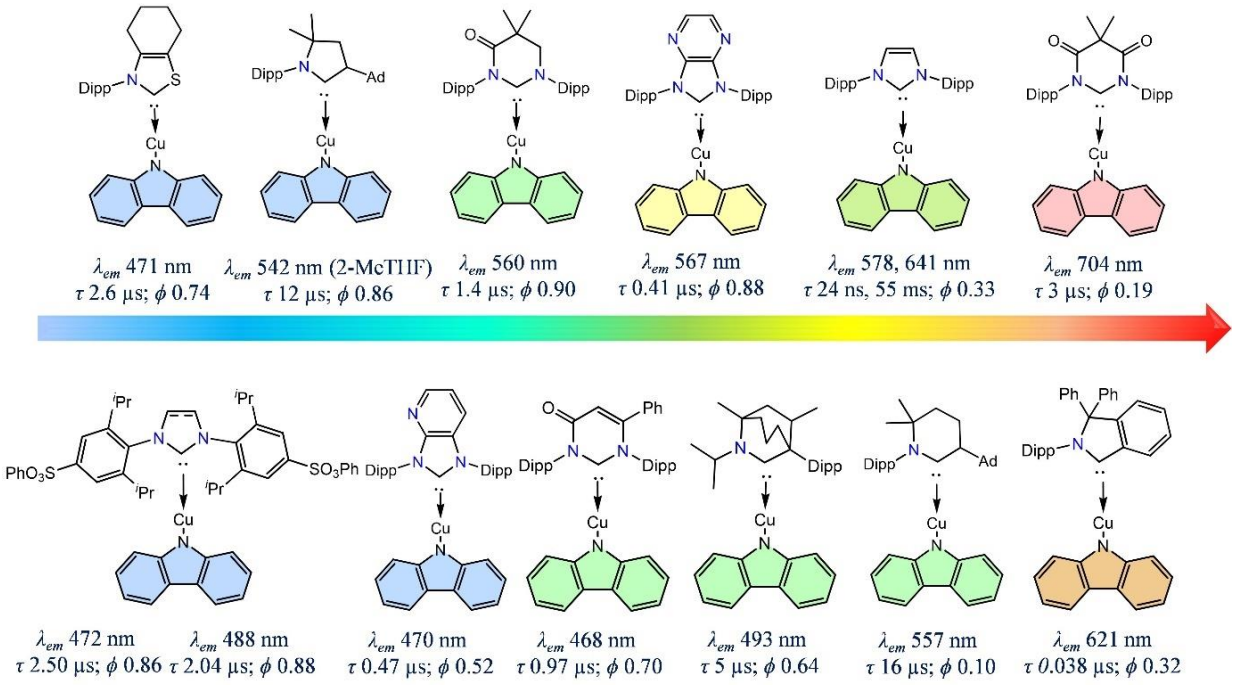

Chart 1C.5. Various carbene ligated Cu(I) carbazolide (amide) complexes and their photophysical data.[127]

The scope of development for NHSi-coinage metal complexes would be photophysical properties. Metallophilic interactions are often responsible for attractive luminescent materials.[47] Recent years have witnessed a sudden growth in the area of carbene [N-heterocyclic carbene (NHC), cyclic alkyl amino carbene (CAAC), diamido carbene (DAC), monoamido carbene (MAC)] coordinated coinage metal amide due to their facile synthesis and distinctive photophysical properties (**Chart 1C.5**).[71, 128-130] In contrast, NHSis-supported coinage metals amide complexes remain elusive. It is important to note that the existing approaches to facilitate the formation of NHSi-coordinated coinage metal amide complexes do not work. Thus, the rational design of substituted NHSi ligated to the coinage metals can trigger some unprecedented photophysical properties. Hence, the work discussed in Chapters 2D and 3 fills this gap with a new synthetic route to access these unavailable NHSis complexes. There is a great likelihood that NHSi-coinage metals will undergo a paradigm shift from purely academic curiosities to commercially relevant materials. Research in this field is dynamic, and in the next two decades, we will certainly see even more exciting progress.

1D Overview of NHC-capped metal nanoparticles (MNPs) and their catalytic scope.

1D.1 Introduction.

NHCs have become the most celebrated ligands in various fields of chemistry due to their unique electronic properties.[3-5, 8, 131] Since the first stable NHC was isolated, many other variations of stable carbenes have also been reported.[132] The cyclic five-membered NHC possesses a formally divalent carbon center, stabilized by σ-electron-withdrawing and π-electron-donating nitrogen atoms next to the carbene carbon (Figure 1D.1). Owing to the presence of a lone-pair of electrons and an empty *p*-orbital, these NHCs have been proven to be the potential ligands for stabilizing a wide range of reactive main-group and transition metal species and found their applications in catalysis and material chemistry.[12, 133, 134] The NHC-modified MNPs have recently attracted attention in catalysis owing to their higher active surface area than bulk metallic complexes. The MNPs have a diameter <100 nm, where 50% of the particles must remain in the 1-100 nm range in one dimension.[135] The proper control over the surface by ancillary ligands makes the MNPs behave more selectively.[136] NHCs have attracted considerable interest as potential surface ligands for MNPs due to their affinity to form strong bonds with the metals.[137, 138] MNPs have drawn much attention over the past decade due to their extensive applications, such as biology, optics, sensors, electronics, and heterogeneous catalysis due to their large surface area.[139] However, preparing stable MNPs for the desired application in catalysis is still challenging as they suffer from agglomeration and subsequent loss of catalytic activity during the catalytic processes (Figure 1D.2).

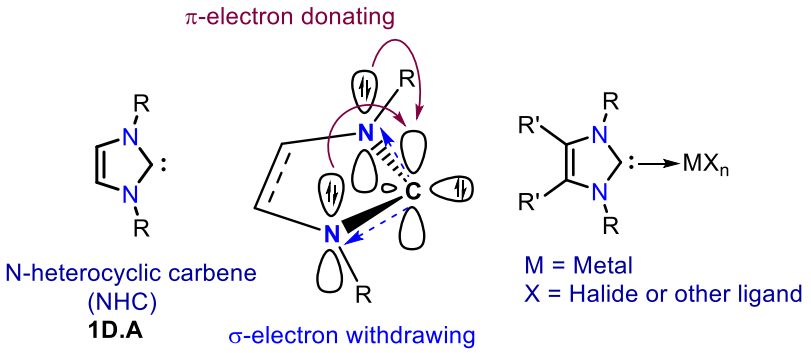

Figure 1D.1. General representation of the NHC used in MNPs stabilization.

1D.1.1 NHCs as surface modulators for the MNPs.

The chemical reactivity and stability of MNPs are associated with their shape, size, composition, morphology, and ligand anchored upon them.[140-142] The role of capping ligands is crucial to overcome the high surface energy and van der Waals interactions between the metal cores, which can otherwise cause aggregation (Figure 1D.2). Moreover, the surface

ligands can also tune the shape, size, and surface properties of MNPs.[137] Thus, the strength of the ligand-metal bonds and their steric environment plays an essential role in stabilizing MNPs. NHCs are already established as powerful ligands for stabilizing several reactive species due to their strong electron-donating ability and tunable steric properties.[3, 143] Hence, in recent nanochemistry, NHCs have become a suitable choice of surface stabilizing agent compared to the widely used long aliphatic chains of thiols (-SH) and amines ($-NH_2$).[8, 12, 133] In 2005, Finke *et al*. reported the first example of NHC on the metal surface (IrNPs),[144] which paved the way for various NHC-stabilized MNPs. Several modifications of NHCs showcase excellent surface stabilization of MNPs.[145] But, the catalytic application of these NHC@MNPs is limited and restricted to a handful of organic transformations. We will discuss the catalytic application of NHC-capped well-defined, and unsupported MNPs[146, 147] and the challenges in this field. The unsupported NP systems mean that two phases are not microscopically available. As the role of the ligand on the surface of supported MNPs is frequently misunderstood due to the presence of external support, we have primarily focused on unsupported MNP systems.[146, 147] To cover the entire range of such NHC-capped MNPs engaged in catalytic activities, we will also briefly discuss NHC-capped supported MNPs. However, we intend to understand the role of NHCs as ligands on metal surfaces, which could help design more targeted catalytic activities.[146, 147]

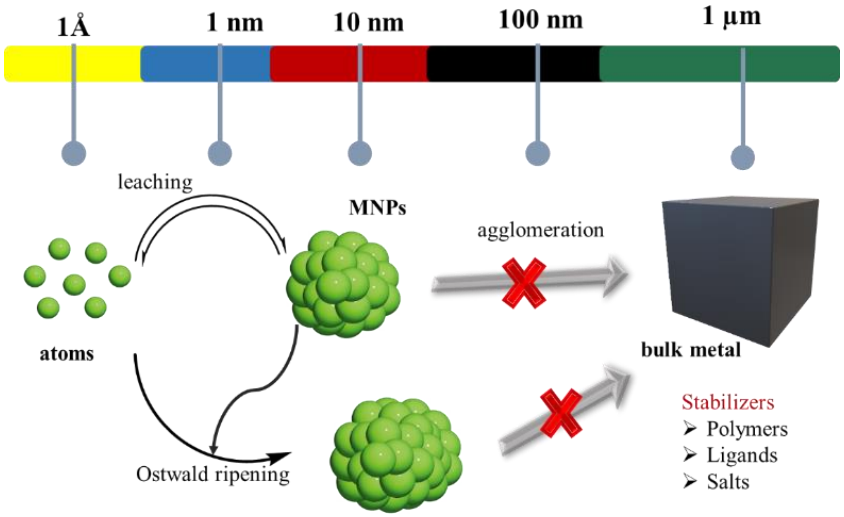

Figure 1D.2. Viable methods to prevent agglomeration of MNPs.

1D.1.2 Synthetic methodology for the preparation of NHC-functionalized MNPs.

The NHC-modified surfaces can be synthesized by three major routes (Figure 1D.3):[10,148] a) Decarboxylation of zwitterionic carbon dioxide adducts of NHCs, which usually leads to high-quality surface modification; b) Chemical reduction of preformed NHC-metal precursors; c) Ligand exchange method using preformed MNPs stabilized by other capping ligands.

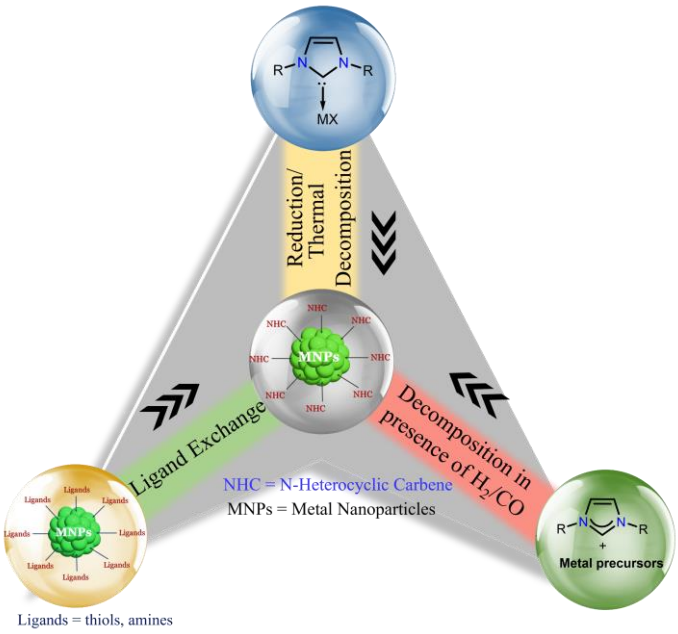

Figure 1D.3. Schematic diagram of the possible synthetic routes of NHC@MNPs.

1D.1.3 NHC-capped MNPs and their catalytic applications.

This section discusses the catalytic applications based on the metal surface (metal = Ni, Ru, Pd, Au, Ir, and Pt) (Figure 1D.4) of the well-characterized and unsupported NHC-capped (Figure 1D.5) MNPs.

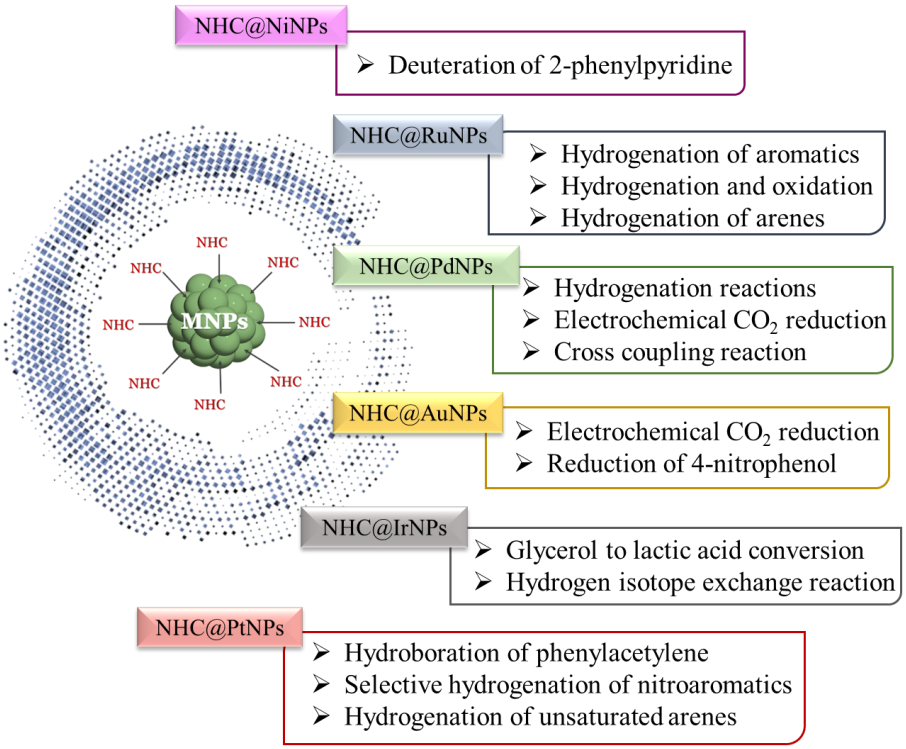

Figure 1D.4. Reported examples of well-defined and unsupported NHC@MNPs as catalysts in organic transformations and electrocatalysis.

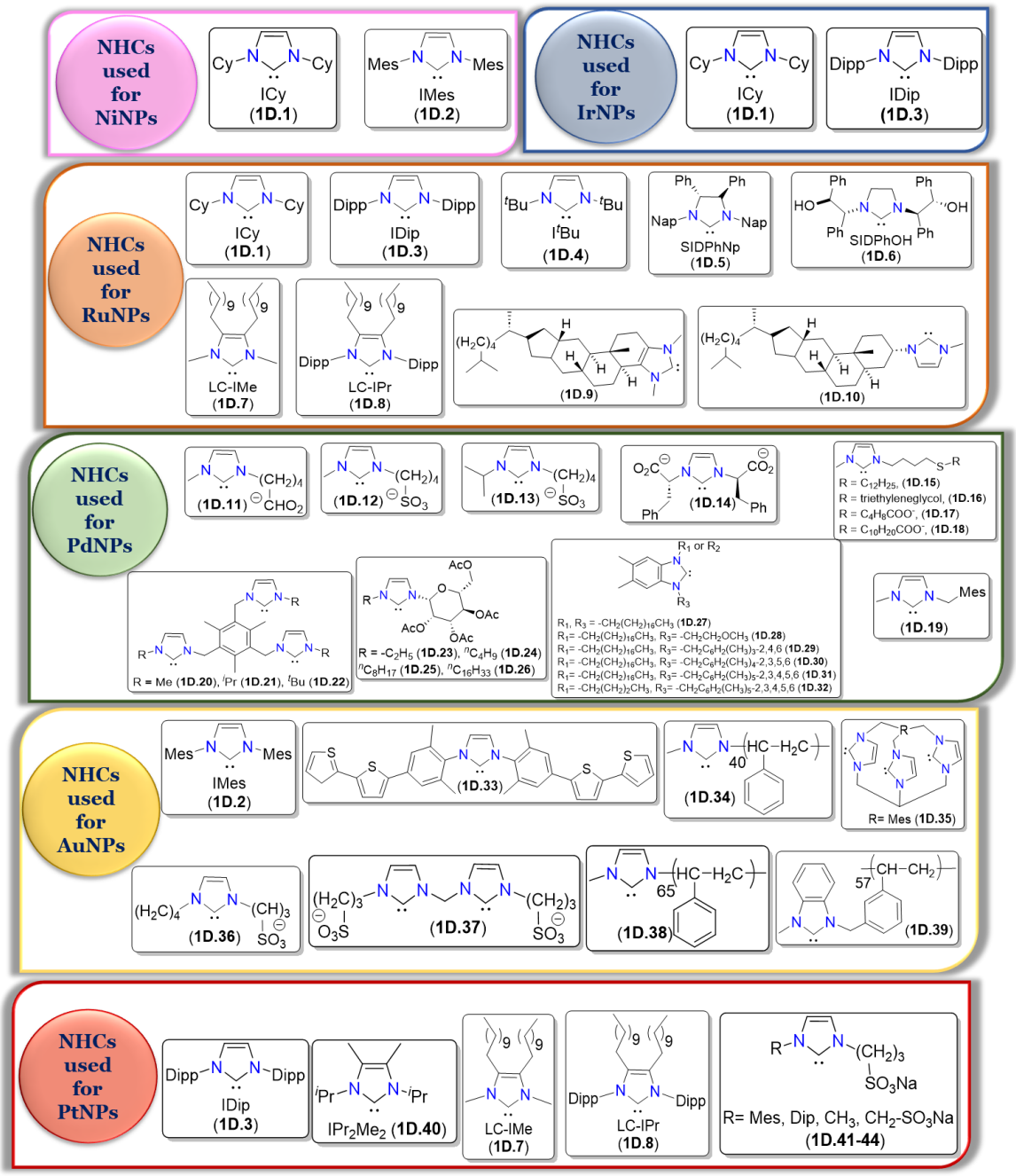

Figure 1D.5. NHCs used to date for unsupported MNPs stabilization towards catalytic applications.

1D.1.4 NHC functionalized nickel nanoparticles (NHC@NiNPs).

The NiNPs are generally redox-active and magnetic in nature. They found enormous applications in organic transformations like transfer hydrogenation reactions.[149] The unsupported NHC@NiNPs were synthesized using the H_2 reduction method, ICy (N,N′-bis(cyclohexylimidazol)-2-ylidene) (**1D.1**) and IMes (N,N′-bis(2,4,6-trimethylphenyl)imidazol)-2-ylidene) (**1D.2**) functionalized NiNPs of 2 and 1.8 nm sizes were synthesized, respectively.[150] These magnetic NiNPs were tested for the deuteration of 2-

phenylpyridine and performed superior over **1D.1@RuNPs** for the same reaction. It was observed that **1D.2@NiNPs** could fully deuterate the *ortho* positions of the phenyl substituents. Although the size and shape of **1D.1@NiNPs** and **2@NiNPs** are the same, **1D.2@NiNPs** perform significantly better **(**Figure 1D.6**)**. It has been established that the NHCs interact with MNPs *via* π-interactions.[151] Due to the presence of the wingtip groups of NHCs, ligand **1D.2** takes up less steric than **1D.3** around the metallic nickel surfaces, leaving enough space for another molecule to approach. This might be attributed to the superior catalytic activity of **1D.2** over **1D.3** when combined with NiNPs.

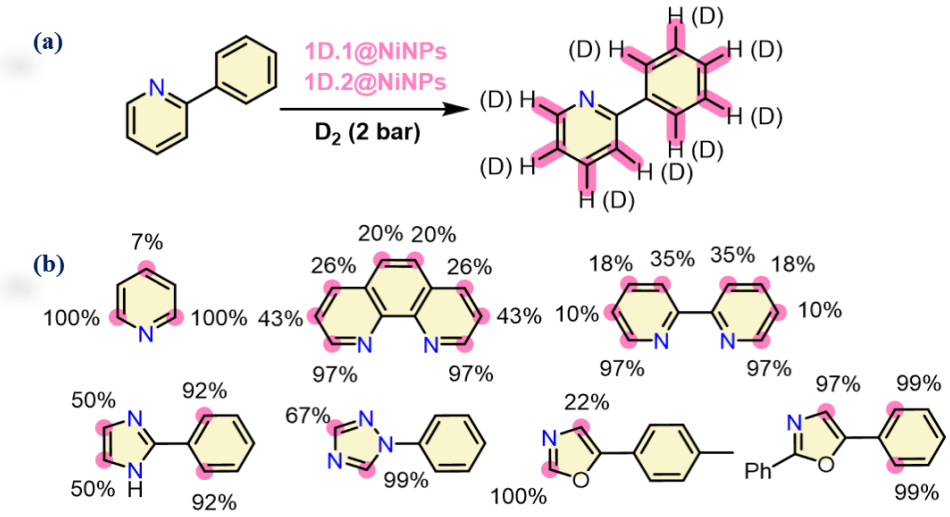

Figure 1D.6. (a) Schematic of deuteration of 2-phenylpyridine catalyzed by **1D.1@NiNPs** and **1D.2@NiNPs**; (b) Substrate scope of **1D.2@NiNPs** using tetrahydrofuran (THF) for 24 h at 55 °C.

1D.1.5 NHC functionalized ruthenium nanoparticles (NHC@RuNPs).

The first NHC@RuNPs were prepared using IDip (**3**) and I^{t}Bu (**1D.4**) as stabilizer ligands and Ru(0)(COD)(COT) as an organometallic complex under the H_2 pressure.[152] These mono-dispersed NHC@RuNPs are extremely air-sensitive and auto-ignite in the presence of oxygen. However, they are very efficient catalysts for the hydrogenation of aromatic compounds. The **1D.4@RuNPs** show a very slow reaction rate compared to **1D.3@RuNPs**, arising from the presence of more I^{t}Bu ligands on the surface. It was also concluded that the presence of aromatic groups in the NHC ligands leads to the formation of more stable catalysts. A chiral version of NHC@RuNPs were synthesized using two non-isolable chiral NHCs [SIDPhNp ((4*S*,5*S*)-1,3-di(naphthalene-1-yl)-4,5-diphenylimidazolidine) (**1D.5**) and SIPhOH ((*S*)-3-((1*S*,2*R*)-2-hydroxy-1,2-diphenylethyl)-1-((*R*)-2-hydroxy-1,2-diphenylethyl)-4,5-dihydro-3H-imidazoline)] (**1D.6**) as the supporting ligands **(**Figure 1D.7**)**.[153]

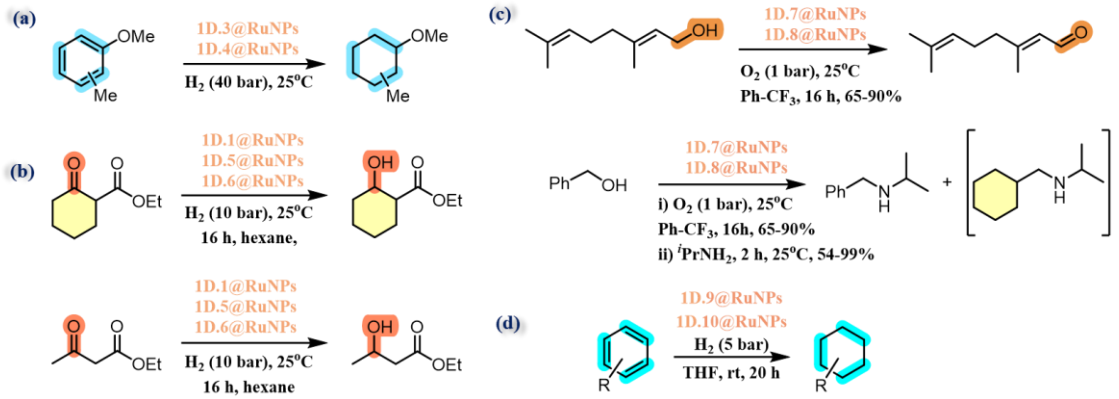

Figure 1D.7. (a) Hydrogenation of methyl anisole by **1D.3** and **1D.4@RuNPs**; (b) Selective hydrogenation by **1D.1**, **1D.5** and **1D.6@RuNPs**; (c) Oxidation of (*E*)-3,7-dimethylocta-2,6-dien-1-ol and transformation of phenyl methanol to *N*-benzylpropan-2-amine using **1D.7** and **1D.8@RuNPs**; (d) Hydrogenation of arenes catalyzed by **1D.9** and **1D.10@RuNPs**.

These chiral NHC@RuNPs orientate themselves around the Ru surface through π-interaction of the aryl groups of the NHC backbone. As a result, the number of active sites accessible on the Ru sites for the catalytic process decreases. These chiral NHCs did not increase the enantioselectivity significantly in the hydrogenation process, giving more room for other intuitive designs of the capping ligand. Furthermore, two NHCs with long aliphatic chains on the backbone [1,3-dimethyl-4,5-diundecyl imidazoline) (LC-IMe, **1D.7**) and (1,3-bis(2,6-diisopropylphenyl)-4,5-diundecyl imidazoline)] (LC-IPr, **1D.8**) were also utilized to isolate the stable NHC@RuNPs. As expected, the presence of a long aliphatic chain at the backbone significantly enhanced the stability of RuNPs, and they were found to be stable for three days in the aerobic condition. These NHC@RuNPs were tested for the one-pot oxidation-hydrogenation processes (Figure 1D.7), and as observed before, the Dip- group substituted NHC@RuNPs displayed better catalytic efficiency due to the availability of more face sites.[154] Similarly, the cholesterol moiety functionalized NHCs (**1D.9-1D.10**) capped RuNPs were found to be very efficient in the catalytic hydrogenation of arenes.[155] Due to the steric demands, **1D.9@RuNPs** and **1D.10@RuNPs** demonstrated an improved hydrogenation activity for arene derivatives. Owing to the biomimetic functionality of the NHC ligand. Due to the presence of biomimetic functionality in the NHC system, future utilization of these NPs in the biological medium is also foreseen.

1D.1.6 NHC functionalized palladium nanoparticles (NHC@PdNPs).

Palladium metal and its organometallic complexes are well known to catalyze various useful reactions in homogeneous catalysis.[156, 157] In several instances, the formation of PdNPs was

observed during the catalytic processes, which triggered the development of the field of PdNPs.[147] The water-soluble NHCs-capped PdNPs (**1D.11-1D.14**) were synthesized using an NHC with the negatively charged sulfonate group *via* the ligand exchange method from preformed dodecylsulfide capped PdNPs of ~4 nm size.[158] Different types of olefins, namely, 1-decene, 3-methyl-2-cyclohexenone, and citronellol, were taken as the substrates to check the catalytic activity and selectivity of the NHC@PdNPs as a catalyst in the hydrogenation reaction. Notably, the reduction of all the substrates using NHC@PdNPs occurred in excellent yield and were found to be efficient over commercially available Pd/C catalysts. Similarly, another variation of stable NHC@PdNPs with an average size between 3.6-5.1 nm were prepared using the thioether-based bidentate NHCs (**1D.15-1D.18**).[159] Due to the presence of thioether spacers at NHC moiety, these PdNPs were found to be soluble in non-polar solvents like hexane or toluene and can hydrogenate di- and tri-substituted alkenes chemoselectively. Recently, monodentate (**1D.19**) and tripodal tris-imidazolium NHCs (**1D.20-1D.22**) capped PdNPs were explored in electrocatalytic CO_2 reduction (Figure 1D.8a). The tripodal NHC@PdNPs have displayed the Faradaic efficiency (FE) of 86% to give CO_2RR products (82% $HCOO^-$ and 4% H_2) at -0.57 V onset potential (Figure 1D.8b-d).[160]

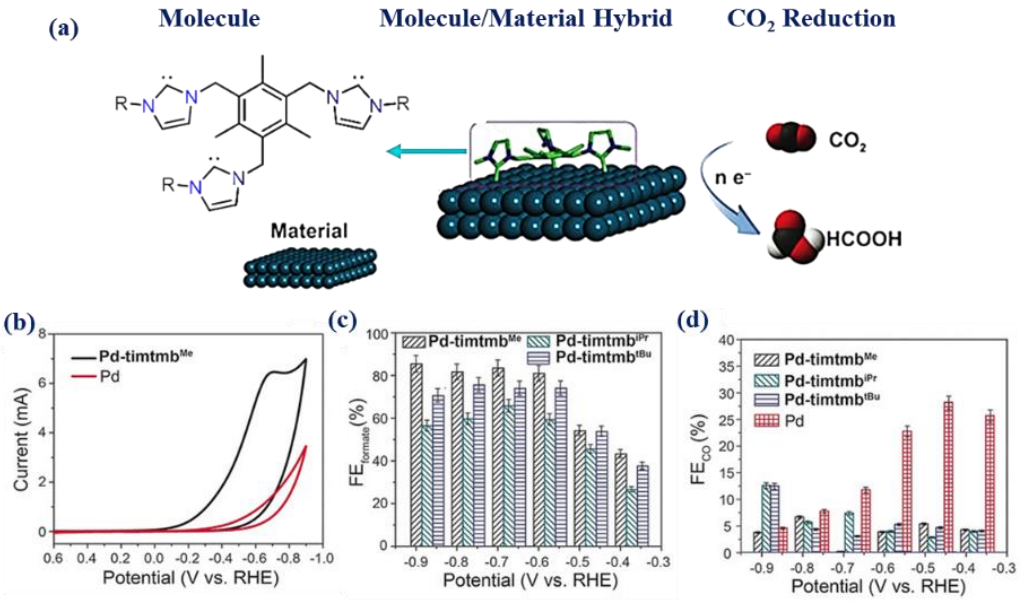

Figure 1D.8. (a) Overview of tris-imidazolium NHC (**1D.20-22**) stabilized PdNPs for electrocatalytic CO_2 reduction; (b) Cyclic Voltagram (CV) trace of unfunctionalized Pd and **1D.20@PdNPs** in CO_2-saturation at pH 7.3; (c) FE of $HCOO^-$ generation by **1D.20**, **1D.21** and **1D.22@PdNPs**; (d) FE of CO generation by **1D.20**, **1D.21**, and **1D.22@PdNPs**. Pd-timtmb^{Me} = **1D.20@PdNPs**, Pd-timtmb^{IPr} = **1D.21@PdNPs** and Pd-timtmb^{ItBu} = **1D.22@PdNPs**. Reproduced with permission from Ref. 138. Copyright 2023 American Chemical Society.

This summarizes an increment of 32-fold catalytic activity compared to standard Pd foil but is not selective toward product formation. Another important catalytic reaction, namely the C−C coupling reaction, was achieved in an aqueous solution of ethanol with a remarkable turnover number (1.96 x 10^4 h^{-1}) and turnover frequency (3.92 x 10^6 h^{-1}) using chiral sugar-substituted NHCs (**1D.23-1D.26**) functionalized ultrasmall PdNPs (1.7-2.1 nm).[161] A new addition to this list is the PEPSI type NHC (**1D.27-1D.32**) ligated PdNPs generated by the dehydrogenation reaction of ammonia borane and also exploited in C-C coupling reactions.[162]

1D.1.7 NHC functionalized AuNPs (NHC@AuNPs).

Homogeneous gold catalysis has been established as a powerful synthetic tool in both total synthesis[163-166] and pharmaceuticals.[167] Similarly, AuNPs have been studied extensively in various areas.[168-171] But NHC@AuNPs are comparatively less explored. This section will briefly discuss the catalytic application of NHC-capped AuNPs.[172] The NHC@AuNPs mediated catalytic activities are mainly dominated by nitroarene reduction,[173-176] and a handful of examples prevail for electrochemical CO_2 reduction. Herein, we will first discuss the nitroarene reduction followed by electrochemical CO_2 reduction.[177, 178] A conducting polymer functionalized NHC-capped (**1D.33**) AuNPs with an average particle size of 4.2-5.3 nm was synthesized and utilized with a loading of 2 mg/ml in the catalytic reduction of 4-nitrophenol (substrate concentration 15 mM), a model reaction for AuNPs (Figure 1D.9).[173] However, an improved catalytic activity towards 4-nitrophenol reduction was obtained by imidazolium-terminated polystyrene (**1D.34**) modified AuNPs (**1D.34@AuNPs**) (Figure 1D.9).[174]

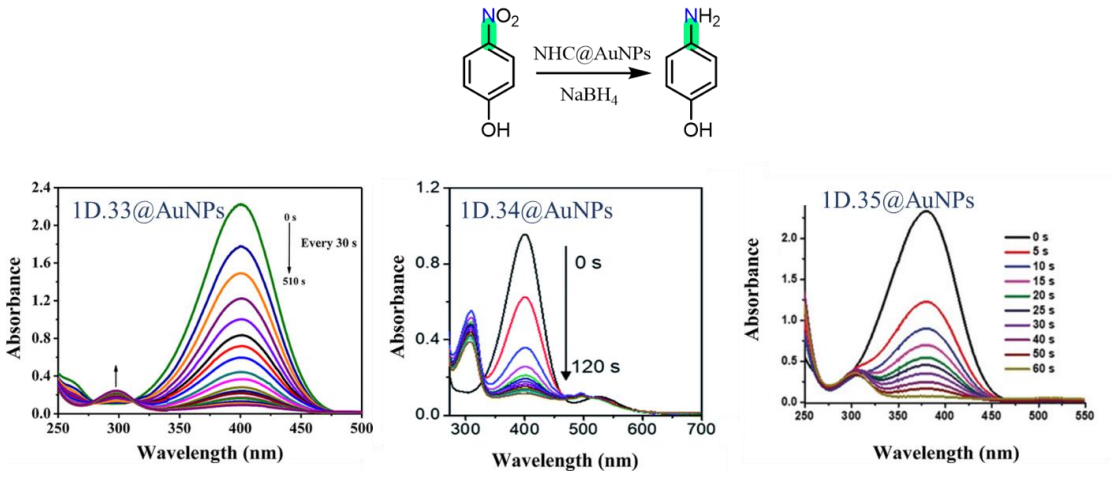

Figure 1D.9. Reduction of 4-nitrophenol to 4-aminophenol catalyzed by various NHC@AuNPs (**1D.33-1D.35@AuNPs**). Advancement and completion of the reaction were monitored *via* UV-Vis spectroscopy. Reproduced with permission from Ref. 138. Copyright 2023 American Chemical Society.

At the same time, three-dimensional polyimidazolium cages (PICs) (**1D.35**) based AuNPs (**1D.35@AuNPs**) demonstrated a superior catalytic activity for 4-nitroarene reduction with excellent stability and durability (Figure 1D.9).[175] A water-soluble version of NHCs capped (**1D.36-1D.37**) AuNPs were obtained using a hydrophilic moiety at the NHC backbone *via* the bottom-up approach, i.e., reducing NHC-Au(I) complex in the presence of $NaBH_4$.[176] This water-soluble AuNPs reduces 4-nitrophenol into 4-aminophenol (81%) within 1.5 min. In 2016, IMes (**1D.2**) capped AuNPs were shown to perform the electrochemical reduction of CO_2, which opened new opportunities for NHC@AuNPs in electrocatalysis.[177] The ~5-6 nm size **1D.2@AuNPs** yielded CO as the primary product with 83% Faradaic efficiency (FE) at an onset potential of -0.57 V **(**Figure 1D.10**)**. However, this catalytic procedure also produced minor products like H_2 and $HCOO^-$. After this work, terminal polymeric NHC (**1D.38-1D.39**) stabilized AuNPs and PdNPs were also used for the electroreduction of CO_2. They observed an increased FE of around 90% with the polymeric NHC@AuNPs at an onset potential of -0.9 V for 2 h **(**Figure 1D.10**)** and 86% for 11 h, demonstrating a better catalytic activity over PdNPs.[178]

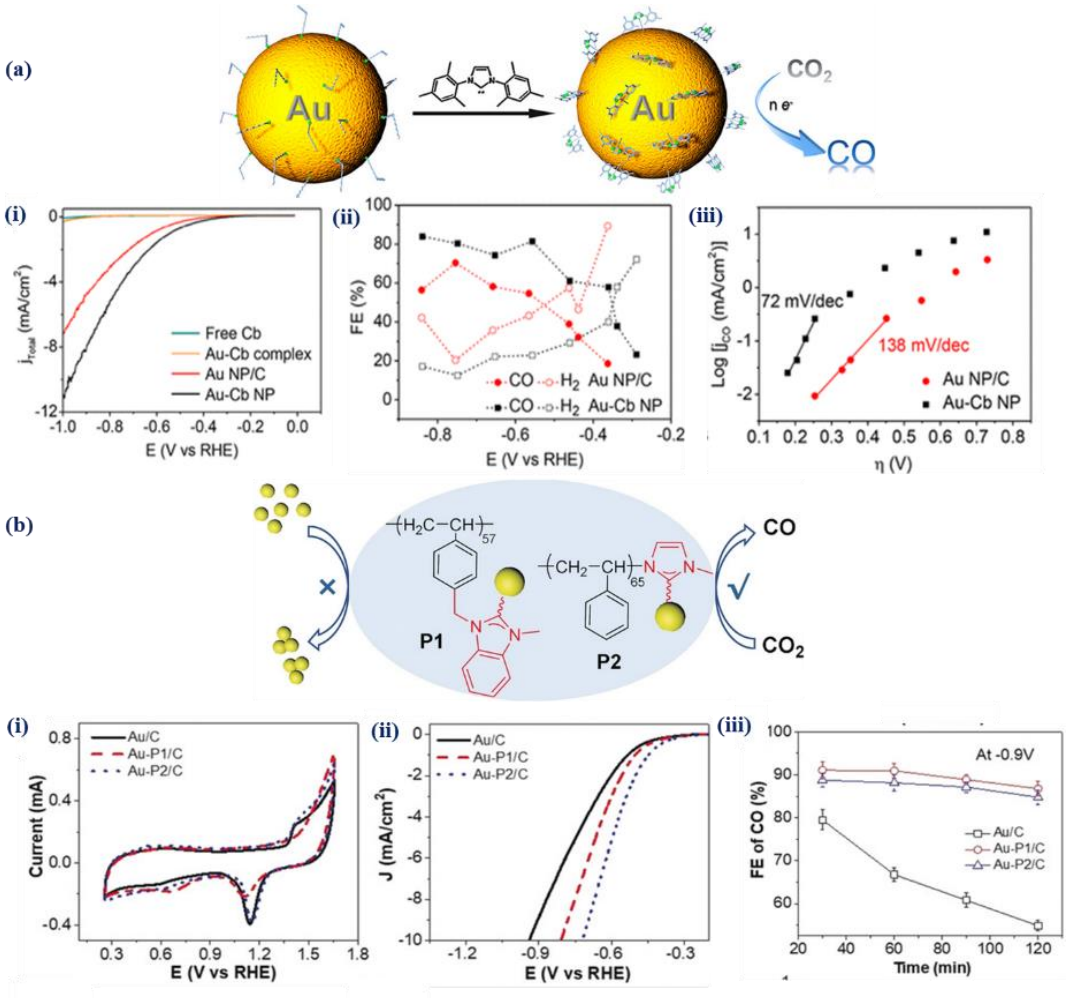

Figure 1D.10. (**a**) General scheme showing electrocatalytic CO_2 reduction to form CO by **1D.2@AuNP**; (i) Linear Sweep Voltammetric (LSV) scans of **1D.2@AuNPs** (Au−Cb NP), bare AuNPs on carbon paper (Au NP/C), free carbene and molecular Au carbene complex (Au−Cb) in CO_2^- saturated at pH 6.8; (ii) FE of products formed during electrolysis for **2@AuNPs** (Au−Cb NP), bare AuNPs (Au NP/C); (iii) Tafel plots for **1D.2@AuNPs** (Au−Cb NP), bare AuNPs (Au NP/C). (**b**) General scheme showing electrocatalytic CO_2 reduction to form CO by **1D.38** (P1) and **1D.39** (P2) capped **AuNPs**; (i) Cyclic Voltagram (CV) trace in 0.5 m H_2SO_4 saturated by N_2 at a scan rate of 100 mVs^{-1} (ii) Linear Sweep Voltametric scans in 0.1 M $KHCO_3$ at a scan rate of 10 mVs^{-1} (iii) FE of CO by bare AuNP/C **1D.38** and **1D.39@AuNPs**. Reproduced with permission from Ref. 138. Copyright 2023 American Chemical Society.

1D.1.8 NHC functionalized iridium nanoparticles (NHC@IrNPs).

Due to its characteristic properties to those of other noble MNPs and good corrosion resistance, nano-dimensional Ir has been used for various catalytic applications over the years.[179] There persist only two reports on NHC@IrNPs. The first report is on IDip (**1D.3**)-capped IrNPs (**1D.3@IrNPs**), which was further used to convert glycerol into lactic acid in the presence of NaOH, featuring a TOF value of 10^4 h^{-1}.[180] This catalyst shows high selectivity for lactic acid (93.0%), and it is completely recyclable. However, **1D.3@IrNPs** on carbon support did not display excellent catalytic activity for the same reaction; instead, it led to a much lower catalytic activity (TOF = $4x10^3$ h^{-1}) and a lower selectivity for the lactic acid. The second well-defined ICy (**1D.1**) capped IrNPs (1.1-1.3 nm sized particles) were prepared by reducing $[(COD)Ir(MeO)]_2$ with H_2.[181]

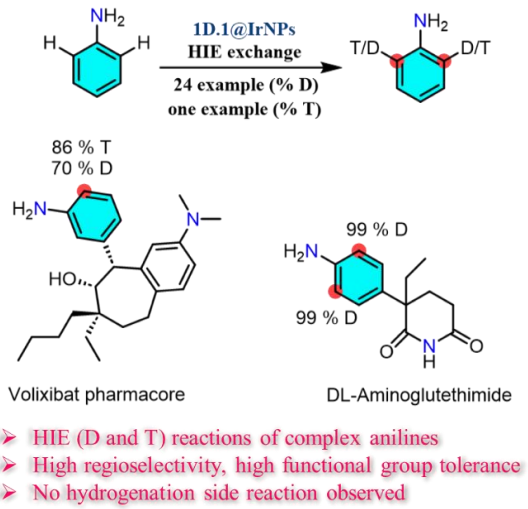

Figure 1D.11. Overview of HIE reaction catalyzed by **1D.1@IrNPs**.

1D.1@IrNPs were used further for the hydrogen isotope exchange (HIE) reaction on aniline by deuterium (D_2) and tritium (T_2) **(**Figure 1D.11**)**. The drugs like aminoglutethimide, sulfadimethoxine, sulfamoxole, menthyl anthranilate, and saccharose 4-aminophenyl-*beta-D*-galactopyranoside were found to undergo HIE with good isotope incorporation.[181] More importantly, direct tritium labeling of the volixibat pharmacophore with a high selectivity and specific activity was also achieved.

1D.1.9 NHC functionalized platinum nanoparticles (NHC@PtNPs).

First NHC stabilized PtNPs (NHC = IDip, **1D.3** and 1,3-diisopropyl-4,5-dimethylimidazol-2-ylidene ($I^iPr_2Me_2$), **1D.40**) was prepared by the reduction of $Pt(dba)_2$ with H_2 and tested as catalysts in the chemoselective hydrogenation of nitroarenes (Figure 1D.12a).[182] The **1D.3@PtNPs** displayed excellent activity and selectivity for the hydrogenation reaction as compared to **1D.40@PtNPs**.[182]

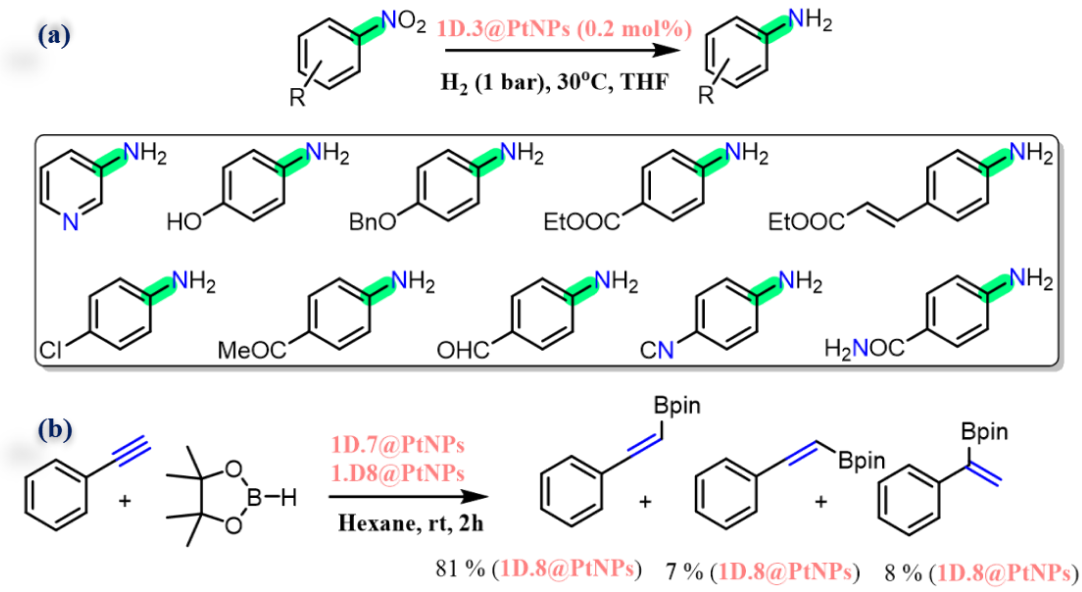

Figure 1D.12. (a) Hydrogenation of nitroarenes catalyzed by **1D.3@PtNPs**; (b) hydroboration of phenylacetylene catalyzed by **1D.7@PtNPs** and **1D.8@PtNPs**.

Two water-soluble PtNPs ligated by different NHCs bearing a long-chain aliphatic group (LC−IMe, **1D.7**; LC−IPr, **1D. 8**) at the backbone were synthesized and probed for the hydroboration of phenylacetylene.[183] The **1D.7@PtNPs** showed negligible catalytic activity, but **1D.8@PtNPs** exhibited good selectivity for the *trans*-isomers (Figure 1D.12b). Another variety of water-soluble sulfonated NHC ligands (**1D.41-44**) capped PtNPs was also synthesized and utilized as the recoverable catalysts for hydrogenating aromatic compounds in an aqueous medium, displaying recyclability up to eleven cycles.[184]

1D.1.10 Limitations in the area of NHC@MNPs.

The catalytic aspects of NHC-capped MNPs are still developing. Considerable attention is being paid to NHC-capped Pd and AuNPs, and a variety of them are being synthesized and explored with the modified NHC backbones. These might be due to the ease of synthesis and stability of these NPs. However, their utilization in catalysis is somewhat limited to the handful of organic transformations. Moreover, other MNPs, such as Ni, Ir, Pt, Ru, and Rh, are very scarce, leaving out the opportunities for further detailed investigation. These NHC@MNPs are utilized mainly for hydrogenation reactions. One of the major limitations of the NHC@MNPs is getting a monodispersed MNP solution, which is essential for efficient catalytic activities.[185, 186] Thus, designing NHCs with functionalized backbones, which can provide a monodispersed solution, is desirable. Less exploration of the MNPs in an unsupported fashion remained one of the challenges to overcome for a better understanding of the electronic and steric influence of NHCs on the NP surface.

1D.1.11 Motivation and objectives.

As discussed in the above sections, selecting a substituent on the backbone of the NHCs is crucial to creating accessible reactive sites on the MNPs. The electronic parameter and the steric environment of the capping ligand play an essential role in the catalytic efficiency of the MNPs.[145] Many well-defined NHC-ligated MNPs have been synthesized and investigated for various catalytic applications. However, the scope of NHCs is limited to mainly electron-donating NHC ligands. There is a variety of stable NHCs available in the literature, such as CAACs, which possess more σ-electron donating and better π-electron accepting behavior due to the substitution of one of the π-electron donating amino groups with a σ-donating alkyl group.[187, 188] It is well established in the literature that a combination of strong σ-donating and π-accepting properties of CAAC ligands could bring a selective product formation in the catalytic reaction.[189] A recent work on the proto-borylation of alkynes using the CAAC-copper halide complexes exhibited an exclusive α-selectivity by the CAAC ligand. At the same time, normal NHCs led to the β-product formation.[190]

Moreover, CAAC and NHCs were found to display different reactivity patterns in stabilizing reactive main group species.[191, 192] Although there are two reports on the deposition of CAAC on the coinage metal surfaces (111) *via* the decomposition method.[69, 193, 194] There is no report on synthesizing CAAC-stabilized MNPs and their catalytic applications. Similarly, another variation of NHCs called abnormal NHCs (*a*NHCs), bind through C4/5-centers of the imidazolium ring and possess better σ-donor properties than NHCs. Due to the significant

difference in electronic properties, they offer different reactivity patterns as a ligand in catalysis and material chemistry.[10] Hence, in the area of NHCs ligated metal surfaces, the future will likely hold a wealth of new possibilities for exploring π-properties of NHC ligands, such as CAACs and abnormal carbenes. The electronic properties and catalytic efficiency of these MNPs need more thorough investigation.

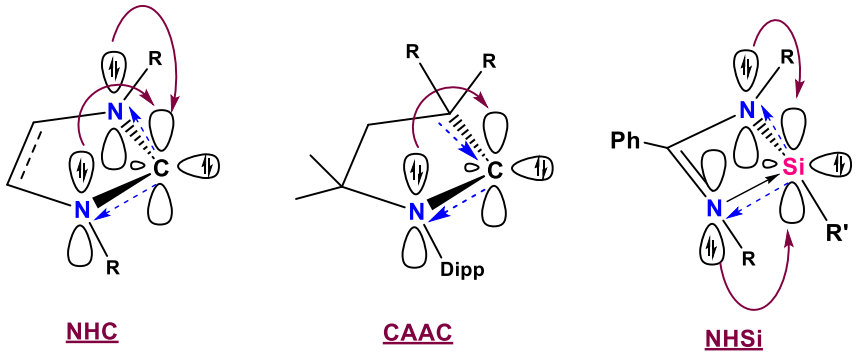

Figure 1D.13. Main class of NHTs used in our work as capping ligands on MNPs surface.

1.2 Bibliography.

(1) Power, P. P. Main-group elements as transition metals. *Nature* **2010**, *463*, 171-177.
(2) Weetman, C.; Inoue, S. The Road Travelled: After Main-Group Elements as Transition Metals. *ChemCatChem* **2018**, *10*, 4213-4228.
(3) Bourissou, D.; Guerret, O.; Gabbai, F. P.; Bertrand, G. Stable carbenes. *Chem. Rev.* **2000**, *100*, 39-92.
(4) Peris, E. Smart N-heterocyclic carbene ligands in catalysis. *Chem. Rev.* **2017**, *118*, 9988-10031.
(5) Huynh, H. V. Electronic properties of N-heterocyclic carbenes and their experimental determination. *Chem. Rev.* **2018**, *118*, 9457-9492.
(6) Igau, A.; Grutzmacher, H.; Baceiredo, A.; Bertrand, G. Analogous a,a'-bis-carbenoid triply bonded species: Synthesis of a stable l^3-phosphinocarbene-l^5-phosphaacetylene. *J. Am. Chem. Soc.* **1988**, *110*, 6463-6466.
(7) Arduengo, A. J.; Harlow, R. L.; Kline, M. A Stable Crystalline Carbene. *J. Am. Chem. Soc.* **1991**, *113*, 361-363.
(8) Hopkinson, M. N.; Richter, C.; Schedler, M.; Glorius, F. An overview of N-heterocyclic carbenes. *Nature* **2014**, *510*, 485-496.
(9) Crudden, C. M.; Allen, D. P. Stability and reactivity of N-heterocyclic carbene complexes. *Coord. Chem. Rev.* **2004**, *248*, 2247-2273.
(10) Sau, S. C.; Hota, P. K.; Mandal, S. K.; Soleilhavoup, M.; Bertrand, G. Stable abnormal N-heterocyclic carbenes and their applications. *Chem. Soc. Rev.* **2020**, *49*, 1233-1252.
(11) Visbal, R.; Gimeno, M. C. N-heterocyclic carbene metal complexes: photoluminescence and applications. *Chem. Soc. Rev.* **2014**, *43*, 3551-3574.
(12) Smith, C. A.; Narouz, M. R.; Lummis, P. A.; Singh, I.; Nazemi, A.; Li, C.-H.; Crudden, C. M. N-Heterocyclic carbenes in materials chemistry. *Chem. Rev.* **2019**, *119*, 4986-5056.
(13) Mizuhata, Y.; Sasamori, T.; Tokitoh, N. Stable heavier carbene analogues. *Chem. Rev.* **2009**, *109*, 3479-3511.
(14) Hanusch, F.; Groll, L.; Inoue, S. Recent advances of group 14 dimetallenes and dimetallynes in bond activation and catalysis. *Chem. Sci.* **2021**, *12*, 2001-2015.

(15) Hadlington, T. J.; Driess, M.; Jones, C. Low-valent group 14 element hydride chemistry: towards catalysis. *Chem. Soc. Rev.* **2018**, *47*, 4176-4197.
(16) Loh, Y. K.; Aldridge, S. Acid-Base Free Main Group Carbonyl Analogues. *Angew. Chem. Int. Ed.* **2021**, *60*, 8626-8648.
(17) Raoufmoghaddam, S.; Zhou, Y.-P.; Wang, Y.; Driess, M. N-heterocyclic silylenes as powerful steering ligands in catalysis. *J. Organomet. Chem.* **2017**, *829*, 2-10.
(18) Sen, N.; Khan, S. Heavier Tetrylenes as Single Site Catalysts. *Chem. Asian J.* **2021**, *16*, 705-719.
(19) Alvarez-Rodriguez, L.; Cabeza, J. A.; Garcia-Alvarez, P.; Polo, D. The transition-metal chemistry of amidinatosilylenes, -germylenes and -stannylenes. *Coord. Chem. Rev.* **2015**, *300*, 1-28.
(20) Blom, B.; Gallego, D.; Driess, M. N-heterocyclic silylene complexes in catalysis: new frontiers in an emerging field. *Inorg. Chem. Front.* **2014**, *1*, 134-148.
(21) Zhou, Y. P.; Driess, M. Isolable Silylene Ligands Can Boost Efficiencies and Selectivities in Metal-Mediated Catalysis. *Angew. Chem. Int. Ed.* **2019**, *58*, 3715-3728.
(22) Ghosh, M.; Khan, S. N-Heterocyclic silylenes in coinage metal chemistry: an account of recent advances. *Dalton Trans.* **2021**, *50*, 10674-10688.
(23) Driess, M.; Grützmacher, H. Main group element analogues of carbenes, olefins, and small rings. *Angew. Chem. Int. Ed.* **1996**, *35*, 828-856.
(24) Sekiguchi, A.; Tanaka, T.; Ichinohe, M.; Akiyama, K.; Tero-Kubota, S. Bis (tri-tert-butylsilyl) silylene: Triplet ground state silylene. *J. Am. Chem. Soc.* **2003**, *125*, 4962-4963.
(25) Sekiguchi, A.; Tanaka, T.; Ichinohe, M.; Akiyama, K.; Gaspar, P. P. Tri-tert-butylsilylsilylenes with Alkali Metal Substituents (t Bu_3Si) SiM (M= Li, K): Electronically and Sterically Accessible Triplet Ground States. *J. Am. Chem. Soc.* **2008**, *130*, 426-427.
(26) Jiang, P.; Gaspar, P. P. Tri-tert-butylsilyl (triisopropylsilyl) silylene ($(^{t}Bu)_3Si{-}Si{-}Si(^{i}Pr)_3$ and Chemical Evidence for Its Reactions from a Triplet Electronic State. *J. Am. Chem. Soc.* **2001**, *123*, 8622-8623.
(27) Ganesamoorthy, C.; Schoening, J.; Wolper, C.; Song, L. J.; Schreiner, P. R.; Schulz, S. A silicon-carbonyl complex stable at room temperature. *Nat. Chem.* **2020**, *12*, 608-614.
(28) Wendel, D.; Porzelt, A.; Herz, F. A. D.; Sarkar, D.; Jandl, C.; Inoue, S.; Rieger, B. From Si(II) to Si(IV) and Back: Reversible Intramolecular Carbon-Carbon Bond Activation by an Acyclic Iminosilylene. *J. Am. Chem. Soc.* **2017**, *139*, 8134-8137.
(29) Protchenko, A. V.; Birjkumar, K. H.; Dange, D.; Schwarz, A. D.; Vidovic, D.; Jones, C.; Kaltsoyannis, N.; Mountford, P.; Aldridge, S. A Stable Two-Coordinate Acyclic Silylene. *J. Am. Chem. Soc.* **2012**, *134*, 6500-6503.
(30) Protchenko, A. V.; Schwarz, A. D.; Blake, M. P.; Jones, C.; Kaltsoyannis, N.; Mountford, P.; Aldridge, S. A Generic One-Pot Route to Acyclic Two-Coordinate Silylenes from Silicon(IV) Precursors: Synthesis and Structural Characterization of a Silylsilylene. *Angew. Chem. Int. Ed.* **2013**, *52*, 568-571.
(31) Roy, M. M.; Ferguson, M. J.; McDonald, R.; Zhou, Y.; Rivard, E. A vinyl silylsilylene and its activation of strong homo-and heteroatomic bonds. *Chem. Sci.* **2019**, *10*, 6476-6481.
(32) Driess, M. Breaking the limits with silylenes. *Nat. Chem.* **2012**, *4*, 525-526.
(33) West, R. Two-armed silicon. *Nature* **2012**, *485*, 49-50.
(34) Fujimori, S.; Inoue, S. Small Molecule Activation by Two-Coordinate Acyclic Silylenes. *Eur. J. Inorg. Chem.* **2020**, *2020*, 3131-3142.
(35) Asay, M.; Inoue, S.; Driess, M. Aromatic Ylide-Stabilized Carbocyclic Silylene. *Angew. Chem. Int. Ed.* **2011**, *50*, 9589-9592.
(36) Ghadwal, R. S.; Roesky, H. W.; Merkel, S.; Henn, J.; Stalke, D. Lewis base stabilized dichlorosilylene. *Angew. Chem. Int. Ed.* **2009**, *48*, 5683-5686.

(37) Abe, T.; Tanaka, R.; Ishida, S.; Kira, M.; Iwamoto, T. New isolable dialkylsilylene and its isolable dimer that equilibrate in solution. *J. Am. Chem. Soc.* **2012**, *134*, 20029-20032.
(38) Krahfuss, M. J.; Radius, U. N-Heterocyclic silylenes as ambiphilic activators and ligands. *Dalton Trans.* **2021**, *50*, 6752-6765.
(39) Alvarado-Beltran, I.; Baceiredo, A.; Saffon-Merceron, N.; Branchadell, V.; Kato, T. Cyclic Amino(Ylide) Silylene: A Stable Heterocyclic Silylene with Strongly Electron-Donating Character. *Angew. Chem. Int. Ed.* **2016**, *55*, 16141-16144.
(40) Rosas-Sanchez, A.; Alvarado-Beltran, I.; Baceiredo, A.; Saffon-Merceron, N.; Massou, S.; Branchadell, V.; Kato, T. Exceptionally Strong Electron-Donating Ability of Bora-Ylide Substituent vis-a-vis Silylene and Silylium Ion. *Angew. Chem. Int. Ed.* **2017**, *56*, 10549-10554.
(41) Khan, S.; Sen, S. S.; Roesky, H. W. Activation of phosphorus by group 14 elements in low oxidation states. *Chem. Commun.* **2012**, *48*, 2169-2179.
(42) Sen, S. S.; Khan, S.; Nagendran, S.; Roesky, H. W. Interconnected bis-silylenes: a new dimension in organosilicon chemistry. *Acc. Chem. Res.* **2012**, *45*, 578-587.
(43) Sen, S. S.; Khan, S.; Samuel, P. P.; Roesky, H. W. Chemistry of functionalized silylenes. *Chem. Sci.* **2012**, *3*, 659-682.
(44) Shan, C. K.; Yao, S. L.; Driess, M. Where silylene-silicon centres matter in the activation of small molecules. *Chem. Soc. Rev.* **2020**, *49*, 6733-6754.
(45) Meltzer, A.; Inoue, S.; Präsang, C.; Driess, M. Steering S−H and N−H Bond Activation by a Stable N-Heterocyclic Silylene: Different Addition of H_2S, NH_3, and Organoamines on a Silicon (II) Ligand versus Its Si (II)→ Ni $(CO)_3$ Complex. *J. Am. Chem. Soc.* **2010**, *132*, 3038-3046.
(46) Arya, P.; Boyer, J.; Carré, F.; Corriu, R.; Lanneau, G.; Lapasset, J.; Perrot, M.; Priou, C. Formation and Reactivity of Silicon–Sulfur and Silicon–Selenium Double Bonds. The First X-Ray Structure of a Silanethione. *Angew. Chem. Int. Ed.* **1989**, *28*, 1016-1018.
(47) Suzuki, H.; Tokitoh, N.; Nagase, S.; Okazaki, R. The First Genuine Silicon-Sulfur Double-Bond Compound - Synthesis and Crystal-Structure of a Kinetically Stabilized Silanethione. *J. Am. Chem. Soc.* **1994**, *116*, 11578-11579.
(48) Suzuki, H.; Tokitoh, N.; Okazaki, R.; Nagase, S.; Goto, M. Synthesis, structure, and reactivity of the first kinetically stabilized silanethione. *J. Am. Chem. Soc.* **1998**, *120*, 11096-11105.
(49) Tokitoh, N.; Sadahiro, T.; Hatano, K.; Sasaki, T.; Takeda, N.; Okazaki, R. Synthesis of kinetically stabilized silaneselone and silanetellone. *Chem. Lett.* **2002**, *31*, 34-35.
(50) Iwamoto, T.; Sato, K.; Ishida, S.; Kabuto, C.; Kira, M. Synthesis, properties, and reactions of a series of stable dialkyl-substituted silicon-chalcogen doubly bonded compounds. *J. Am. Chem. Soc.* **2006**, *128*, 16914-16920.
(51) Mitra, A.; Wojcik, J. P.; Lecoanet, D.; Muller, T.; West, R. A Bis(silaselenone) with Two Donor-Stabilized Si=Se Bonds from an Unexpected Stereoconvergent Hydrolysis of a Diselenadisiletane. *Angew. Chem. Int. Ed.* **2009**, *48*, 4069-4072.
(52) Yao, S.; Xiong, Y.; Brym, M.; Driess, M. An isolable silanoic ester by oxygenation of a stable silylene. *J. Am. Chem. Soc.* **2007**, *129*, 7268-7269.
(53) Yao, S. L.; Xiong, Y.; Brym, M.; Driess, M. A series of isolable silanoic thio-, seleno-, and telluroesters (LSi(=X)OR) with donor-supported Si=X double bonds (L=beta-diketiminate; X = S, Se, Te). *Chem. Asian J.* **2008**, *3*, 113-118.
(54) Yao, S. L.; Xiong, Y.; Driess, M. N-Heterocyclic Carbene (NHC)-Stabilized Silanechalcogenones: NHC -> $Si(R_2)$=E (E = O, S, Se, Te). *Chem. Eur. J.* **2010**, *16*, 1281-1288.
(55) Xiong, Y.; Yao, S. L.; Inoue, S.; Irran, E.; Driess, M. The Elusive Silyliumylidene $[ClSi:]^+$ and Silathionium $[ClSi=S]^+$ Cations Stabilized by Bis(Iminophosphorane) Chelate Ligand. *Angew. Chem. Int. Ed.* **2012**, *51*, 10074-10077.

(56) Tan, G.; Xiong, Y.; Inoue, S.; Enthaler, S.; Blom, B.; Epping, J. D.; Driess, M. From elusive thio-and selenosilanoic acids to copper (I) complexes with intermolecular Si [double bond, length as m-dash] E→Cu–O–Si coordination modes (E= S, Se). *Chem. Commun.* **2013**, *49*, 5595-5597.
(57) Mück, F. M.; Baus, J. A.; Bertermann, R. d.; Burschka, C.; Tacke, R. Lewis Acid/Base Reactions of the Bis(amidinato)silylene [^{i}PrNC(Ph)N^{i}Pr]$_2$Si and Bis(guanidinato)silylene [^{i}PrNC(N^{i}Pr$_2$)N^{i}Pr]$_2$Si with ElPh$_3$ (El= B, Al). *Organometallics* **2016**, *35*, 2583-2588.
(58) Li, J.; Zhong, M.; Keil, H.; Zhu, H.; Herbst-Irmer, R.; Stalke, D.; De, S.; Koley, D.; Roesky, H. W. (PhC(N^{t}Bu)$_2$Al)$_2$(SiH$_2$)$_4$ six-membered heterocycle: comparable in structure to cyclohexane. *Chem. Commun.* **2019**, *55*, 2360-2363.
(59) Nazish, M.; Siddiqui, M. M.; Sarkar, S. K.; Munch, A.; Legendre, C. M.; Herbst-Irmer, R.; Stalke, D.; Roesky, H. W. Synthesis and Coordination Behavior of a New Hybrid Bidentate Ligand with Phosphine and Silylene Donors. *Chem. Eur. J.* **2021**, *27*, 1744-1752.
(60) Mo, Z. B.; Szilvasi, T.; Zhou, Y. P.; Yao, S. L.; Driess, M. An Intramolecular Silylene Borane Capable of Facile Activation of Small Molecules, Including Metal-Free Dehydrogenation of Water. *Angew. Chem. Int. Ed.* **2017**, *56*, 3699-3702.
(61) Nazish, M.; Harinath, A.; Lüert, D.; Köhler, C.; Herbst-Irmer, R.; Stalke, D.; Roesky, H. W. Reactivity of Silylene with Gallium-and Boron Trihalide at Reductive Conditions Resulting in Unforeseen Products. *Chem. Eur. J.* **2023**, e202300310.
(62) Pahar, S.; Karak, S.; Pait, M.; Raj, K. V.; Vanka, K.; Sen, S. S. Access to Silicon(II)– and Germanium(II)–Indium Compounds. *Organometallics* **2018**, *37*, 1206-1213.
(63) Wang, X.; Lei, B.; Zhang, Z.; Chen, M.; Rong, H.; Song, H.; Zhao, L.; Mo, Z. Isolation and characterization of bis (silylene)-stabilized antimony (I) and bismuth (I) cations. *Nat. Commun.* **2023**, *14*, 2968-2978.
(64) Yao, S.; Saddington, A.; Xiong, Y.; Driess, M. Chelating bis-silylenes as powerful ligands to enable unusual low-valent main-group element functions. *Acc. Chem. Res.* **2023**, *56*, 475-488.
(65) Garrison, J. C.; Youngs, W. J. Ag (I) N-heterocyclic carbene complexes: synthesis, structure, and application. *Chem. Rev.* **2005**, *105*, 3978-4008.
(66) Lin, J. C.; Huang, R. T.; Lee, C. S.; Bhattacharyya, A.; Hwang, W. S.; Lin, I. J. Coinage metal− N-heterocyclic carbene complexes. *Chem. Rev.* **2009**, *109*, 3561-3598.
(67) Mora, M.; Gimeno, M. C.; Visbal, R. Recent advances in gold–NHC complexes with biological properties. *Chem. Soc. Rev.* **2019**, *48*, 447-462.
(68) Hossain, J.; Akhtar, R.; Khan, S. Luminescent coinage metal complexes of carbenes. *Polyhedron* **2021**, *201*, 115151-115187.
(69) Jazzar, R.; Soleilhavoup, M.; Bertrand, G. Cyclic (alkyl)-and (aryl)-(amino) carbene coinage metal complexes and their applications. *Chem. Rev.* **2020**, *120*, 4141-4168.
(70) Conaghan, P. J.; Matthews, C. S. B.; Chotard, F.; Jones, S. T. E.; Greenham, N. C.; Bochmann, M.; Credgington, D.; Romanov, A. S. Highly efficient blue organic light-emitting diodes based on carbene-metal-amides. *Nat. Commun.* **2020**, *11*, 1758.
(71) Hamze, R.; Peltier, J. L.; Sylvinson, D.; Jung, M.; Cardenas, J.; Haiges, R.; Soleilhavoup, M.; Jazzar, R.; Djurovich, P. I.; Bertrand, G.; Thompson, M. E. Eliminating nonradiative decay in Cu(I) emitters: > 99% quantum efficiency and microsecond lifetime. *Science* **2019**, *363*, 601-606.
(72) Liu, W. K.; Gust, R. Metal N-heterocyclic carbene complexes as potential antitumor metallodrugs. *Chem. Soc. Rev.* **2013**, *42*, 755-773.
(73) Hashmi, A. S. K. Gold-catalyzed organic reactions. *Chem. Rev.* **2007**, *107*, 3180-3211.
(74) Mohamed, A. A. Advances in the coordination chemistry of nitrogen ligand complexes of coinage metals. *Coord. Chem. Rev.* **2010**, *254*, 1918-1947.

(75) Zeng, C.; Wang, N.; Peng, T.; Wang, S. Copper (I) complexes bearing 1, 2-phenyl-bridged P∧ N, P∧ N∧ P, and N∧ P∧ N chelate ligands: structures and phosphorescence. *Inorg. Chem.* **2017**, *56*, 1616-1625.
(76) Hendrich, C. M.; Sekine, K.; Koshikawa, T.; Tanaka, K.; Hashmi, A. S. K. Homogeneous and heterogeneous gold catalysis for materials science. *Chem. Rev.* **2020**, *121*, 9113-9163.
(77) Boehme, C.; Frenking, G. N-heterocyclic carbene, silylene, and germylene complexes of MCl (M = Cu, Ag, Au). A theoretical study. *Organometallics* **1998**, *17*, 5801-5809.
(78) Jutzi, P.; Möhrke, A. Bis (pentamethylcyclopentadienyl) silylene as Ligand in Gold (I) Chloride Complexes. *Angew. Chem. Int. Ed.* **1990**, *29*, 893-894.
(79) So, C. W.; Roesky, H. W.; Magull, J.; Oswald, R. B. Synthesis and characterization of $[PhC(N^tBu)_2]SiCl$: A stable monomeric chlorosilylene. *Angew. Chem. Int. Ed.* **2006**, *45*, 3948-3950.
(80) Sen, S. S.; Roesky, H. W.; Stern, D.; Henn, J.; Stalke, D. High Yield Access to Silylene RSiCl ($R=PhC(N^tBu)_2$) and Its Reactivity toward Alkyne: Synthesis of Stable Disilacyclobutene. *J. Am. Chem. Soc.* **2010**, *132*, 1123-1126.
(81) Tan, G.; Blom, B.; Gallego, D.; Driess, M. Facile Access to Mono-and Dinuclear Heteroleptic N-Heterocyclic Silylene Copper Complexes. *Organometallics* **2014**, *33*, 363-369.
(82) Khan, S.; Ahirwar, S. K.; Pal, S.; Parvin, N.; Kathewad, N. Silicon(II) Bis(trimethylsilyl)amide ($LSiN(SiMe_3)_2$, $L = PhC(N^tBu)_2$) Supported Copper, Silver, and Gold Complexes. *Organometallics* **2015**, *34*, 5401-5406.
(83) Parvin, N.; Dasgupta, R.; Pal, S.; Sen, S. S.; Khan, S. Strikingly diverse reactivity of structurally identical silylene and stannylene. *Dalton Trans.* **2017**, *46*, 6528-6532.
(84) Parvin, N.; Pal, S.; Khan, S.; Das, S.; Pati, S. K.; Roesky, H. W. Unique Approach to Copper(I) Silylene Chalcogenone Complexes. *Inorg. Chem.* **2017**, *56*, 1706-1712.
(85) Khan, S.; Pal, S.; Kathewad, N.; Purushothaman, I.; De, S.; Parameswaran, P. Stepwise isolation of an unprecedented silylene supported dinuclear gold(I) cation with aurophilic interaction. *Chem. Commun.* **2016**, *52*, 3880-3882.
(86) Bayrakdar, T. A. C. A.; Scattolin, T.; Ma, X. Y.; Nolan, S. P. Dinuclear gold(I) complexes: from bonding to applications. *Chem. Soc. Rev.* **2020**, *49*, 7044-7100.
(87) Schmidbaur, H.; Schier, A. Aurophilic interactions as a subject of current research: an up-date. *Chem. Soc. Rev.* **2012**, *41*, 370-412.
(88) Pearson, R. G. Hard and soft acids and bases. *J. Am. Chem. Soc.* **1963**, *85*, 3533-3539.
(89) Paesch, A. N.; Kreyenschmidt, A. K.; Herbst-Irmer, R.; Stalke, D. Side-Arm Functionalized Silylene Copper(I) Complexes in Catalysis. *Inorg. Chem.* **2019**, *58*, 7000-7009.
(90) Kolb, H. C.; Finn, M. G.; Sharpless, K. B. Click chemistry: Diverse chemical function from a few good reactions. *Angew. Chem. Int. Ed.* **2001**, *40*, 2004-2021.
(91) Tornøe, C. W.; Christensen, C.; Meldal, M. Peptidotriazoles on solid phase:[1, 2, 3]-triazoles by regiospecific copper (I)-catalyzed 1, 3-dipolar cycloadditions of terminal alkynes to azides. *J. Org. Chem.* **2002**, *67*, 3057-3064.
(92) Thirumurugan, P.; Matosiuk, D.; Jozwiak, K. Click chemistry for drug development and diverse chemical–biology applications. *Chem. Rev.* **2013**, *113*, 4905-4979.
(93) Nolte, C.; Mayer, P.; Straub, B. F. Isolation of a copper (I) triazolide: A "click" intermediate. *Angew. Chem. Int. Ed.* **2007**, *46*, 2101-2103.
(94) Badiei, Y. M.; Dinescu, A.; Dai, X.; Palomino, R. M.; Heinemann, F. W.; Cundari, T. R.; Warren, T. H. Copper-Nitrene Complexes in Catalytic C-H Amination. *Angew. Chem. Int. Ed.* **2008**, *47*, 9961-9964.
(95) Gephart, R. T.; McMullin, C. L.; Sapiezynski, N. G.; Jang, E. S.; Aguila, M. J. B.; Cundari, T. R.; Warren, T. H. Reaction of Cu-I with Dialkyl Peroxides: Cu-II-Alkoxides, Alkoxy Radicals, and Catalytic C-H Etherification. *J. Am. Chem. Soc.* **2012**, *134*, 17350-17353.

(96) Osako, T.; Tachi, Y.; Doe, M.; Shiro, M.; Ohkubo, K.; Fukuzumi, S.; Itoh, S. Quantitative evaluation of d-pi interaction in copper(I) complexes and control of copper(I)-dioxygen reactivity. *Chem. Eur. J.* **2004**, *10*, 237-246.
(97) Nako, A. E.; Tan, Q. W.; White, A. J. P.; Crimmin, M. R. Weakly Coordinated Zinc and Aluminum sigma-Complexes of Copper(I). *Organometallics* **2014**, *33*, 2685-2688.
(98) Nako, A. E.; White, A. J. P.; Crimmin, M. R. Bis(sigma-B-H) complexes of copper(I): precursors to a heterogeneous amine-borane dehydrogenation catalyst. *Dalton Trans.* **2015**, *44*, 12530-12534.
(99) Srivastava, R. S.; Khan, M. A.; Nicholas, K. M. Nitrosoarene-Cu(I) complexes are intermediates in copper-catalyzed allylic amination. *J. Am. Chem. Soc.* **2005**, *127*, 7278-7279.
(100) Ma, D. W.; Zhang, Y. D.; Yao, J. C.; Wu, S. H.; Tao, F. G. Accelerating effect induced by the structure of a-amino acid in the copper-catalyzed coupling reaction of aryl halides with alpha-amino acids. Synthesis of benzolactam-V_8. *J. Am. Chem. Soc.* **1998**, *120*, 12459-12467.
(101) Stringer, K. L.; Citir, M.; Metz, R. B. Photofragment spectroscopy of pi complexes: $Au^+(C_2H_4)$ and $Pt^+(C_2H_4)$. *J. Phys. Chem. A* **2004**, *108*, 6996-7002.
(102) Hertwig, R. H.; Koch, W.; Schroder, D.; Schwarz, H.; Hrusak, J.; Schwerdtfeger, P. A comparative computational study of cationic coinage metal-ethylene complexes $(C_2H_4)M(+)$ (M=Cu, Ag, and Au). *J. Phys. Chem.* **1996**, *100*, 12253-12260.
(103) Schroder, D.; Schwarz, H.; Hrusak, J.; Pyykko, P. Cationic gold(I) complexes of xenon and of ligands containing the donor atoms oxygen, nitrogen, phosphorus, and sulfur. *Inorg. Chem.* **1998**, *37*, 624-632.
(104) Schroder, D.; Hrusak, J.; Hertwig, R. H.; Koch, W.; Schwerdtfeger, P.; Schwarz, H. Experimental and Theoretical-Studies of Gold(I) Complexes Au(L)(+) (L=H_2O CO, NH_3, C_2H_4, C_3H_6, C_4H_6, C_6H_6, C_6F_6). *Organometallics* **1995**, *14*, 312-316.
(105) Nechaev, M. S.; Rayon, V. M.; Frenking, G. Energy partitioning analysis of the bonding in ethylene and acetylene complexes of group 6, 8, and 11 metals: $(CO)_5TM\text{-}C_2H_x$ and $Cl_4TM\text{-}C_2H_x$ (TM = Cr, Mo, W), $(CO)_4TM\text{-}C_2H_x$ (TM = Fe, Ru, Os), and $TM^+\text{-}C_2H_x$ (TM = Cu, Ag, Au). *J. Phys. Chem. A* **2004**, *108*, 3134-3142.
(106) Meyer, F.; Khan, F. A.; Armentrout, P. Thermochemistry of transition metal benzene complexes: Binding energies of $M(C_6H_6)x^+$ (x= 1, 2) for M= Ti to Cu. *J. Am. Chem. Soc.* **1995**, *117*, 9740-9748.
(107) Zhang, S. L.; Liu, L.; Fu, Y.; Guo, Q. X. Cation-pi interactions of Cu^+. *J. Mol. Struc. Theochem* **2005**, *757*, 37-46.
(108) Xu, F.-B.; Li, Q.-S.; Wu, L.-Z.; Leng, X.-B.; Li, Z.-C.; Zeng, X.-S.; Chow, Y. L.; Zhang, Z.-Z. Formation of group 11 metal (I)-arene complexes: Bonding mode and molecule-responsive spectral variations. *Organometallics* **2003**, *22*, 633-640.
(109) Mascal, M.; Kerdelhué, J. L.; Blake, A. J.; Cooke, P. A. S-Cylindrophanes: From Metal Tweezers to Metal Sandwiches. *Angew. Chem. Int. Ed.* **1999**, *38*, 1968-1971.
(110) Wright, A. M.; Irving, B. J.; Wu, G.; Meijer, A. J. H. M.; Hayton, T. W. A Copper(I)-Arene Complex With an Unsupported η^6 Interaction. *Angew. Chem. Int. Ed.* **2015**, *54*, 3088-3091.
(111) Parvin, N.; Pal, S.; Echeverria, J.; Alvarez, S.; Khan, S. Taming a monomeric $[Cu(\eta^6\text{-}C_6H_6)]^+$ complex with silylene. *Chem. Sci.* **2018**, *9*, 4333-4337.
(112) Parvin, N.; Hossain, J.; George, A.; Parameswaran, P.; Khan, S. N-heterocyclic silylene stabilized monocordinated copper(I)-arene cationic complexes and their application in click chemistry. *Chem. Commun.* **2020**, *56*, 273-276.
(113) Shahzad, S. A.; Sajid, M. A.; Khan, Z. A.; Canseco-Gonzalez, D. Gold catalysis in organic transformations: A review. *Synthetic Commun.* **2017**, *47*, 735-755.
(114) Wang, W.; Hammond, G. B.; Xu, B. Ligand effects and ligand design in homogeneous gold (I) catalysis. *J. Am. Chem. Soc.* **2012**, *134*, 5697-5705.

(115) Furstner, A.; Davies, P. W. Catalytic carbophilic activation: Catalysis by platinum and gold pi acids. *Angew. Chem. Int. Ed.* **2007**, *46*, 3410-3449.
(116) Weber, S. G.; Rominger, F.; Straub, B. F. Isolated silver intermediate of gold precatalyst activation. *Eur. J. Inorg. Chem.* **2012**, *2012*, 2863-2867.
(117) Herrero-Gómez, E.; Nieto-Oberhuber, C.; López, S.; Benet-Buchholz, J.; Echavarren, A. M. Cationic η^1/η^2-Gold (I) Complexes of Simple Arenes. *Angew. Chem. Int. Ed.* **2006**, *45*, 5455-5459.
(118) Lavallo, V.; Frey, G. D.; Kousar, S.; Donnadieu, B.; Bertrand, G. Allene formation by gold catalyzed cross-coupling of masked carbenes and vinylidenes. *Proc. Natl. Acad. Sci.* **2007**, *104*, 13569-13573.
(119) Parvin, N.; Mishra, B.; George, A.; Neralkar, M.; Hossain, J.; Parameswaran, P.; Hotha, S.; Khan, S. N-Heterocyclic silylene/germylene ligands in Au(I) catalysis. *Chem. Commun.* **2020**, *56*, 7625-7628.
(120) Yu, B. Gold (I)-catalyzed glycosylation with glycosyl o-alkynylbenzoates as donors. *Acc. Chem. Res.* **2018**, *51*, 507-516.
(121) Seeberger, P. H.; Werz, D. B. Synthesis and medical applications of oligosaccharides. *Nature* **2007**, *446*, 1046-1051.
(122) Zhu, X.; Schmidt, R. R. New principles for glycoside-bond formation. *Angew. Chem. Int. Ed.* **2009**, *48*, 1900-1934.
(123) Thadke, S. A.; Mishra, B.; Islam, M.; Pasari, S.; Manmode, S.; Rao, B. V.; Neralkar, M.; Shinde, G. P.; Walke, G.; Hotha, S. [Au]/[Ag]-catalysed expedient synthesis of branched heneicosafuranosyl arabinogalactan motif of Mycobacterium tuberculosis cell wall. *Nat. Commun.* **2017**, *8*, 1-9.
(124) Danopoulos, A. A.; Simler, T.; Braunstein, P. N-heterocyclic carbene complexes of copper, nickel, and cobalt. *Chem. Rev.* **2019**, *119*, 3730-3961.
(125) Abe, S.; Inagawa, Y.; Kobayashi, R.; Ishida, S.; Iwamoto, T. Silyl (silylene) Coinage Metal Complexes Obtained from Isolable Cyclic Alkylsilylenes. *Organometallics* **2022**, *41*, 874-882.
(126) Krahfuss, M. J.; Radius, U. N-Heterocyclic Silylenes as Metal-Metal Bridges and Metal-Halide Activators in Transition Metal Complexes. *Inorg. Chem.* **2020**, *59*, 10976-10985.
(127) Li, T.-Y.; Zheng, S.-J.; Djurovich, P. I.; Thompson, M. E. Two-Coordinate Thermally Activated Delayed Fluorescence Coinage Metal Complexes: Molecular Design, Photophysical Characters, and Device Application. *Chem. Rev.* **2024**, *124*, 4332-4392.
(128) Di, D.; Romanov, A. S.; Yang, L.; Richter, J. M.; Rivett, J. P. H.; Jones, S.; Thomas, T. H.; Jalebi, M. A.; Friend, R. H.; Linnolahti, M.; Bochmann, M.; Credgington, D. High-performance light-emitting diodes based on carbene-metal-amides. *Science* **2017**, *356*, 159-163.
(129) Hamze, R.; Shi, S.; Kapper, S. C.; Ravinson, D. S. M.; Estergreen, L.; Jung, M.-C.; Tadle, A. C.; Haiges, R.; Djurovich, P. I.; Peltier, J. L.; Jazzar, R.; Bertrand, G.; Bradforth, S. E.; Thompson, M. E. "Quick-silver" from a systematic study of highly luminescent, two-coordinate, d10 coinage metal complexes. *J. Am. Chem. Soc.* **2019**, *141*, 8616-8626.
(130) Romanov, A. S.; Jones, S. T.; Gu, Q.; Conaghan, P. J.; Drummond, B. H.; Feng, J.; Chotard, F.; Buizza, L.; Foley, M.; Linnolahti, M.; Credgington, D.; Bochmann, M. Carbene metal amide photoemitters: tailoring conformationally flexible amides for full color range emissions including white-emitting OLED. *Chem. Sci.* **2020**, *11*, 435-446.
(131) Bellotti, P.; Koy, M.; Hopkinson, M. N.; Glorius, F. Recent advances in the chemistry and applications of N-heterocyclic carbenes. *Nat. Rev. Chem* **2021**, *5*, 711-725.
(132) Nesterov, V.; Reiter, D.; Bag, P.; Frisch, P.; Holzner, R.; Porzelt, A.; Inoue, S. NHCs in main group chemistry. *Chem. Rev.* **2018**, *118*, 9678-9842.

(133) Zhong, R.; Lindhorst, A. C.; Groche, F. J.; Kühn, F. E. Immobilization of N-heterocyclic carbene compounds: a synthetic perspective. *Chem. Rev.* **2017**, *117*, 1970-2058.
(134) Zhukhovitskiy, A. V.; MacLeod, M. J.; Johnson, J. A. Carbene ligands in surface chemistry: from stabilization of discrete elemental allotropes to modification of nanoscale and bulk substrates. *Chem. Rev.* **2015**, *115*, 11503-11532.
(135) Jin, R.; Zeng, C.; Zhou, M.; Chen, Y. Atomically precise colloidal metal nanoclusters and nanoparticles: fundamentals and opportunities. *Chem. Rev.* **2016**, *116*, 10346-10413.
(136) Pla, D.; Gomez, M. Metal and metal oxide nanoparticles: a lever for C–H functionalization. *ACS Catal.* **2016**, *6*, 3537-3552.
(137) Shen, H.; Tian, G.; Xu, Z.; Wang, L.; Wu, Q.; Zhang, Y.; Teo, B. K.; Zheng, N. N-heterocyclic carbene coordinated metal nanoparticles and nanoclusters. *Coord. Chem. Rev.* **2022**, *458*, 214425-214451.
(138) Ghosh, M.; Khan, S. N-Heterocyclic Carbenes Capped Metal Nanoparticles: An Overview of Their Catalytic Scope. *ACS Catal.* **2023**, *13*, 9313-9325.
(139) Ghosh Chaudhuri, R.; Paria, S. Core/shell nanoparticles: classes, properties, synthesis mechanisms, characterization, and applications. *Chem. Rev.* **2012**, *112*, 2373-2433.
(140) Herrmann, A.-K.; Formanek, P.; Borchardt, L.; Klose, M.; Giebeler, L.; Eckert, J. r.; Kaskel, S.; Gaponik, N.; Eychmüller, A. Multimetallic aerogels by template-free self-assembly of Au, Ag, Pt, and Pd nanoparticles. *Chem. Mater.* **2014**, *26*, 1074-1083.
(141) Li, N.; Zhao, P.; Astruc, D. Anisotropic gold nanoparticles: synthesis, properties, applications, and toxicity. *Angew. Chem. Int. Ed.* **2014**, *53*, 1756-1789.
(142) Daniel, M.-C.; Astruc, D. Gold nanoparticles: assembly, supramolecular chemistry, quantum-size-related properties, and applications toward biology, catalysis, and nanotechnology. *Chem. Rev.* **2004**, *104*, 293-346.
(143) Wang, Y.; Robinson, G. H. Counterintuitive Chemistry: Carbene Stabilization of Zero-Oxidation State Main Group Species. *J. Am. Chem. Soc.* **2023**, *145*, 5592-5612.
(144) Ott, L. S.; Cline, M. L.; Deetlefs, M.; Seddon, K. R.; Finke, R. G. Nanoclusters in ionic liquids: evidence for N-heterocyclic carbene formation from imidazolium-based ionic liquids detected by ^{2}H NMR. *J. Am. Chem. Soc.* **2005**, *127*, 5758-5759.
(145) Koy, M.; Bellotti, P.; Das, M.; Glorius, F. N-Heterocyclic carbenes as tunable ligands for catalytic metal surfaces. *Nat. Catal.* **2021**, *4*, 352-363.
(146) Mikami, Y.; Dhakshinamoorthy, A.; Alvaro, M.; Garcia, H. Catalytic activity of unsupported gold nanoparticles. *Catal. Sci. Technol.* **2013**, *3*, 58-69.
(147) Gavia, D. J.; Shon, Y. S. Catalytic properties of unsupported palladium nanoparticle surfaces capped with small organic ligands. *ChemCatChem* **2015**, *7*, 892-900.
(148) An, Y. Y.; Yu, J. G.; Han, Y. F. Recent Advances in the Chemistry of N-Heterocyclic-Carbene-Functionalized Metal-Nanoparticles and Their Applications. *Chin. J. Chem.* **2019**, *37*, 76-87.
(149) Alonso, F.; Riente, P.; Yus, M. Nickel Nanoparticles in Hydrogen Transfer Reactions. *Acc. Chem. Res.* **2011**, *44*, 379-391.
(150) Bouzouita, D.; Asensio, J. M.; Pfeifer, V.; Palazzolo, A.; Lecante, P.; Pieters, G.; Feuillastre, S.; Tricard, S.; Chaudret, B. Chemoselective H/D exchange catalyzed by nickel nanoparticles stabilized by N-heterocyclic carbene ligands. *Nanoscale* **2020**, *12*, 15736-15742.
(151) Wang, G.; Rühling, A.; Amirjalayer, S.; Knor, M.; Ernst, J. B.; Richter, C.; Gao, H.-J.; Timmer, A.; Gao, H.-Y.; Doltsinis, N. L.; Glorius, F.; Fuchs, H. Ballbot-type motion of N-heterocyclic carbenes on gold surfaces. *Nat. Chem.* **2017**, *9*, 152-156.
(152) Gonzalez-Galvez, D.; Lara, P.; Rivada-Wheelaghan, O.; Conejero, S.; Chaudret, B.; Philippot, K.; van Leeuwen, P. W. NHC-stabilized ruthenium nanoparticles as new catalysts for the hydrogenation of aromatics. *Catal. Sci. Technol.* **2013**, *3*, 99-105.

(153) Martínez-Prieto, L. M.; Ferry, A.; Lara, P.; Richter, C.; Philippot, K.; Glorius, F.; Chaudret, B. New Route to Stabilize Ruthenium Nanoparticles with Non-Isolable Chiral N-Heterocyclic Carbenes. *Chem. Eur. J.* **2015**, *21*, 17495-17502.
(154) Martínez-Prieto, L.; Ferry, A.; Rakers, L.; Richter, C.; Lecante, P.; Philippot, K.; Chaudret, B.; Glorius, F. Long-chain NHC-stabilized RuNPs as versatile catalysts for one-pot oxidation/hydrogenation reactions. *Chem. Commun.* **2016**, *52*, 4768-4771.
(155) Rakers, L.; Martínez-Prieto, L. M.; López-Vinasco, A. M.; Philippot, K.; van Leeuwen, P. W.; Chaudret, B.; Glorius, F. Ruthenium nanoparticles ligated by cholesterol-derived NHCs and their application in the hydrogenation of arenes. *Chem. Commun.* **2018**, *54*, 7070-7073.
(156) Xu, W.; Li, M.; Qiao, L.; Xie, J. Recent advances of dinuclear nickel-and palladium-complexes in homogeneous catalysis. *Chem. Commun.* **2020**, *56*, 8524-8536.
(157) Chen, Q.-A.; Ye, Z.-S.; Duan, Y.; Zhou, Y.-G. Homogeneous palladium-catalyzed asymmetric hydrogenation. *Chem. Soc. Rev.* **2013**, *42*, 497-511.
(158) Ferry, A.; Schaepe, K.; Tegeder, P.; Richter, C.; Chepiga, K. M.; Ravoo, B. J.; Glorius, F. Negatively charged N-heterocyclic carbene-stabilized Pd and Au nanoparticles and efficient catalysis in water. *ACS Catal.* **2015**, *5*, 5414-5420.
(159) Rühling, A.; Schaepe, K.; Rakers, L.; Vonhören, B.; Tegeder, P.; Ravoo, B. J.; Glorius, F. Modular bidentate hybrid NHC-thioether ligands for the stabilization of palladium nanoparticles in various solvents. *Angew. Chem. Int. Ed.* **2016**, *55*, 5856-5860.
(160) Cao, Z.; Derrick, J. S.; Xu, J.; Gao, R.; Gong, M.; Nichols, E. M.; Smith, P. T.; Liu, X.; Wen, X.; Copéret, C.; Chang, C. J. Chelating N-Heterocyclic Carbene Ligands Enable Tuning of Electrocatalytic CO_2 Reduction to Formate and Carbon Monoxide: Surface Organometallic Chemistry. *Angew. Chem. Int. Ed.* **2018**, *57*, 4981-4985.
(161) Zhou, Z.; Li, M.; Liu, G.; Xu, G.; Xue, J. Ultra-small sugar-substituted N-heterocyclic carbene-protected palladium nanoparticles and catalytic activity. *Appl. Organomet. Chem.* **2019**, *33*, e4942.
(162) Arıcı, H.; Sündü, B.; Fırıncı, R.; Ertuğrul, E.; Özdemir, N.; Cetinkaya, B.; Metin, Ö.; Günay, M. E. The synthesis of new PEPPSI-type N-heterocyclic carbene (NHC)-Pd (II) complexes bearing long alkyl chain as precursors for the synthesis of NHC-stabilized Pd (0) nanoparticles and their catalytic applications. *J. Organomet. Chem.* **2021**, *934*, 121633.
(163) Hashmi, A. S. K. Introduction: Gold Chemistry. *Chem. Rev.* **2021**, *121*, 8309-8310.
(164) Pflaesterer, D.; Hashmi, A. S. K. Gold catalysis in total synthesis–recent achievements. *Chem. Soc. Rev.* **2016**, *45*, 1331-1367.
(165) Rudolph, M.; Hashmi, A. S. K. Gold catalysis in total synthesis—an update. *Chem. Soc. Rev.* **2012**, *41*, 2448-2462.
(166) Hashmi, A. S. K.; Rudolph, M. Gold catalysis in total synthesis. *Chem. Soc. Rev.* **2008**, *37*, 1766-1775.
(167) Liu, L.; Zhang, J. Gold-catalyzed transformations of α-diazocarbonyl compounds: selectivity and diversity. *Chem. Soc. Rev.* **2016**, *45*, 506-516.
(168) Jain, V.; Roy, S.; Roy, P.; Pillai, P. P. When Design Meets Function: The Prodigious Role of Surface Ligands in Regulating Nanoparticle Chemistry. *Chem. Mater.* **2022**, *34*, 7579-7597.
(169) Odom, T. W.; Nehl, C. L. How gold nanoparticles have stayed in the light: The 3M's principle. *ACS Nano* **2008**, *2*, 612-616.
(170) Khlebtsov, N.; Dykman, L. Biodistribution and toxicity of engineered gold nanoparticles: a review of in vitro and in vivo studies. *Chem. Soc. Rev.* **2011**, *40*, 1647-1671.
(171) Astruc, D. Introduction: Nanoparticles in Catalysis. *Chem. Rev.* **2020**, *120*, 461-463.
(172) Eisen, C.; Chin, J. M.; Reithofer, M. R. Catalytically Active Gold Nanomaterials Stabilized by N-heterocyclic Carbenes. *Chem. Asian J.* **2021**, *16*, 3026-3037.

(173) Song, S. G.; Satheeshkumar, C.; Park, J.; Ahn, J.; Premkumar, T.; Lee, Y.; Song, C. N-heterocyclic carbene-based conducting polymer–gold nanoparticle hybrids and their catalytic application. *Macromolecules* **2014**, *47*, 6566-6571.
(174) Zhang, L.; Wei, Z.; Meng, M.; Ung, G.; He, J. Do polymer ligands block the catalysis of metal nanoparticles? Unexpected importance of binding motifs in improving catalytic activity. *J. Mater. Chem. A* **2020**, *8*, 15900-15908.
(175) Gou, X. X.; Liu, T.; Wang, Y. Y.; Han, Y. F. Ultrastable and Highly Catalytically Active N-Heterocyclic-Carbene-Stabilized Gold Nanoparticles in Confined Spaces. *Angew. Chem. Int. Ed.* **2020**, *59*, 16683-16689.
(176) Thomas, S. R.; Yang, W.; Morgan, D. J.; Davies, T. E.; Li, J. J.; Fischer, R. A.; Huang, J.; Dimitratos, N.; Casini, A. Bottom-up Synthesis of Water-Soluble Gold Nanoparticles Stabilized by N-Heterocyclic Carbenes: From Structural Characterization to Applications. *Chem. Eur. J.* **2022**, *28*, e202201575.
(177) Cao, Z.; Kim, D.; Hong, D.; Yu, Y.; Xu, J.; Lin, S.; Wen, X.; Nichols, E. M.; Jeong, K.; Reimer, J. A.; Peidong, Y.; J., C. C. A molecular surface functionalization approach to tuning nanoparticle electrocatalysts for carbon dioxide reduction. *J. Am. Chem. Soc.* **2016**, *138*, 8120-8125.
(178) Zhang, L.; Wei, Z.; Thanneeru, S.; Meng, M.; Kruzyk, M.; Ung, G.; Liu, B.; He, J. A Polymer Solution To Prevent Nanoclustering and Improve the Selectivity of Metal Nanoparticles for Electrocatalytic CO_2 Reduction. *Angew. Chem. Int. Ed.* **2019**, *58*, 15834-15840.
(179) Cui, M.-L.; Chen, Y.-S.; Xie, Q.-F.; Yang, D.-P.; Han, M.-Y. Synthesis, properties and applications of noble metal iridium nanomaterials. *Coord. Chem. Rev.* **2019**, *387*, 450-462.
(180) Oberhauser, W.; Evangelisti, C.; Liscio, A.; Kovtun, A.; Cao, Y.; Vizza, F. Glycerol to lactic acid conversion by NHC-stabilized iridium nanoparticles. *J. Catal.* **2018**, *368*, 298-305.
(181) Valero, M.; Bouzouita, D.; Palazzolo, A.; Atzrodt, J.; Dugave, C.; Tricard, S.; Feuillastre, S.; Pieters, G.; Chaudret, B.; Derdau, V. NHC-Stabilized Iridium Nanoparticles as Catalysts in Hydrogen Isotope Exchange Reactions of Anilines. *Angew. Chem. Int. Ed.* **2020**, *59*, 3517-3522.
(182) Lara, P.; Suarez, A.; Colliere, V.; Philippot, K.; Chaudret, B. Platinum N-Heterocyclic Carbene Nanoparticles as New and Effective Catalysts for the Selective Hydrogenation of Nitroaromatics. *ChemCatChem* **2014**, *6*, 87-90.
(183) Martínez-Prieto, L. M.; Rakers, L.; López-Vinasco, A. M.; Cano, I.; Coppel, Y.; Philippot, K.; Glorius, F.; Chaudret, B.; van Leeuwen, P. W. Soluble Platinum Nanoparticles Ligated by Long-Chain N-Heterocyclic Carbenes as Catalysts. *Chem. Eur. J.* **2017**, *23*, 12779-12786.
(184) Ruiz-Varilla, A. M.; Baquero, E. A.; Chaudret, B.; de Jesus, E.; Gonzalez-Arellano, C.; Flores, J. C. Water-soluble NHC-stabilized platinum nanoparticles as recoverable catalysts for hydrogenation in water. *Catal. Sci. Technol.* **2020**, *10*, 2874-2881.
(185) Zhang, Z.; Shao, C.; Sun, Y.; Mu, J.; Zhang, M.; Zhang, P.; Guo, Z.; Liang, P.; Wang, C.; Liu, Y. Tubular nanocomposite catalysts based on size-controlled and highly dispersed silver nanoparticles assembled on electrospun silica nanotubes for catalytic reduction of 4-nitrophenol. *J. Mater. Chem.* **2012**, *22*, 1387-1395.
(186) Liu, L.; Corma, A. Metal catalysts for heterogeneous catalysis: from single atoms to nanoclusters and nanoparticles. *Chem. Rev.* **2018**, *118*, 4981-5079.
(187) Kundu, S.; Sinhababu, S.; Chandrasekhar, V.; Roesky, H. W. Stable cyclic (alkyl)(amino) carbene (cAAC) radicals with main group substituents. *Chem. Sci.* **2019**, *10*, 4727-4741.
(188) Lavallo, V.; Canac, Y.; Präsang, C.; Donnadieu, B.; Bertrand, G. Stable Cyclic (Alkyl)(Amino)Carbenes as Rigid or Flexible, Bulky, Electron-Rich Ligands for Transition-

Metal Catalysts: A Quaternary Carbon Atom Makes the Difference. *Angew. Chem. Int. Ed.* **2005**, *44*, 5705-5709.
(189) Gao, Y.; Yazdani, S.; Kendrick IV, A.; Junor, G. P.; Kang, T.; Grotjahn, D. B.; Bertrand, G.; Jazzar, R.; Engle, K. M. Cyclic (Alkyl)(amino) carbene Ligands Enable Cu-Catalyzed Markovnikov Protoboration and Protosilylation of Terminal Alkynes: A Versatile Portal to Functionalized Alkenes. *Angew. Chem. Int. Ed.* **2021**, *60*, 19871-19878.
(190) Jang, H.; Zhugralin, A. R.; Lee, Y.; Hoveyda, A. H. Highly selective methods for synthesis of internal (α-) vinylboronates through efficient NHC–Cu-catalyzed hydroboration of terminal alkynes. Utility in chemical synthesis and mechanistic basis for selectivity. *J. Am. Chem. Soc.* **2011**, *133*, 7859-7871.
(191) Schmid, P.; Fantuzzi, F.; Klopf, J.; Schröder, N. B.; Dewhurst, R. D.; Braunschweig, H.; Engel, V.; Engels, B. Twisting versus Delocalization in CAAC-and NHC-Stabilized Boron-Based Biradicals: The Roles of Sterics and Electronics. *Chem. Eur. J.* **2021**, *27*, 5160-5170.
(192) Böhnke, J.; Braunschweig, H.; Ewing, W. C.; Hörl, C.; Kramer, T.; Krummenacher, I.; Mies, J.; Vargas, A. Diborabutatriene: An Electron-Deficient Cumulene. *Angew. Chem. Int. Ed.* **2014**, *53*, 9082-9085.
(193) Bakker, A.; Freitag, M.; Kolodzeiski, E.; Bellotti, P.; Timmer, A.; Ren, J.; Schulze Lammers, B.; Moock, D.; Roesky, H. W.; Mönig, H.; Amirjalayer, S.; Fuchs, H.; Glorius, F. An Electron-Rich Cyclic (Alkyl)(Amino)Carbene on Au(111), Ag(111), and Cu(111) Surfaces. *Angew. Chem. Int. Ed.* **2020**, *59*, 13643-13646.
(194) Ren, J.; Freitag, M.; Gao, Y.; Bellotti, P.; Das, M.; Schulze Lammers, B.; Mönig, H.; Zhang, Y.; Daniliuc, C. G.; Du, S.; Fuchs, H.; Glorius, F. Reversible Self-Assembly of an N-Heterocyclic Carbene on Metal Surfaces. *Angew. Chem. Int. Ed.* **2022**, *61*, e202115104.

Chapter 2: Functionalized N-Heterocyclic Silylenes for Small Molecule Activation and Reactivities

Chapter 2A: The First Bis(Silatellurone) with C-H···Te Interaction

Adapted from: ***M. Ghosh***, P. Panwaria, S. Tothadi, A. Das* and S. Khan*, Bis (silanetellurone) with C–H···Te interaction. *Inorg. Chem.* **2020**, *59*, 17811-17821.

2A.1 Objective of this work.

Herein, we isolated a series of bis(silanechalcogenones) [Ch = Te (**2A.2**), S (**2A.3**), and Se (**2A.4**)] using an NHSi-based SiCSi pincer ligand (**2A.1**). **2A.4** is the first example of a bis(silanetellurone) derivative. The bonding patterns of **2A.2**-**2A.4** were extensively studied by natural bond orbital (NBO), quantum theory of atoms in molecules (QTAIM), and non-covalent interaction (NCI) index analyses and they exhibit weak C-H···Ch interaction. The analogous reaction of **2A.1** with trimethyl *N*-oxide produced a novel bis(cyclosiloxane) derivative (**2A.5**).

2A.2 Introduction.

The scarcity of compounds featuring the Te=C functionality bespeaks the reluctance of tellurium to engage in multiple bonding, which can be attributed to the poor *pπ*-*pπ* overlap of tellurium with the second or third-row elements.[1, 2] Nonetheless, by using the protective influence of bulky substituents, several multiply-bound tellurium compounds with second or third-row elements have been isolated. Braunschweig and co-workers recently reported the first compound with a B=Te double bond obtained from the reaction of a base-stabilized borylene [Cp(OC)$_2$Mn=B*t*Bu(IMe)] with tellurium.[3] The Al=Te doubly bound compound was reported by Inoue's group, where the Al=Te functionality was stabilized by N-heterocyclic carbenes and imine.[4] The situation is relatively better placed with silicon as the telluration of the stable silylenes usually provides access to the silicon-tellurium doubly bound systems. This methodology has been extensively exploited by the groups of Kira,[5] Driess,[6-8] Tacke,[9] So,[10] and Sen[11] to prepare a range of Si=Te double-bonded compounds. However, a compound with two Si=Te double bonds, commonly known as bis(silanetellurone), is not reported in the literature. Even from a much broader perspective, bis(silanechalcogenones) are still very rare (Chart 2A.1). The groups of Müller and West reported the first bis(silanechalcogenones), a novel bis(silaneselone) with two donor-supported Si=Se double bonds (**2A.A**).[12] However, the synthetic route used in their work involved an essential but uncontrolled hydrolysis step. Subsequently, So *et al.* discovered an appropriate synthetic methodology to isolate a bis(silaneselone) (**2A.B**)[13] through the oxidation of Roesky's inter-connected bis-silylene[14] with elemental selenium. However, the scope of this methodology is limited to only selenium, presumably due to the very low-yield of Roesky's bis-silylene. Nonetheless, this protocol shows that bis-silylenes can be the most appropriate precursors for the preparation of such compounds if they are isolated in good yields. In fact, Driess and co-workers recently reported the first bis(silanethione) (**2A.C**) from the ferrocene-derived bis-silylene.[15] However, access to

bis(silanetellurone) has not been reported yet, presumably due to the intrinsic instability of the Si=Te bonds. With the increasing use of silicon tellurides (Si_2Te_2 and Si_2Te_3) as attractive 2-D materials in electronics[16-18] and to understand their aggregation processes and chemical bonding, it is desirable to study their well-defined molecular structures. This work presents the preparation of the first bis(silanetellurone) (**2A.2**) by telluration of a stable 2,6-tert-butyl resorcinolate SiCSi pincer (**2A.1**);[19] a methodology that is also suitable for sulfur (**2A.3**) and selenium (**2A.4**). In fact, this is the first report where an entire series of heavier congeners of bis(silanechalcogenones) (**2A.2-2A.4**) were obtained from the same system. The nature of the double bond between silicon and chalcogens has been a subject of debate because their zwitter-ionic form ($Si^{\delta+}$-$Ch^{\delta-}$) also contributes to the overall structure, especially when the silicon atom is hyper-coordinated.[7] A further impetus comes from the recent works by Lips, Müller and co-workers.[20-22] Hence, the nature of the double bond in **2A.2-2A.4** has been characterized not only by single-crystal X-ray studies but also solution state studies and theoretical investigations. What is even more interesting is the identification of a weak C-H···S/Se/Te interaction in these systems. Unconventional hydrogen bonds with chalcogen atoms as hydrogen bond (HB) acceptors have recently been recognized through various spectroscopic techniques.[23-28]

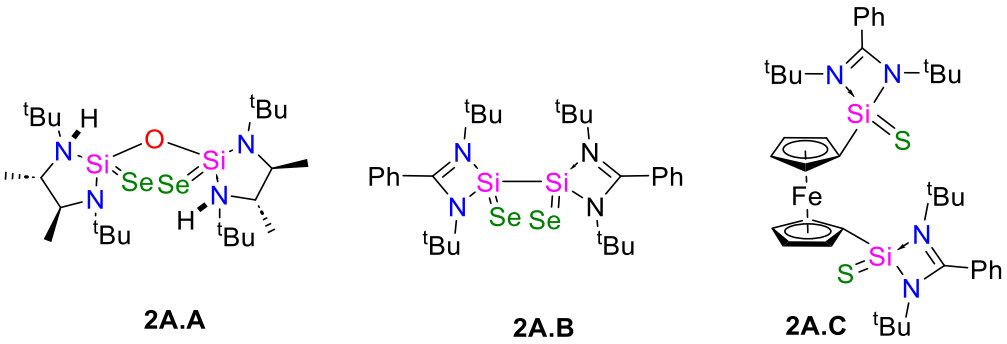

Chart 2A.1. Reported bis(silanechalcogenones). The Te analogue was not reported.

2A.3 Results and Discussion.

2A.3.1 Synthesis of 2A.2-2A.5.

All experiments were conducted under an atmosphere of dry argon or vacuum using the standard Schlenk technique and in a dinitrogen-filled MBRAUN MB 150-G1 glovebox. MBRAUN solvent purification system MB SPS-800 purified the solvents used. Compound **2A.1** has been prepared using the literature procedure.[19] All other chemicals purchased from Sigma Aldrich and Alfa Aesar were used without further purification. ^{1}H, ^{13}C, and ^{29}Si NMR spectra were recorded in $CDCl_3$ and C_6D_6 using a Bruker Avance DRX500 spectrometer, and

were referenced to external $SiMe_4$ and ^{77}Se was referenced to external Me_2Se. Melting points were measured in a sealed glass tube and were not corrected.

2A.3.1.1 Preparation of 2A.2. A Schlenk flask charged with **2A.1** (0.470 g, 0.5 mmol) and tellurium powder (0.128 g, 1 mmol) was taken in 40 ml toluene and kept in stirring overnight. The greenish-yellow color solution was evaporated under reduced pressure, extracted in 50 ml DCM, and filtered off. Concentrating DCM to 2 ml and adding 4 ml *n*-Pentane produced single crystals at room temperature. Yield: 335 mg (56%). ^{1}H NMR (400 MHz, C_6D_6, 298 K) δ 1.30 (s, 36H, NC*Me*$_3$), 1.70 (s, 18H, Ar*Me*$_3$), 6.82-6.99 (m, 8H, arom. H), 7.62 (s, 1H, arom. H), 7.85-7.86 (m, 2H, arom. H), 8.52 (s, 1H, arom. H), ^{13}C{^{1}H} NMR (100.613 MHz, C_6D_6, 298 K): δ 29.92 (ArC($\underline{C}$H$_3$)$_3$), 30.45 (NC($\underline{C}$H$_3$)$_3$), 33.77 (Ar$\underline{C}$(CH$_3$)$_3$), 54.58 (N$\underline{C}$(CH$_3$)$_3$), 110.57, 124.11, 126.62, 126.86, 129.17,129.56,131.88,149.93 (arom. $\underline{C}$), 173.70 (N$\underline{C}$N), ^{29}Si{^{1}H} NMR (79.49 MHz, C_6D_6, 298 K): δ -60.28 M.p. 151.7 ^{o}C HRMS: $C_{44}H_{66}N_4O_2Si_2Te_2$: *m/z* 994.6365 Found *m/z*: 994.4080.

2A.3.1.2 Preparation of 2A.3. A Schlenk flask charged with **2A.1** (0.470 g, 0.5 mmol) and elemental sulfur (0.032 g, 1 mmol) was taken with 40 ml toluene at room temperature. After 2 h of stirring, all volatiles were evaporated under reduced pressure, and residue was extracted in DCM. The solid white powder as **2A.3**, obtained by evaporating DCM, was next taken for further experimental studies. Suitable crystals for X-ray crystallography were obtained from DCM and pentane mixture at 0 °C. Yield: 0.38 g (75.7%). ^{1}H NMR (400 MHz, C_6D_6, 298 K) δ 1.25 (s, 36H, NC*Me*$_3$), 1.74 (s, 18H, Ar*Me*$_3$) 6.81-7.00 (m, 8H, arom. H), 7.63 (s, 1H, arom. H), 7.93-7.95 (m, 2H, arom. H), 8.49 (s, 1H, arom. H), ^{13}C{^{1}H} NMR (100.613 MHz, C_6D_6, 298 K): δ 29.86 (ArC($\underline{C}$H$_3$)$_3$), 30.20 (NC($\underline{C}$H$_3$)$_3$), 33.82 (Ar$\underline{C}$(CH$_3$)$_3$), 54.23(N$\underline{C}$(CH$_3$)$_3$), 111.36, 123.96, 128.13, 128.38, 12.98, 129.44, 131.48, 150.51 (arom. $\underline{C}$), 174.67 (N$\underline{C}$N), ^{29}Si{^{1}H} NMR (79.49 MHz, C_6D_6, 298 K): δ -37.29. M.p. 180-186.2 ^{o}C HRMS: $C_{44}H_{66}N_4O_2Si_2S_2$ Calculated *m/z*: 802.4166; Found *m/z*: 802.4796.

2A.3.1.3 Preparation of 2A.4. A Schlenk flask charged with **2A.1** (0.470 g, 0.5 mmol) and elemental selenium (0.079 g, 1 mmol) was taken in 40 ml of toluene at room temperature. After 5 h of stirring, all volatiles were removed under reduced pressure, and the remaining residue was extracted in DCM. After filtration, DCM was concentrated to 2 ml, and 4 ml of pentane was added and kept for crystallization at room temperature. The compound was obtained as a colorless crystal with a yield of 0.35 g (63.7%). ^{1}H NMR (400 MHz, C_6D_6, 298 K) δ 1.27 (s, 36H, NC*Me*$_3$), 1.73 (s, 18H, Ar*Me*$_3$), 6.81-7.00 (m, 8H, arom. H), 7.62 (s, 1H, arom. H), 7.88-

7.90 (m, 2H, arom. H), 8.55 (s, 1H, arom. H), ^{13}C {^{1}H} NMR (100.613 MHz, $CDCl_3$, 298 K): δ 30.59 (ArC($\underline{C}H_3)_3$), 31.26 (NC($\underline{C}H_3)_3$), 34.40 (Ar$\underline{C}(CH_3)_3$), 55.33 (N$\underline{C}(CH_3)_3$), 111.26, 124.76, 127.11, 129.09, 129.24, 130.99, 132.12, 150.55 (arom. C), 176.02 (N$\underline{C}$N), ^{29}Si{^{1}H} NMR (79.49 MHz, C_6D_6, 298 K): δ -38.04 ^{77}Se {^{1}H} NMR (76.311 MHz, $CDCl_3$, 298 K): δ -514.44 M.p. 190 °C HRMS: $C_{44}H_{66}N_4O_2Si_2Se_2$: *m/z* 898.3055 Found *m/z*: 898.3105.

2A.3.1.4 Preparation of 2A.5. A Schlenk flask with **2A.1** (0.470 g, 0.5 mmol) and Me_3NO (0.0751 g, 1 mmol) were dissolved in 45 ml of toluene at 0^0C and kept for attaining room temperature slowly overnight. All volatiles were removed under reduced pressure, and the white powder was dissolved in *n*-hexane and filtered off. Single crystals suitable for X-ray crystallography were grown from *n*-hexane at room temperature. Yield: 0.4 g (73.38%). ^{1}H NMR (400 MHz, $CDCl_3$, 298 K) δ 1.02 (s, 72 H, NC*Me$_3$*), 1.48 (s, 36 H, 2H, Ar*Me$_3$*), 7.03 (m, 2 H, arom. H), 7.26-7.27 (m, 14H, arom. H), 7.31-7.33 (m, 6H, arom. H) 7.37 (s, 2 H, arom. H), ^{13}C{^{1}H} NMR (100.613 MHz, $CDCl_3$, 298 K): δ 30.57 (ArC($\underline{C}H_3)_3$), 30.66 (NC($\underline{C}H_3)_3$), 33.55 (Ar$\underline{C}(CH_3)_3$), 52.43 (N$\underline{C}(CH_3)_3$), 118.91, 124.48, 126.42, 127.17, 127.97, 129.28, 133.75, 151.09 (arom. C) and 168.79 (N$\underline{C}$N), ^{29}Si{^{1}H} NMR (79.49 MHz, $CDCl_3$, 298K): δ -114.09. M.p. 210 °C. HRMS. $C_{88}H_{132}N_8O_8Si_4$: Calculated *m/z* 1540.9240; Found *m/z* 1540.9460.

2A.3.2 Structural elucidation of 2A.2-2A.4.

The synthesis of the bis(silanetellurone), **2A.2** starts with the previously reported 2,6-*tert*-butyl resorcinolate SiCSi pincer (**2A.1**).[19] The addition of two equivalents of tellurium to **2A.1** in toluene afforded the desired bis(silanetellurone), **2A.2** in 56% yield *via* oxidative addition of the two Si(II) centers in **2A.1** (Scheme 2A.1).

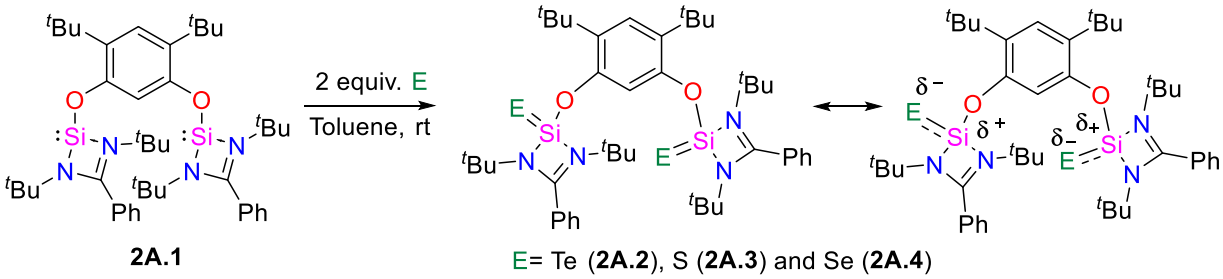

Scheme 2A.1. Syntheses of **2A.2-2A.4**.

The formation of **2A.2** was indicated by the appearance of new resonance in the ^{29}Si NMR spectrum at δ -60.3 ppm, which is significantly upfield shifted than that of **2A.1** (δ -24 ppm). **2A.2** crystallizes in the monoclinic *P2$_1$/c* space group, where both the silicon atoms

exhibit distorted tetrahedral geometry (Figure 2A.1). The Si=Te bond distances are 2.341(2) and 2.332(2) Å, which are bit shorter than the previously reported Si=Te double-bonded compounds featuring tetra-coordinate Si atoms, such as Driess' [HC(CMeNAr){C(=CH_2)NAr}Si(NHC)=Te] (2.383(2) Å),[6-8] So's [PhC(N*t*Bu)$_2$SiN{($SiMe_3$)$_2$}=Te] (2.3720(15) Å),[10] Sen's [PhC(N*t*Bu)$_2$SiSi{($SiMe_3$)$_3$}=Te] (2.3723(8) Å),[11] but shorter than typical Si–Te single bonds (< 2.52 Å). Interestingly, the Si=Te bond lengths in **2A.2** are longer than Kira's three-coordinate Si=Te bond [2.3210(6) Å],[5] but shorter than Tacke's five-coordinate Si=Te bonds [2.4017(6) Å],[9] implying that the increase in the coordination number of Si leads to the decrease the double bond character.[29]

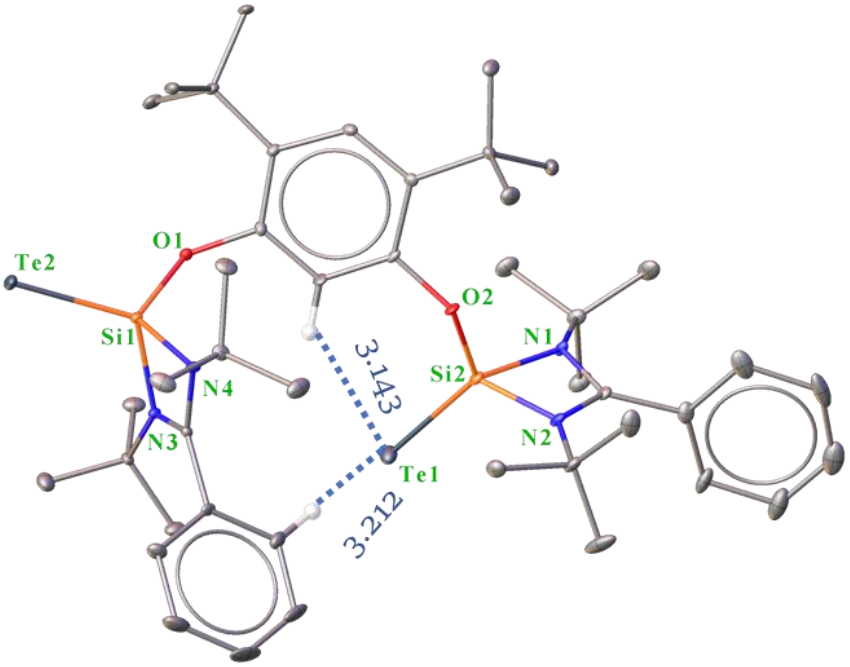

Figure 2A.1. The molecular structure of **2A.2** (ellipsoids are shown at the probability level of 50%). Tert-butyl groups attached to nitrogens (N1, N2, N3, and N4) and hydrogen atoms are omitted for clarity. Selected bond lengths (Å): O1-Si03 1.622(3), Te2-Si03 2.341(2), N3-Si03 1.814(4), N4-Si03 1.802(4), O2-Si04 1.633(3), Te1-Si04 2.332(2), Si04-N1 1.819(4), Si04-N2 1.786(4), and bond angles (°): Te2-Si03-N3 118.8(1), Te2-Si03-O1 115.7(1), Te2-Si03 N4 119.7(1), O1-Si03-N4 111.9(2), N3-Si03-N4 72.3(2), Te1-Si04-O2 123.5(1), Te1-Si04-N2 120.5(1), Te1-Si04-N1 117.2(1), O2-Si04-N1 108.6(2), N2-Si04-N1 72.3(2).

As bis-(silanethione) and –(silaneselenone) have already been reported (Chart 2A.1), we realized it would be useful to prepare analogues of **2A.2** with these elements and compare them to **2A.A**-**2A.C**. To this end, **2A.1** can be treated with two equivalents of sulfur or selenium to afford similar oxidative addition products, **2A.3** and **2A.4**, respectively. The ^{29}Si NMR

spectra for **2A.3** and **2A.4** show singlet resonances at δ -34.21 and -35.27 ppm, respectively, which are downfield than that in **2A.2,** reflecting the gradual upfield shift of ^{29}Si NMR resonance with the decreasing electronegativity of the chalcogens down the group from sulfur to tellurium.[11] The ^{29}Si NMR resonance of **2A.3** is upfield than that in **2A.C** (12.1 ppm) due to the replacement of the σ-donating ferrocenyl substituent with the π-donating resorcinolate moiety. **2A.3** crystallizes in the monoclinic *C2/c* space group (Figure 2A.2) featuring two Si=S fragments with Si-S bond lengths of 1.968(2) and 1.978(2) Å, consistent with those in **2A.C** (1.9867(13) and 1.9858(13) Å)[15] and other related silanethiones with tetra-coordinate silicon atoms, such as Si(S)N(SiMe$_3$)$_2$:1.987(8) Å,[30] {PhC(N*t*Bu)$_2$}Si(S)Si(SiMe$_3$)$_3$:1.9996(6) Å,[11] {PhC(N*t*Bu)$_2$}Si(S)Cl:2.079(6) Å,[13] however, marginally longer than silanethiones reported by Tokitoh (1.948(4) Å)[31] or Kira (1.9575(7) Å),[5] which feature tri-coordinated silicon atoms.

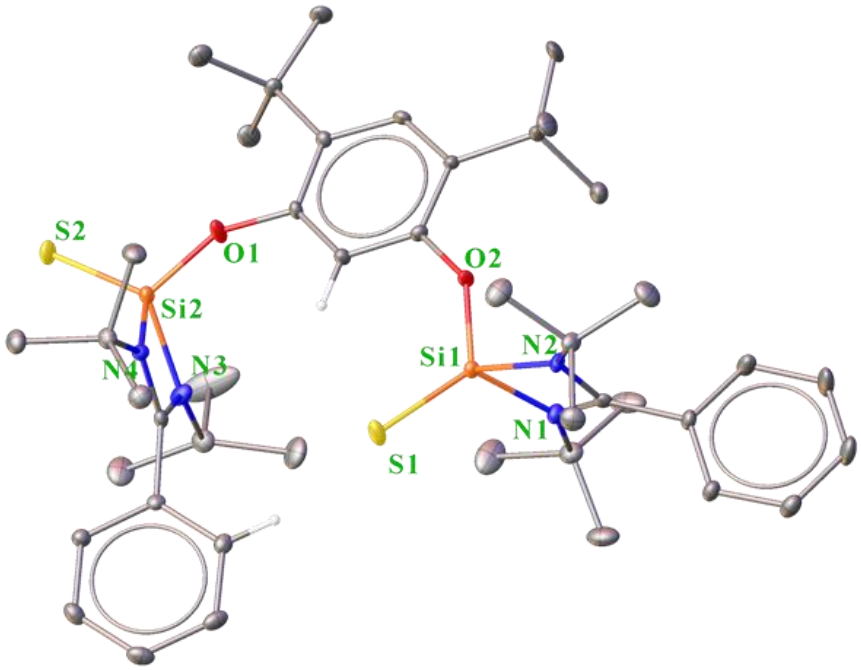

Figure 2A.2. The molecular structure of **2A.3** (ellipsoids are shown at the probability level of 50%). tert-butyl groups and hydrogen atoms are omitted for clarity. Selected bond lengths (Å): S2-Si2 1.978(2), Si1-S1 1.968(2), O1-Si2 1.605(3), O2-Si1 1.620(3), Si2-N4 1.807(3), Si2-N3 1.801(4), Si1-N1 1.817(4), Si1-N2 1.797(3) and bond angles (°): S2-Si2-O1 113.0(1), S2-Si2-N3 121.3(1), S2-Si2-N4 119.5(1), O1-Si2-N4 112.7(2), N3-Si2-N4 72.4(2), S1-Si1-O2 122.9(1), S1-Si1-N1 121.5(1), S1-Si1-N2 121.5(1), O2-Si1-N2 101.4(2), N1-Si1-N2 72.6(2).

2A.4 crystallizes in the triclinic *P*-1 space group (Figure 2A.3). The Si=Se bond lengths in **2A.4** [Si1-Se1: 2.098(1) Si2-Se2: 2.116(1) Å] compare favorably with those in **2A.A** (2.153(1) and 2.156(1) Å),[12] **2A.B** (2.1346(16) Å),[13] and other amidinate based Si=Se doubly

bound compounds, {PhC(N*t*Bu)$_2$}Si(Se)N(SiMe$_3$)$_2$: 2.136(9) Å,[23-28] {PhC(N*t*Bu)$_2$}Si(Se)Si(SiMe$_3$)$_3$: 2.139(4) Å.[11]

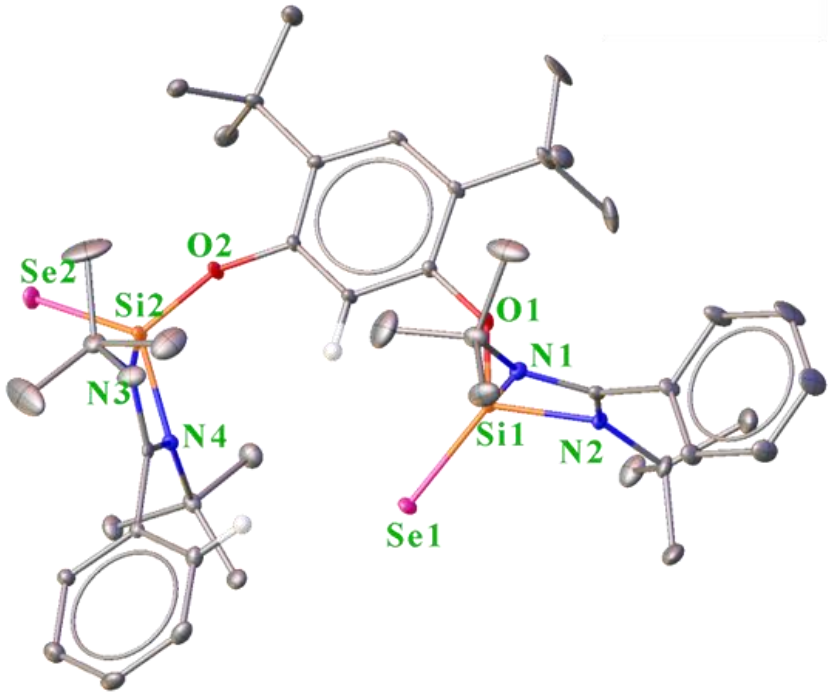

Figure 2A.3. The molecular structure of **2A.4** (ellipsoids are shown at the probability level of 50%). tert-butyl groups attached to nitrogens (N1, N2, N3, and N4) and hydrogen atoms are omitted for clarity. Selected bond lengths (Å): Si1-N1 1.811(3), Si1-N2 1.804(3), Si1-Se1 2.098(1), Si1-O1 1.617(2), Si2-N3 1.809(3), Si2-N4 1.807(3), Si2-Se2 2.116(1), Si2-O2 1.601(2) and bond angles (°): N4-Si2-N3 72.4(1), N4-Si2-Se2 118.7(1), O2-Si2-N3 112.8(1), O2-Si2-Se2 112.9(1), N2-Si1-N1 72.3(1), O1-Si1-Se1 122.8(1), N1-Si1-Se1 121.5(1), N2-Si1-O1 101.6(1).

We have also calculated the percentage bond shortening of **2A.2**-**2A.4** from their respective single bonds (Table 2A.1) using a methodology shown by Iwamoto and Kira.[5] The percent bond shortening among **2A.2**-**2A.4** decreases from sulfur to tellurium, indicating the weakness of Si=E double bonds in the same order.

Table 2A.1. Comparison of shortening of the bond (%Δd^b), which is calculated as follows

%Δd^b =[1 - (Si=E double bond length)/(Si-E single-bond length)]•100%.[5]

Compound	Si-E (Å)	Si=E (Å)	%Δd^b
2A.2	2.52	2.350 (av)	6.72
2A.3	2.27	1.970(av)	7.94
2A.4	2.14	2.107(av)	7.18

2A.3.3 Detection of C-H···Chalcogen (Ch) interaction and solution state confirmation.

While elucidating the molecular structures of **2A.2-2A.4**, we observe that they exhibit C-H···Ch (Ch=S, Se, and Te) interaction, with resorcinolate C-H (Case-I) and benzamidinate C-H (Case-II) (Figure 2A.4). It should be noted here that there is a modicum of precedence for C-H···Se interactions[32-34] and only one report for C-H···Te interaction,[35] which was predicted based on short contacts in the crystal structure. The low electronegativity of tellurium has been ascribed to the paucity of C-H···Te interaction.[36] Recently, there has been an increased interest in understanding C-H···Te interactions that could be exploited for applications in crystal engineering, superconductivity, gas capture, and field-effect transistor studies.[37]

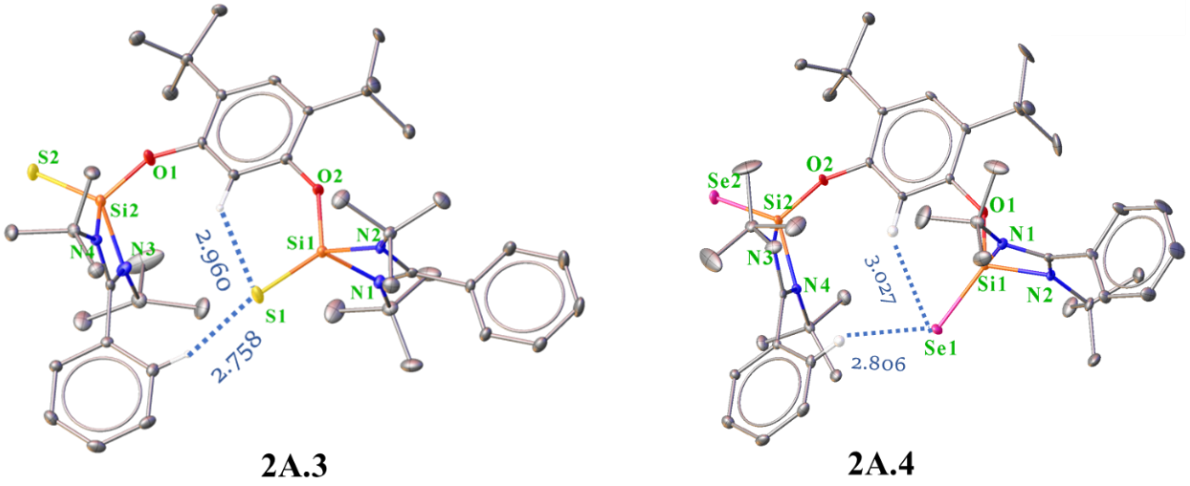

Figure 2A.4. The molecular structures of **2A.3** and **2A.4** showing intramolecular C-H···Ch interactions. C-H···Ch interaction distances (Å) (a) H15···S1 2.971, H4···S1 2.768; (b) H21···Se1 3.027, H36···Se1 2.806, and C-H···Ch angles (°): (a) C15-H15-S1 136.89, C4-H4-S1 137.53; (b) C21-H21-Se1 138.59, C36-H36-Se1 138.68.

2A.2 has a distance of 3.133 Å between H1 and Te1 (Case-I), falling shorter than the sum of their van der Waals radii (3.260 Å), and forms an angle of 132.7° between H1-C1 and Te1 (Figure 2A.5). Of note, the distance between H24 (benzamidinate) and Te1 (Case-II) (3.272 Å) (Figure 2A.5) is larger than the sum of their van der Waals radii by 0.011 Å. Thus, Case-II seems to be very weak. We have also found the presence of two identical intermolecular C-H···Te interactions in the molecular structure of **2A.2**, which has a distance of 3.192 Å between the H atom of the tert-butyl group of one moiety and the tellurium atom of another moiety and ∠C-H-Te of 160.5^0 (Figure 2A.5).

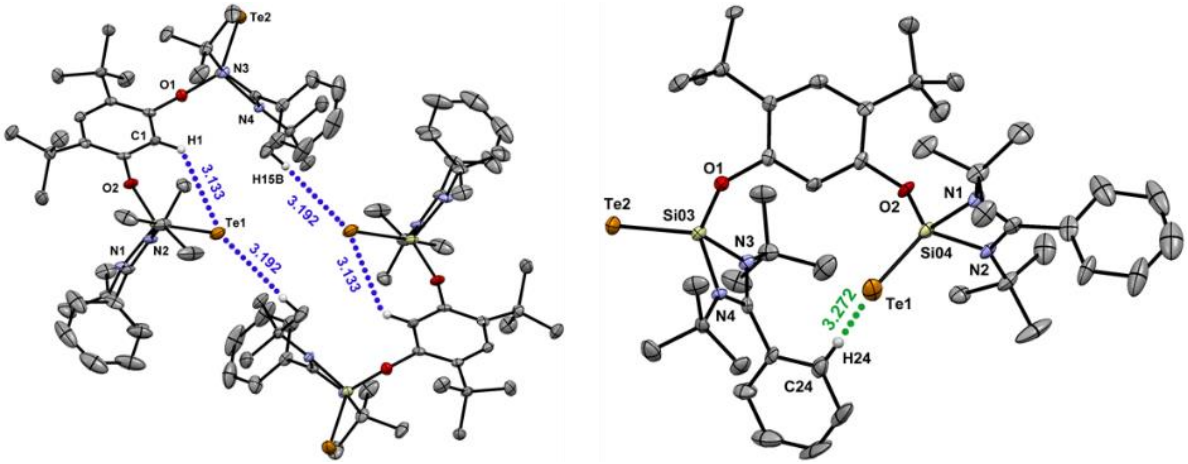

Figure 2A.5. Crystal packing of **2A.2** showing inter and intramolecular C-H···Te interactions.

A difference Fourier map[38] (F_0-F_c) around carbon atoms where hydrogens have interacted with Te atoms has been generated in support of the hydrogen positions for complex **2A.2** (Figures 2A.6). Interestingly here, the intermolecular C-H···Te interaction features sp^3 hybridized C-H bond as acceptor, which is least basic as compared to sp^2 and sp hybridized C-H bond.[39]

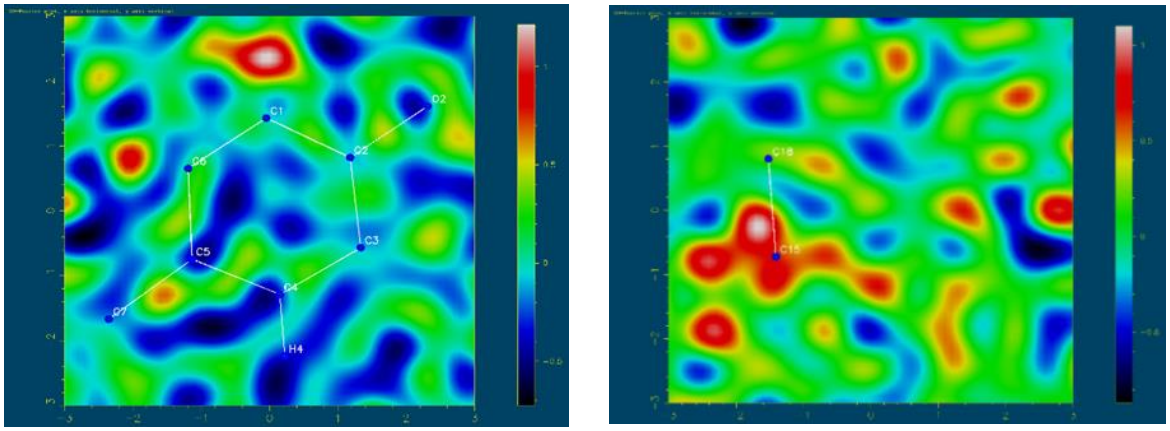

Figure 2A.6. Difference Fourier map (Fo-Fc) of **2A.2**, (i) One aromatic hydrogen can be seen near to C1 (red color), which belongs to C1-H1···Te1, intramolecular interaction; (ii) Hydrogens of the methyl group can be seen around C15 (C15-H15···Te1 intermolecular interaction).

After observing the inter and intramolecular C-H···Te interactions in this work, we remained curious about their presence in the previously reported silanetellurones. We have found a very short C-H···Te distance of 2.561 Å present in NHC-stabilized silanetellurone[6] and 3.052 Å in silanoic telluroester[7] (Chart 2A.2 and Table 2A.2) in their respective molecular structures, which had been unaddressed in the works reported by Driess and co-workers.[6, 7]

Therefore, it can be stated that accumulating abundant negative charge to electropositive tellurium can be turned into a subtle hydrogen bond donor in terms of delocalization of charges and thus further validate their occurrence.

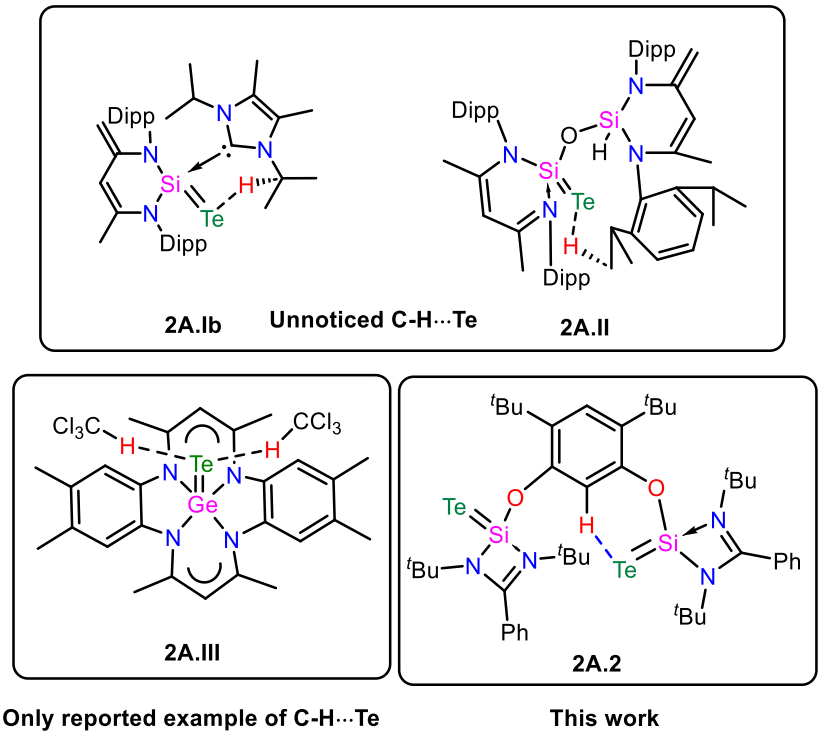

Chart 2A.2. Presence of C-H···Te interactions in previously reported NHC stabilized silanetellurone (**2A.I**) and silanoic telluroester (**2A.II**), which remained unaddressed and only reported C-H···Te interaction (**2A.III**) based on short contacts from crystal structure.

Table 2A.2. Comparison of the structural parameters of the C-H···Te interactions in **2A.I**-**2A.III** and **2A.2**

C-H···Te interaction	Intramolecular		Intermolecular	
	C-H···Te (Å)	∠C-H···Te (^{0})	C-H···Te (Å)	∠C-H···Te (^{0})
2A.I	2.561	154.41	3.013	147.08
2A.II	3.052	103.63	not present	not present
2A.III	not present	not present	2.90 2.67 2.84	151 169 158
2A.2	3.133	132.71	3.192	160.54

Apart from the observation of the C-H···Te interaction in the structure of **2A.2**, we also checked the Te···X (X= N and O) distances (Table 2A.3) to verify the presence of any pnictogen

and chalcogen interactions present there. Although these separations were found to be well considering the non-covalent interaction range for Te···X, further NBO and QTAIM analyses do not support the presence of these interactions either in the crystal structure or the gas phase optimized structure of **2A.2**.

Table 2A.3. Selected bond length of **2A.2** (sum of the vdW radii of Te and N is 3.61 Å while the same of Te and O is 3.58 Å)

Interactions	Bond length (Å)
Te1···O2	3.508(4)
Te2···O1	3.378(4)
Te2···N3	3.587(5)
Te1···N1	3.552(5)

Analogous C-H···S/Se interactions are also observed in **2A.3** and **2A.4**. The H15 and H4 of **2A.3** are close to the sulfur atom at distances 2.971 and 2.768 Å, respectively, which are shorter than the sum of their van der Waals radii (3.00 Å). The angles ∠S1-H15-C15 (136.8°) and ∠S1-H4-C4 (137.5°) indicate a weak interaction between C-H and S atom. In **2A.4,** the H21···Se1 (Case-I) and H36···Se1 distances (Case-II) are 3.027 and 2.806 Å, respectively, which are shorter than their sum of van der Waals radii (3.10 Å) and thus in accordance with the C-H···Se hydrogen bond reported by the group of Tomoda (H···Se = 2.92 Å)[33] but longer than the H···Se hydrogen bond reported by Bertrand and co-workers (H···Se = 2.64, 2.54 Å, respectively).[34]

The variable temperature (VT) ^{1}H NMR was performed in Benzene-d_6 (C_6D_6) in the 288-315 K range using tetramethylsilane (TMS) as an internal standard. Compound **2A.2** shows intra- and intermolecular interactions, whereas compounds **2A.3** and **2A.4** can only form intramolecular ones. The chemical shift of the corresponding C-H···Te bound proton (marked as H_a) got upfielded as the temperature was raised from 288 to 315K for each case. The natural logarithm of chemical shifts (ln δ) is correlated linearly with the inverse of temperature (1/T) within a given temperature range. This can be easily correlated with the Arrhenius-type equation with slope A.[4a] The slope of the ln δ versus 1/T plot denotes energy changes ΔE of the C-H···Ch interaction at a given temperature range and can be calculated from the slope (A) of equation (1) times the universal gas constant (R).

$$\ln(\delta) = \frac{A}{T} + B \quad \text{.....equation (1)}$$

	S	Se	Te
Slope	22.1056	19.1953	18.109
Intercept	15.8827	15.8968	15.897

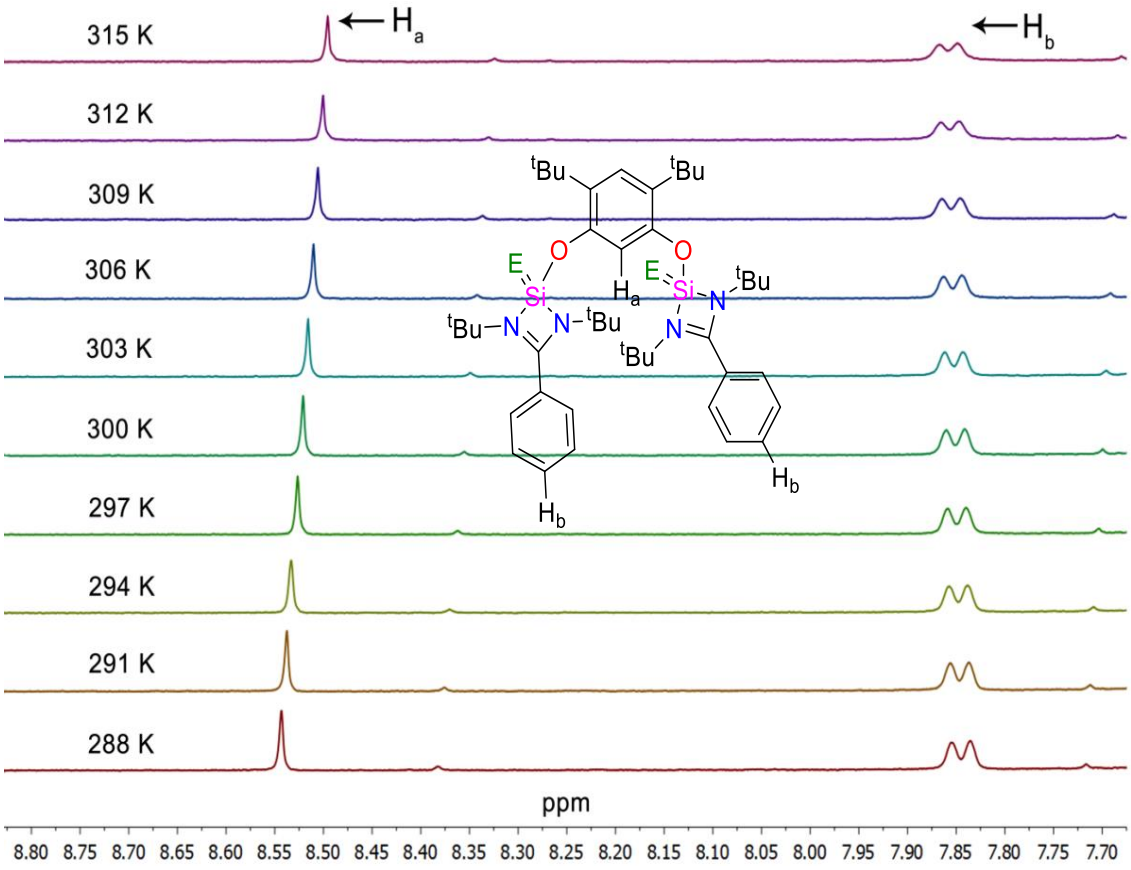

Figure 2A.7. Variable temperature (VT) ^{1}H NMR spectrum of **2A.2** (E = Te).

To prove that these interactions are not arising due to the crystal lattice forces, we have systematically studied ^{1}H NMR with a temperature variation, as Boltzmann's average of the chemical shifts can be correlated linearly with the theoretical binding energy of the hydrogen bond.[40] The ^{1}H NMR of H_a appears at δ 7.87 ppm for **2A.1**, whereupon after complexation, this proton comes at δ 8.52, 8.49, and 8.54 ppm in C_6D_6 at ambient temperature for **2A.2** (Figure 2A.7), **2A.3**, and **2A.4** (Figures 2A.8 and 2A.9 for VT NMR spectra of **2A.3** and **2A.4**), respectively. The prominent gradual upfield shift for H_a for **2A.2** concerning Hb (which is constant) in the VT NMR indicates its hydrogen-bonded nature. Our attempts also dealt with observing the hydrogen-bonded methyl protons of the tert-butyl group of the benzamidinate ring, which is responsible for the intermolecular CH···Te interaction. Due to the fluxional behavior (fast exchange) of the corresponding protons, they remained undetectable in the given temperature range (288 to 315 K).

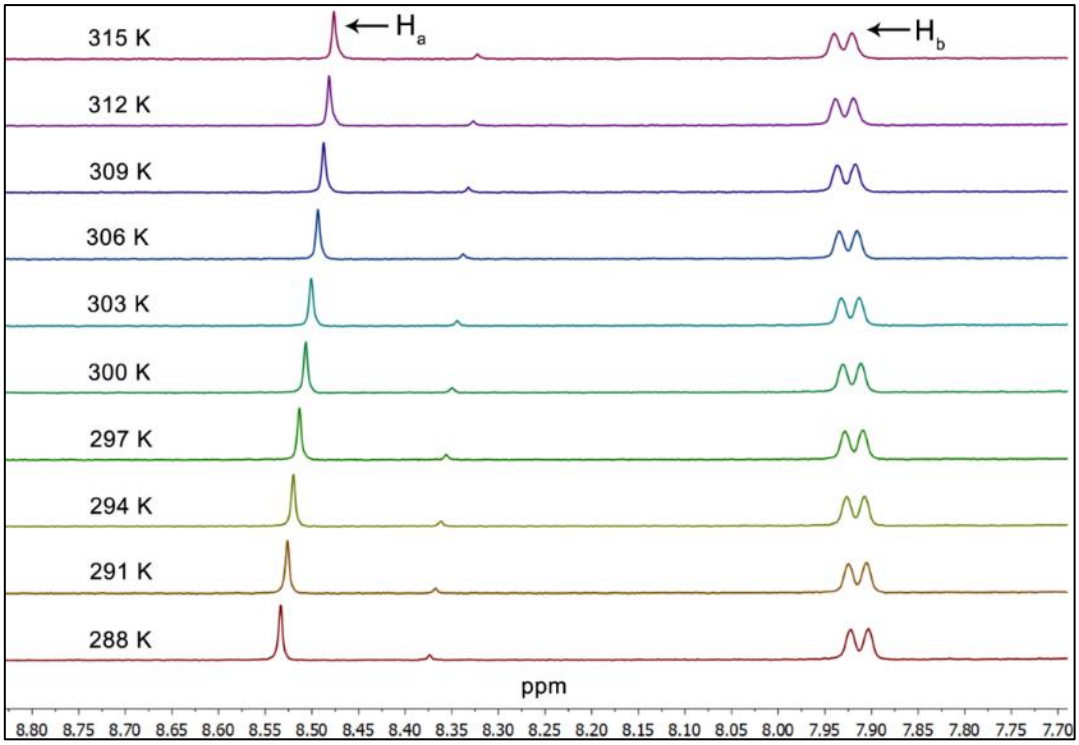

Figure 2A.8. ^{1}H VT NMR of complex **2A.3**.

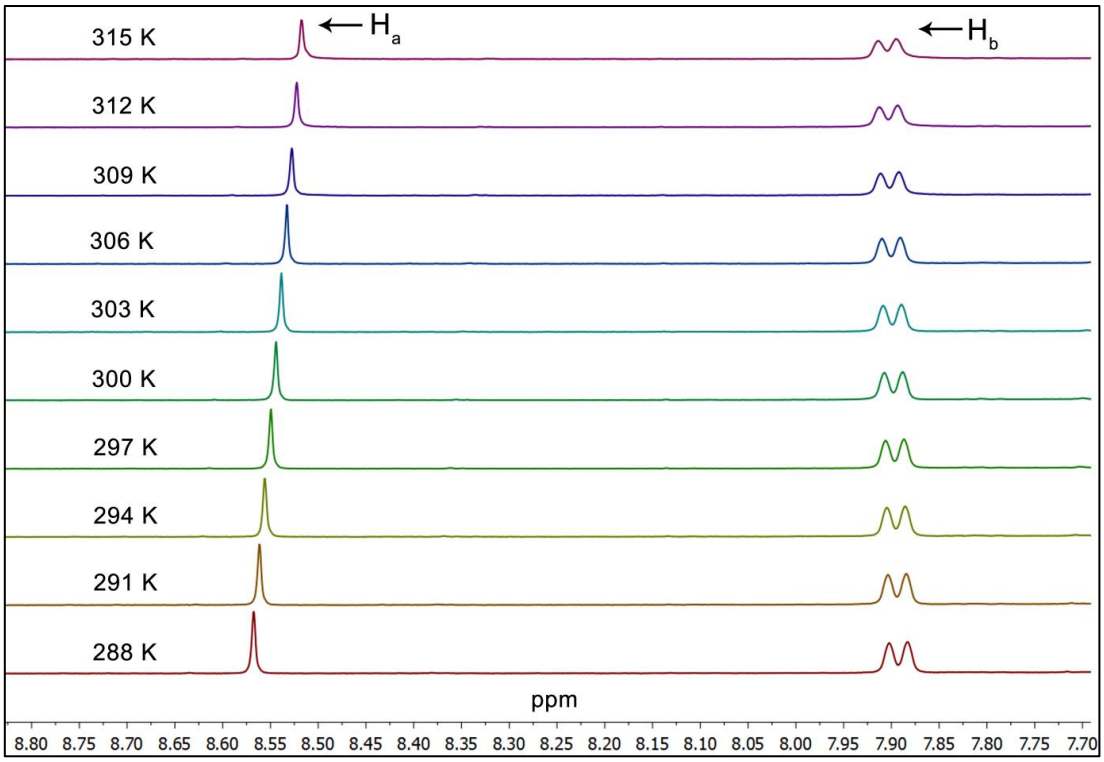

Figure 2A.9. ^{1}H VT NMR of complex **2A.4**.

A linear correlation plot with the natural logarithm of (resorcinolate) proton (H_a) chemical shift (ln δ) with the inverse of the temperature (1/T) (288 to 315 K) with the overall shift of 0.04 ppm is given in Figure 2A.10.

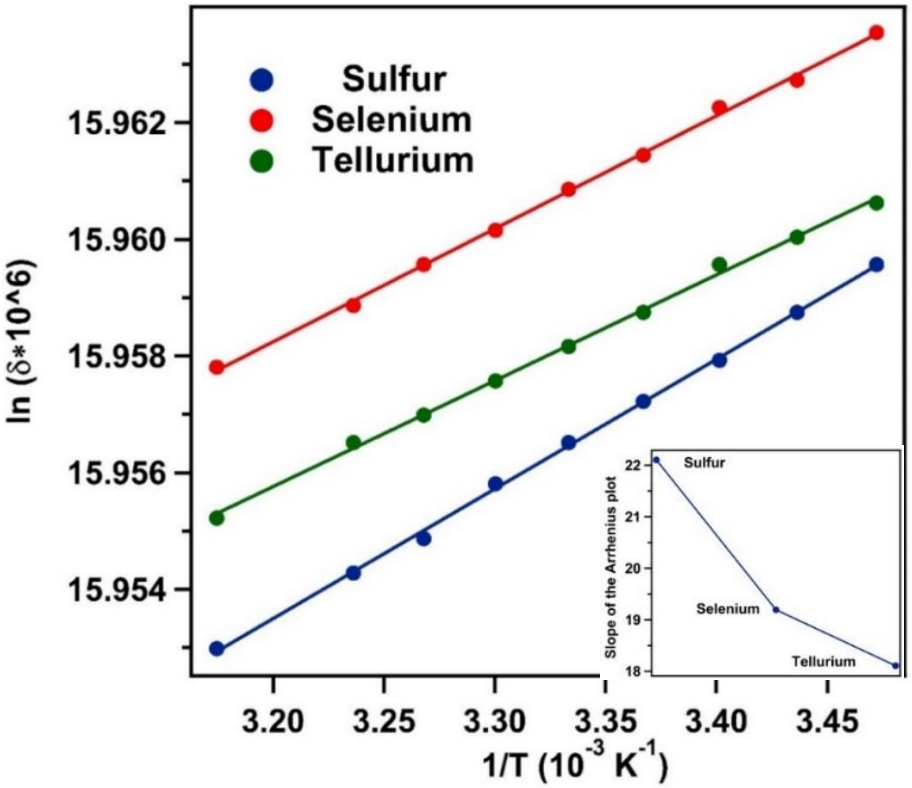

Figure 2A.10. The plot of ln (δ*10^6) vs. 1/T ($10^{-3}K^{-1}$) and comparison of slope (inset).

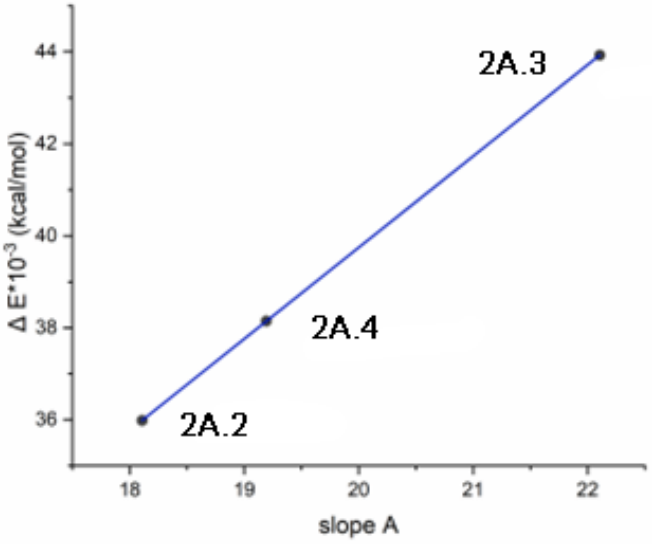

Figure 2A.11. Correlation plot for ΔE and slope A obtained from Figure 2A.10.

We also recorded ^{1}H NMR for complex **2A.2** at 325 K; this gave δ 8.474 ppm for H_a, but the chemical shift for H_b was found to be constant (Figure 2A.7). Unlike the "strong" hydrogen bond, the difference is smaller due to its weak nature and well agreed with weak C-H···O interaction, as documented by Pulay and co-workers in 2003.[41] This comes in line with the Arrhenius-like equation, giving slopes of 18.109, 22.106, and 19.195 for **2A.2**, **2A.3,** and **2A.4**, respectively, and we have plotted the change in the interaction energy (ΔE) with slope

(A) (Figure 2A.11), indicating that the C-H···Ch interaction is relatively the strongest for C-H···S case (inset of Figure 2A.10). This observation corresponds to only Case-I interaction as we could not detect the particular hydrogen for Case-II interaction in ^{1}H NMR due to the overlapping of the peaks for phenyl protons. We have obtained the ^{125}Te and ^{77}Se NMR for complexes **2A.2** and **2A.4 (**Figures 2A.A.4 and 2A.A.12**)**, respectively. The ^{77}Se NMR for **2A.4** comes at -514 ppm, and ^{125}Te for **2A.2** comes at -1242.44 ppm as a sharp singlet. The high field chemical shift of the Te atom indicates the contribution from the ($Si^{\delta+}$-$Te^{\delta-}$) bonding situation as suggested by the groups of Lips and So.[10, 20] A comparison of the ^{125}Te NMR of related Si=Te compounds is given in Table 2A.4. It is also correlated with **2A.Ib**[6] and **2A.II**[7] in Table 2A.4 that despite having a very short distance between C-H···Te in both the compounds, a singlet peak was observed at room temperature for each case and could be attributed to space separation. Unlike downfield chemical shifts of a few reported silanechalcogenones,[42, 43] the upfield chemical shift for both **2A.2** and **2A.4** indicates higher electronic surroundings near the nuclei owing to the presence of lone-pairs (*p*-type) around the chalcogen center.

Table 2A.4. Comparison of ^{125}Te chemical shift for complexes **2A.I-2A.III'** and **2A.2**

Complexes	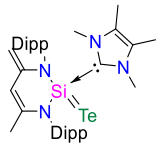 **2A.Ia**	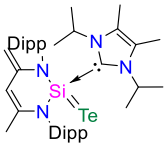 **2A.Ib**	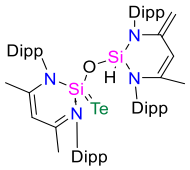 **2A.II**	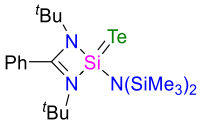 **2A.III'**	**2A.2**
^{125}Te (δ in ppm)	-1010.4	-982.5	-1076.7 and -1105.5	-1093	-1242.4

We have also recorded proton (^{1}H) coupled ^{125}Te and ^{77}Se NMR for **2A.2** and **2A.4** at -53 °C and -50°C, respectively, in $CDCl_3$, which showed a broadening of spectrum for both compounds (Figures 2A.A.5 and 2A.A.13). For compound **2A.2,** we noticed the splitting of ^{125}Te signal, which might be due to the strengthening of ^{125}Te···^{1}H interaction at a lower temperature. However, no resolved J-coupling was observed in either of the ^{125}Te spectra. The splitting is unclear, and it may occur due to the small coupling because of very weak interaction, which may be hidden within the signal broadening. Therefore, we refrained from discussing any resolved spin-spin coupling for both cases.[30]

2A.3.4 Theoretical Studies. Ground state geometry optimization of the complexes **2A.2**-**2A.4** and **(2A.2)$_2$** were performed with tight convergence criteria and ultrafine grid at the B3LYP-

D3/def2-TZVPP level using the Gaussian 09 program package.[44] Various theoretical approaches, such as natural bond orbital (NBO), Wiberg bond index (WBI), quantum theory of atom in molecules (QTAIM), and non-covalent interaction (NCI) index analyses were performed to validate the bonding situation in **2A.2**-**2A.4** and **(2A.2)$_2$** (dimer of **2A.2**).[45-48] The optimized structures of these complexes are denoted as **2A.2m**-**2A.4m** (Figure 2A.12) and **(2A.2m)$_2$** (Figure 2A.13) are confirmed to be energy minima from vibrational frequency calculations. Second-order perturbative energies [$E^{(2)}$] for various interactions, i.e., C-H···Ch interactions, were calculated from the NBO analysis using the NBO6.0 program package.[46] It is found that the C-H···Te, C-H···S, C-H···Se non-bonded distances in the optimized gas-phase structures **2A.2m**-**2A.4m** and **(2A.2m)$_2$** (Figures 2A.12 and 2A.13) are similarly short, as were observed in the crystal structures.

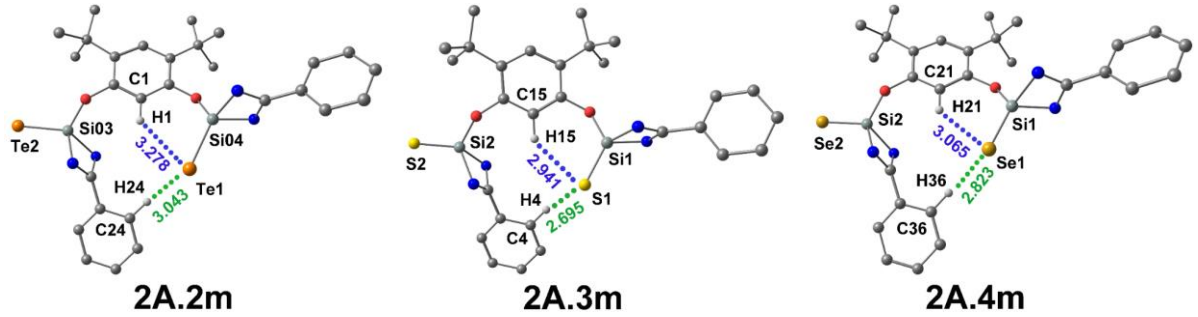

Figure 2A.12. Optimized gas-phase geometries of the complexes **2A.2**-**2A.4** named as **2A.2m**-**2A.4m**, respectively.

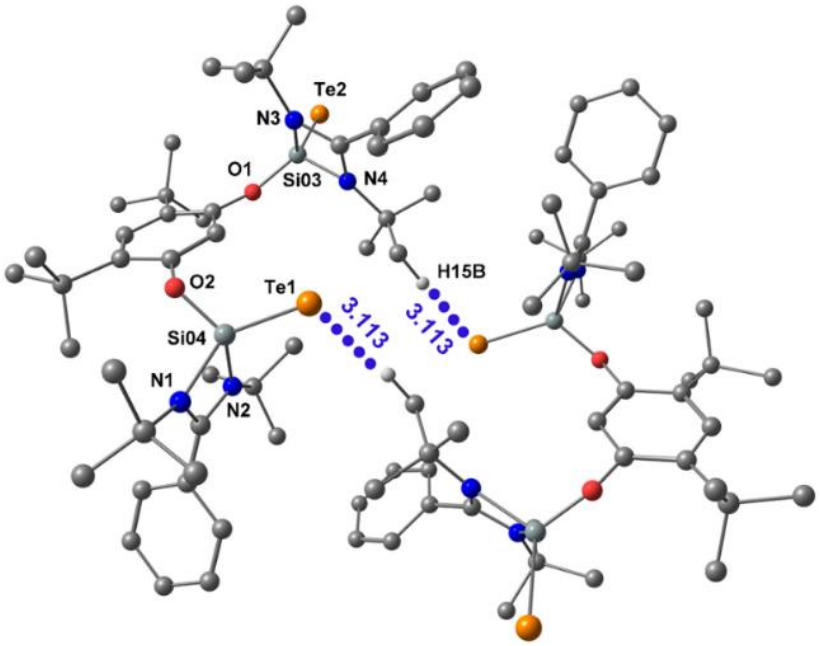

Figure 2A.13. Optimized gas-phase geometries of the dimer of the complex **2A.2** named as **(2A.2m)$_2$**.

As the hydrogen positions in the X-ray crystal structures cannot be determined accurately, we have optimized only the hydrogen atoms of the complexes **2A.2**-**2A.4** and **(2A.2)$_2$**, keeping all other atoms fixed in their respective positions of the crystal structures. Tables 2A.5 and 2A.6 present a comparison of the structural parameters of the complexes **2A.2**-**2A.4** and **(2A.2)$_2$** obtained from their crystal structures with unoptimized hydrogen atoms, crystal structures with optimized hydrogen atoms **2A.2m′**-**2A.4m′** and **(2A.2m′)$_2$**, and gas-phase structures with full optimization **2A.2m**-**2A.4m** and **(2A.2m)$_2$**. It is evident that the structural parameters of the three complexes obtained from the crystal structures are not very different from those obtained from the fully optimized or partially optimized crystal structures. Interestingly, the crystal structure of complex **2A.2**, with the hydrogen positions optimized, shows reasonable short contact for both the Case-I and Case-II types C-H···Te interactions, although the crystal structure shows only the Case-I interaction. It is important to mention that we have performed the NBO and AIM calculations on the crystal structures with optimized hydrogens apart from the gas-phase structures.

Table 2A.5. Structural parameters and $E^{(2)}$ values (kcal/mol) of C-H···Ch interaction of the complexes in the crystal structures (**2A.2**-**2A.4**), crystal structures with optimized hydrogens (**2A.2m′**-**2A.4m′**), and gas-phase optimized structures (**2A.2m**-**2A.4m**)

	Crystal structures		**Crystal structures with optimized hydrogens**		**Gas-phase optimized structures**	
	case-I	**case-II**	**case-I**	**case-II**	**case-I**	**case-II**
Complex 2A.2						
^{d}C-H···Te (Å)	3.133	3.272	3.054	3.137	3.278	3.043
∠C-H-Te (°)	132.7°	153.5°	130.3°	155.2°	132.1°	148.1°
$E^{(2)}$	0.62	0.76	1.37	1.95	0.61	1.96
Complex 2A.3						
^{d}C-H···S (Å)	2.971	2.768	2.875	2.643	2.941	2.695
∠C-H-S (°)	136.9°	137.5°	135.4°	138.8°	130.7°	152.0°
$E^{(2)}$	0.50	1.05	1.16	2.76	0.68	2.57
Complex 2A.4						
^{d}C-H···Se (Å)	3.029	2.813	2.930	2.693	3.065	2.823
∠C-H-Se (°)	138.7°	138.5°	137.3°	139.2°	131.3°	150.6°
$E^{(2)}$	0.63	1.36	1.46	3.41	0.68	2.30

^{d}C-H···Te, ^{d}C-H···S, and ^{d}C-H···Se stand for corresponding distances.

Table 2A.6. Structural parameters and $E^{(2)}$ values (kcal/mol) of intermolecular C-H···Ch interactions in the dimer of complex **2A.2** in the crystal structure **(2A.2)$_2$**, crystal structure with optimized hydrogen atoms **(2A.2m′)$_2$**, gas-phase optimized structure **(2A.2m)$_2$**

	Crystal structures	Crystal structures with optimized hydrogens	Gas-phase optimized structures
Dimer of Complex 2A.2			
[d]C-H···Te (Å)	3.192	3.109	3.113
∠C-H-Te (˚)	160.6˚	156.3˚	162.7˚
$E^{(2)}$	0.68	1.20	1.93

[d]C-H···Te stands for corresponding distance.

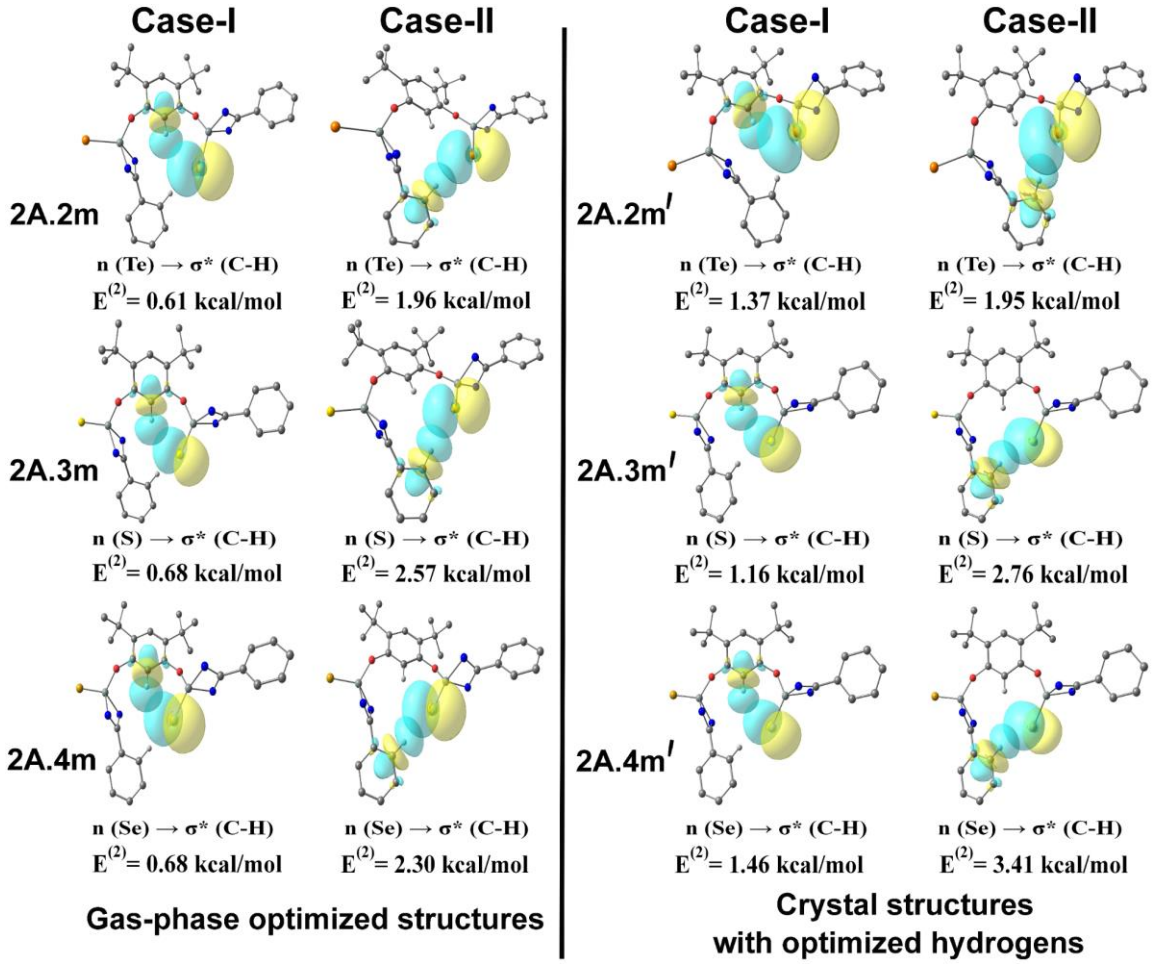

Figure 2A.14. NBO overlaps for the case-I and case-II interactions with $E^{(2)}$ values in the crystal structures with optimized hydrogens (**2A.2m′-2A.4m′**) and gas-phase optimized structures (**2A.2m-2A.4m**) of the complexes **2A.2-2A.4**.

As the present work deals with the C-H···Te interaction, we are engrossing our analysis primarily on compound **2A.2**. NBO analysis shows an overlap between the lone-pair orbital of

the Te atom and the σ* orbital of the C-H bond for the Case-I and Case-II interactions in the gas-phase structure **2A.2m** (Figure 2A.14). It is apparent that the $E^{(2)}$ value for the Case-II (1.96 kcal/mol) is larger than that for the Case-I (0.61 kcal/mol) in **2A.2m.** The same trend in the $E^{(2)}$ value has been found for the Case-I (1.35 kcal/mol) and Case-II (1.88 kcal/mol) interactions in the crystal structure **(2A.2m′)** of **2A.2** (Figure 2A.14). The $E^{(2)}$ value found for the intermolecular C-H···Te interaction in **(2A.2m)₂** is 1.93 kcal/mol. NBO overlap for the Case-I and Case-II interactions in the gas-phase optimized structures **(2A.2m-2A.4m)** and crystal structures with optimized hydrogens (**2A.2m′-2A.4m′**) of the complexes are shown in Figure 2A.14. It is noteworthy that the $E^{(2)}$ values for the C-H···Te, C-H···S, and C-H···Se interactions in the gas-phase structures (**2A.2m-2A.4m)** of the complexes are not very much different from each other. The WBI, Si=Ch charge separation values for the Si=Ch (Ch = S, Se, and Te) bonds, bond-length of Si-Ch bond in the gas phase and crystal structures of the complexes **2A.2-2A.4** have been provided in Table 2A.7. The WBI values for the C-H···Te bound Si-Te and free Si-Te in the gas-phase structure (**2A.2m**) of **2A.2** are 1.551 and 1.570, respectively (Table 2A.7 for **2A.3** and **2A.4**). Further, the higher charge separation (Δq) in the Si-Te1 (2.312 au) compared to that in the Si-Te2 (2.278 a.u.) also implies that the former has more of $Si^{\delta+}$-$Te^{\delta-}$ character than the latter one. Further, hyperconjugation involving delocalization of the electron density from the Te lone-pair orbital to the σ* orbital of the Si-O and Si-N bond is notably absent in **2A.2m'-2A.4m'** and **2A.2m-2A.4m**. However, hyperconjugation from the O and N lone-pair (p-type) orbitals to the σ* orbital of the Si-Ch bond is present in **2A.2m'-2A.4m'** and **2A.2m-2A.4m** (Table 2A.8).

Table 2A.7. WBI of Si=Ch (Ch = S, Se, Te) bond, charges on Si (q_{Si}) and Ch (q_{ch}) atoms, charge separation on Si=Ch ($\Delta q_{S=Ch}$), and bond length of Si=Ch (r, Å) bond in the crystal structures with optimized hydrogens (**2A.2m′-2A.4m′**) and gas-phase optimized structures (**2A.2m-2A.4m**) of the complexes **2A.2-2A.4**

	Crystal structures with optimized hydrogens		**Gas-phase optimized structures**	
	Si1=Ch1	**Si2=Ch2**	**Si1=Ch1**	**Si2=Ch2**
Complex 2A.2				
WBI	1.524	1.549	1.551	1.570
q_{Te}	-0.632	-0.622	-0.611	-0.597
q_{Si}	1.726	1.704	1.701	1.682
$\Delta q_{Te=Si}$	2.358	2.326	2.312	2.279
$r_{Te=Si}$	2.332	2.341	2.346	2.347

Complex 2A.3				
WBI	1.479	1.497	1.505	1.541
q_S	-0.868	-0.842	-0.847	-0.824
q_{Si}	1.908	1.883	1.894	1.865
$\Delta q_{S=Si}$	2.776	2.725	2.741	2.689
$r_{S=Si}$	1.968	1.978	2.119	2.118
Complex 2A.4				
WBI	1.514	1.522	1.542	1.573
q_{Se}	-0.780	-0.760	-0.753	-0.732
q_{Si}	1.836	1.814	1.816	1.790
$\Delta q_{Se=Si}$	2.616	2.574	2.569	2.522
$r_{Se=Si}$	2.100	2.115	1.975	1.973

q_{Ch} and q_{Si} stand for charges on chalcogen (S, Se, and Te) and Si atoms, respectively. Si1=Ch1 is having C-H···Ch interaction, Si2=Ch2 is free from C-H…Ch interaction.

Table 2A.8. $E^{(2)}$ values (kcal/mol) for hyperconjugation from nitrogen/oxygen lone-pair orbital to σ* orbital of Si-Ch bond in the crystal structures with optimized hydrogen (**2A.2m'-2A.4m'**) and gas-phase optimized structures (**2A.2m-2A.4m**)

	n(N)→σ*(Si-Ch)		**n(O)→σ*(Si-Ch)**	
	free arm	**C-H···Ch bound arm**	**free arm**	**C-H···Ch bound arm**
crystal structures with optimized hydrogen				
2A.2m'	6.81	2.15	5.28	8.60
2A.3m'	5.84	6.09	5.96	6.62
2A.4m'	7.34	6.80	6.10	6.70
gas-phase optimized structures				
2A.2m	6.05	6.09	5.02	6.41
2A.3m	6.01	6.00	5.07	6.53
2A.4m	6.71	6.61	5.19	6.53

Si-Te bond is better visualized as $Si^{\delta+}$-$Te^{\delta-}$ (charge-separated species) rather than Si=Te bond. Natural resonance theory (NRT)[49] was performed to understand the partial double bond character of the Si-Te bond. We tried to perform an NRT calculation for **2A.2m** but failed after several attempts. We then tried to perform NRT by substituting all tert-butyl groups by methyl group to speed up the calculation, as handling 120 atoms by NRT is a potential challenge at

such a large basis set, i.e., def2-TZVPP. Then, we made a model compound **2A.2m^{model}** by substituting the tert-butyl group with a methyl group and focussing the resonance on the 4-membered ring (amidinate) and chalcogen atoms. We further optimized **2A.2m^{model}** to confirm that the geometrical parameters do not differ more than 1% from the original, optimized gas-phase structure **2A.2m**. We have found that the Si$^{\delta+}$-Te$^{\delta-}$ structure dominates over the Si=Te structure of the model compound (Figure 2A.15).[21, 22] The NRT calculation reveals that the betaine form of the Si-Te bond is responsible for the C-H···Te interaction.[22, 34]

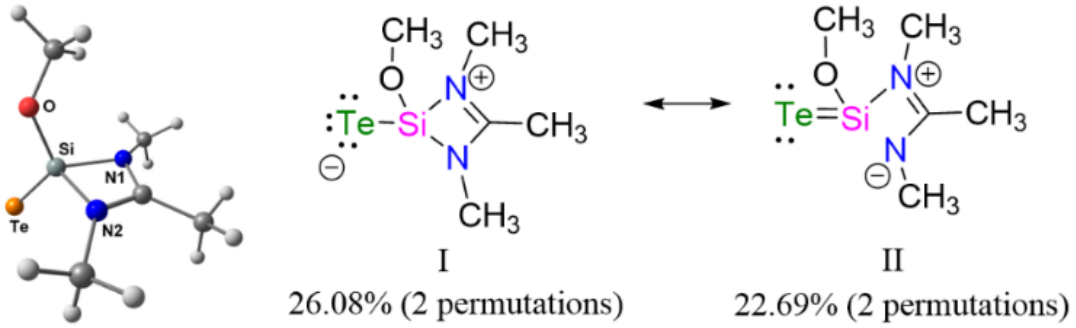

Figure 2A.15. Optimized structure of **2A.2m^{model}** and its leading resonance structure from NRT analysis.

Various molecular orbitals (Figure 2A.16 for **2A.2m**) were scrutinized to understand the bonding pictures of the complexes. The HOMO and HOMO–2 are the lone-pair orbitals on the two Te atoms, while the HOMO-1 and HOMO-3 are the π-type bonding[29] orbitals between Si and Te.

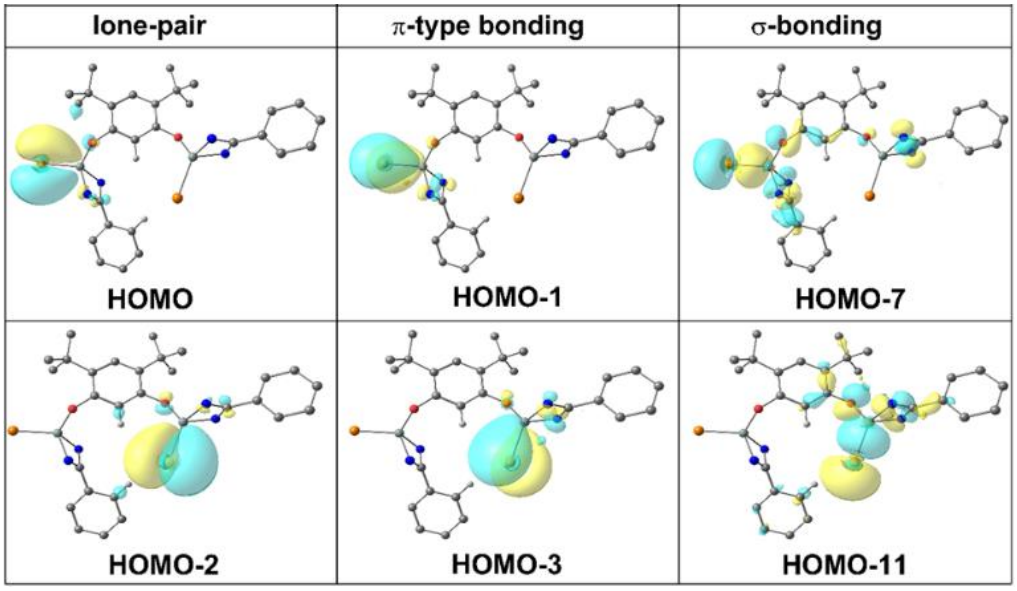

Figure 2A.16. Various MOs of **2A.2m** complex showing lone-pair orbitals on the Te atom, π-type bonding, and σ-bonding orbitals on the Si=Te bonds of both arms.

The MOs of the **2A.3m** and **2A.4m** complexes are provided in Figures 2A.17 and 2A.18, respectively. Each of the HOMO/ HOMO-2 shows the Te lone-pair orbitals, and HOMO-1/HOMO-3 shows the π-type bonding orbitals in Figure 2A.16. Si-Ch bond is a single bond linkage and can be best visualized as $Si^{\delta+}$-$Ch^{\delta-}$ which has a partial double bond character.

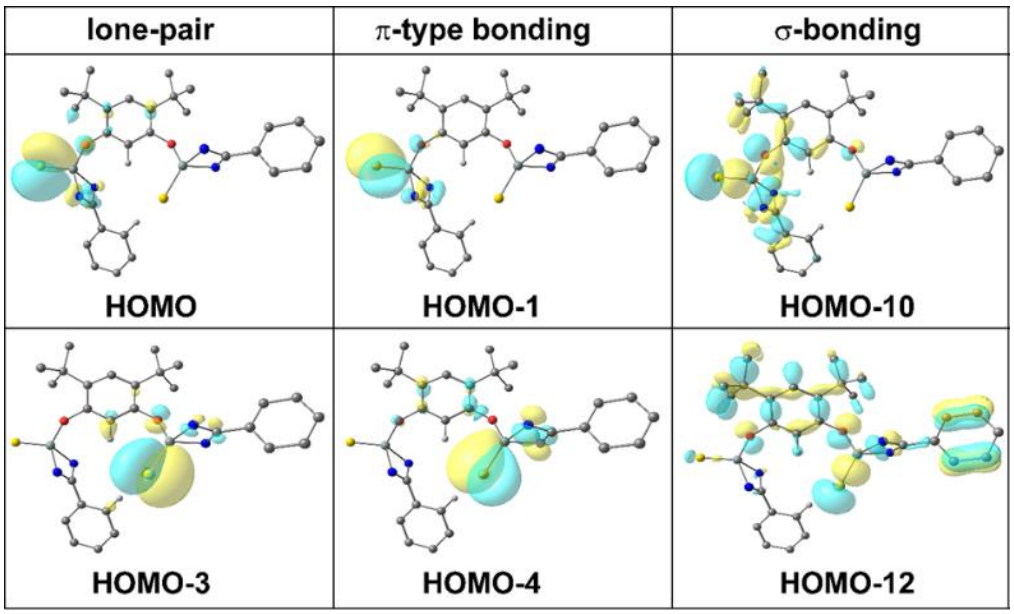

Figure 2A.17. Various MOs of **2A.3m** complex showing lone-pair orbitals on the S atom, π-type bonding, and σ-bonding orbitals on the Si=S bonds of both arms.

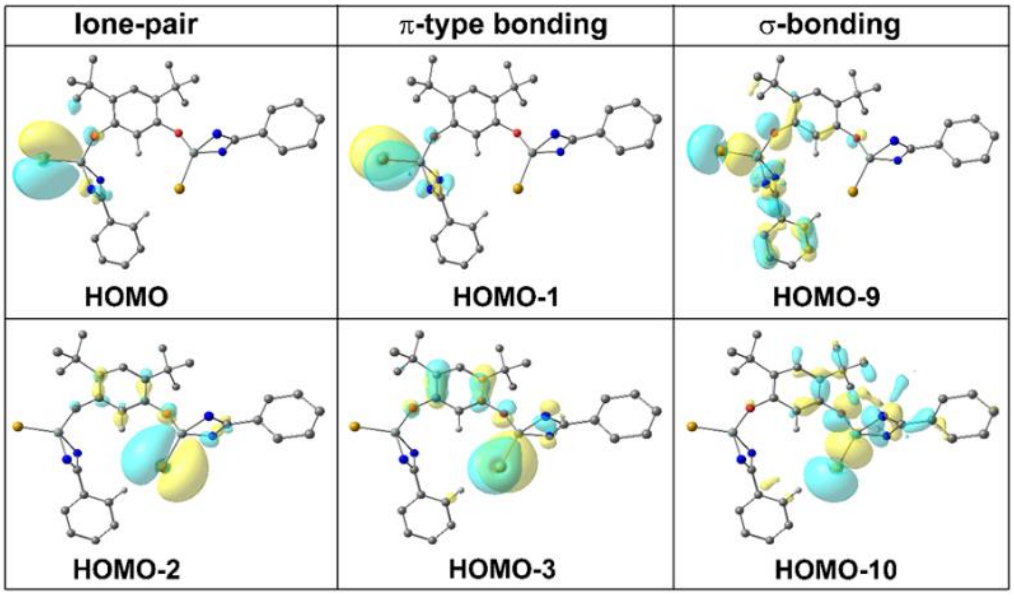

Figure 2A.18. Various MOs of **2A.4m** complex showing lone-pair orbitals on the Se atom, π-type bonding, and σ-bonding orbitals on the Si=Se bonds of both arms.

NBO deletion analysis was also performed for **2A.2m-2A.4m** and **(2A.2m)$_2$** to get a deeper insight into the orbitals involved in the C-H···Ch interactions. It is intriguing to note that

the occupancy of the σ^* orbital of the C-H bond decreases while that of the lone-pair (n) orbitals of the chalcogen atoms increases after the deletion the C-H···Ch interaction in all of the complexes (Table 2A.9). Thus, the delocalization of the electron density from the Ch lone-pair orbitals to the σ^* of the C-H bond due to the presence of the C-H···Ch interaction is re-confirmed.

Table 2A.9. Occupancy of the lone-pair orbital (n_p) of the chalcogen atoms (Ch = S, Se, Te) and σ^* orbital of the C-H bond on deleting case-I and case-II interactions present in the gas-phase optimized structures (**2A.2m-2A.4m**) of the complexes **2A.2-2A.4** calculated by NBO deletion analysis

	Occupancy of orbitals after deletion of interactions		
	None deleted	**case-I deleted**	**case-II deleted**
Complex 2A.2m			
Lone-pair orbital (n_p) of Te atom	1.798	1.801	1.805
σ^*_{C-H} of case-I	0.015	0.012	0.014
σ^*_{C-H} of case-II	0.022	0.022	0.014
Complex 2A.3m			
Lone-pair orbital (n_p) of S atom	1.798	1.800	1.802
σ^*_{C-H} of case-I	0.015	0.012	0.015
σ^*_{C-H} of case-II	0.021	0.021	0.013
Complex 2A.4m			
Lone-pair orbital (n_p) of Se atom	1.796	1.798	1.801
σ^*_{C-H} of case-I	0.015	0.012	0.015
σ^*_{C-H} of case-II	0.022	0.022	0.014
Complex $(2A.2m)_2$			
Lone-pair orbital (n_p) of Te atom	1.806	1.807	
σ^*_{C-H}	0.012	0.007	

Finally, we have performed the topological analysis of electron density in the gas-phase [**2A.2m-2A.4m** and $(2A.2)_2$] as well as crystal structures [**2A.2m′-2A.4m′** and $(2A.2m')_2$] of the complexes using QTAIM analysis to analyze the nature of the bonding in the C-H···Ch interactions. QTAIM analysis has been carried out using Multiwfn software.[45] $\rho(r)$ denotes the electron density at the bond-critical point (BCP) of the C-H···Te interaction, whereas λ_2 is the second eigenvalue of the electron density Hessian (second-derivative) matrix. λ_2 tells about the

type of interaction present in molecular systems. $\lambda_2<0$ and $\lambda_2>0$ correspond to the attractive and repulsive interaction.[45] Molecular graph and contour plots for **2A.2m-2A.4m** and **(2A.2m)$_2$** are given in Figure 2A.19 and Figure 2A.20, respectively.[50]

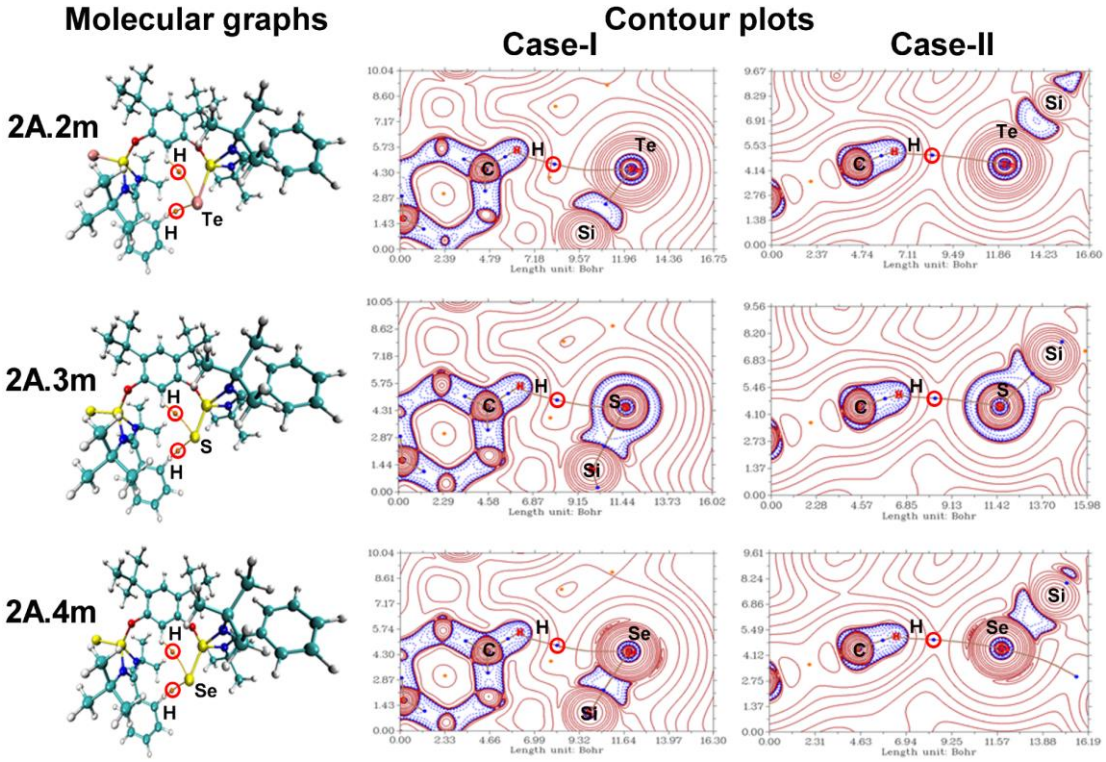

Figure 2A.19. Molecular graphs and contour plots of the $\nabla^2\rho(r)$ in the C-H-Ch plane for the case-I and case-II interactions in the gas-phase optimized structures (**2A.2m-2A.4m)** of the complexes **2A.2-2A.4** calculated from QTAIM analysis.

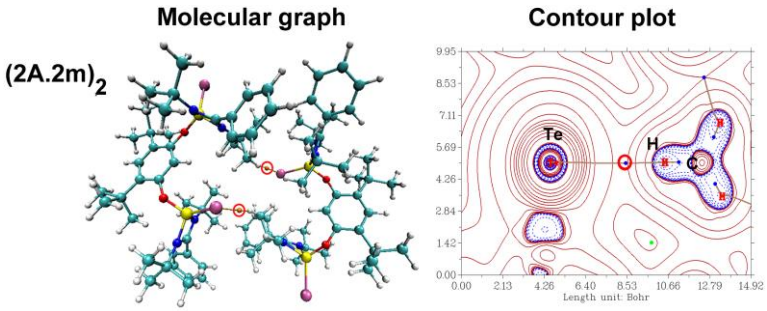

Figure 2A.20. Molecular graph and Contour plot of the $\nabla^2\rho(r)$ in the C-H-Te plane for the intermolecular interactions in the gas-phase optimized structures **(2A.2m)$_2$** of the complexes **(2A.2)$_2$** calculated from QTAIM analysis. For brevity, only the BCPs (marked with the red circle) for the C-H···Te intermolecular interactions are shown in the molecular graphs. In the contour plots, the small blue circles represent bond critical points (BCP) (marked with the red circle), while the red solid and blue dotted lines indicate regions with $\nabla^2\rho(r) <0$ and $\nabla^2\rho(r)> 0$, respectively.

The results obtained from the AIM analysis establish that C-H···Te is a weak interaction. Detailed results of the AIM analysis for the gas-phase and crystal structures of **2A.2-2A.4** and **(2A.2)$_2$** are provided in Table 2A.10, respectively. The strength of the C-H···Ch interaction is also calculated from the potential energy density [V(r)] at the BCP of C-H···Ch interaction obtained from the QTAIM calculation (Table 2A.10).

Table 2A.10. ρ(r), λ_2, and strength of C-H···Ch interaction (E, kcal/mol) calculated from V(r) at the BCP of case-I and case-II in the crystal structures with optimized hydrogen atoms [**2A.2m′-2A.4m′** and **(2A.2m′)$_2$**] and gas-phase optimized structures [**2A.2m-2A.4m** and **(2A.2m)$_2$**] of the complexes **2A.2-2A.4** and (**2A.2**)$_2$

	Crystal structures with optimized hydrogen		**Gas-phase optimized structures**	
	case-I	**case-II**	**case-I**	**case-II**
Complex 2A.2				
ρ	0.010	0.008	0.007	0.010
λ_2	-0.004	-0.005	-0.002	-0.006
E	1.39	1.02	0.92	1.24
Complex 2A.3				
ρ	0.009	0.012	0.009	0.012
λ_2	-0.005	-0.010	-0.004	-0.009
E	1.42	1.94	1.28	1.80
Complex 2A.4				
ρ	0.010	0.013	0.008	0.011
λ_2	-0.005	-0.010	-0.003	-0.008
E	1.44	2.01	1.16	1.59
Dimer of complex (2A.2)$_2$				
ρ	0.007		0.008	
λ_2	-0.004		-0.005	
E	0.90		1.05	

Moreover, we have performed NCI analysis[47, 48] using Multiwfn software[45] to visualize the presence of C-H···Ch interactions in the forms of NCI isosurfaces. NCI isosurface for complexes **2A.2m-2A.4m** are given in Figure 2A.21. The NCI plots clearly indicate the presence of the C-H···Ch interactions in all three complexes.

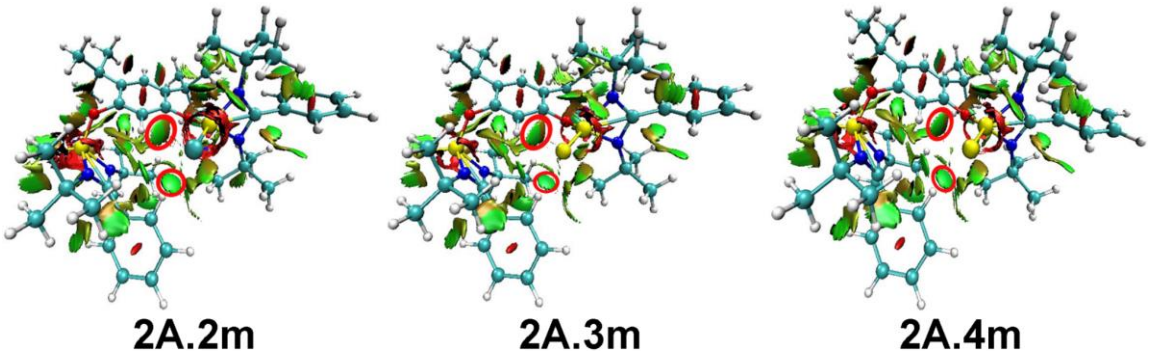

Figure 2A.21. NCI plot for the C-H···Ch interaction in **2A.2m-2A.4m**. Isosurface corresponds to C-H···Ch interaction is marked by red-colored circles. Gradient isosurface following blue-green-red color scheme over the range of -0.05 < Sign (λ_2)ρ(r) < +0.05, where blue, green, and red color denote very strong attraction, weak interaction, and strong repulsion, respectively.

Electrostatic potential mapping for **2A.2m-2A.4m** (Figure 2A.22) shows that the negative charge cloud on chalcogen atoms decreases in the order of S>Se>Te, which is in line with the strength of the C-H···Ch (S, Se, and Te) interaction found in this work.

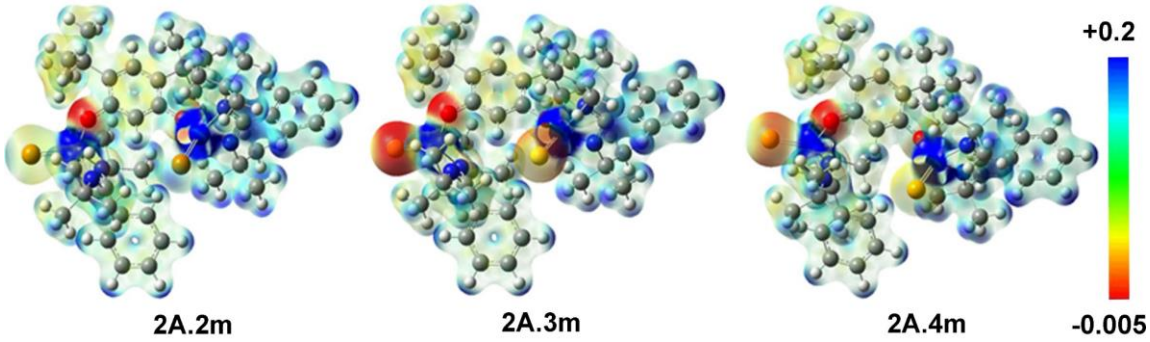

Figure 2A.22. Electrostatic potential maps for **2A.2m-2A.4m** plotted over the range of -0.005 a.u. (red) to +0.2 a.u. (blue). The isosurface is drawn at 0.03 a.u.

2A.3.5 Reaction with oxygen donor. About a century ago, Kipping tried to isolate "silanone" but obtained a polymeric siloxane.[51] In 1998, Tokitoh *et al*. showed that the enhanced reactivity of a putative Si=O is a result of high energy *σ*- and *π*-orbital, i.e., unfavorable overlapping between *pπ*(Si) and *pπ*(O).[32-34] The higher polarity of a $Si^{\delta+}$-$O^{\delta-}$ bond than that of the heavier chalcogen analogues comprise of $Si^{\delta+}$-$Ch^{\delta-}$ bonds, and that can be attributed to the rapid head-to-tail oligomerization process to generate σ bonded siloxane[52] thus resulting in the isolation of "silanone," most desirable compound in main group chemistry for a long time until when Kato *et al*. reported the free Si=O in 2017[53] which paved the way for more results to flourish in.[54] We wanted to use compound **2A.1** in this aspect; for that, we carried out the reaction of **2A.1** with trimethyl N-oxide, but contrary to our expectation, we obtained an unusual

dimerized product **2A.5** with two siloxane moieties (Scheme 2A.2). The ^{1}H NMR of the same shows two sets of singlet at δ 1.02 and 1.48 ppm for *t*Bu groups of resorcinolate moiety and amidinate backbone, respectively, which are shifted upfield than those of **2A.1** (δ 1.24 and 1.74 ppm). The ^{29}Si NMR shows a sharp singlet at δ -114.09 ppm, which is comparable with the penta-coordinated Si atoms.[55-58]

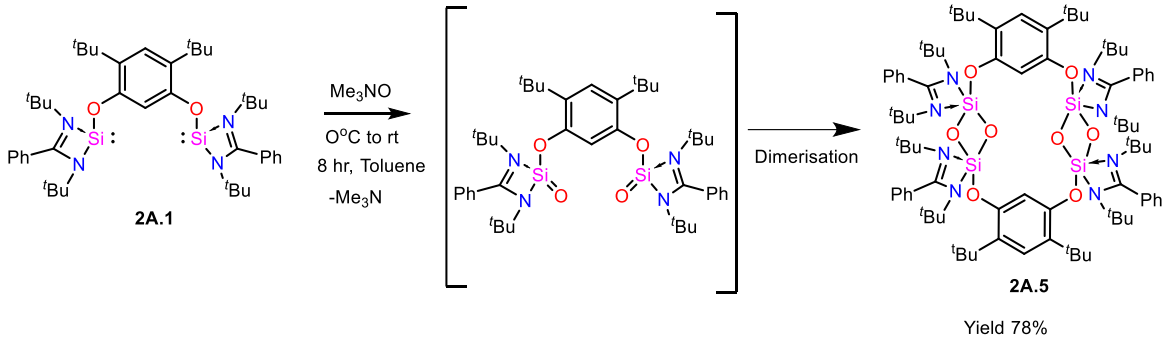

Scheme 2A.2. Synthesis of complex **2A.5**.

Compound **2A.5** crystallizes in the monoclinic space group *C2/c*. The molecular structure of **2A.5** is shown in Figure 2A.23. Each silicon center is five coordinated with two four-membered Si_2O_2 rings, attaining a distorted trigonal bi-pyramidal geometry. Two types of Si-N bonds are present, i.e., N2-Si1 1.948(3) and N1-Si1 1.830(3) Å and three types of Si-O bonds, which are Si1-O3 1.656(3), Si1-O1 1.677(3) and Si1-O2 1.710(3) Å. The penta-coordinated silicon center is differently substituted at axial and equatorial positions. While axial positions are occupied by one nitrogen (N2) of benzamidinate moiety and other being oxygen (O2) of siloxane (Si_2O_2) moiety with O2-Si1-N2 angle of 164.3(1)°, equatorial positions are held by nitrogens (N1) of benzamidinate ring, oxygen (O1) from siloxane (Si_2O_2) moiety and another oxygen (O3) from resorcinolate moiety, respectively. The angles at equatorial positions are as follows O3-Si1-O1 124.7(1)° O1-Si1-N1 120.2(1)° and O3-Si1-N1 112.5(1)°. These differences in bond lengths and bond angles are indicative of its plausible distorted geometry. The Si1···Si2 distance in **2A.5** is 2.490(2) Å, which is 0.14 Å longer than the normal Si-Si σ bond (2.35 Å), and the O1···O2 distance is 2.281(3) Å. Due to the presence of the nitrogen atoms, the electron density is shifted towards the amidinate ligands, leading to the increase in the Si···Si distances. So, the rings can be best described as featuring four equivalent localized Si-O σ-bonds,[11, 41] which is in accordance with the modified neglect of diatomic overlap (MNDO)[59] calculations (a semi-empirical method used in quantum chemical calculations, limited mainly to second-row elements of the periodic table) on the parent cyclodisiloxane, $H_4Si_2O_2$.[60]

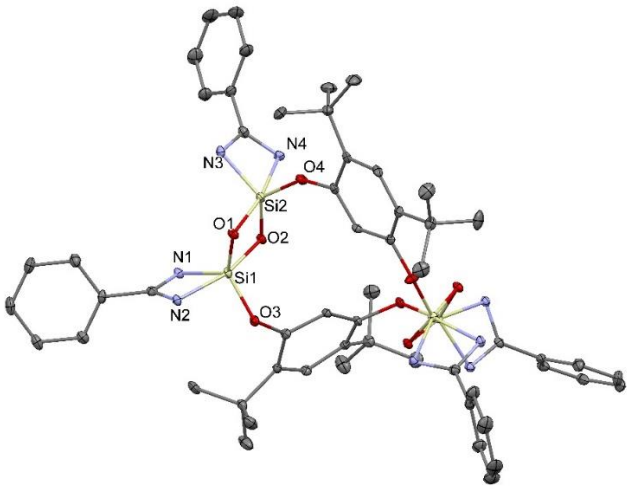

Figure 2A.23. The molecular structure of **2A.5** (ellipsoids are shown at the probability level of 50%). Tert-butyl groups and hydrogen atoms are omitted for clarity. Selected bond lengths (Å): N2-Si1 1.948(3), N1-Si1 1.830(3), Si1-O3 1.656(3), Si1-O1 1.677(3), Si1-O2 1.710(3), O4-Si2 1.651(3), O2-Si2 1.667(3), O1-Si2 1.713(3), N3-Si2 1.835 (3), N4-Si2 1.938 (3) and bond angles (°): O3-Si1-O2 102.9(1), N2-Si1-N1 68.4(1), N1-Si1-O2 99.3(1), N2-Si1-O3 91.1(1), O4-Si2-N4 89.2(1), O4-Si2-O2 128.3(1), N3-Si2-N4 69.3(1), N3-Si2-O1 101.9(1), O1-Si2-O2 84.9(1).

2A.4 Conclusion.

In summary, a systematic study of the synthesis, structure, and spectroscopic properties of a series of bis(silanechalcogenones) [**2A.2** (Te), **2A.3** (S), and **2A.4** (Se)] has been reported through the oxidative addition of a spacer based bis-silylene (**2A.1**) with the respective chalcogens. Among them, **2A.2** is the first compound featuring two Si=Te double bonds. The Si=Ch bond lengths, NMR spectroscopic data, and theoretical calculations demonstrate that the character of the Si–Ch bonds in **2A.2**–**2A.4** are intermediate between a Si=Ch double bond and a strongly delocalized $Si^{\delta+}$-$Te^{\delta-}$ single bond. It is of note here that the presence of the double bond in **2A.2**–**2A.4** is deduced from geometrical features obtained from the structural studies. Topological analysis of the experimentally determined charge density of these bonds will be a more realistic tool for elucidating the nature of the bonding. The analogous reaction with trimethyl N-oxide did not lead to the desired bis(silanone), but a cyclodisiloxane derivative (**2A.5**) was formed, arising from the dimerization of the putative Si=O double bond. The C-H···Ch interactions were delineated experimentally by the downfield shift in the corresponding ^{1}H, VT-NMR, NBO, NCI index calculations, and QTAIM analysis. Perhaps this work will promote further investigation into chalcogen-centered hydrogen bonding interactions, specifically, C–H···Te in small molecules, which are very rare in the literature.

Chapter 2B: Access to N-Heterocyclic Bis-Silylenes Coordinated Cationic Group 13 Species

Adapted from: ***M. Ghosh***, P. Panwaria, S. Tothadi, and S. Khan*, Facile Access to SiNSi Pincer Based Bis-silylene Co-ordinated Group 13 Cations. (***Manuscript under revision***).

2B.1 Objective of this work.

We isolated pyridine functionalized SiNSi pincer-based bis-silylene ligand (**2B.1**) and explored its reactivities towards various halide precursors (X= Br and I) of group 13 elements (M = Al, Ga, and In). These gave us straightforward access to the SiNSi pincer coordinated group 13 cations (**2B.2**-**2B.7**). The complexes are duly characterized by single-crystal X-ray diffraction studies, multinuclear nuclear magnetic resonance (^{1}H, ^{13}C, and ^{29}Si) spectroscopy, and HRMS. Their electronic properties were further analyzed with the help of quantum chemical calculations.

2B.2 Introduction.

NHSis with two lone-pairs and vacant *p*-orbital can act as both electrophilic and nucleophilic in nature.[61-64] NHSis proved potential σ-donor ligand backbones for stabilizing electron-deficient reactive main group species and small molecule activation.[65-70] NHSi generally donates its pair of electrons to the Lewis acid to form the Lewis acid-base adducts.[71, 72] Exploration of reactivity of NHSi towards group 13 elements started in 1996 by Denk and co-workers where they used West's silylene to form an adduct with tris(pentafluorophenyl) borane [$B(C_6F_5)_3$].[73] Braunschweig, Roesky, Iwamoto, So, Driess, Sen, and co-workers later isolated several NHSi-coordinated low valent boron species.[74-85] Roesky and co-workers also isolated NHSi stabilized boron radical and its corresponding cation by reacting benzamidinato-chloro silylene and dibromoarylborane in the presence of potassium graphite.[86, 87] Handful NHSi coordinated Al and Ga complexes are isolated by the groups of Tacke, Roesky, Radius, Alridge, Driess, and co-workers.[88-96] Only two examples prevail for NHSi bound In(III) compounds by Jutzi and Sen co-workers.[97, 98] The scarcity of the successful isolation of heavier group 13 complexes bespeaks the need for further investigation in this direction. The oxidation states of +I and +III are the most prevalent because all elements (M= B, Al, Ga, In, and Tl) of group 13 have a ns^2np^1 electron configuration in the valence shell in the ground state. Nevertheless, group 13 metals—aside from thallium—are more stable in the +III oxidation state. The transition metal-like amphiphilicity of these elements in cationic form makes them more attractive.[99-103] Owing to their electrical properties and importance in improving catalytic performance when used as catalysts, the Lewis acidic main group cations are of great interest.[104-109] Zhao, Mo, and co-workers recently reported 1, 8, 10, 9-triazaboradecalin-based bis-silylene and isolated univalent antimony and bismuth cations.[110] However, the utilization of NHSis for isolating heavier group 13 cations remained unexplored. We stayed motivated to fill this gap because of our recent interest in studying the Lewis acid cations (Chart 2B.1).[111]

Functionalized pyridyl motifs have recently been used in isolating group 13 species.[112, 113] The conformational rigidity of bis(trimethylsilyl) pyridine-2,6-diamine, with a properly placed donor N-atom, aids the ligand motif in stabilizing the reactive species.[114] Thus, we isolated bis(trimethylsilyl) pyridine-2,6-diamide-based bis-silylene (**2B.1**) and probed them for the reaction with halide precursors of group 13 elements. These afforded SiNSi stabilized trivalent cations *via* halide displacement reactions. This reactivity is reminiscent of previously observed bis-NHC-coordinated Al and Ga cations.[115] However, we could isolate a series of SiNSi pincer-based bis-silylene coordinated group 13 cations (**2B.2**-**2B.7**) in moderate to good yield straightforwardly without using any further halogen abstracting agent in the latter steps. This chapter justifies the need for a further quest into NHSis to isolate more elusive main group cations and investigate their catalytic activity.

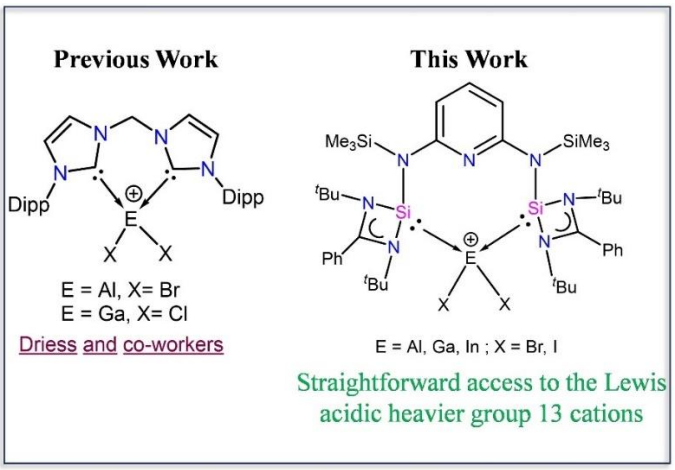

Chart 2B.1. General overview of the present work in the context of the previous work by Driess and co-workers.[115]

2B.3 Results and Discussion.

2B.3.1 Synthesis of 2B.1-2B.8.

^{1}H, ^{13}C, ^{29}Si, and ^{19}F NMR spectra were measured in $CDCl_3$, C_6D_6 using a 400 MHz NMR spectrometer, "Bruker Avance DRX500"; chemical shifts (δ) are expressed in ppm referenced to external $SiMe_4$ (tetramethylsilane, TMS), using the residual solvent as internal standard ($CDCl_3$: ^{1}H, 7.26 ppm and ^{13}C, 77.16 ppm; C_6D_6: ^{1}H, 7.16 ppm and ^{13}C, 128.06 ppm). Coupling constants are expressed in hertz. Individual peaks are reported as multiplicities (s = singlet, d = doublet, dd = doublet of doublet, t = triplet, q = quartet, m = multiplet, integration, coupling constants are given in Hz. Melting points were measured in a sealed glass tube and were not corrected. LSiCl (L= $PhC(N^tBu)_2$) and N^2,N^6-bis(trimethylsilyl)pyridine-2,6-diamine have been prepared as per the literature procedure.[116, 117]

2B.3.1.1 Preparation of 2B.1. N^2,N^6-bis(trimethylsilyl)pyridine-2,6-diamine (862 mg, 3.40 mmol) was taken in 30 ml anhydrous diethyl ether. *n*-BuLi in hexane (2.72 ml, 2.5 M) was added into the solution at -78°C and warmed to room temperature slowly. An ethereal solution of LSiCl (2 g, 6.80 mmol) was added in the flask containing deprotonated N^2,N^6-bis(trimethylsilyl)pyridine-2,6-diamine at -78°C mL of toluene. After overnight stirring at room temperature, LiCl was precipitated from the reaction mixture and filtered off. The volume was reduced to 5 mL, and the mixture was kept at -30°C. The colorless crystals suitable for X-ray analysis were obtained. Yield: 2 g (77%). Mp: 196 °C. ^{1}H NMR (400 MHz, C_6D_6, 298 K): δ 7.59 (t, J = 7.8 Hz, 1H, aromatic C-H), 7.43 (d, J = 7.4 Hz, 2H, aromatic C-H), 7.10 – 7.02 (m, 2H, aromatic C-H), 7.02 – 6.95 (m, 8H, aromatic C-H), 6.89 (t, J = 7.2 Hz, 2H, aromatic C-H), 1.12 (s, 36H, {N-C(C*H*$_3$)$_3$}), 0.90 (s, 18H, Si-C*H*$_3$) ; ^{13}C{^{1}H} NMR (100.613 MHz, C_6D_6, 298 K): δ 160.67 (N*C*N), 159.64 (aromatic C), 135.86 (aromatic C), 134.44 (aromatic C), 129.64 (aromatic C), 129.23 (aromatic C), 108.94 (aromatic C), 53.16 [*C*(CH$_3$)$_3$], 31.52 [C(*C*H$_3$)$_3$], 4.27 [-Si(*C*H$_3$)$_3$]; ^{29}Si{^{1}H} NMR (79.495 MHz, C_6D_6, 298 K): δ 5.4 [{LSiN(*Si*Me$_3$)}$_2$C$_5$H$_3$N], -17.6 [{L*Si*N(SiMe$_3$)}$_2$C$_5$H$_3$N] ppm; HRMS: Calculated for [$C_{41}H_{67}N_7Si_4$]: *m/z* 769.4535. Found *m/z* 769.3762 [M]$^+$

2B.3.1.2 Preparation of 2B.2. 2B.1 (155, 0.25 mmol) and AlI_3 (51 mg,0.125 mmol) were taken in a flask, and 40 mL of toluene was added to the reaction mixture. After overnight stirring at room temperature in the dark, toluene was evaporated to dryness, and 40 mL of DCM was added and filtered off. The colorless crystals suitable for X-ray analysis were obtained from a dichloro-methane and toluene mixture after 1 day at room temperature. Yield: 220 mg (75 %). Mp: 207 °C. ^{1}H NMR (400 MHz, $CDCl_3$, 298 K): δ 7.78 – 7.68 (m, 3H, aromatic C-H), 7.66 – 7.51 (m, 7H, aromatic C-H), 7.41 (d, J = 7.0 Hz, 2H, aromatic C-H), 6.81 (d, J = 8.1 Hz, 2H), 1.35 (s, 36H, {N-C(C*H*$_3$)$_3$}), 0.57 (s, 18H, Si-C*H*$_3$); ^{13}C{^{1}H} NMR (100.613 MHz, $CDCl_3$, 298 K): δ 176.00 (N*C*N), 158.97 (aromatic C), 142.56 (aromatic C), 132.02 (aromatic C), 128.95 (aromatic C), 128.73 – 128.34 (aromatic C), 128.18 (aromatic C), 127.91 (aromatic C), 125.25 (aromatic C), 110.83 (aromatic C), 56.55 [*C*(CH$_3$)$_3$], 55.64 [*C*(CH$_3$)$_3$], 32.21 [C(*C*H$_3$)$_3$], 31.99 [C(*C*H$_3$)$_3$], 2.17 [-Si(*C*H$_3$)$_3$]; ^{29}Si{^{1}H} NMR (79.495 MHz, $CDCl_3$, 298 K): δ 12.7 [{LSiN(*Si*Me$_3$)}$_2$C$_5$H$_3$N], -20.5 [{L*Si*N(SiMe$_3$)}$_2$C$_5$H$_3$N] ppm; HRMS: Calculated for [$C_{41}H_{67}N_7Si_4AlI_2$]$^+$: *m/z* 1050.2435. Found *m/z* 1050.2123 [M]$^+$

2B.3.1.3 Preparation of 2B.3. 2B.1 (155, 0.25 mmol) and $GaBr_3$ (39 mg,0.125 mmol) were taken in a flask, and 40 mL of toluene was added to the reaction mixture. After overnight

stirring at room temperature in the dark, toluene was evaporated to dryness, and 40 mL of DCM was added and filtered off. The colorless crystals suitable for X-ray analysis were obtained from a dichloro-methane and toluene mixture after 1 day at room temperature. Yield: 200 mg (74 %). Mp: 163 °C. ^{1}H NMR (400 MHz, $CDCl_3$, 298 K): δ 7.74 (d, J = 7.5 Hz, 2H, aromatic C-H), 7.69 – 7.51 (m, 10H, aromatic C-H), 6.88 (d, J = 8.1 Hz, 2H, aromatic C-H), 1.38 (s, 36H, {N-C(C*H*$_3$)$_3$}), 0.60 (s, 18H, Si-C*H*$_3$); ^{13}C{^{1}H} NMR (100.613 MHz, $CDCl_3$, 298 K): δ 176.71 (N*C*N), 157.18 (aromatic C), 141.65 (aromatic C), 132.26 (aromatic C), 129.08 (aromatic C), 128.69 (aromatic C), 128.33 (aromatic C), 128.07 (aromatic C), 111.88 (aromatic C), 56.35 [*C*(CH$_3$)$_3$], 31.99 [C(*C*H$_3$)$_3$], 2.22 [-Si(*C*H$_3$)$_3$]; ^{29}Si{^{1}H} NMR (79.495 MHz, $CDCl_3$, 298 K): δ 12.8 [{LSiN(*Si*Me$_3$)}$_2$C$_5$H$_3$N], -16.8 [{L*Si*N(SiMe$_3$)}$_2$C$_5$H$_3$N] ppm; HRMS: Calculated for [$C_{41}H_{67}N_7Si_4GaBr_2$]$^{+}$: *m/z* 998.2132. Found *m/z* 997.3176 [M-1]$^{+}$

2B.3.1.4 Preparation of 2B.4. 2B.1 (155 mg, 0.25 mmol) and GaI_3 (56 mg,0.125 mmol) were taken in a flask, and 40 mL of toluene was added to the reaction mixture. After overnight stirring at room temperature in the dark, toluene was evaporated to dryness, and 40 mL of DCM was added and filtered off. The colorless crystals suitable for X-ray analysis were obtained from a dichloro-methane and toluene mixture after 1 day at room temperature. Yield: 250 mg (82 %). Mp: 199 °C. ^{1}H NMR (400 MHz, $CDCl_3$, 298 K): δ 7.89 (d, J = 7.6 Hz, 2H, aromatic C-H), 7.62 (ddd, J = 23.4, 15.5, 8.7 Hz, 10H, aromatic C-H), 6.92 (d, J = 8.1 Hz, 2H, aromatic C-H), 1.40 (d, J = 7.4 Hz, 36H, {N-C(C*H*$_3$)$_3$}), 0.60 (s, 18H, Si-C*H*$_3$); ^{13}C{^{1}H} NMR (100.613 MHz, $CDCl_3$, 298 K): 176.38 (N*C*N), 156.85 (aromatic C), 141.32 (aromatic C), 131.94 (aromatic C), 129.12 (aromatic C), 128.76 (aromatic C), 128.54 – 127.55 (aromatic C), 125.07 (aromatic C), 111.55 (aromatic C), 56.38 [*C*(CH$_3$)$_3$], 31.66 [C(*C*H$_3$)$_3$], 1.90 [-Si(*C*H$_3$)$_3$]; ^{29}Si{^{1}H} NMR (79.495 MHz, $CDCl_3$, 298 K): δ 12.7 [{LSiN(*Si*Me$_3$)}$_2$C$_5$H$_3$N], -23.3 [{L*Si*N(SiMe$_3$)}$_2$C$_5$H$_3$N] ppm; HRMS: Calculated for [$C_{41}H_{67}N_7Si_4GaI_2$]$^{+}$: *m/z* 1092.1875. Found *m/z* 1131.1696 [M+K]$^{+}$

2B.3.1.5 Preparation of 2B.5. 2B.4 (305 mg, 0.25 mmol) and $GaBr_3$ (78 mg,0.25 mmol) were taken in a flask, and 40 mL of DCM was added to the reaction mixture. After overnight stirring at room temperature in the dark, the solution was filtered off. The colorless crystals suitable for X-ray analysis were obtained from a mixture of chloroform and toluene after 2 days at room temperature. Mp: 202°C.

2B.3.1.6 Preparation of 2B.6. 2B.1 (155 mg, 0.25 mmol) and $InBr_3$ (43 mg,0.125 mmol) were taken in a flask, and 40 mL of toluene was added to the reaction mixture. After overnight

stirring at room temperature in the dark, toluene was evaporated to dryness, and 40 mL of DCM was added and filtered off. The colorless crystals suitable for X-ray analysis were obtained from a dichloro-methane and toluene mixture after 1 day at room temperature. Yield: 180 mg (65 %). Mp: 177 °C. ^{1}H NMR (400 MHz, $CDCl_3$, 298 K): δ 7.71 (d, J = 8.0 Hz, 1H, aromatic C-H), 7.67 – 7.52 (m, 10H, aromatic C-H), 7.43 – 7.38 (m, 2H, aromatic C-H), 6.98 (d, J = 8.0 Hz, 2H, aromatic C-H), 1.39 (s, 36H, {N-C(C*H*$_3$)$_3$), 0.55 (s, 18H, Si-C*H*$_3$); ^{13}C{^{1}H} NMR (100.613 MHz, $CDCl_3$, 298 K): δ 175.97 (N*C*N), 157.55 (aromatic C), 141.82 (aromatic C), 132.35 (aromatic C), 129.66 (aromatic C), 129.00 (aromatic C), 128.55 (aromatic C), 128.50 – 128.01 (aromatic C), 114.68 (aromatic C), 56.47 [*C*(CH$_3$)$_3$], 31.99 [C(*C*H$_3$)$_3$], 2.22 [-Si(*C*H$_3$)]; ^{29}Si{^{1}H} NMR (79.495 MHz, $CDCl_3$, 298 K): δ 14.1 [{LSiN(*Si*Me$_3$)}$_2$C$_5$H$_3$N], -7.6 [{L*Si*N(SiMe$_3$)}$_2$C$_5$H$_3$N] ppm ; HRMS: Calculated for [$C_{41}H_{67}N_7Si_4InBr_3$]: *m/z* 1123.1915. Found *m/z* 1123.1915 [M]$^{+}$

2B.3.1.7 Preparation of 2B.7. 2B.1 (155 mg, 0.25 mmol) and InI_3 (60.5 mg,0.125 mmol) were taken in a flask, and 40 mL of toluene was added to the reaction mixture. After overnight stirring at room temperature in the dark, toluene was evaporated to dryness, and 40 mL of DCM was added and filtered off. The colorless crystals suitable for X-ray analysis were obtained from a dichloro-methane and toluene mixture after 1 day at room temperature. Yield: 220 mg (69 %). Mp: 156 °C. ^{1}H NMR (400 MHz, $CDCl_3$, 298 K): δ 7.73 (s, 1H, aromatic C-H), 7.70 – 7.54 (m, 10H, aromatic C-H), 7.01 (d, J = 8.0 Hz, 2H, aromatic C-H), 1.41 (d, J = 7.6 Hz, 36H, {N-C(C*H*$_3$)$_3$}), 0.56 (s, 18H, Si-C*H*$_3$); ^{13}C{^{1}H} NMR (100.613 MHz, $CDCl_3$, 298 K): δ 176.12 (N*C*N), 167.01 (aromatic C), 157.58 (aromatic C), 141.92 (aromatic C), 132.40 (aromatic C), 129.45 (aromatic C), 129.16 (aromatic C), 128.90 (aromatic C), 128.57 (aromatic C), 128.33 (aromatic C), 128.12 (aromatic C), 114.75 (aromatic C), 57.43 [*C*(CH$_3$)$_3$], 32.39 [C(*C*H$_3$)$_3$], 2.36 [-Si(*C*H$_3$)$_3$]; ^{29}Si{^{1}H} NMR (79.495 MHz, $CDCl_3$, 298 K): δ 13.7 [{LSiN(*Si*Me$_3$)}$_2$C$_5$H$_3$N], -14.2 [{L*Si*N(SiMe$_3$)}$_2$C$_5$H$_3$N] ppm; HRMS: Calculated for [C41H67N7Si4InI3] : *m/z* 1265.0698. Found *m/z* 1265.1403 [M]$^{+}$

2B.3.1.8 Preparation of 2B.8. 2B.1 (155 mg, 0.25 mmol) and BBr_3 (12 µL,0.125 mmol) were taken in a flask, and 40 mL of toluene was added to the reaction mixture. After overnight stirring at room temperature in the dark, toluene was evaporated to dryness, and 40 mL of DCM was added and filtered off. The colorless crystals suitable for X-ray analysis were obtained from a dichloro-methane and toluene mixture after 1 day at room temperature. Yield: 240 mg (75 %). Mp: 256 °C. ^{11}B{^{1}H} (128.387 MHz, $CDCl_3$, 298 K): δ -24.2 ppm ^{29}Si{^{1}H} NMR

(79.495 MHz, $CDCl_3$, 298 K): δ 27.5 [{LSiN(*Si*Me$_3$)}$_2$C$_5$H$_3$N] and 12.6 [{LSiN(*Si*Me$_3$)}$_2$C$_5$H$_3$N].

We began our investigation by isolating bis(trimethylsilyl) pyridine-2,6-diamide-based bis-silylene. To accomplish this, we performed the deprotonation of the N-H functionality of bis(trimethylsilyl) pyridine-2,6-diamine with *n*-BuLi (2.4 equiv.) in diethyl ether at -78°C and gradually raised the reaction mixture to room temperature. The addition of 2 equiv. of [PhC(N^{t}Bu)$_2$SiCl] resulted in compound **2B.1** as an off-white crystalline solid with a 75% yield. (Scheme 2B.1). The ^{29}Si{^{1}H} NMR shows two sharp peaks at δ 5.9 and 17.6 ppm, which denotes the -*Si*Me$_3$ and Si(II) center, respectively. The chemical shift of the Si(II) center is upfield shifted than the previously isolated bis-silylenes **2B.A-2B.D** (Chart 2B.2)[118-121] and comparable to **2B.E**,[122] denoting its stronger electron ability than **2B.D**[121] due to the presence of electron-donating -SiMe$_3$ group. Although ^{29}Si{^{1}H} NMR for compound **2B.1** is downfield shifted than **2B.F**[110] and **2B.G**[19] (Chart 2B.2).

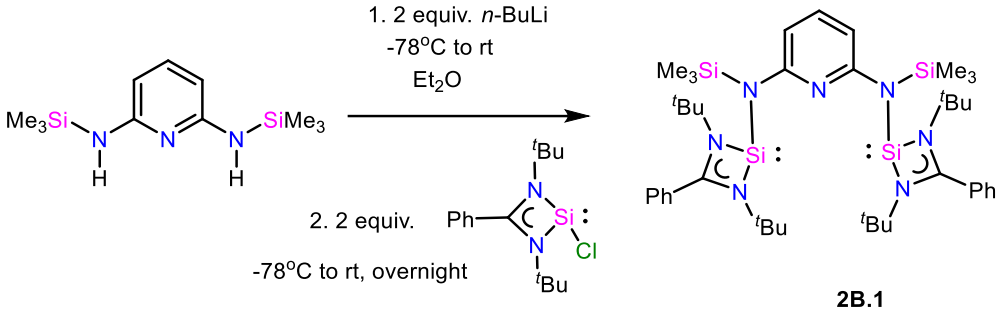

Scheme 2B.1. Synthesis of compound **2B.1**.

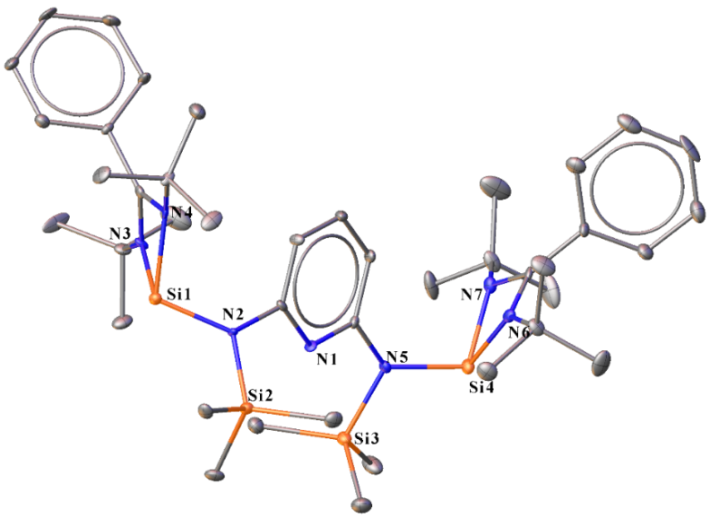

Figure 2B.1. Molecular structure of **2B.1**. Anisotropic displacement parameters are depicted at the 50% probability level. H atoms are omitted for clarity.

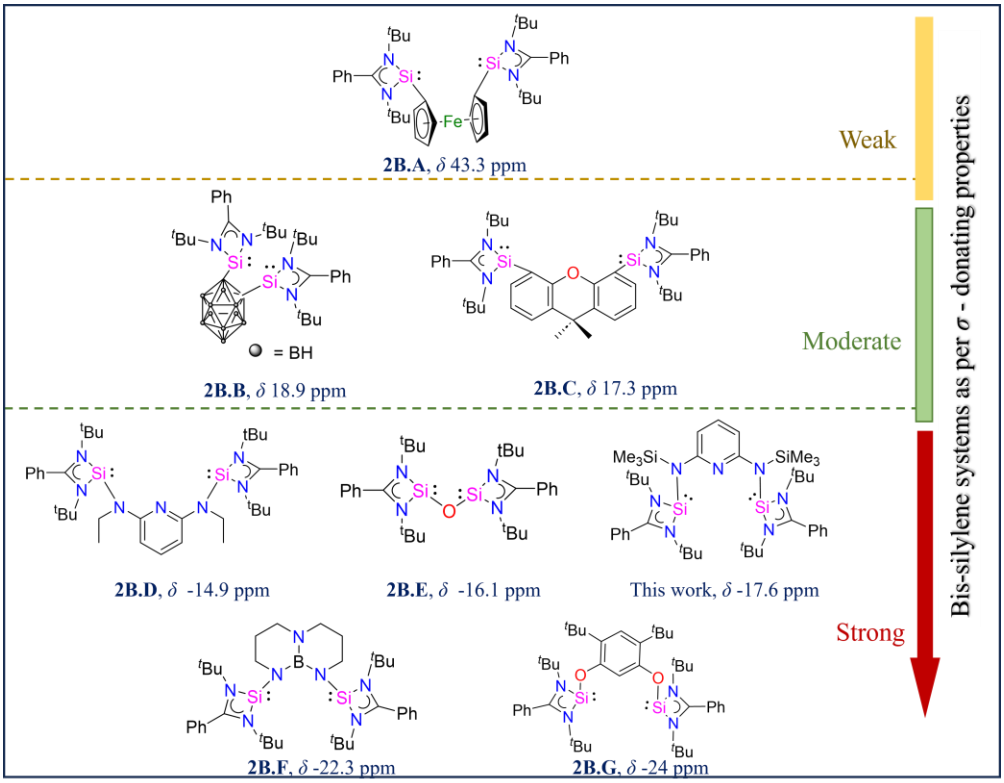

Chart 2B.2. Comparison of σ-donating strength of isolated bis-silylene systems from $^{29}Si\{^{1}H\}$ NMR.[123]

Compound **2B.1** crystallizes in the triclinic *P-1* space group (Figure 2B.1). The silicon (II) center of **2B.1** possesses three coordination and a trigonal-pyramidal geometry with a lone-pair at the apical position. The molecular structure reveals that one rotational conformer in the crystal lattice.[124-126] In the molecular structure **2B.1**, the two silylene subunits point away from the pyridine moiety. However, the rotational ability of compound **2B.1** in solution aids in its pincer-like coordination. Although the molecular structure established its formation, poor crystal quality refrained us from discussing its metrical parameters.

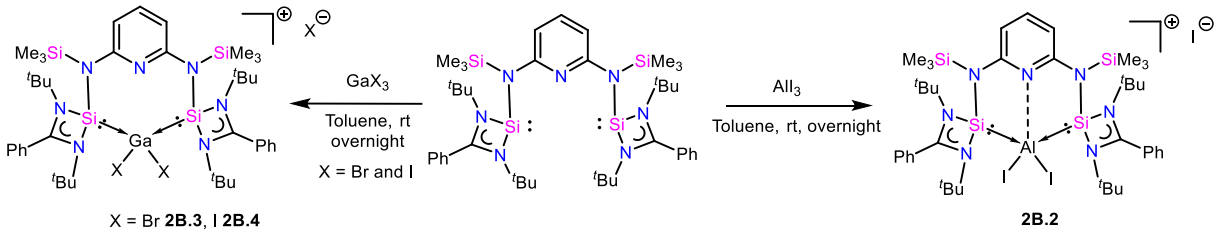

Scheme 2B.2. Reactivity of compound **2B.1** towards the group 13 halide precursors.

As already discussed, we were interested in understanding the reactivity patterns of SiNSi pincer ligand **2B.1** towards the group 13 Lewis acids owing to our infant stride towards Si(II) donors stabilized group 13 and 15 elements.[89] The silylene-aluminum complexes

compared to silyene-boron compounds, are still scarce.[88, 90-92, 94] Only four examples of silylenes that coordinate Al(III) halide complexes are known (Chart 2B.3, **2B.I-2B.VI**).[88, 89, 93] Seeing the paucity of this particular domain, we targeted compound **2B.1**, especially towards halide precursors, as they are extremely moisture sensitive. This is one of the synthetic barriers that have a significant impact on catalytic efficiency when they are used as a catalyst.

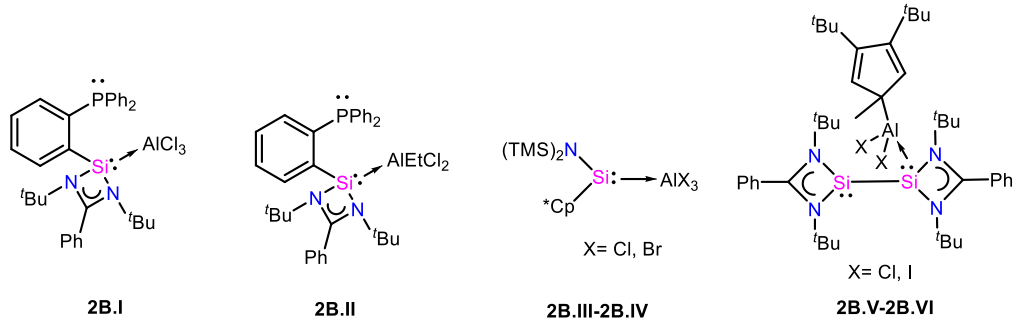

Chart 2B.3. Reported examples of NHSi coordinated Al(III) halide complexes.

We treated compound **2B.1** with AlI_3 in toluene at room temperature (Scheme 2B.2). After stirring the reaction mixture overnight, we obtained an oily residue, which was then treated with DCM. This afforded complex **2B.2** in 65% yield as a white crystalline solid. The 18 protons for the -Si*Me*$_3$ group resonate at δ 0.57 ppm, whereas tert-butyl protons show singlet at δ 1.35 ppm. The $^{29}Si\{^1H\}$ NMR shows a sharp singlet at δ 12.7 ppm and a broad peak at δ -20.5 ppm for -*Si*Me$_3$ and Si(II) centers, respectively. The chemical shift for Si(II) is downfield shifted than **2B.III** (δ -12.6 ppm), **2B.IV**(δ -17.9 ppm), **2B.V** (δ 54.4, 47.8 ppm), and **2B.VI** (δ 54.4, 47.8 ppm).

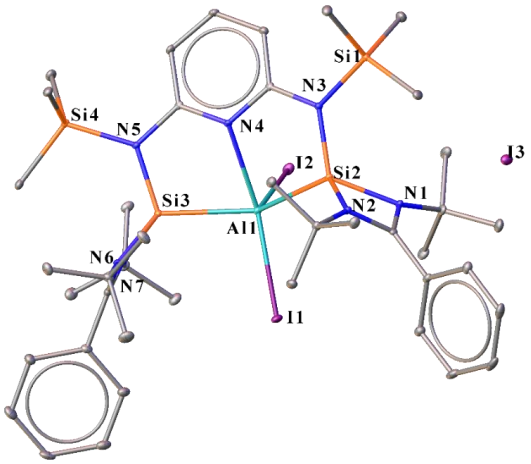

Figure 2B.2. Molecular structure of **2B.2**. Anisotropic displacement parameters are depicted at the 50% probability level. Solvent moiety and H atoms are omitted for clarity. Selected bond distances (Å) and angles (deg): Si3-Al1 2.404(1), Si2-Al1 2.404(1), Al1-I1 2.6522(9), Al1-I2

2.588(1), Al1-N4 2.320(2), N5-Si3 1.734(2), N3-Si2 1.732(2), Si3-N6 1.809(3), Si3-N7 1.804(2), Si2-N2 1.804(3), Si2-N1 1.825(3), N5-Si4 1.794(2), N3-Si1 1.806(2) Al1-I3 9.076 (2) and N4-Al1-I2 89.38(6), N4-Al1-I1 161.82(7), N4-Al1-Si2 75.09(7), I1-Al1-Si2 101.99(4), Si3-Al1-I1 98.38(4), Si3-Al1-I2 105.37(4), N4-Al1-Si3 74.46(7), N5-Si3-Al1 106.06(9), N5-Si3-N7 116.7(1), N5-Si3-Al1 106.06(9), N6-Si3-Al1 122.53(9), N7-Si3-N6 72.6(1), N3-Si2-Al1 104.10(9), N3-Si2-N1 119.4(1), N3-Si2-N2 116.4(1), N2-Si2-Al1 123.65(9), N2-Si2-N1 72.2(1).

Complex **2B.2** crystallizes in the triclinic *P-1* space group with one molecule and three DCM molecules (Figure 2B.2). According to the molecular structure, the Al(III) center has five coordinations: two from the silylene center, two from the iodide center, and one from the pyridyl nitrogen atom, resulting in a distorted square pyramidal geometry. The penta coordinated Al(III) center is differently substituted where one of the Si(II) and pyridyl N centers attain angles N4-Al1-Si2 75.09(7) and N4-Al1-I2 89.38(6)^{o}. Other substituents, on the other hand, attain bond angles as follows: Si3-Al1-I1 98.38(4), I1-Al1-Si2 101.99(4), and Si3-Al1-I2 105.37(4). The two Si-Al bond lengths are identical 2.404(1) Å which are shorter than **2B.I** [2.4509(8) Å], **2B.II** [2.4988(14) Å], **2B.III** [2.4675(9) Å], **2B.IV** [2.463(4) Å], **2B.V** [2.5413(9) Å], and **2B.VI** [2.5505(9) Å]. It is noteworthy that Al(III) possesses the pyridyl N-donation because of its enhanced Lewis acidity. The Al1-N4 bond length is 2.320(2) Å which is significantly longer than the N donor stabilized Al(III) cations, [Al(2-$C(SiMe_3)_2C_5H_4N)_2$][$AlCl_4$] [1.91(2) Å],[127] (Pytsi)AlMe]$^{+}$[$MeB(C_6F_5)_3$]$^{-}$ [(Pytsi)$C(SiMe_3)_2SiMe_2$(2-C_5H_4N)] [1.9485(18) Å].[128, 129] When we tried the same reaction with $AlBr_3$, we found an insoluble oily residue that could not be further characterized. Moving to the next element down the group, we treated compound **2B.1** with 0.5 equivalent GaX_3 (X= Br and I) in toluene at room temperature overnight (Scheme 2B.2). After a few hours of stirring, we observed white precipitation in the reaction mixture. Upon extracting the white residue in DCM, we obtained complexes **2B.3** and **2B.4** in analytically pure form with 60 and 70 % yield, respectively. After recrystallization, both compounds become insoluble in non-polar solvent mediums like toluene and readily soluble in polar solvent mediums like DCM and THF. Previously, there are few examples of differently functionalized benzamidinato silylene-based Ga(III) complexes by Driess, Roesky, and co-workers (Chart 2B.4).[88, 93, 95, 96] Nevertheless, complexes **2B.3** and **2B.4** are the first examples of chelating bis-silylene coordinated cationic Ga(III) complexes. The 18 protons of the -Si*Me*$_3$ group resonate at δ 0.60 ppm for both complexes, whereas the tert-butyl protons of benzamidinate moiety resonate at δ 1.38 and 1.41

ppm for complex **2B.3** and **2B.4**, respectively. The $^{29}Si\{^{1}H\}$ NMR shows two signals at δ 12.8 and -16.8 ppm, whereas 12.6 and -23.2 ppm for -*Si*Me$_3$ and Si(II) center for complexes **2B.3** and **2B.4,** respectively. The chemical shift for Si(II) center for complexes **2B.3** and **2B.4** are downfield shifted than previously reported NHSi coordinated Ga(III) halide complexes (Chart 2B.4), **2B.VII** (δ 129.8 ppm),[95] **2B.VIII** (δ 11.3 ppm),[88] **2B.IX** (δ 1.5 ppm),[96] **2B.X** (δ 54.7, 41.1 ppm),[93] suggesting electron richness of Si(II) centers in complex **2B.3** and **2B.4**.

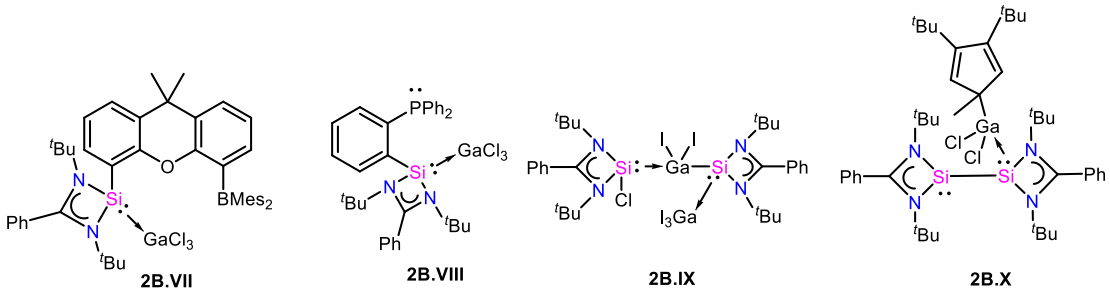

Chart 2B.4. Reported examples of NHSi coordinated Ga(III) halide complexes.

Complex **2B.3** crystallized in the triclinic *P-1* space group (Figure 2B.3); the molecular structure establishes that complex **2B.3** is an ion pair with a bromide counter anion. The asymmetric unit contains one molecule with one unit of DCM. The Ga(III) center is tetracoordinated, where two silylenes and two bromide atoms coordinate the Ga center. The Ga center adopts a distorted tetrahedral geometry. The two bond lengths, Si2-Ga1 2.3882(7) and Si3-Ga1 2.3709(8) Å, which are in line with complex **2B.VII** [2.3904(6) Å], **2B.VIII** [2.3904(6) Å] and longer than **2B.IX** [2.4162(12)–2.4292(12) Å], **2B.X** [2.4910(7) Å]. However, the Si-Ga bonds in complex **2B.3** are significantly longer than the Ga-C bond, observed in the [{(bisNHC)GaCl$_2$}$^+$Cl$^-$] [2.000(4), 2.006(3) Å], (bisNHC = bis(N-Dipp-imidazole-2-ylidene)methylene).[115] The Ga center is separated from its counter bromide anion by a distance of 7.564(2) Å.

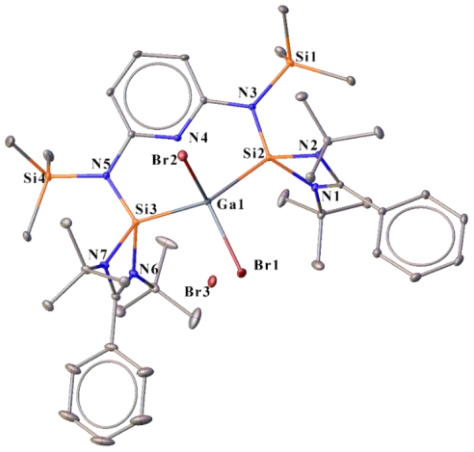

Figure 2B.3. Molecular structure of **2B.3**. Anisotropic displacement parameters are depicted at the 50% probability level. Solvent moiety and H atoms are omitted for clarity. Selected bond distances (Å) and angles (deg): Si2-Ga1 2.3882(7), Si3-Ga1 2.3709(8), Ga1-Br1 2.4165(5), Ga1-Br2 2.4102(5), N2-Si2 1.818(2), N1-Si2 1.804(2), N6-Si3 1.799(2), N7-Si3 1.818(2), N3-Si2 1.725(1), N5-Si3 1.725(2), N5-Si4 1.795(2), N3-Si1 1.798(2) Ga1-Br3 7.564(2) and Br2-Ga1-Br1 112.00(2), Br2-Ga1-Si3 99.96(2), Br1-Ga1-Si3 105.17(2), N3-Si2-Ga1 114.15(7), N3-Si2-N2 117.08(9), N1-Si2-Ga1 118.42(7), N2-Si2-N1 72.30(9), N5-Si3-Ga1 112.63(7), N5-Si3-N7 118.2(1), N6-Si3-Ga1 117.54(7), N6-Si3-N7 72.42(9).

Our attempt to grow better-quality single crystals for complex **2B.4** was unsuccessful. However, we could unambiguously establish the molecular structure of complex **2B.4** (Figure 2B.4). The literature precedence shows monodentate NHC coordinated Ga(III) cations have been utilized in the Lewis acid-mediated homogeneous catalysis.[105, 130-132] Similarly, catalytic activities with complexes **2B.3**-**2B.4** could be apprehended in the near future. Continuing previous reactivities, we treated complex **2B.4** with another equivalent of $GaBr_3$ in a toluene chloroform mixture at room temperature (Scheme 2B.3). This afforded complex **2B.5** with a 30% yield with a mixture of complex **2B.4**. The additional $GaBr_3$ reacts with the iodide counter anion to produce $GaBr_3I^-$ as the counter anion. The poor solubility of this compound restricted us to measure its NMR.

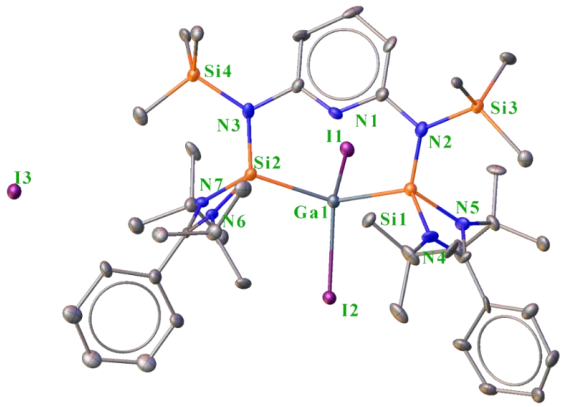

Figure 2B.4. Molecular structure of complex **2B.4**.

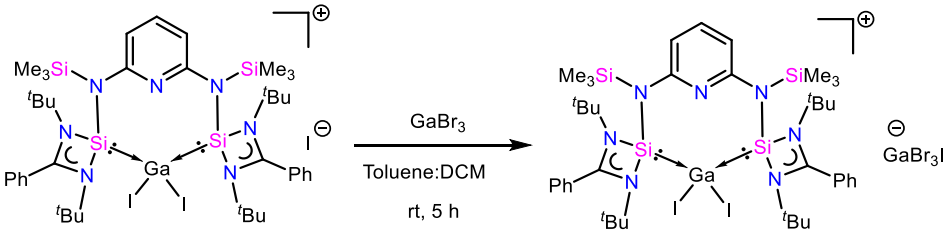

2B.5

Scheme 2B.3. Reactivity of compound **2B.4** in the presence of the Lewis acidic $GaBr_3$.

The molecular structure suggests that complex **2B.5** is crystallized in the monoclinic $P2_1/c$ space group (Figure 2B.5). Complex **2B.5** contains two different types of Ga(III) centers. The SiNSi pincer bound Ga center adopts a distorted tetrahedral geometry with Si-Ga bond lengths in the range of 2.390(2)-2.412(2) Å, which are in the range of Si-Ga bond lengths observed in the complex **2B.VII** and **2B.VIII** by Roesky and co-workers. The Ga center in the anion counterpart also adopts distorted tetrahedral geometry. The Ga2-I1 bond is shorter [2.435(1) Å] than the bis-silylene bound Ga-I bonds [Ga1-I3 2.460(2), Ga1-I2 2.475(1) Å], which could be attributed to the Lewis acidic nature of Ga towards electronegative iodide atom.

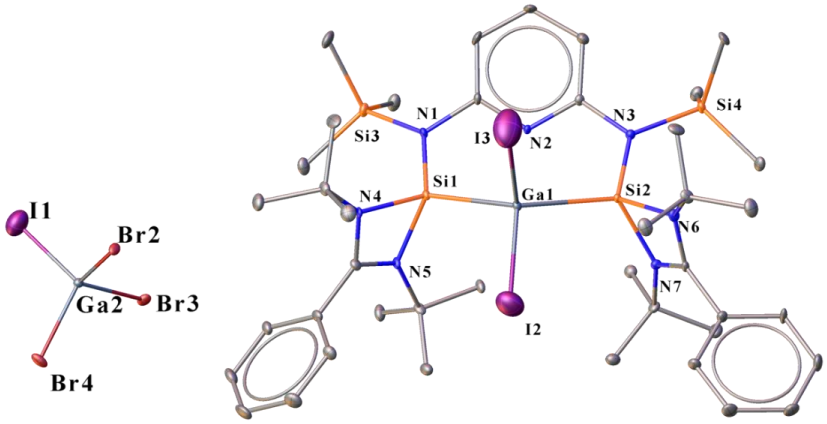

Figure 2B.5. Molecular structure of **2B.5**. Anisotropic displacement parameters are depicted at the 50% probability level. Solvent moiety, anion, and H atoms are omitted for clarity. Selected bond distances (Å) and angles (deg): Ga1-I3 2.460(2), Ga1-I2 2.475(1), Si2-Ga1 2.412(2), Si1-Ga1 2.390(2), N3-Si2 1.721(7), Si2-N7 1.820(9), Si2-N6 1.822(7), N3-Si4 1.796(6), N1-Si3 1.784(7), N1-Si1 1.731(7), Si1-N5 1.811(8), Si1-N4 1.812(6), Ga2-I1 2.435(1), Ga2-Br2 2.348(1), Ga2-Br4 2.363(2), Ga2-Br3 2.410(1), Ga1-Ga2 16.171(2) and I2-Ga1-I3 108.30(5), Si2-Ga1-I3 105.83(7), Si2-Ga1-I2 106.00(6), N1-Si1-Ga1 114.3(2), N1-Si1-N4 116.2(3), N5-Si1-Ga1 115.2(2), N5-Si1-N4 72.6(3), N3-Si2-N6 114.5(3), N7-Si2-Ga1 120.0(3), N3-Si2-Ga1 113.5(2), N6-Si2-N7 72.7(3), I1-Ga2-Br3 111.95(5), Br3-Ga2-Br4 107.40(5), Br4-Ga2-Br2 109.43(5), I1-Ga2-Br2 108.44(5).

Only two reports exist where NHSis have been explored for exploring coordination behavior with In(III) precursors (Chart 2B.5).[97, 98] Jutzi and co-workers showed the reaction of decamethylsilicocene with $InMe_3$, which resulted in $[Cp^*_2Si(Me)]_2InMe$ (**2B.XI**) by insertion reaction instead of NHSi-In(III) adduct.[97] Sen and co-workers recently reported a Lewis acid-base adduct of $[PhC(N^tBu)_2SiN(SiMe_3)_2]$ with InX_3 (X= Cl and Br) (**2B.XII-2B.XIII**).[98] After

the successful isolation of several SiNSi coordinated Al(III) and Ga(III) cations, we remained curious to probe compound **2B.1** with halide precursors of In(III) to isolate chelating bis-silylene coordinated In(III) cations, which are hitherto unknown. We treated **2B.1** with InX_3 (X= Br and I) in toluene at room temperature (Scheme 2B.4). As the reaction proceeded, white precipitation occurred, which was treated with DCM. Single crystals of complexes **2B.6** and **2B.7** were grown from toluene and DCM mixture at room temperature. ^{1}H NMR for both complexes shows sharp singlets at δ 0.55 and 0.56 ppm for 18 protons of the -Si*Me*$_3$ group for complex **2B.6** and **2B.7**, respectively. The tert-butyl groups of benzamidinate moiety resonate at δ 1.39 and 1.42 ppm for complexes **2B.6** and **2B.7**, respectively. The ^{29}Si{^{1}H} NMR for complexes **2B.6** and **2B.7** show two peaks. The sharp peaks at δ 14.1 and 13.7 ppm for **2B.6** and **2B.7** denote the -SiMe3 center, whereas the broad peak at δ -7.6 and -14.2 ppm for **2B.6** and **2B.7** indicate the Si(II) center. The chemical shift for Si(II) centers in complex **2B.6** and **2B.7**, coordinated to cationic In(III) center, are downfield shifted than complex **2B.XI** (δ 20.6 ppm) and upfield shifted than **2B.XII** (^{29}Si CP/MAS δ -54.4 to -84.3 ppm), **2B.XIII** (^{29}Si CP/MAS δ -31.7 ppm).

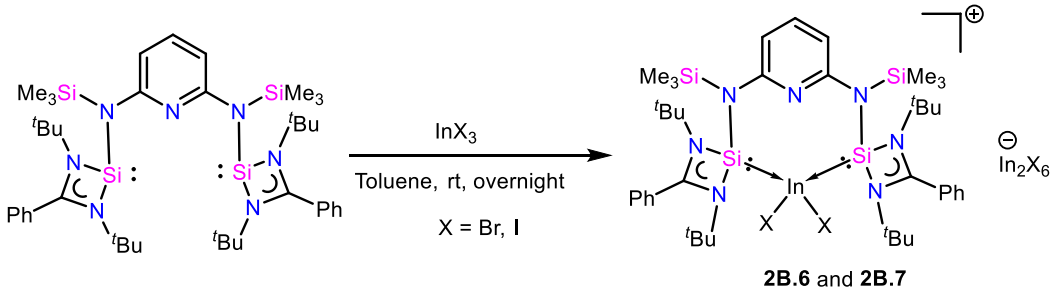

Scheme 2B.4. Reactivity of compound **2B.1** towards the halide precursors of In(III).

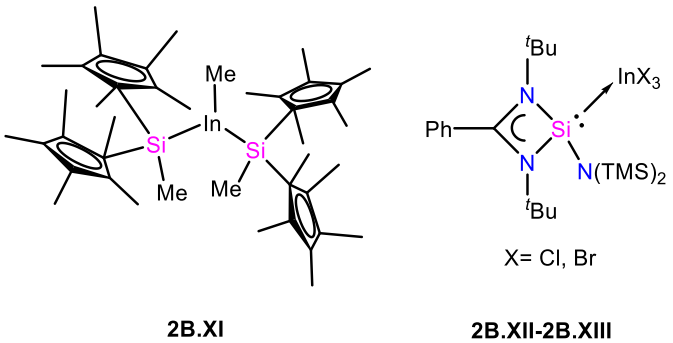

Chart 2B.5. Reported examples of NHSi coordinated In(III) complexes.

Complexes **2B.6** and **2B.7** crystallize in the triclinic *P-1* space group shown in Figures 2B.6 and 2B.7, respectively. The tetra-coordinated In(III) center adopts slightly distorted tetrahedral geometry in both complexes. The Si-In bond lengths in complex **2B.6** are Si1-In1

2.540(4) and Si2-In1 2.541(5) Å in complex **7**, Si2-In1 2.584(3) and Si4-In1 2.577(3) Å. The Si-In bond lengths are in accordance with complex **2B.XII** and **2B.XIII,** which are 2.5804(5) and 2.5840(12) Å, respectively. The Si-In bond lengths in **2B.6** are substantially longer than the In-C bond in IDip (1,3-bis(2,6-diisopropylphenyl) imidazol-2-ylidene) coordinated $InBr_2^+$ complex [2.178(2) Å] reported by Gondon and co-workers. The average In-X bond lengths are 2.568 (for **2B.6**) and 2.763 (for **7**) Å. In **2B.6**, the In-Br average bond distance is marginally longer than the **2B.XII** (2.5206 Å) but significantly longer than the IDip coordinated $InBr_2^+$ complex.[133]

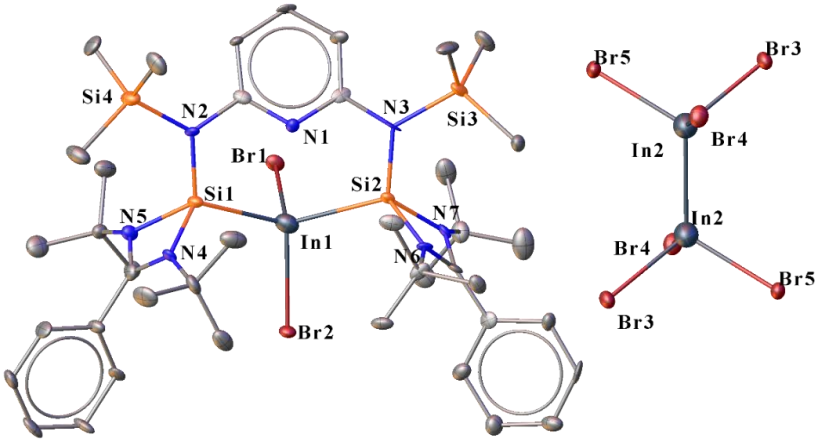

Figure 2B.6. Molecular structure of **2B.6**. Anisotropic displacement parameters are depicted at the 50% probability level. Solvent moiety and H atoms are omitted for clarity. Selected bond distances (Å) and angles (deg): Si1-In1 2.540(4), In1-Si2 2.541(4), In1-Br1 2.561(2), In1-Br2 2.574(2), Si1-N4 1.80(1), Si1-N5 1.84(2), Si1-N2 1.72(1), Si2-N3 1.71(1), Si2-N6 1.77(2), Si2-N7 1.81(1) and Si1-In1-Br1 102.8(1), Si1-In1-Br2 108.0(1), Br2-In1-Si2 106.6(1), Br1-In1-Si2 102.8(1), N2-Si1-N5 117.4(7), N2-Si1-In1 112.6(5), N4-Si1-In1 117.8(5), N4-Si1-N5 72.6(6).

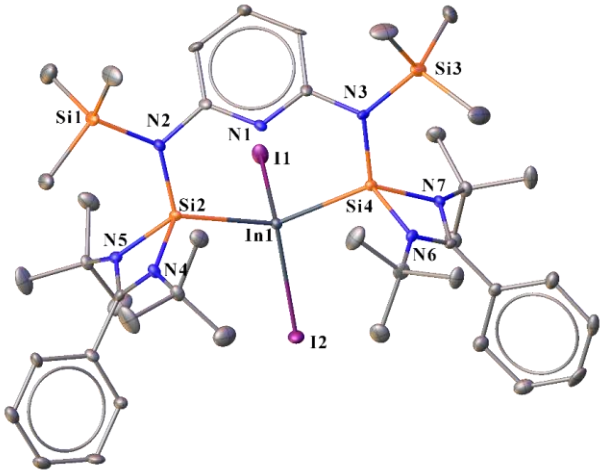

Figure 2B.7. Molecular structure of **2B.7**. Anisotropic displacement parameters are depicted at the 50% probability level. Solvent moiety, disordered anion, and H atoms are omitted for clarity. Selected bond distances (Å) and angles (deg): I1-In1 2.772(1), In1-I2 2.754(1), Si4-In1 2.577(3), Si2-In1 2.584(3), N7-Si4 1.814(8), N6-Si4 1.798(9), N2-Si2 1.72(1), N3-Si4 1.73(1), N2-Si1 1.80(1), N3-Si3 1.79(1) and I1-In1-I2 108.82(4), I1-In1-Si2 101.21(7), I2-In1-Si2 110.13(7), N3-Si4-N7 116.0(4), N3-Si4-In1 111.7(3), N7-Si4-N6 71.4(4), N6-Si4-In1 117.0(3), N2-Si2-In1 112.1(3), N5-Si2-N4 72.1(4), N5-Si2-In1 118.4(3), N2-Si2-N4 116.1(4).

Braunschweig and co-workers have shown reactivity of B-Cl moiety with West's silylene, which underwent oxidative addition at the Si(II) center to form a six-membered C_2BN_2Si-cycle.[134] Similar reactivities were also observed by So and Roesky and co-workers when they treated $PhBCl_2$ with the Si(I) center of the amidinate-supported silicon(I) dimer, which is followed by the ring expansion and LSiCl or LSiMes (L = $PhC(N^tBu)_2$, Mes = 2,4,6-$Me_3C_6H_2$) with RBX_2 (R= Ph, Mes, $N(SiMe_3)_2$; X = Cl and Br), respectively.[77, 135] Apart from these, Mo, So and co-workers utilized BBr_3 with carborane-based bis-silylene and monodentate silylene for stabilizing substituted borylene.[84, 85, 136] Seeing the diverse reactivity patterns, lastly, we treated compound **2B.1** with BBr_3 in toluene at room temperature (Scheme 2B.5) to afford complex **2B.8**. Unlike the LSiCl or LSiMes stabilized organo boron complexes, which readily undergo ring expansion, the complex forms a Si(II)→B adduct.[77]

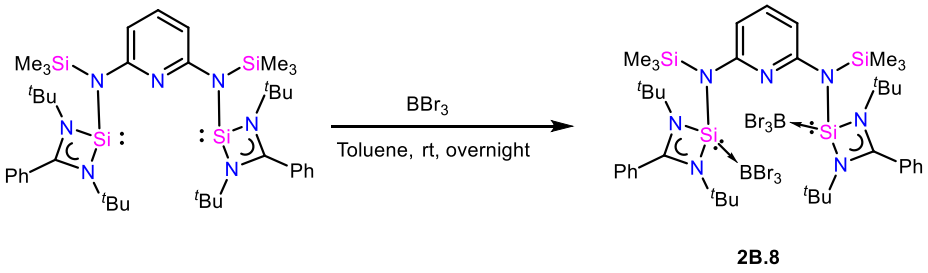

2B.8

Scheme 2B.5. Reactivity of compound **2B.1** with boron tribromide.

The $^{29}Si\{^1H\}$ NMR of the reaction mixture shows two sharp peaks at δ 27.5 and 12.6 ppm. The former denotes the Si(II) center, where the sharp singlet at 12.6 ppm indicates the -*Si*Me_3 group. Because of the low yield and rapid decomposition, we could not perform the ^1H and ^{13}C NMR of the pure product. The molecular structure of **2B.8** (Figure 2B.8) reveals that it crystallizes in a monoclinic *C2/c* space group with one molecule. It shows that the two silylene moieties coordinate independently to the B(III) center, unlike complexes **2B.2**-**2B.7**. It might be due to the larger bite angle of the silylene unit with respect to the small B(III) nuclei. Each B(III) center is tetra-coordinated and displays a distorted tetrahedral geometry. The

molecular structure shows that complex **2B.8** possesses a *C2v* symmetry, passing through the pyridine ring. The Si-B bond length is 2.020(8) Å, which is in accordance with the previously reported [PhC(N^{t}Bu)$_2$Si]BPhCl$_2$ [2.0369(19) Å] but marginally longer than the silylene borane complex [2.019(3) Å].[134] This established that the Si-B bond is coordination in nature. Complex **2B.8** is of special interest as it could be an effective platform for SiNSi pincer-stabilized diborene formation.[137, 138]

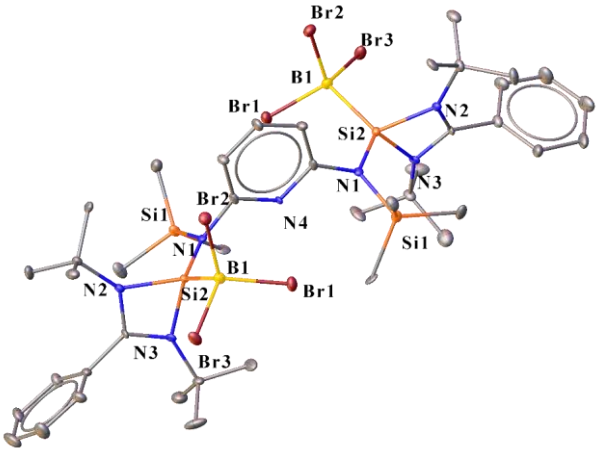

Figure 2B.8. Molecular structure of **2B.8**. Anisotropic displacement parameters are depicted at the 50% probability level. Solvent moiety, anion, and H atoms are omitted for clarity. Selected bond distances (Å) and angles (deg): Si2-B1 2.020(8), B1-Br2 2.013(8), B1-Br1 2.006(9), B1-Br3 2.040(8), N1-Si2 1.731(5), Si2-N2 1.801(6), Si2-N3 1.807(5), Si1-N1 1.833(5) and Si2-B1-Br3 106.1(4), Si2-B1-Br1 110.8(4), Br3-B1-Br2 108.8(4), Br2-B1-Br1 109.1(4), N1-Si2-N3 112.1(2), N1-Si2-B1 119.5(3), N2-Si2-B1 113.2(3), N3-Si2-N2 72.9(2).

2B.3.2 Quantum chemical calculations.

Ground state geometries of various complexes were optimized at the B3LYP-D3(BJ)/def2-TZVPP level by taking crystal structures as initial coordinates. Optimized geometries of these complexes (Figure 2B.9) showed a resemblance with their respective crystal structures. FMO analysis was performed to obtain insights into the bonding situations of various complexes. WBI values depicting bond order, natural charges, and $E^{(2)}$ values for the various delocalizations have been calculated using the NBO3.1 program. The lone-pairs corresponding to the silicon atoms of the silylene moiety of compound **2B.1** can be visualized in HOMO and HOMO-1, showing the higher nucleophilic nature of silylene moiety. HOMO-2 significantly contributes from the σ-orbital of the Si-N_{TMS} bond and the π-orbital of the pyridyl ring. HOMO-3 and HOMO-5 are localized over the pyridyl, amidinato, and TMS-bound nitrogen lone-pairs, whereas HOMO-4 is constituted from the amidinato nitrogen lone-pairs (Figure 2B.10).

However, pyridyl nitrogen lone-pair can be found over the HOMO-6, showing its relative stability over the silylene lone-pairs. LUMO is situated over the phenyl ring of the benzamidinato moiety of the compound **2B.1**. Natural charges of 1.136 was found to be present at both the silylene silicon atoms of NHSi groups. The occupancy of TMS-bound nitrogen lone-pair (1.772) is found to be less as compared to the pyridyl nitrogen lone-pair (1.885) due to the hyperconjugative interactions [n(N1)→σ*(Si2-N2/3)] in the former one.

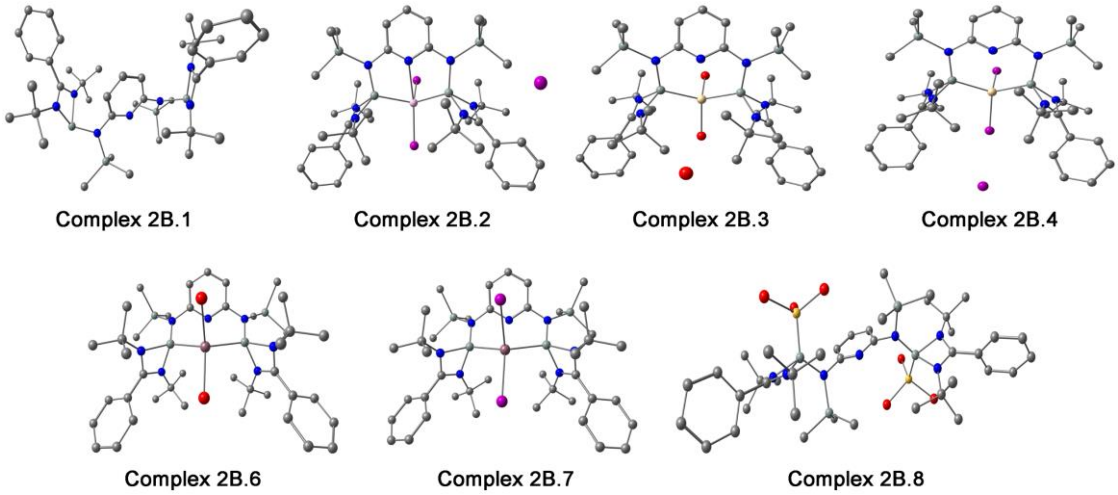

Figure 2B.9. Ground state optimized geometries of various complexes at the B3LYP-D3(BJ)/def2-TZVP level.

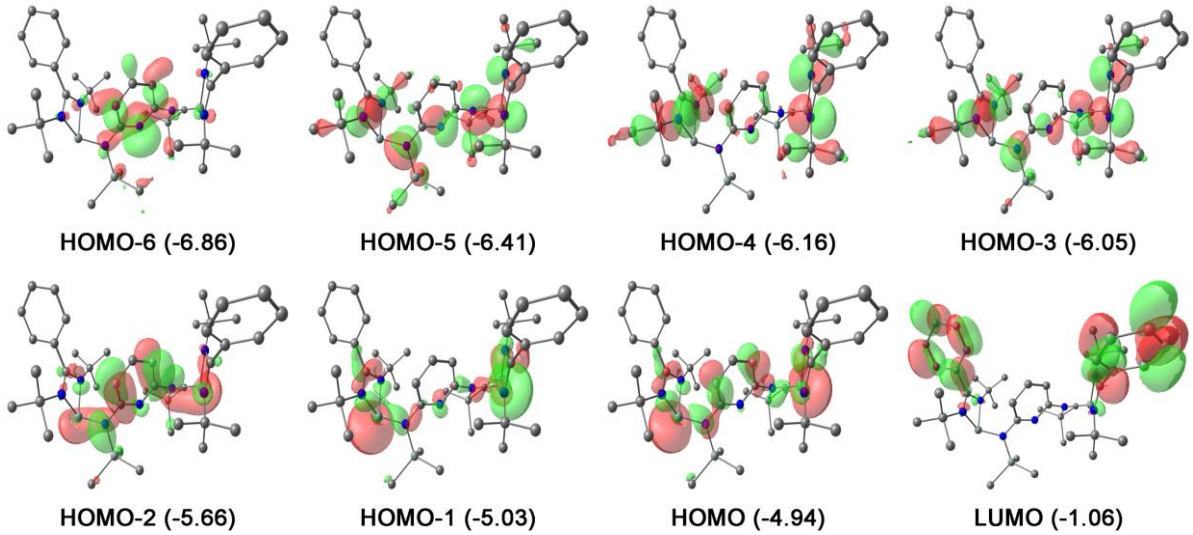

Figure 2B.10. Relevant MOs of compound **2B.1** with their energies (in eV) provided in parentheses.

The lone-pairs of the anionic iodine atom in complex **2B.2** can be observed on HOMO, HOMO-1, and HOMO-2, whereas HOMO-3 is constituted from the TMS-bound nitrogen lone-pair and π-orbital of the pyridine ring (Figure 2B.11). The σ bond of Si(II)→Al(III) can be

visualized in HOMO-4 and HOMO-5, along with the contribution from the lone-pairs of the Al(III)-bound iodide moieties. LUMO is concentrated over one of the benzamidinato groups. LUMO+1 contributes from the Al(III) center along with the contribution from the pyridyl ring and nitrogen of amidinato moieties. The WBI values of 0.785 and 0.754 for the Si2-Al1 and Si3-Al1 show a coordinative bonding nature for Si(II)→Al(III). It is further corroborated by the dispersion of the positive charge of the Al(III) center (0.578) towards the Si(II) centers (1.536 and 1.521). The electron density of the silicon atoms of the NHSi group of complex **2** delocalizes into the σ^* orbital of the Al1-I1 bond, which is predominantly localized over the Al(III) center, with $E^{(2)}$ values of the 12.59 and 10.53 kcal/mol. The WBI value of 0.096 for N4-Al1 confirms the weak N→Al(III) dative bonding situation compared to the Si(II)→Al(III). Hence, the donation from the pyridyl nitrogen to the σ^* orbital of the Al1-I1 bond was also checked and found to be 7.74 kcal/mol.

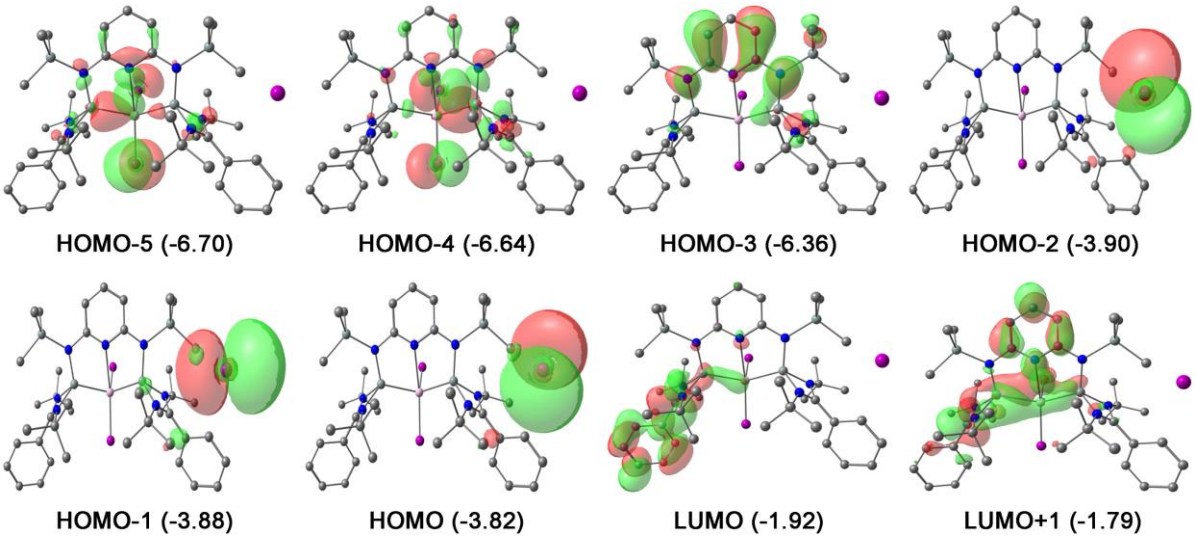

Figure 2B.11. Relevant molecular orbitals of complex **2B.2** with their energies (in eV) provided in parentheses.

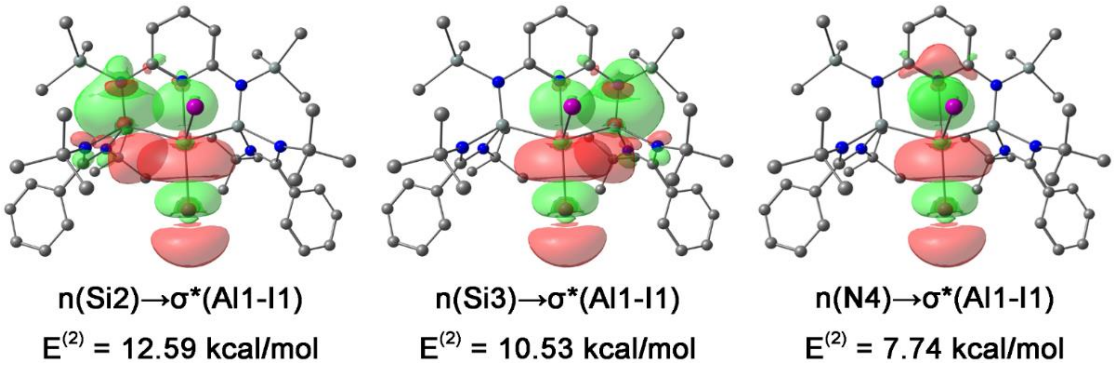

Figure 2B.12: Orbital overlaps for various donor-acceptor interactions in complex **2B.2** with their $E^{(2)}$ values. Anionic counterparts have not been shown for brevity.

Similar to complex **2B.2**, HOMO, HOMO-1, and HOMO-2 show contributions from the lone-pairs of the anionic bromide and iodide atoms in complex **2B.3** and **2B.4**, respectively (Figure 2B.13). HOMO-3 in complex **2B.3** is constituted from the TMS-bound nitrogen lone-pair and π-orbital of the pyridyl ring, whereas HOMO-3 in complex **2B.4** shows the contribution from the Si(II)→Ga(III) bonds along with the contribution from the lone-pair orbital of the Ga(III)-bound iodide moieties. The σ-orbital of both the Si(II)→Ga(III) bonds can be visualized in HOMO-4 along with the contribution from the lone-pairs of Ga(III)-bound halide moieties in complex **2B.3** and **2B.4**. However, HOMO-5 shows the delocalized electron density over the Si(II)→Ga(III)←Si(II) with a contribution from the lone-pairs of pyridyl nitrogen and halide moieties in complexes **2B.3** and **2B.4**. LUMO in complexes **2B.3** and **2B.4** shows the presence of discrete electron density over the amidinato rings and pyridine rings with an electron density at Ga(III) center.

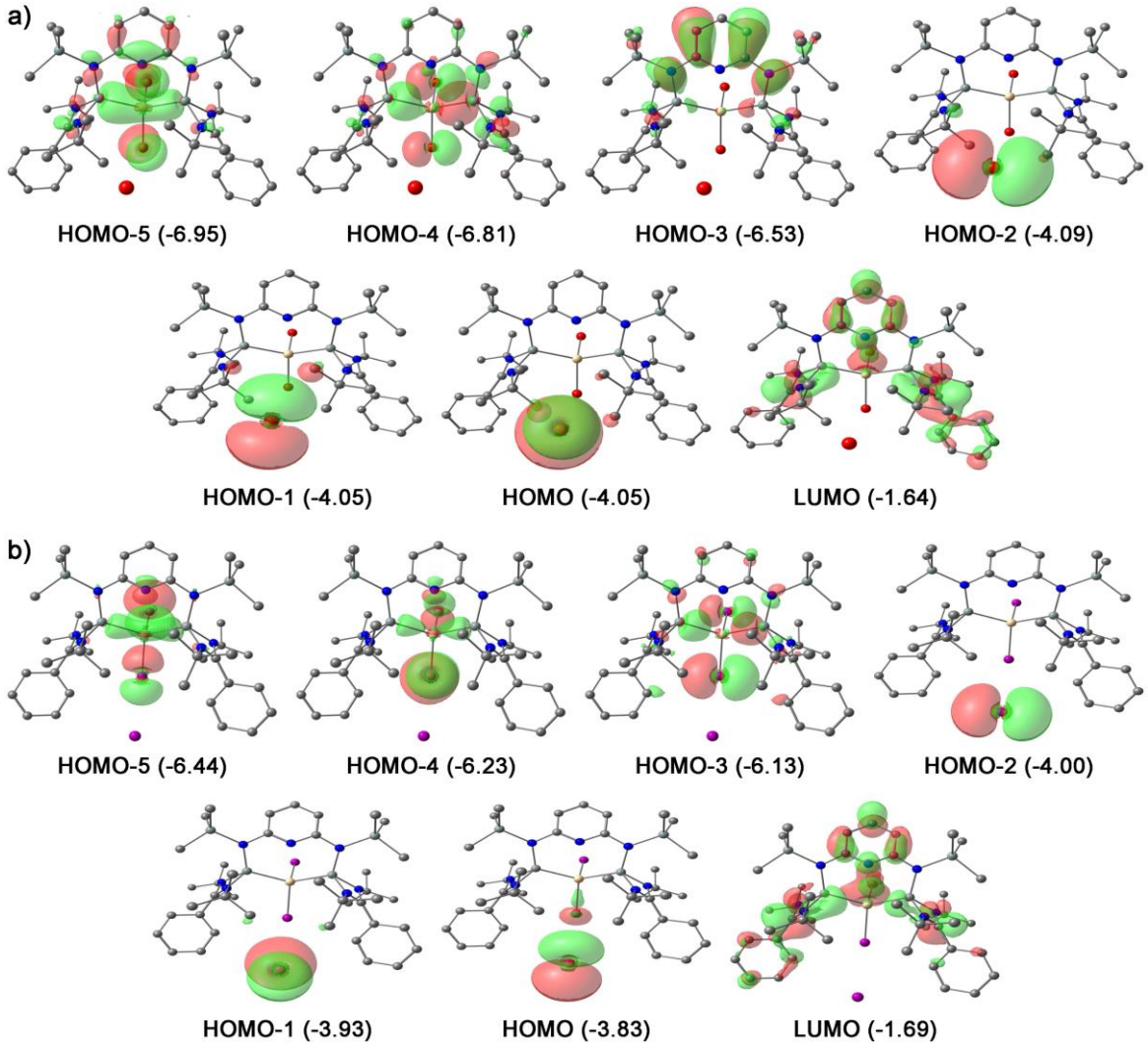

Figure 2B.13. Relevant molecular orbitals of a) complex **2B.3** and b) complex **2B.4** with their energies (in eV) provided in parentheses.

WBI of 0.817 and 0.816 for the Si1-Ga1 and Si2-Ga1 for complex **2B.3** and WBI of 0.819 and 0.818 for the Si1-Ga1 and Si2-Ga1 for complex **2B.4**. The positive charge of the Ga(III) center (0.512) towards the Si(II) centers (1.645 and 1.641) in complex **2B.3** and Ga(III) center (0.216) towards the Si(II) centers (1.654 and 1.651) in complex **2B.4** is dispersed indicating the coordinate bonding. The electron density of lone-pair on the silicon atoms of the NHSi group for complex **2B.3** delocalizes into the σ^* orbital of the Ga1-Br2 bond, which is predominantly localized over Ga(III) center, with $E^{(2)}$ values of the 15.45 kcal/mol. On the contrary, the electron density of lone-pair on both the silicon atoms of the NHSi group for complex **2B.4** delocalizes into the σ^* orbital of the Ga1-I1 bond with $E^{(2)}$ values of the 12.59 and 12.46 kcal/mol. In complex **2B.3**, pyridyl nitrogen lone-pair electron density delocalizes into the lone-vacant orbital of Ga(III) center with an $E^{(2)}$ value of 10.47 kcal/mol. In contrast, pyridyl nitrogen lone-pair electron density delocalizes into the σ^* orbital of the Ga1-I2 with an $E^{(2)}$ value of 4.31 kcal/mol.

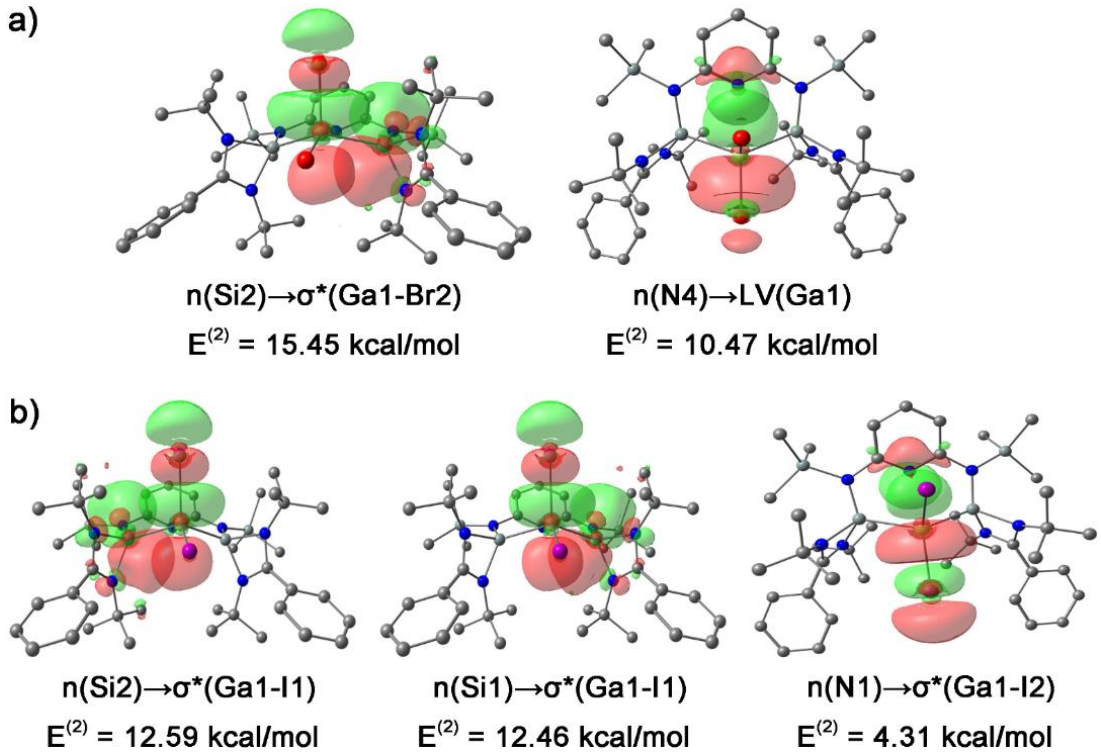

Figure 2B.14. Orbital overlaps for various donor-acceptor interactions in a) complex **2B.3** and b) complex **2B.4** with their $E^{(2)}$ values. Anionic counterparts have not been shown for brevity.

HOMO and HOMO-1 of complexes **2B.6** and **2B.7** are constituted from the lone-pair orbital of the In(III)-bound halide moieties along with the contribution from the Si(II)→In(III) bonds (Figure 2B.15). Also, there is a contribution from the π-orbital of the pyridyl ring in HOMO of **2B.6** and **2B.7** and HOMO-1 of complex **2B.6**. HOMO-2 of the complex **2B.6** shows

a contribution of the delocalized electron density over the Si(II)→Ga(III)←Si(II) with a contribution of the lone-pair of pyridyl nitrogen and bromide moieties. On the other hand, LUMO in complexes **2B.6** and **2B.7** shows the presence of electron density over the benzamidinato with an electron density at the In(III) center. WBI value of 0.788 for both the Si2-In1 and Si4-In1 in complex **2B.7** shows coordinate bonding for Si(II)→In(III). Dispersal of the positive charge of the In(III) center (0.439) towards the Si(II) centers (1.605 and 1.603) also indicates the coordinate behavior. The lone-pair electron density of both the silicon atoms of the NHSi group delocalizes into the σ^* orbital of the In1-I2 bond (predominantly localized over the In(III) center) with E(2) values of the 25.57 and 27.60 kcal/mol. The electron density of the pyridyl nitrogen lone-pair also delocalized into the σ^* orbital of the In1-I2 bond with an E(2) value of 3.83 kcal/mol. The weaker N→In(III) dative bonding situation was also depicted from the lower WBI value of 0.057.

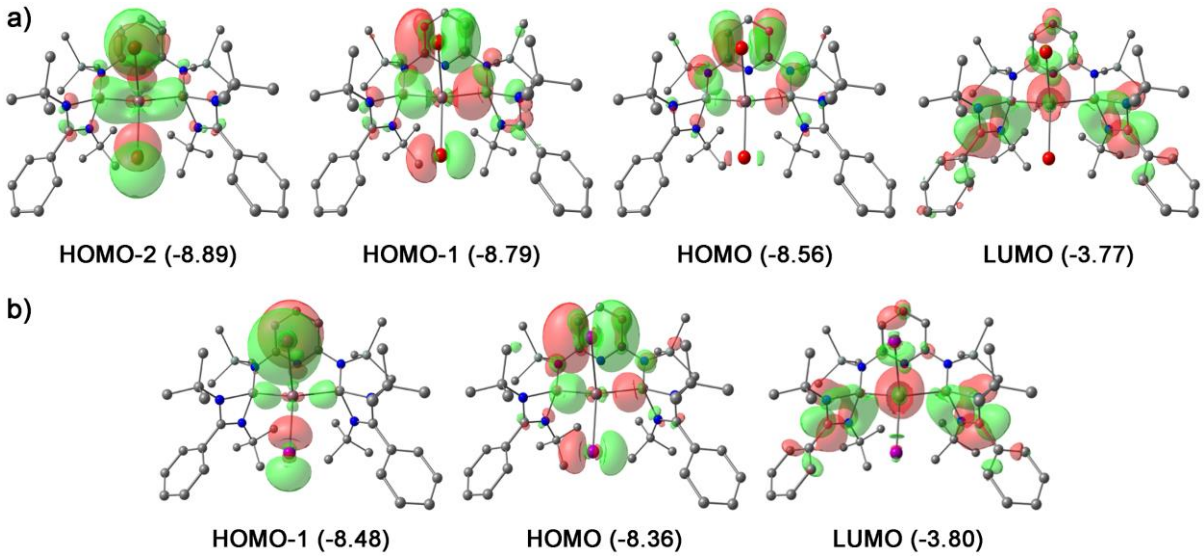

Figure 2B.15. Relevant molecular orbitals of a) complex **2B.6** and b) complex **2B.7** with their energies (in eV) provided in parentheses.

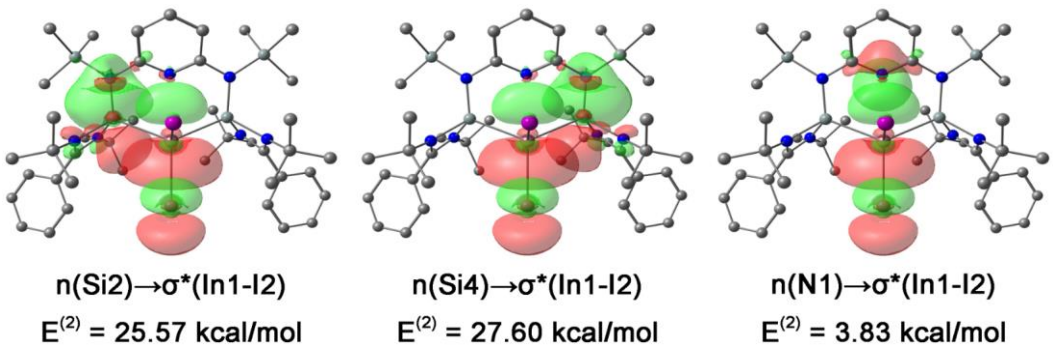

Figure 2B.16. Orbital overlaps for various donor-acceptor interactions in complex **2B.7** with their $E^{(2)}$ values.

Table 2B.1. WBI and natural charges of various complexes

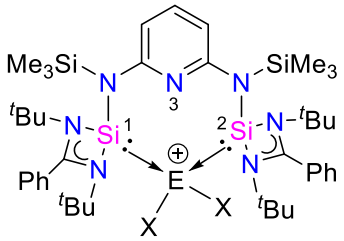

E = Al, Ga, In ; X = Br, I

	WBI			Natural charge		
	Si1-E	**Si2-E**	**N3-E**	**Si1**	**Si2**	**E**
Complex 2B.1	-	-	-	1.136	1.136	-
Complex 2B.2	0.754	0.785	0.096	1.521	1.536	0.578
Complex 2B.3	0.817	0.816	0.066	1.645	1.641	0.512
Complex 2B.4	0.818	0.819	0.050	1.651	1.654	0.216
Complex 2B.6	0.789	0.789	0.056	1.597	1.595	0.631
Complex 2B.7	0.788	0.788	0.057	1.605	1.603	0.439
Complex 2B.8	0.879	0.879	-	2.097	2.097	-0.566

2B.4 Conclusion

In summary, we have prepared and characterized the first bis-silylene stabilized cationic complexes of Al (**2B.2**), Ga (**2B.3**-**2B.5**), In (**2B.6**-**2B.7**) by the reactions of [{PhC(N^{t}Bu)$_2$Si}$_2${N(SiMe$_3$)}$_2$C$_5$H$_3$] (**2B.1**) with AlI_3, $GaBr_3$, GaI_3, $InBr_3$, and InI_3, respectively. The systematic study has been extended to prepare the first NHSi-based Lewis acid cations. Single crystal X-ray diffraction studies authenticated all the complexes. This study reveals the future potentials of SiNSi-based pincer ligands for taming reactive main group species with unusual oxidation states. On the other hand, because of their electron-deficient nature, they might be excellent alternatives to the available Lewis acid catalysts.

Chapter 2C: Carbazole Substituted Amidinato Silylene: Synthesis, Bonding, and Coordination Behavior with Coinage Metals

Adapted from: ***M. Ghosh***, S. Tothadi, and S. Khan*, Carbazole Substituted Amidinato Silylene: Synthesis, Bonding, and Coordination Behavior with Coinage Metals. *Organometallics* **2021**, *40*, 3201-3210.

2C.1 Objective of this work.

This part discusses the synthesis and characterization of a new carbazole substituted amidinatosilylene (**2C.1**) and its coinage metal complexes **2C.3**-**2C.8**. Before the complexation reactions, we prepared [PhC(N^{t}Bu)$_2$Si(Cbz)→Co(CO)Cp] complex (**2C.2**) to estimate the σ-donating strength of the newly synthesized silylene **2C.1**. Further, several commonly available coinage metal salts were utilized for the complexation reactions with **2C.1**, which afforded complexes **2C.3**-**2C.8**. The solid-state structures of **2C.1**-**2C.8** have been validated by single-crystal X-ray diffraction studies, NMR spectroscopy, and mass spectroscopy. DFT studies were also performed to understand the bonding scenario of **2C.1** and **2C.3**-**2C.7**. Of note, **2C.1** consists HOMO on its carbazolide moiety, and HOMO-1 features the silylene character. We also compared the HOMO-LUMO gap of **2C.1** with other amidinato silylenes having different N-substitutions.

2C.2 Introduction.

Recent decades have witnessed tremendous growth in the area of silylene chemistry.[61, 66, 123, 139-143] Ever since Roesky and co-workers reported the facile synthesis of the three-coordinate benzamidinato silylene **2C.A**, the derivatization of the silylene with various functionalities has become more accessible.[116, 144] To date, many variations of benzamidinato silylenes have been reported.[11, 72, 124, 125, 145-147] It is evident from the literature that changing the substituent at the Si(II) center of **2C.A** will directly influence the HOMO-LUMO energy gap[11] and hence the σ-donating ability. Among other N-donor variants, our group has explored [PhC(N^{t}Bu)$_2$Si{N(TMS)$_2$}] to isolate unique cationic copper(I)$\cdots\eta^6$-arene (arene = benzene, hexamethylbenzene) complexes.[148] Subsequently, these complexes were utilized as efficient catalysts in CuAAC reactions.[149] However, a close look at the literature reveals very few monodentate N-donor substituted silylenes. Although benzamidinato silylene ligated coinage metal complexes have been isolated over the years, they are still in their early stages.[88, 148-159] This encouraged us to synthesize a new N-donor substituted three-coordinate benzamidinato silylene and compare the HOMO-LUMO gap and coordination properties with the reported analogues. For this purpose, we choose tricyclic carbazole (Cbz) as an N-donor precursor as it is the main structural moiety of many biologically active compounds, and it has found versatile applications in synthesizing dyes and pigments.[160] In this study, we have synthesized a carbazolideamidinato silylene (**2C.1**), where Cbz can provide a rigid scaffold around the Si(II) center. Moreover, two coplanar aryl rings are expected to reduce π-donation from the *p*-orbital of the N-atom of Cbz to the Si(II) center. Following the synthesis of **2C.1**, we further

investigated its *σ*-donating ability by isolating a carbonyl complex [PhC(N^{t}Bu)$_2$Si(Cbz)Co(Cp)CO] (**2C.2**) *via* the reaction of cyclopentadienylcobalt(I)dicarbonyl [CpCo(CO)$_2$] with **2C.1**. Further, **2C.1** was treated with many group 11 metal precursors to generate several Si(II)→coinage metal complexes (**2C.3-2C.8**). These findings intend to elaborate the substituent effect in benzamidinato silylene towards the coinage metal complexes.

2C.3 Results and Discussion.

2C.3.1 Synthesis of 2C.1-2C.8.

[PhC(N^{t}Bu)$_2$SiCl] (LSiCl) was prepared by following the literature procedure.[116] ^{1}H, ^{13}C, ^{29}Si, and ^{19}F NMR spectra were recorded with the Bruker 400 MHz spectrometer, using $CDCl_3$ and C_6D_6 as a solvent with an external standard ($SiMe_4$ for ^{1}H, ^{13}C, and ^{29}Si and CHF_3 for ^{19}F).

2C.3.1.1 Preparation of 2C.1. LSiCl (2 g, 6.78 mmol) and LiCbz (1.172 g, 6.78 mmol) were taken in 60 mL toluene. After overnight stirring at room temperature, LiCl was precipitated from the reaction mixture and filtered off. The volume was reduced to 5 mL and kept at -30 °C. The colorless crystals suitable for X-ray analysis were observed. Yield: 2.19 g (76.6 %). Mp: 178°C. ^{1}H NMR (400 MHz, C_6D_6, 298 K): *δ* 0.98 (s, 18H, C*Me*$_3$), 7.27-7.60 (m, 8H, Ph), 8.04-8.17 (m, 3H, Ph), 9.02-9.04 (d, 1H, Ph) ppm. ^{13}C{^{1}H} NMR (100.613 MHz, C_6D_6, 298 K): *δ* 30.75 (C*Me*$_3$), 53.28 (*C*Me3), 113.68, 114.63, 119.56, 119.65, 119.89, 120.19, 124.71, 125.48, 128.88, 129.58, 133.54, 147.96, 145.96 (Ph-*C*), 161.21 (N*C*N) ppm. ^{29}Si{^{1}H} NMR (79.495 MHz, C_6D_6, 298 K): *δ* -24.81 ppm. HRMS: Calculated for [$C_{27}H_{31}N_3Si$]: *m/z* 425.2287. Found *m/z* 425.2026 [M]$^+$.

2C.3.1.2 Preparation of 2C.2. 2C.1 (0.213 g, 0.5 mmol) was charged in a flask with 40 ml toluene where $CpCo(CO)_2$ (0.5 ml, 0.5 mmol, 1 M solution in toluene) was added at 0 °C. After overnight stirring at room temperature, the reaction mixture was filtered off and concentrated to 3 ml. **2C.2** was crystallized as red crystals at room temperature. Yield: 225 mg (77.98 %). Mp: 227.7°C. ^{1}H NMR (400 MHz, $CDCl_3$, 298 K): *δ* 1.05 (s, 18H, C*Me*$_3$), 4.93 (s, 5H, C_5H_5), 6.58-6.97 (m, 3H, aromatic CH), 7.28-7.52 (m, 6H, aromatic CH), 8.08 (br, 2H, aromatic CH), 8.43 (m, 1H, aromatic CH), 9.96 (s, 1H, aromatic CH) ppm. ^{13}C{^{1}H} NMR (100.613 MHz, C_6D_6, 298 K): *δ* 30.50 (C*Me*$_3$), 54.53 (*C*Me$_3$), 82.50 (C_5H_5) 114.9, 117.80, 119.39, 120.30, 124.54, 127.94, 127.99, 128.04, 128.07, 130.20, 131.36, (Ph-*C*), 170.56 (N*C*N), 207.23 (CO) ppm. ^{29}Si{^{1}H} NMR (79.495 MHz, CDCl3, 298 K): *δ* 49.73 ppm. HRMS: Calculated for [$C_{33}H_{36}N_3OSiCo$]: *m/z* 577.2748. Found *m/z* 549.3146 ([M-CO]$^+$).

2C.3.1.3 Preparation of 2C.3. 2C.1 (0.106 g, 0.25 mmol) and $AuCl.SMe_2$ (0.0736 g, 0.25 mmol) were taken in a flask, and 40 ml toluene was added to the reaction mixture. After overnight stirring at room temperature in the dark, toluene was evaporated to dryness, and 40 ml DCM was added and filtered off. The colorless crystals suitable for X-ray analysis were obtained from a DCM and *n*-pentane mixture after one day at room temperature. Yield: 110 mg (66.85 %). Mp: 255.4ºC ^{1}H NMR (400 MHz, $CDCl_3$, 298 K): δ 1.09 (s, 18H, C*Me*$_3$), 7.16-7.18 (m, 2H, aromatic CH), 7.33-7.36(m, 2H, aromatic CH), 7.38-7.42 (m, 2H, aromatic CH), 7.45-7.49 (m, 2H, aromatic CH), 8.02-8.04 (d, 2H, aromatic CH), 10.49 (s, 2H, aromatic CH) ppm. ^{13}C{^{1}H} NMR (100.613 MHz, $CDCl_3$, 298 K): δ 31.05 (C*Me*$_3$), 56.19 (*C*Me$_3$), 110.17, 119.42, 120.36, 123.38, 125.85, 128.28, 129.48, 132.07, 139.58, 167.13 (N*C*N) ppm. ^{29}Si{^{1}H} NMR (79.495 MHz, $CDCl_3$, 298 K): δ 9.060 ppm. HRMS: Calculated for [$C_{27}H_{31}N_3SiAuCl$]: *m/z* 657.1641. Found *m/z* 656.4276 ([M-1]$^+$).

2C.3.1.4 Preparation of 2C.4. 2C.1 (0.213 g, 0.50 mmol) and CuBr / $CuBr_2$ (0.0717 g, 0.50 mmol) / (0.112 g, 0.5 mmol) were taken in a flask and 40 ml toluene was added to the reaction mixture. After overnight stirring at room temperature, the reaction mixture was filtered off, and toluene was concentrated. The colorless crystals suitable for X-ray analysis were obtained from DCM and *n*-pentane mixture after one day at 0ºC. Yield: 227 mg (80 %). Mp: 197.3ºC. ^{1}H NMR (400 MHz, $CDCl_3$, 298 K): δ 1.19 (s, 36H, C*Me3*), 7.20-7.33 (m, 3H, aromatic CH), 7.43-7.63 (m, 17H, aromatic CH), 8.04-8.10 (m, 3H, aromatic CH), 9.62 (s, 3H, aromatic CH) ppm. ^{13}C{^{1}H} NMR (100.613 MHz, $CDCl_3$, 298 K): δ 31.06 (C*Me*$_3$), 54.67 (*C*Me$_3$), 114.63, 115.11, 119.43, 120.12, 120.55, 125.32, 126.19, 126.98, 127.96, 128.31, 128.37, 129.56, 130.98, 131.31, 132.26, 144.26, 145.47, 170.20(N*C*N) ppm. ^{29}Si{^{1}H} NMR (79.495 MHz, $CDCl_3$, 298 K): δ -0.72 ppm. HRMS: Calculated for [$C_{54}H_{62}N_6Si_2Cu_2Br_2$]: *m/z* 1134.1533. Found *m/z* 1157.1426 ([M+Na]$^+$).

2C.3.1.5 Preparation of 2C.5. 2C.1 (0.213 g, 0.50 mmol) and CuI (0.191 g, 1 mmol) were taken in a flask. 40 ml toluene and 5 ml THF were added to the reaction mixture. After overnight stirring at room temperature, the reaction mixture was filtered off. The colorless crystals suitable for X-ray analysis were obtained at -30ºC after 4 days. Yield: 300 mg (57.5 %). Mp: 177.2ºC. ^{1}H NMR (400 MHz, $CDCl_3$, 298 K): δ 1.17 (s, 36H, C*Me*$_3$), 7.23-7.28 (m, 3H, aromatic CH), 7.38-7.53 (m, 10H, aromatic CH), 7.63-7.97 (m, 5H, aromatic CH), 8.03-8.05 (d, 4H, aromatic CH), 8.29 (m, 2H, aromatic CH) 8.76 (m, 2H, aromatic CH) ppm. ^{13}C{^{1}H} NMR (100.613 MHz, $CDCl_3$, 298 K): δ 30.23 (C*Me*$_3$), 53.34 (*C*Me$_3$), 113.69, 113.98,

117.99, 118.91, 118.97, 119.24, 123.98, 124.27, 126.63, 126.84, 127.20, 127.50, 128.01, 129.63, 143.56, 144.55, 169.14 (N*C*N) ppm. ^{29}Si{1H} NMR (79.495 MHz, $CDCl_3$, 298 K): δ 5.01 ppm. HRMS: Calculated for [$C_{54}H_{62}N_6Si_2CuI$]: *m/z* 1040.2915. Found *m/z* 1040.1088 ([M]$^+$).

2C.3.1.6 Preparation of 2C.6. 2C.1 (0.213 g, 0.50 mmol) and CuOTF.toluene (0.259 g, 0.5 mmol) were taken in a flask, and 40 ml toluene was added to the reaction mixture. After overnight stirring at room temperature, 20 ml DCM was added additionally due to poor solubility and was filtered off. The colourless crystals suitable for X-ray analysis were obtained from a DCM and toluene mixture at 0 ºC. Yield: 252.5 mg (77.57 %). Mp: 205.0ºC. ^{1}H NMR (400 MHz, $CDCl_3$, 298 K): δ 1.12 (s, 36H, C*Me*$_3$), 7.32-7.34 (m, 2H, aromatic CH), 7.42-7.50 (m, 7H, aromatic CH), 7.54-7.56 (m, 4H, aromatic CH), 7.59-7.62 (m, 3H, aromatic CH), 7.67-7.70 (d, 3H, aromatic CH), 8.02-8.08 (m, 5H, aromatic CH), 8.58-8.60 (d, 2H, aromatic CH) ppm. ^{13}C{^{1}H} NMR (100.613 MHz, $CDCl_3$, 298 K): δ 30.95 (C*Me*$_3$), 55.05 (*C*Me$_3$), 113.71, 120.02, 120.44, 121.38, 127.50, 128.25-128.97 (m, *C*F$_3$), 131.58, 143.53, 144.63, 172.58 (N*C*N) ppm. ^{29}Si{^{1}H} NMR (79.495 MHz, $CDCl_3$, 298 K): δ 0.13 ppm. ^{19}F{^{1}H} NMR (376.49 MHz, $CDCl_3$, 298 K): δ – 77.29 ppm. HRMS: Calculated for [$C_{56}H_{62}N_6O_6S_2F_6Si_2Cu_2$]: *m/z* 1274.2207. Found *m/z* 1275.2217 [M+H]$^+$.

2C.3.1.7 Preparation of 2C.7. 2C.1 (0.213 g, 0.5 mmol) and AgBr (0.094 g, 0.5 mmol) were charged in a flask with 40 ml toluene. After overnight stirring at room temperature in dark conditions, the reaction mixture was filtered off and concentrated. The colorless crystals suitable for X-ray analysis were obtained from a toluene and n-pentane mixture at room temperature. Yield: 221 mg (72 %). Mp: 238ºC. ^{1}H NMR (400 MHz, CDCl3, 298 K): δ 1.20 (s, 36H, C*Me*$_3$), 7.31-7.34(m, 3H, aromatic CH), 7.50-7.67 (m, 11H, aromatic CH), 7.67-7.68 (m, 2H, aromatic CH), 7.82-7.84 (m, 4H, aromatic CH), 8.02-8.10 (m, 4H, aromatic CH), 9.13-9.15 (m, 2H, aromatic CH) ppm. ^{13}C{^{1}H} NMR (100.613 MHz, CDCl3, 298 K): δ 30.01 (C*Me*$_3$), 53.72 (*C*Me$_3$), 113.03, 113.80, 118.38, 119.06, 124.25, 125.36, 125.75, 126.79, 127.17, 127.52, 127.62, 127.98, 129.88, 129.99, 136.76, 143.01, 144.01, 168.66 (N*C*N) ppm. ^{29}Si{^{1}H} NMR (79.495 MHz, CDCl3, 298 K): δ 4.36 ppm. HRMS: Calculated for [$C_{54}H_{62}N_6Si_2Ag_2Br_2$]: *m/z* 1222.1043. Found *m/z* 1222.1062 ([M]$^+$).

2C.3.1.8 Preparation of 2C.8. 2C.1 (0.213 g, 0.5 mmol) and AgI (0.117 g, 0.5 mmol) were charged in a flask with 40 ml toluene. After overnight stirring at room temperature in dark conditions, the reaction mixture was filtered off and evaporated to dryness. The colorless

crystals suitable for X-ray analysis were obtained from a DCM and *n*-pentane mixture at room temperature. Yield: 200 mg (60 %). M.p: 252.4°C. ^{1}H NMR (400 MHz, CDCl3 298 K): δ 1.11 (s, 72H, C*Me*$_3$), 7.14-7.24 (m, 10H, aromatic CH), 7.36-7.58 (m, 21H, aromatic CH), 7.72-7.74 (m, 4H, aromatic CH), 7.85-7.87 (d, 4H, aromatic CH), 7.91-7.93 (d, 4H, aromatic CH), 7.98-8.00 (d, 5H, aromatic CH), 9.03-9.05 (d, 4H, aromatic CH) ppm. ^{13}C{^{1}H} NMR (100.613 MHz, CDCl3, 298 K): δ 310.12 (C*Me*$_3$), 53.71 (*C*Me$_3$), 113.22, 114.45, 118.24, 119.03, 119.54, 119.65, 124.12, 125.05, 125.40, 125.88, 126.66, 127.05, 127.61, 128.63, 129.85, 130.18, 143.16, 144.21, 168.28 (N*C*N) ppm. ^{29}Si{^{1}H} NMR (79.495 MHz, CDCl$_3$, 298 K): δ 2.69 ppm.

The reaction of [PhC(N^{t}Bu)$_2$SiCl] (**2C.A**) with lithium carbazolide (LiCbz) (Scheme 2C.1) at room temperature afforded the Cbz substituted benzamidinato silylene (**2C.1**) in 76 % yield as a pale yellow crystalline solid. The ^{29}Si NMR spectrum of **2C.1** displays a chemical shift at δ -24.81 ppm, which is comparable to the pincer-based bis-silylene (δ -24 ppm)[19] but upfield shifted as compared to any of the N-donor moiety attached benzamidinato silylene reported to date (Chart 2C.1).[124]

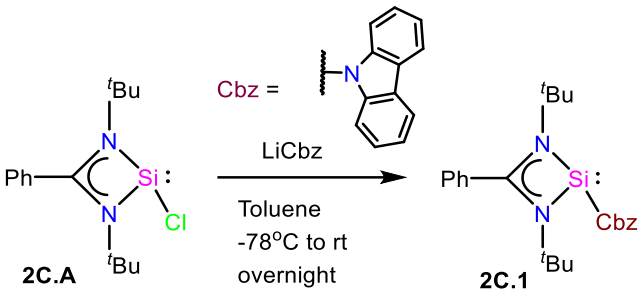

Scheme 2C.1. Synthesis of Cbz substituted benzamidinato silylene (**2C.1**).

Chart 2C.1. ^{29}Si NMR chemical shift in C_6D_6 (δ in ppm) of various N-donor substituted benzamidinato silylenes [{PhC(N^{t}Bu)$_2$}Si(NR$_2$)].

-NR$_2$	**NMe$_2$**	**N^{i}Pr$_2$**	**NPh$_2$**	**NCy$_2$**	**N(TMS)$_2$**	**Cbz**
δ	-2.7	-6.5	-20.5	-5.8	-8.1	-24.8

Compound **2C.1** crystallizes in the triclinic *P-1* space group (Figure 2C.1). The silicon center of **2C.1** possesses three coordination and a trigonal-pyramidal geometry with a lone-pair at the apical position. The Si1-N1 bond length in **2C.1** is 1.813 Å, whereas the other two Si1-N2 and Si1-N3 bond lengths are 1.860 Å and 1.876 Å, respectively. The Si1-N1 bond of **2C.1** is longer than the typical Si-N bond reported for various N-donor attached benzamidinato silylenes,[124] 1.769 Å [PhC(N^{t}Bu)$_2$Si{N(TMS)$_2$}], 1.724 Å [PhC(N^{t}Bu)$_2$Si{N(Me)$_2$}], 1.7432

Å, [PhC(N^{t}Bu)$_2$Si{N(Cy)$_2$}], 1.7434 Å [PhC(N^{t}Bu)$_2$Si{N(^{i}Pr)$_2$}], 1.782 Å [PhC(N^{t}Bu)$_2$Si{N(Me)Py}].[125]

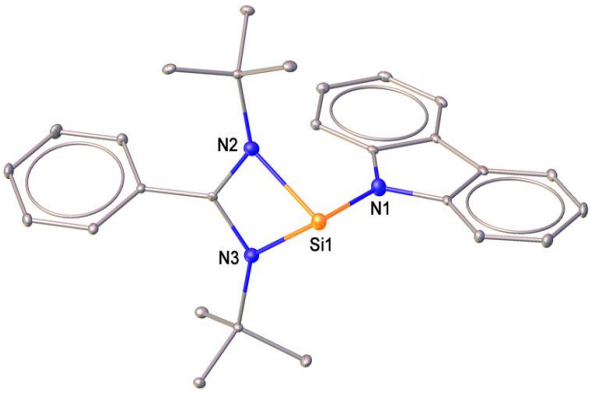

Figure 2C.1. Molecular structure of **2C.1**. Anisotropic displacement parameters are depicted at the 50 % probability level. H atoms are omitted for clarity. Selected bond distances (Å) and angles (°): Si1-N1 1.813(2), Si1-N3 1.876(1), Si1-N2 1.860(2) and N3-Si1-N2 69.37(8), N3-Si1-N1 102.77(8), N1-Si1-N2 101.41(8).

After isolating **2C.1** in the pure form, we intended to investigate its σ donation ability. Despite the precedence of good numbers of isolated silylenes, the comparison of their donor strength remained absent until recently. Radius and co-workers have isolated a few transition metal carbonyl complexes of five-membered NHSi and elaborately discussed their donation strength with the corresponding NHCs and phosphines.[161] Very recently, Nakata and co-workers employed Tolman's electronic parameter to estimate the donor strength of an imino-phosphonamido-chlorosilylene.[162, 163] Our group, also in a recent development, has put forward this idea to understand the role of ligand donation towards the glycosidation reaction.[153, 157] Accordingly, the reaction of **2C.1** with CpCo(CO)$_2$ leads to the formation of **2C.2** with the elimination of CO (Scheme 2C.2). The ^{29}Si NMR spectrum of **2C.2** shows a sharp peak at δ 49.73 ppm, which is upfield shifted than the previously reported complexes [PhC(N^{t}Bu)$_2$Si{N(TMS)$_2$}Co(Cp)CO] (**2C.B**) (δ 50.64 ppm) and [PhC{(N^{t}Bu)$_2$}Si(Cl)Co(Cp)CO] (**2C.C**) (δ 54.71 ppm)[157, 164]

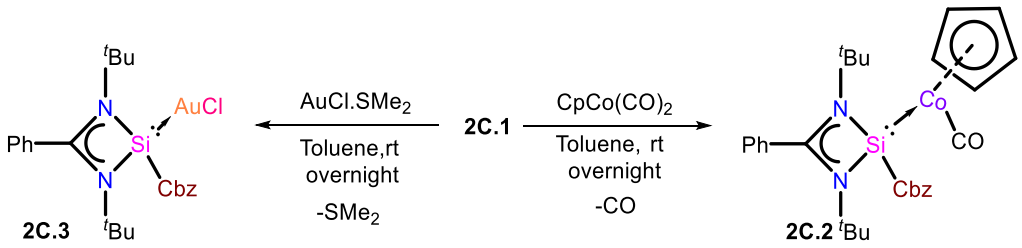

Scheme 2C.2. Reaction of **2C.1** with CpCo(CO)$_2$ and AuCl·SMe$_2$.

Compound **2C.2** crystallizes in the monoclinic $P2_1/n$ space group (Figure 2C.2). Tetra-coordinated Si center of **2C.2** attains a distorted tetrahedral geometry where the Co atom is attached to a carbonyl group, Cp group in η^5 fashion, and a silicon center comprised of benzamidinato backbone. The Si1-Co1 bond length in **2C.2** is 2.1437(7) Å, which is longer than those in [PhC{(N^{t}Bu)$_2$}SiClCo(Cp)CO] (**2C.C**) [2.1143(4) Å] and shorter than our [PhC(N^{t}Bu)$_2$Si{N(TMS)$_2$}Co(Cp)CO] (**2C.B**) [2.172(3) Å]. The Co-CO bond length in **2C.2** is [1.694(3) Å] which is comparable to **2C.C**[164] [1.6985(14) Å] but marginally shorter than **2C.B**[157] [1.686(9) Å]. The IR stretching frequency of CO appears at 1894 cm^{-1} (Figure 2C.3). This stretching frequency of **2C.2** is lower than **2C.C** (1968 cm^{-1}) but slightly higher than **2C.B** (1873 cm^{-1}) (Chart 2C.2). From this, it can be understood that the σ donation ability follows -N(TMS)$_2$ > -Cbz > -Cl trend when attached to the benzamidinato silylene moiety.

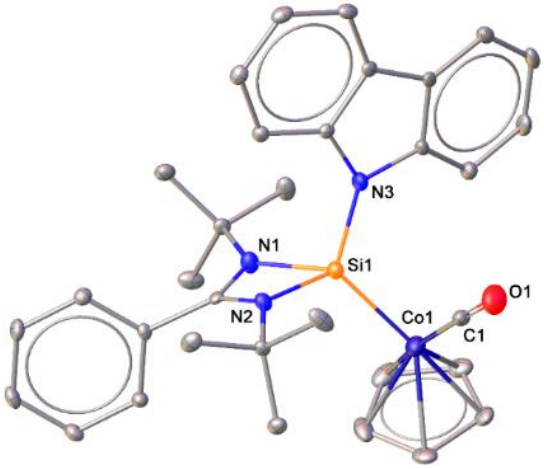

Figure 2C.2. Molecular structure of **2C.2**. Anisotropic displacement parameters are depicted at the 50 % probability level. H atoms are omitted for clarity. Selected bond distances (Å) and angles (°): Si1-Co1 2.1437(7), Co1-C1 1.694(3), Si1-N3 1.780(2), Si1-N1 1.831(2), Si1-N2 1.853(2), Co1-C3 2.097(3), Co1-C4 2.047(3), Co1-C5 2.098(3), Co1-C2 2.110(3), Co1-C6 2.089(3) and C1-Co1-Si1 86.3(1), O1-C1-Co1 178.0(2), Co1-Si1-N3 120.39(7), Co1-Si1-N1 122.89(7), N3-Si1-N2 109.86(9), N2-Si1-N1 70.76(9).

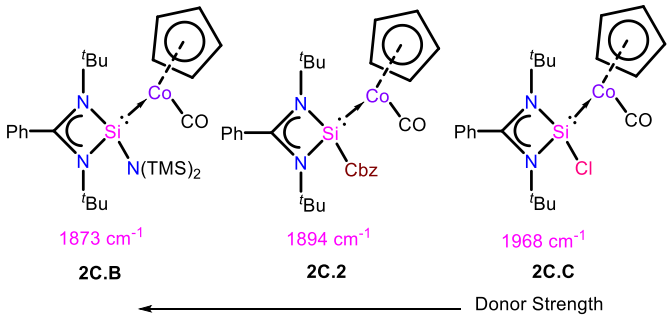

Chart 2C.2. IR stretching frequency of CO in **2C.2** and the reported complexes.

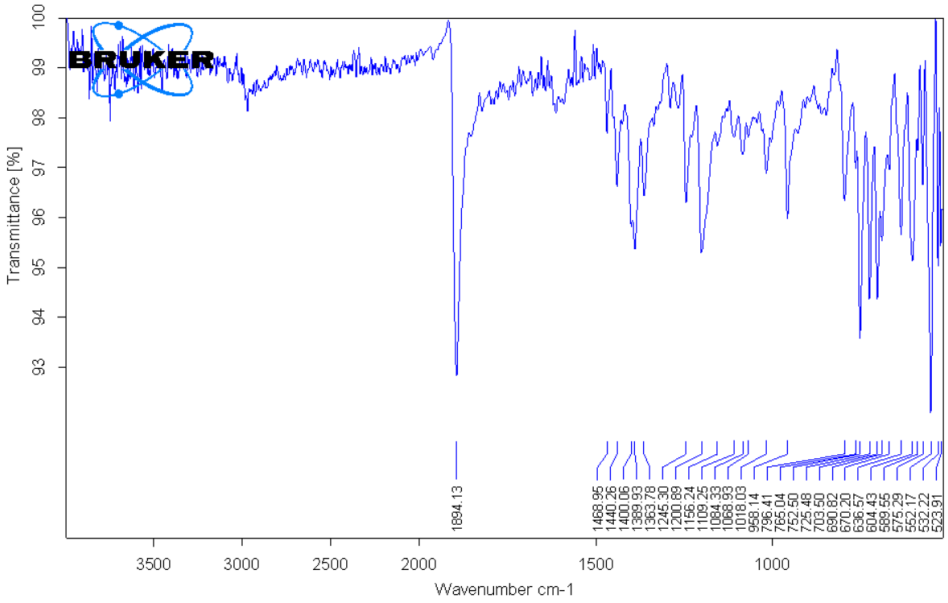

Figure 2C.3. IR spectra of complex **2C.2**.

Next, we wanted to explore the coordination behavior of **2C.1**, and for that purpose, we reacted **2C.1** with several group 11 metal precursors. To start with, the equivalent reaction of **2C.1** with AuCl·SMe_2 produced the complex **2C.3** (Scheme 2C.2). The ^{29}Si NMR spectrum of **2C.3** shows a peak at 9.0 ppm, which is comparatively downfield shifted than the previously reported [PhC(N^tBu)$_2$Si{N(TMS)$_2$}AuCl] (δ 8.76 ppm)[154] and upfield shifted than [PhC(N^tBu)$_2$Si{N(PPh_2)(2,6-^{i}Pr$_2$C$_6$H$_3$)}AuCl] (δ 24.73 ppm).[155] **2C.3** crystalizes in a monoclinic *C2/c* space group (Figure 2C.4). The four coordinated silicon center in **2C.3** attains a distorted tetrahedral geometry with the Si1-Au1 bond length of 2.242(2) Å, which is comparable to those in [PhC(N^tBu)$_2$Si{N(PPh_2)(2,6-^{i}Pr$_2$C$_6$H$_3$)}AuCl] [2.246(2) Å] and shorter than [PhC(N^tBu)$_2$Si{N(TMS)$_2$}AuCl] [2.265(1) Å]. The Si-Au bond length is also in accordance with the theoretically predicted Si(II)–Au(I) bond length (2.227 Å).[165] The Si1-Au1-Cl1 bond angle for **2C.3**, is 176.93(6)° and this is shorter from the linearity as [PhC(N^tBu)$_2$Si{N(PPh_2)(2,6-^{i}Pr$_2$C$_6$H$_3$)}AuCl] and [PhC(N^tBu)$_2$Si{N(TMS)$_2$}AuCl] show Si-Au-Cl bond angle of 177.39° and 179.47(3)°, respectively.

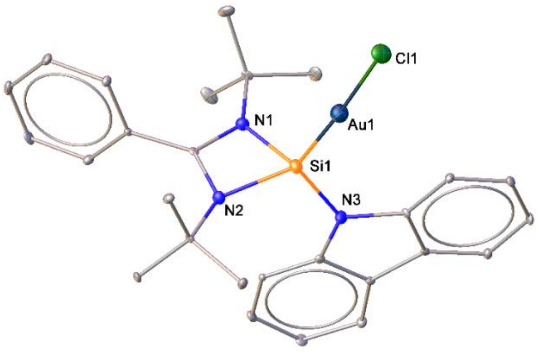

Figure 2C.4. Molecular structure of **2C.3**. Anisotropic displacement parameters are depicted at the 50 % probability level. H atoms are omitted for clarity. Selected bond distances (Å) and angles (°): Si1-Au1 2.242(2), Au1-Cl1 2.333(2), N2-Si1 1.816(7), N1-Si1 1.815(6), N3-Si1 1.760(6) and Si1-Au1-Cl1 176.93(6), Au1-Si1-N2 116.5(2), N2-Si1-N1 72.1(3), N1-Si1-N3 108.9(3), Au1-Si1-N3 120.0(2).

Further, with the aid of **2C.3**, the steric bulk of compound **2C.1** is also calculated. The $\%V_{bur}$ (percent buried volume) of **2C.1** was found to be 59, which is comparatively less bulky than the PhC(N^{t}Bu)$_2$Si{N(TMS)$_2$} ($\%V_{bur}$ = 63.5) (Figure 2C.5).[24] This difference in $\%V_{bur}$ upon substitution also discloses the substitution effect on the steric properties of the Si(II) center, which could be beneficial in designing catalytic reactions.

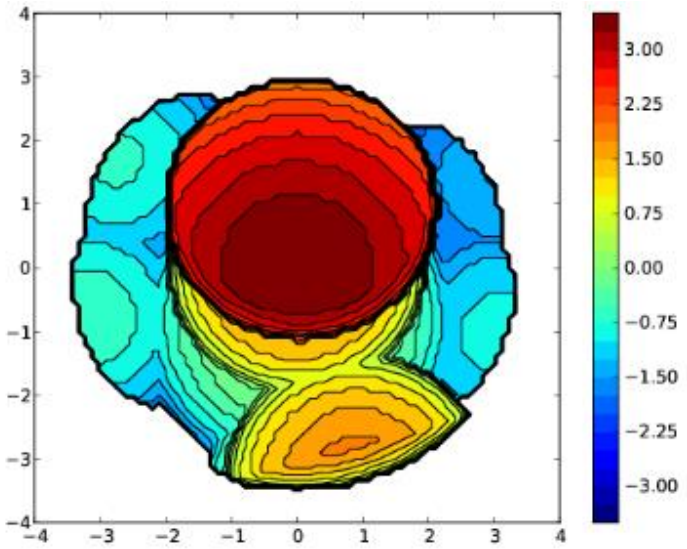

Figure 2C.5. Steric map of complex **2C.1**.

In continuation to the previous reaction, **2C.1** was further treated with CuBr to afford a dimeric complex **2C.4** (Scheme 2C.3). The ^{29}Si NMR of **2C.4** shows a peak at δ -0.72 ppm, which is upfield shifted as compared to [PhC(N^{t}Bu)$_2$Si{N(TMS)$_2$}CuBr]$_2$ (δ 5.72 ppm).[153] Compound **2C.4** crystallizes in triclinic *P-1* space group (Figure 2C.6). This is iso-structural to our previously reported [PhC(N^{t}Bu)$_2$Si{N(TMS)$_2$}CuBr]$_2$. The Si1-Cu1 and Si2-Cu2 bond lengths (2.203(2) and 2.212(2) Å) in **2C.4** are shorter than those in [PhC(N^{t}Bu)$_2$Si{N(TMS)$_2$}CuBr]$_2$ (2.243(3) Å and 2.250(3) Å).[23] After the reaction with Cu(I) halide salt, we intended to see the coordination behavior of **2C.1** towards Cu(II) halide salt. To our surprise, the reaction of **2C.1** with CuBr$_2$ led to the formation of **2C.4** along with the side product [PhC(N^{t}Bu)$_2$Si(Cbz)Br$_2$]. This reaction behavior is presumably due to the halophilic nature of the silylene.[161]

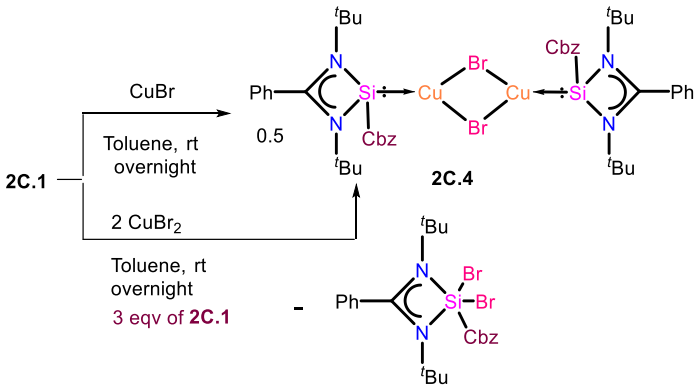

Scheme 2C.3. Synthesis of **2C.4** *via* the reaction of **2C.1** with $CuBr_2$.

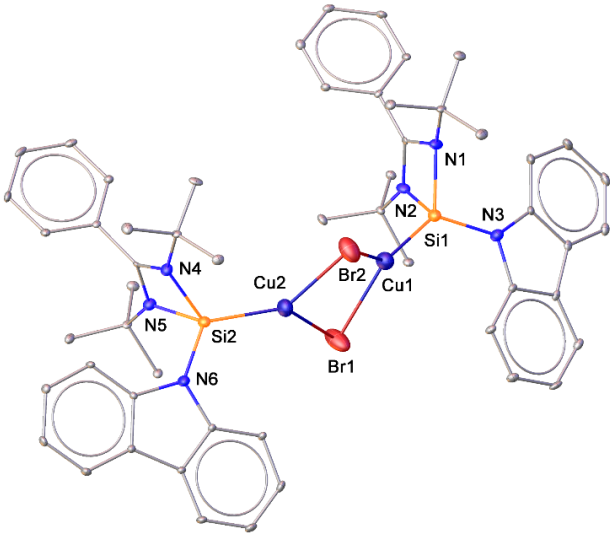

Figure 2C.6. Molecular structure of **2C.4**. Anisotropic displacement parameters are depicted at the 50 % probability level. H atoms and the non-coordinating solvent molecule are omitted for clarity. Selected bond distances (Å) and angles (°): Si2-Cu2 2.212(2), Cu2-Br2 2.4444(9), Cu2-Br1 2.422(1), Br1-Cu1 2.4250(8), Cu1-Si1 2.203(2), Si2-N6 1.780(5), Si1-N3 1.776(4), Si1-N2 1.832(4), Si1-N1 1.838(6), Si2-N5 1.821(4), Si2-N4 1.839(5) and Si2-Cu2-Br2 126.11(5), Br1-Cu2-Br2 96.69(3), Br1-Cu2-Si2 136.70(5), N6-Si2-Cu2 124.5(2), Cu2-Si2-N4 120.1(2), N6-Si2-N4 106.7(2), N5-Si2-N4 71.2(2), Br2-Cu1-Br1 97.30(3), Br2-Cu1-Si1 132.67(5), Si1-Cu1-Br1 129.97(5), Cu1-Si1-N3 122.4(2), Cu1-Si1-N1 119.7(2), N1-Si1-N2 71.2(2), N2-Si1-N3 103.7(2).

The formation of **2C.5** was serendipitous as we intended to see the complexation of **2C.1** with CuSPh, and for the preparation of CuSPh, we used CuI and LiSPh. Assuming the generation of CuSPh *in situ*, we added an equivalent amount of **2C.1** in the reaction mixture. However, X-ray data revealed the formation of **2C.5** where the Cu(I) center is coordinated to two molecules of **2C.1** (Figure 2C.7). The ^{29}Si NMR spectrum of **2C.5** shows a singlet at δ

5.01 ppm. **2C.5** is a structurally unique complex due to the coordination of two molecules of **2C.1** to the one copper(I) center. There are only a few examples of similar coordination of copper(I) with NHCs in the literature.[166, 167] The Cu center adopts a distorted trigonal geometry in **2C.5,** where Cu and I atoms are located at the crystallographic axis of rotation (Figure 2C.7). The silylene moieties are twisted out of the plane, which makes the structure look like a propeller. The Cu1-I1 bond length in **2C.5** is 2.604(1) Å, which is in accordance with the similar Cu-I bond observed with NHCs.[167]

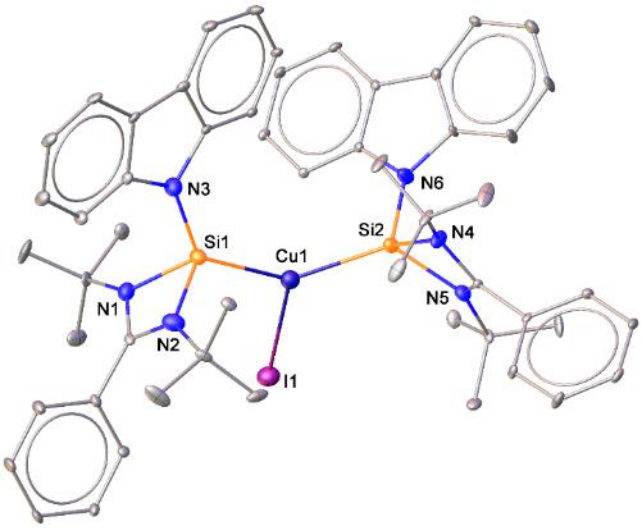

Figure 2C.7. Molecular structure of **2C.5**. Anisotropic displacement parameters are depicted at the 50 % probability level. H atoms are omitted for clarity. Selected bond distances (Å) and angles (°): Si2-Cu1 2.270(1), Si1-Cu1 2.295(1), Cu1-I1 2.604(1), Si2-N6 1.772(4), Si2-N5 1.830(5), Si2-N4 1.843(4), Si1-N3 1.776(4), Si1-N1 1.839(4), Si1-N2 1.831(5) and I1-Cu1-Si2 114.45(4), I1-Cu1-Si1 107.34(4), Si2-Cu1-Si1 138.12(6), Cu1-Si2-N6 116.2(2), Cu1-Si2-N5 122.2(1), N6-Si2-N4 104.8(2), N5-Si2-N4 70.8(2), Cu1-Si1-N3 130.6(1), N3-Si1-N2 105.2(2), N1-Si1-N2 71.0(2), Cu1-Si1-N1 111.1(1).

To standardize the synthetic protocol for **2C.5**, we then performed a reaction of **2C.1** with 0.5 equivalent of CuI, which resulted in the clean formation of **2C.5** (Scheme 2C.4). Our attempts to isolate silylene-CuSPh remained unsuccessful due to the poor solubility of CuSPh in toluene, THF, and diethyl ether. Nevertheless, we targeted cationic copper(I) precursor [CuOTf.toluene complex] to explore other coordination behavior of **2C.1**. The reaction of **2C.1** with CuOTf.toluene in 1:1 ratio afforded a dimeric complex **2C.6** (Scheme 2C.4). The ^{29}Si NMR spectrum of **2C.6** displays a singlet at δ -0.13 ppm, which is downfield shifted as compared to **2C.1**. The ^{19}F NMR spectrum shows a sharp singlet at δ -77.29 ppm. **2C.6** crystallizes in monoclinic $P2_1/c$ space group (Figure 2C.8).

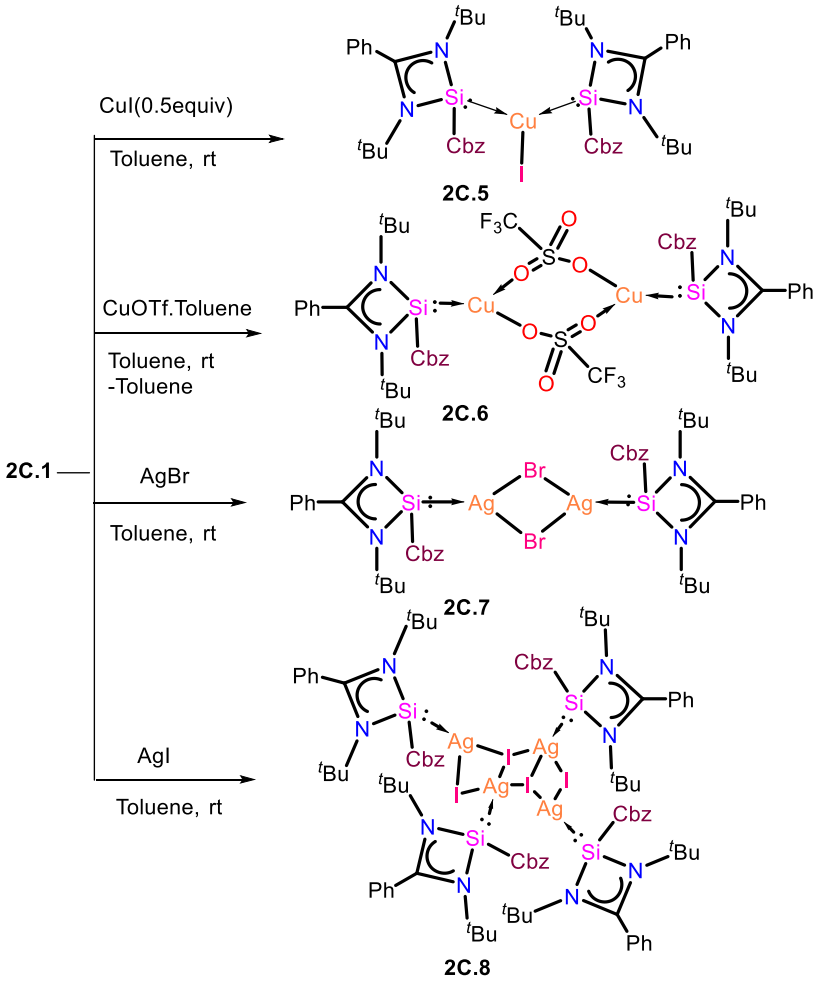

Scheme 2C.4. Syntheses of **2C.5-2C.8**.

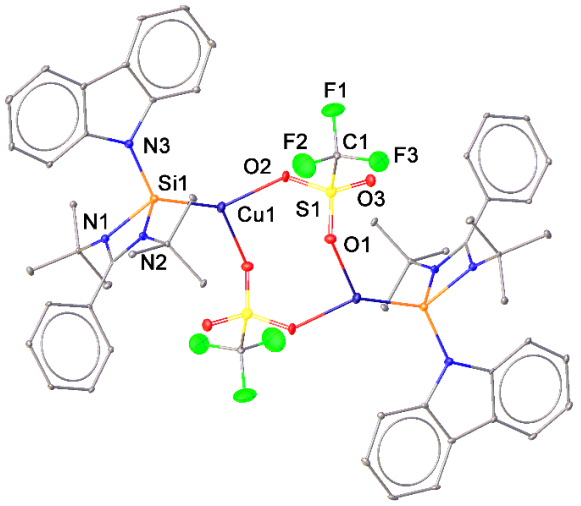

Figure 2C.8. Molecular structure of **2C.6**. Anisotropic displacement parameters are depicted at the 50% probability level. H atoms are omitted for clarity. Selected bond distances (Å) and angles (º): Si1-Cu1 2.186(1), Si1-N1 1.764(3), Si1-N3 1.821(3), Si1-N2 1.837(3), Cu1-O1 2.109(2), S1-O1 1.454(3), S1-O3 1.428(3), S1-O2 1.459(3) and O1-Cu1-Si1 128.92(8), O1-

Cu1-O2 89.5(1), O2-Cu1-Si1 140.51(9), Cu1-Si1-N1 124.0(1), Cu1-Si1-N3 117.4(1), Cu1-Si1-N2 119.5(1), N1-Si1-N2 106.7(1).

The molecular structure of **2C.6** reveals the formation of a unique eight-membered heteroatomic $Cu_2S_2O_4$ ring, where the copper center is ligated to the silylene moiety. Our group in 2015 reported a silver analogue $[PhC(N^tBu)_2Si\{N(TMS)_2\}]_2Ag_2(OTf)_2$ of **2C.6**,[154] where the molecule consists of a four-membered Ag_2O_2 core, unlike **2C.6**. It possesses an inversion center passing through the middle of the eight-membered ring. The Si1-Cu1 bond length of **2C.6** is 2.186(1) Å, which is shorter than Iwamoto's cationic Si-Cu complex[168] [2.268 Å] but comparable to that of heteroleptic NHSi-Cu cationic complexes, reported by Driess and co-workers in 2014.[150, 151] Although, in a recent development, our group has isolated a few benzamidinato silylenes coordinated cationic silver(I) complexes and explored them in three-component A^3 coupling reaction,[158] the structural validation of silver(I) halide complex with benzamidinato silylene is still missing. We employed **2C.1** to react with AgBr and AgI in equivalent amounts. Treatment of **2C.1** with AgBr led to the dimeric compound **2C.7** (Scheme 2C.3). The ^{29}Si NMR spectrum of **2C.7** shows a peak at δ 4.36 ppm. **2C.7** crystallizes in the monoclinic $P2_1/n$ space group (Figure 2C.9). The Si center in **2C.7** adopts a distorted tetrahedral geometry with Si1-Ag1 bond length of 2.3462 Å, which matches well with the reported Si(II)-Ag bond in $[PhC(N^tBu)_2Si\{N(TMS)_2\}]_2Ag_2(OTf)_2$ (2.337(2) and 2.346(2)).

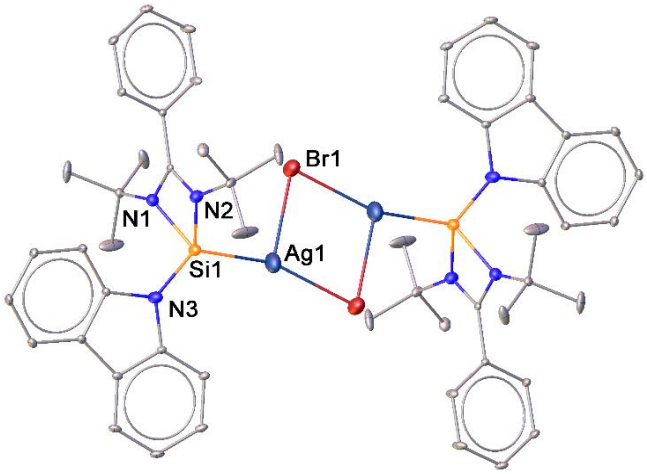

Figure 2C.9. Molecular structure of **2C.7**. Anisotropic displacement parameters are depicted at the 50 % probability level. H atoms are omitted for clarity. Selected bond distances (Å) and angles (°): Si1-Ag1 2.3508(9), Ag1-Br1 2.5296(7), Ag1-Br1 2.8864(8), Si1-N2 1.826(2), Si1-N1 1.830(2), Si1-N3 1.759(2), and Si1-Ag1-Br1 157.85(2), Br1-Ag1-Br1 97.40(1), Br1-Ag1-Si1 104.31(2), Ag1-Si1-N3 125.87(7), Ag1-Si1-N2 113.62(6), N3-Si1-N1 107.72(9), N1-Si1-N2 71.29(8).

The reaction of **2C.1** with AgI produces a unique stair-step tetrameric complex **2C.8** (Scheme 2C.4). The ^{29}Si NMR chemical shift at δ 2.69 ppm indicates the coordination of Si to Ag(I) center. Complex **2C.8** crystallizes in the triclinic *P-1* space group with three molecules of DCM (Figure 2C.10). Due to the larger size of iodide, two Ag_2I_2 moieties fused to release structural strain, and each silver(I) center is ligated with a silylene moiety. This coordination fashion is commonly observed in various phosphine ligated-silver(I) complexes,[169] but never realized with a silylene molecule. The formation of a multinuclear complex (**2C.8**) by the reaction of NHSi and AgI can be attributed to the less bulky nature of **2C.1**, which is also supported by the $\%V_{bur}$ data ($\%V_{bur}$(**2C.1**) = 59; $\%V_{bur}$(PhC(N^{t}Bu)$_2$Si{N(TMS)$_2$}) = 63.5). Additionally, we assume that the bridging ability of the iodide also plays an important role in this multinuclear core. The same observation is made for the complexation reaction of various phosphines with different silver(I) halides.[170] The Si1-Ag1 and Si2-Ag1 bond lengths in **2C.8** are 2.3865(9) and 2.409(1) Å, respectively, which are slightly longer than **7**. The Ag atoms in complex **2C.8** are arranged in a rectangular array with Ag•••Ag distances of 3.305 Å and 3.385 Å, which are marginally close to the borderline limit of argentophilic interaction (3.44 Å, the sum of van der Waal radii of two silver atoms).[171]

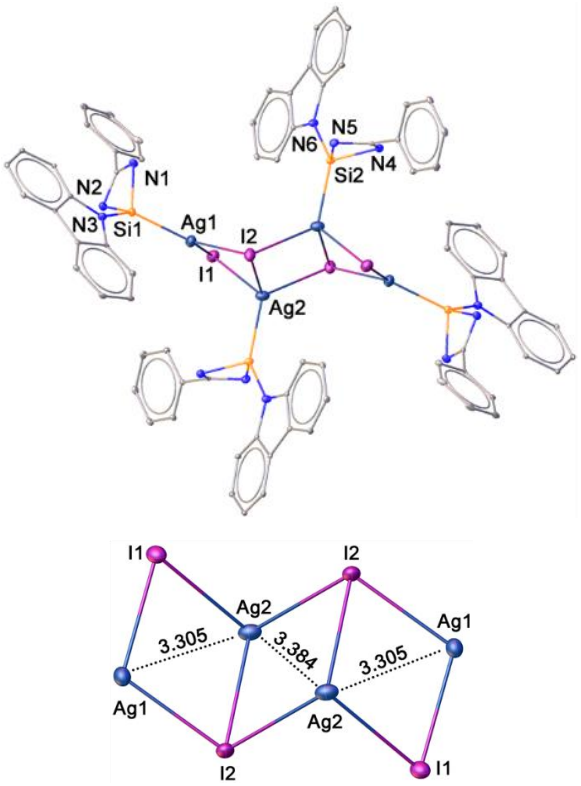

Figure 2C.10. Molecular structure of **2C.8**. Anisotropic displacement parameters are depicted at the 50% probability level. H atoms, tert-butyl groups at N1, N2, N4, N5, and the noncoordinating solvent molecule are omitted for clarity. Selected bond distances (Å) and

angles (°): Si1-Ag1 2.3865(9), Ag1-I1 2.7648(5), Ag1-I2 2.7804(5), I1-Ag2 2.9498(5), Ag2-I2 2.8874(6), Ag2-Si2 2.409(1), Si1-N3 1.759(3), N2-Si1 1.822(3), Si1-N1 1.829(4), Si2-N6 1.778(3), Si2-N4 1.830(3), Si2-N5 1.838(4) and Si1-Ag1-I1 118.04(3), Si1-Ag1-I2 131.82(3), I1-Ag1-I2 109.43(1), Ag1-I2-Ag2 71.31(1), I1-Ag2-I2 101.69(1), Ag1-Si1-N3 127.5(1), N3-Si1-N1 109.1(2), Ag1-Si1-N1 110.8(1).

DFT calculations were performed at the B3LYP-D3/def2-TZVPP level. The HOMO-1 (-5.5157 eV) is present on the silylene part of **2C.1**, whereas LUMO (-1.2349 eV) is spread over the amidinate ring (Figure 2C.11). The HOMO-LUMO gap in **2C.1** was found to be 4.28 eV and compared with other N-donor substituted silylenes. This energy gap of **2C.1** is comparable to that of Roesky's chlorosilylene (4.32 eV).[116] It is evident that aryl rings at N-center (such as phenyl and carbazolide) contribute more to the HOMO, thus making it more energetically stable and increasing the HOMO-LUMO gap. The optimized geometries of **2C.3-2C.6** are akin to their experimentally obtained geometries (Figure 2C.12).

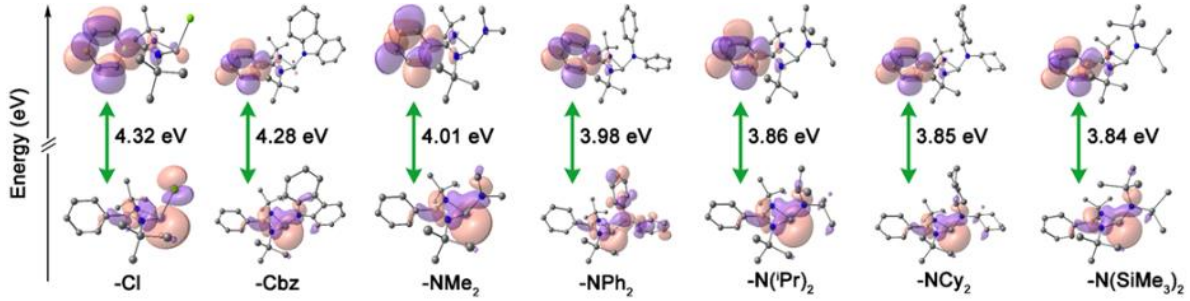

Figure 2C.11. DFT derived surface diagrams of HOMO and LUMOs for several N-donor substituted benzamidinato silylenes. For –Cbz substitution, HOMO-1 is considered.

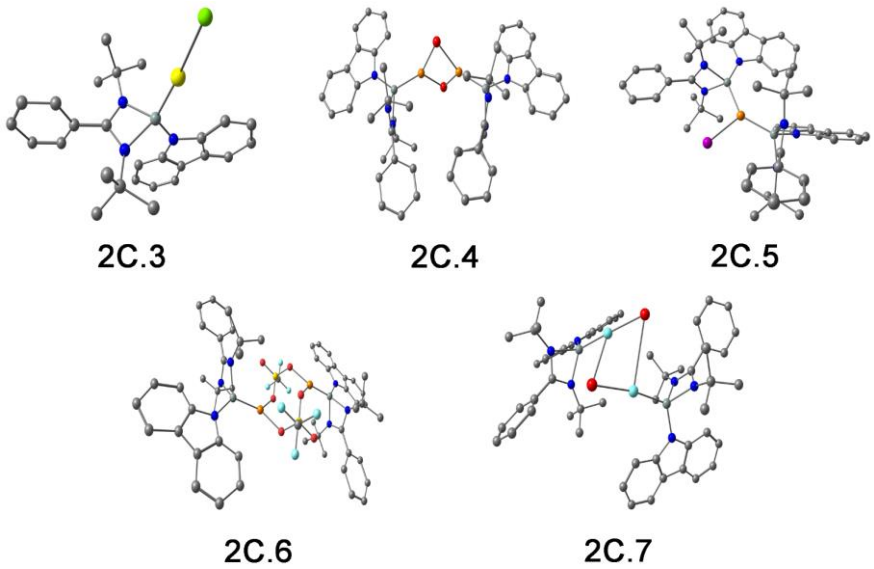

Figure 2C.12. Optimized geometries of **2C.3-2C.7**.

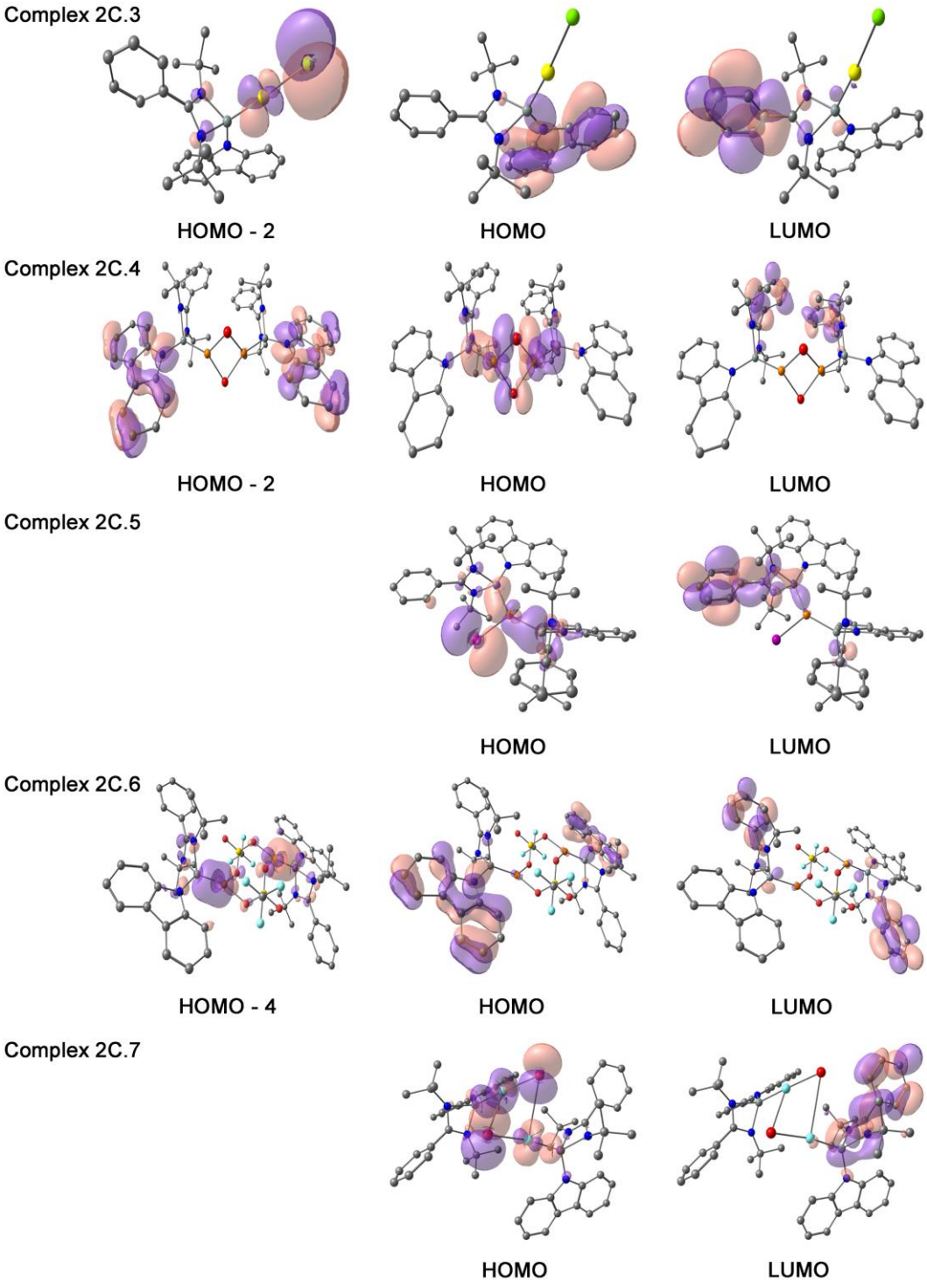

Figure 2C.13. DFT derived surface diagrams of relevant MOs of **2C.3-2C.7** (isosurface value = 0.03). Hydrogens are omitted for clarity.

The relevant MOs of complexes **2C.3**-**2C.7** are mentioned in Figure 2C.13. The HOMO (-6.0654 eV) in **2C.3** is mainly located on the carbazolide moiety, and the HOMO-2 (-6.43005 eV) is associated with the Au-Cl bond. The LUMO (-1.6300 eV) is largely associated with the amidinate ring of complex **2C.3**. The HOMOs of **2C.4** (-5.1674 eV) majorly consists of the

Si→Cu dative bond, whereas HOMO-2 (-5.7443 eV) is located at the carbazolide aromatic ring (Figure 2C.13). The LUMO of **2C.4** (-1.5864 eV) is located on the phenyl ring of the amidinato ligand. HOMO (-5.1538 eV) of complex **2C.5** is located on Si(II)→Cu-I bond, while LUMO (-1.1864 eV) is spread over the amidinate ring. For **2C.6**, the HOMO (-5.7879 eV) is on the carbazolide aromatic ring, but HOMO-4 (-6.0926 eV) has the contribution of Si(II)→Cu dative bond. It is interesting here to note that LUMO (-1.1946 eV) of **2C.6** is located on the amidinate ring despite the presence of the Lewis acidic triflate group. In the case of complex **2C.7**, HOMO (-5.7824 eV) is present on Si(II)→Ag-Br bond while LUMO (-1.3823 eV) is spread over the amidinate ring, denoting possible d-p backbonding. We further recorded the UV-Vis spectra of the complexes **2C.1**, **2C.3**-**2C.7** to see the HOMO-LUMO transitions (Figure 2C.14 and Tables 2C.1-2C.2) and calculated the HOMO-LUMO gaps. The absorption spectrums show only $\pi \rightarrow \pi^*$ transitions (ranging from 290 to 330 nm) for carbazolide moiety and are in accordance with the previously reported carbazolide-based systems.[172, 173] The spectrums showed vibrational features. We observed some scattering effects in the absorption spectra of **2C.3**, **2C.6**, and **2C.7** due to insoluble metal particle suspension. The HOMO-LUMO gaps have been calculated taking the right most transition into account.[174] It was observed that the experimentally obtained HOMO-LUMO gaps follow the same trend as the theoretically calculated ones (Table 2C.2).

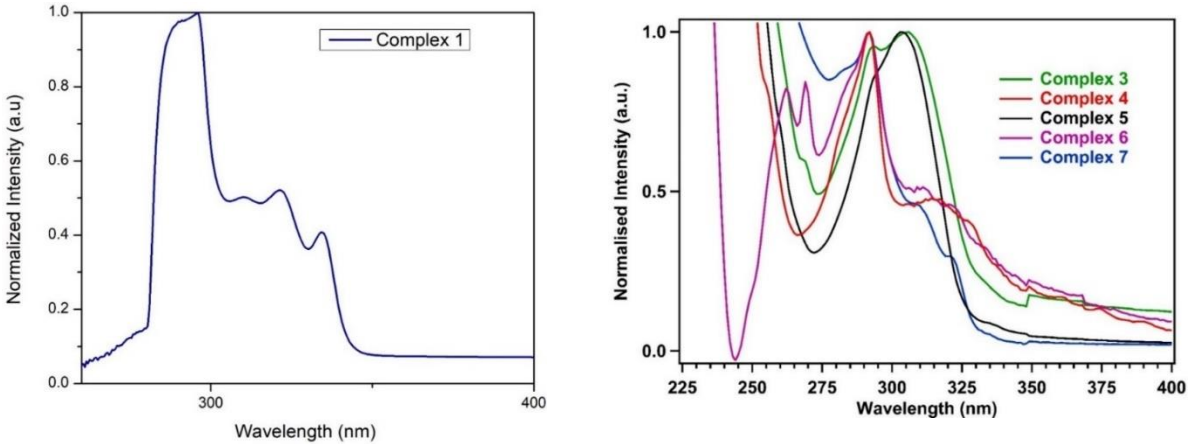

Figure 2C.14. Absorption spectra of **2C.1** (top) (in toluene) and **2C.3**-**2C.7 (**in DCM) with 3μM compound concentration.

Table 2C.1. The observed UV-Visible peaks for **2C.1** and **2C.3**-**2C.7**

Complexes	Peak wavelength (nm)
2C.1	334, 321, 310, 294
2C.3	306, 293

2C.4	327, 314, 292
2C.5	303, 294
2C.6	321, 311, 292, 269, 262
2C.7	322, 310, 292, 282

Table 2C.2. Calculated and observed HOMO-LUMO energies and gaps for **2C.1, 2C.3-2C.7**

Complexes	HOMO	LUMO	E (eV) (Calc.)	λ (nm) (Calc.)	λ (nm) (Obs.)	E (eV) (Obs.)
2C.1	-5.46	-1.23	4.28	290	334	3.71
2C.3	-6.06	-1.63	4.42	280	306	4.06
2C.4	-5.16	-1.58	3.58	346	327	3.79
2C.5	-5.15	-1.18	3.96	313	303	4.10
2C.6	-5.78	-1.19	4.59	269	321	3.87
2C.7	-5.78	-1.38	4.40	282	322	3.85

2C.4 Conclusion.

We have synthesized a new carbazolide substituted benzamidinato silylene **2C.1** and employed it to isolate several silylene-supported group 11 metal complexes. The DFT studies revealed the HOMO and LUMO gap of **2C.1** to be 4.28 eV, which is comparable to **2C.A**. However, the donation ability of **2C.1** was found to be better than **2C.A** as per the IR stretching frequency of the CO group of the respective cobalt carbonyl complexes, which is further supported by the higher HOMO of **2C.1** (-5.45 eV) than that of **2C.A** (-5.53 eV). The σ-donation strength of a ligand depends upon various electronic factors, which are regulated by the substituent attached to the ligand backbone. It is previously reported for NHCs that the +M effect of the -NHR group is higher than a halo (X= F, Cl, Br, and I)[43] substituent, and as a result, the -NHR group increases the overall σ-donation of the ligand. In view of the aforementioned fact, **2C.1** should show a relatively stronger positive mesomeric effect (+M) effect but a lesser negative inductive effect (-I) as compared to **2C.A**. Hence, the donation ability of **2C.1** is expected to be higher than **2C.A**. Further, depending upon metal precursors, the coordination properties of **2C.1** change as AgBr resulted in a dimeric Ag_2Br_2 core, whereas AgI led to a tetrameric Ag_4I_4 core. Cationic copper(I) triflate precursor upon reaction with **2C.1** afforded the complex **2C.6** with a unique $Cu_2S_2O_4$ eight-membered ring. These findings will help design new NHSis, which can be utilized to explore more coinage metal complexes as they are potent enough to emerge as excellent catalysts in various organic transformations.

Chapter 2D: Functionalization of N-Heterocyclic Silylene Coordinated Copper (I) Aryl Complex: Access to Versatile Cu(I) Synthons

Adapted from: ***M. Ghosh***, K. Gaurav, P. Panwaria, S. Tothadi, and S. Khan*, N-Heterocyclic Silylene Supported Copper(I) Aryl Complexes: Multitasking Cu(I) Synthon (***Manuscript under revision***); available at ChemRxiv **2024**.

2D.1 Objective of this work.

In this section, we have prepared [PhC{N(^{t}Bu)}$_2$SiN(SiMe$_3$)$_2$] (**2D.1**) coordinated organocopper(I) complexes (**2D.2** and **2D.3**) and utilized them as a useful synthon for the aryl group transfer and cleavage of a variety of homolytic and heterolytic bonds. Complex **2D.2** was used as a mesityl transfer reagent in the C–C cross-coupling reaction that led to the formation of the coupled products in excellent yields. Further, we have demonstrated the reaction of **2D.2** with compounds having B–B and Se–Se bonds, which led to the formation of dimeric μ-boryl bound Cu(I) complex (**2D.8**) and a new class of unprecedented NHSi-supported copper-selenides (**2D.10** and **2D.11**). Finally, this new synthetic methodology smoothly afforded several elusive NHSi-copper amide complexes (**2D.12-2D.16**). Moreover, the reaction of **2D.1** with mesityl silver afforded a unique dinuclear NHSi-silver(I) complex (**2D.4**), which possesses a three-membered Ag$_2$C ring supported by argentophilic interaction. We have also performed the DFT calculation to understand the bonding situation in all the isolated complexes.

2D.2 Introduction.

NHSis are now considered one of the formidable classes of neutral donor ligand systems as a higher congener of NHCs.[61, 68, 123, 143, 175-179] Over the years, several NHSis have been isolated and utilized in stabilizing reactive main group species,[66] coordinating transition metals for homogeneous catalysis,[119, 180] and activating the small molecules.[70, 123, 181-183] The NHSi stabilized coinage metal complexes are comparatively less explored than the NHC ones, despite their superior catalytic activities in several organic transformations.[67, 159, 184, 185] However, recent years have witnessed a sharp growth in isolating differently functionalized NHSi-coordinated coinage metal complexes and exploring their catalytic activities.[126, 148, 153, 155, 158, 186-190] Given our interest in this field,[126, 148, 153, 158, 186-188] we continue to be intrigued by the future possibilities of NHSi-based coinage metal complexes as useful synthons beyond the coordination of coinage metal halides to encompass the broader range of synthetic possibilities. The coordination of NHSis with coinage metals having heteroatom functionalization remains uncharted territory. This underscores the need for innovative methods to unlock this unexplored facet of coordination chemistry with NHSis. Till date, many NHC-based copper(I) synthons have been isolated and studied for bond activation and homogeneous catalysis.[191-199,200-203] One such complex is [Cu(IPr)(O^{t}Bu)], {IPr= 1,3-bis(2,6-diisopropylphenyl)imidazol-2-ylidene}, which has given access to plenty of important

compounds with various heteroatom bonding linkage.[191-199, 204, 205] Very recently, Nolan and co-workers explored [Cu(IPr)(OC(H)(CF_3)$_2$)] as a versatile synthon for the activation of S–H, N–H, C–H, and P–H bonds.[200] In this context, organocopper(I) reagents are a very reactive class of copper(I) species, often playing an essential role as a *trans*-metallation agent in many catalytic transformations.[193, 206] Moreover, NHC-based Cu(I) complexes with anionic C-donor atoms have already been explored for their catalytic application and functionalization reactions, e.g. formation of Cu-X bonds (-SR, -PR_2, -OR, -NR_2, etc.), intramolecular hydroalkoxylation of alkynes, CuAAC reaction and defluoro-borylation of fluoroalkenes, etc.[207] This inspired us to isolate the NHSi-based Cu(I)–aryl complexes (**2D.2** and **2D.3**), creating a platform for the further functionalization of the Cu–aryl bond (Chart 2D.1). Interestingly, a similar reaction with mesityl silver(I) afforded an NHSi-supported dinuclear Ag(I) complex (**2D.4**), which contains a three-membered Ag_2C ring supported with argentophilic interaction (**2D.4**). The stability of the complex is unique because of the high level of angle strains and torsional strains of the thermodynamically unstable three-membered Ag_2C ring. Sadighi and co-workers isolated a triangular $[Ag_2H]^+$ core stabilized by the 1,3-bis(2,6-diisopropylphenyl)imidazolin-2-ylidene (SIDipp),[208] but there is no precedence of such complex with NHSis till date.

The first part demonstrates the reaction of organo-coinage metal precursors with benzamidinato silylene (**2D.1**) and the utility of the derived NHSi-based organocopper complex **(2D.2**) as an aryl transfer reagent, and the second part showcases the reactivities of **2D.2** towards homolytic and heterolytic bond cleavage reactions. With the aid of NHSi→Cu-mesityl complex (**2D.2**), we first attempted a mesityl group transfer reaction in a Pd-catalyzed C–C cross-coupling reaction, which afforded C–C coupled products in excellent yields with a low-catalyst loading as compared to the previously reported work of Uchiyama and co-workers.[209] Hartwig and co-workers have proved that the generation of phosphine-coordinated silver-aryl bonds during the Pd-catalyzed C–C coupling reaction enables the facile *trans*-metalation at the Pd center, which explains the excellent catalytic activity of **2D.2** as a mesityl transfer reagent in C-C coupling reaction.[210] The feasibility of transferring sterically demanding mesityl group from **2D.2** to aryl halide with lower catalyst loading makes it an attractive alternative to other existing coupling counterparts (such as aryl boronic acid ester, aryl Grignard, and aryl zinc).[211]

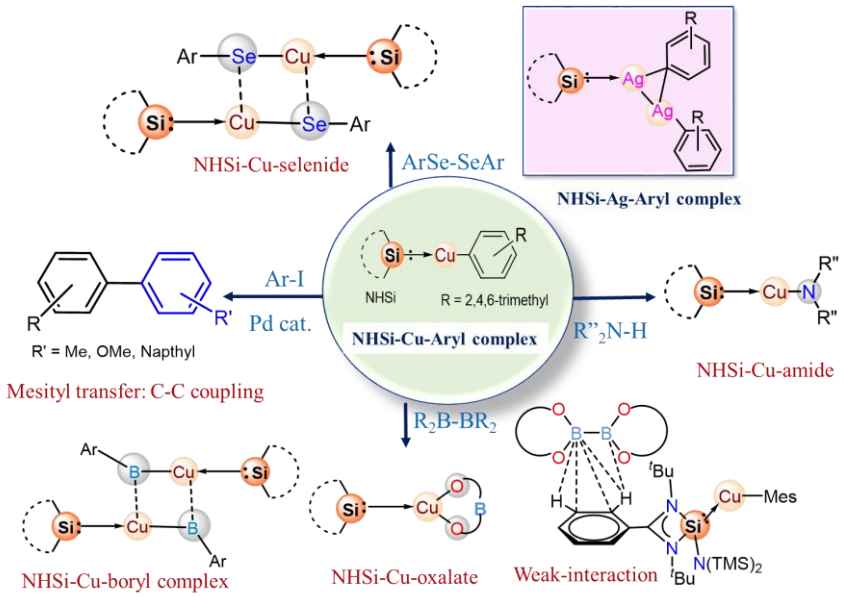

Chart 2D.1. Overview of the present Chapter.

In the second part of our work, we aimed at several homo- and heterolytic bond cleavage reactions with the NHSi-coordinated Cu(I) aryl complex. Sadighi and co-workers successfully isolated the first NHC (IPr and ICy = 1,3-dicyclohexylimidazol-2-ylidene) based Cu(I) boryl complexes [(IPr)Cu(Bpin), (ICy)Cu(Bpin)], which were found to be catalytically active for the reduction of CO_2 to CO.[212-216] We were interested in isolating NHSi-Cu-boryl complexes from diboron bond cleavage as they are proposed to be the intermediates in borylation reactions.[213-216] We thus attempted the reaction of **2D.2** with various diboron reagents, which furnished complexes **2D.6-2D.8** displaying unusual reaction patterns depending on the diboron reagents used.[209] Complex **2D.7** shows a cocrystallized structure with weak C–H···B interactions, while **2D.8** consists of a Cu_2B_2 core. Unlike copper-boryl complexes, NHC/CAAC-supported chalcogenides are limited to a handful of examples,[217-220] and the isolation of an NHSi-coordinated copper chalcogenolate complex remains elusive. Similarly, carbene metal amide (CMA) complexes have gathered special attention recently due to their mesmerizing photophysical properties, and a wide variety of NHC/CAAC ligated metal-amide complexes have already been documented.[221-226] Surprisingly, there is no report on NHSi-coordinated copper amide complexes either. Intrigued by the facts mentioned above, we treated complex **2D.2** with the compounds having Se–Se and N–H functionalities, which led to the formation of the first NHSi-copper arylselenogenolate complexes (**2D.10** and **2D.11**) and NHSi-based copper-amide complexes (**2D.12-2D.16**). Our present study showcases the synthetic versatility and potential applications of the NHSi-Cu-aryl complex (**2D.2**) in catalysis and bond activations.

2D.3 Results and Discussion.

2D.3.1 Synthesis and application of NHSi-Cu-Aryl complexes.

^{1}H, ^{13}C, ^{29}Si, and ^{19}F NMR spectra were measured in $CDCl_3$, C_6D_6 using a 400 MHz NMR spectrometer, "Bruker Avance DRX500"; chemical shifts (δ) are expressed in ppm referenced to external $SiMe_4$ (tetramethylsilane, TMS), ^{77}Se was referenced to external Me_2Se, using the residual solvent as internal standard ($CDCl_3$: ^{1}H, 7.26 ppm and ^{13}C, 77.16 ppm; C_6D_6: ^{1}H, 7.16 ppm and ^{13}C, 128.06 ppm). Melting points were measured in a sealed glass tube and were not corrected. Compounds **2D.1** and **2D.5** were prepared *via* previously reported procedures.[116, 124] According to the literature procedure, Mesityl copper, 2,4,6-triisopropylphenyl copper, and mesityl silver were also prepared.[227-229]

2D.3.1.1 Preparation of 2D.2. A Schlenk flask charged with compound **2D.1** (210.42 mg, 0.5 mmol) and mesityl copper (91.37 mg, 0.5 mmol) followed by the addition of toluene (20 ml) and kept in stirring overnight under an inert atmosphere of Argon (Ar). The greenish-yellow color solution was filtered and evaporated under reduced pressure. Yield: 250 mg (83%). ^{1}H NMR (400 MHz, C_6D_6, 298 K) δ 0.32 (s, 9H, Si-CH_3), 0.70 (s, 9H, Si-CH_3), 1.17 (s, 18H, {N-C(CH_3)$_3$}, 2.44 (s, 3H, *p*-CH_3), 3.06 (s, 6H, *o*-CH_3), 6.85-7.03 (m, 5H, arom. H), 7.14 (d, 2H, arom. H) ppm; $^{13}C\{^{1}H\}$ NMR (100.613 MHz, C_6D_6, 298 K): δ 4.82 (Si-CH_3), 5.98 (Si-CH_3), 21.78 (mesityl CH_3), 29.86 (mesityl CH_3), 31.80 {N-C(CH_3)$_3$}, 54.36 {N-C(CH_3)$_3$}, 125.16, 130.29, 132.03, 133.40, 146.66 (arom. C), 165.93, 167.16 (NCN) ppm; $^{29}Si\{^{1}H\}$ NMR (79.49 MHz, C_6D_6, 298 K): δ 5.28 [-N($SiMe_3$)$_2$], 5.33 [-N($SiMe_3$)$_2$], 6.5 (*Si*-Cu) ppm. HRMS (ESI, CH_3CN) (*m/z*) for [$C_{30}H_{52}CuN_3Si_3$] cacld. 601.2765; found 601.2748 [M^+].

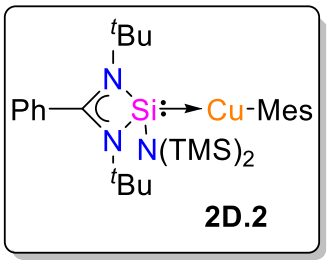

2D.3.1.2 Preparation of 2D.3. A Schlenk flask charged with compound **2D.1** (210.42 mg, 0.5 mmol) and 2,4,6-triisopropylphenyl copper (133.45 mg, 0.5 mmol) followed by the addition of toluene (20 ml) and kept in stirring overnight under an inert atmosphere of Argon (Ar). The greenish-yellow color solution was filtered and evaporated under reduced pressure. Yield: 300 mg (87.2 %). ^{1}H NMR (400 MHz, C_6D_6, 298 K) δ 0.24 (s, 9H, Si-CH_3), 0.60 (s, 9H, Si-CH_3), 1.10 (s, 18H, {N-C(CH_3)$_3$}), 1.38 (s, 6H, *p*-CHCH_3), 1.57 (s, 12H, *o*-CHCH_3), 2.97 (sept, 1H, *p*-CHCH$_3$), 3.74 (sept, 2H, *o*-CHCH$_3$), 6.80 (m, 3H, Ar-H), 6.93 (m, 1H, Ar-H), 7.06 (m, 3H, Ar-H) ppm; $^{13}C\{^{1}H\}$ NMR

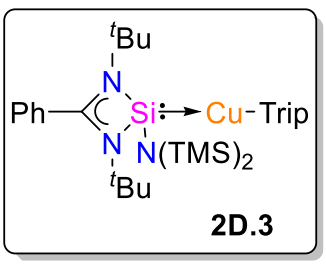

(100.613 MHz, C_6D_6, 298 K): δ 4.93 (Si-CH_3), 5.96 (Si-CH_3), 24.46 {-CH(CH_3)$_2$}, 26.42 {-CH(CH_3)$_2$}, 31.81 {N-C(CH_3)$_3$}, 35.37 {N-C(CH_3)$_3$}, 42.23 {C-(CH_3)$_2$}, 54.41 {N-C(CH_3)$_3$}, 118.71, 122.43, 125.70, 129.34, 130.38, 132.10, 145.40, 158.52, (arom. C), 165.65, 166.84 (NCN) ppm; ^{29}Si{^{1}H} NMR (79.49 MHz, C_6D_6, 298 K): δ 4.9 [-N(SiMe$_3$)$_2$], 5.4 [-N(SiMe$_3$)$_2$], 6.6 (Si-Cu) ppm. HRMS (ESI, CH_3CN) (m/z) for [$C_{36}H_{64}CuN_3Si_3$] cacld. 685.3704; found 708.1825 [M+Na]$^+$. M.p. 178.0 °C.

2D.3.1.3 Preparation of 2D.4. A Schlenk flask charged with compound **2D.1** (210.42 mg, 0.5 mmol) and mesityl silver (113.53 mg, 0.5 mmol) followed by the addition of toluene (20 ml) and kept in stirring overnight under an inert atmosphere of Argon (Ar). The resultant solution was filtered and evaporated under reduced pressure, which afforded single crystals at room temperature. Yield: 350 mg (80 %). ^{1}H NMR (400 MHz, C_6D_6, 298 K) δ 0.31 (s, 9H, Si-CH_3), 0.66 (s, 9H, Si-CH_3), 1.16 (s, 18H, {N-C(CH_3)$_3$}), 2.45 (s, 3H, o-CH_3), 3.02 (s, 6H, p-CH_3), 6.88 (m, 3H, arom. H), 7.00 (d, 1H, arom. H), 7.12 (d, 1H, arom. H), 7.21 (s, 2H, arom. H) ppm; ^{13}C{^{1}H} NMR (100.613 MHz, C_6D_6, 298 K): δ 4.89 (Si-CH_3), 5.92 (Si-CH_3), 14.35 (Mes-CH_3), 21.75 (mesityl CH_3), 23.06 (mesityl CH_3), 31.86 (N-CCH_3), 54.48 {N-C(CH_3)$_3$}, 125.11, 130.35, 131.98, 133.40, 146.16 (arom. C), 166.18 (NCN) ppm; ^{29}Si{^{1}H} NMR (79.49 MHz, C_6D_6, 298 K): δ 6.2 [-N(SiMe$_3$)$_2$], 6.3 [-N(SiMe$_3$)$_2$], 6.9 (Si-Cu) ppm. HRMS (ESI, CH_3CN) (m/z) for [$C_{39}H_{63}Ag_2N_3Si_3$] cacld. 871.2432; found 872.2076 [M+H]$^+$. M.p. 212.5 °C.

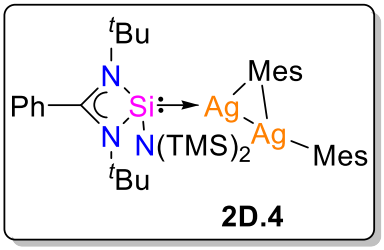

2D.4

2D.3.1.4 Preparation of 2D.5. A Schlenk flask charged with LSiCl (189.32 mg, 0.5 mmol) and mesityl copper (91.37 mg, 0.5 mmol) was taken in 20 ml toluene and kept in stirring overnight under an inert atmosphere of Argon (Ar). The greenish-yellow solution was evaporated under reduced pressure, extracted in 20 ml DCM and filtered off. Concentrating DCM to 2 ml and adding 4 ml n-Pentane produced single crystals at room temperature. Yield: 410 mg (86 %). ^{1}H NMR (400 MHz, C_6D_6, 298 K) δ 1.16 (s, 18H, {N-C(CH_3)$_3$}), 2.23 (s, 3H, mesityl-CH_3), 2.54 (s, 3H, mesityl-CH_3), 3.13 (s, 3H, mesityl-CH_3), 6.78-6.82 (m, 2H, Ar-H), 7.38-7.42 (m, 2H, Ar-H), 7.51 (m, 3H, Ar-H) ppm; ^{13}C{^{1}H} NMR (100.613 MHz, C_6D_6, 298 K): δ 20.36 (N-CCH_3), 21.17 (mesityl CH_3), 27.34 (mesityl CH_3), 31.26 (N-CCH_3), 54.41 {N-C(CH_3)$_3$}, 127.64, 127.94,128.27, 129.61, 130.07, 130.87, 131.69, 141.08, 145.15, 147.52, 167.07 (NCN) ppm;

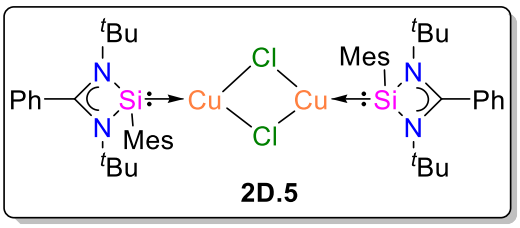

2D.5

$^{29}Si\{^{1}H\}$ NMR (79.49 MHz, C_6D_6, 298 K): δ 32.7 (*Si*-Cu) ppm. HRMS (ESI, CH_3CN) (*m/z*) for [$C_{48}H_{68}C_{12}Cu_2N_4Si_2$] cacld. 952.2952; found 953.1852 $[M+H]^+$. M.p. 279.6 °C.

2D.3.1.5 Preparation of 2D.6. A Schlenk flask charged with compound **2D.1** (210.42 mg, 0.5 mmol) and mesityl copper (91.37 mg, 0.5 mmol) followed by the addition of toluene (20 ml) and kept in stirring for 4 h. Bpin-Bdan[230] (146.98 mg, 0.5 mmol) were added to the solution and kept in stirring overnight under an inert atmosphere of Argon (Ar). The brown-colored solution was filtered off and concentrated to 2 ml to obtain single crystals at room temperature. Yield: 127 mg (35 %). HRMS (ESI, CH_3CN) (*m/z*) for [$C_{33}H_{65}BCuN_3O_4Si_3$] cacld. 725.3672; found 726.1791 $[M+H]^+$. M.p. 209.9 °C.

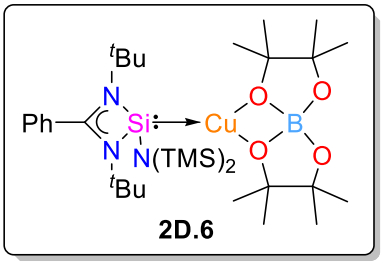

2D.6

2D.3.1.6 Preparation of 2D.7. A Schlenk flask charged with compound **2D.1** (210.42 mg, 0.5 mmol) and mesityl copper (91.37 mg, 0.5 mmol) followed by the addition of toluene (20 ml) and kept in stirring for 4 h. Bpin-Bpin (127mg, 0.5 mmol) was added to the solution and kept in stirring overnight under an inert atmosphere of Argon (Ar). The dark red-colored solution was filtered off and concentrated to 2 ml to obtain single crystals at room temperature. Yield: 171 mg (40 %). ^{1}H NMR (400 MHz, C_6D_6, 298 K): *δ* 0.45 (s, 9H, Si-C*H*$_3$), 0.65 (s, 9H, Si-C*H*$_3$), 1.15 (s, 18H, {N-C(C*H*$_3$)$_3$}), 1.24 (s, 24H, -C*H*$_3$) 2.15 (s, 3H, *p*-C*H*$_3$), 2.55 (s, 6H, *o*-C*H*$_3$), 6.94-6.97 (m, 5H, arom. H), 7.28 (d, 2H, arom. H) ppm; $^{13}C\{^{1}H\}$ NMR (100.613 MHz, C_6D_6, 298 K): *δ* 4.05 (Si-*C*H$_3$), 4.56 (Si-*C*H$_3$), 21.63 (mesityl *C*H$_3$), 23.83 (mesityl *C*H$_3$), 23.97 (-*C*H$_3$ of pinB-pinB) 30.96 {N-C(*C*H$_3$)$_3$}, 52.55 {N-*C*(CH$_3$)$_3$}, 82.01 {-*C*(CH$_3$)$_2$ of pinB-pinB} 123.97, 128.11, 128.60, 133.64, 137.85, 141.83, 145.45, 155.70, (arom. C) ppm $^{29}Si\{^{1}H\}$ NMR (79.49 MHz, C_6D_6, 298 K): *δ* 3.7 [-N(*Si*Me$_3$)$_2$], 2.8 [-N(*Si*Me$_3$)$_2$], -8.1 (*Si*-Cu); ^{11}B $\{^{1}H\}$ NMR (C_6D_6, 298 K, 128 MHz): *δ* 32.8 (pin*B*-*B*pin) ppm. HRMS (ESI, CH_3CN) (*m/z*) for [$C_{42}H_{76}B_2CuN_3O_4Si_3$] cacld. 855.4625; found 855.4675 $[M]^+$.

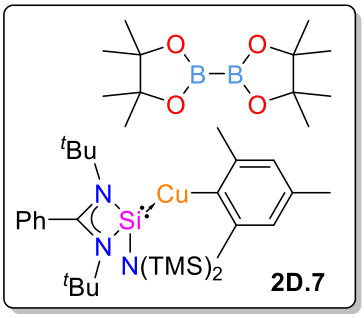

2D.7

2D.3.1.7 Preparation of 2D.9. A Schlenk flask charged with compound **2D.1** (210.42 mg, 0.5 mmol) and mesityl copper (91.37 mg, 0.5 mmol) followed by the addition of toluene (20 ml) and kept in stirring for 4 h. Bis(catecholato)diboron (B_2Cat_2) (127mg, 0.5 mmol) was added to the solution and kept in stirring overnight under an inert atmosphere of Argon (Ar). The dark red-colored solution was filtered off and concentrated to 2 ml to obtain single crystals at room

temperature. The spectroscopic data is in accordance to the previously reported literature.[231] For **2D.8**; ^{1}H NMR (400 MHz, C_6D_6, 298 K) δ 0.34 (s, 9H, Si-CH_3), 0.74 (s, 9H, Si-CH_3), 1.11 (s, 18H, {N-C(CH_3)$_3$}), 6.92 (m, 4H, Ar-H), 7.02 (m, 3H, Ar-H), 7.33 (m, 2H, Ar-H) ppm; ^{13}C{^{1}H} NMR (100.613 MHz, C_6D_6, 298 K): δ 5.04 (Si-CH_3), 6.73 (Si-CH_3), 31.93 {N-C(CH_3)$_3$}, 54.93 {N-C(CH$_3$)$_3$}, 122.95, 125.70, 128.57, 129.34, 131.72 (Ar-C), 153.15 (NCN) ppm; ^{29}Si{^{1}H} NMR (79.49 MHz, C_6D_6, 298 K): δ 3.7 [-N(SiMe$_3$)$_2$], 2.8 [-N(SiMe$_3$)$_2$], -8.1 (Si-Cu); ^{11}B {^{1}H} NMR (C_6D_6, 298 K, 128 MHz): δ 15.26 (Cu-BCat) ppm. HRMS (ESI, CH_3CN) (*m/z*) for [$C_{27}H_{45}N_3CuBO_2Si_3$] cacld. 601.2214; found 601.2728 [M]$^+$. For **2D.9**; ^{1}H NMR (400 MHz, C_6D_6, 298 K): δ ^{1}H NMR (400 MHz, C_6D_6, 298 K) δ 2.11 (s, 3H, Mes-CH_3), 2.55 (s, 6H, Mes-CH_3), 6.78 (s, 2H, Ar-H), 6.84 (dd, 2H, Ar-H), 7.12 (dd, 2H, Ar-H) ppm; ^{13}C{^{1}H} NMR (100.613 MHz, C_6D_6, 298 K): δ 21.35 (Mes-CH_3), 23.26 (Mes-CH_3), 109.01, 112.77, 118.23, 140.99, 145.10, 148.72 (Ar-C) ppm; ^{11}B {^{1}H} NMR (C_6D_6, 298 K, 128 MHz): δ 15.26 (Mes-BCat) ppm. HRMS (ESI, CH_3CN) (*m/z*) for [$C_{15}H_{15}BO_2$] cacld. 238.1165; found 238.0554 [M]$^+$.

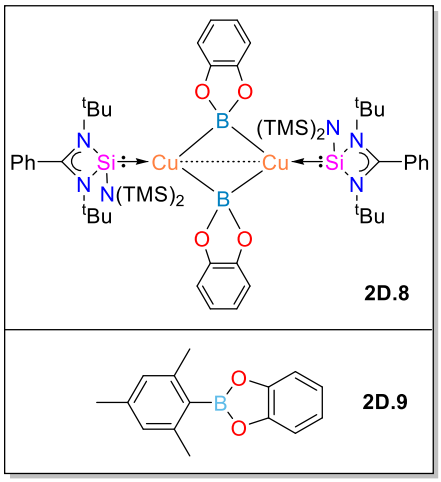

2D.3.1.8 Preparation of 2D.10. A Schlenk flask charged with compound **2D.1** (210.42 mg, 0.5 mmol) and mesityl copper (91.37 mg, 0.5 mmol) followed by addition of toluene (20 ml) and kept in stirring for 4 h. Diphenyl diselenide (Ph_2Se_2) (156.06 mg, 0.5 mmol) was added to the solution and kept in stirring overnight under inert atmosphere of Argon (Ar). The greenish-yellow color solution was filtered off and concentrated to 2 ml, and the addition of 4 ml n-pentane produced single crystals at room temperature. Yield: 255 mg (40 %). ^{1}H NMR (400 MHz, C_6D_6, 298 K) δ 0.38 (s, 9H, Si-CH_3), 0.72 (s, 9H, Si-CH_3), 1.23 (s, 18H, {N-C(CH_3)$_3$}), 6.93 (m, 3H, Ar-H), 7.03 (m, 1H, Ar-H), 7.09 (s, 2H, Ar-H), 7.20 (m, 1H, Ar-H), 7.35 (d, 1H, Ar-H), 8.21 (s, 2H, Ar-H) ppm; ^{13}C{^{1}H} NMR (100.613 MHz, C_6D_6, 298 K): δ 5.29 (Si-CH_3), 6.29 (Si-CH_3), 31.72 {N-C(CH_3)$_3$}, 54.42 {N-C(CH$_3$)$_3$}, 123.40, 127.53, 129.64, 129.86, 132.59, 136.76 (Ar-C), 166.12 (NCN) ppm; ^{29}Si{^{1}H} NMR (79.49 MHz, C_6D_6, 298 K): δ 4.4 [-N(SiMe$_3$)$_2$], 5.9 [-N(SiMe$_3$)$_2$], 5.9 (Si-Cu); ^{77}Se NMR (76.49 MHz, $CDCl_3$, 298 K): δ 37.1 ppm. HRMS (ESI, CH_3CN) (*m/z*) for [$C_{54}H_{92}Cu_2N_6Se_2Si_6$] cacld. 1278.2921; found 1279.2452 [M+H]$^+$. M.p. 152.2 °C.

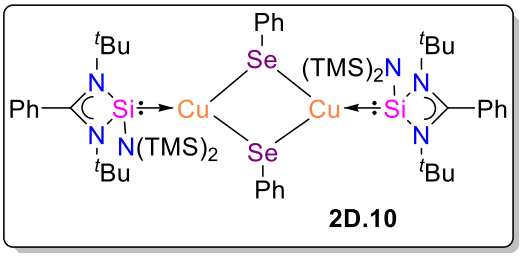

NMR details of mesityl(phenyl)selane: ^{1}H NMR (400 MHz, $CDCl_3$, 298 K): δ 2.33 (s, 3H, *p*-C*H*$_3$), 2.46 (s, 6H, o-C*H*$_3$), 7.02 (m, 2H), 7.14 (m, 5H); ^{13}C{^{1}H} NMR (100.613 MHz, C_6D_6, 298 K): δ 21.20, 24.40, 125.48, 126.89, 128.56, 128.99, 129.25, 133.60, 139.23, 143.78 ppm; ^{77}Se NMR (76.49 MHz, $CDCl_3$, 298 K): δ 290.4 ppm. HRMS (ESI, CH_3CN) (*m/z*) for [$C_{15}H_{16}Se$] cacld. 276.0417; found 276.0455 [M]$^{+}$.

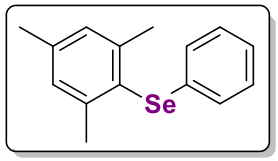

2D.3.1.9 Preparation of 2D.11. A Schlenk flask charged with compound **2D.1** (210.42 mg, 0.5 mmol) and mesityl copper (91.37 mg, 0.5 mmol) followed by the addition of toluene (20 ml) and kept in stirring for 4 h. Bis(2,4,6-trimethylphenyl) diselenide (Mes_2Se_2) (198 mg, 0.5 mmol) was added to the solution and kept in stirring overnight under inert atmosphere of Argon (Ar). The greenish-yellow color solution was filtered off and concentrated to 2 ml, this afforded single crystals at room temperature. Yield: 400 mg (69 %). ^{1}H NMR (400 MHz, C_6D_6, 298 K) δ 0.25 (s, 9H, Si-C*H*$_3$), 0.55 (s, 9H, Si-C*H*$_3$), 1.07 (s, 18H, {N-C(C*H*$_3$)$_3$}), 2.23 (s, 3H, Mes-C*H*$_3$), 3.10 (s, 6H, Mes-C*H*$_3$), 6.86 (m, 1H, Ar-H), 6.95 (m, 2H, Ar-H), 7.02 (s, 3H, Ar-H), 7.07 (s, 1H, Ar-H) ppm; ^{13}C{1H} NMR (100.613 MHz, C6D6, 298 K): δ 4.85 (Si-*C*H3), 5.85 (Si-*C*H$_3$), 21.14 (Mes-*C*H$_3$), 28.85 (Mes-*C*H$_3$), 31.74 {N-C(*C*H$_3$)$_3$}, 54.47 {N-*C*(CH$_3$)$_3$}, 129.46, 130.24, 131.43, 142.23, 155.37 (Ar-*C*), 167.02 (N*C*N) ppm; ^{29}Si{^{1}H} NMR (79.49 MHz, C_6D_6, 298 K): δ 6.7 [-N(*Si*Me$_3$)$_2$], 5.3 [-N(*Si*Me$_3$)$_2$], 3.2 (*Si*-Cu); ^{77}Se NMR (76.49 MHz, $CDCl_3$, 298 K): δ 230.4 ppm. M.p. 178°C.

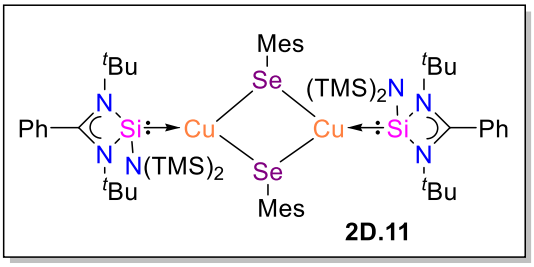

NMR details of dimesityl selane: ^{1}H NMR (400 MHz, $CDCl_3$, 298 K): δ: 2.23 (6H, s, CH_3), 2.25 (12H, s, CH_3), 6.84 (4H, s, ArH) ppm; ^{13}C NMR (100 MHz, $CDCl_3$) δ: 20.96, 23.64, 125.46, 128.39, 129.20,141.50 ppm; ^{77}Se NMR (76.49 MHz, $CDCl_3$, 298 K): δ 334.3 ppm. HRMS (ESI, CH_3CN) (*m/z*) for [$C_{18}H_{22}Se$] cacld. 318.0887; found 319.0959 [M+H]$^{+}$. M.p. <300°C.

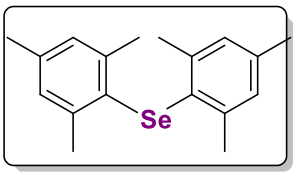

2D.3.1.10 Preparation of 2D.12. A Schlenk flask charged with compound **2D.1** (210.42 mg, 0.5 mmol) and mesityl copper (91.37 mg, 0.5 mmol) followed by the addition of toluene (20 ml) and kept in stirring for 4 h. Pyrrole (33.55 mg, 0.5 mmol) was added to the solution and kept in stirring overnight under an inert atmosphere of Argon (Ar). The resultant solution was filtered and evaporated under reduced pressure, which afforded single crystals at room

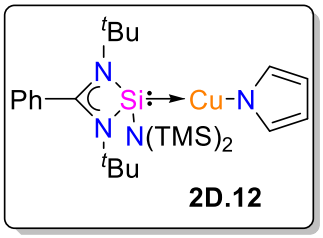

2D.12

temperature. Yield: 190 mg (69 %). ^{1}H NMR (400 MHz, C_6D_6, 298 K) δ 0.25 (s, 9H, Si-C*H*$_3$), 0.61 (s, 9H, Si-C*H*$_3$), 1.05 (s, 18H, {N-C(C*H*$_3$)$_3$}), 6.73 (m, 1H, Ar-H), 6.88 (m, 2H, Ar-H), 6.98 (m, 5H, Ar-H), 7.54 (m, 1H, Ar-H) ppm; ^{13}C{^{1}H} NMR (100.613 MHz, C_6D_6, 298 K): δ 4.65 (Si-*C*H$_3$), 6.06 (Si-*C*H$_3$), 31.78 (N-C*C*H$_3$), 54.63 {N-*C*(CH$_3$)$_3$}, 107.19, 125.69, 126.82, 129.33, 130.58, 131.31, 137.89, (Ar-*C*), 168.25 (N*C*N) ppm; ^{29}Si{^{1}H} NMR (79.49 MHz, C_6D_6, 298 K): δ 5.9 [-N(*Si*Me$_3$)$_2$], 6.7 [-N(*Si*Me$_3$)$_2$], 7.6 (*Si*-Cu) ppm. HRMS (ESI, CH_3CN) (*m/z*) for [$C_{25}H_{45}CuN_4Si_3$] cacld. 548.225; found 549.2099 [M+H]$^{+}$. M.p. 149.6 °C.

2D.3.1.11 Preparation of 2D.13: A Schlenk flask charged with compound **2D.1** (210.42 mg,

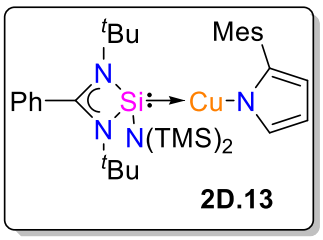

2D.13

0.5 mmol) and mesityl copper (91.37 mg, 0.5 mmol) followed by addition of toluene (20 ml) and kept in stirring for 4 h. 2-mesityl-1H-pyrrole[232] (92.56 mg, 0.5 mmol) was added to the solution and kept in stirring overnight under inert atmosphere of Argon (Ar). The resultant solution was filtered and evaporated under reduced pressure, which afforded single crystals at room temperature. Yield: 233 mg (70 %). ^{1}H NMR (400 MHz, C_6D_6, 298 K) δ 0.50 (s, 9H, Si-C*H*$_3$), 0.81 (s, 9H, Si-C*H*$_3$), 1.24 (s, 18H, {N-C(C*H*$_3$)$_3$}), 2.54 (s, 3H, Mes-C*H*$_3$), 2.79 (s, 6H, Mes-C*H*$_3$), 6.84 (m, 1H, Ar-H), 7.07 (d, 1H, Ar-H), 7.21(m, 2H, Ar-H), 7.27-7.42 (m, 5H, Ar-H), 7.75 (m, 1H, Ar-H) ppm; ^{13}C{^{1}H} NMR (100.613 MHz, C_6D_6, 298 K): δ 4.68 (Si-*C*H$_3$), 5.95 (Si-*C*H$_3$), 21.51 (Mes-*C*H$_3$), 22.00 (Mes-*C*H$_3$), 31.72 ({N-C(*C*H$_3$)$_3$}), 54.47 {N-*C*(CH$_3$)$_3$}, 106.49, 107.94, 125.69, 127.15, 129.33, 130.63, 131.41, 134.51, 137.49, 139.19 (Ar-*C*), 167.89 (N*C*N) ppm; ^{29}Si{^{1}H} NMR (79.49 MHz, C_6D_6, 298 K): δ 5.9 [-N(*Si*Me$_3$)$_2$], 6.6 [-N(*Si*Me$_3$)$_2$], 7.4 (*Si*-Cu) ppm. HRMS (ESI, CH_3CN) (*m/z*) for [$C_{34}H_{54}CuN_4Si_3$] cacld. 666.3031; found 665.1862 [M-H]$^{-}$. M.p. 193.1 °C.

2D.3.1.12 Preparation of 2D.14. A Schlenk flask charged with compound **2D.1** (210.42 mg,

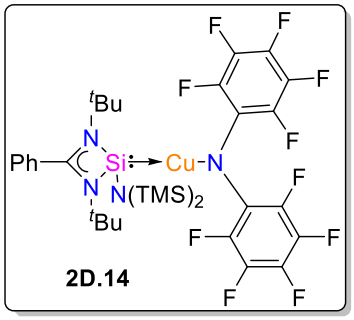

2D.14

0.5 mmol) and mesityl copper (91.37 mg, 0.5 mmol) followed by the addition of toluene (20 ml) and kept in stirring for 4 h. Bis-perfluoroarylamine[233] (174.56 mg, 0.5 mmol) was added to the solution and kept in stirring overnight under an inert atmosphere of Argon (Ar). The resultant solution was filtered and evaporated under reduced pressure, which afforded single crystals at room temperature. Yield: 269 mg (65 %). ^{1}H NMR (400 MHz, C_6D_6, 298 K) δ 0.23 (s, 9H, Si-C*H*$_3$),

0.47 (s, 9H, Si-C*H*$_3$), 1.05 (s, 18H, {N-C(C*H*$_3$)$_3$}), 6.91 (m, 3H, Ar-H), 7.06(m, 2H, Ar-H) ppm; ^{13}C{^{1}H} NMR (100.613 MHz, C_6D_6, 298 K): δ 4.74 (Si-*C*H$_3$), 5.53 (Si-*C*H$_3$), 31.51 {N-C(*C*H$_3$)$_3$}, 54.66 {N-*C*(CH$_3$)$_3$}, 127.34, 130.70, 131.17, 168.59 (N*C*N) ppm; ^{19}F {^{1}H} (376 MHz, C_6D_6, 298 K): δ -174.3, -167.1, -154.7 ppm; ^{29}Si{^{1}H} NMR (79.49 MHz, C_6D_6, 298 K): δ 6.2 [-N(*Si*Me$_3$)$_2$], 7.1 (*Si*-Cu) ppm. HRMS (ESI, CH_3CN) (*m/z*) for [$C_{33}H_{41}CuF_{10}N_4Si_3$] cacld. 830.1775; found 829.1780 [M-H]$^-$. M.p. 211.7 °C.

2D.3.1.13 Preparation of 2D.15. A Schlenk flask charged with compound **2D.1** (210.42 mg, 0.5 mmol) and mesityl copper (91.37 mg, 0.5 mmol) followed by the addition of toluene (20 ml) and kept in stirring for 4 h. *N*-mesitylpyridin-2-amine[234] (106 mg, 0.5 mmol) was added to the solution and kept in stirring overnight under an inert atmosphere of Argon (Ar). The resultant solution was filtered and evaporated under reduced pressure, which afforded single crystals at room temperature. Yield: 190 mg (55 %). ^{1}H NMR (400 MHz, C_6D_6, 298 K) δ 0.40 (s, 9H, Si-C*H*$_3$), 0.72 (s, 9H, Si-C*H*$_3$), 1.27 (s, 18H, {N-C(C*H*$_3$)$_3$}), 2.40 (s, 3H, *p*-C*H*$_3$), 2.69 (s, 6H, *o*-C*H*$_3$), 5.96 (d, 1H, Ar-H), 6.31 (m, 1H, Ar-H) 7.02-7.13 (m, 5H, Ar-H), 7.23-7.32 (m, 2H, Ar-H), 8.22 (d, 1H, Ar-H) ppm; ^{13}C{^{1}H} NMR (100.613 MHz, C_6D_6, 298 K): δ 4.80 (Si-*C*H$_3$), 5.82 (Si-*C*H$_3$), 19.49 (mesityl-*C*H$_3$), 21.23 (mesityl-*C*H$_3$), 31.74 {N-C(*C*H$_3$)$_3$}, 54.57 {N-*C*(CH$_3$)$_3$}, 104.81, 106.69, 129.34, 130.33, 130.64, 132.11, 133.80, 137.11, 146.47, 148.00 (Ar-*C*), 167.13, 168.70 (N*C*N) ppm; ^{29}Si{^{1}H} NMR (79.49 MHz, C_6D_6, 298 K): δ 5.3 [-N(*Si*Me$_3$)$_2$], 6.4 [-N(*Si*Me$_3$)$_2$], 6.9 (*Si*-Cu) ppm. HRMS (ESI, CH_3CN) (*m/z*) for [$C_{35}H_{56}CuN_5Si_3$] cacld. 693.3139; found 692.1946 [M-H]$^-$. M.p. 216.1 °C.

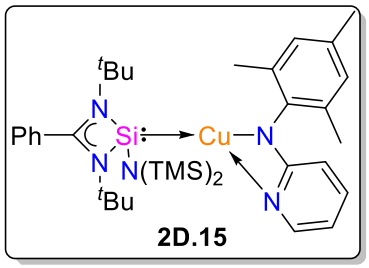

2D.15

2D.3.1.14 Preparation of 2D.16. A Schlenk flask charged with compound **2D.1** (210.42 mg, 0.5 mmol) and mesityl copper (91.37 mg, 0.5 mmol) followed by the addition of toluene (20 ml) and kept in stirring for 4 h. *N, N'*-bis(2,6-diisopropylphenyl)formimidamide[235] (182.29 mg, 0.5 mmol) was added to the solution and kept in stirring overnight under inert atmosphere of Argon (Ar). The resultant solution was filtered and evaporated under reduced pressure, which afforded single crystals at room temperature. Yield: 253 mg (60 %) ^{1}H NMR (400 MHz, C_6D_6, 298 K) δ 0.28 (s, 9H, Si-C*H*$_3$), 0.50 (s, 9H, Si-C*H*$_3$), 1.19 (s, 18H, {N-C(C*H*$_3$)$_3$}), 1.43 (d, 24H, ^{i}Pr-C*H*$_3$), 4.05 (sept, 4H, C*H*-

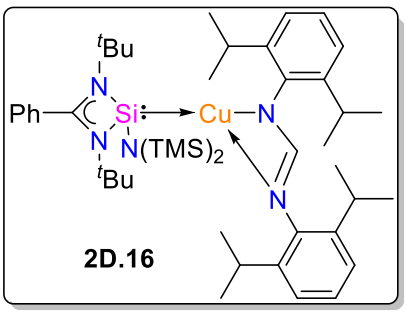

2D.16

CH_3), 6.76 (m, 1H, Ar-H), 6.86 (m, 2H, Ar-H), 7.04(m, 1H, Ar-H), 7.19 (s, 1H, Ar-H), 7.28 (d, 4H, Ar-H), 7.59 (d, 1H, Ar-H), 7.63 (s, 1H, Ar-H) ppm; $^{13}C\{^1H\}$ NMR (100.613 MHz, C_6D_6, 298 K): δ 4.94 (Si-CH_3), 5.97 (Si-CH_3), 24.47 {CH-(CH_3)$_2$}, 26.41 {CH-(CH_3)$_2$}, 31.82 {N-C(CH_3)$_3$}, 42.21 {CH-(CH_3)$_2$}, 54.42 {N-C(CH_3)$_3$}, 118.68, 120.57, 122.42, 125.70, 129.33, 130.41, 132.09, 135.45, 137.88, 145.35, 149.13, 158.51, (Ar-*C*), 165.67, 166.87 (N*C*N) ppm; $^{29}Si\{^1H\}$ NMR (79.49 MHz, C_6D_6, 298 K): δ 4.9 [-N(*Si*Me$_3$)$_2$], 5.4 [-N(*Si*Me$_3$)$_2$], 6.4 (*Si*-Cu) ppm. HRMS (ESI, CH_3CN) (*m/z*) for [$C_{46}H_{76}CuN_5Si_3$] cacld. 845.4705; found 868.4382 $[M+Na]^+$. M.p. 215.2 °C.

2D.3.2 General procedure for C-C cross-coupling reactions with the conventional method.

A 100 mL Schlenk tube charged with compound **2D.1** (210.42 mg, 0.50 mmol) and mesityl-copper (91.37 mg, 0.50 mmol) followed by the addition of toluene (8 ml) and stirred for 30 minutes at room temperature. 0.33 mmol of aryl halide was added to the solution, followed by adding 0.50 mmol of NaO^{t}Bu and 0.50 mol% Pd(dba)$_2$. The reaction mixture was then stirred for 16 h at 110 °C under the Argon (Ar) atmosphere. After 16 h, the reaction mixture was cooled to room temperature and extracted in *n*-hexane. The resulting solution was concentrated on a rota-evaporator and purified by column chromatography (*n*-hexane) to afford the expected product. All the C-C coupled products were characterized by NMR spectroscopy and HRMS.

2D.3.2.1 2'-Methoxy-2,4,6-trimethyl-1,1'-biphenyl (2D.I). Compound **2D.I** was prepared

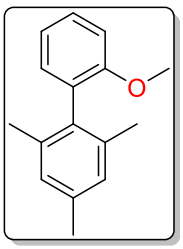

according to the general procedure; 1-iodo-2-methoxybenzene (44 mg, 21.67 µL, 0.33 mmol) was used as aryl halide. The product was obtained as a colorless oil. Yield: 74 mg (99 %). ^1H NMR (400 MHz, $CDCl_3$): δ 1.99 (s, 6H, *o*-C*H*$_3$), 2.34 (s, 3H, *p*-C*H*$_3$), 3.75 (s, 3H, -OC*H*$_3$), 6.95 (s, 2H, aromatic C-*H* of mesityl), 7.03- 6.98 (m, 3H), 7.34 (m, 1H); ^{13}C NMR (100.613 MHz, $CDCl_3$): δ 156.84, 136.62, 135.41, 131.10, 129.62, 128.41, 128.05, 120.76, 55.55 21.28, 20.49. HRMS (ESI, CH_3CN) (*m/z*) for [$C_{16}H_{18}O$] cacld. 226.1358; found 227.1447 $[M+H]^+$. All spectral data are consistent with those previously reported.[236]

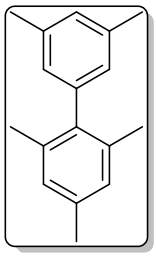

2D.3.2.2 2,3',4,5',6-pentamethyl-1,1'-biphenyl (2D.II). Compound **2D.II** was prepared according to the general procedure; 1-iodo-2-methoxybenzene (77.35 mg, 48 µL, 0.33 mmol) was used as aryl halide. The product was obtained as a colorless oil. Yield: 54 mg (72.3%). ^1H NMR (400 MHz, $CDCl_3$): δ 2.07 (s, 6H, -C*H*$_3$), 2.38 (s, 3H, *p*-C*H*$_3$), 2.40 (s, 6H, *o*-CH_3), 6.81 (s, 2H, aromatic C-*H* of

mesityl), 6.98 (m, 2H), 7.02 (s, 1H); ^{13}C NMR (100.613 MHz, $CDCl_3$): δ 141.12, 139.44, 137.79, 136.37, 136.04, 128.08, 127.13, 125.25, 21.51, 21.14, 20.89. HRMS (ESI, CH_3CN) (*m/z*) for [$C_{17}H_{20}$] cacld. 224.1565; found 225.1642 $[M+H]^+$. All spectral data are consistent with those previously reported.[237]

2D.3.2.3 2,4,6-trimethyl-1,1'-biphenyl (2D.III). Compound **2D.III** was prepared according

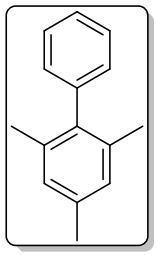

to the general procedure; iodobenzene (68 mg, 37.30 µL, 0.33 mmol) was used as aryl halide. The product was obtained as a colorless oil. Yield: 61.8 mg (94.45 %). ^{1}H NMR (400 MHz, $CDCl_3$): δ 2.39 (s, 3H, o-C*H*$_3$), 2.06 (s, 6H, *p*-C*H*$_3$), 7.00 (m, 2H), 7.21 (m, 2H), 7.37(m, 1H), 7.46 (m, 2H); ^{13}C NMR (100.613 MHz, $CDCl_3$): δ 141.23, 139.20, 136.68, 136.10, 129.43, 128.49, 128.18, 126.63, 21.16, 20.87. HRMS (ESI, CH_3CN) (*m/z*) for [$C_{15}H_{17}$] cacld. 196.1252; found 219.1714 $[M+Na]^+$. All spectral data are consistent with those previously reported.[238-240]

2D.3.2.4 1-mesityl naphthalene (2D.IV). Compound **2D.IV** was prepared according to the

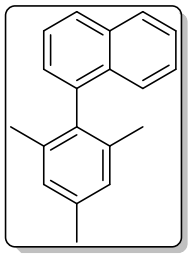

general procedure; 1-iodo-2-methoxybenzene (84.7 mg, 48.6 µL, 0.33 mmol) was used as aryl halide. The product was obtained as a colorless oil. Yield: 64.6 mg (79 %). ^{1}H NMR (400 MHz, $CDCl_3$): δ 1.95 (s, 6H, *o*-C*H*$_3$), 2.46 (s, 3H, *p*-CH_3), 7.08 (s, 2H, aromatic C-*H* of mesityl), 7.33 (d, 1H), 7.43 (m, 2H), 7.52 (t, 1H), 7.59 (t, 1H), 7.97-7.90 (dd, 2H); ^{13}C NMR (100.613 MHz, $CDCl_3$): δ 138.97, 136.99, 136.93, 136.88, 133.89, 132.13, 128.41, 128.20, 127.24, 126.84,126.12 125.85, 125.62, 21.27, 20.43. HRMS (ESI, CH_3CN) (*m/z*) for [$C_{19}H_{19}$] cacld. 246.1409; found 247.1592 $[M+H]^+$. All spectral data are consistent with previous reports.[241]

2D.3.2.5 2-mesityl thiophene (2D.V). Compound **2D.V** was prepared according to the general

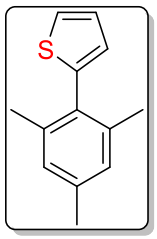

procedure; 2-iodothiophene (70.01 mg, 36.81 µL, 0.33 mmol) was used as aryl halide. The product was obtained as a colorless oil. Yield: 54.6 mg (80.96 %). ^{1}H NMR (400 MHz, $CDCl_3$): δ 2.16 (s, 6H, *o*-C*H*$_3$), 2.37 (s, 3H, *p*-C*H*$_3$), 6.84 (d, 1H), 6.98 (s, 2H, aromatic C-*H* of mesityl), 7.14 (s, 1H), 7.39 (d, 1H); ^{13}C NMR (100.613 MHz, $CDCl_3$): δ 141.63, 138.41, 137.92, 131.22, 128.22, 127.11, 126.54, 125.37, 21.20, 20.81. HRMS (ESI, CH_3CN) (*m/z*) for [$C_{13}H_{15}S$] cacld. 202.0816; found 203.0887 $[M+H]^+$. All spectral data are consistent with those previously reported.[242, 243]

We began our journey by attempting the synthesis of NHSi-based copper amide complexes from a dimeric [PhC{N(^{t}Bu)}$_2$SiN(SiMe$_3$)$_2$}$_2$Cu$_2$Cl$_2$] (**2D.A**) complex (Scheme

2D.1), but the desired complex could not be isolated with the base abstraction method. We mostly observed the decomposition products. Then, we sought to change our synthetic methodology and aimed to utilize organocopper(I) compound as a Cu(I) source. We started our investigation by reacting bis-(trimethylsilyl) amide substituted benzamidinato silylene (**2D.1**) with mesityl copper (CuMes)[228, 229, 244] in toluene at room temperature, which furnished complex **2D.2** (Scheme 2D.2) in 83% yield.

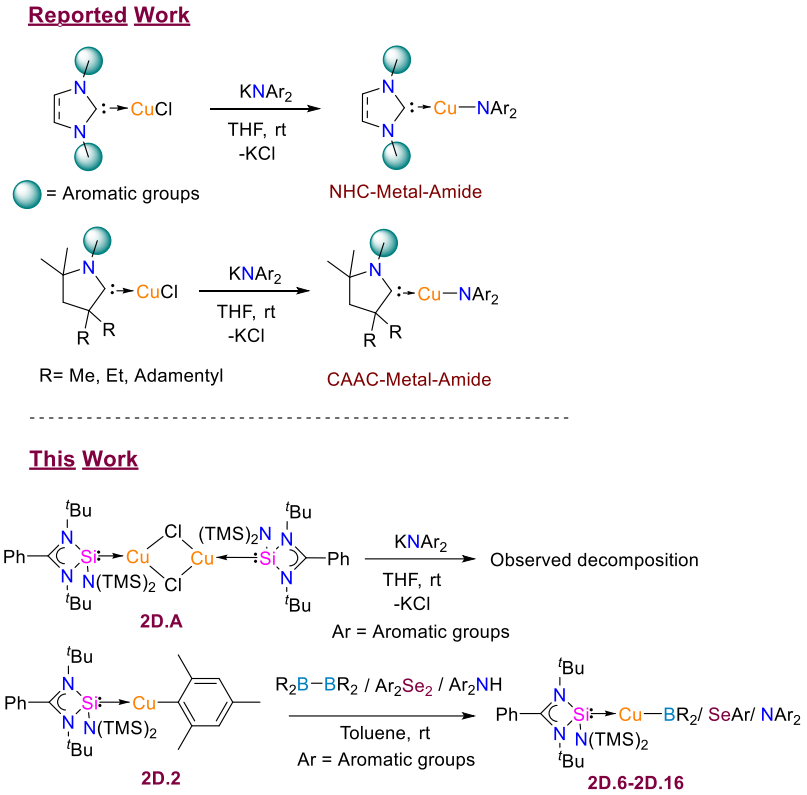

Scheme 2D.1. Attempt to generate NHSi stabilized heteroatom functionalized copper(I) complexes from **2D.A**.

Complex **2D.2** shows two sharp peaks for the –*Si*Me$_3$ groups at δ 5.28 and 5.33 ppm in benzene-d_6 and a broad peak at δ 6.5 ppm for the copper(I) coordinated silicon(II) center in the ^{29}Si{^{1}H} NMR spectrum, respectively.[245] Also, ^{1}H NMR shows two singlets for the mesityl group at δ 2.44 for three protons and 3.66 ppm for six protons. Complex **2D.2** crystallizes in a monoclinic *P2$_1$/c* space group, where the Si(II) center adopts a distorted tetrahedral geometry (Figure 2D.1). The Si–Cu bond length is 2.2590(8) Å, which matches well with the previously reported carbazole substituted benzamidinato silylene stabilized dimeric Cu_2Br_2 complex,[126] but significantly longer than the predicted bond length for NHSi→Cu(I) complex by Frenking and co-workers.[165] **2D.2** features almost linear geometry around the copper(I) center featuring the bond angle Si1–Cu1–C1 of 173.28(6)°, which is in accordance with the previously reported

IMes (1,3-bis-(2,4,6-trimethylphenyl)imidazol-2-ylidene) stabilized copper mesityl complex.[246] Similarly, treatment of **2D.1** with 2,4,6-triisopropylphenyl copper (CuTrip) in toluene at room temperature produced **2D.3** in 87% yield (Scheme 2D.2). The $^{29}Si\{^{1}H\}$ NMR spectrum of **3** shows two sharp singlets at δ 4.9 and 5.4 ppm for the –*Si*Me$_3$ groups and a broad peak at δ 6.6 ppm for *Si*–Cu. The Si–Cu bond length of **2D.3** (Figure 2D.1) is similar to the previously reported dimeric copper(I) halide complexes of **2D.1**.[247] The Si1–Cu1–C1 bond angle in **2D.3** is 170.72 (7)°, which is slightly deviated as compared to that in **2D.2** and the reason can be attributed to the bulkiness of the 2,4,6-triisopropylphenyl group.

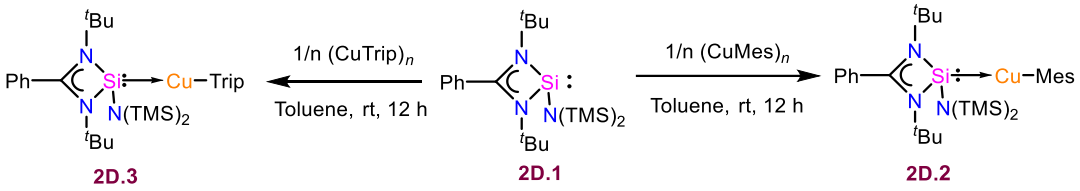

Scheme 2D.2. The reaction of compound **2D.1** with various organocopper compounds.

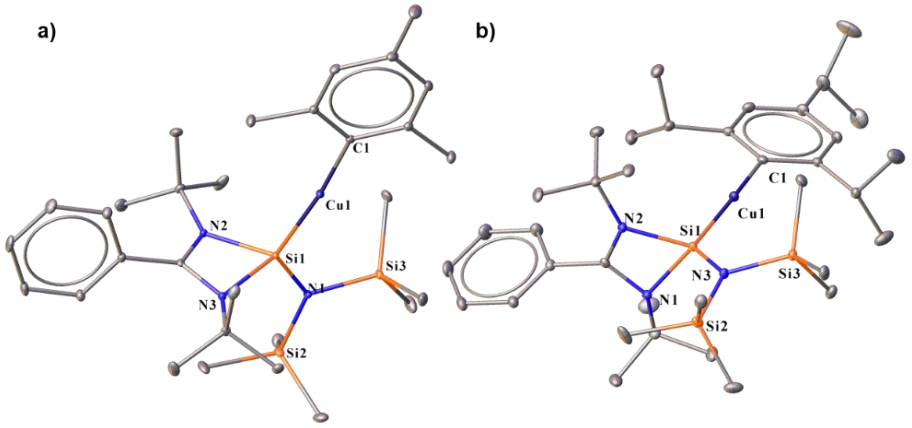

Figure 2D.1. Molecular structure of complexes a) **2D.2** and b) **2D.3**. Anisotropic displacement parameters are depicted at the 50% probability level. Solvent moiety and H atoms are omitted for clarity. Selected bond distances (Å) and angles (deg): for a) Si1–Cu1 2.2509(8), Cu1–C1 1.946(2), Si1–N1 1.735(2), N1–Si2 1.758(2), N1–Si3 1.768(2), Si1–N2 1.845(2), Si1–N3 1.852(2) and Si1–Cu1–C1 173.28(6), N1–Si1–Cu1 124.91(6), N1–Si1–N2 110.71(8), N2–Si1–N3 70.49(7), N3–Si1–Cu1 109.99(5) and for b) Si1–Cu1 2.2407(8), Cu1–C1 1.937(2), N1–Si1 1.861(2), N2–Si1 1.847(2), N3–Si1 1.736(2), N3–Si3 1.768(2), N3–Si2 1.753(2) and Si1–Cu1–C1 170.72(7), N3–Si1–N1 113.42(9), N3–Si1–Cu1 124.77(7), N1–Si1–Cu1 108.56(7).

In complex **2D.2** (Figure 2D.2), HOMO is primarily localized over the Cu *d*-orbital and the π-orbital of the mesityl group. Conversely, the electron density in HOMO-1 predominantly resides over the Cu(I)–C$_{ipso}$ bond, with a marginal distribution extending over the Si(II)→Cu

bond and the mesityl group. Notably, HOMO-3 is majorly localized over the Si(II)→Cu bond, exhibiting a minor dispersion over the Cu(I)–C_{ipso} bond and the amidinate fragment. The HOMO of complex **2D.3** (Figure 2D.2) shows a predominant contribution from the Cu(I)–C_{ipso} bond and a minor involvement from the Si(II)→Cu bond and the trip group. Conversely, HOMO-1 is localized over the Cu *d*-orbital and the π-orbital of the trip group. Intriguingly, unlike HOMO of **2D.2** and **2D.3**, the electron density in HOMO-3 of both complexes exhibits analogous features. Important to note that the electron density on C_{ipso} is more in complex **2D.3** (35.94 %) in HOMO than in complex **2D.2** (26.72 %). However, the LUMO of both complexes is predominantly localized over the benzamidinato fragment.

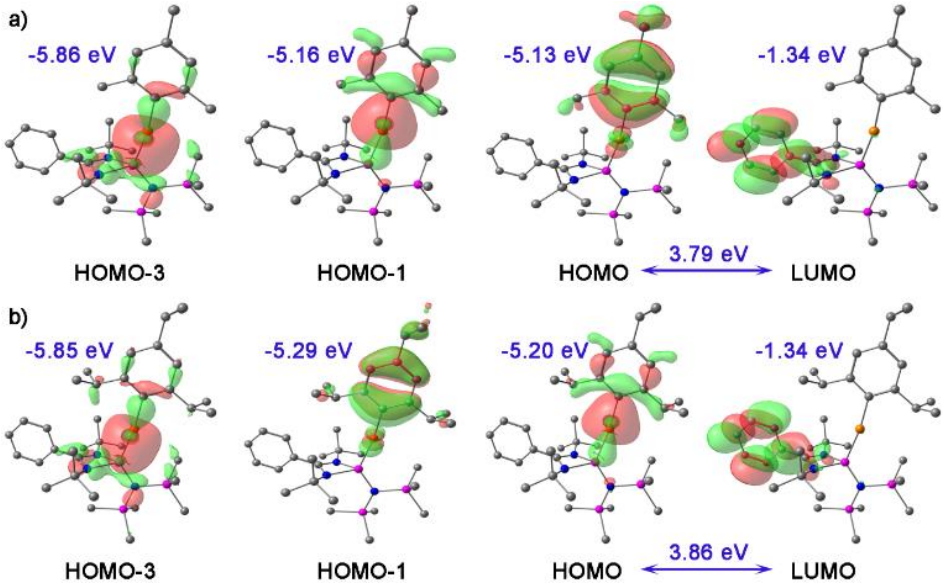

Figure 2D.2. MOs of complexes a) **2D.2** and b) **2D.3** calculated at the B3LYP-D3/def2TZVPP level.

2D.3.3 Synthesis of NHSi-based silver aryl complex.

Unlike organocopper(I) complexes, the chemistry of organosilver(I) complexes has not been explored much. There are very few examples of ligated silver(I)-mesityl moiety in the literature.[248] After the successful isolation and interesting reactivity of the NHSi–Cu–mesityl complex (**2D.2**), we aimed to explore the NHSi–Ag–aryl complex. Upon reaction of compound **2D.1** with mesityl silver[229] in toluene at room temperature, an interesting μ-mesityl bound dimeric silver(I) complex (**2D.4**) was obtained (Scheme 2D.3). A broad peak at δ 6.9 ppm in $^{29}Si\{^{1}H\}$ NMR spectrum of **2D.4** indicated the formation of the desired complex. Complex **2D.4** crystallizes in the triclinic *P-1* space group, featuring a 3c-2e electron bond involving the C_{ipso} atom of the mesityl group with two silver atoms (Figure 2D.3), resulting in close proximity of Ag1–Ag2 (2.7453 (5) Å). The Ag1–Ag2 bond length of **2D.4** is much shorter than the sum

of the van der Waal radii (3.44 Å).[171] The aryl group bound to coinage metal complexes often show μ-bonding in aggregated form to form a polynuclear complex (Figure 2D.3).[249]

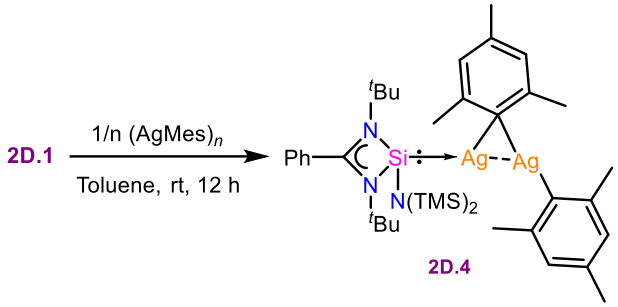

Scheme 2D.3. Reaction of **2D.1** with mesityl silver.

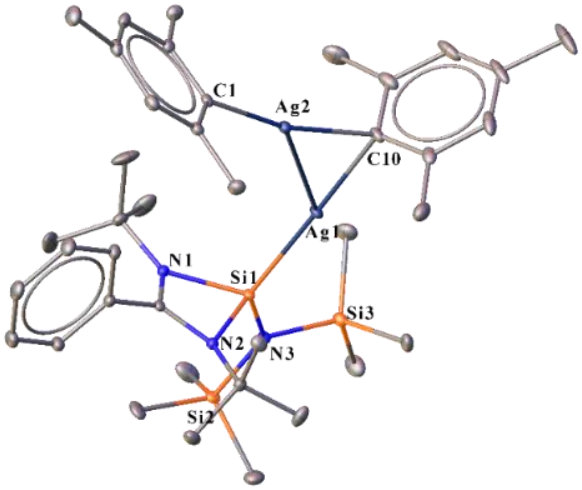

Figure 2D.3. Molecular structure of **2D.4**. Anisotropic displacement parameters are depicted at the 50% probability level. H atoms are omitted for clarity. Selected bond distances (Å) and angles (deg): Si1–Ag1 2.3900(9), Ag1–Ag2 2.7453(5), Ag1–C10 2.215(3), C1–Ag2 2.106(3), C10–Ag2 2.211(3), N1–Si1 1.843(2), N2–Si1 1.844(2), Si1–N3 1.719(2), N3–Si2 1.770(2), N3–Si3 1.768(2) and Si1–Ag1-C10 178.85(7), Si1–Ag1–Ag2 127.28(2), Ag2–Ag1–C10 51.60(7), C10–Ag2–Ag1 51.74(7), N2–Si1–N3 113.9(1), N1–Si1–N3 113.9(1), Ag1–Si1–N2 109.64(7), N3–Si1–Ag1 126.42(8), N1–Si1–N2 70.53(9).

The Si1–Ag1 bond length in **2D.4** is 2.3900(9) Å, which is similar to the carbazole-substituted benzamidinato silylene coordinated tetrameric Ag_4I_4 complex.[126] Kays and co-workers reported an *m*-terphenyl group bound dimeric Ag_2 core with Ag···Ag distance 2.6706(3) Å, which is shorter than the complex **2D.4**.[250] While the Ag1–C1 bond in **2D.4** is shorter (2.106 Å), the μ-bridged mesityl bound Ag atoms are longer (Ag1–C10 2.215(3) and Ag2–C10 2.211(3) Å) and form almost symmetrical bonds with the C10 atom. This is the first NHSi-supported three-membered Ag_2C ring system. The HOMO of complex **2D.4** shows the

contribution over the delocalized mesityl–Ag–C_{ipso} and *d*-orbital of Ag atom bonded to NHSi, whereas HOMO-1 shows the contribution over the localized mesityl–Ag–C_{ipso} and *d*-orbital of Ag atom. HOMO-2 is localized over the mesityl group, whereas HOMO-3 is delocalized over the Si(II)→Ag_2C ring connected to the μ-bridged mesityl group (Figure 2D.4). LUMO of this complex shows the contribution from the benzamidinato fragment.

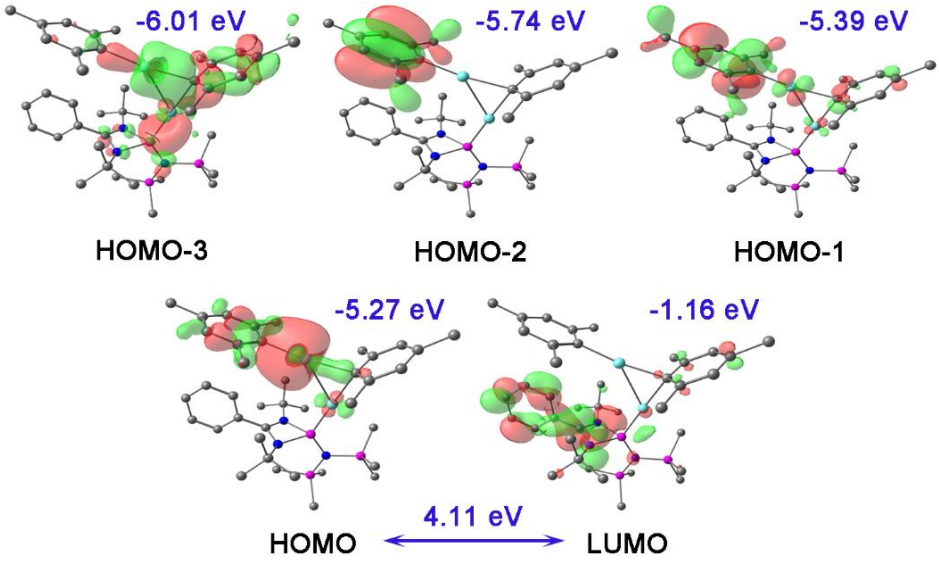

Figure 2D.4. MOs of complex **2D.4**.

NBO discloses the presence of argentophilic interaction in complex **2D.4** (Figure 2D.5). The $E^{(2)}$ value for the delocalization of electron density from the Ag(I) center to the σ^* orbital of the Ag(I)–Si bond was 2.10 kcal/mol. However, the $E^{(2)}$ value for the Ag(I) center attached to the NHSi to the σ^* orbital of the Ag(I)–C_{ipso} bond was found to be 1.71 kcal/mol. The WBI of the Ag···Ag bond was found to be 0.0719, which is in the range (0.022-0.094) of reported literature on argentophilic interaction.[251-255]

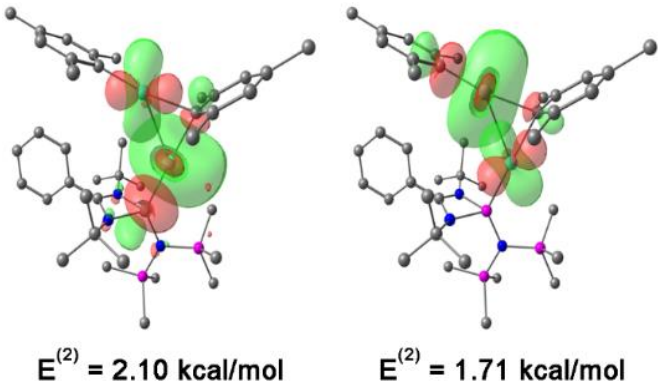

Figure 2D.5. NBO orbital overlap with $E^{(2)}$ values for argentophilic interaction in **2D.4**.

2D.3.4 Reaction of organocopper towards benzamidinato chlorosilylene.

After isolating the organocopper complexes of **2D.1**, we further probed the reactivity pattern of benzamidinato chlorosilylene.[116] For that, we have treated benzamidinato chlorosilylene with the mesityl copper in a 1:1 molar ratio, which furnished complex **2D.5** *via* the σ-bond metathesis (Scheme 2D.4).[256] The reaction proceeded through the σ-bond metathesis at the labile Si–Cl moiety, and the mesityl group migrated to the Si(II) center to form a dimeric Cu_2Cl_2 core.

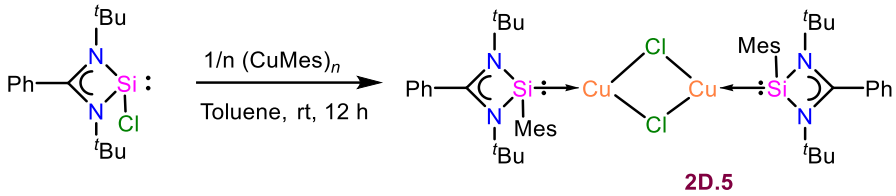

Scheme 2D.4. Synthesis of complex **2D.5**.

The peak at δ 32.4 ppm in $^{29}Si\{^1H\}$ NMR spectrum is highly deshielded than the previously reported dimeric copper(I) chloride of compound **2D.A**,[247] which might be due to the presence of the σ-donating mesityl group at the silicon(II) center. **2D.5** crystallizes in the monoclinic $P2_1/n$ space group (Figure 2D.6) and is isostructural to the dimeric Cu_2Cl_2 complex of **2D.A**.[247] The silicon(II) center of **2D.5** attains a distorted tetrahedral geometry with the Si–Cu bond length of 2.213(1) Å.[247] The electron density at the HOMO of complex **2D.5** is localized over the Si(II)→Cu_2Cl_2←Si(II) moiety, whereas LUMO is localized over the benzamidinato part and along the Si(II)-mesityl group (Figure 2D.7). We attempted a similar reaction of 2,4,6-triisopropylphenyl copper[227] with **2D.4**, but no successful isolation of the desired complex could be made.

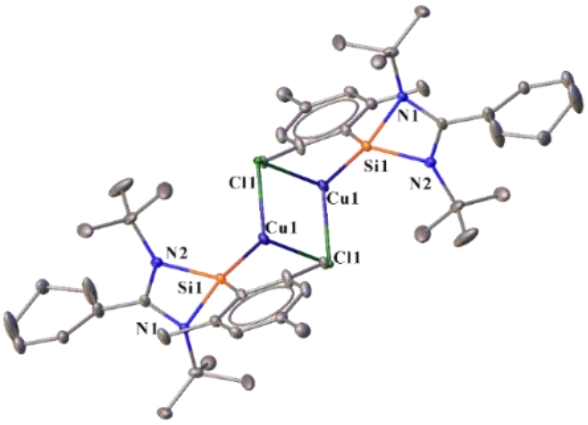

Figure 2D.6. Molecular structure of **2D.5**. Anisotropic displacement parameters are depicted at the 50% probability level. Disordered C atoms of *tert*-butyl, mesityl, phenyl moieties, and H atoms are omitted for clarity, and only asymmetric unit is shown. Selected bond distances (Å)

and angles (deg): Si1–Cu1 2.213(1), Cu1–Cl1 2.345(1), Si1–C16 1.899(5), Si1–N2 1.835(4), Si1–N1 1.842(4) and Si1–Cu1–Cl1 132.14(5), N2–Si1–N1 70.6(2), N2–Si1–Cu1 115.4(1), N1–Si1–C16 110.1(2), C16–Si1–Cu1 125.0(2).

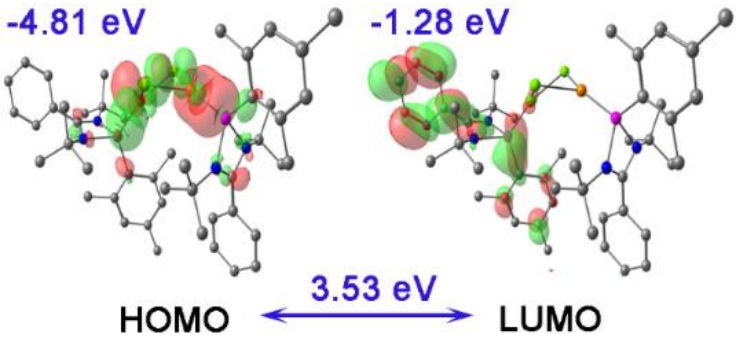

Figure 2D.7. MOs of complex **2D.5**.

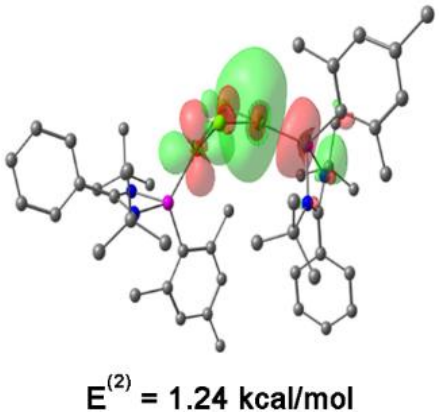

Figure 2D.8: NBO orbital overlap with $E^{(2)}$ values for cuprophilic interaction in complex **2D.5**.

2D.3.5 Use of NHSi-copper mesityl complex as mesityl transfer agent in C–C coupling reaction.

Over the years, the prodigious use of aryl boronic esters and aryl magnesium precursors has dominated the area of C–C cross-coupling reactions.[257, 258] A recent report by Uchiyama and co-workers has shown the applicability of aryl copper in Pd-catalyzed C–C coupling with sterically demanding substrates.[209] If this analogous Cu system can perform the metal-mediated bond-forming processes, then such transformations might be crucial to use as a platform for important catalytic reactions. There are only two reports where NHSis are used as ligands (catalysts **2D.A** and **2D.B**) (Chart 2D.2) for sp^3-sp^2 and sp^2-sp^2 C–C coupling reactions.[122, 259] Since we already had a well-characterized NHSi-Cu-Aryl system (**2D.2**), we utilized it as an efficient mesityl group transfer agent for Pd-catalyzed C–C coupling reactions with aryl iodides (Scheme 2D.5). The C–C coupling reactions with a few aryl iodides were carried out under the optimized conditions with the complex **2D.2** (Table 2D.1).

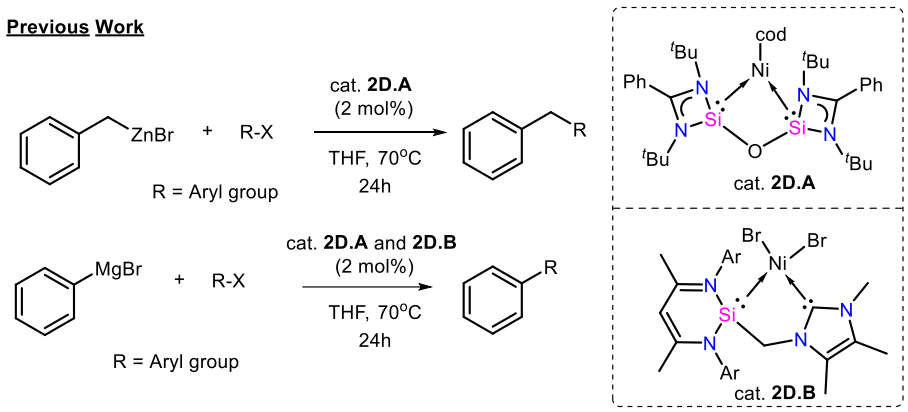

Chart 2D.2. Previous reports on C–C coupling reactions with NHSi as a ligand on the metal center.

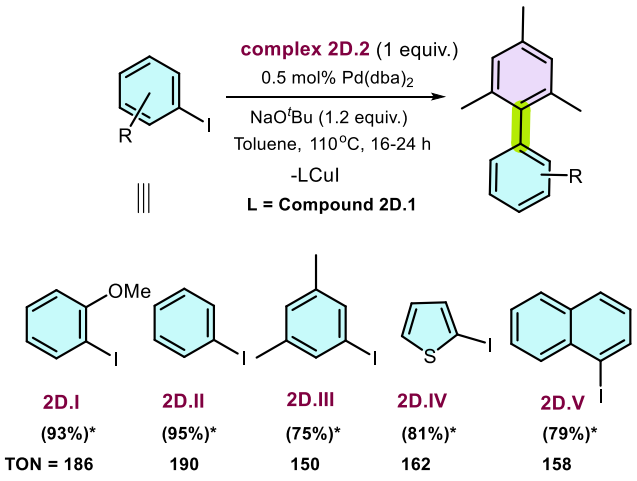

Scheme 2D.5. Pd catalyzed sp^2-sp^2 C–C coupling reaction using **2D.2** as a mesityl transfer reagent. *Isolated yields.

Table 2D.1. Optimization of reaction conditions for C-C coupling reaction

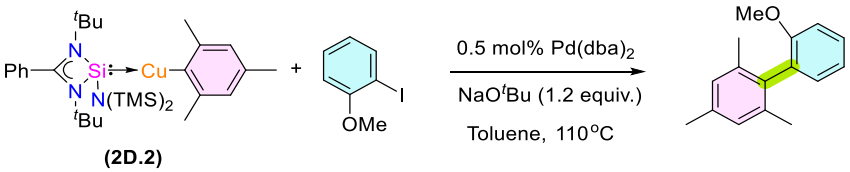

Entry	Substrate	Catalyst	Base	Mol %	Time (h)	Conversion Yield[#] (%)
1	**2D.2**	-	NaO^{t}Bu	-	24	trace
2	**2D.2**	Pd(dba)$_2$	NaO^{t}Bu	0.1	24	60
3	**2D.2**	Pd(dba)$_2$	NaO^{t}Bu	0.5	24	<99
4	***2D.2***	***Pd(dba)$_2$***	*NaO^{t}Bu*	***0.5***	***16***	***<99***
5	Mesityl Copper	Pd(dba)$_2$	NaO^{t}Bu	0.5	24	40

6	**2D.2**	$Pd(dba)_2$	-	0.5	16	62
7	**2D.2**	-	-	-	16	22

We also observed good to excellent product yields for the heteroaromatic (**2D.IV**) and fused aromatic (**2D.V**) systems (Scheme 2D.5). Using NHSi coordinated mesityl copper complex as an alternative to conventional aryl boronic esters provides lower Pd catalyst loading (0.5 mol%) than the conventional C–C coupling reactions.[260] The Pd catalyst loading (5 mol%) for the C–C coupling reaction by Uchiyama and co-workers remains much higher with the use of additional ligand loading (up to 15 mol%) (Table 2D.2). The turnover number (TON) for the formation of compound **2D.I** is observed 186 with our catalytic method, whereas it is 18.2 by utilizing the method of Uchiyama and co-workers (Table 2D.2). Hence, our method utilizing **2D.2** as a mesityl transfer reagent works much more efficiently than the method reported by Uchiyama and co-workers for the C–C cross-coupling reaction. This observation paves the way to explore more electron-donating ligand-coordinated organocopper compounds for important cross-coupling reactions.

Table 2D.2: Pd catalyzed C–C coupling reaction using mesityl copper.

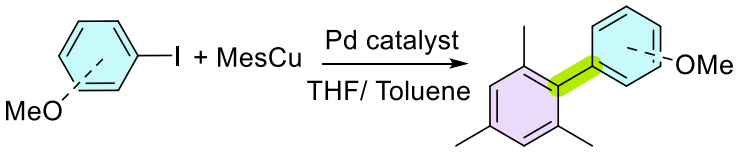

Serial No.	Pd-based Catalyst (mol%)	Temperature (°C)	Yield (%)	TON
1	5	80-140	91[209]	18.2
This work	***0.5***	***110***	***93***	***186***

2D.3.6 Reaction of 2D.2 towards homolytic and heterolytic bond cleavage.

2D.3.6.1 Reaction of 2D.2 with diboron compounds (B–B bond).

Various NHC and CAAC coordinated low-valent boron species have found application in optoelectronics.[261-263] The coinage metal complexes of diborene and boron−boron triple-bonded systems also showcased interesting photophysical behaviour.[264, 265] Thus; we were interested in probing the reaction of **2D.2** with the diboron (B–B bond) reagents[266, 267] in quest of homolytic bond cleavage.[268] We have isolated an unusual complex **2D.6** serendipitously from the reaction of **2D.2** with pinacolato-1,8-diaminonaphthalenato diboron (Bpin-Bdan). The preparation of Bpin-Bdan (Scheme 2D.6) involves the elimination of pinacol as a side product. Due to the high boiling point of pinacol, it remained present along with Bpin-Bdan, which was confirmed by the ^1H NMR spectrum.

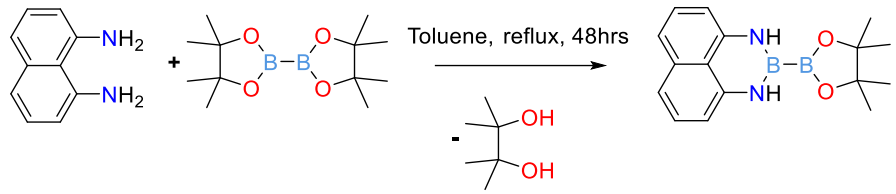

Scheme 2D.6. Preparation of Bpin-Bdan.

We presume that during the reaction of complex **2D.2** with Bpin-Bdan, the interference of pinacol (Scheme 2D.7) leads to the formation of complex **2D.6** (Scheme 2D.8) with concomitant elimination of mesitylene and HBdan. Complex **2D.6** crystallizes in a monoclinic $P2_1/c$ space group with a toluene molecule (Figure 2D.9). The molecular structure of **2D.6** features a Si1–Cu1 bond length of 2.199(4) Å, which is longer than the SIMes (1,3-dimesitylimidazolin-2-ylidene) coordinated Cu(I) oxalate complex.[269] Our attempt to isolate the desired product with purified Bpin-Bdan was unsuccessful, possibly due to the instability of the formed complex at ambient temperature.

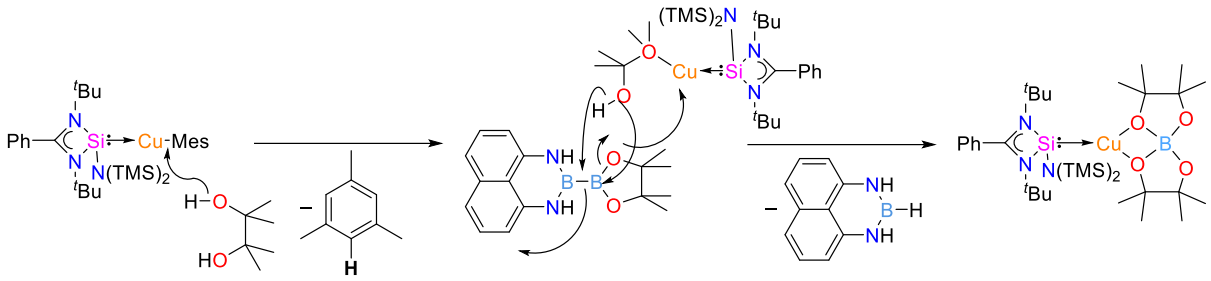

Scheme 2D.7. Plausible mechanism of formation of complex **2D.6**.

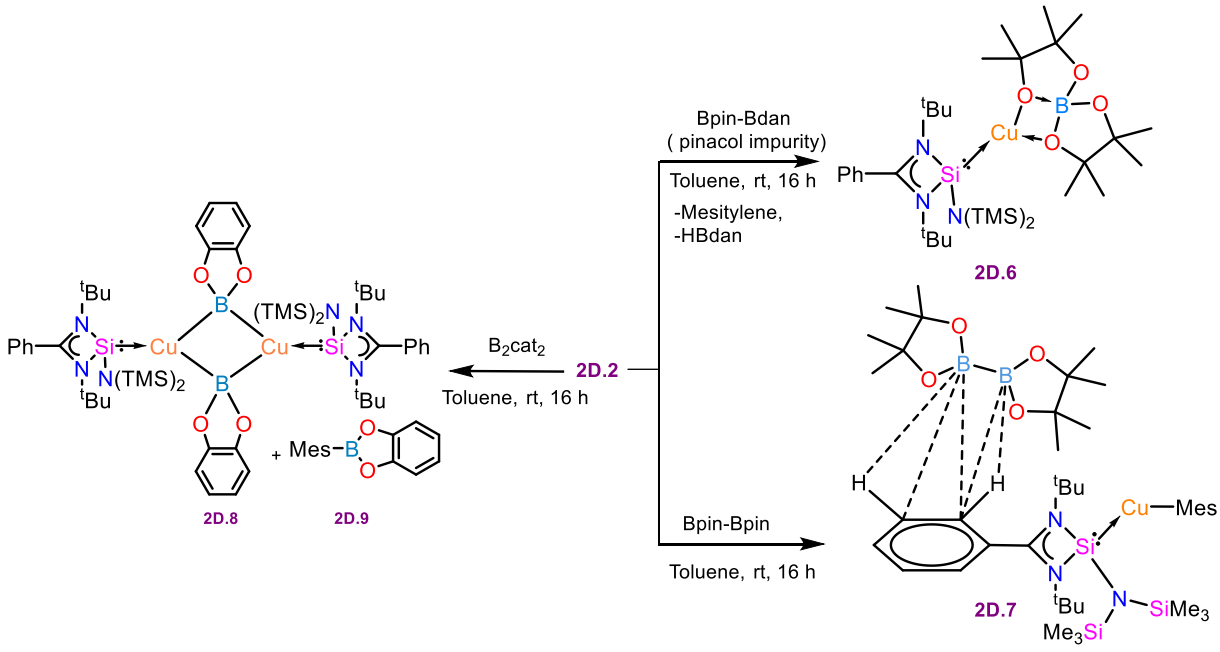

Scheme 2D.8. Reactions of complex **2D.2** with diboron compounds.

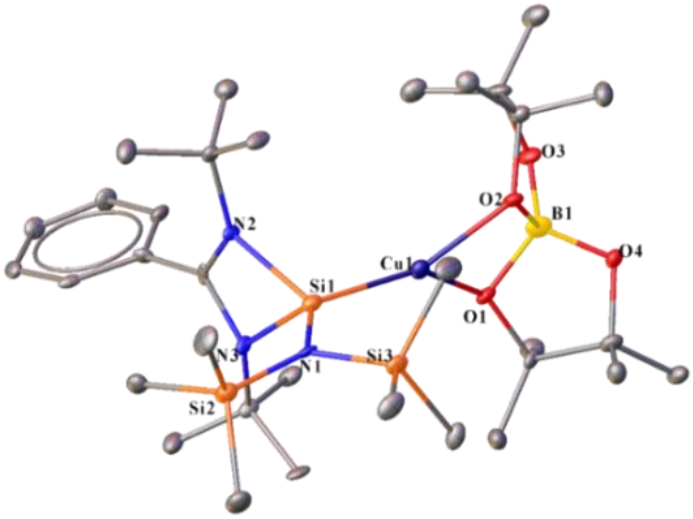

Figure 2D.9. Molecular structure of **2D.6**. Anisotropic displacement parameters are depicted at the 50% probability level. Solvent molecule and H atoms are omitted for clarity. Selected bond distances (Å) and angles (deg): Si1–Cu1 2.199(4), Cu1–O2 2.022(8), Cu1–O1 2.180(7), B1–Cu1 2.69(2), Si1–N1 1.741(7), N1–Si3 1.774(9), N1–Si2 1.749(8), Si1–N3 1.838(9), Si1–N2 1.856(9) and Si1–Cu1–O1 139.6(2), Si1–Cu1–O2 152.2(2), O1–Cu1–O2 67.8(3), O1–B1–O2 101.4(9), O1–B1–O4 105(1), O2–B1–O3 104(1), O4–B1–O3 110(1).

The copper(I) center adopts a distorted trigonal planar geometry with a smaller bite angle of O1–Cu1–O2 67.8(3)º. The Cu–O bond lengths in **2D.6** (Cu1–O2 2.022(8), Cu1–O1 2.180(7) Å) are longer than those reported in the previously tri-coordinated Cu(I) oxalates with olefin and alkyne as coordinated ligands (1.987(1)-2.004(2) Å),[270, 271] but in accordance with the SIMes coordinated Cu(I) oxalate complex.[272, 273] HOMO of complex **2D.6** (Figure 2D.10) is spread over the pinacol fragment and *d*-orbital of Cu, whereas HOMO-1 exhibits a significant contribution from the Si(II)→Cu with a minor spread over the pinacol fragment and LUMO is localized over the benzamidinato part. Oxoborolate moiety of complex **2D.6** forms two O→Cu(I) donations with $E^{(2)}$ values of 13.45 and 14.59 kcal/mol.

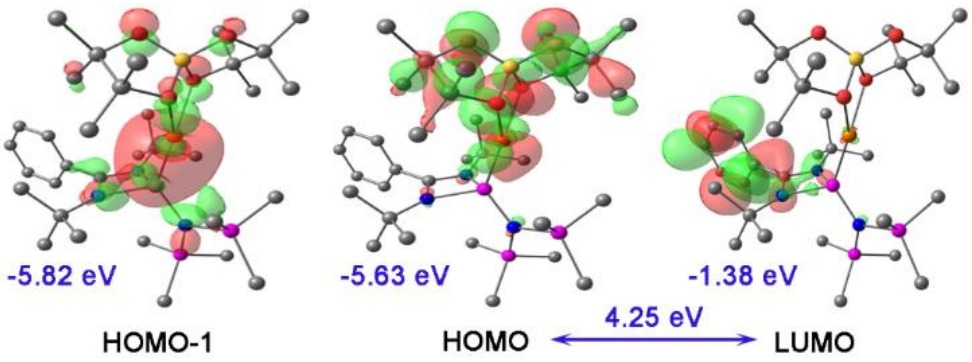

Figure 2D.10. MOs of complex **2D.6**.

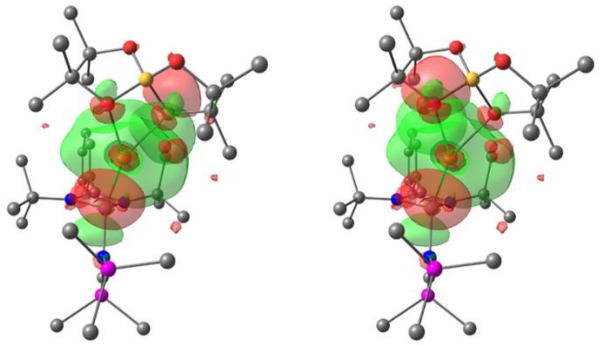

Figure 2D.11: NBO orbital overlap with $E^{(2)}$ values for donations from the oxygen center of oxyborolate moiety in complex **2D.6**.

The NHC-coordinated copper boryl complexes have been explored extensively as nucleophilic boron sources in copper-mediated borylation reactions.[274] Thus, to probe complex **2D.2** for the homolytic diboron bond cleavage, we performed a stoichiometric reaction of complex **2D.2** with bis(pinacolato)diboron (B_2pin_2) in toluene at room temperature. However, we obtained the single crystals of an unprecedented co-crystallized compound **2D.7** (Figure 2D.12) instead of the B–B bond cleavage.

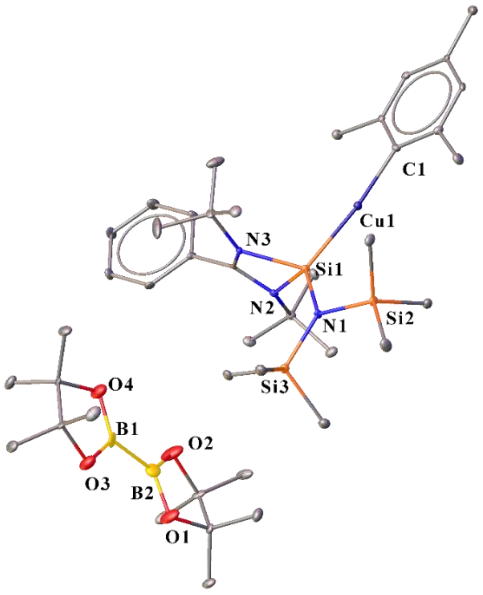

Figure 2D.12. Molecular structure of **2D.7**. Anisotropic displacement parameters are depicted at the 50% probability level. Solvent molecule and H atoms are omitted for clarity. Selected bond distances (Å) and angles (deg): Si1-Cu1 2.246(2), Cu1-C1 1.939(6), Si1-N1 1.732(4), N1-Si3 1.755(5), N1-Si2 1.767(5), Si1-N3 1.848(4), Si1-N2 1.842(4), B2-B1 1.688(6), B2-O2 1.354(7), B2-O1 1.365(6), B1-O3 1.368(6), B1-O4 1.360(6) and Si1-Cu1-C1 172.8(2), N3-Si1-Cu1 113.9(1), N3-Si1-N2 70.3(2), N2-Si1-N1 113.0(2), Cu1-Si1-N1 122.2(2), O2-B2-O1

112.9(5), B1-B2-O2 125.5(5), O1-B2-B1 121.6(5), O3-B1-O4 112.6(4), O3-B1-B2 121.7(4), B2-B1-O4 125.6(4).

The molecular structure of **2D.7** reveals that the two units are stabilized by several non-covalent interactions, as seen from the Hirshfield analysis at 0.5 iso-surface. The Hirshfield analysis shows that the two units are stabilized *via* several C–H···B and O···H interactions—two distinct, independent molecules are crystallized in the asymmetric unit (Figure 2D.13).

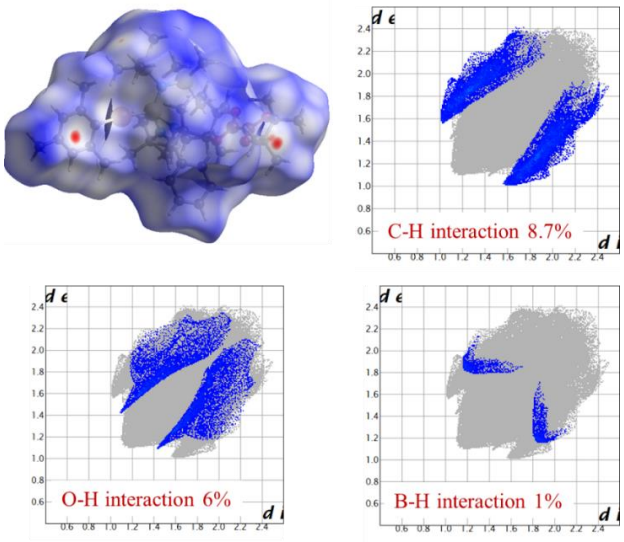

Figure 2D.13. Hirshfield analysis of complex **2D.7**.

The Si1–Cu1 bond length in compound **2D.7** is found to be 2.246(2) Å, which is shorter than the Si–Cu bond in complex **2D.2**. The Cu1–C1 bond [1.939(6)] Å of **2D.7** is marginally shorter than the Cu–C bond [1.946(2)] in the complex **2D.2**. Several non-covalent interactions stabilize complex **2D.7**, which features C–H···B interaction, with a distance ranging from 3.0-3.1 Å (Figure 2D.14), which is marginally shorter than the sum of their van der Waal radii (3.12 Å). Cremer and co-workers recently established B–H···π interaction (Chart 2D.3).[275]

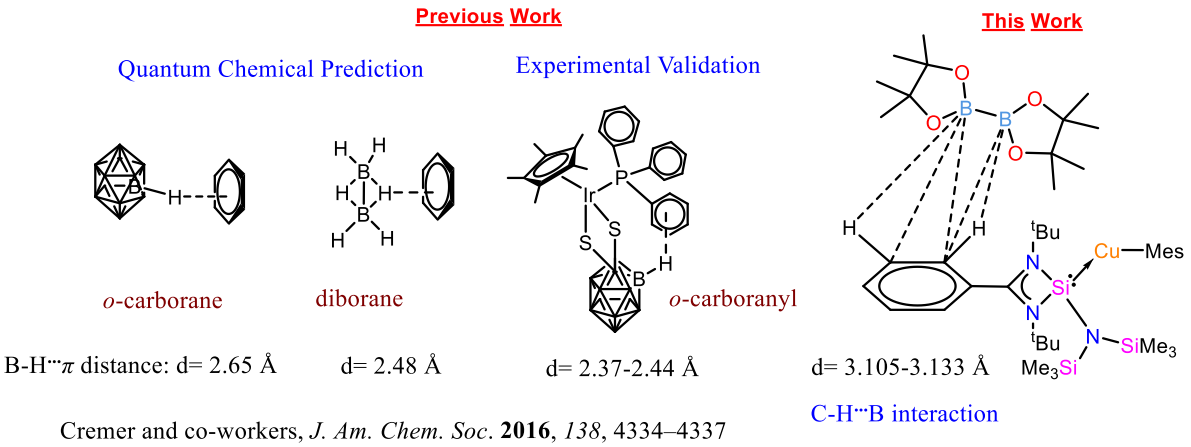

Cremer and co-workers, *J. Am. Chem. Soc.* **2016**, *138*, 4334–4337

Chart 2D.3. Reported examples of B-H···π interactions and this work, representing C-H···B interactions.

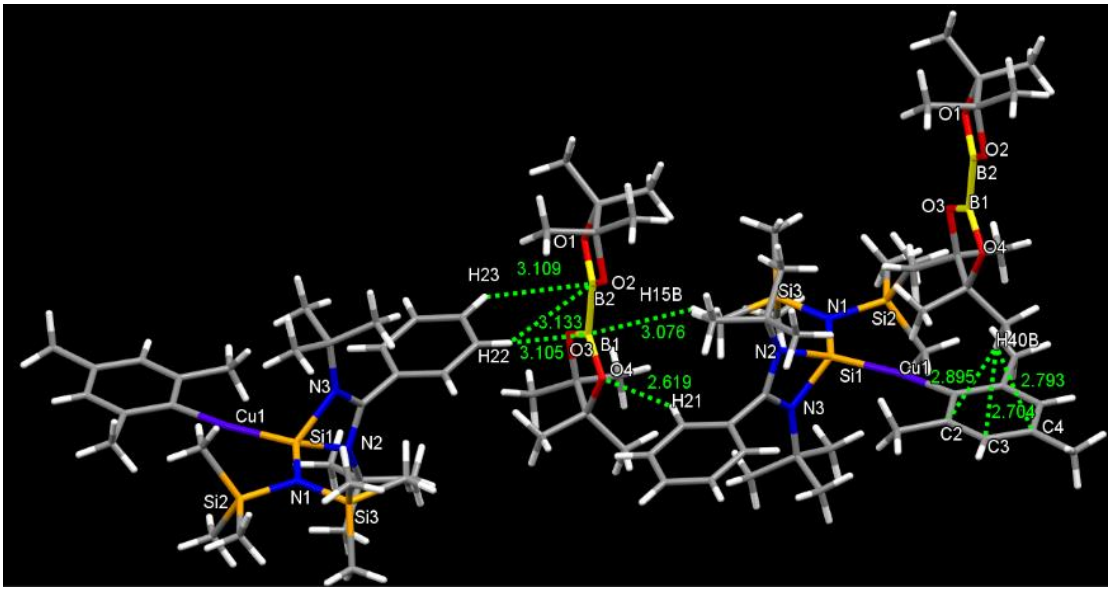

Figure 2D.14. Various weak interactions (C-H···B, C-H···O) stabilizing complex **2D.7**.

We observed charge transfer from the σ-orbital of the C–H group to the vacant *p*-orbital of the boron center in its gas-phase optimized structure shown in Figure 2D.15 along with strong C–H···O interaction (Figure 2D.16).

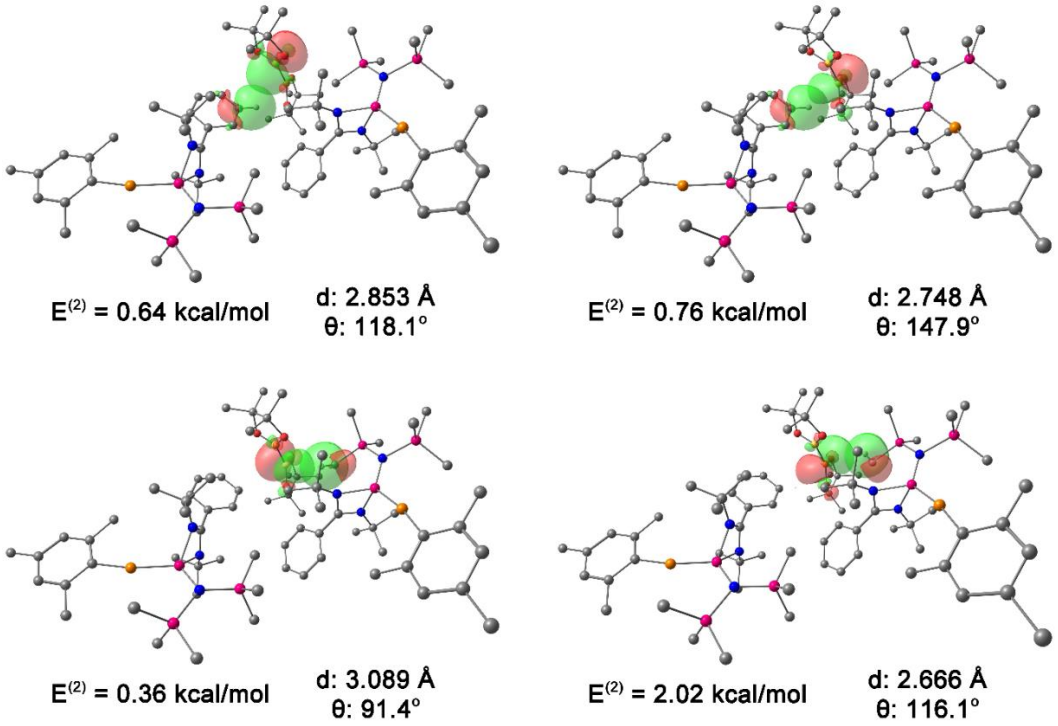

Figure 2D.15. NBO images of **2D.7** with $E^{(2)}$ values for charge transfer from σ-orbital of C-H to vacant *p*-orbital of boron center and geometrical parameters, such as distance and angle.

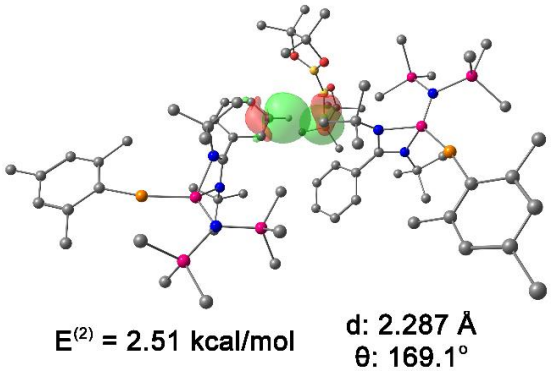

Figure 2D.16. NBO images of complex **2D.7** with second-order perturbative energies for C-H···O interaction and relevant geometrical parameters such as distance (d) and angle (θ).

Conversely, when mesityl copper was treated directly with Bpin–Bpin in the presence of PPh_3, Mes–Bpin was obtained.[276] Observing the reaction pattern, we rationalized that the enhanced steric bulk of B_2pin_2 might have prevented the desired product formation. We also tried the reaction at elevated temperature to access the NHSi–Cu–Bpin complex but could not isolate the desired complex. Thus, we performed a reaction of less sterically bulky B_2cat_2 with complex **2D.2** (Scheme 2D.8) in toluene. In this case, we could obtain dimeric $[PhC\{N(^tBu)\}_2SiN(SiMe_3)_2\}_2Cu_2BCat_2]$ (**2D.8**) and Mes–Bcat (**2D.9**) as a mixture of the products. The isolation of complex **2D.8** also indicated the higher reactivity of sterically less hindered B_2cat_2 over B_2pin_2, which Marder and co-workers also pointed out.[277] The molecular structure of complex **2D.8** (Figure 2D.17) established the μ-coordination mode of boryl linkage to Cu(I) coordinated with NHSi unambiguously. However, the poor quality of the crystals refrained us from discussing the metrical parameters. Analogous NHC stabilized μ-boryl Cu(I) complexes were reported by Sadhigi, Kleeberg, and co-workers, which show μ-boryl Cu(I) core (Chart 2D.4).[278-280,281, 282]

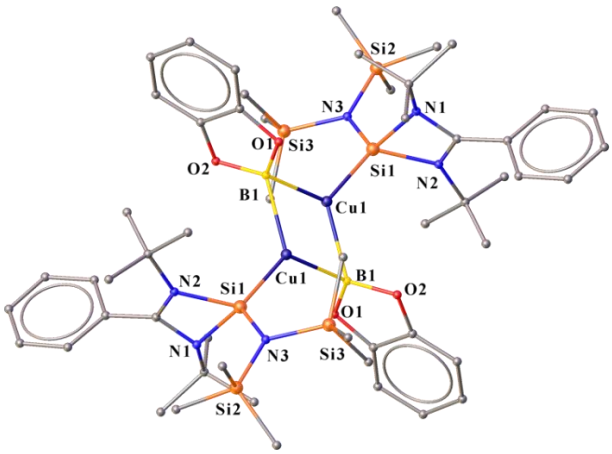

Figure 2D.17. Molecular structure of **2D.8**.

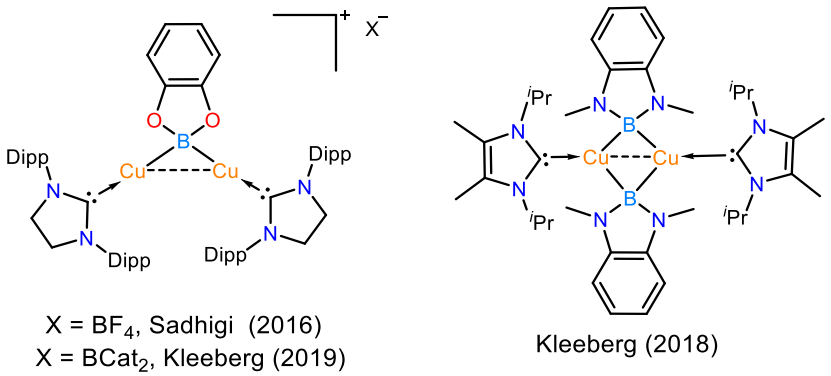

Chart 2D.4. Reported examples of NHC supported μ-boryl Cu(I) complexes.[277-280]

We could not get a clean ^{1}H NMR spectrum of **2D.8** as it was isolated as a mixture with **2D.9** (Figure 2D.18). However, ^{29}Si{^{1}H} NMR spectra revealed two sharp singlets at δ 6.3 and 7.1 ppm, corresponding to the –*Si*Me$_3$ moiety, and a singlet at δ 3.7 ppm, presumably indicating *Si*(II)–Cu(I) bond.

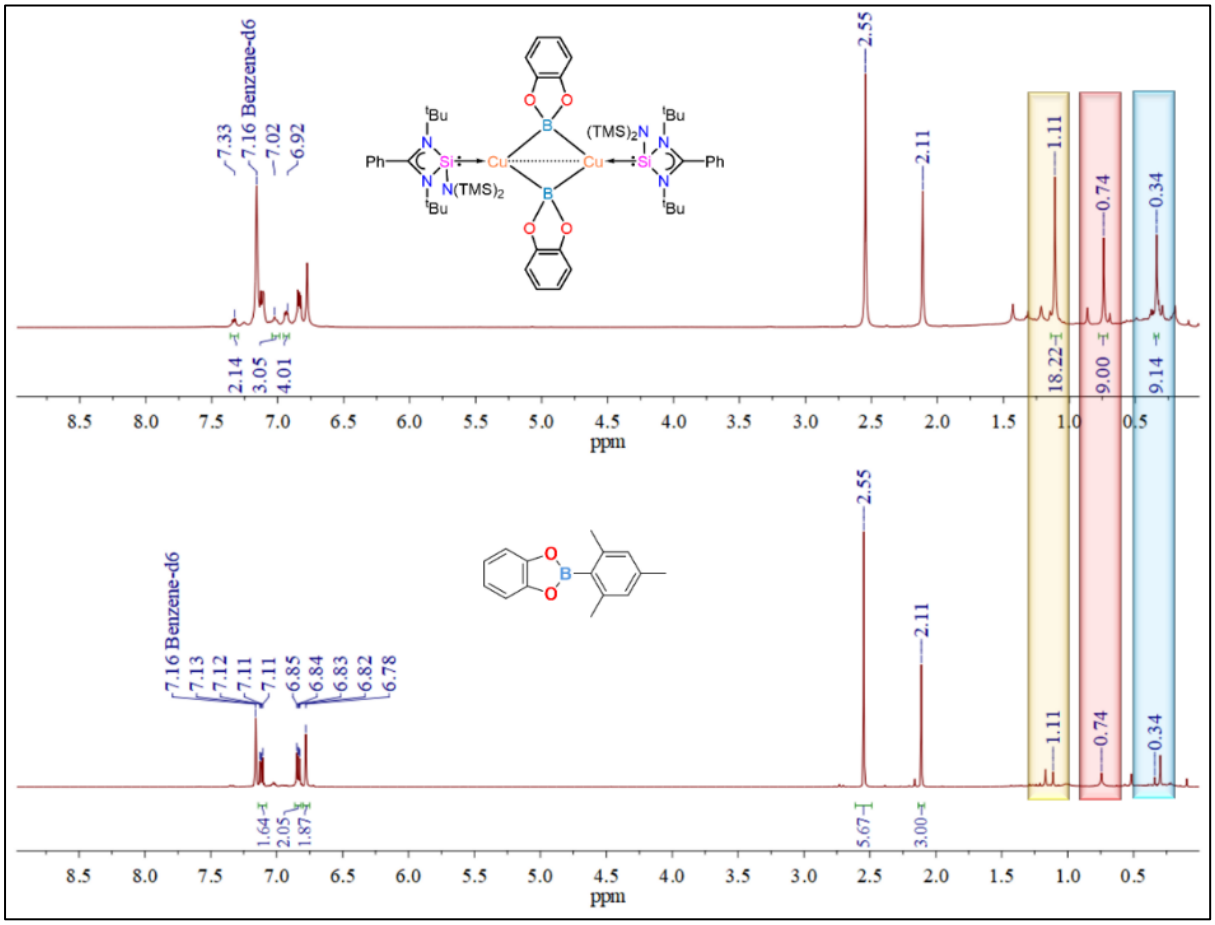

Figure 2D.18. ^{1}H NMR spectrum of complexes **2D.8** and **2D.9**.

The electronic structure analysis reveals that the HOMO of the dimeric Cu(I)–μ^2–Boryl complex (**2D.8**) (Figure 2D.19) is localized over the Cu_2B_2 ring. The orbital composition of

HOMO shows that the localization of electron densities at Cu centers is 18.84% and 13.01 %, while at B centers, 30.46% and 22.40 %, respectively. This 3c-2e bonding scenario was further confirmed by the natural localized molecular orbital (NLMO) analysis, showing that the contribution of each Cu center and B orbital in the Cu–B–Cu bond is 12.51, 6.37, and 72.90 %, respectively. HOMO-1 also has a contribution over the Cu_2B_2 ring along with the Si(II)→Cu bond, whereas the electron density in the HOMO-2 is predominantly localized over the Si(II)→Cu bond, along with the contribution from the catechol-boryl moiety. As observed for the previous complexes, LUMO in **2D.8** is also localized over the benzamidinato fragment.

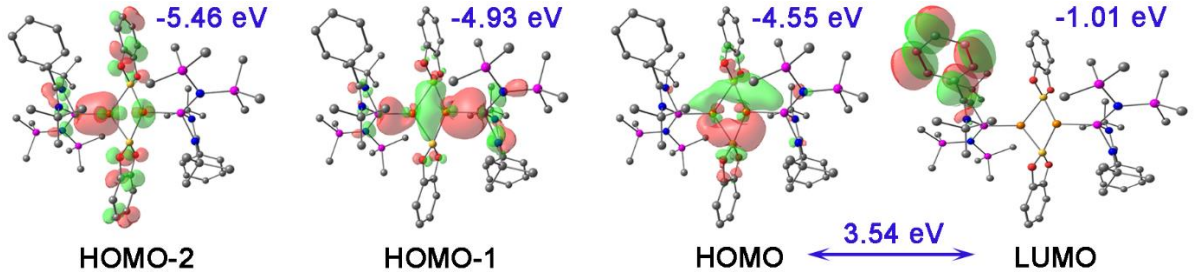

Figure 2D.19. MOs of complex **2D.8**.

Adachi and co-workers prepared Mes–Bcat (**2D.9**) by reacting catechol and mesityl boronic acid at elevated temperatures and purified it by azeotropic distillation.[231] The preparation of aryl boronate esters either involves Suzuki-Miyura cross-coupling for C–B bond formation[283] or by base-mediated $ArB(OH)_2$ formation.[284] Thus, forming **2D.9** in crystalline form gives easy access to mesityl boronic ester (Figure 2D.20). The tri-coordinate boron center in **2D.9** possesses a distorted trigonal planar geometry with a B1–O1 bond length of 1.398 (1) Å, which is in accordance with the B–O bond observed in aryl boronate esters.[285]

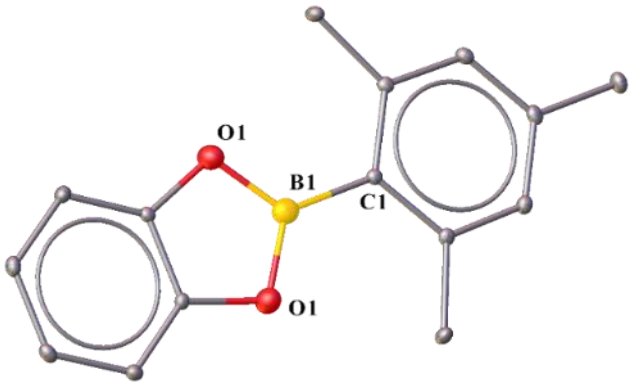

Figure 2D.20. Molecular structure of **2D.9**. Anisotropic displacement parameters are depicted at the 50% probability level. H atoms are omitted for clarity. Selected bond distances (Å) and angles (deg): O1-B1 1.398(1), B1-C1 1.553(3) and C1-B1-O1 125.0(1), O1-B1-O1 110.0(2).

2D.3.6.2 Synthesis of NHSi-based copper selenogenolate complex *via* Se–Se bond cleavage.

The coinage metal clusters of chalcogens are an important class of compound due to their utility in materials chemistry.[286, 287] We treated complex **2D.2** with diphenyl diselenide and sterically demanding bis(2,4,6-trimethylphenyl) diselenide in toluene at room temperature (Scheme 2D.9), which led to the formation of an immediate white precipitate. This was characterized by ^{1}H and ^{77}Se NMR spectra as MesSePh[288] and Mes_2Se,[289] respectively. We filtered the reaction mixture and reduced the solution to obtain suitable single crystals of **2D.10** and **2D.11**. The ^{77}Se NMR confirms the copper(I) bound selenium center in **2D.10** by displaying a broad peak at δ 37.1 ppm, which is upfield shifted than triethyl phosphine stabilized monomeric copper(I) phenylselenogenolate and downfield shifted than trimethyl phosphine stabilized dimeric copper(I) phenylselenogenolate.[290] The ^{29}Si{^{1}H} NMR spectra display two sharp singlets for the –*Si*Me$_3$ groups at δ 4.9 and 5.9 ppm for **2D.10** and 5.3 and 6.7 for **2D.11,** respectively. A broad peak for *Si(II)*–Cu was observed in ^{29}Si NMR spectra at δ 6.7 and 3.2 for **2D.10** and **2D.11**, respectively.

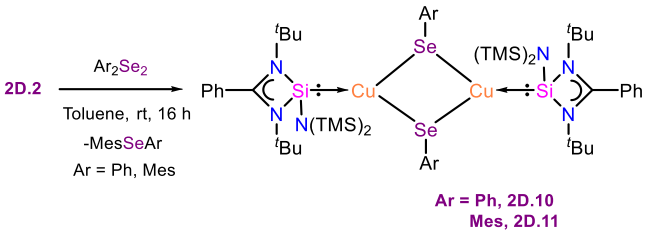

Scheme 2D.9. The reaction of complex **2D.2** with diaryl diselenide (Ar_2Se_2).

Complexes **2D.10** and **2D.11** (Figure 2D.20) display a dimeric Cu_2Se_2 core with the Si-Cu bond lengths of 2.248(3) and 2.2631(6) Å, respectively. The marginal elongation of the Si–Cu bond in complex **2D.11** can be attributed to the sterically demanding mesityl group. Lang and co-workers prepared a multinuclear $(CuSe)_n$ cluster using a bipyridyl ligand.[291] The Cu1–Se1 distances in **2D.10** and **2D.11** are 2.456(1) and 2.5076(6) Å, which are marginally longer than those in $Ph_3PCu(\mu\text{-}SePh)_2Cu(PPh_3)_2.CH_3CN$ complex {2.406(1) Å} by Oliver and co-workers.[220] The Cu···Cu distances in **2D.10** and **2D.11** are 2.938(2) and 3.4398(6) Å, respectively, which are longer than the Cu···Cu distance in the $Ph_3PCu(\mu\text{-}SePh)_2Cu(PPh_3)_2.CH_3CN$ complex {2.738(1) Å},[292] but shorter than the Cu···Cu distance in $[PhC(N^tBu)_2N(TMS)_2SiCu_2X_2]$ (X= Cl and Br).[247] We also tried similar reactions with diphenyl sulfide (Ph_2S_2) and diphenyl telluride (Ph_2Te_2) but could not obtain the desired compounds.

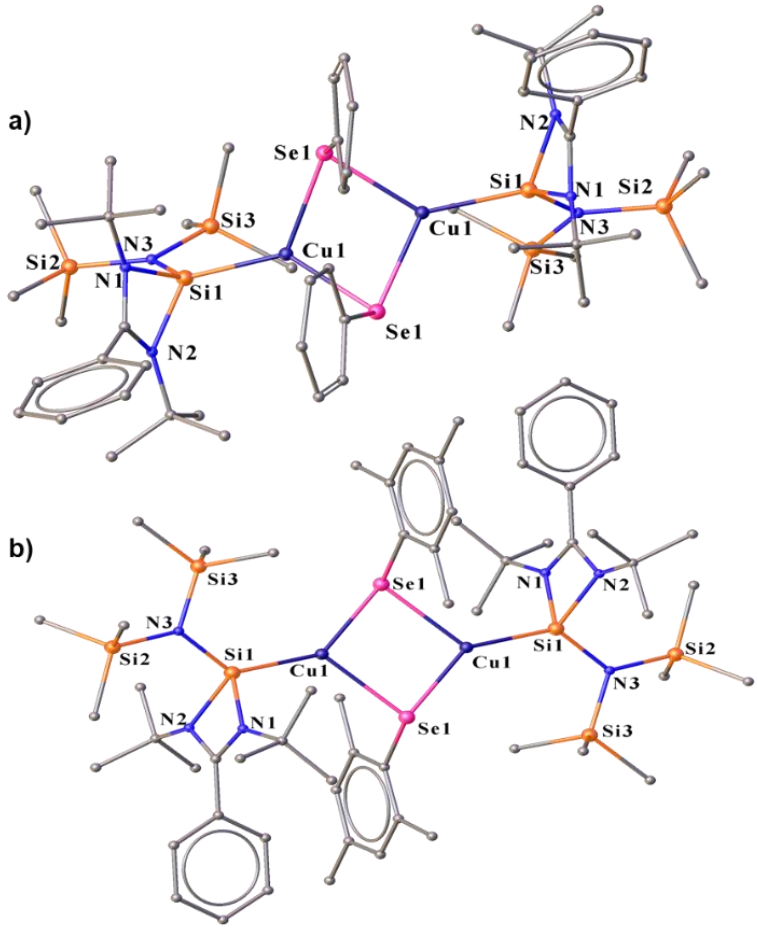

Figure 2D.21. Molecular structure of a) **2D.10** and b) **2D.11**. Anisotropic displacement parameters are depicted at the 50% probability level. Disordered aromatic rings and H atoms are omitted for clarity. Selected bond distances (Å) and angles (deg): for a) Si1–Cu1 2.248(3), Cu1–Se1 2.456(1), Si1–N3 1.743(7), N3–Si3 1.770(8), N3–Si2 1.76(1), Si1–N2 1.848(6), Si1–N1 1.862(6) and Si1–Cu1–Se1 133.89(8), N3–Si1–Cu1 125.8(3), N3–Si1–N1 112.6(3), N2–Si1–Cu1 117.0(2), N1–Si1–N2 70.4(3) and for b) Si1–Cu1 2.2631(6), Cu1–Se1 2.4579(6), Cu1–Se1 2.5076(6), Si1–N3 1.743(1), Si1–N2 1.848(1), Si1–N1 1.853(1), Cu1–Cu1 3.4398(6) and Si1–Cu1–Se1 143.51(2), Si1–Cu1–Se1 124.12(2), Se1–Cu1–Se1 92.31(1), N3–Si1–Cu1 128.42(5), N3–Si1–N1 109.30(7), N2–Si1–Cu1 113.93(5), N1–Si1–N2 70.45(6).

FMO analysis shows that the HOMO of complexes **2D.10** (Figure 2D.22) and **2D.11** (Figure 2D.24) is prominently concentrated over the dimeric Cu_2Se_2 ring, demonstrating substantial contributions from the Si(II) centers and the phenyl rings. Consistently, HOMO-1 and HOMO-3 exhibit concentrated electron density on the Cu_2Se_2 ring for complex **2D.10**, whereas HOMO-3 is localized over the Si(II)→Cu bond for complex **2D.11**. The LUMO resides on the benzamidinato ring. To understand the thermal stability of the dimeric form of **2D.10**, zero-point energy and basis-set superposition error corrected binding energy (ΔE_0) were

calculated in the gas-phase (-29.44 kcal/mol) as well as in the solution-phase (-24.57 kcal/mol) using toluene as a solvent. We have also calculated the change in the Gibbs free energy (ΔG) of **2D.10** in the temperature range of 0-450 K to investigate the thermal stability. It was found that **2D.10** is stable in the dimeric form up to the temperatures of 380 and 420 K in the solution- and gas-phase, respectively (Figure 2D.25).

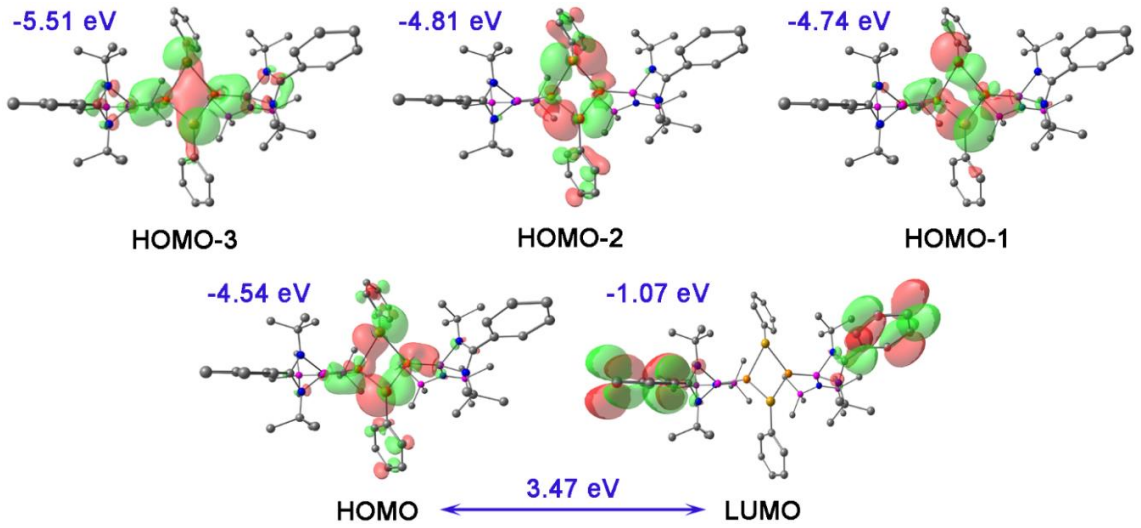

Figure 2D.22. MOs of complex **2D.10**.

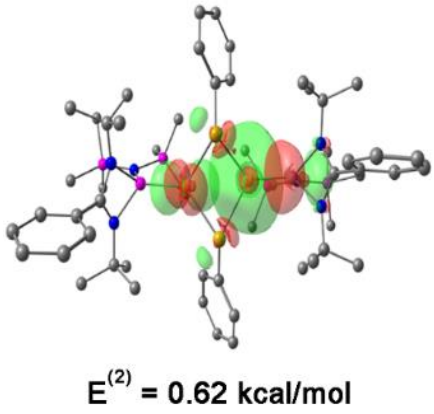

Figure 2D.23. NBO orbital overlap with $E^{(2)}$ values for cuprophilic interaction in complex **2D.10**.

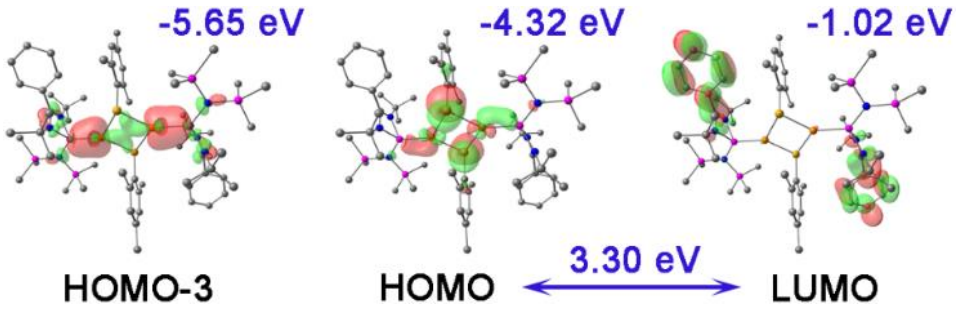

Figure 2D.24. MOs of complex **2D.11**.

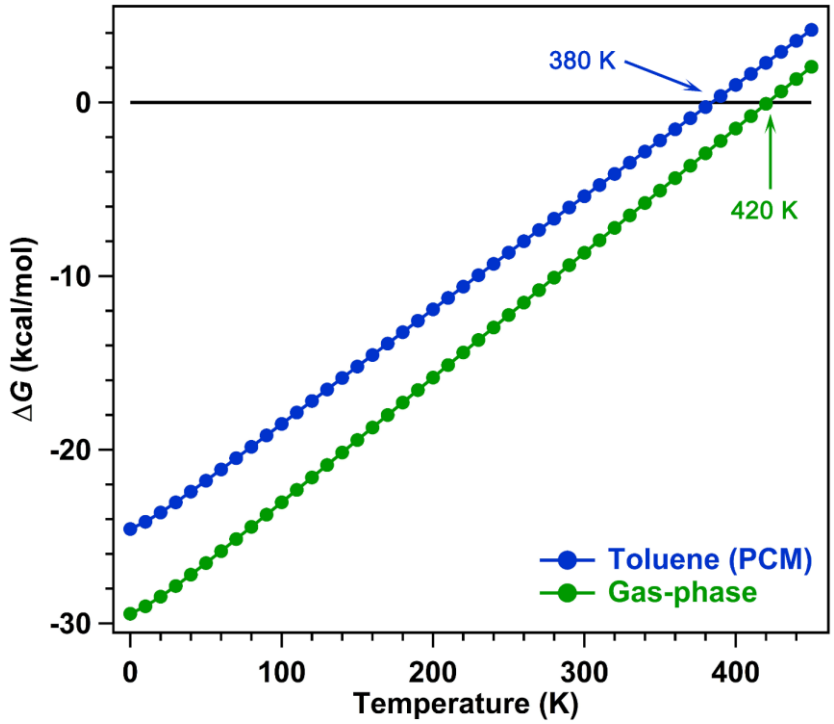

Figure 2D.25. Plot of change in Gibbs free energy (Δ*G*, kcal/mol) of complex **2D.10** in gas and solution-phase as a function of temperature (0-450 K).

2D.3.6.3 Reaction of 2D.2 towards N–H bond (heterolytic) cleavage: synthesis of NHSi-based copper amide complexes.

The N–H bond activation is a vital step for a successful C–N bond formation in the presence of a suitable catalyst. There are several reports on activating such bonds,[293-295] but facile and general preparative methods to obtain these amido species are still relatively scarce.[296, 297] There are prodigious examples of NHC-coordinated copper alkyl complexes that work as intermediates to different E–H (E = N, O, and C) bond functionalized products, which even led to the isolation of the first NHC-based copper amido and anilido complexes.[207,298-300] Recently, CMA complexes have gathered special attention due to their mesmerizing photophysical properties.[221-226, 301-303] Motivated by the fact that NHSi-metal amide complexes were not isolated to date, we delved into the reactivity of the NHSi-ligated copper aryl complex towards N–H bond cleavage, which facilitated a straightforward route for NHSi-coordinated copper amide complexes (**2D.12**-**2D.16**). Hence, the isolation of complex **2D.2** prompted us to functionalize the copper-mesityl bonds further with the polar N–H bonds (Scheme 2D.10). The stoichiometric reaction of **2D.2** with the N–H containing compounds gives access to the variety of NHSi copper amide complexes (**2D.12**-**2D.16**) (Scheme 2D.10). The complexes are stable for several days in the solid state under an inert atmosphere in the dark at room temperature and for several months at 0 °C. However, we could perform all the spectroscopic measurements

at room temperature, including heteronuclear NMR. The treatment of **2D.2** with pyrrole forms complex **2D.12**.

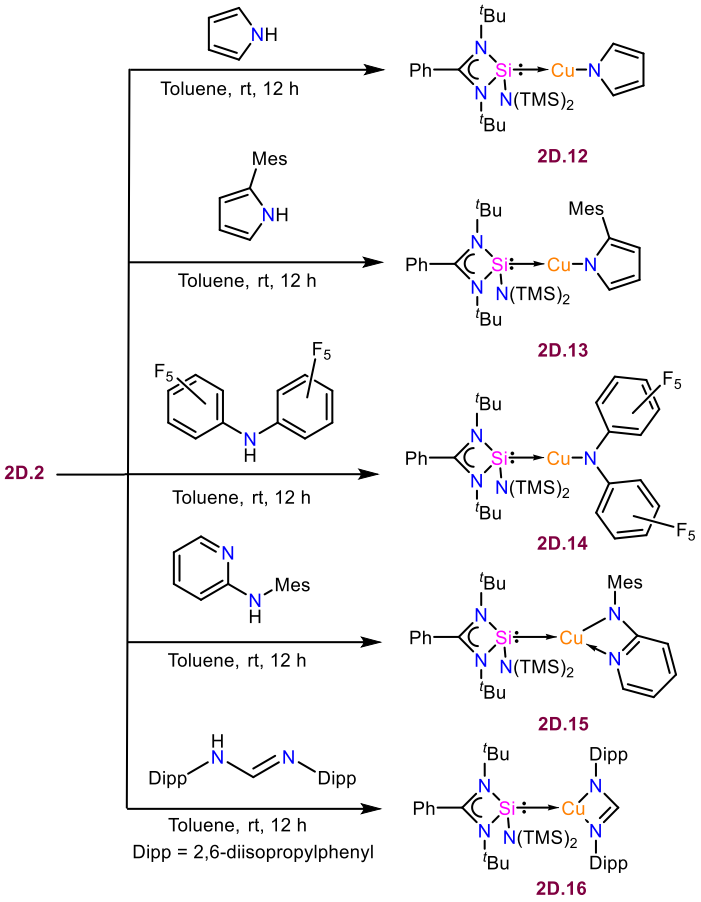

Scheme 2D.10. Syntheses of various NHSi coordinated copper amide complexes from **2D.2**.

The $^{29}Si\{^{1}H\}$ NMR spectrum of **2D.12** shows a broad peak for the Si(II) center at δ 7.6 ppm. The single-crystal X-ray diffraction studies further confirmed the molecular structure of **2D.12** (Figure 2D.26). However, because of the poor quality of the crystals, we refrain from discussing any metrical parameters.

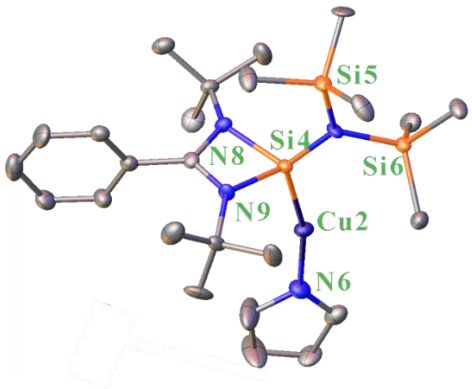

Figure 2D.26. Molecular structure of complex **2D.12**.

Peterson and co-workers also demonstrated the formation of (IPr)Cu–C_5H_4N complex with the help of NMR spectroscopy from (IPr)Cu(Me) complex *via* the facile elimination of CH_4. However, its molecular structure could not be established.[302] After that, we performed a reaction of complex **2D.2** with 2-mesityl–1H-pyrrole, yielding complex **2D.13**. The $^{29}Si\{^1H\}$ NMR spectrum of **2D.13** shows a broad peak at δ 7.4 ppm for the Si(II) coordinated to the Cu center, which is deshielded as compared to **2D.2** due to the π-electron-donating nature of the mesityl group functionalized pyrrole group. Complex **2D.13** possesses a Si1–Cu1 bond length of 2.203(1) Å (Figure 2D.27), which is comparable to the heteroleptic [Cu(tmeda)(PhC(N^tBu)$_2$Si{O^tBu})][OTf] complex (2.2003 (6) Å) reported by Driess and co-workers.[150] The Cu1–N1 bond length of **2D.13** was found as 1.874(3) Å with the Si1–Cu1–N1 angle of 177.5(1)°. In complex **2D.13**, the HOMO is predominantly localized on the 2-mesitylpyrrolide moiety, while the HOMO-1 is distributed across the Cu(I)–N_{amide} fragment. The HOMO-2 is extended over the Si(II)→Cu bond (Figure 2D.28). The bis-perfluoroarylamine is more Lewis acidic than SbF_5, which causes extremely low nucleophilicity of the amide nitrogen and weak coordination of the bis-perfluoroarylamide group.[304] Hence, cleaving the N–H bond of bis-perfluoroarylamine is challenging.[233, 305, 306] Thus, we treated **2D.2** with the bis-pentafluorophenylamine in toluene, which afforded complex **2D.14**. Complex **2D.14** contains a bis-perfluoroarylamide group attached to the copper(I) center, which shows the peak at δ 7.1 ppm for the Si(II) center in the $^{29}Si\{^1H\}$ NMR spectrum. The molecular structure of complex **2D.14** (Figure 2D.27) features a Si–Cu bond length of 2.220(1) Å and a Si1–Cu1–N1 bond angle of 169.3(1)°. This angle shows a significant deviation from the linearity because of the fluorine atoms in the benzene groups. The two *ortho*-fluorine atoms (F5 and F10) are in Cu···F contacts (Cu–F *ortho* distances are Cu1–F10 2.791(3) and Cu1–F5 2.727(2) Å). This leads to an elongation of one of the corresponding C–F bonds (C–F5 and C–F2 distances are 1.350(6) and 1.358(3) Å, respectively) (Figure 2D.29). The intermolecular π-stacking between the phenyl group of amidinate moiety and perfluoro-substituted benzene ring further stabilizes complex **2D.14**. Also, this complex features intermolecular F···F interaction (Figure 2D.29). In complex **2D.14**, the HOMO is centered on the Cu–N_{amide} moiety, while HOMO-1 and HOMO-2 derive significant contributions from the Si(II)→Cu fragment. The LUMO in both complexes **2D.13** and **2D.14** is delocalized over the benzamidinate moieties (Figure 2D.28). The distance between Cu and *ortho*-F atoms in complex **2D.14**, obtained from the optimized geometries and crystal structures, correlates with their $E^{(2)}$ values. Dual Cu···F short contacts between Cu(I) and *ortho*-fluorine atoms of the

pentafluorophenyl ring were observed in complex **2D.14**. $E^{(2)}$ values of Cu···F short contacts from the F5 and F10 were found to be 0.70 and 3.06 kcal/mol (Figure 2D.30).

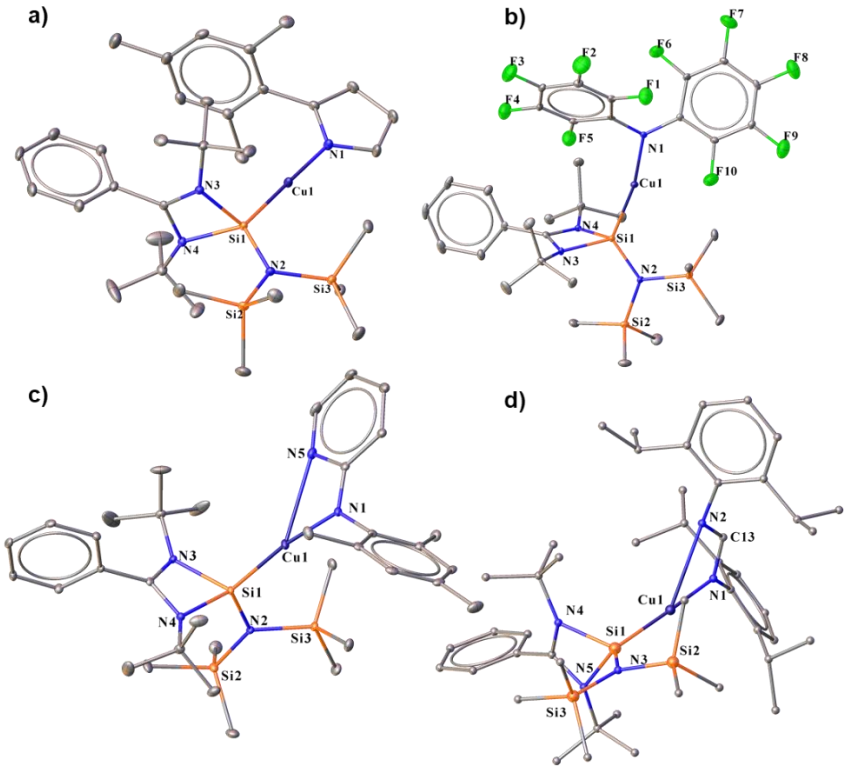

Figure 2D.27. Molecular structure of **2D.13**, **2D.14**, **2D.15**, and **2D.16**. Anisotropic displacement parameters are depicted at the 50% probability level. H atoms are omitted for clarity. Selected bond distances (Å) and angles (deg): for **a)** Si1–Cu1 2.203(1), Cu1–N1 1.874(3), Si1–N2 1.730(5), N2–Si2 1.761(4), N2–Si3 1.770(3), Si1–N3 1.842(3), Si1–N4 1.837(4) and Si1–Cu1–N1 177.5(1), N2–Si1–Cu1 118.8(1), N2–Si1–N4 112.5(2), N3–Si1–Cu1 113.4(1), N3–Si1–N4 71.2(2); **b)** Si1–Cu1 2.220(1), Cu1–N1 1.929(4), N1–C1 1.387(5), N1–C7 1.383(5), Si1–N2 1.724(3), N2–Si2 1.754(4), N2–Si3 1.774(3), Si1–N3 1.836(4), Si1–N4 1.846(3) and Si1–Cu1–N1 169.3(1), N4–Si1–N3 70.7(2), N4–Si1–N2 112.4(2), N2–Si1–Cu1 123.5(1), N4–Si1–Cu1 113.3(1); **c)** Si1–Cu1 2.1964(8), Cu1–N1 1.906(2), Cu1–N5 2.654(2), Si1–N4 1.842(2), Si1–N3 1.838(2), Si1–N2 1.740(2), N2–Si3 1.770(2), N2–Si2 1.754(2) and Si1–Cu1–N1 172.44(7), Si1–Cu1–N5 128.28(6), N5–Cu1–N1 57.09(8), N3–Si1–Cu1 114.98(8), N3–Si1–N2 112.6(1), N4–Si1–N2 112.6(1), Cu1–Si1–N2 118.48(8); and **d)** Si1–Cu1 2.194(1), Cu1–N1 1.903(3), Cu1–N2 2.712(3), N2–C13 1.294(4), C13–N1 1.337(4), Si1–N5 1.837(3), Si1–N4 1.845(3), Si1–N3 1.719(3), N3–Si3 1.761(3), N3–Si2 1.768(3) and Si1–Cu1–N1 171.24(9), Si1–Cu1–N2 129.22(6), N1–Cu1–N2 56.1(1), N1–C13–N2 120.6(3), N3–Si1–N5 112.4(1), N3–Si1–N4 114.2(1), Cu1–Si1–N5 112.4(1), N3–Si1–Cu1 124.8(1), N4–Si1–N5 70.7(1).

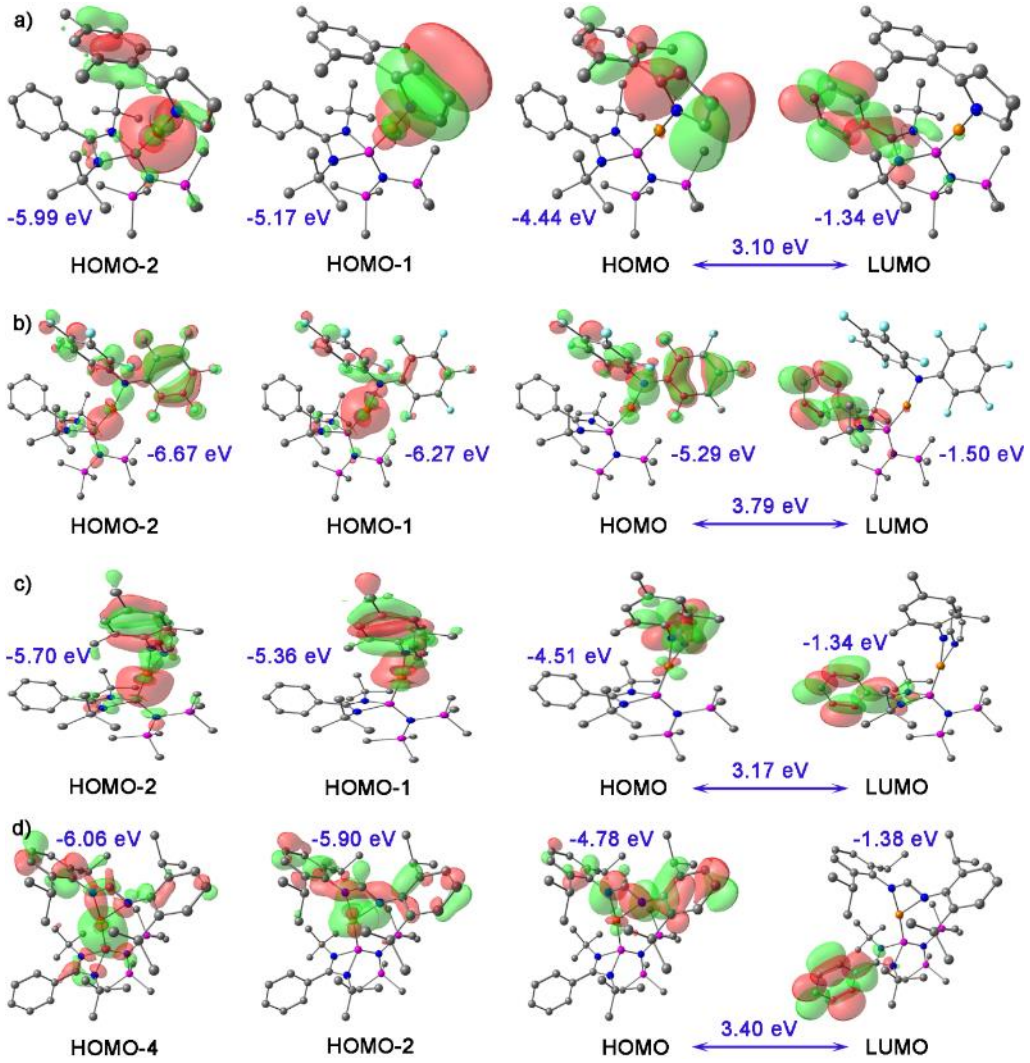

Figure 2D.28. MOs of complexes a) **2D.13**, b) **2D.14**, c) **2D.15**, and d) **2D.16**.

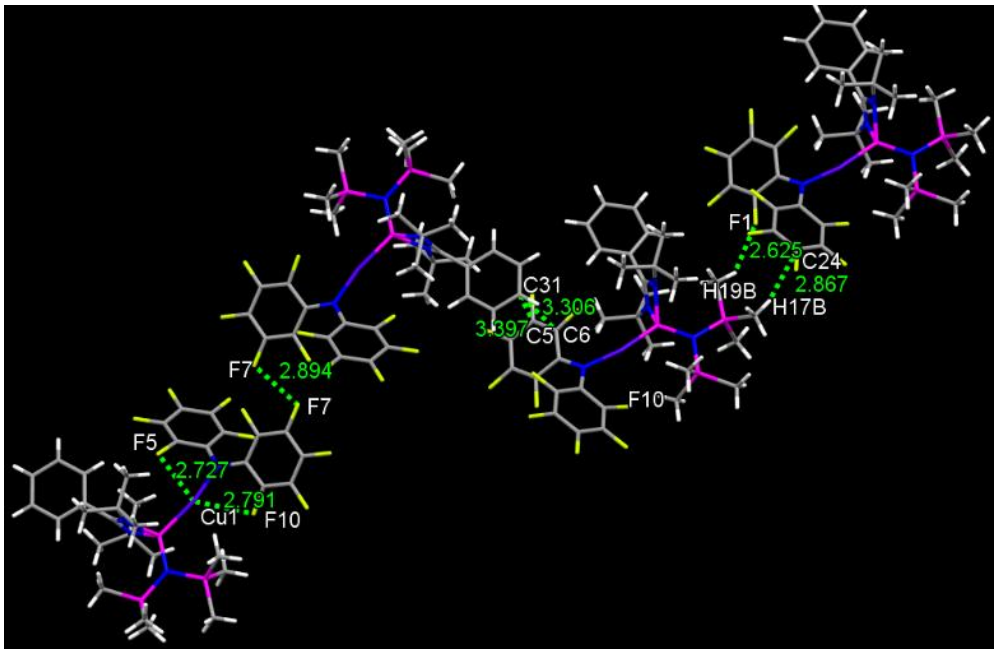

Figure 2D.29. Cu···F interactions in complex **2D.14**.

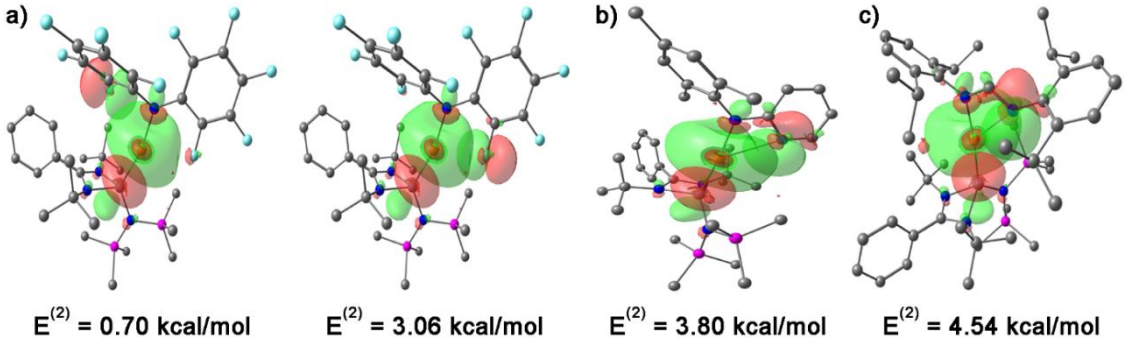

Figure 2D.30. NBO images of a) Cu···F interaction in complex **2D.14**, b and c) showing N→Cu interactions for complex **2D.15** and **2D.16**, respectively.

After isolating the complexes **2D.12-2D.14**, we were curious to investigate the coordinative variability of N-donor functionalized secondary amines. To explore the coordination ability of N–H systems containing auxiliary N-donor atoms, we obtained a few coordinated Cu(I) complexes (**2D.15** and **2D.16**). The three coordinate NHSi-copper(I) complex (**2D.15**) was isolated by treating **2D.2** with *N*-mesitylpyridin-2-amine, which gives a broad peak at δ 6.9 ppm for Si(II) center in the $^{29}Si\{^{1}H\}$ NMR spectrum. Complex **2D.15** features the Si1–Cu1 bond length of 2.1964(8) Å (Figure 2D.27), which is shorter than the Si(II)→Cu(I) bond in complex **2D.12-2D.14**. The Cu1–N5 bond length of **2D.15** is 2.654(2) Å, which is significantly longer than the reported IPr coordinated three copper(I) complexes attached to the 2-(2,3,4,5-tetrafluorophenyl) pyridine group.[307] Thompson and co-workers isolated a few (NHC)Cu(py_2BMe_2) {py_2BMe_2=di(2-pyridyl)dimethylborate} complexes, which features N^N donation to copper(I) centre. These complexes possess Cu–N bond lengths ranging from 1.9929(16)-2.0288(15) Å.[308] The Si1–Cu1–N1 bond angle in **2D.16** is 172.44(7)°, which deviates from the linearity due to the additional *N*-donation. Stalke and co-workers isolated *N*-mesitylpyridin-2-amine substituted benzamidinato silylene coordinated trimeric copper(I) halide complexes,[156] which also features pyridyl N-donation to copper(I) center with the N→Cu bond lengths from 1.995(4) to 2.009(2) Å. These bonds are significantly shorter than the observed N→Cu bond in **2D.15**, denoting a greater extent of electron donation in the former one. The amidinate ligands are infinitely versatile in terms of potential structure and substitution patterns.[309] This prompted us to isolate complex **2D.16** containing 2,6-diisopropylphenyl (Dipp) group substituted formamidine moiety (Scheme 2D.10). This features a broad peak at δ 4.8 ppm for Si(II) attached to three coordinate copper(I) centers in the $^{29}Si\{^{1}H\}$ NMR spectrum. Due to an additional N-donor atom, the Si(II) center is more shielded than the complexes **2D.12-2D.14**. Complex **2D.16** is structurally reminiscent of CAAC stabilized three-coordinate formamidinate copper(I) complex[310] and crystallizes in the

monoclinic *Cc* space group (Figure 2D.27). The molecular structure of **2D.16** reveals the Si1–Cu1–N1 angle of 171.24(9)°, whereas, for the CAAC one, the C–Cu–N angle is 175.09(7)°.[310, 311] The Si1–Cu1 and Cu1–N1 bond lengths are 2.194(1) and 1.903(3) Å, respectively. The Cu1–N2 bond length is 2.712(3) Å, shorter than their sum of van der Waal radius (2.94 Å), suggesting the coordinative nature. This is also shorter than the formamidinate copper(I) complex of CAAC (Cu–N 2.912(14) Å).[310] The C–N bond lengths in the formamidinate backbone are different, with long N1–C13 and short N2–C13 distances of 1.337(4) and 1.294(4) Å, respectively, and match well with the localized C–N single and double bonds in the formamidinate system.

Table 2D.3. Bond lengths of NHSi coordinated Cu-mesityl and Cu-amide complexes

Complexes	^{29}Si{^{1}H} Chemical shift (δ) ppm	Si(II)→Cu(I) bond length (Å)	Cu-C/N bond length (Å)
2D.2	6.5	2.2509(8)	1.946(2)
2D.13	7.4	2.203(1)	1.874(3)
2D.14	7.1	2.220(1)	1.929(4)
2D.15	6.9	2.1964(8)	1.906(2)
2D.16	6.6	2.194(1)	1.903(3)

HOMO of complex **2D.15** exhibits that there is a major contribution from the 2-mesitylpyridyl moiety and *d*-orbital of the Cu atom. The electron density at the HOMO-1 is predominantly localized over the Cu–N_{amide} bond with a minor contribution over the pyridine ring, whereas electron density is delocalized over the Si(II)→Cu–N–mesityl in HOMO-2 with a minor contribution from the pyridine ring. NBO calculation further shows that the N→Cu bond is stabilized by $E^{(2)}$ values 3.80 and 4.54 kcal/mol for complexes **2D.15** and **2D.16**, respectively (Figure 2D.30). An apparent trend emerges after observing the chemical shifts of ^{29}Si{^{1}H} NMR and bonding parameters of the Cu-amide complexes (**2D.13**-**2D.16**) with **2D.2** (Table 2D.3). We observe a deshielding effect on the Si(II) centers for complexes **2D.13**-**2D.16** that can be attributed to the electrophilic nature of the amide group. Furthermore, the Si(II)→Cu and Cu–N_{amide} bond lengths of complexes **2D.13**-**2D.16** are notably shorter than the corresponding Si(II)→Cu and Cu–C_{ipso} bond lengths in complex **2D.2**. This discrepancy suggests an enhanced electropositive character of the Cu(I) center in complexes **2D.13**-**2D.16**, as also realized from the Mulliken charge analysis (Table 2D.4) on the Si, Cu, C_{ipso}, and N_{amide}. It was found that the electropositive character of the Cu(I) center indeed increases in **2D.13**-

2D.16 with a gradual increase in the electrophilic nature of the amide ligand as compared to the mesityl group of **2D.2**.

Table 2D.4. Mulliken charges on Si(II), Cu(I), C_{ipso}, and N_{amide} centres

	2	**13**	**14**	**15**	**16**
q_{Si}	0.6172	0.7934	0.8198	0.8569	0.8369
q_{Cu}	-0.4735	-0.1931	-0.2265	-0.2137	-0.2031
$q_{C/N}$	-0.1829	-0.2091	-0.2386	-0.2477	-0.2395

2D.4 Conclusion

The functionalization of NHC or CAAC-based coinage metal complexes become important lately because of the efficient optoelectronic applications of carbene-metal-amide complexes. However, the functionalization of NHSi-copper(I) complexes was unknown to date. In summary, we have established a versatile route to utilize the NHSi-organocopper complex as an efficient precursor for heteroatom functionalization. We have shown the successful mesityl group transfer from **2D.2** in Pd-catalyzed C–C cross-coupling reactions, affording excellent yields of the products. Importantly, we could also isolate an interesting NHSi coordinated dimeric mesityl silver complex (**2D.4**) with argentophilic interaction. Our adopted methodology allows facile generation of NHSi-supported Cu–O (**2D.6**), Cu–B (**2D.8**), Cu–Se (**2D.10** and **2D.11**) and Cu–N (**2D.12-2D.16**) bonds. Moreover, utilizing N-donor attached secondary amines gives structurally unique three-coordinate copper(I) complexes (**2D.15** and **2D.16**). Our future attempts will fine-tune the methodology to explore the optoelectronic properties of such relevant compounds. Our future efforts will also focus on using these complexes for the different organic transformations for which we believe they have great potential.

2.1 Bibliography.

(1) Minoura, M.; Kawashima, T.; Tokitoh, N.; Okazaki, R. Weak coordination of a telluroketone in an η^1-mode complex: Synthesis and characterization of pentacarbonyl(1,1,3,3-tetramethylindantellone)tungsten. *Chem. Commun.* **1996**, 123-124.
(2) Chivers, T.; Laitinen, R. S. Tellurium: a maverick among the chalcogens. *Chem. Soc. Rev.* **2015**, *44*, 1725-1739.
(3) Liu, S. Y.; Legare, M. A.; Auerhammer, D.; Hofmann, A.; Braunschweig, H. The First Boron-Tellurium Double Bond: Direct Insertion of Heavy Chalcogens into a Mn=B Double Bond. *Angew. Chem. Int. Ed.* **2017**, *56*, 15760-15763.
(4) Franz, D.; Szilvasi, T.; Irran, E.; Inoue, S. A monotopic aluminum telluride with an Al = Te double bond stabilized by N-heterocyclic carbenes. *Nat. Commun.* **2015**, *6*, 10037-10043.

(5) Iwamoto, T.; Sato, K.; Ishida, S.; Kabuto, C.; Kira, M. Synthesis, properties, and reactions of a series of stable dialkyl-substituted silicon-chalcogen doubly bonded compounds. *J. Am. Chem. Soc.* **2006**, *128*, 16914-16920.
(6) Yao, S. L.; Xiong, Y.; Driess, M. N-Heterocyclic Carbene (NHC)-Stabilized Silanechalcogenones: NHC -> $Si(R_2)$=E (E = O, S, Se, Te). *Chem. Eur. J.* **2010**, *16*, 1281-1288.
(7) Yao, S. L.; Xiong, Y.; Brym, M.; Driess, M. A series of isolable silanoic thio-, seleno-, and telluroesters (LSi(=X)OR) with donor-supported Si=X double bonds (L=beta-diketiminate; X = S, Se, Te). *Chem. Asian J.* **2008**, *3*, 113-118.
(8) Xiong, Y.; Yao, S. L.; Inoue, S.; Irran, E.; Driess, M. The Elusive Silyliumylidene $[ClSi:]^+$ and Silathionium $[ClSi=S]^+$ Cations Stabilized by Bis(Iminophosphorane) Chelate Ligand. *Angew. Chem. Int. Ed.* **2012**, *51*, 10074-10077.
(9) Junold, K.; Baus, J. A.; Burschka, C.; Auerhammer, D.; Tacke, R. Stable Five-Coordinate Silicon(IV) Complexes with SiN4X Skeletons (X=S, Se, Te) and Si?X Double Bonds. *Chem. Eur. J.* **2012**, *18*, 16288-16291.
(10) Chan, Y. C.; Li, Y. X.; Ganguly, R.; So, C. W. Acyclic Amido-Containing Silanechalcogenones. *Eur. J. Inorg. Chem.* **2015**, 3821-3824.
(11) Bisai, M. K.; Swamy, V. S. V. S. N.; Das, T.; Vanka, K.; Gonnade, R. G.; Sen, S. S. Synthesis and Reactivity of a Hypersilylsilylene. *Inorg. Chem.* **2019**, *58*, 10536-10542.
(12) Mitra, A.; Wojcik, J. P.; Lecoanet, D.; Muller, T.; West, R. A Bis(silaselenone) with Two Donor-Stabilized Si=Se Bonds from an Unexpected Stereoconvergent Hydrolysis of a Diselenadisiletane. *Angew. Chem. Int. Ed.* **2009**, *48*, 4069-4072.
(13) Zhang, S. H.; Yeong, H. X.; So, C. W. Reactivity of a Silylsilylene Bearing a Functionalized Diaminochlorosilyl Substituent. *Chem. Eur. J.* **2011**, *17*, 3490-3499.
(14) Sen, S. S.; Jana, A.; Roesky, H. W.; Schulzke, C. A Remarkable Base-Stabilized Bis(silylene) with a Silicon(I)-Silicon(I) Bond. *Angew. Chem. Int. Ed.* **2009**, *48*, 8536-8538.
(15) Luecke, M. P.; Pens, E.; Yao, S. L.; Driess, M. An Isolable Bis(Silanone-Borane) Adduct. *Chem. Eur. J.* **2020**, *26*, 4500-4504.
(16) Saito, Y.; Tominaga, J.; Fons, P.; Kolobov, A. V.; Nakano, T. Ab-initio calculations and structural studies of $(SiTe)_2$ $(Sb_2Te_3)n$ (n: 1, 2, 4 and 6) phase-change superlattice films. *Phys. Status Solidi-Rapid Res. Lett.* **2014**, *8*, 302-306.
(17) Ma, Y. D.; Kou, L. Z.; Dai, Y.; Heine, T. Proposed two-dimensional topological insulator in SiTe. *Phys. Rev. B* **2016**, *94*, 201104-201109.
(18) Keuleyan, S.; Wang, M. J.; Chung, F. R.; Commons, J.; Koski, K. J. A Silicon-Based Two-Dimensional Chalcogenide: Growth of Si_2Te_3 Nanoribbons and Nanoplates. *Nano Lett.* **2015**, *15*, 2285-2290.
(19) Wang, W. Y.; Inoue, S.; Irran, E.; Driess, M. Synthesis and Unexpected Coordination of a Silicon(II)-Based SiCSi Pincerlike Arene to Palladium. *Angew. Chem. Int. Ed.* **2012**, *51*, 3691-3694.
(20) Siemes, L. C.; Keuter, J.; Hepp, A.; Lips, F. Reactions of a Silicon-Based Cyclic Silylone with Chalcogens. *Inorg. Chem.* **2019**, *58*, 13142-13149.
(21) Lutters, D.; Merk, A.; Schmidtmann, M.; Muller, T. The Silicon Version of Phosphine Chalcogenides: Synthesis and Bonding Analysis of Stabilized Heavy Silaaldehydes. *Inorg. Chem.* **2016**, *55*, 9026-9032.
(22) Chan, Y. C.; Leong, B. X.; Li, Y. X.; Yang, M. C.; Li, Y.; Su, M. D.; So, C. W. A Dimeric NHC-Silicon Monotelluride: Synthesis, Isomerization, and Reactivity. *Angew. Chem. Int. Ed.* **2017**, *56*, 11565-11569.
(23) Mundlapati, V. R.; Sahoo, D. K.; Ghosh, S.; Purame, U. K.; Pandey, S.; Acharya, R.; Pal, N.; Tiwari, P.; Biswal, H. S. Spectroscopic Evidences for Strong Hydrogen Bonds with Selenomethionine in Proteins. *J. Phys. Chem. Lett.* **2017**, *8*, 794-800.

(24) Mishra, K. K.; Singh, S. K.; Ghosh, P.; Ghosh, D.; Das, A. The nature of selenium hydrogen bonding: gas phase spectroscopy and quantum chemistry calculations. *Phys. Chem. Chem. Phys.* **2017**, *19*, 24179-24187.
(25) Chand, A.; Sahoo, D. K.; Rana, A.; Jena, S.; Biswal, H. S. The Prodigious Hydrogen Bonds with Sulfur and Selenium in Molecular Assemblies, Structural Biology, and Functional Materials. *Acc. Chem. Res.* **2020**, *53*, 1580-1592.
(26) Ghosh, S.; Chopra, P.; Wategaonkar, S. C-H···S interaction exhibits all the characteristics of conventional hydrogen bonds. *Phys. Chem. Chem. Phys.* **2020**, *22*, 17482-17493.
(27) Mishra, K. K.; Singh, S. K.; Kumar, S.; Singh, G.; Sarkar, B.; Madhusudhan, M. S.; Das, A. Water-Mediated Selenium Hydrogen-Bonding in Proteins: PDB Analysis and Gas-Phase Spectroscopy of Model Complexes. *J. Phys. Chem. A* **2019**, *123*, 5995-6002.
(28) Biswal, H. S.; Bhattacharyya, S.; Bhattacherjee, A.; Wategaonkar, S. Nature and strength of sulfur-centred hydrogen bonds: laser spectroscopic investigations in the gas phase and quantum-chemical calculations. *Int. Rev. Phys. Chem.* **2015**, *34*, 99-160.
(29) Epping, J. D.; Yao, S.; Karni, M.; Apeloig, Y.; Driess, M. Si=X Multiple Bonding with Four-Coordinate Silicon? Insights into the Nature of the Si=O and Si=S Double Bonds in Stable Silanoic Esters and Related Thioesters: A Combined NMR Spectroscopic and Computational Study. *J. Am. Chem. Soc.* **2010**, *132*, 5443-5455.
(30) Parvin, N.; Pal, S.; Khan, S.; Das, S.; Pati, S. K.; Roesky, H. W. Unique Approach to Copper(I) Silylene Chalcogenone Complexes. *Inorg. Chem.* **2017**, *56*, 1706-1712.
(31) Suzuki, H.; Tokitoh, N.; Nagase, S.; Okazaki, R. The First Genuine Silicon-Sulfur Double-Bond Compound - Synthesis and Crystal-Structure of a Kinetically Stabilized Silanethione. *J. Am. Chem. Soc.* **1994**, *116*, 11578-11579.
(32) Mukherjee, A. J.; Zade, S. S.; Singh, H. B.; Sunoj, R. B. Organoselenium Chemistry: Role of Intramolecular Interactions. *Chem. Rev.* **2010**, *110*, 4357-4416.
(33) Iwaoka, M.; Tomoda, S. First Observation of a C-H···Se Hydrogen-Bond. *J. Am. Chem. Soc.* **1994**, *116*, 4463-4464.
(34) Junor, G. P.; Lorkowski, J.; Weinstein, C. M.; Jazzar, R.; Pietraszuk, C.; Bertrand, G. The Influence of C(sp^3)H-Selenium Interactions on the ^{77}Se NMR Quantification of the p-Accepting Properties of Carbenes. *Angew. Chem. Int. Ed.* **2020**, *132*, 22212-22217.
(35) Steiner, T. Chloroform molecules donate hydrogen bonds to S, Se, and Te acceptors: evidence from a published series of terminal chalcogenido complexes. *J. Mol. Struct.* **1998**, *447*, 39-42.
(36) Desiraju, G. R.; Steiner, T. *The weak hydrogen bond: in structural chemistry and biology* (International Union of Crystal, 2001).
(37) Chand, A.; Biswal, H. S. Hydrogen Bonds with Chalcogens: Looking Beyond the Second Row of the Periodic Table. *J. Indian Inst. Sci.* **2020**, 77-100.
(38) Thakur, T. S.; Azim, Y.; Srinu, T.; Desiraju, G. R. N–H···O and C–H···O interaction mimicry in the 1: 1 molecular complexes of 5, 5diethylbarbituric acid with urea and acetamide. *Curr. Sci.* **2010**, 793-802.
(39) Jensen, S. J. K.; Tang, T. H.; Csizmadia, I. G. Hydrogen-bonding ability of a methyl group. *J. Phys. Chem. A* **2003**, *107*, 8975-8979.
(40) Kumar, G. A.; McAllister, M. A. Theoretical investigation of the relationship between proton NMR chemical shift and hydrogen bond strength. *J. Org. Chem.* **1998**, *63*, 6968-6972.
(41) Wang, B.; Hinton, J. F.; Pulay, P. C–H···O hydrogen bond between N-methyl maleimide and dimethyl sulfoxide: A combined NMR and Ab initio study. *J. Phys. Chem. A* **2003**, *107*, 4683-4687.
(42) Tokitoh, N.; Sadahiro, T.; Hatano, K.; Sasaki, T.; Takeda, N.; Okazaki, R. Synthesis of kinetically stabilized silaneselone and silanetellone. *Chem. Lett.* **2002**, *31*, 34-35.

(43) Protchenko, A. V.; Vasko, P.; Do, D. C. H.; Hicks, J.; Fuentes, M. A.; Jones, C.; Aldridge, S. Reduction of Carbon Oxides by an Acyclic Silylene: Reductive Coupling of CO. *Angew. Chem. Int. Ed.* **2019**, *58*, 1808-1812.
(44) Frisch, M. J.; Trucks, G. W.; Schlegel, H. B.; Scuseria, G. E.; Robb, M. A.; Cheeseman, J. R.; Scalmani, G.; Barone, V.; Mennucci, B.; Petersson, G. A.; Nakatsuji, H.; Caricato, M.; Li, X.; Hratchian, H. P.; Izmaylov, A. F.; Bloino, J.; Zheng, G.; Sonnenberg, J. L.; Hada, M.; Ehara, M.; Toyota, K.; Fukuda, R.; Hasegawa, J.; Ishida, M.; Nakajima, T.; Honda, Y.; Kitao, O.; Nakai, H.; Vreven, T.; Montgomery Jr., J. A.; Peralta, J. E.; Ogliaro, F.; Bearpark, M.; Heyd, J. J.; Brothers, E.; Kudin, K. N.; Staroverov, V. N.; Kobayashi, R.; Normand, J.; Raghavachari, K.; Rendell, A.; Burant, J. C.; Iyengar, S. S.; Tomasi, J.; Cossi, M.; Rega, N.; Millam, N. J.; Klene, M.; Knox, J. E.; Cross, J. B.; Bakken, V.; Adamo, C.; Jaramillo, J.; Gomperts, R.; Stratmann, R. E.; Yazyev, O.; Austin, A. J.; Cammi, R.; Pomelli, C.; Ochterski, J. W.; Martin, R. L.; Morokuma, K.; Zakrzewski, V. G.; Voth, G. A.; Salvador, P.; Dannenberg, J. J.; Dapprich, S.; Daniels, A. D.; Farkas, Ö.; Foresman, J. B.; Ortiz, J. V.; Cioslowski, J.; Fox, D. J. *M. J. Frisch et al., GAUSSIAN 09, Revision D.01, Gaussian, Inc., Wallingford CT (2009).*
(45) Lu, T.; Chen, F. W. Multiwfn: A multifunctional wavefunction analyzer. *J. Comput. Chem.* **2012**, *33*, 580-592.
(46) Glendening, E. D.; Landis, C. R.; Weinhold, F. NBO 6.0: Natural bond orbital analysis program. *J. Comput. Chem.* **2013**, *34*, 1429-1437.
(47) Johnson, E. R.; Keinan, S.; Mori-Sanchez, P.; Contreras-Garcia, J.; Cohen, A. J.; Yang, W. T. Revealing Noncovalent Interactions. *J. Am. Chem. Soc.* **2010**, *132*, 6498-6506.
(48) Contreras-Garcia, J.; Johnson, E. R.; Keinan, S.; Chaudret, R.; Piquemal, J. P.; Beratan, D. N.; Yang, W. T. NCIPLOT: A Program for Plotting Noncovalent Interaction Regions. *J. Chem. Theory Comput.* **2011**, *7*, 625-632.
(49) Glendening, E. D.; Landis, C. R.; Weinhold, F. NBO 7.0: New vistas in localized and delocalized chemical bonding theory. *J. Comput. Chem.* **2019**, *40*, 2234-2241.
(50) Popelier, P. L. A. Characterization of a dihydrogen bond on the basis of the electron density. *J. Phys. Chem. A* **1998**, *102*, 1873-1878.
(51) Kipping, F. S.; Lloyd, L. L. XLVII.—Organic derivatives of silicon. Triphenylsilicol and alkyloxysilicon chlorides. *J. Chem. Soc., Trans.* **1901**, *79*, 449-459.
(52) Kimura, M.; Nagase, S. The quest of stable silanones: Substituent effects. *Chem. Lett.* **2001**, 1098-1099.
(53) Rodriguez, R.; Gau, D.; Saouli, J.; Baceiredo, A.; Saffon-Merceron, N.; Branchadell, V.; Kato, T. A Stable Monomeric SiO_2 Complex with Donor-Acceptor Ligands. *Angew. Chem. Int. Ed.* **2017**, *56*, 3935-3939.
(54) Loh, Y. K.; Aldridge, S. Acid-Base Free Main Group Carbonyl Analogues. *Angew. Chem. Int. Ed.* **2020**, *60*, 8626-8648.
(55) Khan, S.; Sen, S. S.; Kratzert, D.; Tavcar, G.; Roesky, H. W.; Stalke, D. Synthesis of Stable Silicon Heterocycles by Reaction of Organic Substrates with a Chlorosilylene [$PhC(N^tBu)_2SiCl$]. *Chem. Eur. J.* **2011**, *17*, 4283-4290.
(56) Sen, S. S.; Hey, J.; Kratzert, D.; Roesky, H. W.; Stalke, D. A Remarkable End-On Activation of Diazoalkane and Cleavage of Both C-Cl Bonds of Dichloromethane with a Silylene to a Single Product with Five-Coordinate Silicon Atoms. *Organometallics* **2012**, *31*, 435-439.
(57) Sen, S. S.; Tavcar, G.; Roesky, H. W.; Kratzert, D.; Hey, J.; Stalke, D. Synthesis of a Stable Four-Membered Si_2O_2 Ring and a Dimer with Two Four-Membered Si_2O_2 Rings Bridged by Two Oxygen Atoms, with Five-Coordinate Silicon Atoms in Both Ring Systems. *Organometallics* **2010**, *29*, 2343-2347.
(58) Tavčar, G. p.; Sen, S. S.; Roesky, H. W.; Hey, J.; Kratzert, D.; Stalke, D. Reactions of a Bis-silylene (LSi− SiL, L= PhC ($N^tBu)_2$) and a Heteroleptic Chloro Silylene (LSiCl) with

Benzil: Formation of Bis (siladioxolene) and Monosiladioxolene Analogue with Five-Coordinate Silicon Atoms in Both Ring Systems. *Organometallics* **2010**, *29*, 3930-3935.
(59) Dewar, M. J. S.; Thiel, W. Ground-States of Molecules. 38.[1] MNDO Method. Approximations and Parameters. *J. Am. Chem. Soc.* **1977**, *99*, 4899-4907.
(60) Kudo, T.; Nagase, S. Theoretical-Study on the Dimerization of Silanone and the Properties of the Polymeric Products $(H_2SiO)_n$ (n = 2, 3, and 4) - Comparison with Dimers $(H_2SiS)_2$ and $(H_2CO)_2$. *J. Am. Chem. Soc.* **1985**, *107*, 2589-2595.
(61) Haaf, M.; Schmedake, T. A.; West, R. Stable silylenes. *Acc. Chem. Res.* **2000**, *33*, 704-714.
(62) Gehrhus, B.; Lappert, M. F. Chemistry of thermally stable bis (amino) silylenes. *J. Organomet. Chem.* **2001**, *617*, 209-223.
(63) Mizuhata, Y.; Sasamori, T.; Tokitoh, N. Stable heavier carbene analogues. *Chem. Rev.* **2009**, *109*, 3479-3511.
(64) Asay, M.; Jones, C.; Driess, M. N-Heterocyclic carbene analogues with low-valent group 13 and group 14 elements: syntheses, structures, and reactivities of a new generation of multitalented ligands. *Chem. Rev.* **2011**, *111*, 354-396.
(65) Fujimori, S.; Inoue, S. Small Molecule Activation by Two-Coordinate Acyclic Silylenes. *Eur. J. Inorg. Chem.* **2020**, *2020*, 3131-3142.
(66) Shan, C. K.; Yao, S. L.; Driess, M. Where silylene-silicon centres matter in the activation of small molecules. *Chem. Soc. Rev.* **2020**, *49*, 6733-6754.
(67) Weetman, C.; Inoue, S. The Road Travelled: After Main-Group Elements as Transition Metals. *ChemCatChem* **2018**, *10*, 4213-4228.
(68) Sen, S. S.; Khan, S.; Samuel, P. P.; Roesky, H. W. Chemistry of functionalized silylenes. *Chem. Sci.* **2012**, *3*, 659-682.
(69) Yao, S.; Xiong, Y.; Driess, M. Zwitterionic and donor-stabilized N-heterocyclic silylenes (NHSis) for metal-free activation of small molecules. *Organometallics* **2011**, *30*, 1748-1767.
(70) Wang, Y.; Karni, M.; Yao, S.; Kaushansky, A.; Apeloig, Y.; Driess, M. Synthesis of an isolable bis (silylene)-stabilized silylone and its reactivity toward small gaseous molecules. *J. Am. Chem. Soc.* **2019**, *141*, 12916-12927.
(71) Blom, B.; Driess, M. Recent advances in silylene chemistry: small molecule activation en-route towards metal-free catalysis. *Functional Molecular Silicon Compounds II: Low Oxidation States* **2014**, 85-123.
(72) Alvarez-Rodriguez, L.; Cabeza, J. A.; Garcia-Alvarez, P.; Polo, D. The transition-metal chemistry of amidinatosilylenes, -germylenes and -stannylenes. *Coord. Chem. Rev.* **2015**, *300*, 1-28.
(73) Metzler, N.; Denk, M. Synthesis of a silylene–borane adduct and its slow conversion to a silylborane. *Chem. Commun.* **1996**, 2657-2658.
(74) Seufert, J.; Welz, E.; Krummenacher, I.; Paprocki, V.; Böhnke, J.; Hagspiel, S.; Dewhurst, R. D.; Tacke, R.; Engels, B.; Braunschweig, H. Isolation and Characterization of Crystalline, Neutral Diborane (4) Radicals. *Angew. Chem. Int. Ed.* **2018**, *57*, 10752-10755.
(75) Wang, H.; Wu, L.; Lin, Z.; Xie, Z. Transition-Metal-Like Behavior of Monovalent Boron Compounds: Reduction, Migration, and Complete Cleavage of CO at a Boron Center. *Angew. Chem. Int. Ed.* **2018**, *57*, 8708-8713.
(76) Wang, H.; Zhang, J.; Lee, H. K.; Xie, Z. Borylene insertion into cage B–H bond: a route to electron-precise B–B single bond. *J. Am. Chem. Soc.* **2018**, *140*, 3888-3891.
(77) Li, J.; Liu, Y.; Kundu, S.; Keil, H.; Zhu, H.; Herbst-Irmer, R.; Stalke, D.; Roesky, H. W. Reactions of amidinate-supported silylene with organoboron dihalides. *Inorg. Chem.* **2020**, *59*, 7910-7914.
(78) Sarkar, S. K.; Chaliha, R.; Siddiqui, M. M.; Banerjee, S.; Münch, A.; Herbst-Irmer, R.; Stalke, D.; Jemmis, E. D.; Roesky, H. W. A Neutral Three-Membered 2π Aromatic

Disilaborirane and the Unique Conversion into a Four-Membered BSi_2N-Ring. *Angew. Chem. Int. Ed.* **2020**, *59*, 23015-23019.
(79) Bisai, M. K.; Swamy, V.; Raj, K. V.; Vanka, K.; Sen, S. S. Diverse reactivity of hypersilylsilylene with boranes and three-component reactions with aldehyde and HBpin. *Inorg. Chem.* **2021**, *60*, 1654-1663.
(80) Fan, J.; Yang, M.-C.; Su, M.-D.; So, C.-W. Amidinatoamidosilylene–Dibromodiborene. *Inorg. Chem.* **2021**, *60*, 16065-16069.
(81) Feng, Z.; Tang, S.; Su, Y.; Wang, X. Recent advances in stable main group element radicals: preparation and characterization. *Chem. Soc. Rev.* **2022**, *51*, 5930-5973.
(82) Nazish, M.; Ding, Y.; Legendre, C. M.; Kumar, A.; Graw, N.; Schwederski, B.; Herbst-Irmer, R.; Parvathy, P.; Parameswaran, P.; Stalke, D. Excellent yield of a variety of silicon-boron radicals and their reactivity. *Dalton Trans.* **2022**, *51*, 11040-11047.
(83) Zhang, Y.; Wu, L.; Wang, H. Neutral Homoaromatic Diboradisilacyclobutene: Synthesis, Structure, and Reactivity. *J. Am. Chem. Soc.* **2022**, *144*, 22446-22450.
(84) Chen, X.; Yang, Y.; Wang, H.; Mo, Z. Cooperative Bond Activation and Catalytic CO_2 Functionalization with a Geometrically Constrained Bis (silylene)-Stabilized Borylene. *J. Am. Chem. Soc.* **2023**, *145*, 7011-7020.
(85) Fan, J.; Yang, M.-C.; Su, M.-D.; So, C.-W. N-Phosphinoamidinato Silylene–and Phosphine–Borylborylene Complexes. *Inorg. Chem.* **2023**, *62*, 863-870.
(86) Nazish, M.; Legendre, C. M.; Sarkar, S. K.; Lücken, J.; Goffitzer, D. J.; Diefenbach, M.; Schwederski, B.; Herbst-Irmer, R.; Stalke, D.; Holthausen, M. C. Selective Route to Stable Silicon–Boron Radicals and Their Corresponding Cations. *Inorg. Chem.* **2021**, *60*, 10100-10104.
(87) Nazish, M.; Legendre, C. M.; Ding, Y.; Schluschaß, B.; Schwederski, B.; Herbst-Irmer, R.; Parvathy, P.; Parameswaran, P.; Stalke, D.; Kaim, W.; Roesky, H. W. A Neutral Borylene and its Conversion to a Radical by Selective Hydrogen Transfer. *Inorg. Chem.* **2023**, *62*, 9343-9349.
(88) Nazish, M.; Siddiqui, M. M.; Sarkar, S. K.; Munch, A.; Legendre, C. M.; Herbst-Irmer, R.; Stalke, D.; Roesky, H. W. Synthesis and Coordination Behavior of a New Hybrid Bidentate Ligand with Phosphine and Silylene Donors. *Chem. Eur. J.* **2021**, *27*, 1744-1752.
(89) Sen, N.; Parvin, N.; Tothadi, S.; Khan, S. Reactivity of $(TMS)_2N(\eta^1\text{-}Cp^*)Si{=}Si(\eta^1\text{-}Cp^*)N(TMS)_2$ toward the Halides of Groups 13–15. *Organometallics* **2021**, *40*, 1874-1883.
(90) Xiong, Y.; Yao, S.; Driess, M. Versatile Conversion of N-Heterocyclic Silylene to Silyl Metal Compounds by Insertion of Divalent Silicon into Metal–Carbon and Metal–Hydrogen Bonds. *Chem. Eur. J.* **2012**, *18*, 3316-3320.
(91) Belzner, J.; Ronneberger, V.; Schär, D.; Brönnecke, C.; Herbst-Irmer, R.; Noltemeyer, M. Reactions of a cyclotrisilane with Lewis acids—formation of new cyclotrisilanes and siliconium ions. *J. Organomet. Chem.* **1999**, *577*, 330-336.
(92) Li, J.; Zhong, M.; Keil, H.; Zhu, H.; Herbst-Irmer, R.; Stalke, D.; De, S.; Koley, D.; Roesky, H. W. $(PhC(N^tBu)_2Al)_2(SiH_2)_4$ six-membered heterocycle: comparable in structure to cyclohexane. *Chem. Commun.* **2019**, *55*, 2360-2363.
(93) Ding, Y.; Nazish, M.; Ruth, P. N.; Herbst-Irmer, R.; Stalke, D.; Roesky, H. W. One silicon atom of bis (silylene) functions as a selective Lewis base under adduct formation with a Lewis acid. *Dalton Trans.* **2023**, *52*, 6175-6179.
(94) Mück, F. M.; Baus, J. A.; Bertermann, R. d.; Burschka, C.; Tacke, R. Lewis Acid/Base Reactions of the Bis(amidinato)silylene $[^iPrNC(Ph)N^iPr]_2Si$ and Bis(guanidinato)silylene $[^iPrNC(N^iPr_2)N^iPr]_2Si$ with $ElPh_3$ (El= B, Al). *Organometallics* **2016**, *35*, 2583-2588.
(95) Mo, Z. B.; Szilvasi, T.; Zhou, Y. P.; Yao, S. L.; Driess, M. An Intramolecular Silylene Borane Capable of Facile Activation of Small Molecules, Including Metal-Free Dehydrogenation of Water. *Angew. Chem. Int. Ed.* **2017**, *56*, 3699-3702.

(96) Nazish, M.; Harinath, A.; Lüert, D.; Köhler, C.; Herbst-Irmer, R.; Stalke, D.; Roesky, H. W. Reactivity of Silylene with Gallium-and Boron Trihalide at Reductive Conditions Resulting in Unforeseen Products. *Chem. Eur. J.* **2023**, e202300310.
(97) Kühler, T.; Jutzi, P.; Stammler, A.; Stammler, H.-G. Easy formation of indium–silicon bonds: reaction of decamethylsilicocene with trimethylindium. *Chem. Commun.* **2001**, 539-540.
(98) Pahar, S.; Karak, S.; Pait, M.; Raj, K. V.; Vanka, K.; Sen, S. S. Access to Silicon(II)– and Germanium(II)–Indium Compounds. *Organometallics* **2018**, *37*, 1206-1213.
(99) Wehmschulte, R. J.; Peverati, R.; Powell, D. R. Convenient Access to Gallium(I) Cations through Hydrogen Elimination from Cationic Gallium(III) Hydrides. *Inorg. Chem.* **2019**, *58*, 12441-12445.
(100) Lichtenthaler, M. R.; Stahl, F.; Kratzert, D.; Heidinger, L.; Schleicher, E.; Hamann, J.; Himmel, D.; Weber, S.; Krossing, I. Cationic cluster formation versus disproportionation of low-valent indium and gallium complexes of 2,2'-bipyridine. *Nat. Commun.* **2015**, *6*, 8288-8296.
(101) Higelin, A.; Sachs, U.; Keller, S.; Krossing, I. Univalent Gallium and Indium Phosphane Complexes: From Pyramidal $M(PPh_3)_3^+$ to Carbene-Analogous Bent $M(PtBu_3)_2^+$ (M= Ga, In) Complexes. *Chem. Eur. J.* **2012**, *18*, 10029-10034.
(102) Higelin, A.; Keller, S.; Göhringer, C.; Jones, C.; Krossing, I. Unusual Tilted Carbene Coordination in Carbene Complexes of Gallium(I) and Indium(I). *Angew. Chem. Int. Ed.* **2013**, *52*, 4941-4944.
(103) Glootz, K.; Himmel, D.; Kratzert, D.; Butschke, B.; Scherer, H.; Krossing, I. Why Do Five Ga+ Cations Form a Ligand-Stabilized $[Ga_5]^{5+}$ Pentagon and How Does a 5:1 Salt Pack in the Solid State? *Angew. Chem. Int. Ed.* **2019**, *58*, 14162-14166.
(104) Fliedel, C.; Schnee, G.; Aviles, T.; Dagorne, S. Group 13 metal (Al, Ga, In, Tl) complexes supported by heteroatom-bonded carbene ligands. *Coord. Chem. Rev.* **2014**, *275*, 63-86.
(105) Michelet, B.; Tang, S.; Thiery, G.; Monot, J.; Li, H.; Guillot, R.; Bour, C.; Gandon, V. Catalytic applications of $[IPr{\cdot}GaX_2][SbF_6]$ and related species. *Org. Chem. Front.* **2016**, *3*, 1603-1613.
(106) Kozma, Á.; Gopakumar, G.; Farès, C.; Thiel, W.; Alcarazo, M. Synthesis and structure of carbene-stabilized N-centered cations $[L_2N]^+$,$[L_2NR]^{2+}$,$[LNR_3]^{2+}$, and $[L_3N]^{3+}$. *Chem. Eur. J.* **2013**, *19*, 3542-3546.
(107) Khan, S.; Gopakumar, G.; Thiel, W.; Alcarazo, M. Stabilization of a two-coordinate $[GeCl]^+$ cation by simultaneous σ and π donation from a monodentate carbodiphosphorane. *Angew. Chem. Int. Ed.* **2013**, *52*, 5644-5647.
(108) Kozma, Á.; Rust, J.; Alcarazo, M. Bis [(dialkylamino) cyclopropenimine]-Stabilized P^{III}-and P^{V}-Centered Dications. *Chem. Eur. J.* **2015**, *21*, 10829-10834.
(109) van der Zee, L. J. C.; Pahar, S.; Richards, E.; Melen, R. L.; Slootweg, J. C. Insights into Single-Electron-Transfer Processes in Frustrated Lewis Pair Chemistry and Related Donor–Acceptor Systems in Main Group Chemistry. *Chem. Rev.* **2023**, *123*, 9653-9675.
(110) Wang, X.; Lei, B.; Zhang, Z.; Chen, M.; Rong, H.; Song, H.; Zhao, L.; Mo, Z. Isolation and characterization of bis (silylene)-stabilized antimony (I) and bismuth (I) cations. *Nat. Commun.* **2023**, *14*, 2968-2978.
(111) Sen, N.; Gothe, P.; Sarkar, P.; Das, S.; Tothadi, S.; Pati, S. K.; Khan, S. Donor free stibenium cation as an efficient cyanosilylation catalyst. *Chem. Commun.* **2022**, *58*, 10380-10383.
(112) Bawari, D.; Negi, C.; Jaiswal, K.; Prashanth, B.; Choudhury, A. R.; Singh, S. Group 13 element containing conformationally rigid "N–E–N" heteroatomic bridged [3.3](2, 6) pyridinophanes (E= B, Al). *Chem. Commun.* **2018**, *54*, 8857-8860.

(113) Parsons, L. W.; Fettinger, J. C.; Berben, L. A. Group 13 ion coordination to pyridyl models NAD+ reduction potentials. *Chem. Commun.* **2023**, *59*, 9110-9113.
(114) Guillet, G. L.; Arpin, K. Y.; Boltin, A. M.; Gordon, J. B.; Rave, J. A.; Hillesheim, P. C. Synthesis and Characterization of a Linear Triiron (II) Extended Metal Atom Chain Complex with Fe–Fe Bonds. *Inorg. Chem.* **2020**, *59*, 11238-11243.
(115) Tan, G.; Szilvási, T.; Inoue, S.; Blom, B.; Driess, M. An elusive hydridoaluminum (I) complex for facile C–H and C–O bond activation of ethers and access to its isolable hydridogallium (I) analogue: syntheses, structures, and theoretical studies. *J. Am. Chem. Soc.* **2014**, *136*, 9732-9742.
(116) Sen, S. S.; Roesky, H. W.; Stern, D.; Henn, J.; Stalke, D. High Yield Access to Silylene RSiCl (R=PhC(N^tBu)$_2$) and Its Reactivity toward Alkyne: Synthesis of Stable Disilacyclobutene. *J. Am. Chem. Soc.* **2010**, *132*, 1123-1126.
(117) Beer, L.; Britten, J. F.; Brusso, J. L.; Cordes, A. W.; Haddon, R. C.; Itkis, M. E.; MacGregor, D. S.; Oakley, R. T.; Reed, R. W.; Robertson, C. M. Prototypal dithiazolodithiazolyl radicals: Synthesis, structures, and transport properties. *J. Am. Chem. Soc.* **2003**, *125*, 14394-14403.
(118) Wang, W.; Inoue, S.; Enthaler, S.; Driess, M. Bis(silylenyl)- and Bis(germylenyl)-Substituted Ferrocenes: Synthesis, Structure, and Catalytic Applications of Bidentate Silicon(II)–Cobalt Complexes. *Angew. Chem. Int. Ed.* **2012**, *51*, 6167-6171.
(119) Zhou, Y.-P.; Raoufmoghaddam, S.; Szilvási, T.; Driess, M. A Bis(silylene)-Substituted *ortho*-Carborane as a Superior Ligand in the Nickel-Catalyzed Amination of Arenes. *Angew. Chem. Int. Ed.* **2016**, *55*, 12868-12872.
(120) Wang, Y.; Kostenko, A.; Yao, S.; Driess, M. Divalent silicon-assisted activation of dihydrogen in a bis (N-heterocyclic silylene) xanthene nickel (0) complex for efficient catalytic hydrogenation of olefins. *J. Am. Chem. Soc.* **2017**, *139*, 13499-13506.
(121) Gallego, D.; Inoue, S.; Blom, B.; Driess, M. Highly electron-rich pincer-type iron complexes bearing innocent bis (metallylene) pyridine ligands: syntheses, structures, and catalytic activity. *Organometallics* **2014**, *33*, 6885-6897.
(122) Wang, W.; Inoue, S.; Yao, S.; Driess, M. An isolable bis-silylene oxide ("disilylenoxane") and its metal coordination. *J. Am. Chem. Soc.* **2010**, *132*, 15890-15892.
(123) Zhou, Y. P.; Driess, M. Isolable Silylene Ligands Can Boost Efficiencies and Selectivities in Metal-Mediated Catalysis. *Angew. Chem. Int. Ed.* **2019**, *58*, 3715-3728.
(124) Azhakar, R.; Ghadwal, R. S.; Roesky, H. W.; Wolf, H.; Stalke, D. Facile Access to the Functionalized N-Donor Stabilized Silylenes PhC(N^tBu)$_2$SiX (X = PPh_2, NPh_2, NCy_2, $NiPr_2$, NMe_2, $N(SiMe_3)_2$, O^tBu). *Organometallics* **2012**, *31*, 4588-4592.
(125) Qi, X. H.; Zheng, T. T.; Zhou, J. H.; Dong, Y. H.; Zuo, X.; Li, X. Y.; Sun, H. J.; Fuhr, O.; Fenske, D. Synthesis and Catalytic Activity of Iron Hydride Ligated with Bidentate N-Heterocyclic Silylenes for Hydroboration of Carbonyl Compounds. *Organometallics* **2019**, *38*, 268-277.
(126) Ghosh, M.; Tothadi, S.; Khan, S. Carbazole Substituted Amidinato Silylene: Synthesis, Bonding, and Coordination Behavior with Coinage Metals. *Organometallics* **2021**, *40*, 3201-3210.
(127) Engelhardt, L. M.; Kynast, U.; Raston, C. L.; White, A. H. Alkylaluminum Cations: Synthesis and Structure of. *Angew. Chem. Int. Ed.* **1987**, *26*, 681-682.
(128) Stanga, O.; Lund, C. L.; Liang, H.; Quail, J. W.; Müller, J. Synthesis and Characterization of Neutral and Cationic Intramolecularly Coordinated Aluminum Compounds. Structural Determination of $[(Pytsi)AlMe]^+[MeB(C_6F_5)_3]^-$ [(Pytsi=$C(SiMe_3)_2SiMe_2$ (2-C_5H_4N)]. *Organometallics* **2005**, *24*, 6120-6125.
(129) Franz, D.; Inoue, S. Cationic complexes of boron and aluminum: an early 21st century viewpoint. *Chem. Eur. J.* **2019**, *25*, 2898-2926.

(130) Tang, S.; Monot, J.; El-Hellani, A.; Michelet, B.; Guillot, R.; Bour, C.; Gandon, V. Cationic Gallium (III) Halide Complexes: A New Generation of π-Lewis Acids. *Chem. Eur. J.* **2012**, *18*, 10239-10243.
(131) El-Hellani, A.; Monot, J.; Guillot, R. g.; Bour, C.; Gandon, V. Molecular versus ionic structures in adducts of GaX3 with monodentate carbon-based ligands. *Inorg. Chem.* **2013**, *52*, 506-514.
(132) Bour, C.; Monot, J.; Tang, S.; Guillot, R. g.; Farjon, J.; Gandon, V. Structure, Stability, and Catalytic Activity of Fluorine-Bridged Complexes IPr·$GaCl_2$(μ-F)EF_{n-1} (EF^{n-}= SbF^{6-}, PF^{6-}, or BF^{4-}). *Organometallics* **2014**, *33*, 594-599.
(133) Michelet, B.; Colard-Itté, J.-R.; Thiery, G.; Guillot, R.; Bour, C.; Gandon, V. Dibromoindium (iii) cations as a π-Lewis acid: characterization of [IPr·$InBr_2$][SbF_6] and its catalytic activity towards alkynes and alkenes. *Chem. Commun.* **2015**, *51*, 7401-7404.
(134) Gackstatter, A.; Braunschweig, H.; Kupfer, T.; Voigt, C.; Arnold, N. N-Heterocyclic Silylenes in Boron Chemistry: Facile Formation of Silylboranes and Silaborinines. *Chem. Eur. J.* **2016**, *22*, 16415-16419.
(135) Khoo, S.; Shan, Y.-L.; Yang, M.-C.; Li, Y.; Su, M.-D.; So, C.-W. B–H Bond Activation by an Amidinate-Stabilized Amidosilylene: Non-Innocent Amidinate Ligand. *Inorg. Chem.* **2018**, *57*, 5879-5887.
(136) Wang, H.; Wu, L.; Lin, Z.; Xie, Z. Synthesis, Structure and Reactivity of a Borylene Cation $[(NHSi)_2B(CO)]^+$ Stabilized by Three Neutral Ligands. *J. Am. Chem. Soc.* **2017**, *139*, 13680-13683.
(137) Wang, Y.; Quillian, B.; Wei, P.; Wannere, C. S.; Xie, Y.; King, R. B.; Schaefer, H. F.; Schleyer, P. v. R.; Robinson, G. H. A stable neutral diborene containing a BB double bond. *J. Am. Chem. Soc.* **2007**, *129*, 12412-12413.
(138) Böhnke, J.; Arrowsmith, M.; Braunschweig, H. Reactivity enhancement of a zerovalent diboron compound by desymmetrization. *J. Am. Chem. Soc.* **2018**, *140*, 10368-10373.
(139) Arduengo, A. J.; Harlow, R. L.; Kline, M. A Stable Crystalline Carbene. *J. Am. Chem. Soc.* **1991**, *113*, 361-363.
(140) Veith, M.; Werle, E.; Lisowsky, R.; Köppe, R.; Schnöckel, H. Spektroskopischer Nachweis eines Bis (amino) silylens. *Chem. Ber.* **1992**, *125*, 1375-1377.
(141) Heinicke, J.; Oprea, A.; Kindermann, M. K.; Karpati, T.; Nyulaszi, L.; Veszpremi, T. Unsymmetrical carbene homologues: Isolable pyrido[b]-1,3,2 l^2-diazasilole, -germole and -stannole and quantum-chemical comparison with unstable pyrido[c] isomers. *Chem. Eur. J.* **1998**, *4*, 541-545.
(142) Gehrhus, B.; Hitchcock, P. B.; Lappert, M. F.; Maciejewski, H. Silylenenickel(0) or silyl(silylene)platinum(II) complexes by reaction of Si[(NCH_2Bu^t)$_2C_6H_4$-1,2] with [$NiCl_2(PPh_3)_2$], [Ni(cod)$_2$], or [$PtCl_2$(PPh3)$_2$]. *Organometallics* **1998**, *17*, 5599-5601.
(143) Blom, B.; Gallego, D.; Driess, M. N-heterocyclic silylene complexes in catalysis: new frontiers in an emerging field. *Inorg. Chem. Front.* **2014**, *1*, 134-148.
(144) So, C. W.; Roesky, H. W.; Magull, J.; Oswald, R. B. Synthesis and characterization of [PhC(N^tBu)$_2$]SiCl: A stable monomeric chlorosilylene. *Angew. Chem. Int. Ed.* **2006**, *45*, 3948-3950.
(145) Kaufmann, S.; Kratschmer, F.; Koppe, R.; Schon, T.; Schoo, C.; Roesky, P. W. A cyclopentadienyl functionalized silylene - a flexible ligand for Si- and C-coordination. *Chem. Sci.* **2020**, *11*, 12446-12452.
(146) Ghosh, M.; Panwaria, P.; Tothadi, S.; Das, A.; Khan, S. Bis(silanetellurone) with C-H···Te Interaction. *Inorg. Chem.* **2020**, *59*, 17811-17821.
(147) Sun, X.; Röder, C.; Roesky, P. W. Zinc and Cadmium Complexes of Chelating N-Heterocyclic Silylene and Their Reactivity toward Elemental Chalcogens. *Inorg. Chem.* **2021**, *60*, 13861-13868.

(148) Parvin, N.; Pal, S.; Echeverria, J.; Alvarez, S.; Khan, S. Taming a monomeric $[Cu(\eta^6\text{-}C_6H_6)]^+$ complex with silylene. *Chem. Sci.* **2018**, *9*, 4333-4337.
(149) Troadec, T.; Prades, A.; Rodriguez, R.; Mirgalet, R.; Baceiredo, A.; Saffon-Merceron, N.; Branchadell, V.; Kato, T. Silacyclopropylideneplatinum (0) complex as a robust and efficient hydrosilylation catalyst. *Inorg. Chem.* **2016**, *55*, 8234-8240.
(150) Tan, G.; Blom, B.; Gallego, D.; Driess, M. Facile Access to Mono-and Dinuclear Heteroleptic N-Heterocyclic Silylene Copper Complexes. *Organometallics* **2014**, *33*, 363-369.
(151) Frisch, P.; Inoue, S. Coinage metal complexes of NHC-stabilized silyliumylidene ions. *Chem. Commun.* **2018**, *54*, 13658-13661.
(152) Frisch, P.; Inoue, S. Lewis base-stabilized silyliumylidene ions in transition metal coordination chemistry. *Dalton Trans.* **2020**, *49*, 6176-6182.
(153) Parvin, N.; Mishra, B.; George, A.; Neralkar, M.; Hossain, J.; Parameswaran, P.; Hotha, S.; Khan, S. N-Heterocyclic silylene/germylene ligands in Au(I) catalysis. *Chem. Commun.* **2020**, *56*, 7625-7628.
(154) Khan, S.; Ahirwar, S. K.; Pal, S.; Parvin, N.; Kathewad, N. Silicon(II) Bis(trimethylsilyl)amide ($LSiN(SiMe_3)_2$, $L = PhC(N^tBu)_2$) Supported Copper, Silver, and Gold Complexes. *Organometallics* **2015**, *34*, 5401-5406.
(155) Khan, S.; Pal, S.; Kathewad, N.; Purushothaman, I.; De, S.; Parameswaran, P. Stepwise isolation of an unprecedented silylene supported dinuclear gold(I) cation with aurophilic interaction. *Chem. Commun.* **2016**, *52*, 3880-3882.
(156) Paesch, A. N.; Kreyenschmidt, A. K.; Herbst-Irmer, R.; Stalke, D. Side-Arm Functionalized Silylene Copper(I) Complexes in Catalysis. *Inorg. Chem.* **2019**, *58*, 7000-7009.
(157) Falivene, L.; Cao, Z.; Petta, A.; Serra, L.; Poater, A.; Oliva, R.; Scarano, V.; Cavallo, L. Towards the online computer-aided design of catalytic pockets. *Nat. Chem.* **2019**, *11*, 872-879.
(158) Parvin, N.; Sen, N.; Tothadi, S.; Muhammed, S.; Parameswaran, P.; Khan, S. Synthesis and Application of Silylene-Stabilized Low-Coordinate Ag (I)–Arene Cationic Complexes. *Organometallics* **2021**, *40*, 1626-1632.
(159) Ghosh, M.; Khan, S. N-Heterocyclic silylenes in coinage metal chemistry: an account of recent advances. *Dalton Trans.* **2021**, *50*, 10674-10688.
(160) Gluszynska, A. Biological potential of carbazole derivatives. *Eur. J. Med. Chem.* **2015**, *94*, 405-426.
(161) Krahfuss, M. J.; Radius, U. N-Heterocyclic Silylenes as Metal-Metal Bridges and Metal-Halide Activators in Transition Metal Complexes. *Inorg. Chem.* **2020**, *59*, 10976-10985.
(162) Krahfuss, M. J.; Nitsch, J.; Bickelhaupt, F. M.; Marder, T. B.; Radius, U. N-Heterocyclic Silylenes as Ligands in Transition Metal Carbonyl Chemistry: Nature of Their Bonding and Supposed Innocence. *Chem. Eur. J.* **2020**, *26*, 11276-11292.
(163) Takahashi, S.; Sekiguchi, J.; Ishii, A.; Nakata, N. An Iminophosphonamido-Chlorosilylene as a Strong σ-Donating NHSi Ligand: Synthesis and Coordination Chemistry. *Angew. Chem. Int. Ed.* **2021**, *60*, 4055-4059.
(164) Azhakar, R.; Ghadwal, R. S.; Roesky, H. W.; Hey, J.; Stalke, D. Facile Access to Transition-Metal-Carbonyl Complexes with an Amidinate-Stabilized Chlorosilylene Ligand. *Chem. Asian J.* **2012**, *7*, 528-533.
(165) Boehme, C.; Frenking, G. N-heterocyclic carbene, silylene, and germylene complexes of MCl (M = Cu, Ag, Au). A theoretical study. *Organometallics* **1998**, *17*, 5801-5809.
(166) Kuehn, L.; Eichhorn, A. F.; Marder, T. B.; Radius, U. Copper(I) complexes of N-alkyl-substituted N-Heterocyclic carbenes. *J. Organomet. Chem.* **2019**, *881*, 25-33.
(167) Venkatachalam, G.; Heekenroth, M.; Neels, A.; Albrecht, M. Synthesis, Structural Diversity, and Ligand-Transfer Potential of (Carbene)copper(I) Complexes. *Helv. Chim. Acta.* **2009**, *92*, 1034-1045.

(168) Inagawa, Y.; Ishida, S.; Iwamoto, T. Two-coordinate Dialkylsilylene-Coinage Metal Complexes. *Chem. Lett.* **2014**, *43*, 1665-1667.
(169) Kumar, S.; Mondal, D.; Balakrishna, M. S. Diverse Architectures and Luminescence Properties of Group 11 Complexes Containing Pyrimidine-Based Phosphine, N-((Diphenylphosphine)methyl)pyrimidin-2-amine. *ACS Omega* **2018**, *3*, 16601-16614.
(170) Potwana, F. S.; Pillay, M. N.; Staples, R. J.; Adeniyi, A. A.; Singh, P.; van Zyl, W. E. Silver (I) bis (phosphanylamino) naphthalene complexes: Synthesis, structures and density functional theory (DFT) calculations. *Inorganica Chim. Acta* **2021**, *515*, 120041.
(171) Schmidbaur, H.; Schier, A. Argentophilic Interactions. *Angew. Chem. Int. Ed.* **2015**, *54*, 746-784.
(172) Siraj, N.; Das, S.; Hasan, F.; Lu, C.; Kiruri, L. W.; Gall, K. E. S.; Warner, I. M. Enhanced S_2 emission in carbazole-based ionic liquids. *RSC Adv.* **2015**, *5*, 9939-9945.
(173) Abro, H. A.; Zhou, T.; Han, W.; Xue, T.; Wang, T. Carbazole-based compounds containing aldehyde and cyanoacetic acid: Optical properties and applications in photopolymerization. *RSC Adv.* **2017**, *7*, 55382-55388.
(174) Leonat, L.; Sbarcea, G.; Branzoi, I. V. Cyclic voltammetry for energy levels estimation of organic materials. *UPB Sci. Bull. Ser. B* **2013**, *75*, 111-118.
(175) Blom, B.; Stoelzel, M.; Driess, M. New Vistas in N-Heterocyclic Silylene (NHSi) Transition-Metal Coordination Chemistry: Syntheses, Structures and Reactivity towards Activation of Small Molecules. *Chem. Eur. J.* **2013**, *19*, 40-62.
(176) Yao, S.; Saddington, A.; Xiong, Y.; Driess, M. Chelating bis-silylenes as powerful ligands to enable unusual low-valent main-group element functions. *Acc. Chem. Res.* **2023**, *56*, 475-488.
(177) Wang, L.; Li, Y.; Li, Z.; Kira, M. Isolable silylenes and their diverse reactivity. *Coord. Chem. Rev.* **2022**, *457*, 214413-214441.
(178) Takahashi, S.; Bellan, E.; Baceiredo, A.; Saffon-Merceron, N.; Massou, S.; Nakata, N.; Hashizume, D.; Branchadell, V.; Kato, T. A Stable N-Hetero-Rh-Metallacyclic Silylene. *Angew. Chem. Int. Ed.* **2019**, *58*, 10310-10314.
(179) Alvarado-Beltran, I.; Baceiredo, A.; Saffon-Merceron, N.; Branchadell, V.; Kato, T. Cyclic Amino(Ylide) Silylene: A Stable Heterocyclic Silylene with Strongly Electron-Donating Character. *Angew. Chem. Int. Ed.* **2016**, *55*, 16141-16144.
(180) Gallego, D.; Brück, A.; Irran, E.; Meier, F.; Kaupp, M.; Driess, M.; Hartwig, J. F. From bis (silylene) and bis (germylene) pincer-type nickel (II) complexes to isolable intermediates of the nickel-catalyzed Sonogashira cross-coupling reaction. *J. Am. Chem. Soc.* **2013**, *135*, 15617-15626.
(181) Wang, Y.; Szilvási, T.; Yao, S.; Driess, M. A bis (silylene)-stabilized diphosphorus compound and its reactivity as a monophosphorus anion transfer reagent. *Nat. Chem.* **2020**, *12*, 801-807.
(182) Luecke, M. P.; Giarrana, L.; Kostenko, A.; Gensch, T.; Yao, S.; Driess, M. A Striking Mode of Activation of Carbon Disulfide with a Cooperative Bis (silylene). *Angew. Chem. Int. Ed.* **2022**, *61*, e202110398.
(183) Xiong, Y.; Dong, S.; Yao, S.; Zhu, J.; Driess, M. Unexpected White Phosphorus (P_4) Activation Modes with Silylene-Substituted *o*-Carboranes and Access to an Isolable 1,3-Diphospha-2,4-disilabutadiene. *Angew. Chem. Int. Ed.* **2022**, *61*, e202205358.
(184) Zhu, H.; Kostenko, A.; Franz, D.; Hanusch, F.; Inoue, S. Room Temperature Intermolecular Dearomatization of Arenes by an Acyclic Iminosilylene. *J. Am. Chem. Soc.* **2023**, *145*, 1011-1021.
(185) Wendel, D.; Reiter, D.; Porzelt, A.; Altmann, P. J.; Inoue, S.; Rieger, B. Silicon and oxygen's bond of affection: an acyclic three-coordinate silanone and its transformation to an iminosiloxysilylene. *J. Am. Chem. Soc.* **2017**, *139*, 17193-17198.

(186) Hossain, J.; Gopinath, J. S.; Tothadi, S.; Parameswaran, P.; Khan, S. NHSi/NHGe-Supported Copper Halide and Pseudohalide Complexes: Synthesis and Application. *Organometallics* **2022**, *41*, 3706-3717.
(187) Ghosh, M.; Khan, S. Silylene coordinated coinage metal complexes: An itinerary of their utilities. In *Advances in Inorganic Chemistry*, (Elsevier, 2023); pp 279-303.
(188) Parvin, N.; Hossain, J.; George, A.; Parameswaran, P.; Khan, S. N-heterocyclic silylene stabilized monocordinated copper(I)-arene cationic complexes and their application in click chemistry. *Chem. Commun.* **2020**, *56*, 273-276.
(189) Nazish, M.; Bai, H.; Legendre, C. M.; Herbst-Irmer, R.; Zhao, L.; Stalke, D.; Roesky, H. W. A neutral vicinal silylene/phosphane supported six-membered C_2PSiAu_2 ring and a silver (I) complex. *Chem. Commun.* **2022**, *58*, 12704-12707.
(190) Yadav, R.; Sun, X.; Köppe, R.; Gamer, M. T.; Weigend, F.; Roesky, P. W. Stimuli Responsive Silylene: Electromerism Induced Reversible Switching Between Mono- and Bis-Silylene. *Angew. Chem. Int. Ed.* **2022**, *61*, e202211115.
(191) Xie, W.; Chang, S. [Cu(NHC)]-Catalyzed C−H Allylation and Alkenylation of both Electron-Deficient and Electron-Rich (Hetero)arenes with Allyl Halides. *Angew. Chem. Int. Ed.* **2016**, *55*, 1876-1880.
(192) Bonet, A.; Lillo, V.; Ramírez, J.; Díaz-Requejo, M. M.; Fernández, E. The selective catalytic formation of β-boryl aldehydes through a base-free approach. *Org. Biomol. Chem.* **2009**, *7*, 1533-1535.
(193) Ohishi, T.; Nishiura, M.; Hou, Z. Carboxylation of organoboronic esters catalyzed by N-heterocyclic carbene copper (I) complexes. *Angew. Chem. Int. Ed.* **2008**, *47*, 5792-5795.
(194) Herron, J. R.; Ball, Z. T. Synthesis and reactivity of functionalized arylcopper compounds by transmetalation of organosilanes. *J. Am. Chem. Soc.* **2008**, *130*, 16486-16487.
(195) Zhang, L.; Li, Z.; Takimoto, M.; Hou, Z. Carboxylation Reactions with Carbon Dioxide Using N-Heterocyclic Carbene-Copper Catalysts. *Chem. Rec.* **2020**, *20*, 494-512.
(196) Bagherzadeh, S.; Mankad, N. P. Catalyst control of selectivity in CO_2 reduction using a tunable heterobimetallic effect. *J. Am. Chem. Soc.* **2015**, *137*, 10898-10901.
(197) English, L. E.; Downie, T. M. H.; Lyall, C. L.; Mahon, M. F.; McMullin, C. L.; Neale, S. E.; Saunders, C. M.; Liptrot, D. J. Selective hydroboration of electron-rich isocyanates by an NHC-copper (i) alkoxide. *Chem. Commun.* **2023**, *59*, 1074-1077.
(198) Horsley Downie, T. M.; Mahon, M. F.; Lowe, J. P.; Bailey, R. M.; Liptrot, D. J. A Copper (I) Platform for One-Pot P–H Bond Formation and Hydrophosphination of Heterocumulenes. *ACS Catal.* **2022**, *12*, 8214-8219.
(199) Downie, T. M. H.; Hall, J. W.; Finn, T. P. C.; Liptrot, D. J.; Lowe, J. P.; Mahon, M. F.; McMullin, C. L.; Whittlesey, M. K. The first ring-expanded NHC–copper(I) phosphides as catalysts in the highly selective hydrophosphination of isocyanates. *Chem. Commun.* **2020**, *56*, 13359-13362.
(200) Ostrowska, S.; Arnaut, P.; Liptrot, D. J.; Cazin, C. S.; Nolan, S. P. An air-stable [Cu(NHC)(OR)] (R=C(H)$(CF_3)_2$) complex for C–H, N–H and S–H bond activation. *Chem. Commun.* **2023**, *59*, 9126-9129.
(201) Zhang, L.; Hou, Z. N-Heterocyclic carbene (NHC)–copper-catalysed transformations of carbon dioxide. *Chem. Sci.* **2013**, *4*, 3395-3403.
(202) Lazreg, F.; Nahra, F.; Cazin, C. S. J. Copper-NHC complexes in catalysis. *Coord. Chem. Rev.* **2015**, *293*, 48-79.
(203) Hossain, J.; Akhtar, R.; Khan, S. Luminescent coinage metal complexes of carbenes. *Polyhedron* **2021**, *201*, 115151-115187.
(204) Díez-González, S.; Stevens, E. D.; Scott, N. M.; Petersen, J. L.; Nolan, S. P. Synthesis and characterization of $[Cu(NHC)_2]X$ complexes: Catalytic and mechanistic studies of hydrosilylation reactions. *Chem. Eur. J.* **2008**, *14*, 158-168.

(205) Yang, L.; Wang, H. Recent Advances in Carbon Dioxide Capture, Fixation, and Activation by using N-Heterocyclic Carbenes. *ChemSusChem* **2014**, *7*, 962-998.
(206) Stollenz, M.; Meyer, F. Mesitylcopper–a powerful tool in synthetic chemistry. *Organometallics* **2012**, *31*, 7708-7727.
(207) Danopoulos, A. A.; Simler, T.; Braunstein, P. N-heterocyclic carbene complexes of copper, nickel, and cobalt. *Chem. Rev.* **2019**, *119*, 3730-3961.
(208) Tate, B. K.; Wyss, C. M.; Bacsa, J.; Kluge, K.; Gelbaum, L.; Sadighi, J. P. A dinuclear silver hydride and an umpolung reaction of CO_2. *Chem. Sci.* **2013**, *4*, 3068-3074.
(209) Oi, M.; Takita, R.; Kanazawa, J.; Muranaka, A.; Wang, C.; Uchiyama, M. Organocopper cross-coupling reaction for C–C bond formation on highly sterically hindered structures. *Chem. Sci.* **2019**, *10*, 6107-6112.
(210) Lee, S. Y.; Hartwig, J. F. Palladium-catalyzed, site-selective direct allylation of aryl C–H bonds by silver-mediated C–H activation: a synthetic and mechanistic investigation. *J. Am. Chem. Soc.* **2016**, *138*, 15278-15284.
(211) Suzuki, A. Cross-coupling reactions of organoboranes: an easy way to construct C–C bonds (Nobel Lecture). *Angew. Chem. Int. Ed.* **2011**, *50*, 6722-6737.
(212) Laitar, D. S.; Müller, P.; Sadighi, J. P. Efficient homogeneous catalysis in the reduction of CO_2 to CO. *J. Am. Chem. Soc.* **2005**, *127*, 17196-17197.
(213) Segawa, Y.; Yamashita, M.; Nozaki, K. Boryl Anion Attacks Transition-Metal Chlorides To Form Boryl Complexes: Syntheses, Spectroscopic, and Structural Studies on Group 11 Borylmetal Complexes. *Angew. Chem. Int. Ed.* **2007**, *46*, 6710-6713.
(214) Charman, R. S.; Hobson, J. A.; Jackson, R. A.; Mahon, M. F.; Neale, S. E.; Liptrot, D. J. Acyclic Boryl Complexes of Copper (I). *Chem. Eur. J.* **2023**, e202302704.
(215) Babula, D. J.; Charman, R. S.; Jerome, T. H.; Horsley Downie, T. M.; Mahon, M. F.; Liptrot, D. J. Ring-Expanded N-Heterocyclic Copper (I) Boryl Complexes: The Structures of [(6-Dipp)CuBcat], [(6-Dipp)CuBneop], and [(6-Dipp)CuBhex]. *Eur. J. Inorg. Chem.* **2023**, e202300043.
(216) Drescher, W.; Borner, C.; Kleeberg, C. Stability and decomposition of copper (I) boryl complexes:[(IDipp)Cu–Bneop],[(IDipp*)Cu–Bneop] and copper clusters. *New J. Chem.* **2021**, *45*, 14957-14964.
(217) Romanov, A. S.; Becker, C. R.; James, C. E.; Di, D.; Credgington, D.; Linnolahti, M.; Bochmann, M. Copper and gold cyclic (alkyl)(amino) carbene complexes with sub-microsecond photoemissions: structure and substituent effects on redox and luminescent properties. *Chem. Eur. J.* **2017**, *23*, 4625-4637.
(218) Zou, W.; Zhu, Q.; Fettinger, J. C.; Power, P. P. Dimeric Copper and Lithium Thiolates: Comparison of Copper Thiolates with Their Lithium Congeners. *Inorg. Chem.* **2021**, *60*, 17641-17648.
(219) Azizpoor Fard, M.; Polgar, A. M.; Corrigan, J. F. Tethered Polynuclear Copper–Chalcogenolate Assemblies Enabled *via* NHC Ligation. *Organometallics* **2020**, *39*, 2900-2906.
(220) Kampf, J.; Kumar, R.; Oliver, J. P. Electrochemical synthesis and the molecular structure of a benzeneselenolato complex of copper, $Ph_3PCu(m\text{-}SePh)_2Cu(PPh_3)_2 \cdot CH_3CN$, containing both three-and four-coordinate copper. *Inorg. Chem.* **1992**, *31*, 3626-3629.
(221) Jazzar, R.; Soleilhavoup, M.; Bertrand, G. Cyclic (alkyl)-and (aryl)-(amino) carbene coinage metal complexes and their applications. *Chem. Rev.* **2020**, *120*, 4141-4168.
(222) Hamze, R.; Peltier, J. L.; Sylvinson, D.; Jung, M.; Cardenas, J.; Haiges, R.; Soleilhavoup, M.; Jazzar, R.; Djurovich, P. I.; Bertrand, G.; Thompson, M. E. Eliminating nonradiative decay in Cu(I) emitters: > 99% quantum efficiency and microsecond lifetime. *Science* **2019**, *363*, 601-606.

(223) Conaghan, P. J.; Matthews, C. S. B.; Chotard, F.; Jones, S. T. E.; Greenham, N. C.; Bochmann, M.; Credgington, D.; Romanov, A. S. Highly efficient blue organic light-emitting diodes based on carbene-metal-amides. *Nat. Commun.* **2020**, *11*, 1758.
(224) Gernert, M.; Balles-Wolf, L.; Kerner, F.; Müller, U.; Schmiedel, A.; Holzapfel, M.; Marian, C. M.; Pflaum, J.; Lambert, C.; Steffen, A. Cyclic (amino)(aryl) carbenes enter the field of chromophore ligands: Expanded π system leads to unusually deep red emitting CuI compounds. *J. Am. Chem. Soc.* **2020**, *142*, 8897-8909.
(225) Romanov, A. S.; Jones, S. T.; Gu, Q.; Conaghan, P. J.; Drummond, B. H.; Feng, J.; Chotard, F.; Buizza, L.; Foley, M.; Linnolahti, M.; Credgington, D.; Bochmann, M. Carbene metal amide photoemitters: tailoring conformationally flexible amides for full color range emissions including white-emitting OLED. *Chem. Sci.* **2020**, *11*, 435-446.
(226) Tang, R.; Xu, S.; Lam, T.-L.; Cheng, G.; Du, L.; Wan, Q.; Yang, J.; Hung, F.-F.; Low, K.-H.; Phillips, D. L.; Che, C.-M. Highly Robust Cu^{I}-TADF Emitters for Vacuum-Deposited OLEDs with Luminance up to 222 200 cd m^{-2} and Device Lifetimes (LT_{90}) up to 1300 hours at an Initial Luminance of 1000 cd m^{-2}. *Angew. Chem. Int. Ed.* **2022**, *61*, e202203982.
(227) Bhattacharjee, H.; Zhu, J.; Müller, J. Unique Bora [1] ferrocenophanes with Sterically Protected Boron: A Potential Gateway to Helical Polyferrocenes. *Angew. Chem. Int. Ed.* **2019**, *58*, 16575-16582.
(228) Tsuda, T.; Yazawa, T.; Watanabe, K.; Fujii, T.; Saegusa, T. Preparation of thermally stable and soluble mesitylcopper (I) and its application in organic synthesis. *J. Org. Chem.* **1981**, *46*, 192-194.
(229) Meyer, E. M.; Gambarotta, S.; Floriani, C.; Chiesi-Villa, A.; Guastini, C. Polynuclear aryl derivatives of Group 11 metals. Synthesis, solid state-solution structural relationship, and reactivity with phosphines. *Organometallics* **1989**, *8*, 1067-1079.
(230) Yoshida, H.; Murashige*, Y.; Osaka, I. Preparation of (pin) B–B (dan). *Org. Synth.* **2003**, *95*, 218-230.
(231) Umemoto, T.; Adachi, K. New method for trifluoromethylation of enolate anions and applications to regio-, diastereo-and enantioselective trifluoromethylation. *J. Org. Chem.* **1994**, *59*, 5692-5699.
(232) Rieth, R. D.; Mankad, N. P.; Calimano, E.; Sadighi, J. P. Palladium-catalyzed cross-coupling of pyrrole anions with aryl chlorides, bromides, and iodides. *Org. Lett.* **2004**, *6*, 3981-3983.
(233) Yin, H.; Lewis, A. J.; Williams, U. J.; Carroll, P. J.; Schelter, E. J. Fluorinated diarylamide complexes of Uranium (III, IV) incorporating ancillary fluorine-to-uranium dative interactions. *Chem. Sci.* **2013**, *4*, 798-805.
(234) Manna, S.; Serebrennikova, P. O.; Utepova, I. A.; Antonchick, A. P.; Chupakhin, O. N. Hypervalent iodine (III) in direct oxidative amination of arenes with heteroaromatic amines. *Org. Lett.* **2015**, *17*, 4588-4591.
(235) Kuhn, K. M.; Grubbs, R. H. A facile preparation of imidazolinium chlorides. *Org. Lett.* **2008**, *10*, 2075-2077.
(236) Sumida, A.; Ogawa, K.; Imoto, H.; Naka, K. Steric and electronic effects of arsa-Buchwald ligands on Suzuki–Miyaura coupling reaction. *Dalton Trans.* **2023**, *52*, 2838-2844.
(237) Yang, J.; Han, Q.-Y.; Zhao, C.-L.; Dong, T.; Hou, Z.-Y.; Qin, H.-L.; Zhang, C.-P. Pd-catalyzed divergent trifluoroethylation and arylation of arylboronic acids by aryl (2, 2, 2-trifluoroethyl) iodonium triflates. *Org. Biomol. Chem.* **2016**, *14*, 7654-7658.
(238) Wang, S. M.; Wang, X. Y.; Qin, H. L.; Zhang, C. P. Palladium-Catalyzed Arylation of Arylboronic Acids with Yagupolskii–Umemoto Reagents. *Chem. Eur. J.* **2016**, *22*, 6542-6546.
(239) Hatakeyama, T.; Hashimoto, S.; Ishizuka, K.; Nakamura, M. Highly selective biaryl cross-coupling reactions between aryl halides and aryl Grignard reagents: a new catalyst

combination of N-heterocyclic carbenes and iron, cobalt, and nickel fluorides. *J. Am. Chem. Soc.* **2009**, *131*, 11949-11963.
(240) Biswas, A.; Bhunia, A.; Mandal, S. K. Mechanochemical solid state single electron transfer from reduced organic hydrocarbon for catalytic aryl-halide bond activation. *Chem. Sci.* **2023**, *14*, 2606-2615.
(241) Su, W.; Urgaonkar, S.; McLaughlin, P. A.; Verkade, J. G. Highly active palladium catalysts supported by bulky proazaphosphatrane ligands for Stille cross-coupling: Coupling of aryl and vinyl chlorides, room temperature coupling of aryl bromides, coupling of aryl triflates, and synthesis of sterically hindered biaryls. *J. Am. Chem. Soc.* **2004**, *126*, 16433-16439.
(242) Lu, D.-D.; He, X.-X.; Liu, F.-S. Bulky yet flexible Pd-PEPPSI-IPentAn for the synthesis of sterically hindered biaryls in air. *J. Org. Chem.* **2017**, *82*, 10898-10911.
(243) Organ, M. G.; Abdel-Hadi, M.; Avola, S.; Hadei, N.; Nasielski, J.; O'brien, C. J.; Valente, C. Biaryls made easy: PEPPSI and the Kumada–Tamao–Corriu reaction. *Chem. Eur. J.* **2007**, *13*, 150-157.
(244) Gambarotta, S.; Floriani, C.; Chiesi-Villa, A.; Guastini, C. Ring contraction in an arylcopper (I) compound promoted by a sulphur donor ligand: penta [mesitylcopper (I)] forms a tetra [mesitylcopper (I)] compound. *J. Chem. Soc., Chem. Commun.* **1983**, 1156-1158.
(245) Sen, S. S.; Hey, J.; Herbst-Irmer, R.; Roesky, H. W.; Stalke, D. Striking stability of a substituted silicon (II) bis (trimethylsilyl) amide and the facile Si–Me bond cleavage without a transition metal catalyst. *J. Am. Chem. Soc.* **2011**, *133*, 12311-12316.
(246) Kuehn, L.; Eichhorn, A. F.; Schmidt, D.; Marder, T. B.; Radius, U. NHC-stabilized copper (I) aryl complexes and their transmetalation reaction with aryl halides. *J. Organomet. Chem.* **2020**, *919*, 121249.
(247) Parvin, N.; Dasgupta, R.; Pal, S.; Sen, S. S.; Khan, S. Strikingly diverse reactivity of structurally identical silylene and stannylene. *Dalton Trans.* **2017**, *46*, 6528-6532.
(248) Dahlen, M.; Seifert, T. P.; Lebedkin, S.; Gamer, M. T.; Kappes, M. M.; Roesky, P. W. Tetra-and hexanuclear string complexes of the coinage metals. *Chem. Commun.* **2021**, *57*, 13146-13149.
(249) Tate, B. K.; Jordan, A. J.; Bacsa, J.; Sadighi, J. P. Stable mono-and dinuclear organosilver complexes. *Organometallics* **2017**, *36*, 964-974.
(250) Liu, Y.; Taylor, L. J.; Argent, S. P.; McMaster, J.; Kays, D. L. Group 11 *m*-Terphenyl Complexes Featuring Metallophilic Interactions. *Inorg. Chem.* **2021**, *60*, 10114-10123.
(251) Lemon, C. M.; Powers, D. C.; Huynh, M.; Maher, A. G.; Phillips, A. A.; Tripet, B. P.; Nocera, D. G. Ag (III)···Ag (III) Argentophilic Interaction in a Cofacial Corrole Dyad. *Inorg. Chem.* **2022**, *62*, 3-17.
(252) Carranza, M. P.; Manzano, B. R.; Jalón, F. A.; Rodriguez, A. M.; Santos, L.; Moreno, M. Experimental and theoretical evidence of unsupported Ag–Ag interactions in complexes with triazine-based ligands. Subtle effects of the symmetry of the triazine substituents. *New J. Chem.* **2013**, *37*, 3183-3194.
(253) Carranza, M. P.; Manzano, B. R.; Jalon, F. A.; Rodriguez, A. M.; Santos, L.; Moreno, M. First Examples of a Modulated Bridging μ_2-1:2κN-Triazine in Double Helical Silver Compounds. Experimental and Theoretical Evidence. *Inorg. Chem.* **2010**, *49*, 3828-3835.
(254) Ray, L.; Shaikh, M. M.; Ghosh, P. Shorter argentophilic interaction than aurophilic interaction in a pair of dimeric $\{(NHC)MCl\}_2$ (M= Ag, Au) complexes supported over a N/O-functionalized N-heterocyclic carbene (NHC) ligand. *Inorg. Chem.* **2008**, *47*, 230-240.
(255) Aguado, J. E.; Calhorda, M. J.; Costa, P. J.; Crespo, O.; Félix, V.; Gimeno, M. C.; Jones, P. G.; Laguna, A. Synthesis and Theoretical Studies of a Double Helical Complex with the Ligand 4′, 4‴-Bis (ferrocenyl)-2, 2′: 6′, 2″: 6″, 2‴: 6‴, 2⁗-quinquepyridine. *Eur. J. Inorg. Chem.* **2004**, *2004*, 3038-3047.

(256) Waterman, R. σ-Bond metathesis: a 30-year retrospective. *Organometallics* **2013**, *32*, 7249-7263.
(257) Yin, L.; Liebscher, J. Carbon−carbon coupling reactions catalyzed by heterogeneous palladium catalysts. *Chem. Rev.* **2007**, *107*, 133-173.
(258) Busch, M.; Wodrich, M. D.; Corminboeuf, C. A generalized picture of C–C cross-coupling. *ACS Catal.* **2017**, *7*, 5643-5653.
(259) Someya, C. I.; Haberberger, M.; Wang, W.; Enthaler, S.; Inoue, S. Application of a Bis (silylene) Nickel Complex as Precatalyst in C–C Bond Formation Reactions. *Chem. Lett.* **2013**, *42*, 286-288.
(260) Martin, R.; Buchwald, S. L. Palladium-catalyzed Suzuki−Miyaura cross-coupling reactions employing dialkylbiaryl phosphine ligands. *Acc. Chem. Res.* **2008**, *41*, 1461-1473.
(261) Hollister, K. K.; Molino, A.; Breiner, G.; Walley, J. E.; Wentz, K. E.; Conley, A. M.; Dickie, D. A.; Wilson, D. J.; Gilliard Jr, R. J. Air-Stable Thermoluminescent Carbodicarbene-Borafluorenium Ions. *J. Am. Chem. Soc.* **2022**, *144*, 590-598.
(262) Wentz, K. E.; Molino, A.; Freeman, L. A.; Dickie, D. A.; Wilson, D. J.; Gilliard Jr, R. J. Activation of Carbon Dioxide by 9-Carbene-9-borafluorene Monoanion: Carbon Monoxide Releasing Transformation of Trioxaborinanone to Luminescent Dioxaborinanone. *J. Am. Chem. Soc.* **2022**, *144*, 16276-16281.
(263) Sarkar, S. K.; Hollister, K. K.; Molino, A.; Obi, A. D.; Deng, C.-L.; Tra, B. Y. E.; Stewart, B. M.; Dickie, D. A.; Wilson, D. J. D.; Gilliard, R. J., Jr. Bis(9-Boraphenanthrene) and Its Stable Biradical. *J. Am. Chem. Soc.* **2023**, *145*, 21475-21482.
(264) Bissinger, P.; Steffen, A.; Vargas, A.; Dewhurst, R. D.; Damme, A.; Braunschweig, H. Unexpected Luminescence Behavior of Coinage Metal π-Diborene Complexes. *Angew. Chem. Int. Ed.* **2015**, *54*, 4362-4366.
(265) Braunschweig, H.; Dellermann, T.; Dewhurst, R. D.; Hupp, B.; Kramer, T.; Mattock, J. D.; Mies, J.; Phukan, A. K.; Steffen, A.; Vargas, A. Strongly Phosphorescent Transition Metal π-Complexes of Boron–Boron Triple Bonds. *J. Am. Chem. Soc.* **2017**, *139*, 4887-4893.
(266) Neeve, E. C.; Geier, S. J.; Mkhalid, I. A.; Westcott, S. A.; Marder, T. B. Diboron (4) compounds: from structural curiosity to synthetic workhorse. *Chem. Rev.* **2016**, *116*, 9091-9161.
(267) Dewhurst, R. D.; Neeve, E. C.; Braunschweig, H.; Marder, T. B. sp^2–sp^3 diboranes: astounding structural variability and mild sources of nucleophilic boron for organic synthesis. *Chem. Commun.* **2015**, *51*, 9594-9607.
(268) Eichhorn, A. F.; Kuehn, L.; Marder, T. B.; Radius, U. Facile insertion of a cyclic alkyl (amino) carbene carbon into the B–B bond of diboron (4) reagents. *Chem. Commun.* **2017**, *53*, 11694-11696.
(269) Stollenz, M.; Fischer, S.; Gehring, H.; Resch, S. G.; Dechert, S.; Große, C.; Meyer, F. Molecular dicopper (I) oxalate stabilized by two N-heterocyclic carbenes: A potential precursor for copper deposition. *J. Organomet. Chem.* **2016**, *821*, 106-111.
(270) Köhler, K.; Eichhorn, J.; Meyer, F.; Vidovic, D. Dicopper (I) oxalate complexes stabilized by Lewis bases: Potential precursors for copper deposition. *Organometallics* **2003**, *22*, 4426-4432.
(271) Teichgräber, J.; Dechert, S.; Meyer, F. Dicopper (I) oxalate complexes as molecular precursors for the deposition of copper compounds. *J. Organomet. Chem.* **2005**, *690*, 5255-5263.
(272) Trose, M.; Nahra, F.; Cazin, C. S. Dinuclear N-heterocyclic carbene copper (I) complexes. *Coord. Chem. Rev.* **2018**, *355*, 380-403.
(273) Lan, J.; Liao, T.; Zhang, T.; Chung, L. W. Reaction mechanism of Cu (I)-mediated reductive CO_2 coupling for the selective formation of oxalate: cooperative CO_2 reduction to

give mixed-valence $Cu_2(CO_2^{\bullet-})$ and nucleophilic-like attack. *Inorg. Chem.* **2017**, *56*, 6809-6819.
(274) Cid, J.; Gulyas, H.; Carbo, J. J.; Fernandez, E. Trivalent boron nucleophile as a new tool in organic synthesis: reactivity and asymmetric induction. *Chem. Soc. Rev.* **2012**, *41*, 3558-3570.
(275) Zhang, X.; Dai, H.; Yan, H.; Zou, W.; Cremer, D. B–H···π interaction: A new type of nonclassical hydrogen bonding. *J. Am. Chem. Soc.* **2016**, *138*, 4334-4337.
(276) Yoshida, H.; Kawashima, S.; Takemoto, Y.; Okada, K.; Ohshita, J.; Takaki, K. Copper-Catalyzed Borylation Reactions of Alkynes and Arynes. *Angew. Chem. Int. Ed.* **2012**, *51*, 235-238.
(277) Dang, L.; Zhao, H.; Lin, Z.; Marder, T. B. Understanding the higher reactivity of B_2cat_2 versus B_2pin_2 in copper (I)-catalyzed alkene diboration reactions. *Organometallics* **2008**, *27*, 1178-1186.
(278) Wyss, C. M.; Bitting, J.; Bacsa, J.; Gray, T. G.; Sadighi, J. P. Bonding and reactivity of a dicopper (I) μ-boryl cation. *Organometallics* **2016**, *35*, 71-74.
(279) Kleeberg, C.; Borner, C. Syntheses, structures, and reactivity of NHC copper (I) boryl complexes: a systematic study. *Organometallics* **2018**, *37*, 4136-4146.
(280) Borner, C.; Anders, L.; Brandhorst, K.; Kleeberg, C. Elusive phosphine copper (I) boryl complexes: synthesis, structures, and reactivity. *Organometallics* **2017**, *36*, 4687-4690.
(281) Rutz, P. M.; Grunenberg, J. r.; Kleeberg, C. Unsymmetrical diborane (4) as a precursor to PBP boryl pincer complexes: synthesis and Cu (I) and Pt (II) PBP complexes with unusual structural features. *Organometallics* **2022**, *41*, 3044-3054.
(282) Ríos, P.; See, M. S.; Handford, R. C.; Teat, S. J.; Tilley, T. D. Robust dicopper (I) μ-boryl complexes supported by a dinucleating naphthyridine-based ligand. *Chem. Sci.* **2022**, *13*, 6619-6625.
(283) Molander, G. A.; Trice, S. L.; Dreher, S. D. Palladium-catalyzed, direct boronic acid synthesis from aryl chlorides: a simplified route to diverse boronate ester derivatives. *J. Am. Chem. Soc.* **2010**, *132*, 17701-17703.
(284) Oka, N.; Yamada, T.; Sajiki, H.; Akai, S.; Ikawa, T. Aryl Boronic Esters Are Stable on Silica Gel and Reactive under Suzuki–Miyaura Coupling Conditions. *Org. Lett.* **2022**, *24*, 3510-3514.
(285) Rochette, É.; Desrosiers, V.; Soltani, Y.; Fontaine, F. d. r.-G. Isodesmic C–H borylation: perspectives and proof of concept of transfer borylation catalysis. *J. Am. Chem. Soc.* **2019**, *141*, 12305-12311.
(286) Fuhr, O.; Dehnen, S.; Fenske, D. Chalcogenide clusters of copper and silver from silylated chalcogenide sources. *Chem. Soc. Rev.* **2013**, *42*, 1871-1906.
(287) Corrigan, J. F.; Fuhr, O.; Fenske, D. Metal chalcogenide clusters on the border between molecules and materials. *Adv. Mater.* **2009**, *21*, 1867-1871.
(288) An, R.; Liao, L.; Liu, X.; Song, S.; Zhao, X. Acid-catalyzed oxidative cleavage of S–S and Se–Se bonds with DEAD: efficient access to sulfides and selenides. *Org. Chem. Front.* **2018**, *5*, 3557-3561.
(289) Kolay, S.; Wadawale, A.; Das, D.; Kisan, H. K.; Sunoj, R. B.; Jain, V. K. Cyclopalladation of dimesityl selenide: synthesis, reactivity, structural characterization, isolation of an intermediate complex with C–H···Pd intra-molecular interaction and computational studies. *Dalton Trans.* **2013**, *42*, 10828-10837.
(290) Kluge, O.; Grummt, K.; Biedermann, R.; Krautscheid, H. Trialkylphosphine-stabilized copper (I) phenylchalcogenolate complexes-Crystal structures and copper–Chalcogenolate bonding. *Inorg. Chem.* **2011**, *50*, 4742-4752.

(291) Cabral, B. N.; Zawatski, L. E.; Abram, U.; Lang, E. S. Synthesis and Structural Characterization of Copper (I) Phenylselenolate Complexes Stabilized by N, N′-Donor Ligands. *Z. Anorg. Allg. Chem.* **2015**, *641*, 739-743.
(292) Harisomayajula, N. V. S.; Makovetskyi, S.; Tsai, Y. C. Cuprophilic Interactions in and between Molecular Entities. *Chem. Eur. J.* **2019**, *25*, 8936-8954.
(293) Tolentino, D. R.; Neale, S. E.; Isaac, C. J.; Macgregor, S. A.; Whittlesey, M. K.; Jazzar, R.; Bertrand, G. Reductive elimination at carbon under steric control. *J. Am. Chem. Soc.* **2019**, *141*, 9823-9826.
(294) Yang, X.; Reijerse, E. J.; Bhattacharyya, K.; Leutzsch, M.; Kochius, M.; Nöthling, N.; Busch, J.; Schnegg, A.; Auer, A. A.; Cornella, J. Radical activation of N–H and O–H bonds at bismuth (II). *J. Am. Chem. Soc.* **2022**, *144*, 16535-16544.
(295) Meng, Q.; Zhu, B.; Sakaki, S. Theoretical study of N–H σ-bond activation by nickel (0) complex: reaction mechanism, electronic processes, and prediction of better ligand. *Inorg. Chem.* **2022**, *61*, 8715-8728.
(296) Giri, R.; Hartwig, J. F. Cu(I)−amido complexes in the Ullmann Reaction: Reactions of Cu(I)−amido complexes with iodoarenes with and without autocatalysis by CuI. *J. Am. Chem. Soc.* **2010**, *132*, 15860-15863.
(297) Mankad, N. P.; Antholine, W. E.; Szilagyi, R. K.; Peters, J. C. Three-coordinate copper (I) amido and aminyl radical complexes. *J. Am. Chem. Soc.* **2009**, *131*, 3878-3880.
(298) Stollenz, M.; John, M.; Gehring, H.; Dechert, S.; Grosse, C.; Meyer, F. Oligonuclear Homoleptic Copper (I) Pyrazolates with Multinucleating Ligand Scaffolds: High Structural Diversity in Solid-State and Solution. *Inorg. Chem.* **2009**, *48*, 10049-10059.
(299) van der Vlugt, J. I. Advances in selective activation and application of ammonia in homogeneous catalysis. *Chem. Soc. Rev.* **2010**, *39*, 2302-2322.
(300) Chase, P. A.; Stephan, D. W. Hydrogen and Amine Activation by a Frustrated Lewis Pair of a Bulky N-Heterocyclic Carbene and $B(C_6F_5)_3$. *Angew. Chem. Int. Ed.* **2008**, *47*, 7433-7437.
(301) Scattolin, T.; Logvinov, A. A.; Tzouras, N. V.; Cazin, C. S. J.; Nolan, S. P. Advances in the Synthesis and Applications of N-Heterocyclic Carbene Metal Complexes with a Focus on the Weak Base Route. *Organometallics* **2023**, *42*, 2692-2730.
(302) Goj, L. A.; Blue, E. D.; Munro-Leighton, C.; Gunnoe, T. B.; Petersen, J. L. Cleavage of X− H bonds (X= N, O, or C) by copper (I) alkyl complexes to form monomeric two-coordinate copper (I) systems. *Inorg. Chem.* **2005**, *44*, 8647-8649.
(303) Goj, L. A.; Blue, E. D.; Delp, S. A.; Gunnoe, T. B.; Cundari, T. R.; Pierpont, A. W.; Petersen, J. L.; Boyle, P. D. Chemistry surrounding monomeric copper (I) methyl, phenyl, anilido, ethoxide, and phenoxide complexes supported by N-heterocyclic carbene ligands: reactivity consistent with both early and late transition metal systems. *Inorg. Chem.* **2006**, *45*, 9032-9045.
(304) Kögel, J.; Sorokin, D.; Khvorost, A.; Scott, M.; Harms, K.; Himmel, D.; Krossing, I.; Sundermeyer, J. The Lewis superacid $Al[N(C_6F_5)_2]_3$ and its higher homolog $Ga[N(C_6F_5)_2]_3$ – structural features, theoretical investigation and reactions of a metal amide with higher fluoride ion affinity than SbF_5. *Chem. Sci.* **2018**, *9*, 245-253.
(305) Yin, H.; Lewis, A. J.; Carroll, P.; Schelter, E. J. Electrophilic Ln (III) Cations Protected by C–F→Ln Interactions and Their Coordination Chemistry with Weak σ-and π-Donors. *Inorg. Chem.* **2013**, *52*, 8234-8243.
(306) Roueindeji, H.; Ratsifitahina, A.; Roisnel, T.; Dorcet, V.; Kahlal, S.; Saillard, J. Y.; Carpentier, J. F.; Sarazin, Y. Metal···F−C Bonding in Low-Coordinate Alkaline Earth Fluoroarylamides. *Chem. Eur. J.* **2019**, *25*, 8854-8864.

(307) Molteni, R.; Edkins, K.; Haehnel, M.; Steffen, A. C–H activation of fluoroarenes: synthesis, structure, and luminescence properties of copper (I) and gold (I) complexes bearing 2-phenylpyridine ligands. *Organometallics* **2016**, *35*, 629-640.
(308) Krylova, V. A.; Djurovich, P. I.; Conley, B. L.; Haiges, R.; Whited, M. T.; Williams, T. J.; Thompson, M. E. Control of emission colour with N-heterocyclic carbene (NHC) ligands in phosphorescent three-coordinate Cu (I) complexes. *Chem. Commun.* **2014**, *50*, 7176-7179.
(309) Barry, S. T. Amidinates, guanidinates and iminopyrrolidinates: Understanding precursor thermolysis to design a better ligand. *Coord. Chem. Rev.* **2013**, *257*, 3192-3201.
(310) Romanov, A. S.; Chotard, F.; Rashid, J.; Bochmann, M. Synthesis of copper (I) cyclic (alkyl)(amino) carbene complexes with potentially bidentate N^ N, N^ S and S^ S ligands for efficient white photoluminescence. *Dalton Trans.* **2019**, *48*, 15445-15454.
(311) Chotard, F.; Sivchik, V.; Linnolahti, M.; Bochmann, M.; Romanov, A. S. Mono-versus Bicyclic Carbene Metal Amide Photoemitters: Which Design Leads to the Best Performance? *Chem. Mater.* **2020**, *32*, 6114-6122.

Chapter 3: N-Heterocyclic Silylenes Coordinated Copper(I) Complexes as Potential Luminogens

Adapted from: ***M. Ghosh***, J. Chatterjee, P. Panwaria, A. Kudlu, S. Tothadi, and S. Khan*, Silylene-Copper-Amide Emitters: From Thermally Activated Delayed Fluorescence to Dual Emission. *Angew. Chem. Int. Ed.* **2024**, e202410792.

3.1 Objective of this work.

In this work, we report the inaugural instance of NHSi-coordinated copper amide-based thermally activated delayed fluorescence (TADF) and singlet-triplet dual emitters. By applying a systematic designing strategy, we isolated a series of NHSi [Ph(^{t}BuN)$_2$CSiN(TMS)$_2$] stabilized Cu amide complexes (**3.2**-**3.5**). Carbene-copper-amide, its well-known predecessor, has recently emerged as a potential emitter to be utilized in the field of optoelectronics, photosensitization, and photocatalysis. These silylene-metal-amide (SiMA) emitters display TADF and dual emissive behavior in anaerobic conditions. The NHSi-Cu-diphenylamide (**3.2**) complex shows TADF with a very small ΔE_{ST} gap (0.01 eV) absolute quantum yield of 11 % and radiative rate of 2.22×10^6 s^{-1} and short τ_{TADF} 0.45 μs in the solid state. The dual emissive complexes show an absolute quantum yield of upto 20 % in the solid state with a k_{ISC} rate of 1.82×10^8 s^{-1}. These complexes show room temperature phosphorescence (RTP) with a lifetime of up to 9 ms. The TD-DFT calculation shows that the TADF originates from the LL'CT state, whereas the dual emissive states originate from ^{3}LE and ^{1}LLCT in nature. This work intends to deepen the understanding of SiMA-type emitters, which are hitherto unknown, and modulate them as more efficient Cu(I)-based TADF or RTP emitters.

3.2 Introduction.

The isolation of two coordinate carbene metal amides is a breakthrough discovery because of their excellent OLED performance characteristics.[1-3] The electron donation occurs from the generally π-donating amide fragment to the π-accepting carbene part by enabling a TADF mechanism (Figure 3.1). The TADF process occurs from the lowest excited singlet state S_1 to the ground state S_0 *via* reverse intersystem crossing (RISC) from the triplet excited state T_1 to S_1 upon thermal activation at room temperature.[4] These complexes usually have very short $\Delta E(S_1\text{-}T_1)$ gaps because of the larger spatial separation between electrons and holes located over acceptor and donor moieties, respectively.[5] The four- and three-coordinate Cu complexes that were extensively studied feature metal-to-ligand-centered charge transfer (MLCT) and halogen-to-ligand-centered charge transfer (XLCT).[6, 7] The structural rearrangements (Rener-Teller and Jahn-Teller effect) associated with complexes reduce the emission efficiency;[6-11] thus, the need to lower the coordination number is an effective way by either using the sterically demanding ligand or enhancing the ligand's electronic effect.[2]

A wide range of carbenes, including CAACs[12-19] and mono and di amido carbenes (MAC and DAC)[20-25] and variously substituted NHCs[26-30] have been explored in this direction (Chart 3.1a). A plethora of carbazole substituents have been scrutinized for fine-tuning the

emission properties. Various structural aspects, planarity, angle distortion of amide functionalities,[31-33] and chirality of carbene[34, 35] have been meticulously examined in recent times in quest of highly efficient TADF emitters.

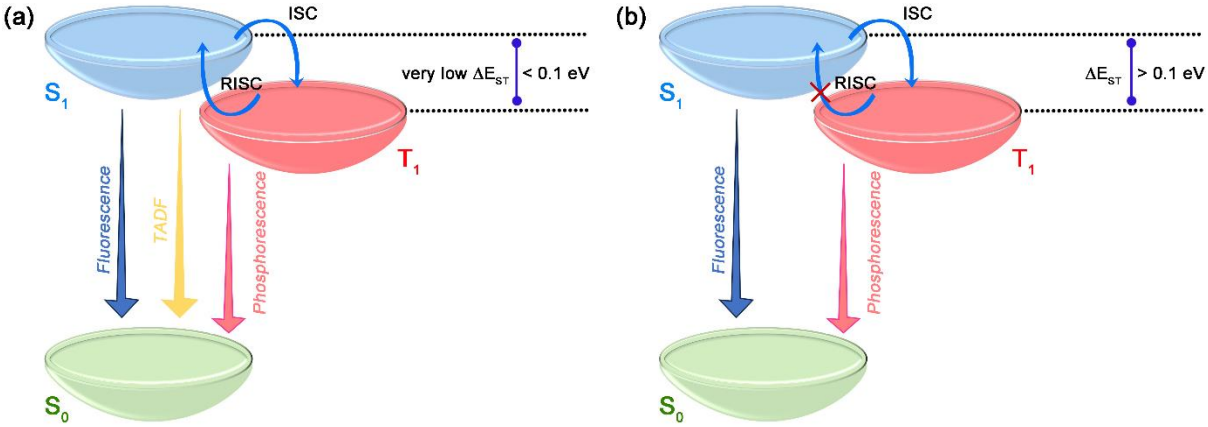

Figure 3.1. The energy diagram represents various electronic transitions, including fluorescence, phosphorescence, (a) TADF; (b) dual emission.

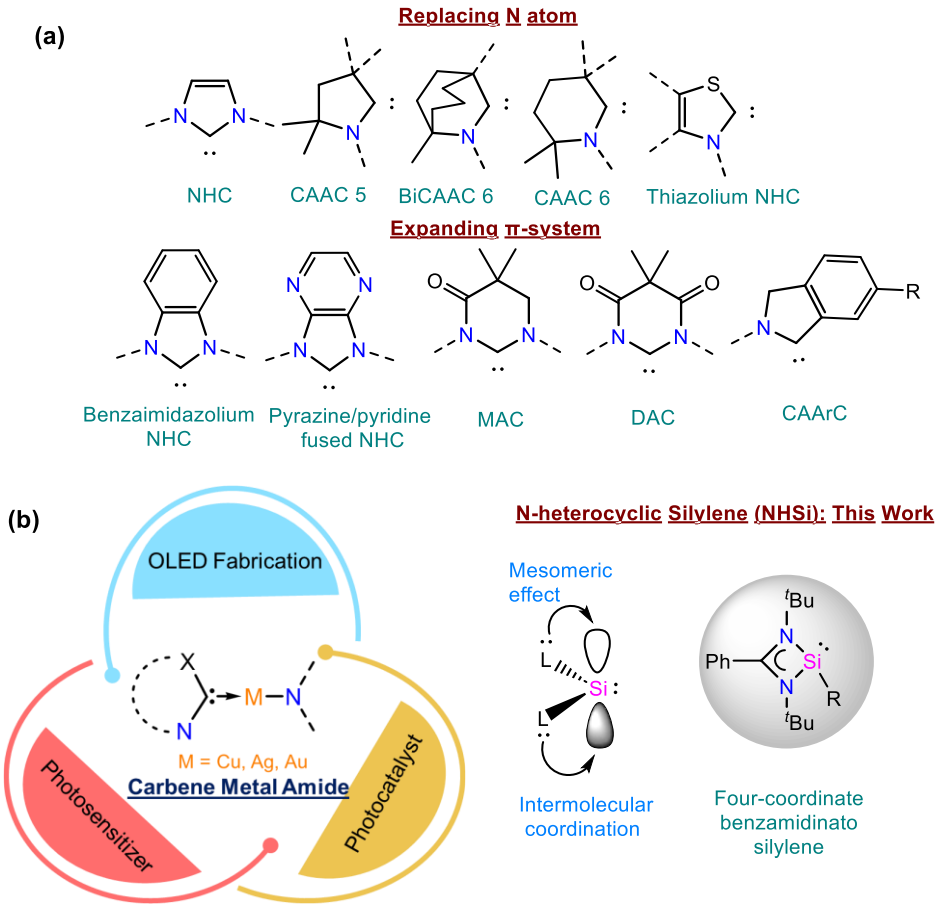

Chart 3.1. (a) Reported carbenes used till date for exploration of luminescent properties of metal amide complexes.[5] (b) Use of carbene metal amide in various applicative domains[36] and use of NHSi coordinated Cu amide for luminescent properties in this work.

NHSis, the higher analogs of NHCs, have never been utilized in this context. However, functionalized disilines have been found to show interesting luminescent properties.[37-40] NHSi were isolated first in 1994 by West and Denk,[41, 42] where the Si(II) center generally prefers a $3s^2 3p^2$ configuration due to its less inclination to hybridize *s*- and *p*-orbital. Thus, they have an out-of-plane *3p*-orbital for electron acceptance.[43] This makes them electronically different than the conventional carbenes, which usually possess a *sp* hybridized orbital as accepting orbital to obey the "octet rule." This electronic difference has enabled NHSis to show diverse reactivities compared to the NHCs in small molecule activation.[44, 45] Jutzi, West, Roesky, Kira, Driess, Iwamoto, Power, Jones, Aldridge, Baceiredo, Kato, Inoue, and others have pioneered remarkable work that highlights the potential of silylene as a potential ligand backbone in stabilizing various elusive and highly reactive species.[41, 45-56] Apart from investigating the reactivity patterns of functionalized NHSi, exploration of their utility in fabricating luminescent materials has unexplored,[57, 58] unlike the other low valent reactive main group precursors.[59-63] Transition metal complexes of NHSis also have been isolated over the years and probed in various organic transformations.[44, 64, 65] However, exploration of the coinage metal precursors (Cu, Ag, and Au) is still infancy. Despite the recent exploration of promising luminescence properties of the carbene functionalized two coordinated coinage metal precursors,[36] surprisingly, no report of such complex of NHSi persists till date. Among all the reported NHSis, benzamidinato chlorosilylene [Ph(^{t}BuN)$_2$CSiCl] is the most studied NHSi ligand owing to its high thermal stability and ease of functionalization at the halide center.[66] Various pioneer groups, including us, have isolated several Cu complexes with functionalized benzamidinato silylenes ranging from neutral to cationic species.[67-73] Owing to our interest in this domain, we have long sought to isolate luminescent coinage metal complexes of NHSi. The overwhelming performance of two coordinated NHC stabilized coinage metal amides[12, 74, 75] inspired us to the isolation of their NHSi analog. For that, we choose hexamethyldisilazide substituted benzamidinato silylene [Ph(^{t}BuN)$_2$CSiN(TMS)$_2$] as our ligand of choice because of its success in isolation of unusual η^6 coordinated Cu(I)···arene complex.[70] It was postulated that the π-acceptance properties of this NHSi ligand can diminish the electron repulsion of the d^{10} system to form η^6 coordination. The π-acceptance is one of the crucial criteria for the charge transfer (CT) process in such emissive two-coordinated metal-amide systems. Copper is an attractive alternative for this purpose due to its cost-effectivity and high earth abundance. The unique structural diversities and distinctive photophysical properties of Cu(I) containing complexes have received significant attention over the years in organic light-emitting diodes and organic photocatalytic properties.[76-81] Hence, we treated [Ph(^{t}BuN)$_2$CSiN(TMS)$_2$] (Chart

3.1b) with mesityl copper to isolate complex **3.1**, which can easily undergo mesitylene elimination in the presence of any secondary amide having polar N-H bonds. For this, we turned our focus towards acyclic secondary amines. We isolated the NHSi-coordinated Cu-diphenylamide (**3.2**) complex, which showed TADF (Figure 3.1). However, when we used amides with a combination of electron donor (Dipp and Trip) and acceptor (-CF_3) substituents (complexes **3.3** and **3.4**), we found that dual emission mechanisms became operative (Figure 3.1) in excited states. For a comparison, we also prepared their NHC counterparts. All complexes were isolated in pure form, and their formation was established *via* XRD, multinuclear NMR, and HRMS. Detailed photophysical and TD-DFT investigations were performed. According to the best of our knowledge, our results mark the inauguration of SiMA emitters, which show TADF and dual emission properties.

3.3 Results and Discussion.

3.3.1 Synthesis of compounds 3.I-3.III and complexes 3.1-3.6, 3.8, and 3.9.

^{1}H, ^{13}C, ^{29}Si, and ^{19}F NMR spectra were measured in $CDCl_3$, C_6D_6 using a 400 MHz NMR spectrometer, "Bruker Avance DRX500"; chemical shifts (δ) are expressed in ppm referenced to external $SiMe_4$ (tetramethylsilane, TMS), using the residual solvent as internal standard ($CDCl_3$: ^{1}H, 7.26 ppm and ^{13}C, 77.16 ppm; C_6D_6: ^{1}H, 7.16 ppm and ^{13}C, 128.06 ppm). Coupling constants are expressed in hertz. Individual peaks are reported as multiplicities (s = singlet, d = doublet, dd = doublet of doublet, t = triplet, q = quartet, m = multiplet, integration, coupling constants are given in Hz. The spectra were processed and analyzed using *MestReNova* software. Melting points were measured in a sealed glass tube and were not corrected. LSiNTMS was prepared *via* previously reported procedures.[82] According to the literature procedure, Mesityl copper and complex **3.7** were also prepared.[83-85]

3.3.1.1 Synthesis procedure for C-N cross-coupling reactions for synthesizing compounds 3.I-3.III.

A 250 mL Schlenk tube was charged with aryl halide (2 mmol) and substituted aniline (2 mmol), followed by the addition of toluene (50 ml), followed by the addition of 0.5 mol% $Pd(dba)_2$, 0.5 mol % PCy_3, and 1.2 equiv. NaO^tBu (Scheme 3.1). The reaction mixture was then refluxed for 48 h at 110 °C. The reaction mixture was cooled to room temperature and extracted in DCM. The resulting solution was concentrated on a rota-evaporator and purified by column chromatography (*n*-hexane and ethyl acetate mixture) to afford the expected product. All the

C-N coupled products were characterized by NMR spectroscopy and mass spectrometry and matched well with the reported literature.[86]

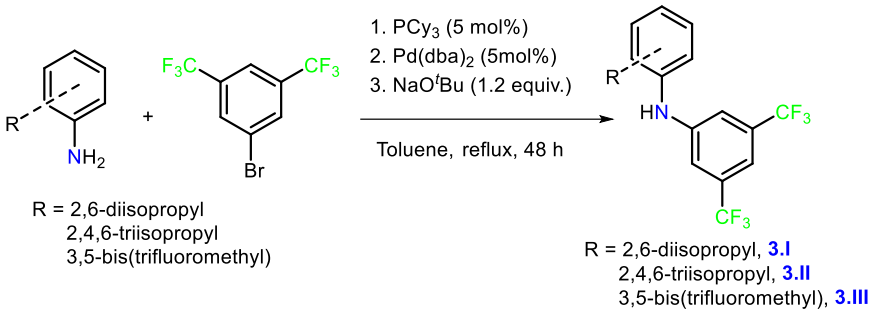

Scheme 3.1. General methodology for syntheses of the compounds **3.I-3.III**.

3.3.1.1.1 Compound 3.II. ^{1}H NMR (400 MHz, $CDCl_3$): δ 7.41 (s, 1H, aromatic C-H), 7.33 (s, 2H, aromatic C-H), 7.26 (s, 2H, aromatic C-H), 7.00 (s, 1H, -N*H*$_2$), 3.23 (hept, J = 6.9 Hz, 2H, -C*H*$(CH_3)_2$), 3.16 – 3.06 (m, 1H, -C*H*$(CH_3)_2$), 1.47 (d, J = 6.9 Hz, 6H, -CH(C*H*$_3)_2$), 1.31 (d, J = 6.9 Hz, 12H, -CH(C*H*$_3)_2$) ppm; ^{13}C NMR (100.613 MHz, $CDCl_3$): δ 149.05 (aromatic C), 148.70 (aromatic C), 146.87 (aromatic C), 132.80 (aromatic C), 132.47 (aromatic C), 132.15 (aromatic C), 131.82 (aromatic C), 130.16 (aromatic C), 124.76 (aromatic C), 122.16 (aromatic C), 111.76 (aromatic C), 110.30 (dq, J = 7.9, 4.0 Hz, -*C*-CF_3), 34.12 (-*C*H$(CH_3)_2$)), 28.28 (-CH(*C*H$_3)_2$)), 23.87 (-CH(*C*H$_3)_2$) ppm; ^{19}F NMR (377 MHz, $CDCl_3$) δ -63.18 ppm.

3.3.1.1.2 Compound 3.III. ^{1}H NMR (400 MHz, $CDCl_3$): δ 7.53 (s, 2H, aromatic C-H), 7.50 (s, 4H, aromatic C-H), 6.27 (s, 1H, -N*H*$_2$) ppm; ^{13}C NMR (100.613 MHz, $CDCl_3$): δ 142.62 (aromatic C), 133.73 -132.79 (-*C*F_3), 126.91 (aromatic C), 124.20 (aromatic C), 121.49 (aromatic C), 118.78 (aromatic C), 117.58 (aromatic C), 115.77 (dt, J = 7.7, 3.8 Hz, -*C*(CF_3)) ppm; ^{19}F NMR (377 MHz, $CDCl_3$): δ -63.42 ppm.

3.3.1.2 Synthesis procedure for complexes 3.1-3.6, 3.8, and 3.9.

We performed the reactions of **3.1** with diphenylamine, *N*-(3,5-bis(trifluoromethyl)phenyl)-2,4,6-triisopropylaniline, *N*-(3,5-bis(trifluoromethyl)phenyl)-2,6-diisopropylaniline and *N*-(3,5-bis(trifluoromethyl)phenyl)-2,6-bis(trifluoromethyl)aniline to afford complex **3.2**, **3.3**, **3.4**, and **3.5**, respectively (Scheme 3.2), which shows good solubility in toluene and THF.

3.3.1.2.1 Preparation of 3.1. A Schlenk flask was charged with compound **3.1** (210.42 mg, 0.5 mmol) and mesityl copper (91.37 mg, 0.5 mmol), followed by the addition of toluene (20 ml) and kept in stirring overnight under an inert atmosphere of Argon (Ar). The greenish-yellow color solution was filtered and evaporated under reduced pressure. Yield: 250 mg

(83%). ^{1}H NMR (400 MHz, C_6D_6, 298 K) δ 0.32 (s, 9H, Si-C*H*$_3$), 0.70 (s, 9H, Si-C*H*$_3$), 1.17 (s, 18H, {N-C(C*H*$_3$)$_3$}, 2.44 (s, 3H, *p*-C*H*$_3$), 3.06 (s, 6H, *o*-C*H*$_3$), 6.85-7.03 (m, 5H, arom. H), 7.14 (d, 2H, arom. H) ppm; ^{13}C{^{1}H} NMR (100.613 MHz, C_6D_6, 298 K): δ 4.82 (Si-*C*H$_3$), 5.98 (Si-*C*H$_3$), 21.78 (mesityl *C*H$_3$), 29.86 (mesityl *C*H$_3$), 31.80 {N-C(*C*H$_3$)$_3$}, 54.36 {N-*C*(CH$_3$)$_3$}, 125.16, 130.29, 132.03, 133.40, 146.66 (arom. C), 165.93, 167.16 (N*C*N) ppm; ^{29}Si{^{1}H} NMR (79.49 MHz, C_6D_6, 298 K): δ 5.28 [-N(*Si*Me$_3$)$_2$], 5.33 [-N(*Si*Me$_3$)$_2$], 6.5 (*Si*-Cu) ppm. HRMS (ESI, CH_3CN) (*m/z*) for [$C_{30}H_{52}CuN_3Si_3$] cacld. 601.2765; found 601.2748 [M^+].

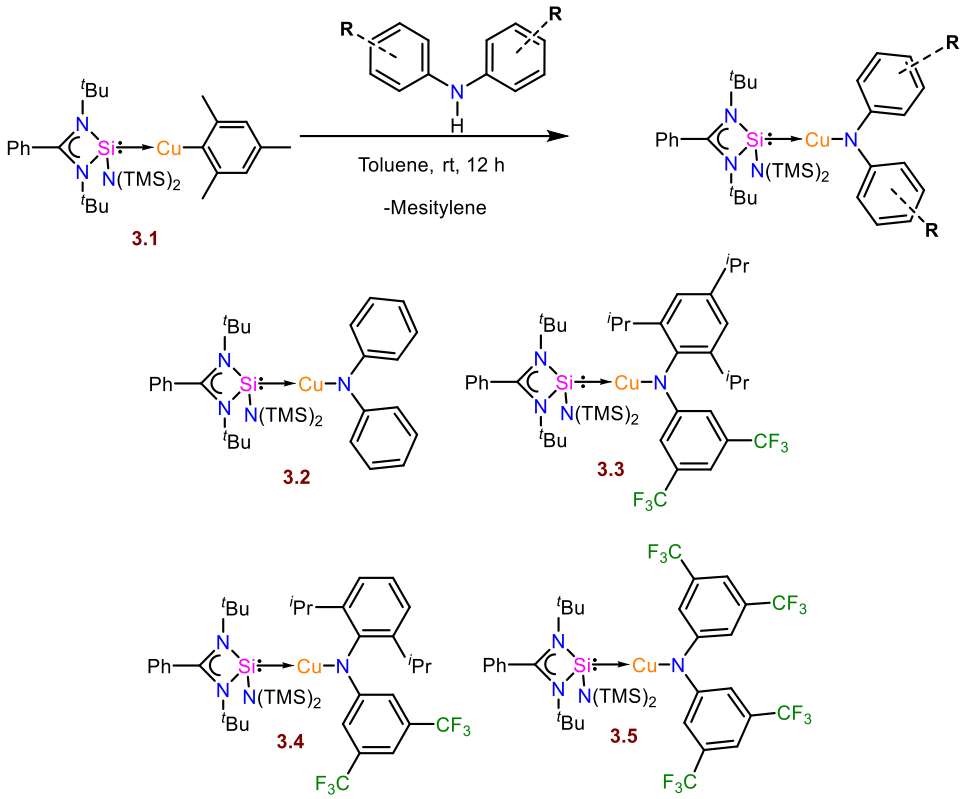

Scheme 3.2. Syntheses of NHSi coordinated copper amide complexes (**3.2**-**3.5**).

3.3.1.2.2 Preparation of 3.2. A Schlenk flask was charged with compound **3.1** (210.42 mg, 0.5 mmol) and mesityl copper (91.37 mg, 0.5 mmol), followed by the addition of toluene (20 ml) and kept in stirring for 4 h. Diphenyl amine (84.6 mg, 0.5 mmol) was added to the solution and kept in stirring overnight under an inert atmosphere of Argon (Ar). The resultant solution was filtered and evaporated under reduced pressure, which afforded single crystals at room temperature. Yield: 200 mg (62 %). ^{1}H NMR (400 MHz, C_6D_6): δ 7.69 (d, J = 8.5 Hz, 4H, aromatic C-H), 7.38 – 7.31 (m, 4H, aromatic C-H), 6.93 – 6.82 (m, 7H, aromatic C-H), 1.07 (s, 18H, {N-C(C*H*$_3$)$_3$}), 0.57 (s, 9H, Si-C*H*$_3$), 0.25 (s, 9H, Si-C*H*$_3$) ppm; ^{13}C{^{1}H} NMR (100.613 MHz, C_6D_6, 298 K): δ 167.63 (N*C*N), 156.44 (aromatic C), 143.26 (aromatic C), 131.13 (aromatic C), 130.08 (aromatic C), 129.18 (aromatic C), 129.06 (aromatic C), 120.79

(aromatic C), 120.56 (aromatic C), 117.84 (aromatic C), 116.42 (aromatic C), 54.21 ({N-*C*(CH_3)$_3$}), 31.16 {N-C(*C*H_3)$_3$}, 4.36 (Si-*C*H_3), 5.60 (Si-*C*H_3) ppm; ^{29}Si{^{1}H} NMR (79.49 MHz, C_6D_6, 298 K): δ 5.70 [-N(*Si*Me_3)$_2$], 6.9 [-N(*Si*Me_3)$_2$], 8.0 (*Si*-Cu) ppm. HRMS (ESI, CH_3CN) (*m/z*) for [$C_{33}H_{51}CuN_4Si_3$] cacld. 650.2717; found 650.1326 [M^+]. M.p. 153 °C.

3.3.1.2.3 Preparation of 3.3. A Schlenk flask was charged with compound **3.1** (210.42 mg, 0.5 mmol) and mesityl copper (91.37 mg, 0.5 mmol), followed by the addition of toluene (20 ml) and kept in stirring for 4 h. *N*-(3,5-bis(trifluoromethyl)phenyl)-2,4,6-triisopropylaniline (**3.II**) (216 mg, 0.5 mmol) was added to the solution and kept in stirring overnight under inert atmosphere of Argon (Ar). The resultant solution was filtered and evaporated under reduced pressure, which afforded single crystals at room temperature. Yield: 340 mg (74 %). ^{1}H NMR (400 MHz, C_6D_6): δ 7.71 (s, 1H, aromatic C-H), 7.26 (d, J = 7.7 Hz, 1H, aromatic C-H), 7.06 (s, 3H, aromatic C-H), 7.04 – 6.95 (m, 3H, aromatic C-H), 6.87 (t, J = 7.5 Hz, 1H, aromatic C-H), 6.81 (t, J = 7.6 Hz, 1H, aromatic C-H), 6.58 (s, 1H, aromatic C-H), 3.83 – 3.70 (m, 2H, -C*H*(CH_3)$_2$), 2.90 – 2.74 (m, 1H, -C*H*(CH_3)$_2$), 1.36 (d, J = 6.9 Hz, 6H, -CH(C*H*$_3$)$_2$), 1.23 (d, J = 6.8 Hz, 6H, -CH(C*H*$_3$)$_2$), 1.19 (d, J = 6.9 Hz, 6H, -CH(C*H*$_3$)$_2$), 0.97 (s, 18H, {N-C(C*H*$_3$)$_3$), 0.32 (s, 9H, Si-C*H*$_3$), 0.14 (s, 9H, Si-C*H*$_3$) ppm; ^{13}C NMR (100.613 MHz, C_6D_6): δ 168.56 (N*C*N), 159.98 (aromatic C), 147.42 (aromatic C), 144.70 (aromatic C), 144.28 (aromatic C), 142.98 (aromatic C), 131.07 (aromatic C), 130.63 (aromatic C), 128.25 (aromatic C), 127.16 (aromatic C), 122.38 (aromatic C), 121.69 (aromatic C), 116.66 (aromatic C), 111.13 (aromatic C), 54.44 {N-*C*(CH_3)$_3$}, 34.44 {-*C*H(CH_3)$_2$}, 31.43 {N-C(*C*H_3)$_3$}, 28.33 {-*C*H(CH_3)$_2$}, 25.03 {-CH(*C*H_3)$_2$}, 24.58 {-CH(*C*H_3)$_2$}, 24.35 {-CH(*C*H_3)$_2$}, 5.60 (Si-*C*H_3), 4.55 (Si-*C*H_3). ^{29}Si{^{1}H} NMR (79.49 MHz, C_6D_6, 298 K): δ 6.2 [-N(*Si*Me_3)$_2$], 6.9 [-N(*Si*Me_3)$_2$], 7.6 (*Si*-Cu) ppm; ^{19}F NMR (377 MHz, C_6D_6): δ -63, -62.1 ppm. HRMS (ESI, CH_3CN) (*m/z*) for [$C_{44}H_{67}CuF_6N_4Si_3$] cacld. 912.3873; found 913.4285 [M+1]. M.p. 178 °C.

3.3.1.2.4 Preparation of 3.4. A Schlenk flask was charged with compound **3.1** (210.42 mg, 0.5 mmol) and mesityl copper (91.37 mg, 0.5 mmol), followed by the addition of toluene (20 ml) and kept in stirring for 4 h. *N*-(3,5-bis(trifluoromethyl)phenyl)-2,6-diisopropylaniline (**3.I**) (195 mg, 0.5 mmol) was added to the solution and kept in stirring overnight under an inert atmosphere of Argon (Ar). The resultant solution was filtered and evaporated under reduced pressure, which afforded single crystals at room temperature. Yield: 310 mg (71 %). ^{1}H NMR (400 MHz, C_6D_6) δ 7.80 (s, 1H, aromatic C-H), 7.38 (d, J = 7.6 Hz, 1H, aromatic C-H), 7.31 (d, J = 8.0 Hz, 2H, aromatic C-H), 7.23 (d, J = 6.8 Hz, 1H, aromatic C-H), 7.13 – 7.06 (m, 3H,

aromatic C-H), 6.97 (t, J = 7.6 Hz, 1H, aromatic C-H), 6.90 (t, J = 7.6 Hz, 1H, aromatic C-H), 6.65 (s, 1H, aromatic C-H), 3.90 – 3.82 (m, 2H, -C*H*(CH_3)$_2$), 1.41 (d, J = 6.9 Hz, 6H, -CH(CH_3)$_2$), 1.27 (d, J = 6.9 Hz, 6H, -CH(CH_3)$_2$), 1.07 (s, 18H, {N-C(CH_3)$_3$}), 0.40 (s, 9H, Si-CH_3), 0.23 (s, 9H, Si-CH_3). ppm; ^{13}C NMR (100.613 MHz, C_6D_6): δ 168.48 (N*C*N), 159.75 (aromatic C), 147.35 (aromatic C), 145.24 (aromatic C), 144.88 (aromatic C), 130.91 (aromatic C), 130.50 (aromatic C), 124.56 (aromatic C), 124.34 (aromatic C), 123.91 (aromatic C), 116.54 (aromatic C), 111.05 (aromatic C), 103.02 (aromatic C), 54.30 {N-*C*(CH_3)$_3$}, 31.29{N-C(*C*H_3)$_3$}, 28.09{-*C*H(CH_3)$_2$}, 24.74{-CH(*C*H_3)$_2$}, 24.29{-CH(*C*H_3)$_2$}, 5.48 (Si-*C*H_3), 4.40 (Si-*C*H_3) ppm; ^{29}Si{^{1}H} NMR (79.49 MHz, C_6D_6, 298 K): δ 6.2 [-N(*Si*Me$_3$)$_2$], 6.9 [-N(*Si*Me$_3$)$_2$], 7.5 (*Si*-Cu) ppm; ^{19}F NMR (377 MHz, C_6D_6): δ -62.0, -63.1 ppm. HRMS (ESI, CH_3CN) (*m/z*) for [$C_{41}H_{61}CuF_6N_4Si_3$] cacld. 870.3404; found 893.5298 [M+Na]. M.p. 146 °C.

3.3.1.2.5 Preparation of 3.5. A Schlenk flask was charged with compound **3.1** (210.42 mg, 0.5 mmol) and mesityl copper (91.37 mg, 0.5 mmol), followed by the addition of toluene (20 ml) and kept in stirring for 4 h. *N*-(3,5-bis(trifluoromethyl)phenyl)-2,6-bis(trifluoromethyl)aniline (**3.III**) (221 mg, 0.5 mmol) was added to the solution and kept in stirring overnight under inert atmosphere of Argon (Ar). The resultant solution was filtered and evaporated under reduced pressure, which afforded single crystals at room temperature. Yield: 290 mg (63%). ^{1}H NMR (400 MHz, C_6D_6): δ 6.66 (s, 2H, aromatic C-H), 6.48 (s, 2H, aromatic C-H), 6.38 (d, J = 8.3 Hz, 1H, aromatic C-H), 6.28 – 6.17 (m, 3H, aromatic C-H), 6.05 (d, J = 7.1 Hz, 1H, aromatic C-H), 0.38 (s, 18H, {N-C(C*H*$_3$)$_3$}), -0.21 (s, 9H, Si-C*H*$_3$), -0.45 (s, 9H, Si-C*H*$_3$) ppm; ^{13}C NMR (100.613 MHz, C_6D_6): δ 168.96 (N*C*N), 156.06 (aromatic C), 132.90 (aromatic C), 132.27-133.22 (-*C*F$_3$), 130.60 (aromatic C), 126.96 (aromatic C), 125.82 (aromatic C), 123.11 (aromatic C), 119.76 (aromatic C), 110.69 (aromatic C), 54.51 (N-*C*(CH_3)$_3$), 31.38 (N-C(*C*H_3)$_3$), 5.49 (Si-*C*H_3), 4.38 (Si-*C*H_3) ppm; ^{29}Si{^{1}H} NMR (79.49 MHz, C_6D_6, 298 K): δ 6.6 [-N(*Si*Me$_3$)$_2$], 7.0 [-N(*Si*Me$_3$)$_2$], 6.7 (*Si*-Cu) ppm; ^{19}F NMR (377 MHz, C_6D_6): δ -62.8 ppm. HRMS (ESI, CH_3CN) (*m/z*) for [$C_{37}H_{47}CuF_{12}N_4Si_3$] cacld. 922.2213; found 923.0352 [M+1]. M.p. 143 °C.

3.3.1.2.6 Preparation of 3.6. A Schlenk flask was charged with compound **3.1** (210.42 mg, 0.5 mmol) and mesityl copper (91.37 mg, 0.5 mmol), followed by the addition of toluene (20 ml) and kept in stirring for 4 h. Carbazole (83.5 mg, 0.5 mmol) was added to the solution and kept in stirring overnight under an inert atmosphere of Argon (Ar). The resultant solution was filtered and evaporated under reduced pressure, which afforded single crystals at room

temperature. Yield: 280 mg (86 %). ^{1}H NMR (400 MHz, C_6D_6): δ 8.43 (d, J = 7.7 Hz, 2H, aromatic C-H), 8.12 (d, J = 8.1 Hz, 2H, aromatic C-H), 7.70 (t, J = 7.0 Hz, 2H, aromatic C-H), 7.36 (t, J = 7.3 Hz, 2H, aromatic C-H), 7.06 (d, J = 7.5 Hz, 2H, aromatic C-H), 6.84 (dd, J = 16.2, 6.1 Hz, 3H, aromatic C-H), 1.10 (s, 18H, {N-C(CH_3)$_3$}), 0.63 (s, 9H, Si-CH_3), 0.27 (s, 9H, Si-CH_3) ppm; ^{13}C NMR (100.613 MHz, C_6D_6): δ 168.34 (N*C*N)151.26 (aromatic C), 131.05 (aromatic C), 130.35 (aromatic C), 125.51 (aromatic C), 123.89 (aromatic C), 120.52 (aromatic C), 116.00 (aromatic C), 114.42 (aromatic C), 54.43 ({N-*C*(CH_3)$_3$}), 31.59 ({N-C(*C*H_3)$_3$}), 5.79 (Si-*C*H_3), 4.41 (Si-*C*H_3) ppm; ^{29}Si{^{1}H} NMR (79.49 MHz, C_6D_6, 298 K): δ 6.2 [-N(*Si*Me_3)$_2$], 7.1 [-N(*Si*Me_3)$_2$], 7.5 (*Si*-Cu) ppm. HRMS (ESI, CH_3CN) (*m/z*) for [$C_{33}H_{49}CuN_4Si_3$] cacld. 649.2717; found 648.0386 [M-1]$^{+}$. M.p. 155 °C.

3.3.1.2.7 Preparation of 3.8. A Schlenk flask was charged with compound **3.1** (210.42 mg, 0.5 mmol) and mesityl copper (91.37 mg, 0.5 mmol), followed by the addition of toluene (20 ml) and kept in stirring for 4 h. *N*-(3,5-bis(trifluoromethyl)phenyl)-2,4,6-triisopropylaniline (**3.II**) (216 mg, 0.5 mmol) was added to the solution and kept in stirring overnight under inert atmosphere of Argon (Ar). The resultant solution was filtered and evaporated under reduced pressure, which afforded single crystals at room temperature. Yield: 400 mg (90 %). ^{1}H NMR (400 MHz, C_6D_6): δ 7.26 (t, J = 7.8 Hz, 2H, aromatic C-H), 7.09 – 7.02 (m, 6H, aromatic C-H), 6.95 (s, 1H, aromatic C-H), 6.77 (s, 1H, aromatic C-H), 6.42 (s, 1H, aromatic C-H), 6.24 (s, 2H, -NC*H*=C*H*N-), 3.35 – 3.24 (m, 2H, -C*H*(CH_3)$_2$ from amide part), 2.83 (dt, J = 13.8, 6.9 Hz, 1H, -C*H*(CH_3)$_2$ from amide part), 2.60 – 2.48 (m, 4H, -C*H*(CH_3)$_2$), 1.26 (d, J = 6.9 Hz, 6H, -CH(CH_3)$_2$ from amide part), 1.17 (d, J = 6.9 Hz, 12H, -CH(CH_3)$_2$), 1.10 (d, J = 6.8 Hz, 6H, -CH(CH_3)$_2$ from amide part), 1.00 (d, J = 6.9 Hz, 12H, -CH(CH_3)$_2$), 0.84 (d, J = 6.9 Hz, 6H, -CH(CH_3)$_2$ from amide part) ppm; ^{13}C NMR (100.613 MHz, C_6D_6) δ 181.53 (carbene C), 159.75 (aromatic C), 147.43 (aromatic C), 145.14 (aromatic C), 144.69 (aromatic C), 143.95 (aromatic C), 142.22 (aromatic C), 134.74 (aromatic C), 130.78 (aromatic C), 124.32 (aromatic C), 123.14 (aromatic C), 122.37 (aromatic C), 121.54 (aromatic C), 116.49 (aromatic C), 111.55 (aromatic C), 103.60 – 102.50 (-*C*F_3), 34.41 (-*C*H(CH_3)$_2$), 28.72 (-*C*H(CH_3)$_2$), 27.79 (-*C*H(CH_3)$_2$), 24.43 (d, -CH(*C*H_3)$_2$), 24.00 (d, -CH(*C*H_3)$_2$) ppm; ^{19}F NMR (377 MHz, C_6D_6): δ -61.3, 63.2 ppm. HRMS (ESI, CH_3CN) (*m/z*) for [$C_{50}H_{62}CuF_6N_3$] cacld. 881.4143; found 881.0219 [M^{+}]. M.p. 232 °C.

3.3.1.2.8 Preparation of 3.9. A Schlenk flask was charged with compound **3.1** (210.42 mg, 0.5 mmol) and mesityl copper (91.37 mg, 0.5 mmol), followed by the addition of toluene (20

ml) and kept in stirring for 4 h. *N*-(3,5-bis(trifluoromethyl)phenyl)-2,6-diisopropylaniline (**3.I**) (195 mg, 0.5 mmol) was added to the solution and kept in stirring overnight under an inert atmosphere of Argon (Ar). The resultant solution was filtered and evaporated under reduced pressure, which afforded single crystals at room temperature. Yield: 345 mg (82 %). ^{1}H NMR (400 MHz, C_6D_6): δ 7.25 (t, J = 7.8 Hz, 2H, aromatic C-H), 7.11 (s, 3H, aromatic C-H), 7.06 (d, J = 7.8 Hz, 4H, aromatic C-H), 6.98 (s, 1H, aromatic C-H), 6.81 (s, 1H), 6.38 (s, 1H, aromatic C-H), 6.23 (s, 2H, -NC*H*=C*H*N-), 3.28 (dt, J = 13.7, 6.9 Hz, 2H, {-C*H*$(CH_3)_2$ from amide part), 2.54 (dt, J = 13.7, 6.8 Hz, 4H, {-C*H*$(CH_3)_2$}), 1.17 (d, J = 6.9 Hz, 12H, {-CH(C*H*$_3)_2$}), 1.04 (d, J = 6.8 Hz, 6H, {-CH(C*H*$_3)_2$} from amide part), 0.99 (d, J = 6.9 Hz, 12H, {-CH(C*H*$_3)_2$}), 0.80 (d, J = 6.9 Hz, 6H, {-CH(C*H*$_3)_2$} from amide part) ppm; ^{13}C NMR (100.613 MHz, C_6D_6) δ 181.40 (carbene C), 159.65 (aromatic C), 145.10 (d, J = 5.2 Hz, aromatic C), 144.71 (aromatic C), 134.70 (aromatic C), 130.78 (aromatic C), 124.42 (d, J = 13.0 Hz), 123.83 (s), 123.13 (s), 122.90 (aromatic C), 116.55 (dd, J = 6.6, 3.2 Hz, -*C*F_3), 28.72 (-*C*H$(CH_3)_2$), 27.72 (-*C*H$(CH_3)_2$), 24.38 (-CH(*C*H$_3)_2$), 24.09 (-CH(*C*H$_3)_2$), 23.88 (-CH(*C*H$_3)_2$), 22.35 (-CH(*C*H$_3)_2$) ppm; ^{19}F NMR (377 MHz, C_6D_6): δ -61.3, 63.2 ppm. HRMS (ESI, CH_3CN) (*m/z*) for [$C_{47}H_{56}CuF_6N_3$] cacld. 839.3674; found 839.5033 [M^+]. M.p. 240 °C.

3.3.2 Structural elucidation.

Complex **3.2**, **3.3**, and **3.4** show broad peaks at δ 8.0, 7.6, and 7.5 ppm, respectively, along with two other sharp singlets for trimethylsilyl (TMS) group. This confirms the Si(II)→Cu-amide coordination. The ^{29}Si{^{1}H} NMR shows a broad peak at δ 6.7 ppm for complex **3.5**. The upfield shift of ^{29}Si{^{1}H} resonances of these complexes show the trend of deshielding **3.2**<**3.3**~**3.4**<**3.5** (Table 3.1).

Table 3.1. ^{29}Si{^{1}H} chemical shift and bond parameters of NHSi coordinated Cu-mesityl and Cu-amide complexes.

Complexes	^{29}Si{^{1}H} Chemical shift (δ) ppm	Si(II)→Cu(I) bond length (Å)	Cu-C/N bond length (Å)	α^a angle	β^b angle
3.1	6.5	2.2509(8)	1.946(2)	-	-
3.2	8.0	2.2164(8)	1.896(2)	21.5	170.5
3.3	7.6	2.204(2)	1.872(5)	28.1	162.1
3.4	7.5	2.2302(15)	1.884(3)	40.9	159.1
3.5	6.7	2.2153(8)	1.901(2)	75.9	171.0
3.6	7.5	2.2068(12)	1.873(2)	18.9	171.9

[a]torsion angle (α) between the NHSi ligand and amide moiety. [b]β is the tilt angle between the Cu and the amide group. Cg centroid and for acyclic secondary amide (C23, C22, N1, C28, C29 for **3.2**; C14, N1, C1, C2, C9 for **3.3**; C22, N1, C27, C30, C31 for **3.4**; C14, C9, N1, C1, C2 for **3.5**) and for the carbazolide five-membered ring (N1, C32, C27, C26, C37 for **3.6)**

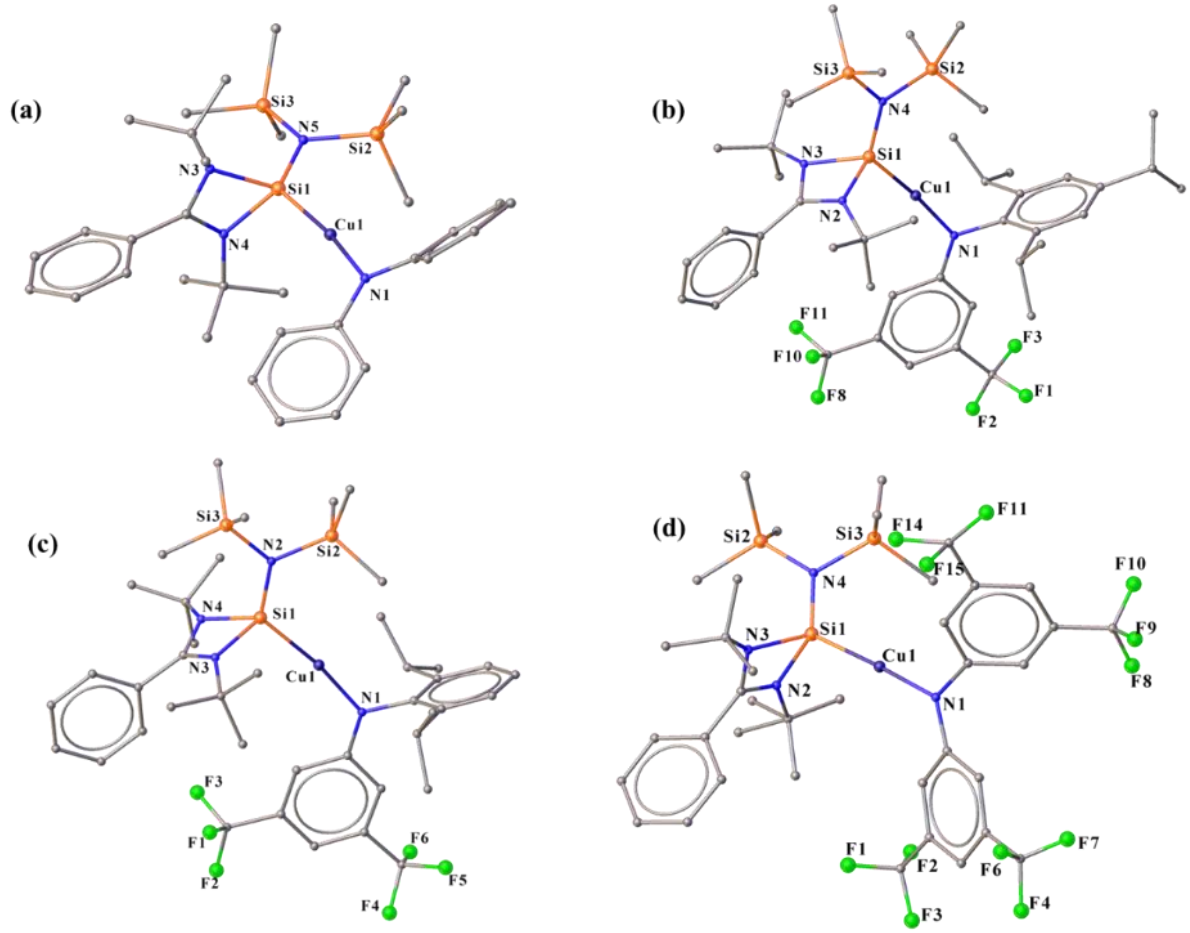

Figure 3.2. Molecular structure of **3.2-3.5**. Anisotropic displacement parameters are depicted at the 50% probability level. Solvent moiety, anion, and H atoms are omitted for clarity. Selected bond distances (Å) and angles (deg): for complex **3.2 (a)** Cu1-Si1 2.2164(8), Cu1-N1 1.896(2), Si1-N3 1.844(2), Si1-N4 1.8405(19), Si1-N5 1.730(2), Si2-N5 1.771(2), Si3-N5 1.755(2) and N1-Cu1-Si1 171.91(6), Si1-N5-Si3 125.78(11), Si3-N5-Si2 120.43(11), N3-Si1-Cu1 111.38(7), N4-Si1-Cu1 111.16(7), N4-Si1-N3 70.78(8), N5-Si1-Cu1 125.01(7), N5-Si1-N3 113.17(9), N5-Si1-N4 112.71(9); for complex **3.3 (b)** Cu1-Si1 2.204(2), Cu1-N1 1.872(5), Si1-N2 1.841(6), Si1-N3 1.826(6), Si1-N4 1.719(6), Si2-N4 1.780(6), Si3-N4 1.749(6) and N1-Cu1-Si1 172.43(19), N2-Si1-Cu1 110.13(18), N3-Si1-Cu1 112.51(19), N3-Si1-N2 70.7(3), N4-Si1-Cu1 125.4(2), N4-Si1-N2 112.5(3), N4-Si1-N3 112.7(3); for complex **3.4 (c)** Cu1-Si1 2.2302(15), Cu1-N1 1.884(3), Si1-N4 1.838(4), Si1-N3 1.839(4), Si1-N2 1.709(4), Si2-N2 1.766(4), Si3-N2 1.764(4) and N1-Cu1-Si1 172.28(11), N4-Si1-Cu1 111.47(12), N4-Si1-N3

70.97(16), N3-Si1-Cu1 110.23(12), N2-Si1-Cu1 124.98(15), N2-Si1-N4 113.14(18), N2-Si1-N3 113.51(19), Si1-N2-Si2 115.7(2), Si1-N2-Si3 125.5(2), Si3-N2-Si2 118.6(2); for complex **3.5 (d)** Cu1-N1 1.901(2), Cu1-Si1 2.2153(8), Si1-N2 1.837(2), Si1-N3 1.841(2), Si1-N4 1.720(2), Si2-N4 1.757(2), Si3-N4 1.771(2) and N1-Cu1-Si1 177.21(8), N2-Si1-Cu1 112.90(8), N2-Si1-N3 70.86(11), N3-Si1-Cu1 110.74(8), N4-Si1-Cu1 122.49(8), N4-Si1-N2 114.01(11), N4-Si1-N3 114.63(11), Si1-N4-Si2 126.42(14), Si1-N4-Si3 113.39(13), Si2-N4-Si3 119.92(13).

Complex **3.2** crystallized in a monoclinic $P2_1/c$ space group with Si1-Cu1 and Cu1-N1 bond lengths, 2.2164(8) and 1.896(2) Å, respectively (Figure 3.2). The Si-Cu and Cu-N bond lengths in complex **3.2** are longer than the five-membered CAAC coordinated Cu-diphenylamide complex (1.882 (5); 1.854(4) Å).[12] Both complexes **3.3** and **3.4** crystallize in the triclinic *P-1* space group, featuring a distorted tetrahedral Si(II) and trigonal planar Cu(I) center (Figure 3.2). The Si1-Cu1 bond lengths are 2.204(2) and 2.2302(15) Å for complexes **3.3** and **3.4**, respectively. The Si-Cu bond lengths are shorter than the complex **3.1**, denoting a greater extent of charge delocalization. The tri-coordinated Cu center showcases a N-Cu-Si bond angle of 172.43(19) and 172.28(11)° for **3.3** and **3.4**, respectively. Complex **3.5** crystallized in a monoclinic $P2_1/c$ space group, featuring Si1-Cu1 and Cu1-N1 bond lengths, 2.2153(8) and 1.901(2) Å, respectively. The Si1-Cu1 bond length for complex **3.5** is shorter than **3.2** and **3.4** and longer than **3.3**. The Si-Cu-N bond angles for complexes **3.2**, **3.3**, **3.4**, and **3.5** are 171.91(6), 172.43(19), 172.28(11), and 177.21(8)°, respectively. These molecular complexes are stabilized *via* several C-H···F and C-H···π interactions. The amide planes and Cu-N bond are not completely coplanar and deviate from linearity (Table 3.1). We measured the distortion by angle β while taking the angle between the Cu-N-Cg (centroid of the amide moieties). This shows the deviation of planarity is significant for complexes **3.3** (162.1°) and **3.4** (159.1°), while it is similar for complexes **3.6** (171.9°), **3.4** (170.5°), and **3.5** (171.0°), which are in line with CAAC coordinated metal amide complexes.[13, 33] The torsion angles (α) between NHSi and amide moieties have also been calculated (Table 3.1), which also discloses the deviation of coplanarity. We also treated the copper mesityl complex of trimethylsilyl substituted benzamidinato silylene (**3.1**) with carbazole in toluene at room temperature to afford complex **3.6**. As suggested by Liu and co-workers, we synthesized carbazole in our lab to probe the complex for any photophysical experiment.[87, 88] The broad peak at δ 7.5 ppm in $^{29}Si\{^1H\}$ NMR supports the coordination of NHSi to Cu carbazolide centre. The Si(II) center in complex **3.6** is more shielded than in complex **3.1** due to the donating nature of carbazole.

The molecular complex shows it crystallized in the triclinic *P-1* space group (Figure 3.3). The Si(II) center features a distorted tetrahedral geometry, whereas Cu(I) features a trigonal planar geometry. The Si1-Cu1 and Cu1-N1 bond lengths are 2.2068(12) and 1.873(2), which are shorter than the complex **3.1** (Table 3.1).

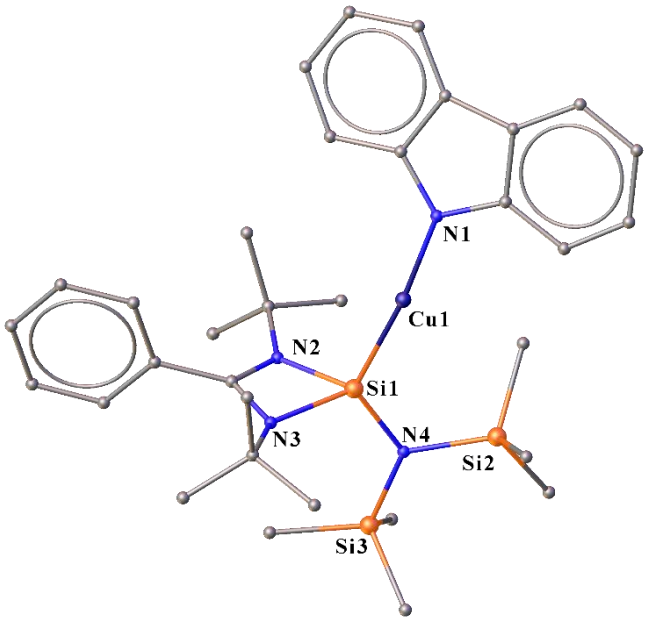

Figure 3.3. Molecular structure of **3.6**. Anisotropic displacement parameters are depicted at the 50% probability level. Solvent moiety, anion, and H atoms are omitted for clarity. Selected bond distances (Å) and angles (deg): Cu1-Si1 2.2068(12), Cu1-N1 1.873(2), Si1-N2 1.823(2), Si1-N3 1.841(2), Si1-N4 1.722(2), Si2-N4 1.764(2), Si3-N4 1.755(2) and N1-Cu1-Si1 172.37(8), N2-Si1-Cu1 111.44(8), N2-Si1-N3 71.03(10), N3-Si1-Cu1 113.16(7), N4-Si1-Cu1 122.95(8), N4-Si1-N2 111.35(11), N4-Si1-N3 115.25(10).

After isolating the NHSi-coordinated Cu amides (**3.2**-**3.6**), we attempted to synthesize IDip-coordinated Cu(I) amides. Radius and co-workers isolated the IDip-coordinated copper mesityl complex. We isolated and characterized the same (**3.7**) and proceeded with the reaction of functionalized secondary amines (Scheme 3.3), which afforded complexes **3.8**-**3.9**. The $^{13}C\{^{1}H\}$ NMR values are δ 181.5 and 181.4 ppm for **3.8** and **3.9**, respectively. The chemical shift of the carbene center is in accordance with the electronic effect of the -CF_3 substituent attached to the amide functionalities. Complexes **3.8** and **3.9** crystallized in the monoclinic $P2_1/n$ space group (Figure 3.4). The C-Cu bond lengths are 1.868(3) and 1.877(6) Å for **3.8** and **3.9**, respectively, which are shorter than the precursor complex **3.7** and NHSi coordinated Cu amides (**3.2**-**3.6**). The observed C-Cu bond lengths are marginally shorter than the CAAC-coordinated Cu amides (1.88 to 1.89 Å).[12] The tri-coordinated Cu centers feature a near linear

geometry with C-Cu-N bond angles 174.96(13) and 178.0(2) for complex **3.8** and **3.9**, respectively. The deviation of coplanarity was measured by angle *β*, which shows the distortion is maximum for complex **3.8**, followed by **3.9** (Table 3.2).

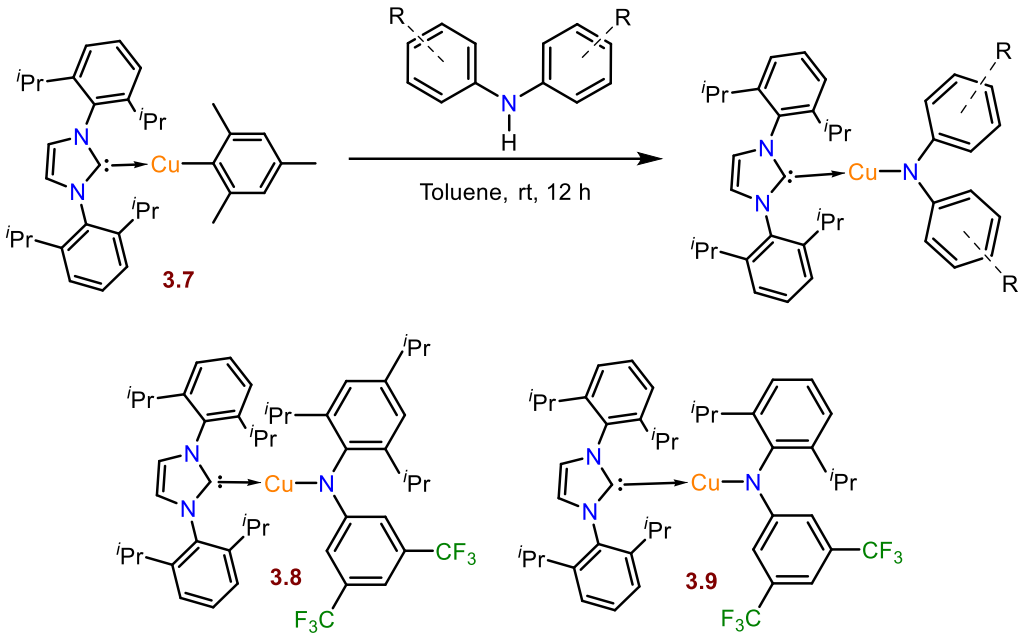

Scheme 3.3. Syntheses of NHC coordinated copper amide complexes.

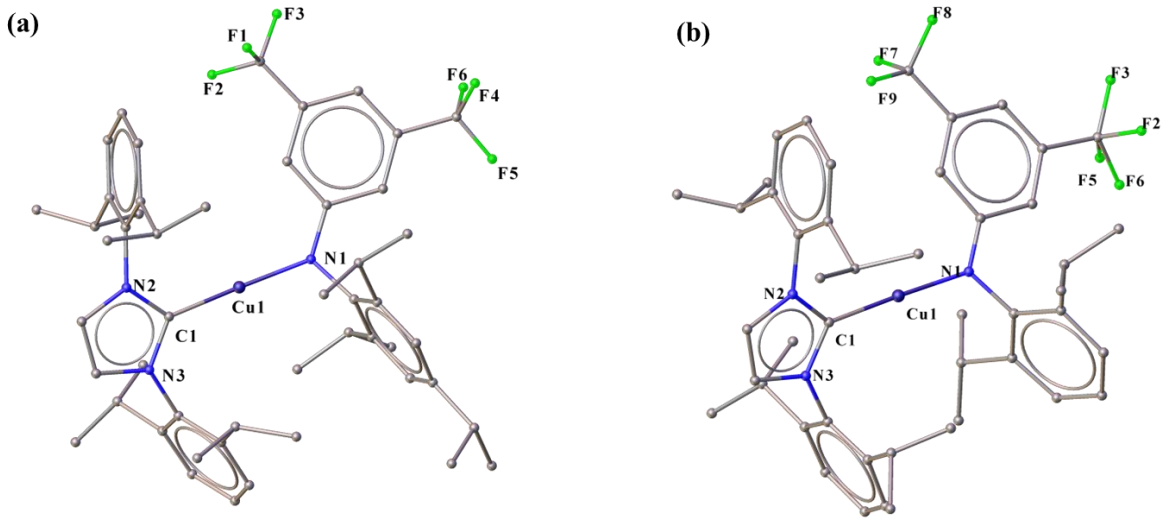

Figure 3.4. Molecular structures of **3.8** and **3.9**. Anisotropic displacement parameters are depicted at the 50% probability level. Solvent moiety, anion, and H atoms are omitted for clarity. Selected bond distances (Å) and angles (deg): for complex **3.8 (a)** Cu1-C1 1.878(3), Cu1-N1 1.868(3), C1-N2 1.359(4), C1-N3 1.364(4) and N1-Cu1-C1 174.96(13), N2-C1-Cu1 125.4(2), N2-C1-N3 103.4(3), N3-C1-Cu1 131.0(2); for complex **3.9 (b)** Cu1-C1 1.883(7), Cu1-N1 1.877(6), C1-N2 1.349(7), C1-N3 1.352(7) and N1-Cu1-C1 178.0(2), N2-C1-Cu1 128.6(4), N2-C1-N3 103.9(5), N3-C1-Cu1 127.4(4).

Table 3.2. $^{13}C\{^{1}H\}$ chemical shift and bond parameters of NHC coordinated Cu-mesityl and Cu-amide complexes

Complexes	$^{13}C\{^{1}H\}$ Chemical shift (δ) ppm	Carbenic C→Cu(I) bond length (Å)	Cu-C/N bond length (Å)	α^a angle	β^b angle
3.7	186.4	1.9006(19)	1.919(2)	-	-
3.8	181.5	1.878(3)	1.868(3)	29.0	154.7
3.9	181.4	1.883(7)	1.877(6)	33.7	164.4

[a]torsion angle (α) between the NHSi ligand and amide moiety. [b]β is the tilt angle between the Cu and the amide group. Cg centroid for the acyclic amide moiety.

3.3.3 HOMO-LUMO energy gaps of complexes 3.2-3.5 and 3.8-3.9.

In all silylene complexes, HOMO resides on the π-donor amide moiety, and LUMO resides on the π-acceptor silylene moiety (Figure 3.5a). Therefore, the nature of the lowest energy electronic transition is assigned to be ligand-to-ligand charge transfer (LL'CT).

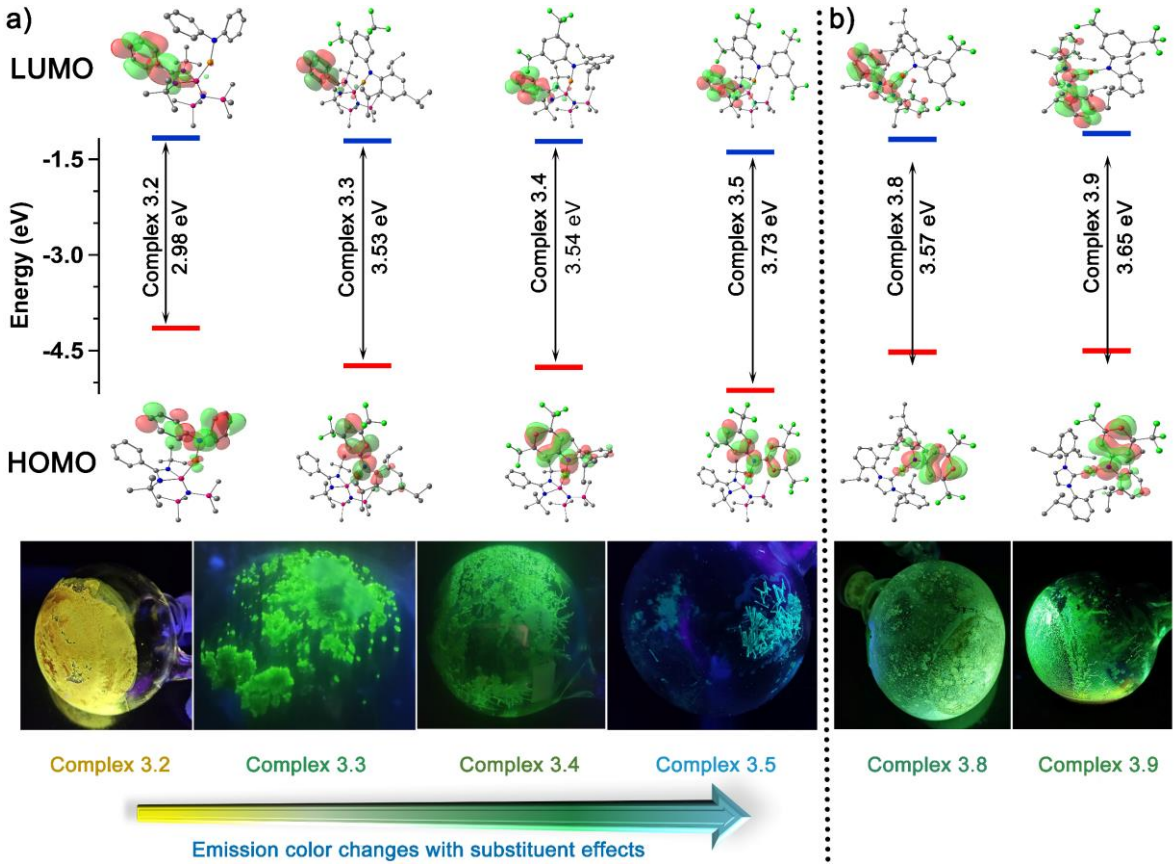

Figure 3.5. HOMO-LUMO orbitals and their energy gaps in the ground state and their emission at 360 nm under UV irradiation of (a) NHSi Cu-amide complexes; (b) NHC Cu-amide complexes.

In the case of **3.2**, the electron-withdrawing effect is the minimum; hence, the HOMO acquires the highest energy. On the other hand, in **3.5**, the electron-withdrawing effect of four -CF_3 groups attached to the amide stabilizes the HOMO to a much greater extent, making it energetically lowest. In the case of **3.3** and **3.4**, the electron-withdrawing effects of -CF_3 groups are equal, but the hyperconjugation effects of isopropyl groups are lower in **3.4**. As a result, the overall electron-withdrawing effect in **3.4** is more significant, resulting in a higher stability of HOMO in this complex compared to **3.3**. Therefore, the HOMO stability order in these complexes is as follows, **3.5** > **3.4** > **3.3**> **3.2**. As the LUMO-containing silylene moiety remains the same in all the complexes hence, the same trend is also observed in the order of the HOMO-LUMO energy gap (Figure 3.5a). Here, the HOMO-LUMO energy gap is particularly important as it dictates the energy of LL'CT states. The optical excitation of the complex with a larger HOMO-LUMO energy gap will result in the formation of high-energy LL'CT states. As we used the same amide moieties for carbene complexes, their HOMO energies and HOMO-LUMO energy gaps exhibit exactly the same trend as the silylene complexes (Figure 3.5b).

3.3.4 Photophysical properties of complex 3.2.

Complex **3.2** shows a long absorption tail in the 320-500 nm range and an absorption peak at ~290 nm (see Appendix). Complex **3.3** and **3.4** show similar absorption characteristics where a broad shoulder peak is observed in the range of 350-420 nm, along with two peaks at ~325 nm and 290 nm. Complex **3.5** shows an absorption tail extended to ~425 nm along with a peak at 340 nm and two peaks in the range of 290-300 nm. The long absorption tail of complex **3.2** is attributed to the LL'CT excitation to the low-lying excited states. Here, the vertical excitation energy for the S_1 state is much lower compared to the higher energy excited states and corresponds to its long absorption range, which is in accordance with the nature of excited states from natural transition orbital (NTO) analysis (*vide infra*) and simulated absorption spectra (see Appendix). The higher energy peak at 290 nm can be attributed to intra-ligand excitations within the amide and NHSi moieties.[89] The shoulder peak in complexes **3.3** and **3.4** is attributed to the LL'CT excitation to two low-lying S_1 and S_2 states having close vertical excitation energy, corroborating with the nature of excited states from NTO analysis (vide infra) and simulated absorption spectra (see Appendix). The absorption peak at 325 nm can be attributed to the higher energy LL'CT states, and the peak at 290 nm is attributed to intra-ligand excitations. In complex **3.5**, LL'CT excitations are higher in energy than **3.3** and **3.4**, and vertical excitation energies are much closer, resulting in a shorter absorption tail (see

Appendix). The peak at 340 nm can be attributed to the higher energy LL'CT states, and the peaks ranging between 290-300 nm can be assigned to the intra-ligand excitations. Complex **3.2** exhibits bright green-yellow emission under exposure of UV light. Inside an inert condition, it shows a single broad emission band having a maximum at ~560 nm (Figure 3.6a).

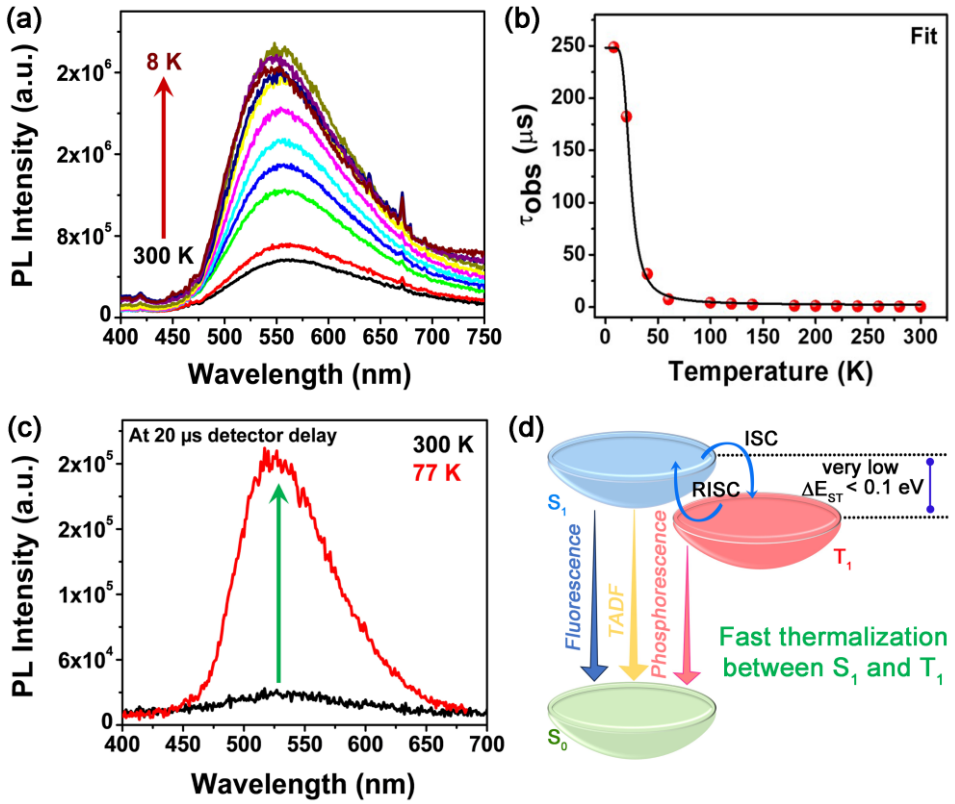

Figure 3.6. (a) Temperature-dependent emission spectra of **3.2**, (b) τ_{obs} *vs.* temperature plot of **3.2**, (c) gated emission spectra at different temperatures (gated emission spectra of **3.2** was collected without correction factor, hence the spectra is blue-shifted compared to that of Figure 3.6a), and (d) schematic representation of TADF mechanism in **3.2**.

The NTO analysis and TD-DFT calculations of this complex show that the lowest singlet (S_1) and triplet (T_1) excited states are LL'CT in nature with a small ΔE_{ST} value of 0.015 eV (Figure 3.7). Despite having a similar charge transfer nature in the S_1 and T_1 states, a high intersystem crossing rate is anticipated in this complex due to the small ΔE_{ST} value.[90] In addition, significantly high spin-orbit coupling matrix elements (SOCME) values between S_1 and T_n states (0.46-7.4 cm^{-1}) indicate a strong ISC process taking place in this complex (Table 3.3). However, the energy diagram indicates the occurrence of the ISC process mainly between S_1 and T_1 states since the other singlet and triplet states are located at much higher energy than S_1 and T_1 (Figure 3.7).[90] The high charge transfer nature and small ΔE_{ST} value prompted us to explore the possibility of TADF in this complex. Temperature-dependent emission studies

manifest that the emission intensity increases sequentially with decreasing temperature from 300 K to about 8 K, and no spectral shift occurs within the temperature range (Figure 3.6a).

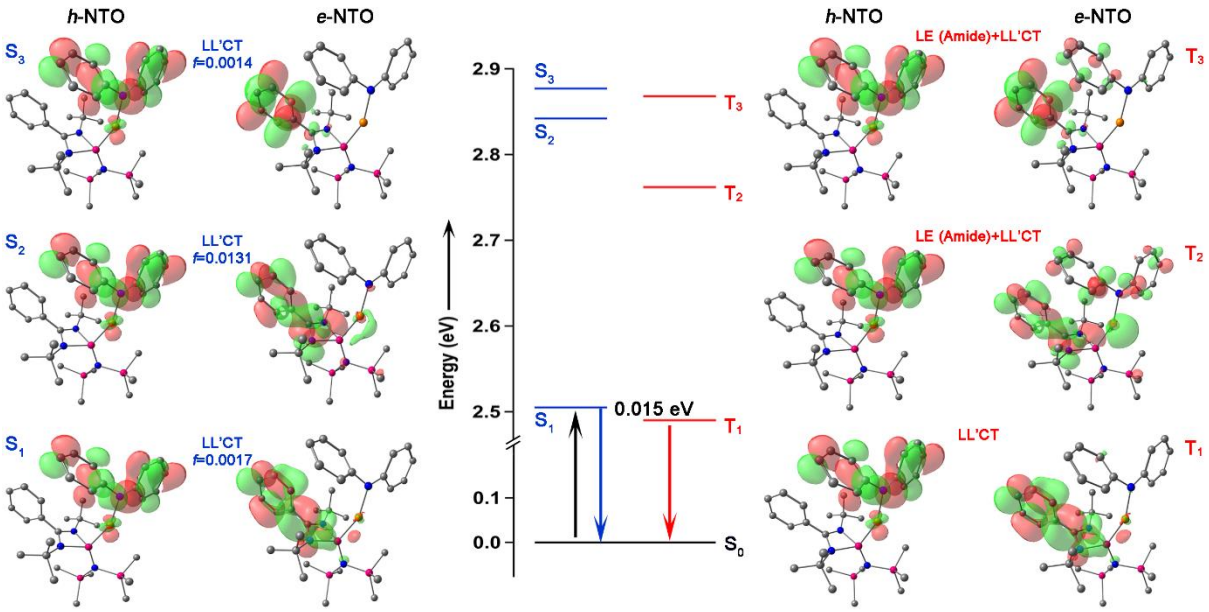

Figure 3.7. Excited-state energies and NTO orbitals for complex **3.2**.

Table 3.3. SOCME values for complexes **3.2-3.5**

In cm^{-1}	3.2	3.3	3.4	3.5
S_0-T_1	7.9545	2.37488	2.45882	2.29984
S_0-T_2	7.44416	10.25825	10.8566	5.36437
S_0-T_3	2.91866	7.92575	7.16796	4.57244
S_1-T_1	0.46434	2.30017	2.26608	0.87546
S_1-T_2	7.46503	4.77955	4.75505	3.55405
S_1-T_3	3.60067	7.5996	7.63303	5.67904

The room temperature lifetime of the complex was found to be 0.45 μs (Figure 3.8a and Table 3.4). The lifetime of this complex sequentially increases upon lowering the temperature to 180 K (Figures 3.6b and 3.8a). However, upon further lowering the temperature to 60 K, the lifetime increases up to ~7.4 μs (Figure 3.8a) and is enormously enhanced in the 60-8 K temperature range (Figures 3.6b and 3.8b). The sharp increment in the lifetime clearly indicates the activation of emissive states with much longer lifetime values within this temperature range, which are essentially triplet states. The temperature dependence of the lifetime represents a Boltzmann-type thermal distribution between a singlet and triplet state under a three-state TADF model. Assuming it is a very fast thermalization process, it can be fitted to equation 1 (Figure 3.6b).[12, 91]

$$\tau_{obs} = \frac{3+ e^{-\frac{\Delta E_{ST}}{k_B T}}}{\frac{3}{\tau(T_1)}+ \frac{1}{\tau(S_1)} e^{-\frac{\Delta E_{ST}}{k_B T}}} \qquad \ldots \text{Eq 1}$$

Where, $\tau_{obs}, k_B, \tau(T_1), \text{and } \tau(S_1)$ represents experimentally observed lifetime, Boltzmann constant, intrinsic lifetime of triplet state, and intrinsic lifetime of singlet state, respectively. ΔE_{ST}, $\tau(T_1), \text{and } \tau(S_1)$ were evaluated from the fitting parameters and found to be 0.01 eV, 250 µs, and 421 ns, respectively. Notably, the experimentally derived ΔE_{ST} in this case matches well with the value obtained from TD-DFT calculations. The absence of any experimentally detectable prompt fluorescence in this complex indicates a significantly high ISC rate. Hence, the observed emission lifetime is solely governed by the thermal population distribution between S_1 and T_1 (Figure 3.6d). At room temperature, the S_1 state is thermally repopulated at the expense of the triplet state population, leading to TADF from the S_1 state having a short lifetime of 0.45 µs. However, at a lower temperature range, thermal reciprocation of the population is restricted, thereby suppressing the delayed emission process, and subsequently, the proportion of phosphorescence is enhanced. The enormous enhancement in the emission intensity at lower temperatures can be attributed to the suppression of the non-radiative decay pathways and the increasing population of the low-energy triplet state. Temperature-dependent gated emission studies can also demonstrate this particular restriction in the thermal reciprocation of the population. Under 20 µs detector delay, the complex shows feeble emission intensity at room temperature, confirming the occurrence of emission from a state with a lower lifetime (Figure 3.6c). Under the same delay, the emission enormously increases at 77 K, indicating that the emission corresponds to a state with a much higher lifetime at lower temperatures (Figure 3.6c). It is worth mentioning that the reasonably short lifetime of this complex falls under the shorter lifetime region of the MAC coordinated Cu-amides.[5, 21] The absolute quantum yield of this TADF-active silylene-Cu-amide emitter was found to be 11.51% with a very radiative rate of 2.22×10^6 s^{-1}, comparable to the carbene analogs.[13, 20, 23] Its notably low quantum yield compared to its contemporary carbene analogs can be attributed to the contributions of metal-centered *d*-orbitals in the electronic transition.[8, 92] In these linear coordination complexes, the involvement of *d*-orbitals in electronic transitions can result in significant Renner-Teller bending distortion of the excited states, reducing emission yield.[8, 92] Nevertheless, a reasonably short lifetime (0.45 µs) of this complex firmly upholds its potential to be utilized in fabricating LED devices and photocatalytic applications.

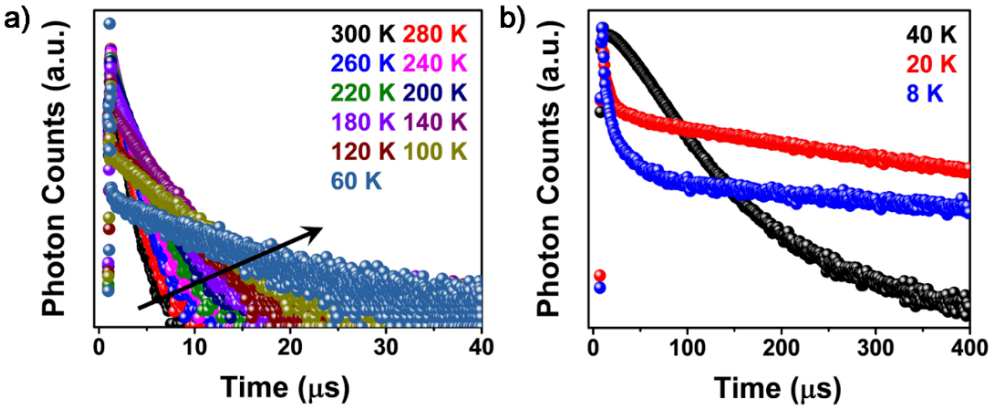

Figure 3.8. PL decay profiles of **3.2** in the temperature range of (a) 300-60 K and (b) 40-8 K.

Table 3.4. Lifetime at different temperatures for **3.2** collected at 560 nm

Temperature (K)	τ_{obs}
300	0.45 μs
280	0.53 μs
260	0.61 μs
240	0.79 μs
220	0.87 μs
200	1.16 μs
180	1.29 μs
140	2.43 μs
120	3.2 μs
100	4.09 μs
60	7.39 μs
40	31.66 μs

3.3.5 Photophysical properties of complexes 3.3-3.5, 3.8, and 3.9.

Complexes **3.3** and **3.4** show bright green emissions under UV light. Under an inert atmosphere, each of them exhibits two successive emission bands, with the emission maximum located at ~450 nm and ~520 nm (Figures 3.9a and 3.9e). In order to resolve the dual emissive nature of these two complexes with respect to their lifetimes, gated emission spectra were collected within the μs timescale. The emission spectra collected at a detector delay of 50 μs show complete depletion of the high-energy (HE) emission band for both complexes, and only the low-energy (LE) bands were obtained (Figures 3.9a and 3.9e). This observation clearly indicates that the two emission bands significantly differ in their emission lifetimes, and the LE band has a much higher lifetime than the HE emission band. We collected the PL decay

profiles at each emission maximum for both complexes to explore further. Lifetime values were found to be 5.77 and 5.23 ns upon collecting the emission at 450 nm for **3.4** and **3.5**, respectively (Figures 3.9d and 3.9h, Table 3.5). When PL decay profiles were collected at 520 nm, the lifetime parameters were found to be 0.41 and 3.37 ms for **3.3** and **3.4**, respectively (Figures 3.9c and 3.9g, Table 3.5). Consequently, the high-energy band is assigned to the fluorescence emission and the low-energy band to the phosphorescence emission.

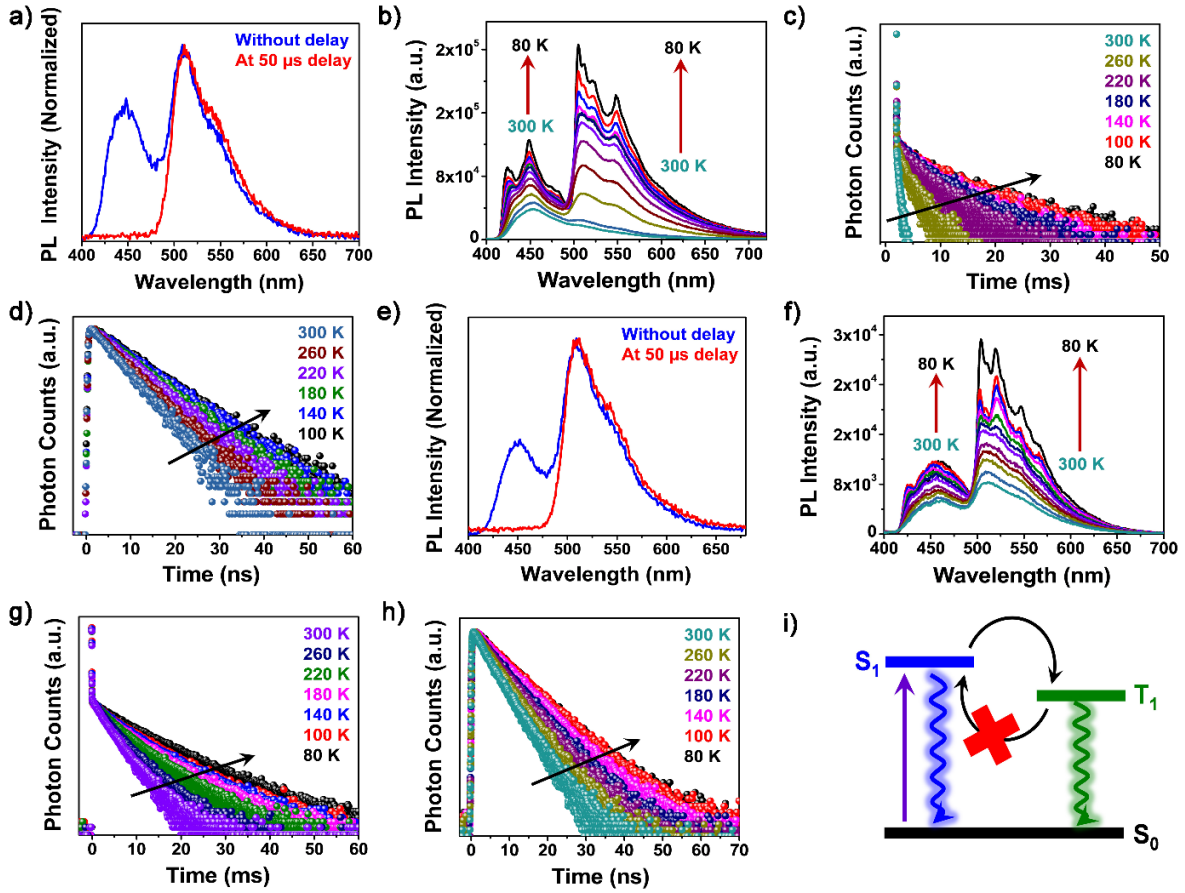

Figure 3.9. (a) Time-gated emission spectra of complex **3.4**; (b) temperature-dependent emission spectra of complex **3.4**; (c) temperature-dependent PL decay profile of complex **3.4** collected at 520 nm; (d) temperature-dependent PL decay profile of complex **3.4** collected at 450 nm, (e) time-gated emission spectra of complex **3.5**; (f) temperature-dependent emission spectra of complex **3.5**; (g) Temperature-dependent PL decay profile of complex **3.5** collected at 520 nm; (h) Temperature-dependent PL decay profile of complex **3.5** collected at 460 nm; and (i) schematic energy diagram for this class of complexes.

Table 3.5. Lifetime at different temperatures for **3.3** and **3.4** collected at 450 and 520 nm

Temperature (K)	Lifetime (ns) collected at 450 nm		Lifetime (ms) collected at 520 nm	
	3.3	3.4	3.3	3.4

300	5.77	5.23	0.41	3.37
260	6.77	5.99	2.16	4.99
220	7.69	6.79	4.44	6.23
180	8.28	7.43	5.56	6.88
140	9.09	8.28	6.16	7.32
100	9.65	9.18	7.86	7.54
80	-	9.11	8.70	8.55

In order to gain insight into the nature of the excited states, TD-DFT calculations were employed. The NTO analysis of these complexes reveals that the electronic structure of the lowest excited singlet (S_1) state is LL'CT in nature, where the electron densities in *e*-NTO and *h*-NTO represent the charge transfer from the π-donor amide to the π-acceptor silylene moiety (Figures 3.10a-b). The lowest excited triplet (T_1) state, on the other hand, represents LE nature, where the electron density is localized over the amide moiety (Figures 3.10a-b). The single-point TD-DFT calculation also suggests the ΔE_{ST} to be reasonably high in these complexes, with a value of 0.44 eV and 0.45 eV for **3.3** and **3.4**, respectively, which is also substantiated by their singlet-triplet dual-emissive nature (Figures 3.10a-b). Because of this intriguing difference in the electronic configuration of the S_1 and T_1 states, a reasonably strong spin-orbit coupling is anticipated between those two states, along with a higher inter-system crossing (ISC) rate.[93] This is also supported by the SOCME obtained for S_1-T_n pairs (n=1-3), which were found to be adequately high (2.26 cm^{-1} to 7.63 cm^{-1}) (Table 3.3). Considering the singlet-triplet dual emission process, we further investigate the thermal distribution of the singlet and triplet state populations in these complexes with the help of temperature-dependent emission studies. Both the HE and LE bands were found to increase with decreasing temperature, from 300 K to 80 K (Figures 3.9b and 3.9f). This indicates that the non-radiative decay pathways get effectively suppressed at lower temperatures, enhancing the emission intensity. However, the extent of enhancement was found to be much higher in the case of the phosphorescence band than that of the singlet emission band (Figures 3.9b and 3.9f). A significant portion of the singlet population that undergoes non-radiative decay at room temperature can participate in the ISC process at lower temperatures to populate the lowest triplet state. Hence, at lower temperatures, the suppression of non-radiative decay pathways can concomitantly pave the way for an increase in the ISC rate between the singlet and triplet states. As a result, the temperature-dependent relative increment in the phosphorescence emission is much higher than that of the singlet emission.

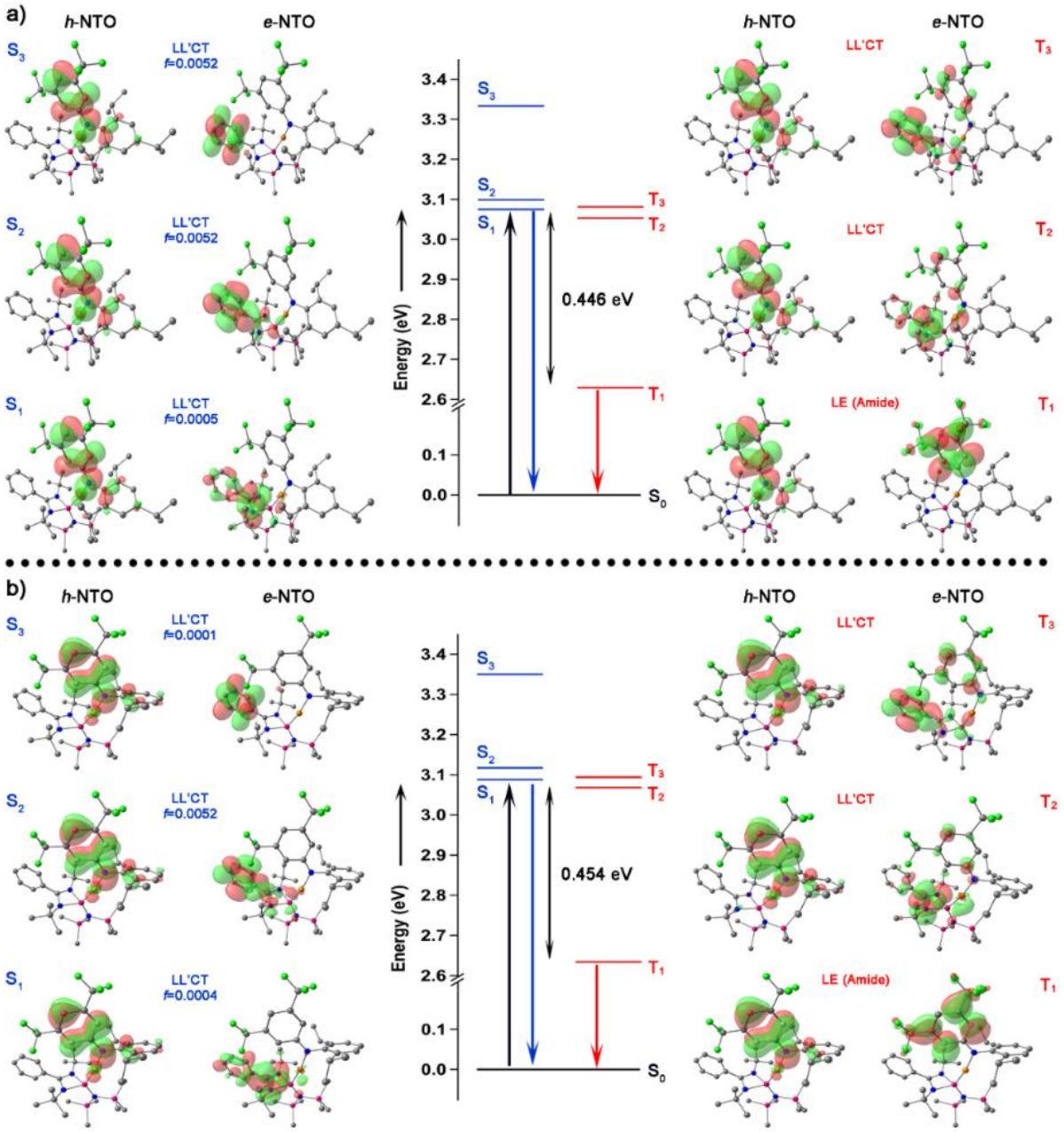

Figure 3.10. (a) Excited-state energies and NTO orbitals for complex **3.3**; (b) Excited-state energies and NTO orbitals for complex **3.4**.

At 300 K, the PL decay profile collected at 450 nm shows no longer lifetime components (Figures 3.9d and 3.9h, Table 3.5). Hence, the singlet states in these complexes emit only through prompt fluorescence and do not participate in any reverse intersystem crossing (RISC), effectively ruling out the possibility of thermally activated delayed fluorescence (TADF). The lifetime of the singlet state was observed to increase up to the range of ~9.1-9.6 ns when the temperature was decreased to 80 K, which is attributed to the suppressed non-radiative decay channels (Figures 3.9d and 3.9h). Furthermore, the absence of any longer lifetime component at 80 K confirms that emission from higher triplet states is not

present even at low temperatures (Figures 3.9d and 3.9h). Interestingly, at 300 K, the decay profile collected at 520 nm exhibited an undetectable fast component with a significant contribution, followed by the millisecond decay components (Figures 3.9c and 3.9g). Here, the appearance of an undetectable fast component is attributed to the prompt fluorescence that comes from the long tail of the broad singlet emission band overlapping with the triplet emission. It should be noted that the charge-transfer nature of the S_1 (^{1}LL'CT) state is evident from the higher broadness of the singlet emission band, which is well-corroborated with the DFT results. As the temperature decreases to 80 K, the lifetime of the triplet state undergoes a sequential increase up to the range of ~8.5-8.7 ms (Figures 3.9c and 3.9g), which is a simultaneous effect of suppressed non-radiative decay pathways and a higher ISC rate at lower temperatures. Interestingly, the emissive behavior of complex **3.5** broadly differs from that of complex **3.3** and **3.4**. Under inert atmospheric conditions, similar dual emissions were obtained in this complex but with a significantly suppressed HE band (Figure 3.11a). In addition, the maximum of the HE band and LE band are located at ~425 nm and ~480 nm, respectively, which are largely blue-shifted compared to the previous complexes (Figure 3.11a). At room temperature, the emission collected at 425 nm shows a lifetime value of 5.49 ns. It lacks any longer microsecond or millisecond component, confirming the band to emerge from a singlet state through prompt fluorescence (Figure 3.11c and Table 3.6). The PL decay profile at 480 nm yields a lifetime value of 0.63 ms, therefore confirming the band to emerge from a triplet state *via* phosphorescence emission (Figure 3.11b and Table 3.6).

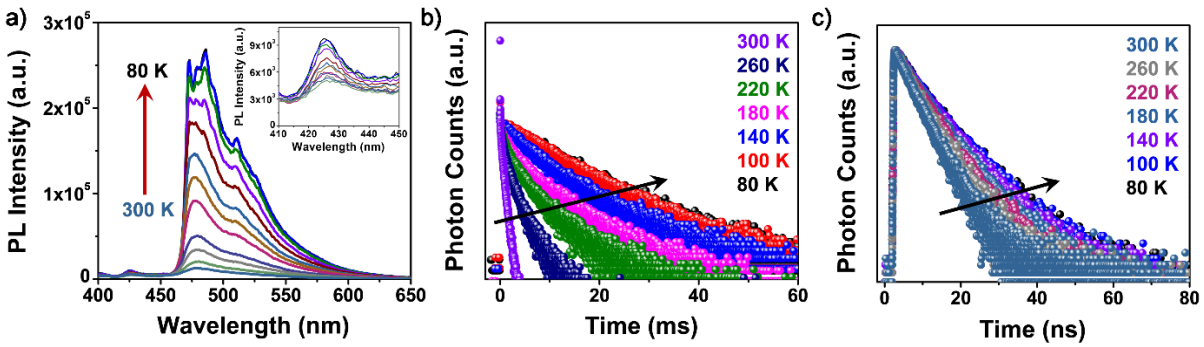

Figure 3.11. (a) Temperature-dependent emission spectra of complex **3.5**; (b) temperature-dependent PL decay profile of complex **3.5** collected at 485 nm; and (c) temperature-dependent PL decay profile of complex **3.5** collected at 425 nm.

A large blue-shift in the spectral bands can be attributed to an increased number of -CF_3 groups. -CF_3 is a strong electron-withdrawing group, which stabilizes the HOMO to a much greater extent, leading to an energetically increased HOMO-LUMO gap. As a result, the

energy of the LL'CT state is highly increased, and the corresponding emission band is blue-shifted. This is also supported by the NTO calculations where the ΔE_{ST} value is 0.52 eV, much higher than **3.3** and **3.4**. The large blue-shift in the singlet emission band with an increasing electron-withdrawing effect from **3.4** to **3.5** also substantiates that the emission emerges from an LL'CT state. Similar to its predecessor complexes, the LE triplet band of this complex was found to be massively enhanced upon lowering the temperature sequentially to 80 K (Figure 3.11a). Upon lowering the temperature to 80 K, the triplet and singlet state lifetimes increased to ~8.84 ms and ~9.65 ns, respectively (Figures 3.11b-c, Table 3.6).

Table 3.6. Lifetime at different temperatures for **3.5** collected at 425 nm

Temperature (K)	Collected at 425 nm		Collected at 480 nm	
	Lifetime	Lifetime	Lifetime	Lifetime
300	-	5.49 ns	0.26 ms	0.63 ms
260	-	6.10 ns	0.65 ms	2.30 ms
220	-	6.73 ns	1.28 ms	5.36 ms
180	-	7.32 ns	1.68 ms	6.56 ms
140	4.46 ns	8.96 ns	-	6.67 ms
100	4.26 ns	9.45 ns	-	8.54 ms
80	4.76 ns	9.65 ns	-	8.84 ms

This increment in the emission lifetime can be attributed to a collective effect of suppressed non-radiative decay pathways and increased ISC rate at low temperatures. The significant suppression of the singlet emission compared to the previous complexes can be addressed with the help of TD-DFT calculations along with references to El-Sayed's rule.[93] In **3.3** and **3.4**, the NTO calculations of the first three lowest triplet states (T_1-T_3) suggest the electronic structure of T_1 to be completely different from T_2 and T_3 (Figure 3.10). T_1 possesses a pure LE (amide-centered) character, and T_2 and T_3 possess an LL'CT character (Figure 3.10). As the S_1 state comprises a pure LL'CT character, its electronic wave function significantly overlaps with that of the T_2 and T_3 states. As a result, according to the El-Sayed rule, the S_1 state can only participate in an effective ISC process with the T_1 state. On the other hand, in **3.5**, all the triplet LL'CT states are much higher in energy due to the strong electron-withdrawing effect of four -CF_3 groups (Figure 3.12). As a result, low-lying triplet states (T_1-T_3) are predominantly LE in nature (Figure 3.12). Here, the S_1 state, which possesses LL'CT

character, can simultaneously participate in the ISC process with T_1, T_2, and T_3 states, leading to a feeble emission yield from the singlet state through prompt fluorescence.

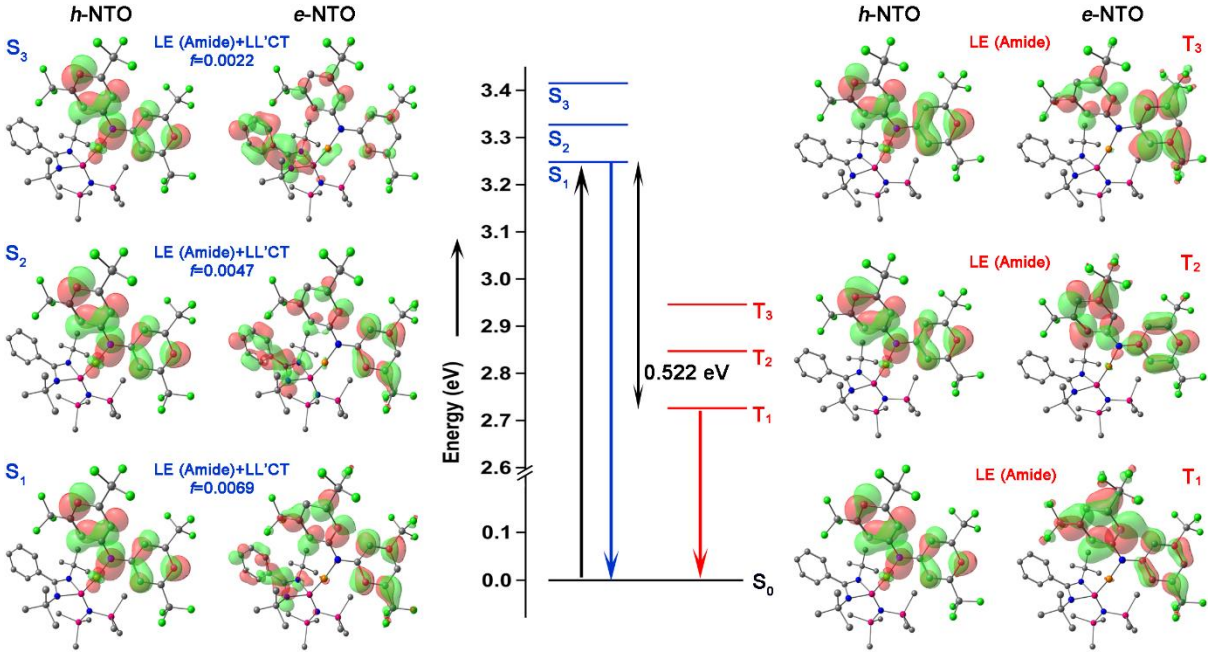

Figure 3.12. Excited-state energies and NTO orbitals for complex **3.5**.

As a proof of concept for this prodigious SiMA emitters, we further extend the work by tailoring the silylene and the amide frameworks of the complex. The silylene moiety was replaced by similarly functionalized NHC, and we obtained complexes by structural modulations named as complexes **3.8** and **3.9**. Complexes **3.8** and **3.9** show similar absorption features with peaks at 300 nm and 340 nm and a shoulder band in 360-420 nm region. The peak at 340 nm and the shoulder region can be attributed to the excitation of the low-lying LL'CT states, which also matches the nature of excited states from NTO analysis and simulated absorption spectra. The peak at 300 nm and the associated band can be assigned to the intra-ligand excitations. All three complexes exhibited dual singlet-triplet emission behavior similar to the respective silylene complexes (Figure 3.13). The fluorescence lifetimes for complexes **3.8** and **3.9** were determined to be 4.54 and 4.3 ns, respectively (Figures 3.13d and 3.13h, Table 3.7). The phosphorescence lifetimes were found to be 1.44 and 2.1 ms, respectively (Figures 3.13c and 3.13g, Table 3.7). Notably, the phosphorescence lifetimes obtained from these emitters are much shorter than those of the previously reported dual-emissive CMA emitters.[27, 94] The shorter lifetime of these complexes also shows that the extent of spin-orbit coupling between the ground state and low-lying triplet states is reasonably high, which is supported by

the T_1-S_0 values obtained from DFT calculations. The shorter lifetime of triplet states has a significant role in suppressing the efficiency roll-off effects in OLED devices.[95]

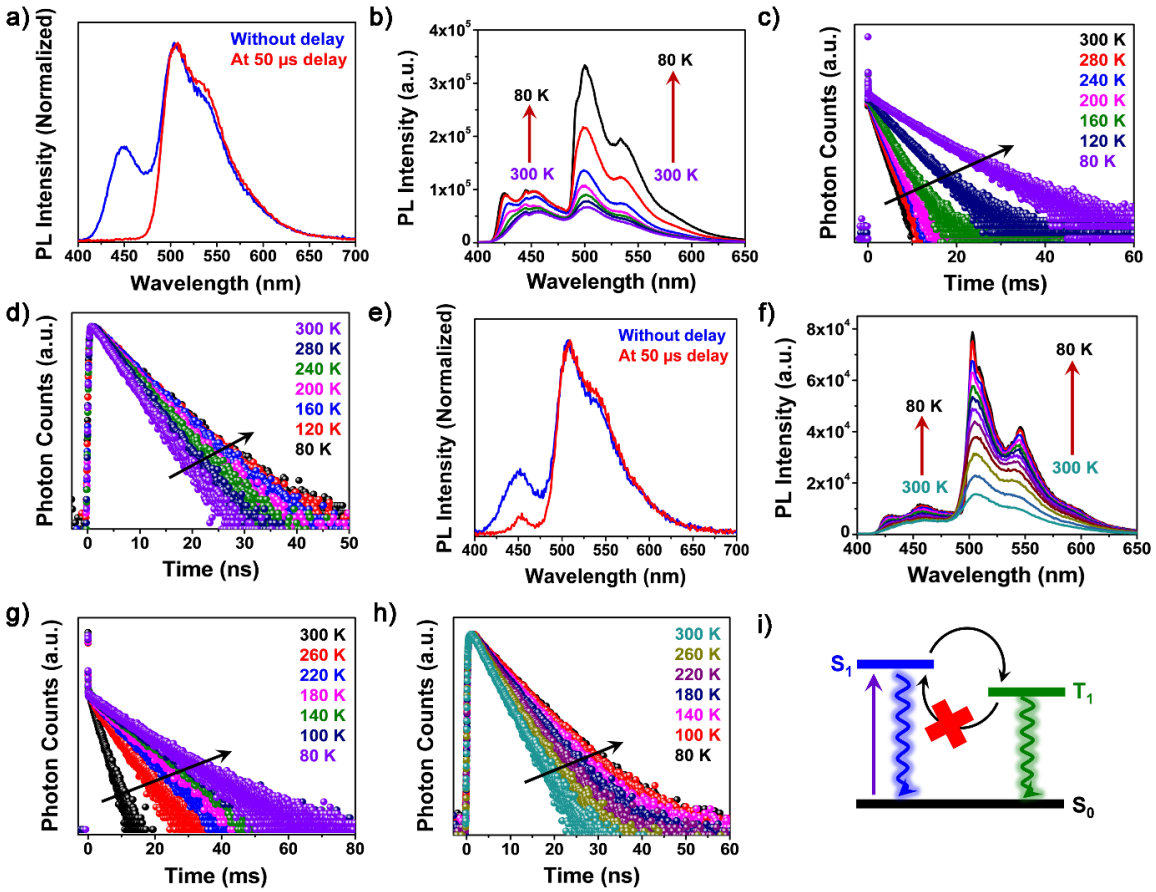

Figure 3.13. (a) Time-gated emission spectra of complex **3.8**; (b) temperature-dependent emission spectra of complex **3.8**; (c) temperature-dependent PL decay profile of complex **3.8** collected at 520 nm; (d) temperature-dependent PL decay profile of complex **3.8** collected at 450 nm; (e) time-gated emission spectra of complex **3.9**; (f) temperature-dependent emission spectra of complex **3.9**; (g) Temperature-dependent PL decay profile of complex **3.9** collected at 520 nm; (h) Temperature-dependent PL decay profile of complex **3.9** collected at 450 nm; and (i) schematic energy diagram for this class of complexes.

Table 3.7. Lifetime at different temperatures for **3.8** and **3.9** collected at 450 nm

Lifetime of 3.8			**Lifetime of 3.9**		
Temperature (K)	**Collected at 450 nm**	**Collected at 520 nm**	**Temperature (K)**	**Collected at 450 nm**	**Collected at 520 nm**
300	4.54 ns	1.44 ms	300	4.30 ns	2.10 ms
280	4.92 ns	1.62 ms	260	4.94 ns	4.90 ms
240	5.53 ns	1.86 ms	220	5.58 ns	7.18 ms

200	5.83 ns	2.09 ms	180	6.22 ns	8.48 ms
160	6.48 ns	2.66 ms	140	6.82 ns	9.36 ms
120	6.59 ns	4.28 ms	100	7.43 ns	10.14 ms
80	6.64 ns	7.21 ms	80	7.58 ns	10.42 ms

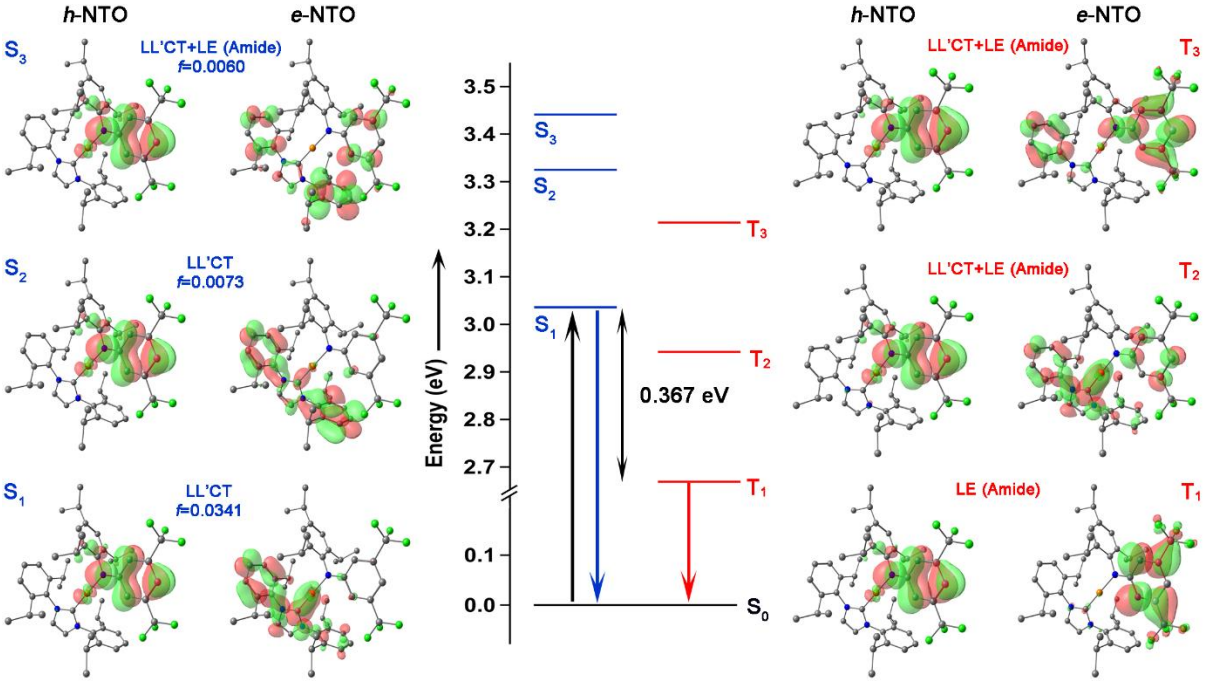

Figure 3.14. Excited-state energies and NTO orbitals for complex **3.8**.

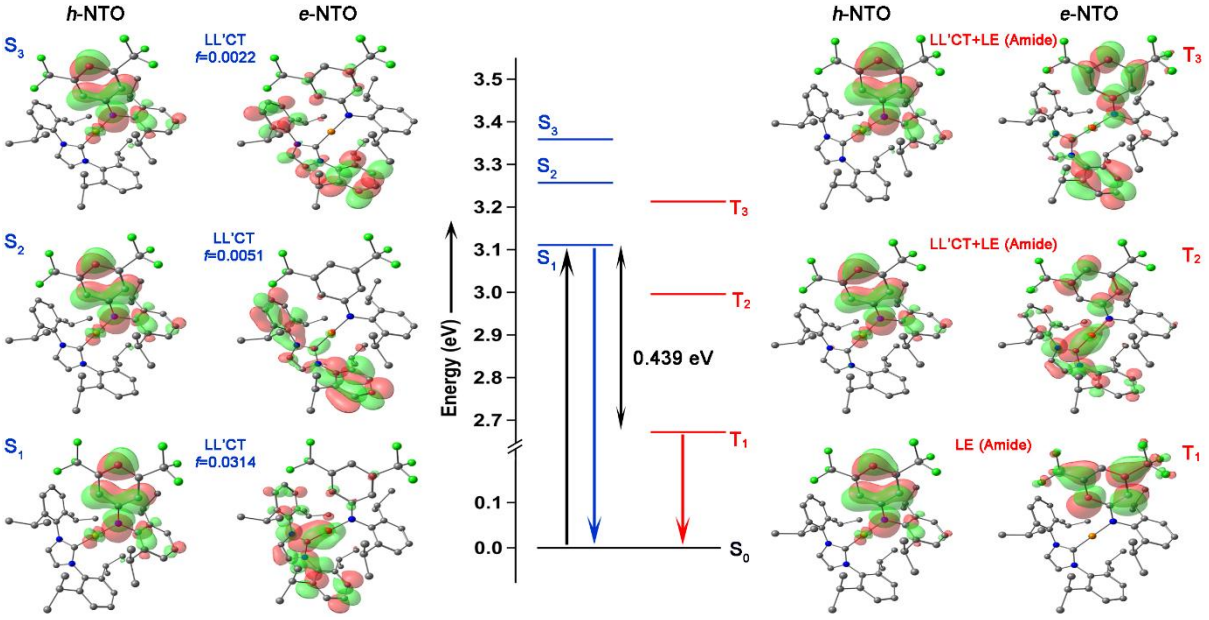

Figure 3.15. Excited-state energies and NTO orbitals for complex **3.9**.

3.3.6 From TADF-active $^{1/3}$LL'CT emission to ^{1}LL'CT-^{3}LE dual emission: The role of -CF_3 groups.

Sequential insertion of strong electron-withdrawing -CF_3 groups in these complexes has a key role in introducing this kind of extreme versatility in the emission mechanism, which is also observed by Romanov and co-workers in designing carbene Au-amide emitter.[96] Previously, we discussed the role of electron-withdrawing groups in increasing the HOMO-LUMO energy gap, where we mentioned the effect of these -CF_3 groups in increasing the energy of LL'CT states. The electron-withdrawing effect is absent in **3.2**, significantly stabilizing the $^{1/3}$LL'CT states. As a result, these charge-transfer states become energetically lower than the ^{3}LE states. This effect is also reflected in the single-point energy calculations, where it was brought about that the S_1 and T_1 states of **3.2** are LL'CT in nature, while the higher energy triplet states are partially LE in nature (Figure 3.7). Therefore, the resultant emission is derived from S_1 and T_1 through the TADF mechanism due to the small exchange energy mediated by a high charge-transfer nature in the lowest excited states. The energy of LL'CT states sequentially increases with an inclining electron-withdrawing effect in **3.3/3.8**, **3.4/3.9**, and **3.5**. As a result, the lowest triplet state becomes ^{3}LE in nature, while the high-energy triplet states are of LL'CT character in these complexes (Figures 3.10, 3.12, 3.14, and 3.15). The lowest singlet state retains its LL'CT character here but is at much higher energy than the ^{3}LE (T_1) state. This is also supported by TD-DFT calculations, which revealed that the S_1 and T_1 have LL'CT and LE characters, respectively. For **3.3**, **3.4**, and **3.5**, the energy gaps were found to be 0.44 eV, 0.46 eV, and 0.52 eV, respectively. For the carbene complexes, the energy gaps are 0.37 eV and 0.44 eV, respectively, for **3.8** and **3.9**. Consequently, the S_1 and T_1 states in these complexes are found to be involved in an efficient ISC process. However, the RISC process is energetically restricted, and the complexes behave as singlet-triplet dual-emitters.

3.4 Conclusion.

In conclusion, we have synthesized a series of copper amide emitters utilizing NHSi, exhibiting TADF and dual emission characteristics modulated by functionalization at the amide moiety. Additionally, analogous NHC-based copper amides were synthesized. Notably, after 40 years of West and co-workers' first isolation of bottleable NHSis, the use of NHSis is majorly restricted in small molecule activation and transition metal-based homogeneous catalysis. Herein, we extend the concept of NHSi-based Cu amide complexes for their photophysical properties. Nevertheless, various carbene-coordinated Cu complexes have found huge room for their fascinating optoelectronic properties. Despite the extensive investigation into carbene-coordinated copper complexes and their remarkable optoelectronic properties, our work

suggests significant potential for using NHSis in this field remains. Thus, we anticipate that our findings in this chapter will be the beginning of the prodigious use of NHSis in this domain.

3.5 Bibliography.

(1) Jazzar, R.; Soleilhavoup, M.; Bertrand, G. Cyclic (alkyl)-and (aryl)-(amino) carbene coinage metal complexes and their applications. *Chem. Rev.* **2020**, *120*, 4141-4168.
(2) Beaudelot, J.; Oger, S.; Perusko, S.; Phan, T.-A.; Teunens, T.; Moucheron, C.; Evano, G. Photoactive copper complexes: properties and applications. *Chem. Rev.* **2022**, *122*, 16365-16609.
(3) Amouri, H. Luminescent complexes of platinum, iridium, and coinage metals containing N-heterocyclic carbene ligands: Design, structural diversity, and photophysical properties. *Chem. Rev.* **2023**, *123*, 230-270.
(4) Hong, G.; Gan, X.; Leonhardt, C.; Zhang, Z.; Seibert, J.; Busch, J. M.; Bräse, S. A brief history of OLEDs—emitter development and industry milestones. *Adv. Mater.* **2021**, *33*, 2005630.
(5) Ying, A.; Gong, S. A Rising Star: Luminescent Carbene-Metal-Amide Complexes. *Chem. Eur. J.* **2023**, *29*, e202301885.
(6) Zhang, Y.; Schulz, M.; Wächtler, M.; Karnahl, M.; Dietzek, B. Heteroleptic diimine–diphosphine Cu (I) complexes as an alternative towards noble-metal based photosensitizers: Design strategies, photophysical properties and perspective applications. *Coord. Chem. Rev.* **2018**, *356*, 127-146.
(7) Chen, X.-L.; Lin, C.-S.; Wu, X.-Y.; Yu, R.; Teng, T.; Zhang, Q.-K.; Zhang, Q.; Yang, W.-B.; Lu, C.-Z. Highly efficient cuprous complexes with thermally activated delayed fluorescence and simplified solution process OLEDs using the ligand as host. *J. Mater. Chem. C* **2015**, *3*, 1187-1195.
(8) Wegeberg, C.; Wenger, O. S. Luminescent first-row transition metal complexes. *JACS Au* **2021**, *1*, 1860-1876.
(9) Lee, L. C.-C.; Lo, K. K.-W. Luminescent and photofunctional transition metal complexes: From molecular design to diagnostic and therapeutic applications. *J. Am. Chem. Soc.* **2022**, *144*, 14420-14440.
(10) Zhang, Q.; Li, B.; Huang, S.; Nomura, H.; Tanaka, H.; Adachi, C. Efficient blue organic light-emitting diodes employing thermally activated delayed fluorescence. *Nat. Photonics* **2014**, *8*, 326-332.
(11) Ito, A.; Iwamura, M.; Sakuda, E. Excited-state dynamics of luminescent transition metal complexes with metallophilic and donor–acceptor interactions. *Coord. Chem. Rev.* **2022**, *467*, 214610.
(12) Hamze, R.; Peltier, J. L.; Sylvinson, D.; Jung, M.; Cardenas, J.; Haiges, R.; Soleilhavoup, M.; Jazzar, R.; Djurovich, P. I.; Bertrand, G.; Thompson, M. E. Eliminating nonradiative decay in Cu(I) emitters: > 99% quantum efficiency and microsecond lifetime. *Science* **2019**, *363*, 601-606.
(13) Chotard, F.; Sivchik, V.; Linnolahti, M.; Bochmann, M.; Romanov, A. S. Mono-versus Bicyclic Carbene Metal Amide Photoemitters: Which Design Leads to the Best Performance? *Chem. Mater.* **2020**, *32*, 6114-6122.
(14) Gernert, M.; Balles-Wolf, L.; Kerner, F.; Müller, U.; Schmiedel, A.; Holzapfel, M.; Marian, C. M.; Pflaum, J.; Lambert, C.; Steffen, A. Cyclic (amino)(aryl) carbenes enter the field of chromophore ligands: Expanded π system leads to unusually deep red emitting CuI compounds. *J. Am. Chem. Soc.* **2020**, *142*, 8897-8909.

(15) Lin, S.; Peng, Q.; Ou, Q.; Shuai, Z. Strong Solid-State Fluorescence Induced by Restriction of the Coordinate Bond Bending in Two-Coordinate Copper (I)–Carbene Complexes. *Inorg. Chem.* **2019**, *58*, 14403-14409.
(16) Song, X.-F.; Li, Z.-W.; Chen, W.-K.; Gao, Y.-J.; Cui, G. Thermally Activated Delayed Fluorescence Mechanism of a Bicyclic "Carbene–Metal–Amide" Copper Compound: DFT/MRCI Studies and Roles of Excited-State Structure Relaxation. *Inorg. Chem.* **2022**, *61*, 7673-7681.
(17) Spence, K. A.; Chari, J. V.; Di Niro, M.; Susick, R. B.; Ukwitegetse, N.; Djurovich, P. I.; Thompson, M. E.; Garg, N. K. π-Extension of heterocycles *via* a Pd-catalyzed heterocyclic aryne annulation: π-extended donors for TADF emitters. *Chem. Sci.* **2022**, *13*, 5884-5892.
(18) Romanov, A. S.; Yang, L.; Jones, S. T.; Di, D.; Morley, O. J.; Drummond, B. H.; Reponen, A. P.; Linnolahti, M.; Credgington, D.; Bochmann, M. Dendritic carbene metal carbazole complexes as photoemitters for fully solution-processed OLEDs. *Chem. Mater.* **2019**, *31*, 3613-3623.
(19) Conaghan, P. J.; Matthews, C. S.; Chotard, F.; Jones, S. T.; Greenham, N. C.; Bochmann, M.; Credgington, D.; Romanov, A. S. Highly efficient blue organic light-emitting diodes based on carbene-metal-amides. *Nat. Commun.* **2020**, *11*, 1758.
(20) Hamze, R.; Shi, S.; Kapper, S. C.; Ravinson, D. S. M.; Estergreen, L.; Jung, M.-C.; Tadle, A. C.; Haiges, R.; Djurovich, P. I.; Peltier, J. L.; Jazzar, R.; Bertrand, G.; Bradforth, S. E.; Thompson, M. E. "Quick-silver" from a systematic study of highly luminescent, two-coordinate, d10 coinage metal complexes. *J. Am. Chem. Soc.* **2019**, *141*, 8616-8626.
(21) Schaab, J.; Shi, S.; Jung, M. C.; Coburn, C.; Tadle, A.; Sylvinson, D. M. R.; Djurovich, P. I.; Forrest, S. R.; Thompson, M. E. Highly efficient photo-and electroluminescence from two-coordinate Cu (I) complexes featuring nonconventional N-heterocyclic carbenes. *J. Am. Chem. Soc* **2023**, *145*, 746-747.
(22) Muniz, C. N.; Archer, C. A.; Applebaum, J. S.; Alagaratnam, A.; Schaab, J.; Djurovich, P. I.; Thompson, M. E. Two-coordinate coinage metal complexes as solar photosensitizers. *J. Am. Chem. Soc.* **2023**, *145*, 13846-13857.
(23) Muniz, C. N.; Schaab, J.; Razgoniaev, A.; Djurovich, P. I.; Thompson, M. E. π-Extended ligands in two-coordinate coinage metal complexes. *J. Am. Chem. Soc.* **2022**, *144*, 17916-17928.
(24) Ying, A.; Huang, Y.-H.; Lu, C.-H.; Chen, Z.; Lee, W.-K.; Zeng, X.; Chen, T.; Cao, X.; Wu, C.-C.; Gong, S. High-Efficiency Red Electroluminescence Based on a Carbene–Cu (I)–Acridine Complex. *ACS Appl. Mater. Interfaces* **2021**, *13*, 13478-13486.
(25) Ying, A.; Tan, Y.; Gong, S. Highly Efficient Copper (I) Emitters Supported by Secondary Metal-Ligand Interactions. *Adv. Opt. Mater.* **2024**, 2303333.
(26) Wang, H. J.; Liu, Y.; Yu, B.; Song, S. Q.; Zheng, Y. X.; Liu, K.; Chen, P.; Wang, H.; Jiang, J.; Li, T. Y. A Configurationally Confined Thermally Activated Delayed Fluorescent Two-Coordinate CuI Complex for Efficient Blue Electroluminescence. *Angew. Chem. Int. Ed.* **2023**, *62*, e202217195.
(27) Li, J.; Wang, L.; Zhao, Z.; Li, X.; Yu, X.; Huo, P.; Jin, Q.; Liu, Z.; Bian, Z.; Huang, C. Two-coordinate copper (I)/NHC complexes: Dual emission properties and ultralong room-temperature phosphorescence. *Angew. Chem. Int. Ed.* **2020**, *59*, 8210-8217.
(28) Ma, J.; Schaab, J.; Paul, S.; Forrest, S. R.; Djurovich, P. I.; Thompson, M. E. Luminescent Bimetallic Two-Coordinate Gold (I) Complexes Utilizing Janus Carbenes. *J. Am. Chem. Soc.* **2023**, *145*, 20097-20108.
(29) Ruduss, A.; Jece, A.; Stucere, K. A.; Chen, K.-W.; Turovska, B.; Belyakov, S.; Vembris, A.; Chang, C.-H.; Traskovskis, K. Sulfonyl-functionalized benzo [d] imidazo [5, 1-b] thiazole-based carbenes as building blocks for two-coordinate Cu (i) complexes exhibiting fast and efficient thermally activated delayed fluorescence. *J. Mater. Chem. C* **2024**, *12*, 2968-2980.

(30) Ruduss, A.; Turovska, B.; Belyakov, S.; Stucere, K. A.; Vembris, A.; Baryshnikov, G.; Ågren, H.; Lu, J.-C.; Lin, W.-H.; Chang, C.-H. Thiazoline Carbene–Cu (I)–Amide complexes: Efficient White Electroluminescence from Combined Monomer and Excimer Emission. *ACS Appl. Mater. Interfaces* **2022**, *14*, 15478-15493.
(31) Li, T.-Y.; Schaab, J.; Djurovich, P. I.; Thompson, M. E. Toward rational design of TADF two-coordinate coinage metal complexes: understanding the relationship between natural transition orbital overlap and photophysical properties. *J. Mater. Chem. C* **2022**, *10*, 4674-4683.
(32) Gu, Q.; Chotard, F.; Eng, J.; Reponen, A.-P. M.; Vitorica-Yrezabal, I. J.; Woodward, A. W.; Penfold, T. J.; Credgington, D.; Bochmann, M.; Romanov, A. S. Excited-state lifetime modulation by twisted and tilted molecular design in carbene-metal-amide photoemitters. *Chem. Mater.* **2022**, *34*, 7526-7542.
(33) Romanov, A. S.; Jones, S. T.; Gu, Q.; Conaghan, P. J.; Drummond, B. H.; Feng, J.; Chotard, F.; Buizza, L.; Foley, M.; Linnolahti, M.; Credgington, D.; Bochmann, M. Carbene metal amide photoemitters: tailoring conformationally flexible amides for full color range emissions including white-emitting OLED. *Chem. Sci.* **2020**, *11*, 435-446.
(34) Ying, A.; Ai, Y.; Yang, C.; Gong, S. Aggregation-Dependent Circularly Polarized Luminescence and Thermally Activated Delayed Fluorescence from Chiral Carbene-CuI-Amide Enantiomers. *Angew. Chem. Int. Ed.* **2022**, *61*, e202210490.
(35) Muthig, A. M.; Wieland, J.; Lenczyk, C.; Koop, S.; Tessarolo, J.; Clever, G. H.; Hupp, B.; Steffen, A. Towards Fast Circularly Polarized Luminescence in 2-Coordinate Chiral Mechanochromic Copper (I) Carbene Complexes. *Chem. Eur. J.* **2023**, *29*, e202300946.
(36) Li, T.-Y.; Zheng, S.-J.; Djurovich, P. I.; Thompson, M. E. Two-Coordinate Thermally Activated Delayed Fluorescence Coinage Metal Complexes: Molecular Design, Photophysical Characters, and Device Application. *Chem. Rev.* **2024**, *124*, 4332-4392.
(37) Obeid, N. M.; Klemmer, L.; Maus, D.; Zimmer, M.; Jeck, J.; Bejan, I.; White, A. J. P.; Huch, V.; Jung, G.; Scheschkewitz, D. (Oligo)aromatic species with one or two conjugated Si□Si bonds: near-IR emission of anthracenyl-bridged tetrasiladiene. *Dalton Trans.* **2017**, *46*, 8839-8848.
(38) Kobayashi, M.; Matsuo, T.; Fukunaga, T.; Hashizume, D.; Fueno, H.; Tanaka, K.; Tamao, K. Air-Stable, Room-Temperature Emissive Disilenes with π-Extended Aromatic Groups. *J. Am. Chem. Soc.* **2010**, *132*, 15162-15163.
(39) Kobayashi, M.; Hayakawa, N.; Matsuo, T.; Li, B.; Fukunaga, T.; Hashizume, D.; Fueno, H.; Tanaka, K.; Tamao, K. (Z)-1,2-Di(1-pyrenyl)disilene: Synthesis, Structure, and Intramolecular Charge-Transfer Emission. *J. Am. Chem. Soc.* **2016**, *138*, 758-761.
(40) Hayakawa, N.; Nishimura, S.; Kazusa, N.; Shintani, N.; Nakahodo, T.; Fujihara, H.; Hoshino, M.; Hashizume, D.; Matsuo, T. π-Conjugation between a Si═Si Double Bond and Thiophene Rings: Synthesis, Structural Characteristics, and Photophysical Properties of 1,2-Bis(thiophen-2-yl)disilene and 1,2-Bis(2,2′-bithiophen-5-yl)disilene. *Organometallics* **2017**, *36*, 3226-3233.
(41) Denk, M.; Lennon, R.; Hayashi, R.; West, R.; Belyakov, A. V.; Verne, H. P.; Haaland, A.; Wagner, M.; Metzler, N. Synthesis and Structure of a Stable Silylene. *J. Am. Chem. Soc.* **1994**, *116*, 2691-2692.
(42) Haaf, M.; Schmedake, T. A.; West, R. Stable silylenes. *Acc. Chem. Res.* **2000**, *33*, 704-714.
(43) Shan, C. K.; Yao, S. L.; Driess, M. Where silylene-silicon centres matter in the activation of small molecules. *Chem. Soc. Rev.* **2020**, *49*, 6733-6754.
(44) Raoufmoghaddam, S.; Zhou, Y.-P.; Wang, Y.; Driess, M. N-heterocyclic silylenes as powerful steering ligands in catalysis. *J. Organomet. Chem.* **2017**, *829*, 2-10.

(45) Wang, L.; Li, Y.; Li, Z.; Kira, M. Isolable silylenes and their diverse reactivity. *Coord. Chem. Rev.* **2022**, *457*, 214413-214441.
(46) Jutzi, P.; Holtmann, U.; Kanne, D.; Krüger, C.; Blom, R.; Gleiter, R.; Hyla-Kryspin, I. Decamethylsilicocene — The first stable silicon(II) compound: Synthesis, structure, and bonding. *Chem. Ber.* **1989**, *122*, 1629-1639.
(47) So, C. W.; Roesky, H. W.; Magull, J.; Oswald, R. B. Synthesis and characterization of [PhC(N^{t}Bu)$_2$]SiCl: A stable monomeric chlorosilylene. *Angew. Chem. Int. Ed.* **2006**, *45*, 3948-3950.
(48) Kira, M.; Ishida, S.; Iwamoto, T.; Kabuto, C. The first isolable dialkylsilylene. *J. Am. Chem. Soc.* **1999**, *121*, 9722-9723.
(49) Asay, M.; Inoue, S.; Driess, M. Aromatic Ylide-Stabilized Carbocyclic Silylene. *Angew. Chem. Int. Ed.* **2011**, *50*, 9589-9592.
(50) Rekken, B. D.; Brown, T. M.; Fettinger, J. C.; Tuononen, H. M.; Power, P. P. Isolation of a Stable, Acyclic, Two-Coordinate Silylene. *J. Am. Chem. Soc.* **2012**, *134*, 6504-6507.
(51) Protchenko, A. V.; Birjkumar, K. H.; Dange, D.; Schwarz, A. D.; Vidovic, D.; Jones, C.; Kaltsoyannis, N.; Mountford, P.; Aldridge, S. A Stable Two-Coordinate Acyclic Silylene. *J. Am. Chem. Soc.* **2012**, *134*, 6500-6503.
(52) Rosas-Sanchez, A.; Alvarado-Beltran, I.; Baceiredo, A.; Saffon-Merceron, N.; Massou, S.; Branchadell, V.; Kato, T. Exceptionally Strong Electron-Donating Ability of Bora-Ylide Substituent vis-a-vis Silylene and Silylium Ion. *Angew. Chem. Int. Ed.* **2017**, *56*, 10549-10554.
(53) Fujimori, S.; Inoue, S. Small Molecule Activation by Two-Coordinate Acyclic Silylenes. *Eur. J. Inorg. Chem.* **2020**, *2020*, 3131-3142.
(54) Guthardt, R.; Jones, C. A bromo (boryloxy) silylene and its heavier analogues. *Chem. Commun.* **2024**, *60*, 1583-1586.
(55) Roy, M. M.; Ferguson, M. J.; McDonald, R.; Zhou, Y.; Rivard, E. A vinyl silylsilylene and its activation of strong homo-and heteroatomic bonds. *Chem. Sci.* **2019**, *10*, 6476-6481.
(56) Garg, P.; Carpentier, A.; Douair, I.; Dange, D.; Jiang, Y.; Yuvaraj, K.; Maron, L.; Jones, C. Activation of CO Using a 1,2-Disilylene: Facile Synthesis of an Abnormal N-Heterocyclic Silylene. *Angew. Chem. Int. Ed.* **2022**, *61*, e202201705.
(57) Kushvaha, S. K.; Kallenbach, P.; Rohman, S. S.; Pandey, M. K.; Hendi, Z.; Rüttger, F.; Herbst-Irmer, R.; Stalke, D.; Parameswaran, P.; Roesky, H. W. A Neutral Planar Four-Membered Si2B2 2π-Aromatic Ring. *J. Am. Chem. Soc.* **2023**, *145*, 25523-25527.
(58) Fan, J.; Yue, L.; Liu, C.; Rao, B.; Zhou, G.; Li, A.; Su, B. Isolation of Fluorescent 2π-Aromatic 1,3-Disiladiboretenes. *J. Am. Chem. Soc.* **2024**, *146*, 39-44.
(59) Deng, C.-L.; Obi, A. D.; Tra, B. Y. E.; Sarkar, S. K.; Dickie, D. A.; Gilliard, R. J. Air- and photo-stable luminescent carbodicarbene-azaboraacenium ions. *Nat. Chem.* **2024**, *16*, 437-445.
(60) Sarkar, S. K.; Hollister, K. K.; Molino, A.; Obi, A. D.; Deng, C.-L.; Tra, B. Y. E.; Stewart, B. M.; Dickie, D. A.; Wilson, D. J. D.; Gilliard, R. J., Jr. Bis(9-Boraphenanthrene) and Its Stable Biradical. *J. Am. Chem. Soc.* **2023**, *145*, 21475-21482.
(61) Wentz, K. E.; Molino, A.; Freeman, L. A.; Dickie, D. A.; Wilson, D. J.; Gilliard Jr, R. J. Activation of Carbon Dioxide by 9-Carbene-9-borafluorene Monoanion: Carbon Monoxide Releasing Transformation of Trioxaborinanone to Luminescent Dioxaborinanone. *J. Am. Chem. Soc.* **2022**, *144*, 16276-16281.
(62) Hollister, K. K.; Molino, A.; Breiner, G.; Walley, J. E.; Wentz, K. E.; Conley, A. M.; Dickie, D. A.; Wilson, D. J.; Gilliard Jr, R. J. Air-Stable Thermoluminescent Carbodicarbene-Borafluorenium Ions. *J. Am. Chem. Soc.* **2022**, *144*, 590-598.
(63) Wentz, K. E.; Molino, A.; Freeman, L. A.; Dickie, D. A.; Wilson, D. J. D.; Gilliard, R. J., Jr. Systematic Electronic and Structural Studies of 9-Carbene-9-Borafluorene Monoanions and Transformations into Luminescent Boron Spirocycles. *Inorg. Chem.* **2022**, *61*, 17049-17058.

(64) Blom, B.; Gallego, D.; Driess, M. N-heterocyclic silylene complexes in catalysis: new frontiers in an emerging field. *Inorg. Chem. Front.* **2014**, *1*, 134-148.
(65) Zhou, Y. P.; Driess, M. Isolable Silylene Ligands Can Boost Efficiencies and Selectivities in Metal-Mediated Catalysis. *Angew. Chem. Int. Ed.* **2019**, *58*, 3715-3728.
(66) Sen, S. S.; Roesky, H. W.; Stern, D.; Henn, J.; Stalke, D. High Yield Access to Silylene RSiCl (R=PhC(N^tBu)$_2$) and Its Reactivity toward Alkyne: Synthesis of Stable Disilacyclobutene. *J. Am. Chem. Soc.* **2010**, *132*, 1123-1126.
(67) Tan, G.; Blom, B.; Gallego, D.; Driess, M. Facile Access to Mono-and Dinuclear Heteroleptic N-Heterocyclic Silylene Copper Complexes. *Organometallics* **2014**, *33*, 363-369.
(68) Khan, S.; Ahirwar, S. K.; Pal, S.; Parvin, N.; Kathewad, N. Silicon(II) Bis(trimethylsilyl)amide (LSiN($SiMe_3$)$_2$, L = PhC(N^tBu)$_2$) Supported Copper, Silver, and Gold Complexes. *Organometallics* **2015**, *34*, 5401-5406.
(69) Ghosh, M.; Tothadi, S.; Khan, S. Carbazole Substituted Amidinato Silylene: Synthesis, Bonding, and Coordination Behavior with Coinage Metals. *Organometallics* **2021**, *40*, 3201-3210.
(70) Parvin, N.; Pal, S.; Echeverria, J.; Alvarez, S.; Khan, S. Taming a monomeric [Cu(η^6-C_6H_6)]$^+$ complex with silylene. *Chem. Sci.* **2018**, *9*, 4333-4337.
(71) Parvin, N.; Hossain, J.; George, A.; Parameswaran, P.; Khan, S. N-heterocyclic silylene stabilized monocordinated copper(I)-arene cationic complexes and their application in click chemistry. *Chem. Commun.* **2020**, *56*, 273-276.
(72) Paesch, A. N.; Kreyenschmidt, A. K.; Herbst-Irmer, R.; Stalke, D. Side-Arm Functionalized Silylene Copper(I) Complexes in Catalysis. *Inorg. Chem.* **2019**, *58*, 7000-7009.
(73) Nazish, M.; Siddiqui, M. M.; Sarkar, S. K.; Munch, A.; Legendre, C. M.; Herbst-Irmer, R.; Stalke, D.; Roesky, H. W. Synthesis and Coordination Behavior of a New Hybrid Bidentate Ligand with Phosphine and Silylene Donors. *Chem. Eur. J.* **2021**, *27*, 1744-1752.
(74) Hossain, J.; Akhtar, R.; Khan, S. Luminescent coinage metal complexes of carbenes. *Polyhedron* **2021**, *201*, 115151-115187.
(75) Di, D.; Romanov, A. S.; Yang, L.; Richter, J. M.; Rivett, J. P. H.; Jones, S.; Thomas, T. H.; Jalebi, M. A.; Friend, R. H.; Linnolahti, M.; Bochmann, M.; Credgington, D. High-performance light-emitting diodes based on carbene-metal-amides. *Science* **2017**, *356*, 159-163.
(76) Marzo, L.; Pagire, S. K.; Reiser, O.; König, B. Visible-light photocatalysis: does it make a difference in organic synthesis? *Angew. Chem. Int. Ed.* **2018**, *57*, 10034-10072.
(77) Prier, C. K.; Rankic, D. A.; MacMillan, D. W. Visible light photoredox catalysis with transition metal complexes: applications in organic synthesis. *Chem. Rev.* **2013**, *113*, 5322-5363.
(78) Mohankumar, M.; Holler, M.; Meichsner, E.; Nierengarten, J.-F.; Niess, F.; Sauvage, J.-P.; Delavaux-Nicot, B.; Leoni, E.; Monti, F.; Malicka, J. M.; Cocchi, M.; Bandini, E.; Armaroli, N. Heteroleptic Copper(I) Pseudorotaxanes Incorporating Macrocyclic Phenanthroline Ligands of Different Sizes. *J. Am. Chem. Soc.* **2018**, *140*, 2336-2347.
(79) Hashimoto, M.; Igawa, S.; Yashima, M.; Kawata, I.; Hoshino, M.; Osawa, M. Highly efficient green organic light-emitting diodes containing luminescent three-coordinate copper (I) complexes. *J. Am. Chem. Soc.* **2011**, *133*, 10348-10351.
(80) Liu, Z.; Qayyum, M. F.; Wu, C.; Whited, M. T.; Djurovich, P. I.; Hodgson, K. O.; Hedman, B.; Solomon, E. I.; Thompson, M. E. A Codeposition route to CuI− pyridine coordination complexes for organic light-emitting diodes. *J. Am. Chem. Soc.* **2011**, *133*, 3700-3703.
(81) Bissember, A. C.; Lundgren, R. J.; Creutz, S. E.; Peters, J. C.; Fu, G. C. Transition-metal-catalyzed alkylations of amines with alkyl halides: Photoinduced, copper-catalyzed couplings of carbazoles. *Angew. Chem. Int. Ed.* **2013**, *52*, 5129-5133.

(82) Azhakar, R.; Ghadwal, R. S.; Roesky, H. W.; Wolf, H.; Stalke, D. Facile Access to the Functionalized N-Donor Stabilized Silylenes PhC(N^{t}Bu)$_2$SiX (X = PPh$_2$, NPh$_2$, NCy$_2$, NiPr$_2$, NMe$_2$, N(SiMe$_3$)$_2$, O^{t}Bu). *Organometallics* **2012**, *31*, 4588-4592.
(83) Tsuda, T.; Yazawa, T.; Watanabe, K.; Fujii, T.; Saegusa, T. Preparation of thermally stable and soluble mesitylcopper (I) and its application in organic synthesis. *J. Org. Chem.* **1981**, *46*, 192-194.
(84) Meyer, E. M.; Gambarotta, S.; Floriani, C.; Chiesi-Villa, A.; Guastini, C. Polynuclear aryl derivatives of Group 11 metals. Synthesis, solid state-solution structural relationship, and reactivity with phosphines. *Organometallics* **1989**, *8*, 1067-1079.
(85) Kuehn, L.; Eichhorn, A. F.; Schmidt, D.; Marder, T. B.; Radius, U. NHC-stabilized copper (I) aryl complexes and their transmetalation reaction with aryl halides. *J. Organomet. Chem.* **2020**, *919*, 121249.
(86) Kathewad, N.; Anagha, M.; Parvin, N.; Parambath, S.; Parameswaran, P.; Khan, S. Facile Buchwald–Hartwig coupling of sterically encumbered substrates effected by PNP ligands. *Dalton Trans.* **2019**, *48*, 2730-2734.
(87) Chen, C.; Chi, Z.; Chong, K. C.; Batsanov, A. S.; Yang, Z.; Mao, Z.; Yang, Z.; Liu, B. Carbazole isomers induce ultralong organic phosphorescence. *Nat. Mater.* **2021**, *20*, 175-180.
(88) Brannan, A. C.; Phuoc, N. L.; Linnolahti, M.; Romanov, A. S. Organic persistent room temperature phosphorescence enabled by carbazole impurity. *Frontiers in Chemistry* **2023**, *10*, 1008658.
(89) Tang, R.; Xu, S.; Lam, T.-L.; Cheng, G.; Du, L.; Wan, Q.; Yang, J.; Hung, F.-F.; Low, K.-H.; Phillips, D. L.; Che, C.-M. Highly Robust Cu^I-TADF Emitters for Vacuum-Deposited OLEDs with Luminance up to 222 200 cd m^{-2} and Device Lifetimes (LT$_{90}$) up to 1300 hours at an Initial Luminance of 1000 cd m^{-2}. *Angew. Chem. Int. Ed.* **2022**, *61*, e202203982.
(90) Li, E. Y.-T.; Jiang, T.-Y.; Chi, Y.; Chou, P.-T. Semi-quantitative assessment of the intersystem crossing rate: an extension of the El-Sayed rule to the emissive transition metal complexes. *Phys. Chem. Chem. Phys.* **2014**, *16*, 26184-26192.
(91) Yersin, H.; Rausch, A. F.; Czerwieniec, R.; Hofbeck, T.; Fischer, T. The triplet state of organo-transition metal compounds. Triplet harvesting and singlet harvesting for efficient OLEDs. *Coord. Chem. Rev.* **2011**, *255*, 2622-2652.
(92) Li, T.-y.; Ravinson, D. S. M.; Haiges, R.; Djurovich, P. I.; Thompson, M. E. Enhancement of the luminescent efficiency in carbene-au (i)-aryl complexes by the restriction of renner–teller distortion and bond rotation. *J. Am. Chem. Soc.* **2020**, *142*, 6158-6172.
(93) Baba, M. Intersystem Crossing in the 1nπ* and 1ππ* States. *J. Phys. Chem. A* **2011**, *115*, 9514-9519.
(94) Ruduss, A.; Belyakov, S.; Stucere, K. A.; Vembris, A.; Traskovskis, K. Light emission mechanism in dimers of carbene–metal–amide complexes. *Phys. Chem. Chem. Phys.* **2023**, *25*, 3220-3231.
(95) Murawski, C.; Leo, K.; Gather, M. C. Efficiency roll-off in organic light-emitting diodes. *Adv. Mater.* **2013**, *25*, 6801-6827.
(96) Reponen, A.-P. M.; Chotard, F.; Lempelto, A.; Shekhovtsev, V.; Credgington, D.; Bochmann, M.; Linnolahti, M.; Greenham, N. C.; Romanov, A. S. Donor N-Substitution as Design Principle for Fast and Blue Luminescence in Carbene-Metal-Amides. *Adv. Opt. Mater.* **2022**, *10*, 2200312.

Chapter 4: Carbene Capped Nanoparticle Synthesis and Their Catalytic Applications

Chapter 4A: Cyclic(Alkyl)(Amino)Carbene Stabilized Gold Nanoparticles for Selective CO_2 Reduction

Adapted from: ***M. Ghosh***, P. Saha, S. Roy, S. Barman, P. P. Pillai*, A. Dey*, and S. Khan*, Cyclic(Alkyl)(Amino)Carbene Stabilized Gold Nanoparticles for Selective CO_2 Reduction. *ACS Catal.* **2024**, *14*, 7011-7019 (*Published at Front Cover*); also available at ChemRxiv **2023**.

4A.1 Objective of this work.

NHCs have recently gained significant attention as capping ligands for AuNPs due to their strong σ-donation properties. It has already been established that the strong σ-donation of NHCs enriches the surface of the AuNPs, which controls the catalytic activity of the metal nanoparticles. CAAC is a special class of carbene that offers stronger σ-donation than NHCs. This extremely electron-rich nature of CAAC projects it as a better surface capping ligand upon extrapolating on the Au(0) surface. In this work, we have isolated stable CAAC-stabilized AuNPs *via* a top-down method and studied their catalytic behavior towards electrochemical CO_2 reduction. These newly synthesized CAAC-stabilized AuNPs furnish a remarkable FE of 94% [at pH 6.3 for 2 h of controlled potential electrolysis at -0.7 V *vs* NHE (Normal Hydrogen Electrode)] towards selective CO formation. This work sets the platform for CAAC as a robust main group ligand on the surface of different metal nanoparticles, bridging the gap between main group ligands and surface chemistry.

4A.2 Introduction.

In recent years, NHCs have emerged as excellent spectator ligands and have never failed to excite the scientific community due to their flexible σ-donating and π-accepting properties.[1, 2] Because of the successful coordination of NHCs to most periodic elements, the main group chemists took great enthusiasm to anchor them as surface ligands for settling metal(loid) nanoparticles.[3] Owing to its ease of synthesis, diverse stability, and delocalized back bonding, various C2 functionalized NHCs become potential candidates as surface capping agents in comparison to widely used long aliphatic chains of thiol (-SH) and amines ($-NH_2$) in the recent nano-chemistry.[2] MNPs are commonly synthesized by the reduction of metal salt precursor compounds in the liquid phase (bottom-up) or *via* ligand exchange (top-down).[4] The catalytic performance and stability of the MNPs are largely controlled by the surface ligands, particle size, shape, and defect sites.[5] The NHC functionalized AuNPs is a milestone discovery from the main group chemistry perspective.[2] Apart from imidazolium and benzimidazolium based NHCs, acyclic[6] and mesoionic[7-11] NHCs have also found their use as surface capping ligands very recently. The stabilization of AuNPs by NHCs can be best rationalized using the hard-soft Lewis acid-base concept.[12] Seeing the vast development of C2 functionalized NHCs on gold surfaces, we envisioned using CAAC on the surface of the AuNPs, which possess better σ-donation and π-acceptor properties (Figure 4A.1).[13, 14] The main difference between conventional NHCs and CAAC lies in substituting one neighboring nitrogen atom with sp^3 hybridized carbon atom adjacent to the carbene center (α-position). This modification

significantly alters the electronic properties of CAAC, making it more nucleophilic (σ-donating) and electrophilic (π-accepting) than NHCs (Figure 4A.1). It is already demonstrated that NHC ligands can boost the catalytic activity of the MNPs.[1, 3, 4, 15, 16] Hence, CAAC was anticipated to perform better than the reported ligands as it has already been proven an excellent ligand for stabilizing several unusual compounds and radical species due to its electron-rich nature.[13, 17-26] It has already been shown that the support of CAAC can stabilize a dimeric Au(0) complex, but NHCs fail to do the same due to their difference in electronic properties.[27, 28] Moreover, there is no precedence of CAAC functionalization on the surface of the MNPs, invoking curiosity about its effect on the surface. Very recently, deposition of CAAC has been utilized on the surfaces of Au(111), Ag(111), and Cu(111).[29, 30] Many pioneers in the field mentioned the possibility of CAAC on the MNP surfaces as a capping agent.[2, 14, 16] However, it remains unexplored. This paved the way for us to anticipate a successful anchoring of DiMeCAAC (methyl substitution at the sp^3 carbon center neighbouring to the CAAC carbene centre) on the surface of AuNPs.

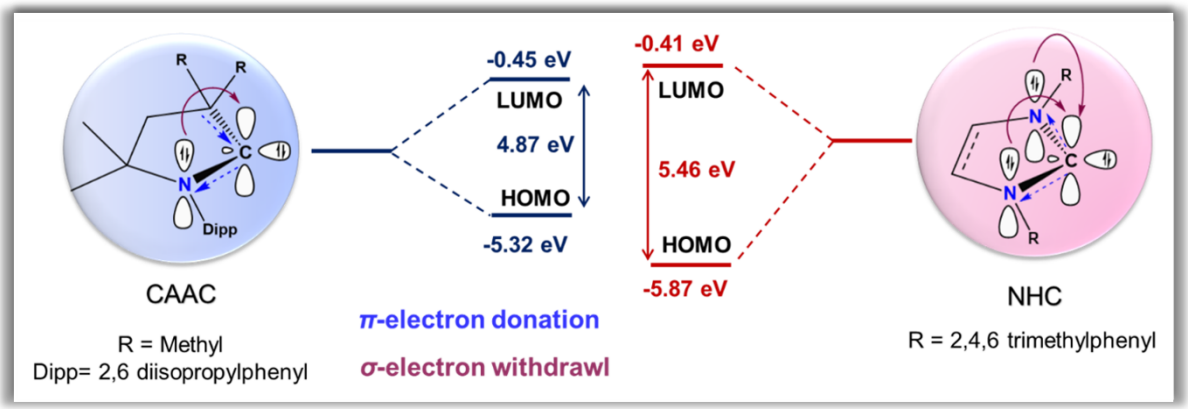

Figure 4A.1. Comparison of the electronic properties of NHC and CAAC carbenes. The HOMO and LUMO energy levels were calculated at the B3LYP-D3/Def2-TZVPP level.

Accordingly, DiMeCAAC functionalized AuNPs (DiMeCAAC@AuNPs) were prepared using the ligand exchange method. The successful isolation of DiMeCAAC@AuNP prompted us to investigate their catalytic activity, so we performed an electrocatalytic CO_2 reduction reaction (CO_2RR) because controlling greenhouse gas emissions is an emerging requirement to mitigate global warming and using the emitted CO_2 as a feedstock to obtain value-added chemicals is a viable alternative. The selective reduction of CO_2 to CO has been an active area of research as CO serves as a substrate in the Fischer-Tropsch synthesis of liquid fuels[31] or methanol synthesis.[32] Over the years, many homogeneous and heterogeneous catalysts have been designed for this purpose.[33-43] Recent years have witnessed tremendous

growth in utilizing MNPs as heterogeneous catalysts for the electrochemical reduction of CO_2 to CO, CH_4, and $HCOO^-$.[44] CAAC has proven its superior activity as ligand backbone over NHC in small molecule activation[45, 46] and homogeneous catalysis[47, 48] to give selective products compared to the NHCs. Seminal work by Bertrand and co-workers on CAAC coordinated trinuclear Cu, Ag, and Au(0) clusters[49] showed that catalytic reduction of CO_2 is possible with CAAC coordinated trinuclear Cu(0) cluster in the presence of bis(neopentyl glycolato)diboron to produce CO with 1000 TON. Interestingly, they did not observe any reaction with its Ag and Au(0) counterparts. This also motivated us to use the isolated AuNPs for CO_2 electroreduction.

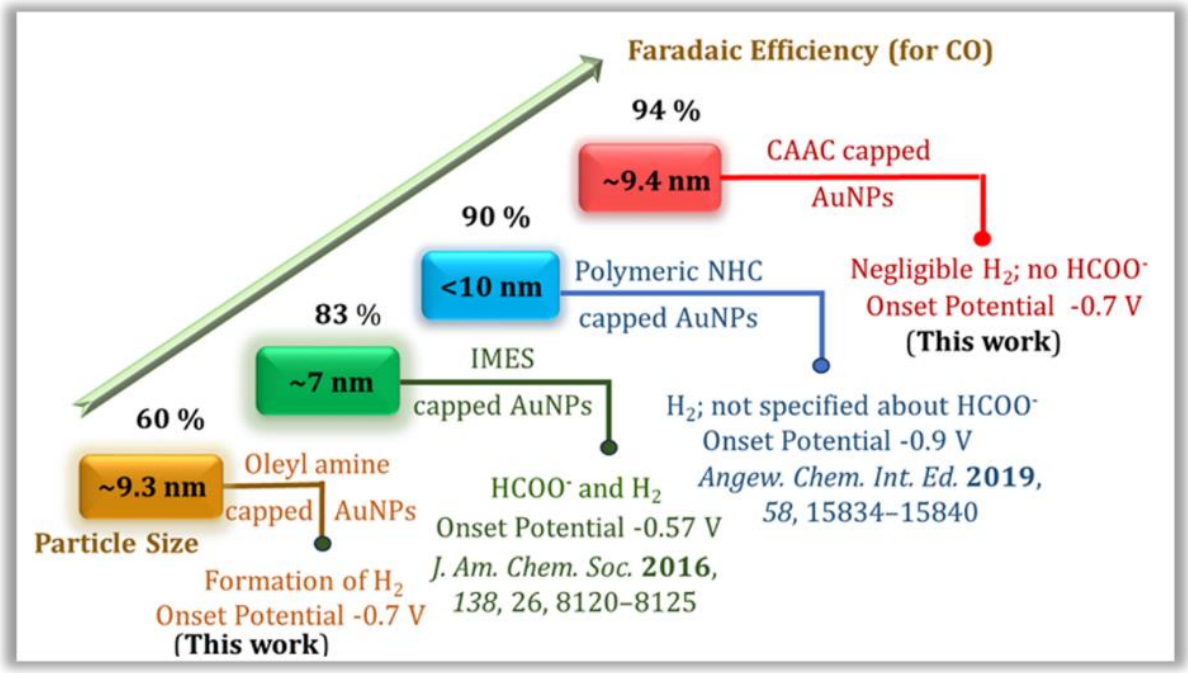

Figure 4A.2. Comparison of electrochemical CO_2 reduction performances of NHC capped AuNPs [8] with CAAC modified AuNPs, major CO_2RR product is CO in all cases, minor side products are also mentioned for different systems.

The first utilization of NHC (IMes) stabilized AuNPs for the electrochemical CO_2 reduction was documented in 2016, followed by the reports on polymeric NHC stabilized AuNPs for the same in 2019.[50, 51, 52] Recently, NHC-capped gold nanoclusters were also utilized for the electrochemical CO_2 reduction.[53-55] The FE of 83-90% towards the electro-reduction of CO_2 to CO was good in all the previous cases of NHC-functionalized AuNPs. However, side product formation (in these cases, $HCOO^-$ and H_2) could not be completely inhibited. Our newly synthesized DiMeCAAC@AuNPs have performed as an efficient and stable catalyst for CO_2 electroreduction, displaying an exclusive CO selectivity (FE = 94%) (Figure 4A.2). We

also synthesized IMES@AuNPs of similar particle size distribution and compared its electrocatalytic performance under identical reaction conditions. We obtained CO formation with 78% FE and H_2 (FE 22%) at -0.7 V.

4A.3 Results and Discussion.

The DiMeCAAC@AuNPs were prepared *via* a ligand exchange method from oleyl amine-capped AuNPs (OA@AuNPs).[56] Subsequently, ~50-fold excess of DiMeCAAC in THF was added to OA@AuNPs in anhydrous toluene under an inert atmosphere. Instantaneous dark purple precipitation of AuNPs was observed, and the solution was kept undisturbed overnight to complete ligand exchange. The purification of DiMeCAAC@AuNPs was performed *via* centrifugation, followed by washing with toluene to remove the free excess ligands. Finally, the DiMeCAAC@AuNPs were dispersed in DMSO after sonication for ~5 min (Scheme 4A.1). Unlike OA@AuNPs, DiMeCAAC@AuNPs were not dispersed in non-polar mediums like toluene and *n*-hexane.

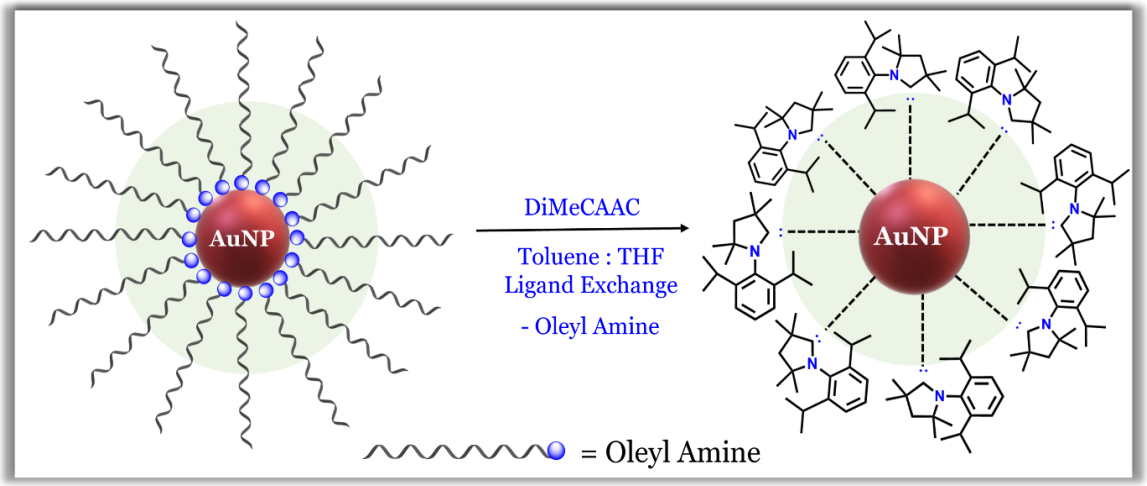

Scheme 4A.1. Representative synthesis of DiMeCAAC@AuNPs *via* the ligand exchange method from pre-synthesized OA@AuNPs.

The UV-visible spectra of DiMeCAAC@AuNPs in DMSO exhibit the characteristic localized surface plasmonic resonance (LSPR) peak at ~525 nm, confirming the formation and stability of the newly synthesized AuNPs in this matrix (Figure 4A.3a). A detailed transmission electron microscopy (TEM) study was carried out to understand the morphology of the DiMeCAAC@AuNPs (Figure 4A.3b). The TEM studies confirmed the formation of monodisperse DiMeCAAC@AuNPs with an average size of 9.5±1.3 nm, comparable with OA@AuNPs (Figure 4A.3c-d and Figure 4A.4). The uniformity in size and shape of the particles prove that DiMeCAAC is a suitable ligand for the surface functionalization of AuNPs.

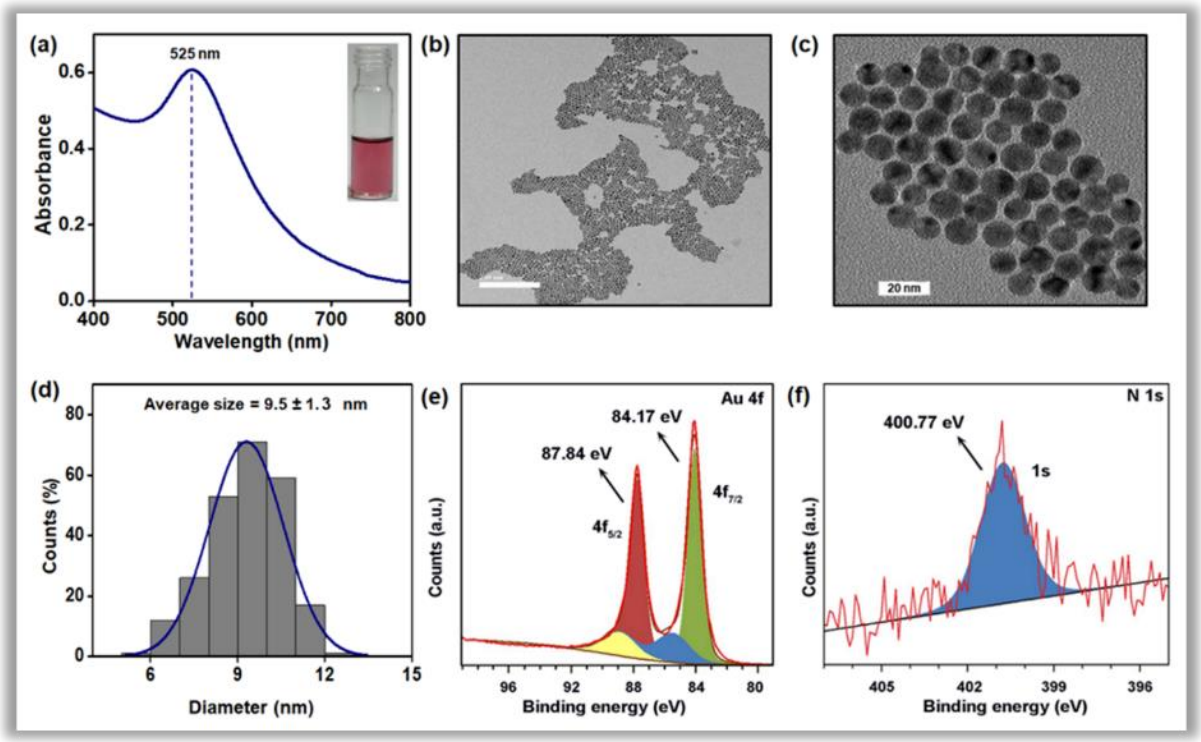

Figure 4A.3. (a) UV-vis spectra of DiMeCAAC@AuNPs in DMSO showing the characteristic LSPR band at ~525 nm (inset shows the photograph of a vial of DiMeCAAC@AuNPs); (b) A representative TEM image of DiMeCAAC@AuNPs; (c) Magnified TEM image at 20 nm scale (d) The corresponding size distribution histogram (from ~250 NPs); (e) XPS spectrum of DiMeCAAC@AuNPs displaying Au 4f peaks; (f) XPS spectrum of DiMeCAAC@AuNPs displaying N1s peak.

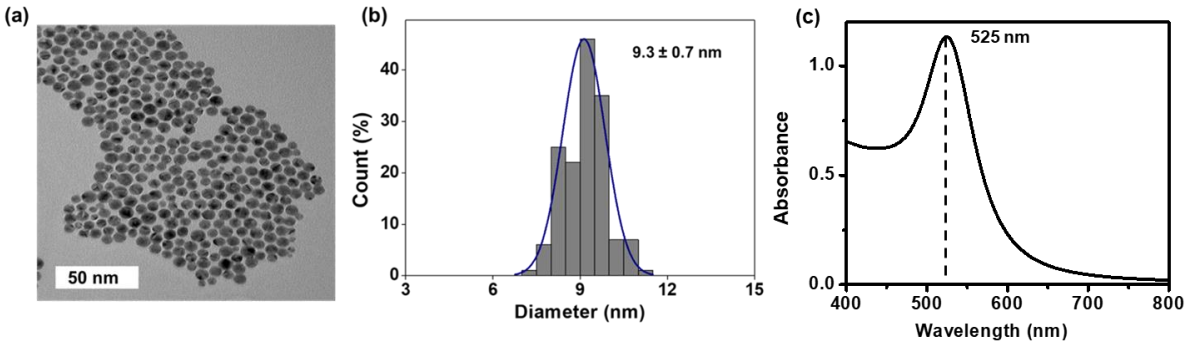

Figure 4A.4. (a) A representative TEM image of OA@AuNPs; (b) The corresponding size distribution histogram; (c) UV-vis spectra of OA@AuNPs in toluene showing the characteristic LSPR band at ~525 nm.

We also performed the Fourier transform infrared spectroscopy (FT-IR) to further prove the successful functionalization of DiMeCAAC ligand on the surface of AuNPs. From the reported examples of NHC functionalized AuNPs, it is evident that the primary hydrocarbon

stretching frequencies of the carbene backbone appeared at ν_{as}(C−H) ≈ 2922 cm^{-1} and ν_{s}(C−H) ≈ 2853 cm^{-1}, while the stretching frequency of the oleyl amine (–NH_2) (3373 cm^{-1}) disappeared upon binding with the gold surfaces.[57, 58] The appearance of the peaks at 2869, 2930, and 2965 cm^{-1} corresponds to the stretching frequencies of the isopropyl groups attached to the Dipp moiety of the DiMeCAAC backbone (Figure 4A.5).

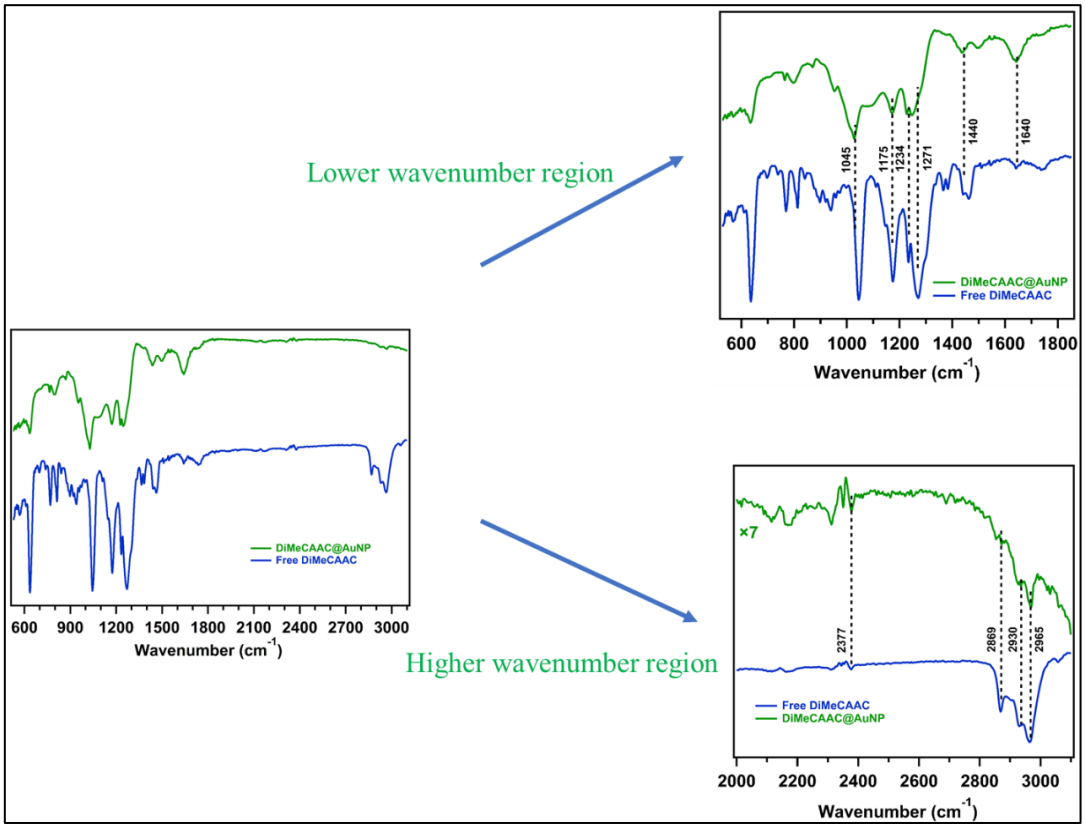

Figure 4A.5. IR spectra for DiMeCAAC@AuNPs and DiMeCAAC. The findings are listed in Table 4A.1.

Table 4A.1. Peak assignments from Figure 4A.5

Peak Position (cm^{-1})	**Assignments**
2965, 2930, 2869	C-H stretching frequency of isopropyl group
1640	Aromatic C-H bending
1440	C-H bending of the methyl group
1271	C-C, C-N stretching; CH_2 twisting
1234, 1175	C-C, C-N, C-H deformation
1045	Aromatic C-H out of plane bending

The X-ray photoelectron spectroscopy (XPS) was performed to observe the presence of signature signals for C 1s and N 1s of the NHC ligand on AuNPs.[59-61] A detailed XPS

analysis of DiMeCAAC@AuNPs confirmed the presence of DiMeCAAC on the AuNP surface. We observed peaks at 84.07 and 87.75 eV for Au $4f_{7/2}$ and Au $4f_{5/2}$ (Figure 4A.3e) transitions, respectively, indicating the presence of Au^0 (ΔeV= 3.68). Shoulder peaks at 85.46 and 88.88 eV correspond to the +1 oxidation states of Au present at the surface of AuNPs along with Au (0), which arises due to the oxidation of the uncoordinated surface Au atoms.[62, 63] The presence of a single chemical environment for N in DiMeCAAC was used as a marker of the successful coordination, as probed by Glorius and co-workers in a recent study of DiMeCAAC on the Au(111) surface.[29, 30] Similarly, we also observed a single peak at 400.77 eV (Figure 4A.3f) corresponding to the N 1s binding energy for DiMeCAAC@AuNPs, which is in accordance with the reported N 1s XPS data (400.7 eV) for CAAC on Au(111) surface.[29, 30] The peak at 400-401 eV for N 1s is the typical region for NHC-bound AuNPs.[2, 59-61, 64-66] The observed binding energy for N 1s confirms the absence of any iminium salt or protonated carbene.[67] The XPS data of OA@AuNPs was also recorded for comparative purposes, which displays two peaks of N 1s binding energy. The peak at 401.01 eV can be attributed to the $–NH_2$ bound AuNPs, and this is in accordance with the previous reports (Figure 4A.6).[57]

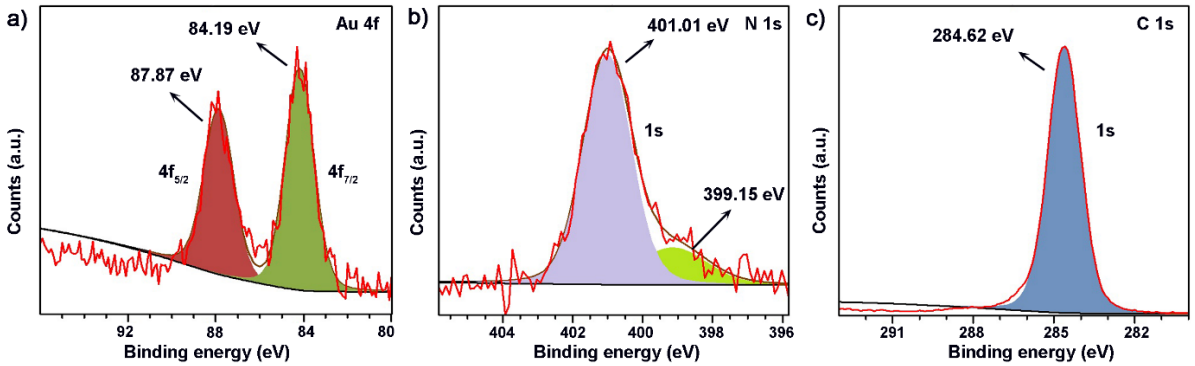

Figure 4A.6. X-ray photoelectron spectra for OA@AuNPs showing (a) Au 4f Au 4f showing spin-pair doublets at 84.19 and 87.87 eV for $4f_{7/2}$ and $4f_{5/2}$, respectively, confirming the presence of Au^0 OA@AuNPs, (b) N 1s showing two peaks at 401.01 and 399.15 eV for $–NH_2$ functionalized N of oleyl amine and oxidized $–NH_2$ functionality of oleyl amine during AuNPs synthesis, respectively, in accordance to the literature.[57] (c) C 1s, showing a peak at 284.62 and for oleyl amine backbone from OA@AuNPs.

Further, we observed the presence of $[M+H]^+$ ion peak (observed *m/z* = 286.2584 for DiMeCAAC) in the ESI-MS spectrum (Figure 4A.A.1) of DiMeCAAC@AuNPs, rationalizing that the observed $[M+H]^+$ ion originates from the detachment of the ligand from the surface of the particles during ionization .[68, 69] Finally, the thermogravimetric analysis (TGA) method was applied to estimate the DiMeCAAC ligand and AuNPs ratio, as reported by Crudden, Camden,

and co-workers.[59, 70] From the weight loss diagram, it is clear that the ligand density on the surface of AuNPs decreases after the ligand exchange with DiMeCAAC ligands (DiMeCAAC:Au ratio for DiMeCAAC@AuNPs= 44.46:51.04 and OA:Au ratio of OA@AuNPs = 82.35:14.75. Figure 4A.7).

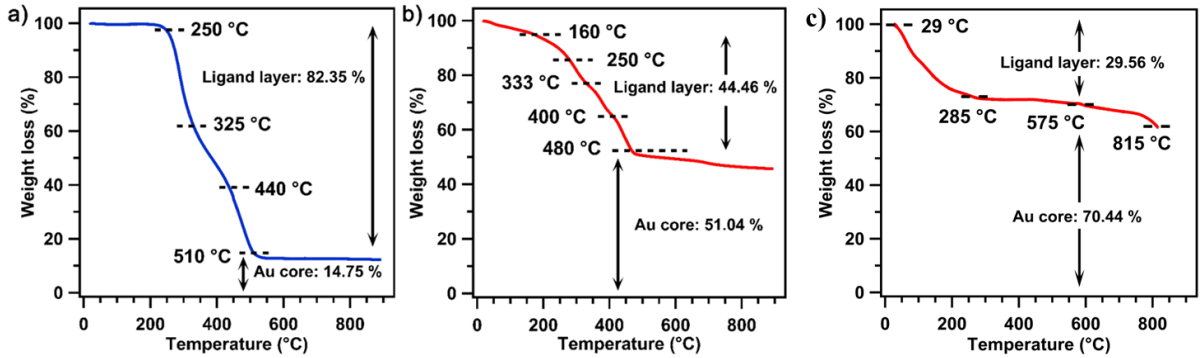

Figure 4A.7. TGA curve for (a) OA@AuNPs; OA@AuNPs, it is 82.35:14.75; (b) DiMeCAAC@AuNPs; DiMeCAAC:Au ratio was found to be 44.46:51.04 and (c) IMES@AuNPs; IMES:Au ratio found to be 29.56:70.44.

Based on the studies mentioned above, we conclusively support the successful functionalization of the AuNPs surface with DiMeCAAC ligands. We have encountered repeated failures in measuring solid-state ^{13}C NMR, which prompted us to check the magnetic properties. Hence, we measured magnetization (*M*) *vs.* magnetic field (*H*) at 300 K using SQUID magnetometry (Figure 4A.8), which discloses the magnetic nature of DiMeCAAC@AuNPs, originating from ferromagnetic as well as paramagnetic contributions.[71-73] We also synthesized IMES@AuNPs following the same procedure.

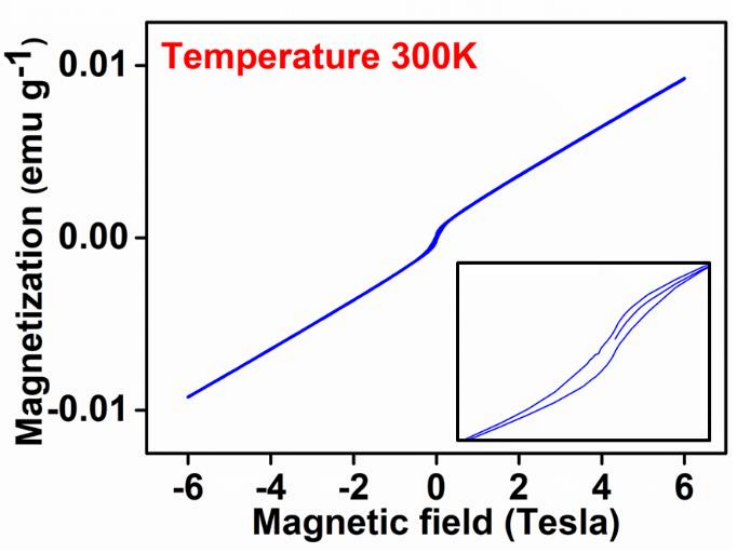

Figure 4A.8. Magnetization curve measured by applying an external magnetic field at 300 K. *M* vs H plot (a, b) for DiMeCAAC@AuNPs. (*M* = Magnetization, *H* = applied magnetic field)

4A.3.1 Stability of DiMeCAAC@AuNPs.

The stability of the DiMeCAAC@AuNPs interface is crucial for catalytic applications. To understand the robustness of DiMeCAAC@AuNPs surface, we introduced an external ligand, dodecanethiol (DDT) (0.2 mM), to the solution of DiMeCAAC@AuNPs. As thiols (-SH) have been extensively used for stabilizing colloidal gold due to their affinity towards the Au surface, adding external thiol, e.g., DDT, should test the robustness of DiMeCAAC on the AuNP surface.[12] After the treatment of DDT, the SPR band remained unchanged even after 12 hours. However, a slight red shift (~ 2 nm) in the SPR band was observed afterward (Figure 4A.9a), which might be due to the change in the dielectric constant of the medium upon the addition of DDT to the DiMeCAAC@AuNPs in the DMSO matrix.[74] After adding a higher concentration of DDT (15 mM) to DiMeCAAC@AuNPs, the colloidal stability was evaluated by tracking alterations in the SPR band for 8 days (Figure 4A.9b). The SPR band shifted to 529 nm (around 4 nm) within 24 hours. Within 24 hours, there was a 1.8% drop in peak intensity; 4 later, there was a 3% decline. The SPR band was then observed at 531 and 532 nm, respectively, following 4 and 8 days (Figure 4A.9c).

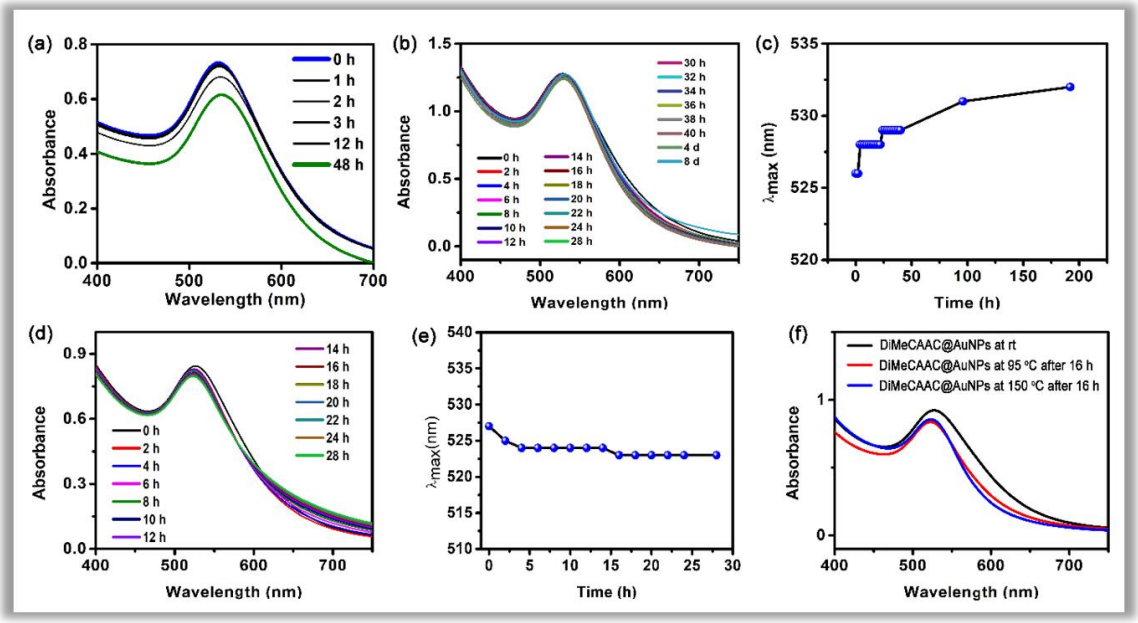

Figure 4A.9. The UV-Vis spectra showing the change in the SPR band upon treatment with DDT depicting the robustness of the DiMeCAAC@AuNPs (a) DDT concentration taken 0.2 mM, a slight red-shift (~2 nm) was observed in the absorption maxima (λ_{max}) after 12 h, but the overall colloidal stability was intact till 48 h; (b) DDT concentration taken 15 mM, a red-

shift (~2 nm) was observed in the absorption maxima (λ_{max}) after 4 h, but the overall colloidal stability was intact till 192 h, with a red-shift in SPR band (upto 532 nm) (c) λ_{max} *vs*. time plot showing the retention of SPR band over time (up to 196 h, i.e., 8 days) for the DDT treatment (15mM) of DiMeCAAC@AuNPs; (d) DiMeCAAC@AuNPs in DMSO at 65ºC upto 28 h; (e) λ_{max} *vs*. time plot showing the retention of SPR band over time (up to 28 h) at 65ºC; (f) DiMeCAAC@AuNPs in DMSO at 95 and 150ºC for 16 h.

The XPS spectrum for S2p shows two spin doublets at 163.63 and 164.93 eV for S $2p_{1/2}$ and S $2p_{3/2}$, respectively (Figure 4A10). The binding energy supports the presence of free thiol (binding energy 163.6 and 164.9 eV for S $2p_{3/2}$ and S $2p_{1/2}$, respectively. Although the XPS studies confirm that the DDT is not bound to the AuNP surface, it could be possible that DDT may adsorb on the vacant sites on DiMeCAAC@AuNPs, as proposed by Fensterbank, Ribot, and co-workers.[10] The TEM image shows the decrement of particle size to 8.5±1.4 nm (Figure 4A.11).

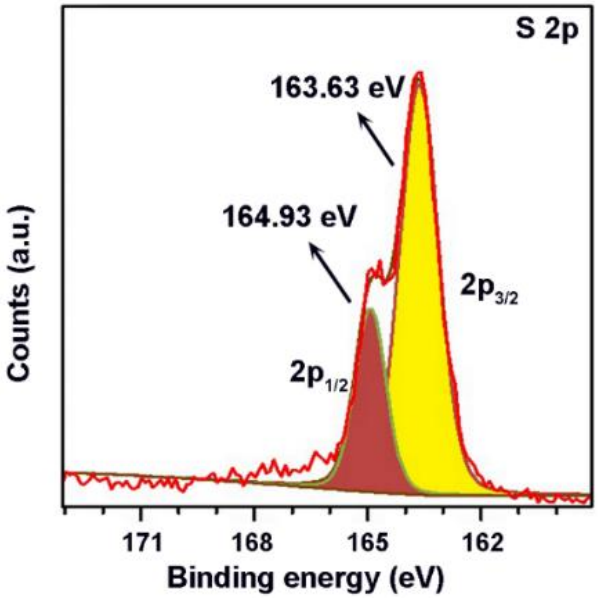

Figure 4A.10. XPS spectrum of S 2p of DiMeCAAC@AuNPs after DDT treatment.

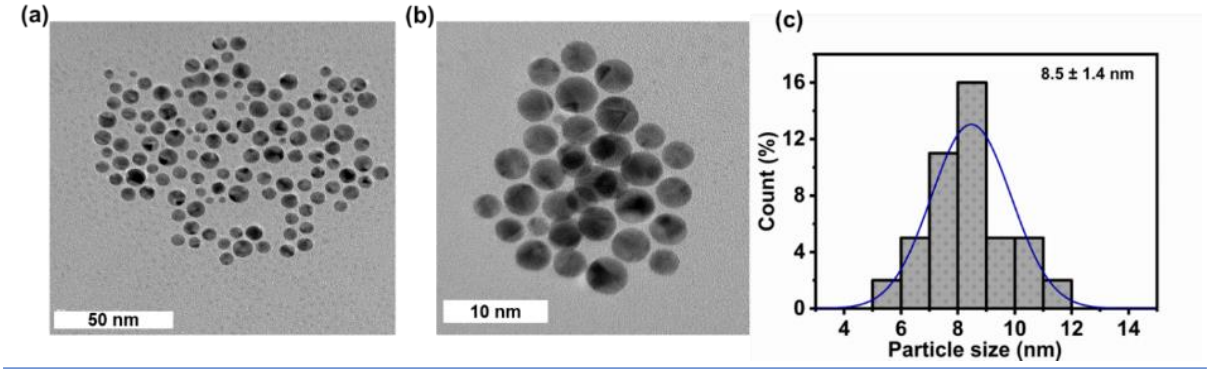

Figure 4A.11. (a) and (b) TEM image of DiMeCAAC@AuNPs after DDT treatment for 8 days; (c) The corresponding size distribution histogram.

We also checked the thermal stability of the DiMeCAAC at different temperatures (Figure 4A.9d-f). We first monitored the colloidal stability at 65°C at 2 h intervals till 28 h. In the 16 h, the SPR band blue-shifted by ~2 nm to 523 nm and remained there until the 28 h. The same observation was also obtained when DiMeCAAC@AuNPs were treated at 95 and 150°C for 16 h. The SPR band shifted to 523 nm, which denotes the synthesized NPs overall stability over various temperature ranges. The corresponding TEM images show the retention of the spherical size of the particles (Figure 4A.12-14). The effect of oxidant (H_2O_2) was also studied. The colloidal stability of NPs collapses in the presence of H_2O_2 (0.5 mM). They instantly formed aggregates in the presence of H_2O_2. Since DiMeCAAC@AuNPs are not stable in water, we could not observe their stability in different *p*H. Negligible changes in the time-dependent absorption studies (~18 h) confirm the long-term stability of DiMeCAAC@AuNPs in DMSO (Figure 4A.15).

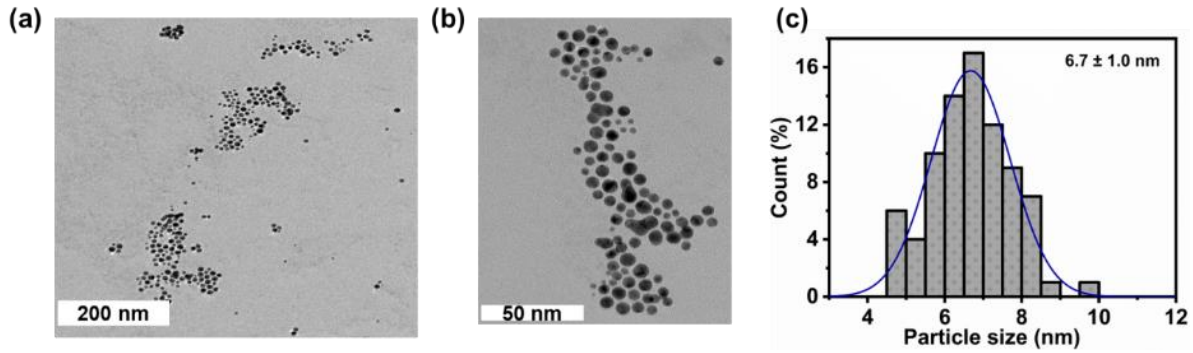

Figure 4A.12. (a) and (b) TEM image of DiMeCAAC@AuNPs after heating at 65°C for 28 h; (c) The corresponding size distribution histogram.

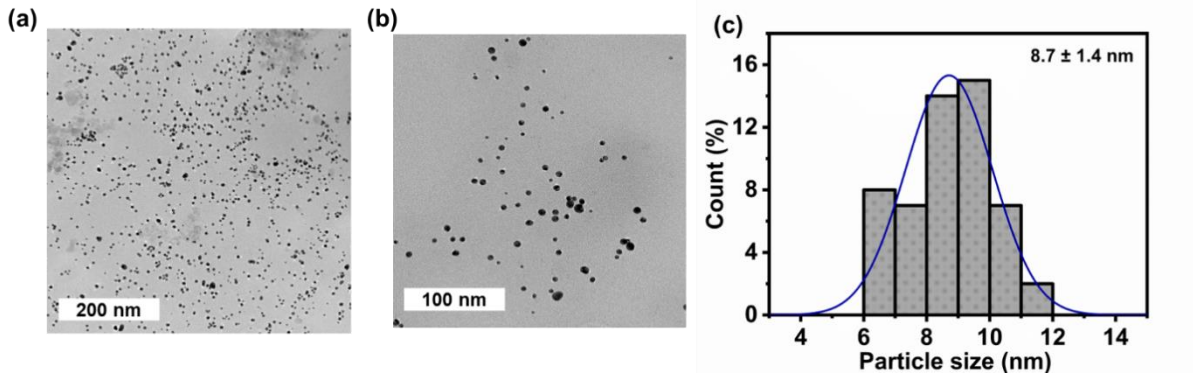

Figure 4A.13. (a) and (b) TEM image of DiMeCAAC@AuNPs after heating at 95°C for 16 h; (c) The corresponding size distribution histogram.

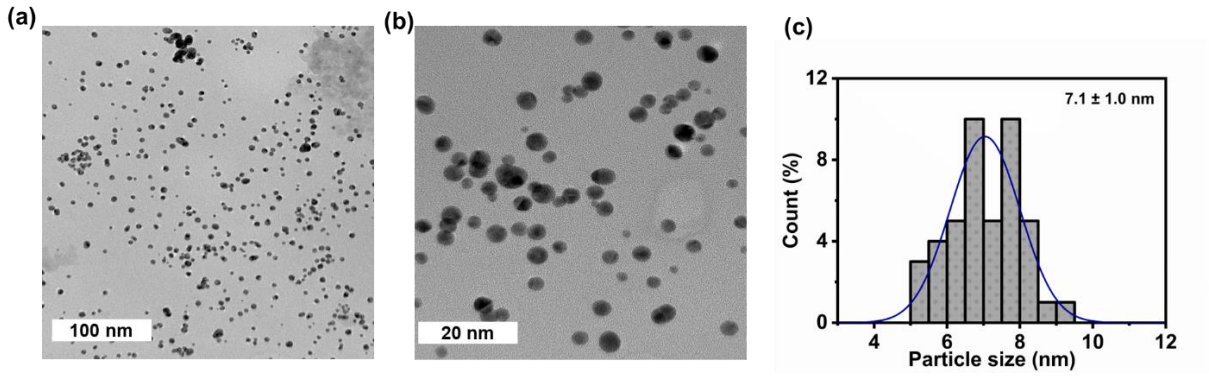

Figure 4A.14. (a) and (b) TEM image of DiMeCAAC@AuNPs after heating at 150ºC for 16 h; (c) The corresponding size distribution histogram.

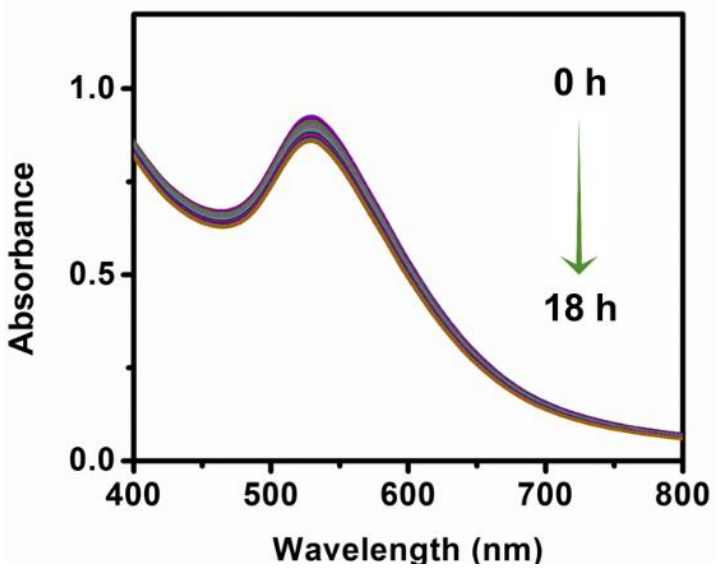

Figure 4A.15. Time dependent absorption spectra of DiMeCAAC@AuNPs in DMSO upto 18 h.

4A.3.2 Electrocatalytic CO_2 reduction.

The NHC-capped AuNPs are known to reduce CO_2 electrocatalytically under heterogeneous electrochemical conditions.[75-80] In 2016, IMes-capped AuNPs were used for the electrochemical reduction of CO_2 to CO, which showed an FE of 83% at -0.57 V *vs* RHE.[50] Following this, the polymeric NHC-capped AuNPs also provide an efficient CO_2 electroreduction (FE = 90% at -0.9 V *vs* RHE) (Reference Hydrogen Electrode) by preventing the nanoclustering of nanoparticles.[51] However, the side products ($HCOO^-$ and H_2) formation was also observed in both cases. In this work, we have performed the electrocatalytic reduction of CO_2 to CO catalyzed by DiMeCAAC@AuNPs and OA@AuNPs. 100 µL from 50 nM DiMeCAAC@AuNPs catalyst solution in DMSO was drop-casted on carbon paper to construct the working electrode to prevent sintering. As a control, an OA@AuNP-coated carbon paper

working electrode was also prepared to perform a comparative study of its CO_2RR performance. To ensure the structural integrity of the ligand backbone to the AuNP surface after drop-casting it to the working electrode, ATR-IR (attenuated total reflectance) (Figure 4A.16d**)** and TEM (Figure 4A.17a) data of the working electrode surface was recorded before and after the electrochemical experiments and compared with that of the DiMeCAAC@AuNPs catalyst. The cyclic voltammogram (CV) manifests $Au^{I/0}$ redox potential for DiMeCAAC@AuNPs shifted anodically under CO_2-saturated buffer with the generation of a pre-catalytic quasi-reversible CV indicating CO_2 binding to DiMeCAAC@AuNPs.

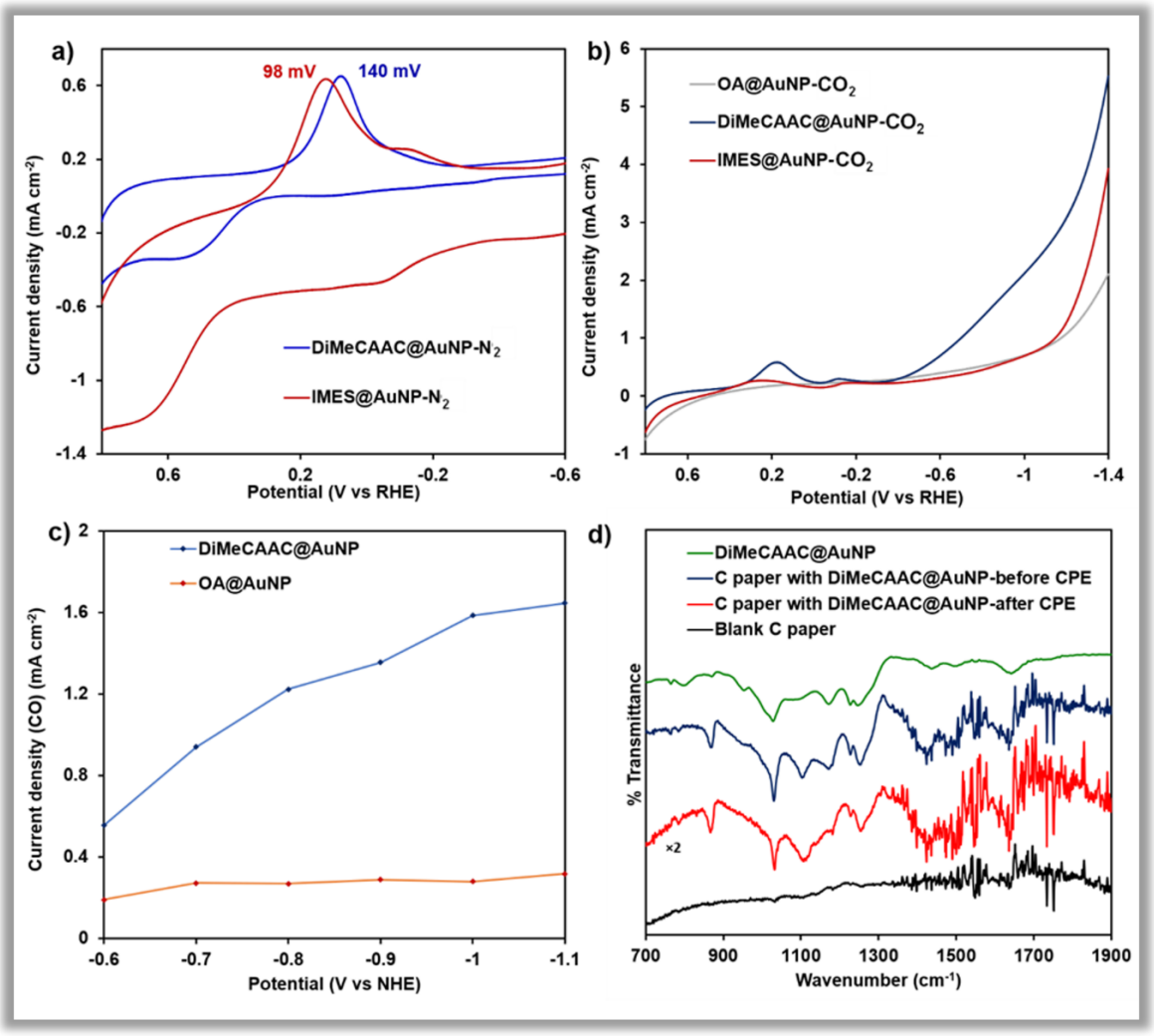

Figure 4A.16. (a) Overlay of cyclic voltammograms of DiMeCAAC@AuNPs, and IMES@AuNPs physisorbed on carbon paper, under N_2 saturation; (b) Electrochemical CO_2 reduction: overlay of LSV scans of OA@AuNPs, IMES@AuNPs and DiMeCAAC@AuNPs physisorbed on carbon paper, under CO_2 saturation. Voltammograms were recorded at 0.1 Vs^{-1} in 0.5 M $KHCO_3$ buffer; (c) Partial current density for CO formation *vs.* potential for DiMeCAAC@AuNPs and OA@AuNPs; (d) ATR spectra of DiMeCAAC@AuNPs (solid)

(green), DiMeCAAC@AuNPs physisorbed on carbon paper before (blue), and after the electrolysis (red), and blank carbon paper (black).

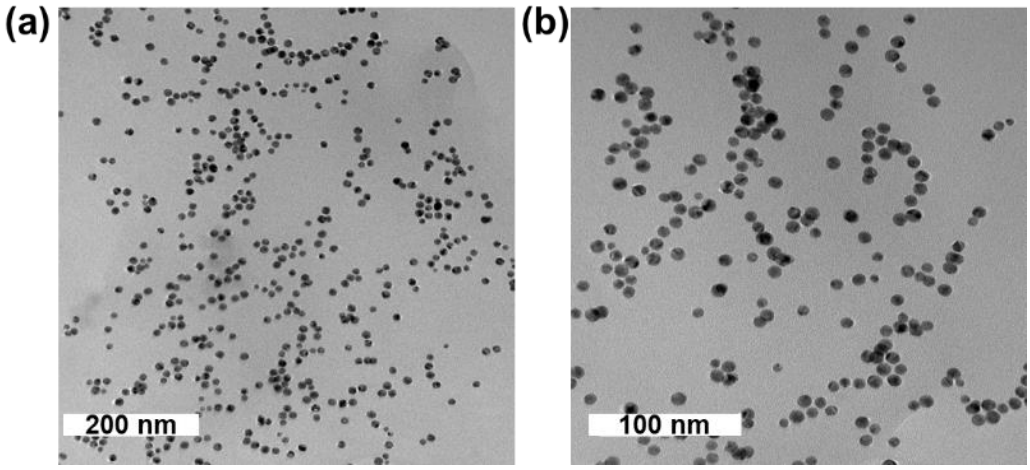

Figure 4A.17. TEM images of DiMeCAAC@AuNPs (a) before; (b) after the electrocatalysis show negligible change in the morphology of AuNPs.

DiMeCAAC@AuNPs resulted in a higher catalytic current and positively shifted onset potential than OA@AuNPs and IMES@AuNPs (Figure 4A.16b). The specific current density for CO formation (j_{CO}) as a function of applied potential for both DiMeCAAC@AuNPs and OA@AuNPs was extracted from the controlled potential electrolysis (CPE) data (Figure 4A.16c), showing a higher value for DiMeCAAC@AuNPs. The electronic effects of the two capping agents, DiMeCAAC and IMES, can be understood well from a more cathodic reduction wave for DiMeCAAC@AuNP under the N_2 atmosphere as compared to IMES@AuNPs (Figure 4A.16a). Although the difference is not substantial, electrochemical experiments are highly sensitive to the electronic structure of the analyte. This 42 mV difference may explain the anticipated electronic structure. DiMeCAAC, having a higher electron density, has a more cathodic reduction potential than IMES. After that, CPE in CO_2-saturated $KHCO_3$ buffer was carried out at different potentials (-0.7 V, -0.8 V, -0.9 V, -1 V, and -1.1 V *vs* RHE) to identify the CO_2RR products for DiMeCAAC@AuNPs and OA@AuNPs coated on a carbon paper. Since extensive electrochemical studies have already been reported for IMES@AuNPs[50], we did not include a detailed study in our work. By analyzing headspace gas using gas chromatography (GC) over different time intervals, CO was obtained as the major product (retention time 6.3 min) with slight traces of H_2 formation (retention time 1.2 min) at higher cathodic potentials (Figure 4A.18). The ion chromatography of the electrolyte solution, obtained after 2 h of CPE, was performed to check the formation of $HCOO^-$ as a side product of CO_2RR (Figure 4A.19).

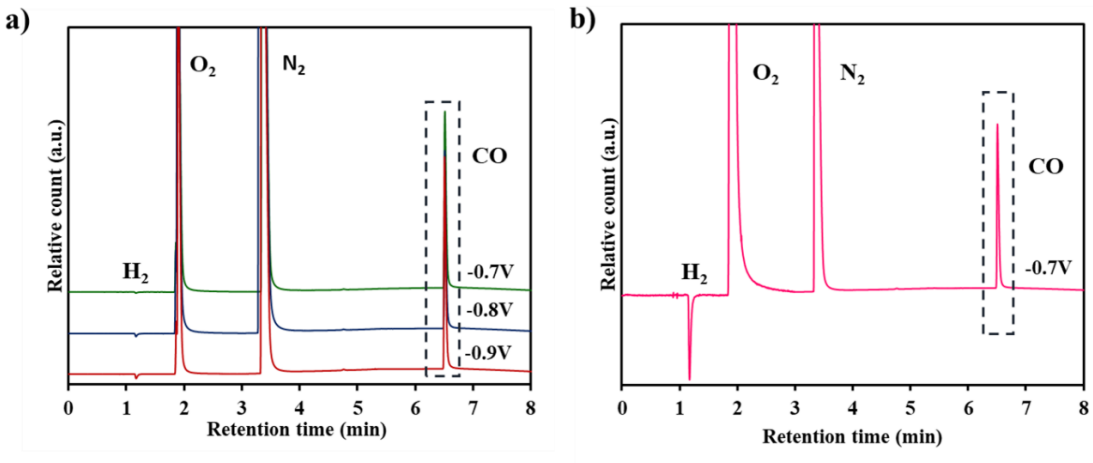

Figure 4A.18. Gas Chromatographic (GC) traces after 2 hours of CPE for (a) DiMeCAAC@AuNPs showing the formation of CO (Retention time 6.5 min) at different potentials (-0.7 to -0.9 V) with near zero production of H_2; (b) OA@AuNPs showing the formation of CO (Retention time 6.5 min) along with H_2 formation (Retention time 1.2 min)

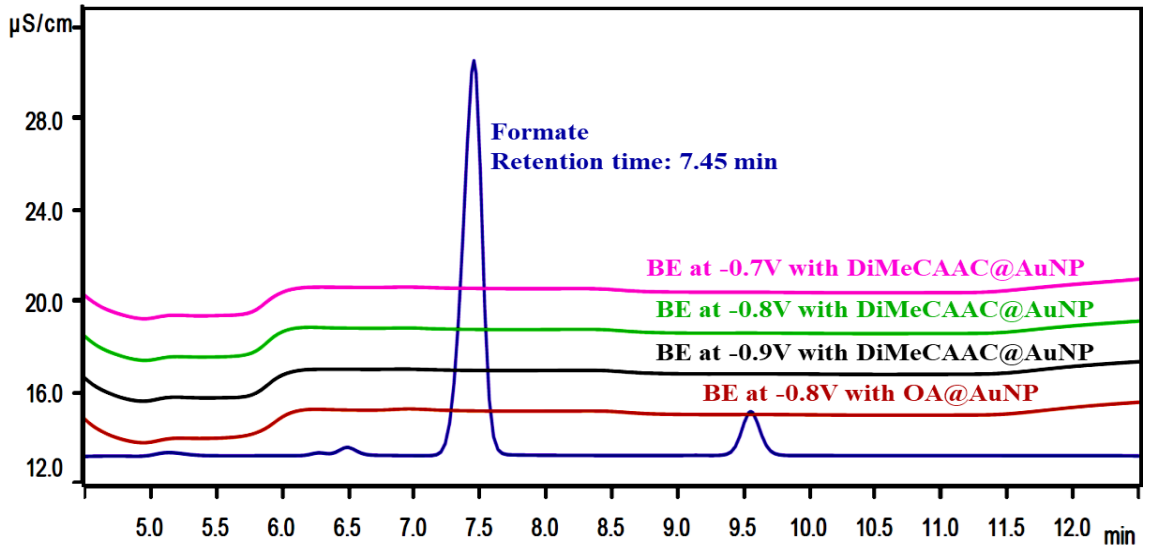

Figure 4A.19. Ion Chromatography (IC) trace for DiMeCAAC@AuNPs and OA@AuNPs indicating zero formation of formate ($HCOO^-$) after 2 hours of CPE at -0.7 and -0.8 V.

Gratifyingly, no $HCOO^-$ formation was observed during the course of the electrolysis. At -0.7 V, DiMeCAAC@AuNPs showed FE of 94% (for CO), while OA@AuNPs showed only 60% FE for CO (Figure 4A.20a). Despite the same size of OA@AuNPs and DiMeCAAC@AuNPs, a lower FE for CO with OA@AuNPs further confirms the significant role of the capping ligand on the surface of AuNPs in controlling the catalytic activity. The CV reveals a similar feature of the traces after 5 h of CPE (Figure 4A.21a). The GC data collected after 5 h shows 90% FE for CO at -0.7 V (Figure 4A.21b).

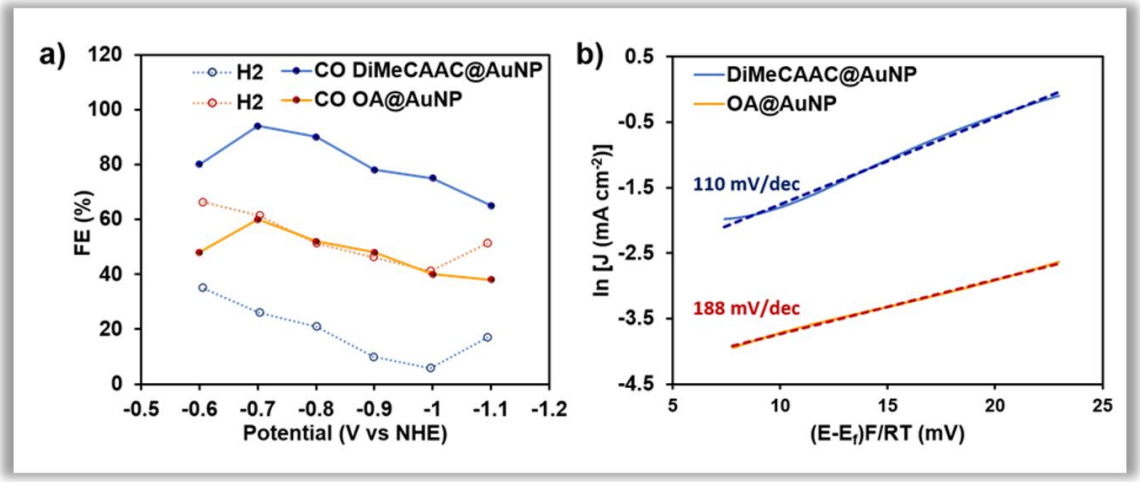

Figure 4A.20. (a) Faradaic efficiency (%) of CO and H_2 *vs.* Potential (V *vs.* NHE) plot showing DiMeCAAC@AuNPs manifested 94%, whereas OA@AuNPs gives 60% CO yield at -0.7 V after 2 h of CPE (b) Tafel plots of DiMeCAAC@AuNPs and OA@AuNPs.

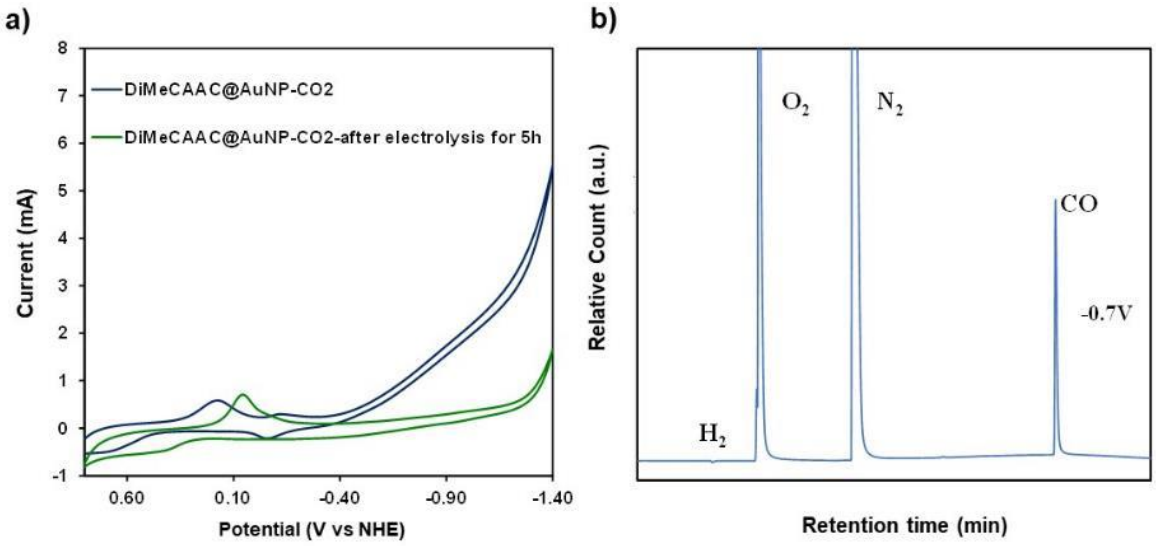

Figure 4A.21. (a) Overlay of cyclic voltammogram of DiMeCAAC@AuNPs under CO_2 saturation and after 5 hours of CPE. Voltammograms were recorded at 0.1 Vs^{-1} in 0.5 M $KHCO_3$ buffer. (b) Gas Chromatographic (GC) traces after 5 hours of CPE for DiMeCAAC@AuNPs showing the formation of CO (Retention time 6.5 min) at -0.7 V with 90 % FE.

To check the structural integrity of the ligand backbone on prolonged electrolysis, ATR-IR (Figure 4A.16d), XPS (Figure 4A.22a-b), and TEM (Figure 4A.17b) data of the working electrode (DiMeCAAC@AuNPs coated carbon paper) were recorded after CPE for 2 h, revealing no structural deformation of the ligand backbone. Hence, the catalyst is stable under working conditions.

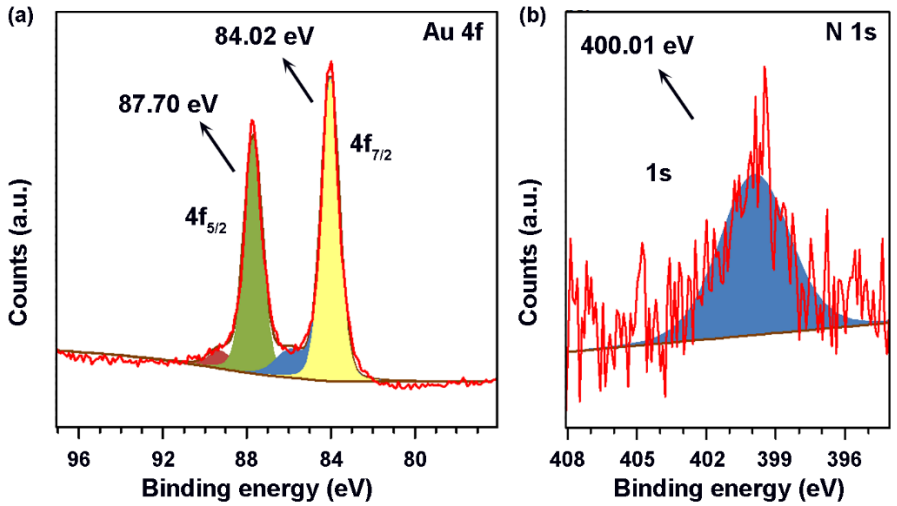

Figure 4A.22. X-ray Photoelectron Spectra for IMES@AuNPs coated Carbon paper showing (a) Au 4f showing spin-pair doublets at 84.02 and 87.70 eV for $4f_{7/2}$ and $4f_{5/2}$, respectively, after electrocatalysis; (b) N 1s spectra showing peak at 400.01 eV, after electrolysis.

The noise in the ATR spectra on the carbon paper is probably due to the water vapor (1350-1950 cm^{-1}).[81] The CPE has been performed with IMES@AuNP under the same conditions as that of DiMeCAAC@AuNPs. It was found that at -0.7 V, IMES@AuNP showed a 78% FE for CO formation (Figure 4A.23). The Tafel slope of 110 $mVdec^{-1}$ for DiMeCAAC (Figure 4A.20b), which is closer to 118 $mVdec^{-1}$, implies that the rate-determining step for CO_2 reduction is the initial step of the $CO_2^{\bullet-}$ generation.[82] On the contrary, the Tafel slope of 188 $mVdec^{-1}$ for OA@AuNPs indicates poor kinetics for CO_2RR (Figure 4A.20b).[83] For our catalyst, the energy efficiency[84] for the conversion of CO_2 to CO is calculated to be 51%, while for IMes[50] and polymeric NHC,[51] 46% and 45.8%, respectively. So, our synthesized catalyst demonstrates superior performance than the previously reported ones.

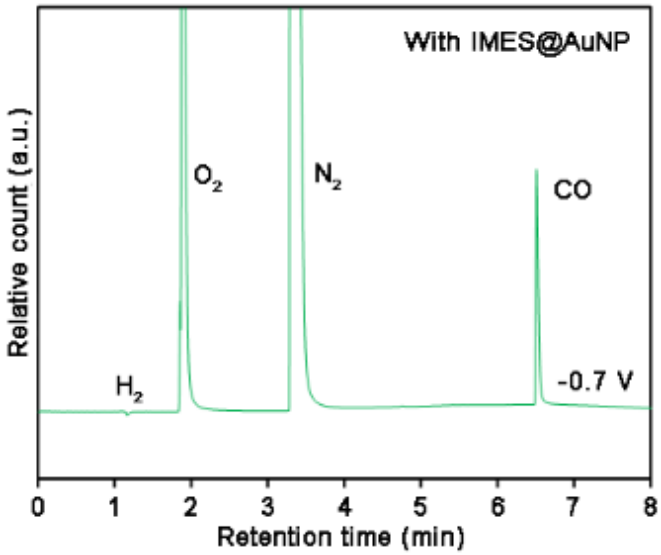

Figure 4A.23. Gas Chromatographic (GC) traces after 5 hours of CPE for IMES@AuNPs showing the formation of CO (Retention time 6.5 min) at -0.7 V with 78 % FE.

It is important to note that all other normal C2 functionalized NHC-ligated AuNPs showed the formation of a considerable amount of H_2 and $HCOO^-$ side products during the CO_2 reduction, which undoubtedly reduces the selectivity and efficiency of the catalyst performance (Table 4A.2). In our case, we did not observe the formation of any detectable side products. Hence, the surface modification of AuNPs with DiMeCAAC provides an exclusive selectivity toward CO_2RR product formation.

Table 4A.2. Comparison of electrochemical CO_2 reduction with literature reports for NHC capped AuNPs and Au nanoclusters. [#]

Catalyst	**FE**	**Onset potential (V)**	**Side products**
IMES capped AuNPs[50]	83 % (for CO)	-0.57	$HCOO^-$ and H_2
Polymeric NHC capped AuNPs[51]	90 % (for CO)	-0.90	H_2 but not specified about $HCOO^-$
NHC capped Au nanocluster[53]	Up to 80 % (for CO)	-1.00	$HCOO^-$ and H_2
NHC capped Au nanocluster[54]	> 90 %	-	H_2 but not specified about $HCOO^-$
CAAC capped AuNP (***This work***)	94 % (for CO)	-0.70	Negligible formation of H_2, no $HCOO^-$

[#]The experimental conditions/catalyst loading adopted to study the AuNPs catalyzed electrochemical reduction of CO_2 is different in different reports. Thus, no quantitative conclusions should be made from the comparison table.

4A.4 Conclusion.

In summary, we have synthesized CAAC-capped AuNPs and demonstrated their catalytic efficiency towards electrochemical CO_2 reduction. The surface functionalization of AuNPs with CAAC enhanced the catalytic activity and selectivity towards the electrocatalytic CO_2 to CO reduction (FE = 94%). This study establishes the advantage of CAAC as a surface capping ligand over conventionally used long-chain aliphatic amines and thiols onto the gold surface. This infers a potential application domain for CAAC-stabilized MNPs to flourish in organic and electrocatalytic transformations.

Chapter 4B: Exploration of Magnetism and Catalytic Properties of Cyclic (Alkyl)(Amino)Carbene (CAAC) Stabilized Gold Nanoparticles

Adapted from: ***M. Ghosh***, R. Akhtar, S. Roy, A. Pandikasaala, M. P. Sangole, K. Singh*, S. Kurungot*, P. P. Pillai*, and S. Khan*, Exploration of Magnetism and Catalytic Properties of Cyclic (Alkyl)(Amino)Carbene (CAAC) Stabilized Gold Nanoparticles (***Manuscript under preparation***).

4B.1 Objective of this work.

NHC-capped MNPs are a burgeoning area nowadays. Exploration of NHCs as a surface capping ligand is a new aspect of the chemistry of nanomaterials due to their unique electronic properties. The advancement of the field spans various domains, including studying their physical properties and catalytic activities. Herein, we have investigated the magnetic and catalytic properties of CAAC-capped AuNPs in relation to nitroarene reduction and electrocatalytic FAO. This opens avenues to unexplored applications and future research opportunities for investigating fundamental properties of such carbene-capped MNPs.

4B.2 Introduction.

NHCs are flexible ligands that have recently attracted much attention from the scientific community.[1, 85] Their versatility as strong σ-donating and π-accepting ligands is superior to other ligands reported in the literature on organometallic chemistry.[86-88] NHC is used in materials and pharmaceutical chemistry, and optoelectronics has demonstrated its wide-ranging influence in various scientific fields.[1, 89, 90] Recently, NHC has been used as surface ligands for stabilizing metal(loid) nanoparticles.[3] The NHC-capped MNPs are mainly synthesized either by the reduction of metal salt precursor compounds in the liquid phase (bottom-up) or *via* ligand exchange (top-down).[15, 16] The NPs are catalytically very active due to the large surface area per atom of volume.[5] The NHCs presumably stabilize AuNPs *via* the hard-soft Lewis acid-base concept proposed by Mittoussi and co-workers.[12] The stability and catalytic activity of NHC-capped NPs are influenced by modifying wingtip groups at NHCs.[2, 64, 65, 91, 92] To date, many functionalized imidazole and benzimidazole-based C2 NHCs,[4] mesoionic and acyclic NHCs, have been utilized as surface capping agents for AuNPs.[6-11] Recently, we reported that CAAC capped AuNPs and utilized them as electrocatalysts for CO_2 reduction. The AuNPs display interesting physicochemical properties due to SPR.[93] However, the AuNPs show magnetism in certain cases, which were reported in several cases but are less understood. The bulk gold is diamagnetic and it becomes magnetic when prepared in the form of functionalized nanoparticles. The AuNPs documented in the literature preferred ferromagnetic behavior.[94-96] In 1999, Hori *et al.* reported that the mean diameter of 3nm in Pd and Au nanoparticles embedded in polyN-vinyl-2-pyrrolidone exhibit superparamagnetic behavior at low temperatures.[97] Additionally, in 2004, the same group reported the ferromagnetic behavior in Au NPs with protective agents polyacrylonitrile and polyallyl amine hydrochloride (PAAHC).[98] Using X-ray magnetic circular dichroism, the ferromagnetic spin polarization of Au nanoparticles shielded by PAAHC with a mean diameter of 1.9 nm has been

determined.[99] Crespo *et al.* discovered the experimental observation of magnetic hysteresis in DDT-capped Au NPs with a 1.4 nm size up to room temperature.[96] The thiol-capped AuNPs apparent ferromagnetism is linked to 5d localized holes produced by covalent Au-S bonds. The high spin-orbit coupling of gold and the symmetry reduction linked to Au-Au and Au-S bonding result in localized magnetic moments that are fixed as a result of these holes. Whereas in 2006, Gracia and co-workers documented that the oleic acid and oleylamine-capped AuNps with 6.7 nm show ferromagnetic behavior.[100] Miyeke and co-workers proposed this can emerge from the spin polarization resulting from the Fermi hole effect.[98] By far no theoretical study has been conducted to reason out the origin of such behaviour. Magnetic behavior of NHC capped NiNPs has been explored.[101] In our previous work, we observed that DiMeCAAC@AuNPs show ferromagnetic behavior. This prompted us to study the magnetism of DiMeCAAC@AuNPs elaboratively using superconducting quantum interference device (SQUID) magnetometry.

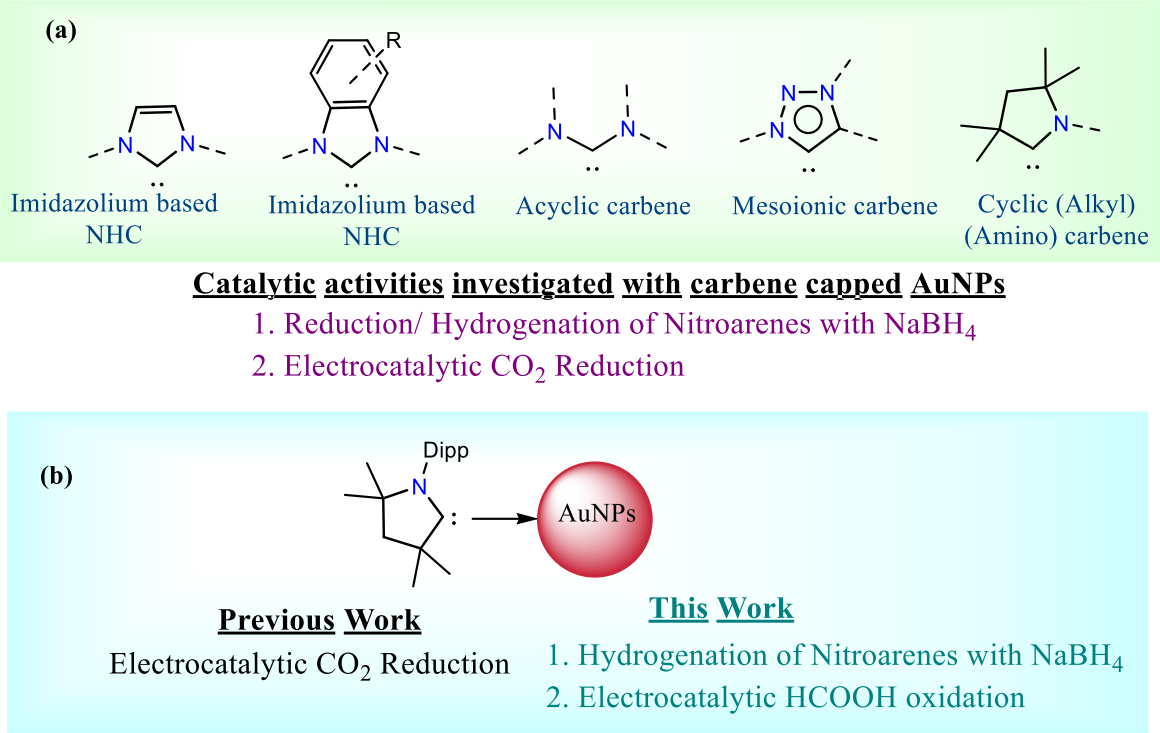

Figure 4B.1. (a) Reported class of carbenes on unsupported AuNPs and their catalytic activities explored; (b) Overview of present work in the context of our previous work.

We also explored the catalytic activity of DiMeCAAC@AuNPs in organic transformation (Figure 4B.1). For this, we performed a reduction of nitroarenes to amines in the presence of $NaBH_4$.[102] It was shown that NHC-capped AuNPs could be used to reduce 4-nitrophenol to 4-aminophenol with sodium borohydride, which is a benchmark reaction for gold

nanocomposites.[103-106] As we screened other nitroarenes in this study, we also used 2-nitroaniline as one of the substrates. 2-nitroaniline is an extremely toxic pollutant. Due to its very poisonous, carcinogenic, and mutagenic qualities, 2-nitroaniline presents severe dangers to aquatic life as well as human health, even at low doses. It can build up in food chains and throw off biological cycles. The US Environmental Protection Agency has classified 2-nitroaniline as a hazardous waste and a priority toxic pollutant;[107] thus, urgent measurement is needed to create effective methods for eliminating 2-nitroaniline from industrial effluent and other sources. However, due to the toxicity of nitro compounds, it is therefore essential that they be eliminated or converted into beneficial goods for the sake of environmental safety.[108] DiMeCAAC@AuNPs acted as an efficient catalyst to reduce nitro arenes to its corresponding amine conjugate. Catalytic applications of NHC-modified AuNPs are very limited[64] and are in their early developing stages. Thus, we sought to explore its electrocatalytic activity towards FAO, which is an anodic reaction in a direct formic acid fuel cell (DFAFC).[109, 110] DFAFC is a promising and sturdy alternative for power consumption because of lower toxicity of formic acid than other liquid fuel cells (methanol and ethanol), high-energy output, and improved oxidation kinetics[111, 112]. Formic acid is liquid fuel where recovery of formic acid does not occur and is fed directly to the fuel cell, producing high electromotive force (emf) and low fuel crossover. Till now, noble metals like palladium, platinum, and gold nanocomposites have been probed for FAO towards more durable and efficient conversion.[112] Having said this, our newly synthesized DiMeCAAC@AuNP has acted as an efficient and stable catalyst for both aforementioned reactions. Through this chapter, we intended to study CAAC as robust ligand backbone for stabilizing MNPs and enhanced catalytic activities both for organic and electrochemical transformations.

4B.3 Results and Discussion.

Following the top-down procedure, we synthesized DiMeCAAC-modified AuNPs (DiMeCAAC@AuNP) *via* the ligand exchange method from oleylamine-capped AuNPs (OA@AuNP) reported in our previous work.[93]

4B.3.1 Magnetic properties.

Magnetic measurements have been performed using a SQUID. The DiMeCAAC@AuNPs were synthesized and measured four times to check the reproducibility of the results. The magnetic properties of the DiMeCAAC@AuNPs were studied by recording both the temperature-dependent magnetization (M-T) and magnetic field-dependent magnetization (M-

H) curves. These curves help us to analyze the nature of the complexes and provide magnetic susceptibility. M-T curves of the complexes are composed of zero-field-cooled (ZFC) and field-cooled (FC) curves.[73] For the ZFC measurement, the samples were cooled to 5 K without an external magnetic field. Hence, the magnetic moments of each atom are frozen to an easy axis of particles. Therefore, the total magnetization of the system is zero. A field of 100 Oe was then applied, and simultaneously, the magnetization was measured with increasing temperature. In the FC measurement, the sample is subjected to the same field, and the temperature is lowered to a lower temperature. After that, the magnetic moment will be measured against increasing temperature. The M-H curve of the complexes informs us of the nature of the complex, whether it is paramagnetic, diamagnetic, ferromagnetic, antiferromagnetic, or supermagnetic in behavior.[72] We have recorded the M-H curve at 5 K and 300 K to study the nature of complexes. At 300 K, the sigmoidal curve in Figure 4B.2a depicts that complex DiMeCAAC@AuNPs show ferromagnetic behavior, which is confirmed by magnetic irreversibility (opening of the loop) extending up to the high field and lack of magnetic saturation up to 6 T with a loop at low field regime.[113] Lack of magnetic saturation in the M(H) curve may be further added due to the paramagnetic contribution of disordered surface spins of the nanoparticles.[100]

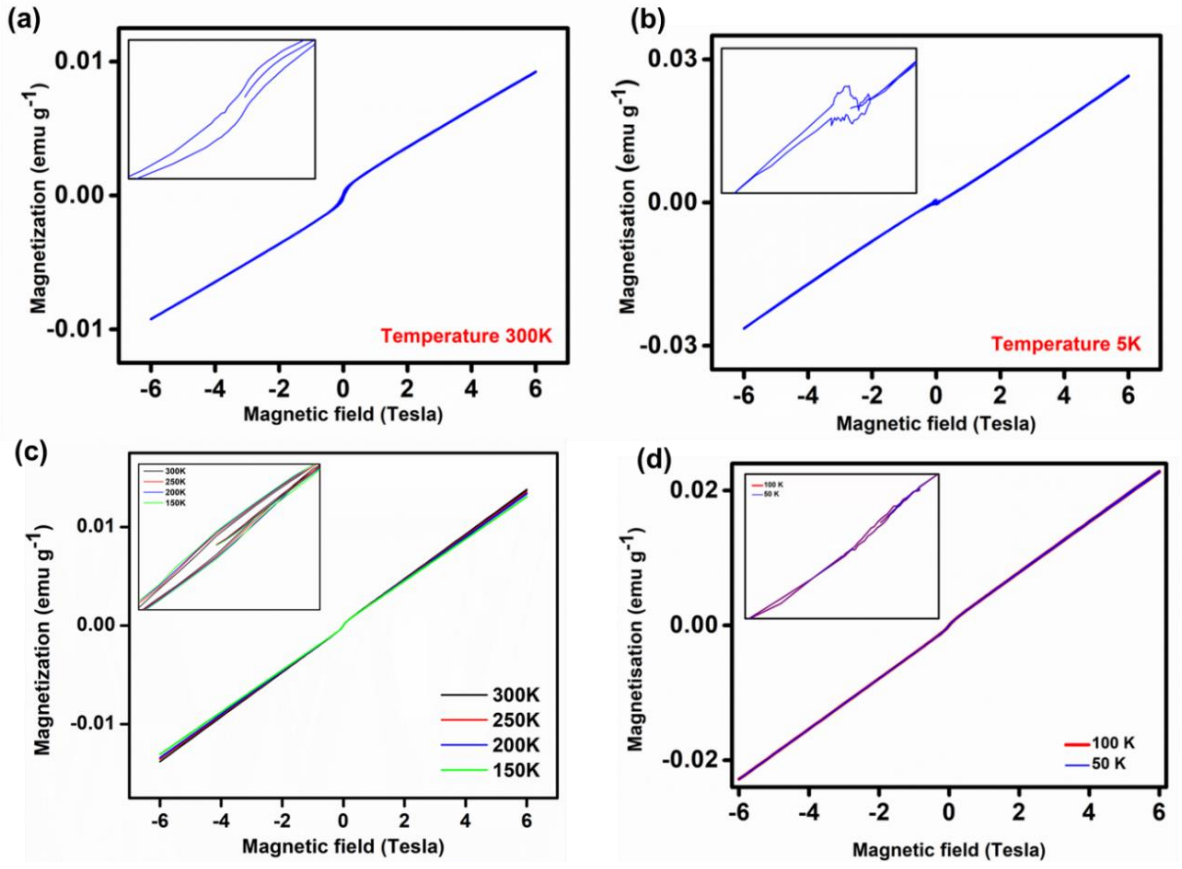

Figure 4B.2. (a) M *vs.* H at 300 K (VSM mode); (b) M vs. H at 5 K (VSM mode); (c) M *vs.* H for DiMeCAAC@AuNPs at variable temperature (300 K, 250 K, 200 K, 150 K) (VSM mode); (d) M *vs.* H for DiMeCAAC@AuNPs at variable temperature (100 K and 50 K) (SQUID mode).

At a lower temperature (5 K), the complex DiMeCAAC@AuNPs shows a straight line with an anomaly at the origin Figure 4B.2b. Figure 4B.2 shows the ferromagnetic behavior of the DiMeCAAC@AuNPs with a Curie temperature above 300 K. The magnetization has remained the same even at low temperature by a field of 6 T, saturation is not achieved from 50 to 300 K, and superparamagnetic behavior is not observed. At 150 K, there is a noticeable coercive field of about 200 Oe, which decreases to 50 Oe at 300 K (Figure 4B.2c).[100] From temperatures 100 and 50 K, a crossover was observed (Figure 4B.2c), which is neither for the paramagnetic nor the superparamagnetic behavior. Figure 4B.3 displays the thermal dependence of magnetization of AuNPs under a direct applied field of 100 Oe for 9.5 nm average mean particle size; the bifurcation in magnetization is observed at 150 K. A phase transition is observed with decreasing temperature.

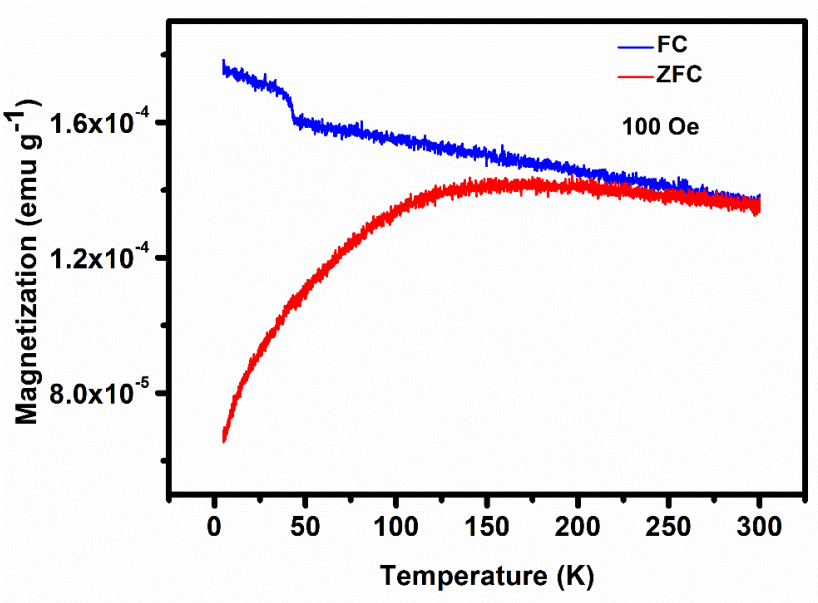

Figure 4B.3. ZFC and FC magnetization curves as a function of temperature for DiMeCAAC@AuNPs measured with an applied field of 100 Oe between 5-300 K.

4B.3.2 Origin of magnetism.

Magnetism in AuNPs is well-reported but not conclusive.[114] The origin of the magnetic order observed in the DiMeCAAC@AuNPs might be very similar to that of the thiol-capped AuNPs.[100] In the case of the thiol-capped one, the Au-S covalent bond is stronger, and the

electronegativity of carbon and sulfur is close by, which leads to the same covalent character as the Au-S bond. The involvement of 5*d* electrons of the Au center in electron redistribution due to size effects can lead to hybridization with 6*s* electrons closer to the Fermi energy level. The significant affinity between Au surface atoms and the surface capping ligand (DiMeCAAC) can result in a substantial charge transfer from Au surface atoms to the donor center of the surface capping ligands, potentially involving the participation of 5*d* electrons. Consequently, unoccupied *d*-state densities situated at Au surface atoms emerge, rendering these atoms prone to magnetic susceptibility.[72] The relationship of the surface to the core electrons is greater than in the DiMeCAAC@AuNPs case due to the smaller size of the former, leading to a negligible diamagnetic contribution.[100] In the case of DiMeCAAC@AuNPs, no longer organic chain was observed, which is present in oleic acid, oleylamine, and DDT-capped NPs, which could lead to a higher contact potential acting on the surface atoms. From here, we could also conclude that a longer CH_2 chain is not a necessary criterion for the ferromagnetic-like behavior in the AuNPs. Hernandez *et al.* have explained the reason behind the "ferromagnetic-like behavior" of AuNPs.[115] They stated that the orbital moment created in atomic-like localized states can be explained by the interaction of contact potential at the large radius domain boundaries with spin-orbit coupling. In this case, electron holes created by electron transport to the organic molecule are the source of the contact potential. Electrostatic forces between trapped electrons in the orbital provide spin alignment, which causes orbital moment alignment *via* spin-orbit coupling.

4B.3.3 Catalytic reduction of nitroarenes.

To check the catalytic activity of the synthesized DiMeCAAC@AuNP, a model reduction in NP catalysis was performed: the reduction of 4-nitrophenol by sodium borohydride ($NaBH_4$) in the presence of AuNPs.[103-105, 116-118] Some NHC-capped AuNPs are known to reduce the nitroarenes in a homogeneous medium, displaying superior activity over many other existing surface-capping ligands.[2, 64-66] Glorius and co-workers also employed NHC-capped bimetallic Au-PdNPs to hydrogenate nitroarenes.[119] Although it showed good functional group tolerance and chemoselectivity, the catalyst loading and conversion time remained higher. Fensterbank, Ribot and co-workers reported the reduction of 4-nitrophenol in a biphasic medium, i.e., in H_2O/CH_2Cl_2.[10] In our case, the DiMeCAAC@AuNPs are not stable in such biphasic medium. To begin with the reduction, we first drop-casted the DiMeCAAC@AuNPs on the Whatman filter paper (1×1 cm) and dried it for 1 hour at 90 °C in an oven before use.[120] A heterogeneous support system (Whatman filter paper) was taken up in our case as the AuNP is not stable in

an aqueous medium, which immediately gets precipitated out in the presence of substrate and $NaBH_4$, nullifying the possibility of the homogeneous mode of operation. Notably, the catalyst-loaded filter paper does not leach out AuNPs upon immersion in the organic and aqueous medium, indicating strong adsorption of AuNPs to the filter paper surface *via* van-der Waals interaction.[120] The progress of the reaction was monitored with the aid of UV-Vis spectroscopy. The instantaneous reaction started to occur when the solution of 4-nitrophenol (6 µL of 50 mM) and $NaBH_4$ (300 µL of 0.1 M) was added to an aqueous solution of DiMeCAAC@AuNPs (18 nM in terms of NPs). The decrease in the peak at ~400 nm, along with the concomitant emergence of a peak at ~300 nm, confirms the conversion of the 4-nitrophenolate ion to 4-aminophenol (Figure 4B.4).[121] The nitro-to-amine reduction catalyzed by DiMeCAAC@AuNPs was completed within 160 min, which was found to follow pseudo-first-order kinetics. The rate constant was calculated to be 0.026 min^{-1} (Figure 4B.4).

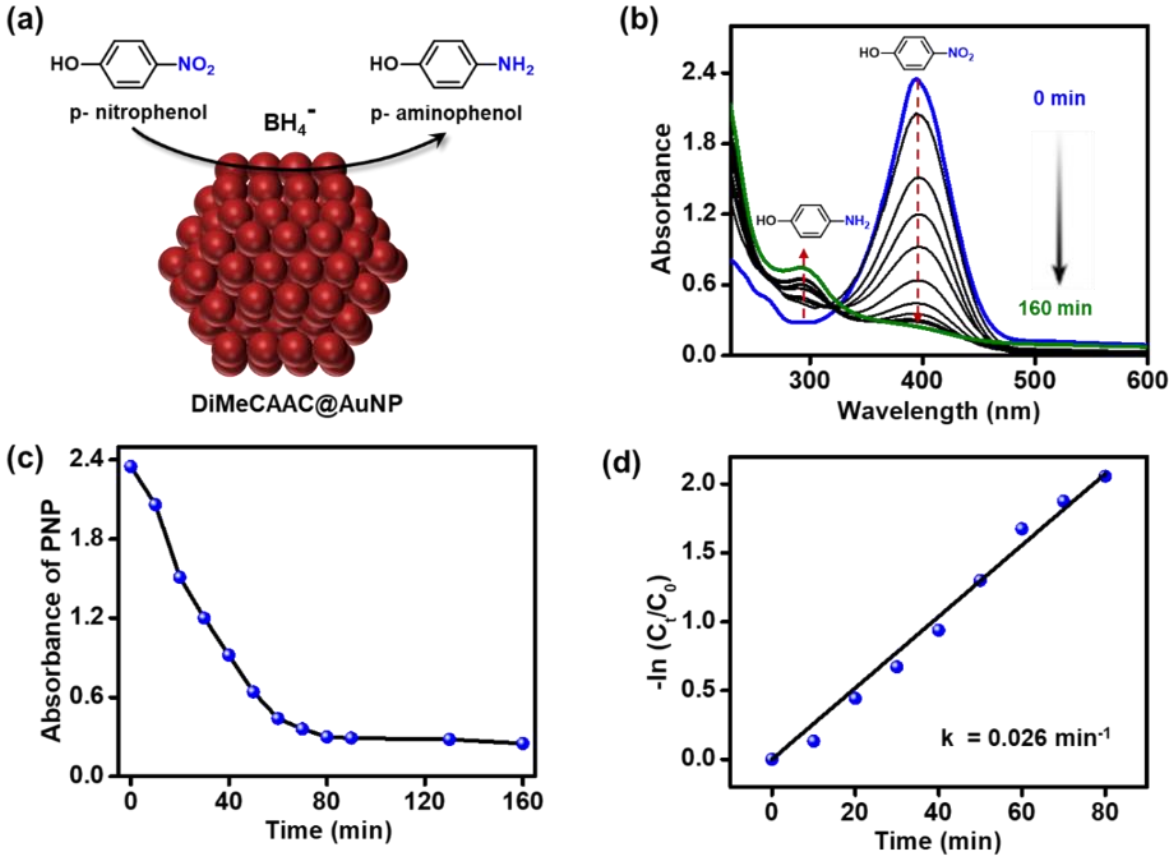

Figure 4B.4. DiMeCAAC@AuNP catalyzed PNP reduction. (a) Schematics showing the DiMeCAAC@AuNP catalyzed PNP reduction by $NaBH_4$. (b) Time-dependent absorption study shows a gradual decrease in the 4-nitrophenolate absorption at ~400 nm along with a concomitant formation of a new band at ~300 nm, corresponding to 4-aminophenolate. (c) Progress of the reaction by monitoring the absorbance changes at 400 nm. (d) Linearized data

for the pseudo-first-order analysis by monitoring the absorption changes of the PNP peak at ~400 nm.

We also performed a control reaction in the presence of only 4-nitrophenol and $NaBH_4$ (without DiMeCAAC@AuNP) for 4 hours, which showed a negligible reduction (Figure 4B.5), confirming the catalyst requirement. Upon increasing the catalyst loading to ~220 nM, the reaction was completed within 10 min (Figure 4B.5). Similarly, by reducing the 4-nitrophenol concentration (6 µL of 25 mM) and keeping the AuNP loading fixed at 220 nM, the reduction was completed within 1 min. (Figure 4B.5).

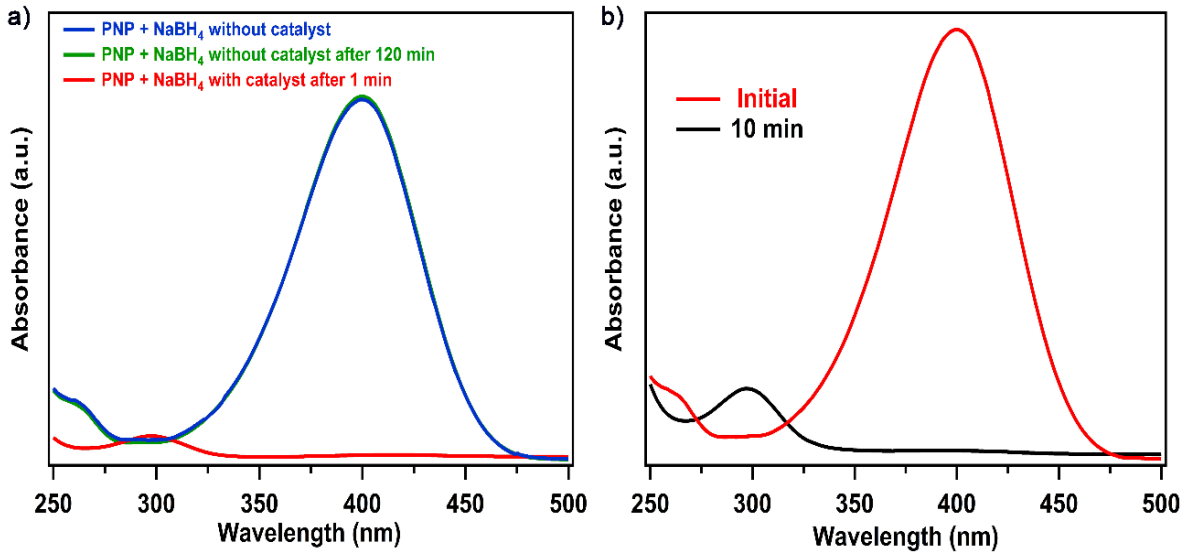

Figure 4B.5. (a) Controlled experiment for *p*-nitrophenol (PNP) reduction (DiMeCAAC@AuNP concentration 220 nM, PNP concentration 25Mm and $NaBH_4$ concentration 0.1M) (b) PNP reduction keeping DiMeCAAC@AuNP concentration 220 nM, PNP concentration 50 mM and $NaBH_4$ concentration 0.1 M.

We have also screened different nitroarenes to broaden the substrate scope, which displayed excellent conversion with the functional group tolerance (Figure 4B.6**)**. In order to showcase the versatility in NP catalysis, we performed the reduction of ferricyanide ($[Fe(CN)_6]^{3-}$) to ferrocyanide ($[Fe(CN)_6]^{4-}$) by BH_4^- catalyzed by DiMeCAAC@AuNP (18 nM) (Figure 4B.6a). The characteristic absorption band of $[Fe(CN)_6]^{3-}$ at 420 nm disappeared upon the completion of the reaction within 1.5 min. In the presence of $NaBH_4$, AuNP possesses negative charges, which are imparted by BH_4^- ions. These negative charges on AuNPs help to promote the $Fe^{3+} \rightarrow Fe^{2+}$ reaction.[116] We also screened different substrates like 2-nitroaniline and 4-nitroacetophenone. For 2-nitroaniline, the reduction was completed within 140 min as the peak at 413 nm disappeared[122] (Figure 4B.6) with 94% yield. For 4-nitroacetophenone

(Figure 4B.6c), the reaction progressed till 130 min; thereafter, no substantial decay of the peak at 277 nm was observed, indicating saturated activity of the catalyst. Based on these catalytic results, we established DiMeCAAC@AuNPs as an effective catalyst for the nitroarene and ferricyanide reduction reactions.

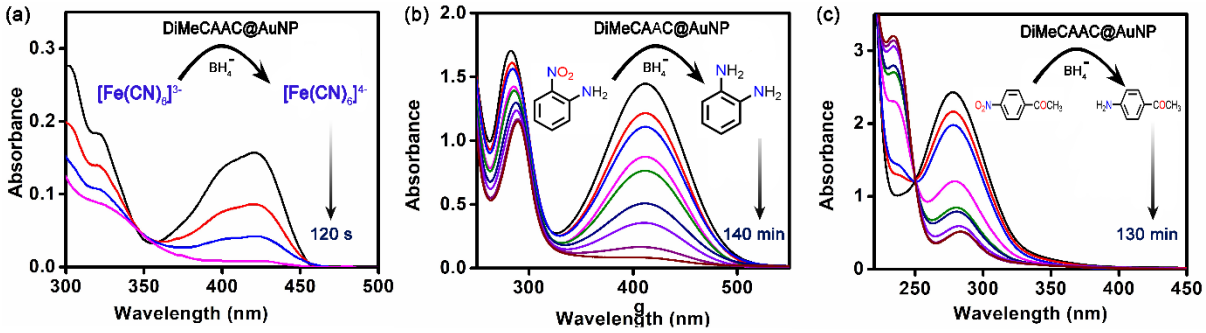

Figure 4B.6. DiMeCAAC@AuNP catalyzed Nitro-arene reduction. Decrements of (a) peak at ~420 nm for potassium ferricyanide; (b) peak at ~413 nm for 2-nitroaniline; (c) peak at ~277 nm for 4-nitroacetophenone and were observed in the presence of 18 nM DiMeCAAC@AuNP and 0.1 M $NaBH_4$.

4B.3.4 Electrocatalytic formic acid oxidation (FAO).

Isolation of DiMeCAAC@AuNP also prompted us to check its electrocatalytic behavior. The electrocatalytic oxidation of formic acid (HCOOH) was conducted using DiMeCAAC@AuNP, OA@AuNP, and bare carbon paper, the latter serving as the substrate for all samples, as illustrated in Figure 4B.7a. The aqueous solution of 0.5 M H_2SO_4 was used as an electrolyte while keeping the scan rate at 50 mV s^{-1}. Nitrogen gas was purged throughout the experiment. After the CV has been stabilized, the fifth scan is plotted. The first four measurement cycles were omitted to avoid the interference of absorbed gases in the solution. Cyclic voltammetry trace shows oxidation potential at the range of 1.3 <V <1.7 (*vs.* RHE) for DiMeCAAC@AuNP, whereas OA@AuNP shows 1.6 V *vs.* RHE (Figure 4B.7a). Lower oxidation potential value and higher peak current density delineate the superior activity of DiMeCAAC over oleyl amine-modified AuNPs. FAO at varying concentrations (0, 0.25, 0.5, and 1.0 M) was carried out individually for DiMeCAAC@AuNP and OA@AuNP, depicted in Figures 4B.7b and 4B.7c, respectively. The oxidation potential observed agrees with forming a single formate ion as an active intermediate, as proposed by Jacob and co-workers.[123] The higher potential (above 1.1 V *vs.* RHE) for formic acid oxidation of Au surfaces is consistent with the oxide formation of gold, which is stable in an acidic electrolytic solution.[124, 125] In the reverse sweep, the Au oxide gets reduced, and then only further oxidation takes place at the anode. We also observed

peak current density increases with increasing concentration of HCOOH. The observed anodic peak starting from 1.8 V *vs.* RHE corroborates the oxygen evolution reaction (OER) occurring during the electrochemical analysis. This is further confirmed by analyzing the OER activity of DiMeCAAC@AuNP in N_2 saturated 0.5 M H_2SO_4 electrolyte, and the corresponding linear sweep voltammogram (LSV) is presented in Figure 4B.7d.

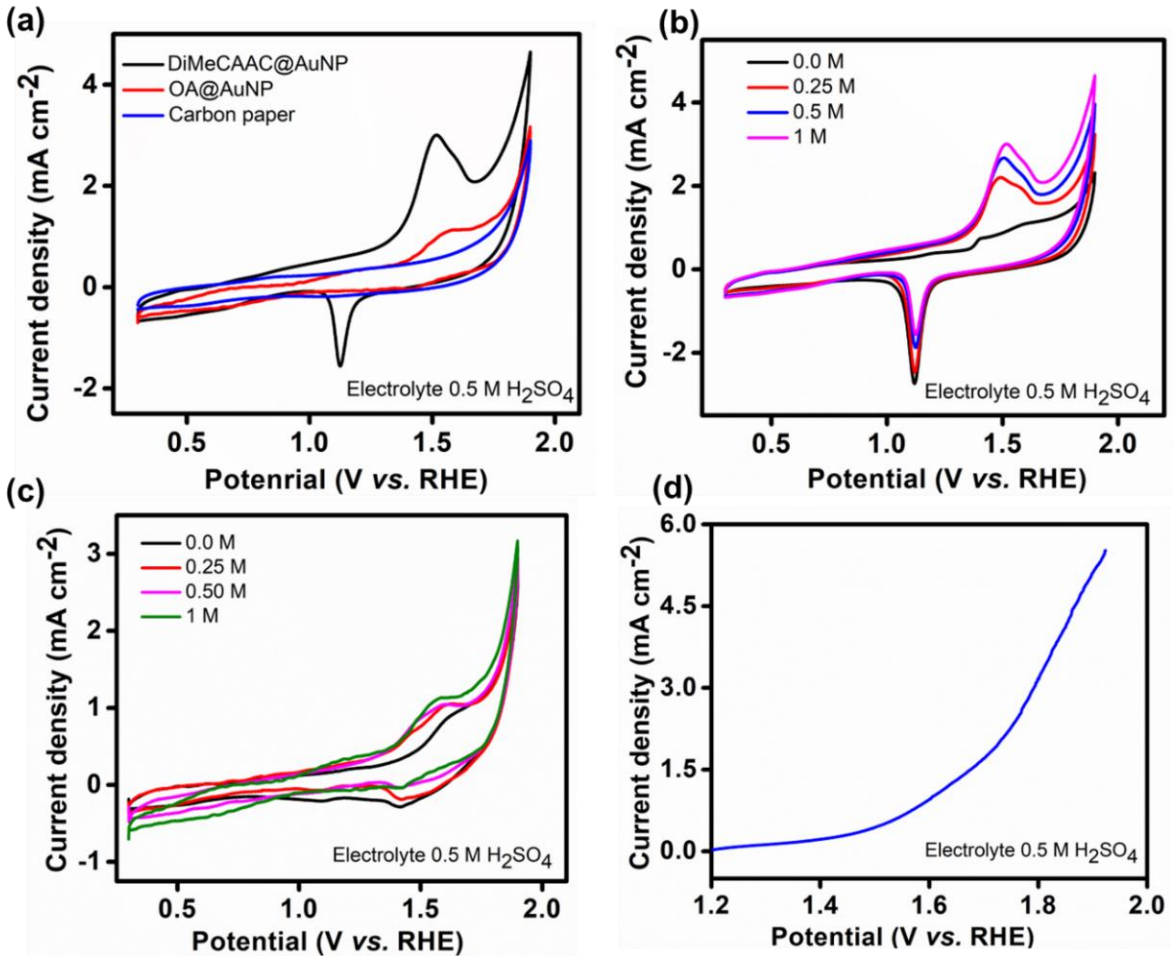

Figure 4B.7. (a) CV traces for HCOOH oxidation at 1.0 M concentration of HCOOH using DiMeCAAC@AuNP, OA@AuNP, and bare carbon paper;(b) CV traces for HCOOH oxidation at various concentrations of HCCOH when the electrocatalyst is DiMeCAAC@AuNP; (c) CV traces for HCOOH oxidation at various concentrations of HCOOH when the electrocatalyst is OA@AuNP; (d) OER linear sweep voltammogram (LSV) of CAAC AuNP recorded in 0.5 M H_2SO_4 electrolyte.

The long-term stability and durability of the catalyst are mainly apprehended when designing an efficient fuel cell. In order to evaluate the catalyst efficiency, it is necessary to investigate the long-term stability in corrosive electrochemical conditions. Thus, the chronoamperometric measurement of DiMeCAAC@AuNP was carried out for 24 hours at a

current density of 3.5 mA cm^{-2}, and the results are shown in Figure 4B.8b. Furthermore, the activity of the DiMeCAAC@AuNP is analyzed for 500 continued cycles of CV (Figure 4B.8a), which shows the gradual increase of efficiency up to 250 cycles and could survive up to 500 cycles. The system demonstrates a stable performance under high current density conditions in the investigated period. The findings support the higher structural integrity of DiMeCAAC@AuNP towards the oxidation of HCOOH. The electrochemical active surface area (ECSA) is an important parameter to study and compare any electrocatalyst, which correlates the active sites of the catalyst and its activity. ECSA of DiMeCAAC@AuNP and OA@AuNP were calculated coulometrically, which is found to be 31.92 and 15.39 $m^2\ g^{-1}_{Au}$ (Table 4B.1).[126] It is evident that ECSA for the former is higher than the latter, which further confirms the enhanced activity of DiMeCAAC@AuNP over oleylamine-capped AuNPs. Apart from that, mass activity and specific activity values are also higher for DiMeCAAC@AuNP (Table 4B.1).

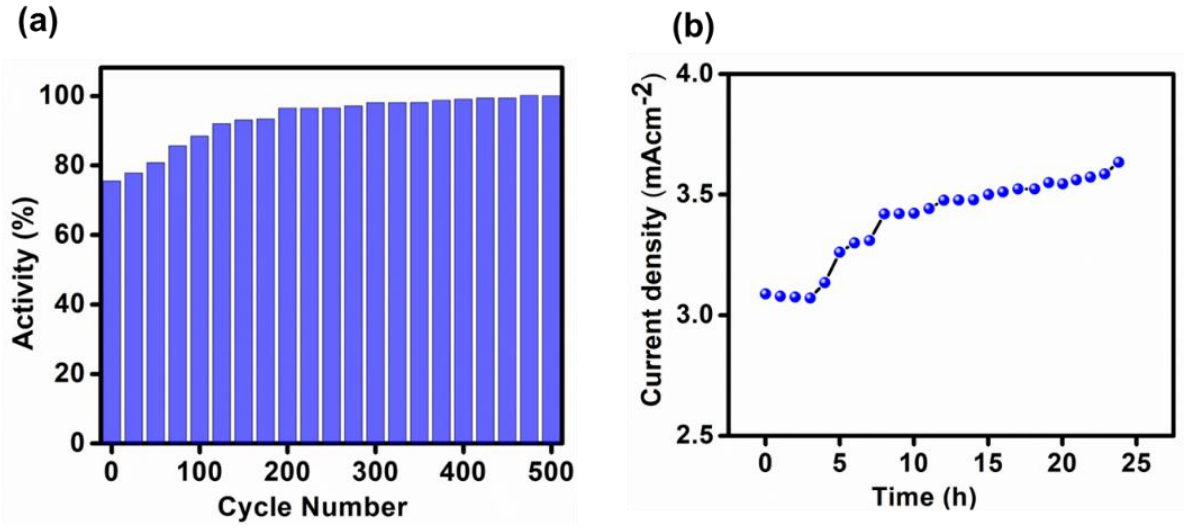

Figure 4B.8. (a) Electrocatalytic durability test of DiMeCAAC@AuNPs in HCOOH (1 M) + H_2SO_4 (0.5 M) electrolyte solution; (b) Chronoamperometric response of DiMeCAAC@AuNPs during formic acid oxidation in 0.5 M H_2SO_4+1 M HCCOH for 24 h at a current density of 3.5 mA cm^{-2}.

Table 4B.1. Details of ECSA, mass activity, and specific activity of DiMeCAAC@AuNP and OA@AuNP

	ECSA ($m^2\ g^{-1}_{Au}$)	**Mass Activity (mA mg^{-1})**	**Specific Activity (mA cm^{-2})**
DiMeCAAC@AuNP	31.92	33.33	9.39

OA@AuNP	15.39	12.59	7.36

4B.4 Conclusion.

Herein, we have demonstrated the catalytic efficiency of CAAC on the AuNPs surface in nitro-arene reduction and formic acid oxidation. We investigate the magnetic properties of DiMeCAAC@AuNPs. The enhanced activity of DiMeCAAC@AuNP towards FAO over oleylamine-capped AuNP has been observed. This infers potential application domain for CAAC stabilized MNPs to flourish in organic transformations and even by exploiting the unique SPR properties of AuNPs.

Chapter 4C: N-heterocyclic Silylene Capped Gold Nanoparticles for CO_2 Functionalization

Adapted from: ***M. Ghosh*** and S. Khan*, N-heterocyclic silylene capped gold nanoparticles for CO_2 functionalization (***Manuscript under preparation***).

4C.1 Objective of this work.

Thus far, N-heterocyclic carbenes have been found to be extensively used in numerous significant catalytic transformations and as a surface-capping ligand on the surface of nanoparticles. It has not yet been reported how useful silicon(II), namely NHSi ligands, can be as auxiliary ligands. Hence, in this work, we wanted to explore NHSi as a surface capping ligand on the surface of AuNPs. Since carbon dioxide reduction is a significant reaction, we aimed to utilize NHSi@AuNPs for this purpose. NMR, IR, UV, XPS spectroscopies, and TEM were used to study the structures and chemical bonding.

4C.2 Introduction.

Over the past years, NHSis have garnered considerable attention primarily for their isolation, structural elucidation, and their remarkable ability to activate small molecules.[127] What sets silylenes apart from carbenes is their unique capacity to access *d*-orbitals, a feat beyond the reach of carbenes. This characteristic, stemming from the presence of lone electron pairs and the accessibility of both vacant *p*- and *d*-orbitals, positions silylenes as superior ligands compared to carbenes. Expanding the scope of Si(II) compounds holds promise for addressing challenges in catalysis and synthetic chemistry.[128, 129] With this work, we seek to introduce a synthetic methodology for fabricating nanoparticles employing NHSis a novel avenue that remains largely unexplored. Moreover, the catalytic potential of Si(II)-AuNPs will be scrutinized for demanding transformations like CO_2 reduction. Furthermore, synthesizing silylene-stabilized metalloid nanoparticles heralds a new era in both organosilicon and nanomaterials disciplines. Tailoring diverse silylenes, predominantly N-heterocyclic amidinate-stabilized silylenes, to stabilize metal nanoparticles represents a noteworthy advancement in silylene chemistry.

4C.3 Results and Discussion.

4C.3.1 Synthesis of NHSi@AuNPs.

The preparation of NHSi@AuNPs generally entails two methods: the reduction method being the primary approach. In this process, the initial step involves the synthesis of ligand-metal complexes, which are then subjected to reduction under varying reaction conditions. Parameters such as temperature, complex concentration, and the nature of the reducing agents play crucial roles in controlling the size and shape of the resulting nanoparticles. Another effective technique is ligand exchange, also known as place exchange, which offers a convenient means to tailor the surface ligands of nanoparticles. In this method, pre-synthesized

nanoparticles are treated with electron-donating ligand stabilizers. This treatment prompts the replacement of the existing ligands with stronger electron-donating ligands. Remarkably, this ligand exchange process typically maintains the size and shape of the nanoparticles while altering their surface chemistry and properties.[4]

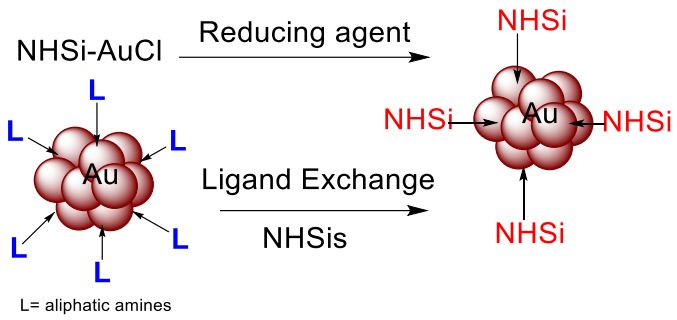

Scheme 4C.1. Synthetic route for the preparation of NHSi@AuNPs.

Due to our success in synthesizing DiMeCAAC@AuNPs with the ligand exchange method, we initially screened many NHSis for the ligand exchange method. However, we could not isolate NHSi@AuNPs. Then, we turned our focus on our previously synthesized compound **2C.3** for the reduction method. We treated complex **2C.3** with potassium selectride (K-selectride), which afforded NHSi@AuNPs as precipitation. The obtained precipitate was then washed, centrifuged, and redispersed in DMSO-d_6.

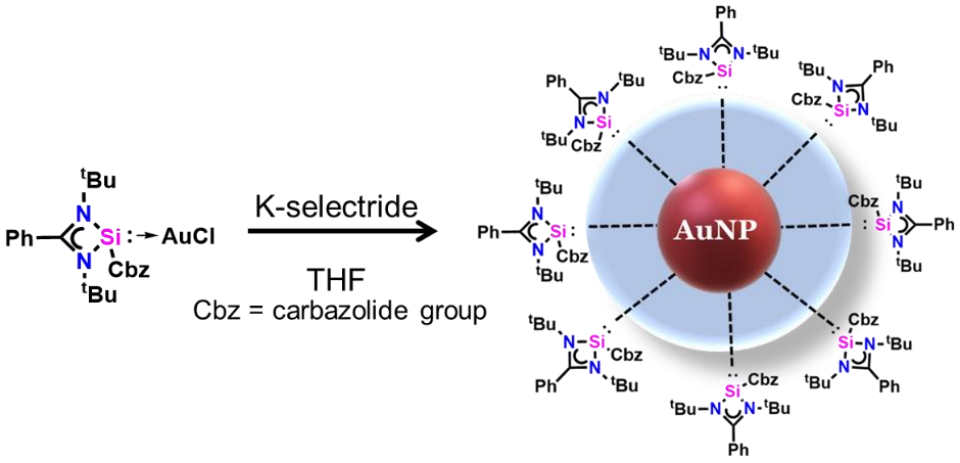

Scheme 4C.2. Synthesis of NHSi@AuNPs synthesis by a bottom-up approach.

The UV-Vis spectra show the SPR band at 535 nm, and TEM analysis shows an average particle size of 5.4 nm. The existence of signature signals for Au 4f, Si 2p, and N 1s of the NHSi ligand on AuNPs was investigated using XPS. For the Au $4f_{7/2}$ and Au $4f_{5/2}$ transitions (Figure 4C.1), we found peaks at 84 and 87.66 eV, respectively, suggesting the sole existence of Au(0).

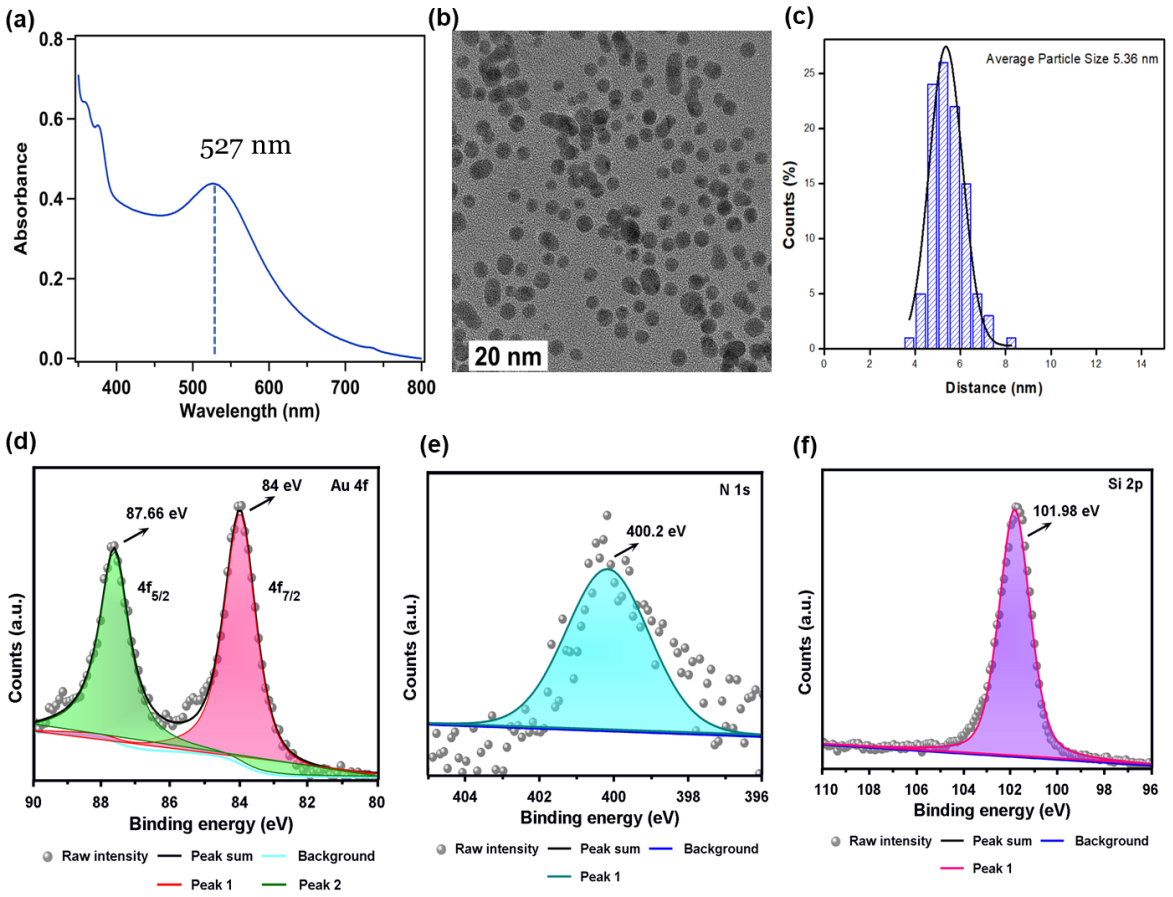

Figure 4C1. (a) UV-Vis spectra of NHSi@AuNPs in DMSO showing the characteristic LSPR band at ~527 nm; (b) A representative TEM image of NHSi@AuNPs; (c) The corresponding size distribution histogram; (d) XPS spectrum NHSi@AuNPs displaying Au 4f peaks; (e) XPS spectrum of NHSi@AuNPs displaying N1s peak; (f) XPS spectrum of NHSi@AuNPs displaying Si 2p peak.

The corresponding Au 4f peaks for NHSi→AuCl appeared at 82.9 and 86.5 eV, which indicates the Au(I) oxidation state (Figure 4C.2). The Si 2p peak at 101.9 and 101.8 eV for NHSi@AuNPs and NHSi→AuCl, respectively, attributed Si(II) oxidation state. The binding energy for N 2p at 400.2 and 399.5 eV for NHSi@AuNPs and NHSi→AuCl, respectively, denotes the structural integrity of the benzamidinate backbone. This binding energy for Au 4f and N 1s aligns with the NHC capped AuNPs.[9, 10, 29, 30, 59-61, 130-132]

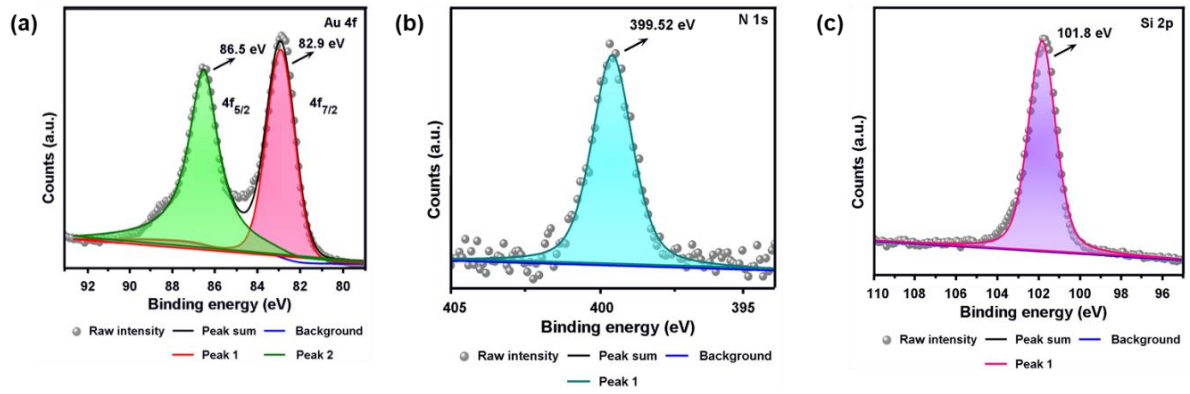

Figure 4C.2. XPS spectra of NHSi→AuCl for (a) Au 4f; (b) N 1s; (c) Si 2p.

After synthesizing the NHSi@AuNPs, we probe it for the hydroboration of CO_2. A growing number of literature reports describing transition metal or metal-free catalytic methods aiming at reducing CO_2 to useful bulk chemicals like methanol (CH_3OH) and HCOOH has raised interest in the chemical utilization of CO_2.[133-135] Homogeneous hydroboration of CO_2 to form various useful C1 products has been obtained.[136] Utilizing pressurized, potentially explosive gases like H_2 poses safety concerns and entails considerable expenses in terms of production, storage, and transportation.[137, 138] Boron-based compounds possess inherent Lewis acidity and oxophilicity, making them adept at activating the C=O bond of carbon dioxide.[139, 140] When CO_2 undergoes reduction by a hydroborane (as illustrated in Scheme 4C.3), it can yield a range of products including formoxyborane (**4C.A**), bis(boryl)-acetal (**4C.B**), methoxyborane (**4C.C**), and bis(boryl)ether (**4C.D**).[141-143] Consequently, achieving high process selectivity is crucial to ensure optimal atom efficiency and to circumvent the need for distillation in separating the diverse products within the reaction mixtures.[140]

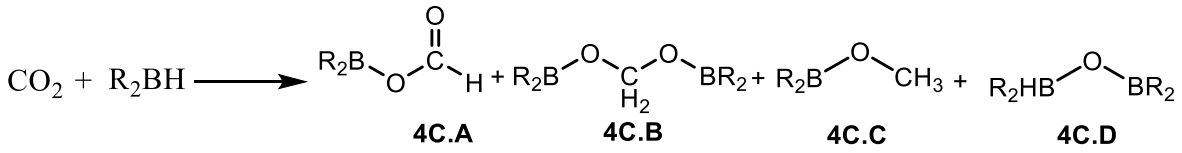

Scheme 4C.3. Various possible products formed during hydroboration of CO_2.

We treated CO_2 in the presence of pinacolborane with NHSi@AuNPs as a catalyst at 80 °C. The crude ^1H NMR shows the exclusive formation of methoxyborane, which, upon hydrolysis and distillation, produces methanol with <90 % yield (Scheme 4C.4 and Figure 4C.3).

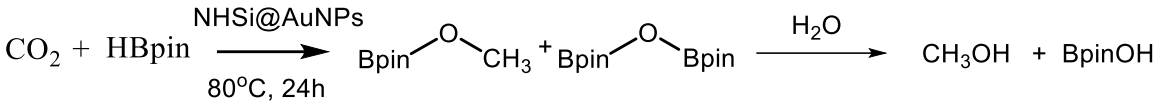

Scheme 4C.4. Hydroboration of CO_2 to methanol with NHSi@AuNPs.

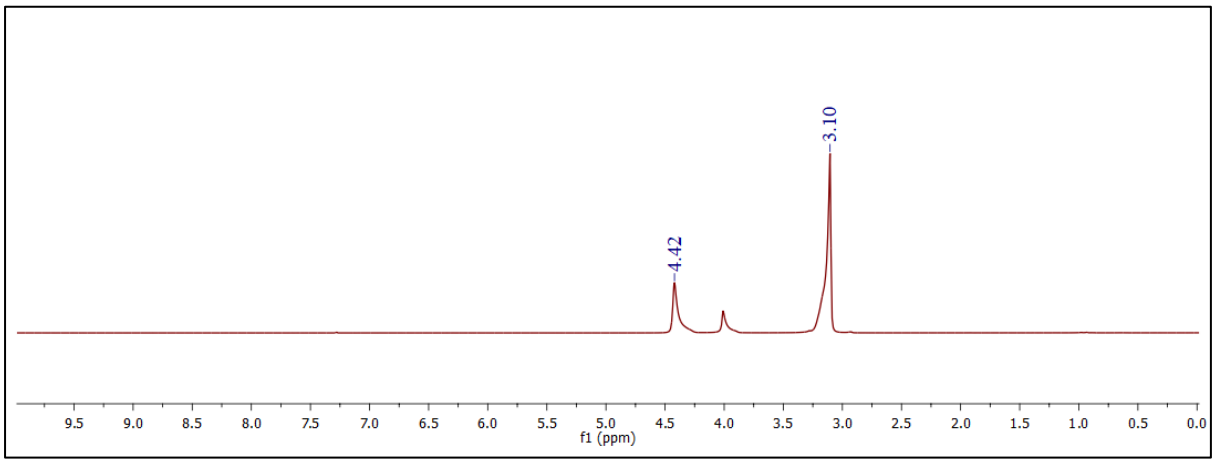

Figure 4C.3. ^{1}H NMR of CH_3OH in $CDCl_3$ obtained after hydrolysis and distillation of methoxyborane.

4C.4 Conclusion.

In summary, our study has showcased the capability of NHSi@AuNPs to facilitate the selective hydroboration of CO_2, resulting in the formation of methoxyborane, which, upon hydrolysis, produces methanol. This exemplifies an innovative application of CO_2 as a C1 building block for chemical synthesis. In the future, we would be interested in utilizing CO_2 in various feedstocks and establishing NHSi as surface capping ligands for other MNP surfaces.

4.1 Bibliography.

(1) Hopkinson, M. N.; Richter, C.; Schedler, M.; Glorius, F. An overview of N-heterocyclic carbenes. *Nature* **2014**, *510*, 485-496.
(2) Koy, M.; Bellotti, P.; Das, M.; Glorius, F. N-Heterocyclic carbenes as tunable ligands for catalytic metal surfaces. *Nat. Catal.* **2021**, *4*, 352-363.
(3) Zhong, R.; Lindhorst, A. C.; Groche, F. J.; Kühn, F. E. Immobilization of N-heterocyclic carbene compounds: a synthetic perspective. *Chem. Rev.* **2017**, *117*, 1970-2058.
(4) Ghosh, M.; Khan, S. N-Heterocyclic Carbenes Capped Metal Nanoparticles: An Overview of Their Catalytic Scope. *ACS Catal.* **2023**, *13*, 9313-9325.
(5) Jain, V.; Roy, S.; Roy, P.; Pillai, P. P. When Design Meets Function: The Prodigious Role of Surface Ligands in Regulating Nanoparticle Chemistry. *Chem. Mater.* **2022**, *34*, 7579-7597.
(6) Rúbio, G. M.; Keppler, B. K.; Chin, J. M.; Reithofer, M. R. Synthetically versatile nitrogen acyclic carbene stabilized gold nanoparticles. *Chem. Eur. J.* **2020**, *26*, 15859-15862.
(7) Cui, L.; Du, M.; Guo, S. Preparation, Characterization and Stability Studies of Gold Nanoparticles Capped by 1, 2, 3-Triazole-Based Mesoionic Carbenes. *Chemistry Select* **2022**, *7*, e202201999.

(8) Nguyen, D. T. H.; Shultz, L. R.; Jurca, T.; Nazemi, A. Monomeric and Polymeric Mesoionic N-Heterocyclic Carbene-Tethered Silver Nanoparticles: Synthesis, Stability, and Catalytic Activity. *Langmuir* **2023**, *39*, 3204-3215.
(9) Nguyen, D. T.; Bélanger-Bouliga, M.; Shultz, L. R.; Maity, A.; Jurca, T.; Nazemi, A. Robust water-soluble gold nanoparticles *via* polymerized mesoionic N-heterocyclic carbene–gold (I) complexes. *Chem. Mater.* **2021**, *33*, 9588-9600.
(10) Porcheron, A.; Sadek, O.; Sowid, S. B.; Bridonneau, N.; Hippolyte, L.; Mercier, D.; Marcus, P.; Mutalliev, L.; Chauvier, C.; Chanéac, C. Direct Synthesis of Mesoionic Carbene (MIC)-Stabilized Gold Nanoparticles from 1, 2, 3-Triazolium Salts. *Chem. Mater.* **2023**, *35*, 6865-6876.
(11) Lee, D. S.; Singh, I.; Veinot, A. J.; Aloisio, M. D.; Lomax, J. T.; Ragogna, P. J.; Crudden, C. M. Mesoionic carbene-based self-assembled monolayers on gold. *Chem. Sci.* **2024**, *15*, 2480-2485.
(12) Nosratabad, N. A.; Jin, Z.; Du, L.; Thakur, M.; Mattoussi, H. N-heterocyclic carbene-stabilized gold nanoparticles: mono-versus multidentate ligands. *Chem. Mater.* **2021**, *33*, 921-933.
(13) Melaimi, M.; Jazzar, R.; Soleilhavoup, M.; Bertrand, G. Cyclic (alkyl)(amino) carbenes (CAACs): recent developments. *Angew. Chem. Int. Ed.* **2017**, *56*, 10046-10068.
(14) Shen, H.; Tian, G.; Xu, Z.; Wang, L.; Wu, Q.; Zhang, Y.; Teo, B. K.; Zheng, N. N-heterocyclic carbene coordinated metal nanoparticles and nanoclusters. *Coord. Chem. Rev.* **2022**, *458*, 214425-214451.
(15) Smith, C. A.; Narouz, M. R.; Lummis, P. A.; Singh, I.; Nazemi, A.; Li, C.-H.; Crudden, C. M. N-Heterocyclic carbenes in materials chemistry. *Chem. Rev.* **2019**, *119*, 4986-5056.
(16) Zhukhovitskiy, A. V.; MacLeod, M. J.; Johnson, J. A. Carbene ligands in surface chemistry: from stabilization of discrete elemental allotropes to modification of nanoscale and bulk substrates. *Chem. Rev.* **2015**, *115*, 11503-11532.
(17) Kundu, S.; Sinhababu, S.; Chandrasekhar, V.; Roesky, H. W. Stable cyclic (alkyl)(amino) carbene (cAAC) radicals with main group substituents. *Chem. Sci.* **2019**, *10*, 4727-4741.
(18) Soleilhavoup, M.; Bertrand, G. Cyclic (alkyl)(amino) carbenes (CAACs): stable carbenes on the rise. *Acc. Chem. Res.* **2015**, *48*, 256-266.
(19) Wang, Y.; Robinson, G. H. Counterintuitive Chemistry: Carbene Stabilization of Zero-Oxidation State Main Group Species. *J. Am. Chem. Soc.* **2023**, *145*, 5592-5612.
(20) Hahn, F. E. Heterocyclic carbenes. *Angew. Chem. Int. Ed.* **2006**, *45*, 1348-1352.
(21) Melaimi, M.; Soleilhavoup, M.; Bertrand, G. Stable cyclic carbenes and related species beyond diaminocarbenes. *Angew. Chem. Int. Ed.* **2010**, *49*, 8810-8849.
(22) Légaré, M.-A.; Rang, M.; Bélanger-Chabot, G.; Schweizer, J. I.; Krummenacher, I.; Bertermann, R.; Arrowsmith, M.; Holthausen, M. C.; Braunschweig, H. The reductive coupling of dinitrogen. *Science* **2019**, *363*, 1329-1332.
(23) Légaré, M.-A.; Bélanger-Chabot, G.; Rang, M.; Dewhurst, R. D.; Krummenacher, I.; Bertermann, R.; Braunschweig, H. One-pot, room-temperature conversion of dinitrogen to ammonium chloride at a main-group element. *Nat. Chem.* **2020**, *12*, 1076-1080.
(24) Légaré, M.-A.; Bélanger-Chabot, G.; Dewhurst, R. D.; Welz, E.; Krummenacher, I.; Engels, B.; Braunschweig, H. Nitrogen fixation and reduction at boron. *Science* **2018**, *359*, 896-900.
(25) Oldroyd, N. L.; Chitnis, S. S.; Annibale, V. T.; Arz, M. I.; Sparkes, H. A.; Manners, I. Metal-free dehydropolymerisation of phosphine-boranes using cyclic (alkyl)(amino) carbenes as hydrogen acceptors. *Nat. Commun.* **2019**, *10*, 1370.
(26) Mondal, K. C.; Roy, S.; Maity, B.; Koley, D.; Roesky, H. W. Estimation of σ-donation and π-backdonation of cyclic alkyl (amino) carbene-containing compounds. *Inorg. Chem.* **2016**, *55*, 163-169.

(27) Weinberger, D. S.; Melaimi, M.; Moore, C. E.; Rheingold, A. L.; Frenking, G.; Jerabek, P.; Bertrand, G. Isolation of neutral mono-and dinuclear gold complexes of cyclic (alkyl)(amino) carbenes. *Angew. Chem. Int. Ed.* **2013**, *52*, 8964-8967.
(28) Tsui, E. Y.; Müller, P.; Sadighi, J. P. Reactions of a Stable Monomeric Gold(I) Hydride Complex. *Angew. Chem. Int. Ed.* **2008**, *47*, 8937-8940.
(29) Bakker, A.; Freitag, M.; Kolodzeiski, E.; Bellotti, P.; Timmer, A.; Ren, J.; Schulze Lammers, B.; Moock, D.; Roesky, H. W.; Mönig, H.; Amirjalayer, S.; Fuchs, H.; Glorius, F. An Electron-Rich Cyclic (Alkyl)(Amino)Carbene on Au(111), Ag(111), and Cu(111) Surfaces. *Angew. Chem. Int. Ed.* **2020**, *59*, 13643-13646.
(30) Ren, J.; Freitag, M.; Gao, Y.; Bellotti, P.; Das, M.; Schulze Lammers, B.; Mönig, H.; Zhang, Y.; Daniliuc, C. G.; Du, S.; Fuchs, H.; Glorius, F. Reversible Self-Assembly of an N-Heterocyclic Carbene on Metal Surfaces. *Angew. Chem. Int. Ed.* **2022**, *61*, e202115104.
(31) Mahmoudi, H.; Mahmoudi, M.; Doustdar, O.; Jahangiri, H.; Tsolakis, A.; Gu, S.; LechWyszynski, M. A review of Fischer Tropsch synthesis process, mechanism, surface chemistry and catalyst formulation. *Biofuels Eng.* **2017**, *2*, 11-31.
(32) Cañete, B.; Gigola, C. E.; Brignole, N. B. Synthesis gas processes for methanol production *via* CH_4 reforming with CO_2, H_2O, and O_2. *Ind. Eng. Chem. Res.* **2014**, *53*, 7103-7112.
(33) Benson, E. E.; Kubiak, C. P.; Sathrum, A. J.; Smieja, J. M. Electrocatalytic and homogeneous approaches to conversion of CO_2 to liquid fuels. *Chem. Soc. Rev.* **2009**, *38*, 89-99.
(34) Amanullah, S.; Saha, P.; Nayek, A.; Ahmed, M. E.; Dey, A. Biochemical and artificial pathways for the reduction of carbon dioxide, nitrite and the competing proton reduction: effect of 2nd sphere interactions in catalysis. *Chem. Soc. Rev.* **2021**, *50*, 3755-3823.
(35) Appel, A. M.; Bercaw, J. E.; Bocarsly, A. B.; Dobbek, H.; DuBois, D. L.; Dupuis, M.; Ferry, J. G.; Fujita, E.; Hille, R.; Kenis, P. J. A.; Kerfeld, C. A.; Morris, R. H.; Peden, C. H. F.; Portis, A. R.; Ragsdale, S. W.; Rauchfuss, T. B.; Reek, J. N. H.; Seefeldt, L. C.; Thauer, R. K.; Waldrop, G. L. Frontiers, Opportunities, and Challenges in Biochemical and Chemical Catalysis of CO_2 Fixation. *Chem. Rev.* **2013**, *113*, 6621-6658.
(36) Massie, A. A.; Schremmer, C.; Ruter, I.; Dechert, S.; Siewert, I.; Meyer, F. Selective Electrocatalytic CO2 Reduction to CO by an NHC-Based Organometallic Heme Analogue. *ACS Catal.* **2021**, *11*, 3257-3267.
(37) Barrett, J. A.; Miller, C. J.; Kubiak, C. P. Electrochemical reduction of CO_2 using Group VII Metal catalysts. *Trends Chem.* **2021**, *3*, 176-187.
(38) Clark, M. L.; Ge, A.; Videla, P. E.; Rudshteyn, B.; Miller, C. J.; Song, J.; Batista, V. S.; Lian, T.; Kubiak, C. P. CO_2 reduction catalysts on gold electrode surfaces influenced by large electric fields. *J. Am. Chem. Soc.* **2018**, *140*, 17643-17655.
(39) Cheung, P. L.; Kapper, S. C.; Zeng, T.; Thompson, M. E.; Kubiak, C. P. Improving photocatalysis for the reduction of CO_2 through non-covalent supramolecular assembly. *J. Am. Chem. Soc.* **2019**, *141*, 14961-14965.
(40) Lu, X.; Wu, Y.; Yuan, X.; Huang, L.; Wu, Z.; Xuan, J.; Wang, Y.; Wang, H. High-performance electrochemical CO_2 reduction cells based on non-noble metal catalysts. *ACS Energy Lett.* **2018**, *3*, 2527-2532.
(41) An, L.; Zhang, H.; Zhu, J.; Xi, S.; Huang, B.; Sun, M.; Peng, Y.; Xi, P.; Yan, C. H. Balancing activity and stability in spinel cobalt oxides through geometrical sites occupation towards efficient electrocatalytic oxygen evolution. *Angew. Chem. Int. Ed.* **2023**, *62*, e202214600.
(42) Pugliese, E.; Gotico, P.; Wehrung, I.; Boitrel, B.; Quaranta, A.; Ha-Thi, M.-H.; Pino, T.; Sircoglou, M.; Leibl, W.; Halime, Z.; Aukauloo, A. Dissection of Light-Induced Charge

Accumulation at a Highly Active Iron Porphyrin: Insights in the Photocatalytic CO_2 Reduction. *Angew. Chem. Int. Ed.* **2022**, *61*, e202117530.
(43) Gotico, P.; Roupnel, L.; Guillot, R.; Sircoglou, M.; Leibl, W.; Halime, Z.; Aukauloo, A. Atropisomeric hydrogen bonding control for CO_2 binding and enhancement of electrocatalytic reduction at iron porphyrins. *Angew. Chem. Int. Ed.* **2020**, *59*, 22451-22455.
(44) Pei, Y. H.; Zhong, H.; Jin, F. M. A brief review of electrocatalytic reduction of CO_2: Materials, reaction conditions, and devices. *Energy Sci. Eng.* **2021**, *9*, 1012-1032.
(45) Frey, G. D.; Lavallo, V.; Donnadieu, B.; Schoeller, W. W.; Bertrand, G. Facile splitting of hydrogen and ammonia by nucleophilic activation at a single carbon center. *Science* **2007**, *316*, 439-441.
(46) Kumar Kushvaha, S.; Mishra, A.; Roesky, H. W.; Chandra Mondal, K. Recent advances in the domain of cyclic (alkyl)(amino) carbenes. *Chem. Asian J.* **2022**, *17*, e202101301.
(47) Gao, Y.; Yazdani, S.; Kendrick IV, A.; Junor, G. P.; Kang, T.; Grotjahn, D. B.; Bertrand, G.; Jazzar, R.; Engle, K. M. Cyclic (Alkyl)(amino) carbene Ligands Enable Cu-Catalyzed Markovnikov Protoboration and Protosilylation of Terminal Alkynes: A Versatile Portal to Functionalized Alkenes. *Angew. Chem. Int. Ed.* **2021**, *60*, 19871-19878.
(48) Romero, E. A.; Jazzar, R.; Bertrand, G. Copper-catalyzed dehydrogenative borylation of terminal alkynes with pinacolborane. *Chem. Sci.* **2017**, *8*, 165-168.
(49) Peltier, J. L.; Soleilhavoup, M.; Martin, D.; Jazzar, R.; Bertrand, G. Absolute templating of M (111) cluster surrogates by galvanic exchange. *J. Am. Chem. Soc.* **2020**, *142*, 16479-16485.
(50) Cao, Z.; Kim, D.; Hong, D.; Yu, Y.; Xu, J.; Lin, S.; Wen, X.; Nichols, E. M.; Jeong, K.; Reimer, J. A.; Peidong, Y.; J., C. C. A molecular surface functionalization approach to tuning nanoparticle electrocatalysts for carbon dioxide reduction. *J. Am. Chem. Soc.* **2016**, *138*, 8120-8125.
(51) Zhang, L.; Wei, Z.; Thanneeru, S.; Meng, M.; Kruzyk, M.; Ung, G.; Liu, B.; He, J. A Polymer Solution To Prevent Nanoclustering and Improve the Selectivity of Metal Nanoparticles for Electrocatalytic CO_2 Reduction. *Angew. Chem. Int. Ed.* **2019**, *58*, 15834-15840.
(52) Luo, Q.; Duan, H.; McLaughlin, M. C.; Wei, K.; Tapia, J.; Adewuyi, J. A.; Shuster, S.; Liaqat, M.; Suib, S. L.; Ung, G. Why surface hydrophobicity promotes CO_2 electroreduction: a case study of hydrophobic polymer N-heterocyclic carbenes. *Chem. Sci.* **2023**, *14*, 9664-9677.
(53) Narouz, M. R.; Osten, K. M.; Unsworth, P. J.; Man, R. W. Y.; Salorinne, K.; Takano, S.; Tomihara, R.; Kaappa, S.; Malola, S.; Dinh, C.-T.; Padmos, J. D.; Ayoo, K.; Garrett, P. J.; Nambo, M.; Horton, J. H.; Sargent, E. H.; Häkkinen, H.; Tsukuda, T.; Crudden, C. M. N-heterocyclic carbene-functionalized magic-number gold nanoclusters. *Nat. Chem.* **2019**, *11*, 419-425.
(54) Kulkarni, V. K.; Khiarak, B. N.; Takano, S.; Malola, S.; Albright, E. L.; Levchenko, T. I.; Aloisio, M. D.; Dinh, C.-T.; Tsukuda, T.; Häkkinen, H.; Crudden, C. M. N-Heterocyclic Carbene-Stabilized Hydrido Au_{24} Nanoclusters: Synthesis, Structure, and Electrocatalytic Reduction of CO_2. *J. Am. Chem. Soc.* **2022**, *144*, 9000-9006.
(55) Albright, E. L.; Malola, S.; Jacob, S. I.; Yi, H.; Takano, S.; Mimura, K.; Tsukuda, T.; Häkkinen, H.; Nambo, M.; Crudden, C. M. Enantiopure Chiral Au_{13} Nanoclusters Stabilized by Ditopic N-Heterocyclic Carbenes: Synthesis, Characterization, and Electrocatalytic Reduction of CO_2. *Chem. Mater.* **2024**.
(56) Liu, S.; Chen, G.; Prasad, P. N.; Swihart, M. T. Synthesis of monodisperse Au, Ag, and Au–Ag alloy nanoparticles with tunable size and surface plasmon resonance frequency. *Chem. Mater.* **2011**, *23*, 4098-4101.

(57) Aslam, M.; Fu, L.; Su, M.; Vijayamohanan, K.; Dravid, V. P. Novel one-step synthesis of amine-stabilized aqueous colloidal gold nanoparticles. *J. Mater. Chem.* **2004**, *14*, 1795-1797.
(58) Polavarapu, L.; Venkatram, N.; Ji, W.; Xu, Q.-H. Optical-limiting properties of oleylamine-capped gold nanoparticles for both femtosecond and nanosecond laser pulses. *ACS Appl. Mater. Interfaces* **2009**, *1*, 2298-2303.
(59) DeJesus, J. F.; Sherman, L. M.; Yohannan, D. J.; Becca, J. C.; Strausser, S. L.; Karger, L. F. P.; Jensen, L.; Jenkins, D. M.; Camden, J. P. A Benchtop Method for Appending Protic Functional Groups to N-Heterocyclic Carbene Protected Gold Nanoparticles. *Angew. Chem. Int. Ed.* **2020**, *59*, 7585-7590.
(60) Wang, G.; Rühling, A.; Amirjalayer, S.; Knor, M.; Ernst, J. B.; Richter, C.; Gao, H.-J.; Timmer, A.; Gao, H.-Y.; Doltsinis, N. L.; Glorius, F.; Fuchs, H. Ballbot-type motion of N-heterocyclic carbenes on gold surfaces. *Nat. Chem.* **2017**, *9*, 152-156.
(61) Sherman, L. M.; Strausser, S. L.; Borsari, R. K.; Jenkins, D. M.; Camden, J. P. Imidazolinium N-Heterocyclic Carbene Ligands for Enhanced Stability on Gold Surfaces. *Langmuir* **2021**, *37*, 5864-5871.
(62) Murphy, C. J.; Sau, T. K.; Gole, A. M.; Orendorff, C. J.; Gao, J.; Gou, L.; Hunyadi, S. E.; Li, T. Anisotropic metal nanoparticles: synthesis, assembly, and optical applications. *J. Phys. Chem. B* **2005**, *109*, 13857-13870.
(63) Sardar, R.; Funston, A. M.; Mulvaney, P.; Murray, R. W. Gold nanoparticles: past, present, and future. *Langmuir* **2009**, *25*, 13840-13851.
(64) Eisen, C.; Chin, J. M.; Reithofer, M. R. Catalytically Active Gold Nanomaterials Stabilized by N-heterocyclic Carbenes. *Chem. Asian J.* **2021**, *16*, 3026-3037.
(65) Gou, X. X.; Liu, T.; Wang, Y. Y.; Han, Y. F. Ultrastable and Highly Catalytically Active N-Heterocyclic-Carbene-Stabilized Gold Nanoparticles in Confined Spaces. *Angew. Chem. Int. Ed.* **2020**, *59*, 16683-16689.
(66) Kaur, G.; Thimes, R. L.; Camden, J. P.; Jenkins, D. M. Fundamentals and applications of N-heterocyclic carbene functionalized gold surfaces and nanoparticles. *Chem. Commun.* **2022**, *58*, 13188-13197.
(67) Moock, D.; Wiesenfeldt, M. P.; Freitag, M.; Muratsugu, S.; Ikemoto, S.; Knitsch, R.; Schneidewind, J.; Baumann, W.; Schäfer, A. H.; Timmer, A.; Tada, M.; Hansen, M. R.; Glorius, F. Mechanistic Understanding of the Heterogeneous, Rhodium-Cyclic (Alkyl)(Amino)Carbene-Catalyzed (Fluoro-)Arene Hydrogenation. *ACS Catal.* **2020**, *10*, 6309-6317.
(68) Reddy, S.; Stephan, C. Analysis of Surface Bound Organic Ligands on Gold Nanomaterials Using Direct Sample Analysis–Time of Flight Mass Spectrometry. PerkinElmer Inc: 2015.
(69) Dominique, N. L.; Strausser, S. L.; Olson, J. E.; Boggess, W. C.; Jenkins, D. M.; Camden, J. P. Probing N-Heterocyclic Carbene Surfaces with Laser Desorption Ionization Mass Spectrometry. *Anal. Chem.* **2021**, *93*, 13534-13538.
(70) Narouz, M. R.; Li, C.-H.; Nazemi, A.; Crudden, C. M. Amphiphilic N-heterocyclic carbene-stabilized gold nanoparticles and their self-assembly in polar solvents. *Langmuir* **2017**, *33*, 14211-14219.
(71) Van Roosbroeck, R.; Van Roy, W.; Stakenborg, T.; Trekker, J.; D'Hollander, A.; Dresselaers, T.; Himmelreich, U.; Lammertyn, J.; Lagae, L. Synthetic antiferromagnetic nanoparticles as potential contrast agents in MRI. *ACS Nano* **2014**, *8*, 2269-2278.
(72) Garitaonandia, J. S.; Insausti, M.; Goikolea, E.; Suzuki, M.; Cashion, J. D.; Kawamura, N.; Ohsawa, H.; Gil de Muro, I.; Suzuki, K.; Plazaola, F.; Rojo, T. Chemically Induced Permanent Magnetism in Au, Ag, and Cu Nanoparticles: Localization of the Magnetism by Element Selective Techniques. *Nano Lett.* **2008**, *8*, 661-667.

(73) Nealon, G. L.; Donnio, B.; Greget, R.; Kappler, J.-P.; Terazzi, E.; Gallani, J.-L. Magnetism in gold nanoparticles. *Nanoscale* **2012**, *4*, 5244-5258.
(74) Mahmoud, M. A.; Chamanzar, M.; Adibi, A.; El-Sayed, M. A. Effect of the dielectric constant of the surrounding medium and the substrate on the surface plasmon resonance spectrum and sensitivity factors of highly symmetric systems: silver nanocubes. *J. Am. Chem. Soc.* **2012**, *134*, 6434-6442.
(75) Zhao, S.; Jin, R.; Jin, R. Opportunities and challenges in CO_2 reduction by gold-and silver-based electrocatalysts: from bulk metals to nanoparticles and atomically precise nanoclusters. *ACS Energy Lett.* **2018**, *3*, 452-462.
(76) Zhu, W.; Michalsky, R.; Metin, O. n.; Lv, H.; Guo, S.; Wright, C. J.; Sun, X.; Peterson, A. A.; Sun, S. Monodisperse Au nanoparticles for selective electrocatalytic reduction of CO_2 to CO. *J. Am. Chem. Soc.* **2013**, *135*, 16833-16836.
(77) Rogers, C.; Perkins, W. S.; Veber, G.; Williams, T. E.; Cloke, R. R.; Fischer, F. R. Synergistic enhancement of electrocatalytic CO_2 reduction with gold nanoparticles embedded in functional graphene nanoribbon composite electrodes. *J. Am. Chem. Soc.* **2017**, *139*, 4052-4061.
(78) Trindell, J. A.; Clausmeyer, J.; Crooks, R. M. Size stability and H_2/CO selectivity for Au nanoparticles during electrocatalytic CO_2 reduction. *J. Am. Chem. Soc.* **2017**, *139*, 16161-16167.
(79) Souza, M. L.; Lima, F. H. Dibenzyldithiocarbamate-functionalized small gold nanoparticles as selective catalysts for the electrochemical reduction of CO_2 to CO. *ACS Catal.* **2021**, *11*, 12208-12219.
(80) Cao, Z.; Zacate, S. B.; Sun, X.; Liu, J.; Hale, E. M.; Carson, W. P.; Tyndall, S. B.; Xu, J.; Liu, X.; Liu, X.; Song, C.; Luo, J.-H.; Cheng, M.-J.; Wen, X.; Liu, W. Tuning Gold Nanoparticles with Chelating Ligands for Highly Efficient Electrocatalytic CO_2 Reduction. *Angew. Chem. Int. Ed.* **2018**, *57*, 12675-12679.
(81) Lasch, P. Spectral pre-processing for biomedical vibrational spectroscopy and microspectroscopic imaging. *Chemom. Intell. Lab. Syst.* **2012**, *117*, 100-114.
(82) Sun, Z.; Ma, T.; Tao, H.; Fan, Q.; Han, B. Fundamentals and challenges of electrochemical CO_2 reduction using two-dimensional materials. *Chem.* **2017**, *3*, 560-587.
(83) Liu, S.; Tao, H.; Zeng, L.; Liu, Q.; Xu, Z.; Liu, Q.; Luo, J.-L. Shape-dependent electrocatalytic reduction of CO_2 to CO on triangular silver nanoplates. *J. Am. Chem. Soc.* **2017**, *139*, 2160-2163.
(84) Garg, S.; Li, M.; Weber, A. Z.; Ge, L.; Li, L.; Rudolph, V.; Wang, G.; Rufford, T. E. Advances and challenges in electrochemical CO_2 reduction processes: an engineering and design perspective looking beyond new catalyst materials. *J. Mater. Chem. A* **2020**, *8*, 1511-1544.
(85) Bellotti, P.; Koy, M.; Hopkinson, M. N.; Glorius, F. Recent advances in the chemistry and applications of N-heterocyclic carbenes. *Nat. Rev. Chem* **2021**, *5*, 711-725.
(86) Bourissou, D.; Guerret, O.; Gabbai, F. P.; Bertrand, G. Stable carbenes. *Chem. Rev.* **2000**, *100*, 39-92.
(87) Visbal, R.; Gimeno, M. C. N-heterocyclic carbene metal complexes: photoluminescence and applications. *Chem. Soc. Rev.* **2014**, *43*, 3551-3574.
(88) Hahn, F. E. Introduction: carbene chemistry. ACS Publications: 2018; Vol. 118, pp 9455-9456.
(89) Mercs, L.; Albrecht, M. Beyond catalysis: N-heterocyclic carbene complexes as components for medicinal, luminescent, and functional materials applications. *Chem. Soc. Rev.* **2010**, *39*, 1903-1912.

(90) Amouri, H. Luminescent complexes of platinum, iridium, and coinage metals containing N-heterocyclic carbene ligands: Design, structural diversity, and photophysical properties. *Chem. Rev.* **2023**, *123*, 230-270.
(91) Song, S. G.; Satheeshkumar, C.; Park, J.; Ahn, J.; Premkumar, T.; Lee, Y.; Song, C. N-heterocyclic carbene-based conducting polymer–gold nanoparticle hybrids and their catalytic application. *Macromolecules* **2014**, *47*, 6566-6571.
(92) Crespo, J.; Guari, Y.; Ibarra, A.; Larionova, J.; Lasanta, T.; Laurencin, D.; López-de-Luzuriaga, J. M.; Monge, M.; Olmos, M. E.; Richeter, S. Ultrasmall NHC-coated gold nanoparticles obtained through solvent free thermolysis of organometallic Au (I) complexes. *Dalton Trans.* **2014**, *43*, 15713-15718.
(93) Ghosh, M.; Saha, P.; Roy, S.; Pillai, P.; Dey, A.; Khan, S. Cyclic (Alkyl)(Amino) Carbene Stabilized Gold Nanoparticles: Efficient Catalyst for Selective Electrochemical Reduction of CO_2 to CO. *ChemRxiv* **2023**.
(94) Jin, R.; Zeng, C.; Zhou, M.; Chen, Y. Atomically precise colloidal metal nanoclusters and nanoparticles: fundamentals and opportunities. *Chem. Rev.* **2016**, *116*, 10346-10413.
(95) Krishna, K. S.; Tarakeshwar, P.; Mujica, V.; Kumar, C. S. Chemically induced magnetism in atomically precise gold clusters. *Small* **2014**, *10*, 907-911.
(96) Crespo, P.; Litrán, R.; Rojas, T. C.; Multigner, M.; de la Fuente, J. M.; Sánchez-López, J. C.; García, M. A.; Hernando, A.; Penadés, S.; Fernández, A. Permanent Magnetism, Magnetic Anisotropy, and Hysteresis of Thiol-Capped Gold Nanoparticles. *Phys. Rev. Lett.* **2004**, *93*, 087204-087207.
(97) Hori, H.; Teranishi, T.; Nakae, Y.; Seino, Y.; Miyake, M.; Yamada, S. Anomalous magnetic polarization effect of Pd and Au nano-particles. *Phys. Lett. A* **1999**, *263*, 406-410.
(98) Hori, H.; Yamamoto, Y.; Iwamoto, T.; Miura, T.; Teranishi, T.; Miyake, M. Diameter dependence of ferromagnetic spin moment in Au nanocrystals. *Phys. Rev. B* **2004**, *69*, 174411-174415.
(99) Yamamoto, Y.; Miura, T.; Suzuki, M.; Kawamura, N.; Miyagawa, H.; Nakamura, T.; Kobayashi, K.; Teranishi, T.; Hori, H. Direct observation of ferromagnetic spin polarization in gold nanoparticles. *Phys. Rev. Lett.* **2004**, *93*, 116801-116804.
(100) de la Presa, P.; Multigner, M.; de la Venta, J.; García, M. A.; Ruiz-González, M. L. Structural and magnetic characterization of oleic acid and oleylamine-capped gold nanoparticles. *J. Appl. Phys.* **2006**, *100*, 123915-123920.
(101) Bouzouita, D.; Asensio, J. M.; Pfeifer, V.; Palazzolo, A.; Lecante, P.; Pieters, G.; Feuillastre, S.; Tricard, S.; Chaudret, B. Chemoselective H/D exchange catalyzed by nickel nanoparticles stabilized by N-heterocyclic carbene ligands. *Nanoscale* **2020**, *12*, 15736-15742.
(102) Fountoulaki, S.; Daikopoulou, V.; Gkizis, P. L.; Tamiolakis, I.; Armatas, G. S.; Lykakis, I. N. Mechanistic studies of the reduction of nitroarenes by NaBH4 or hydrosilanes catalyzed by supported gold nanoparticles. *ACS Catal.* **2014**, *4*, 3504-3511.
(103) Herves, P.; Pérez-Lorenzo, M.; Liz-Marzán, L. M.; Dzubiella, J.; Lu, Y.; Ballauff, M. Catalysis by metallic nanoparticles in aqueous solution: model reactions. *Chem. Soc. Rev.* **2012**, *41*, 5577-5587.
(104) Zhao, P.; Feng, X.; Huang, D.; Yang, G.; Astruc, D. Basic concepts and recent advances in nitrophenol reduction by gold-and other transition metal nanoparticles. *Coord. Chem. Rev.* **2015**, *287*, 114-136.
(105) Aditya, T.; Pal, A.; Pal, T. Nitroarene reduction: a trusted model reaction to test nanoparticle catalysts. *Chem. Commun.* **2015**, *51*, 9410-9431.
(106) Neal, R. D.; Inoue, Y.; Hughes, R. A.; Neretina, S. Catalytic reduction of 4-nitrophenol by gold catalysts: the influence of borohydride concentration on the induction time. *J. Phys. Chem. C* **2019**, *123*, 12894-12901.

(107) Dong, Z.; Le, X.; Li, X.; Zhang, W.; Dong, C.; Ma, J. Silver nanoparticles immobilized on fibrous nano-silica as highly efficient and recyclable heterogeneous catalyst for reduction of 4-nitrophenol and 2-nitroaniline. *Appl. Catal. B: Environ.* **2014**, *158*, 129-135.
(108) Naeem, H.; Ajmal, M.; Muntha, S.; Ambreen, J.; Siddiq, M. Synthesis and characterization of graphene oxide sheets integrated with gold nanoparticles and their applications to adsorptive removal and catalytic reduction of water contaminants. *RSC Adv.* **2018**, *8*, 3599-3610.
(109) El-Nagar, G. A.; Mohammad, A. M. Enhanced electrocatalytic activity and stability of platinum, gold, and nickel oxide nanoparticles-based ternary catalyst for formic acid electro-oxidation. *Int. J. Hydrog. Energy* **2014**, *39*, 11955-11962.
(110) Yu, X.; Pickup, P. G. Recent advances in direct formic acid fuel cells (DFAFC). *J. Power Sources* **2008**, *182*, 124-132.
(111) Fang, Z.; Chen, W. Recent advances in formic acid electro-oxidation: From the fundamental mechanism to electrocatalysts. *Nanoscale Adv.* **2021**, *3*, 94-105.
(112) Rajendra, R.; Gangadharan, P. K.; Tripathi, S.; Kurungot, S.; Ballav, N. High-index faceted Au nanocrystals with highly controllable optical properties and electro-catalytic activity. *Nanoscale* **2016**, *8*, 19224-19228.
(113) Ulloa, J. A.; Lorusso, G.; Evangelisti, M.; Camón, A.; Barberá, J.; Serrano, J. L. Magnetism of dendrimer-coated gold nanoparticles: A size and functionalization study. *J. Phys. Chem. C* **2021**, *125*, 20482-20487.
(114) Gréget, R.; Nealon, G. L.; Vileno, B.; Turek, P.; Mény, C.; Ott, F.; Derory, A.; Voirin, E.; Rivière, E.; Rogalev, A. Magnetic properties of gold nanoparticles: a room-temperature quantum effect. *ChemPhysChem* **2012**, *13*, 3092-3097.
(115) Hernando, A.; Crespo, P.; García, M. A. Origin of Orbital Ferromagnetism and Giant Magnetic Anisotropy at the Nanoscale. *Phys. Rev. Lett.* **2006**, *96*, 057206-057209.
(116) Roy, S.; Rao, A.; Devatha, G.; Pillai, P. P. Revealing the role of electrostatics in gold-nanoparticle-catalyzed reduction of charged substrates. *ACS Catal.* **2017**, *7*, 7141-7145.
(117) Shirin, S.; Roy, S.; Rao, A.; Pillai, P. P. Accelerated Reduction of 4-Nitrophenol: Bridging Interaction Outplays Reducing Power in the Model Nanoparticle-Catalyzed Reaction. *J. Phys. Chem. C* **2020**, *124*, 19157-19165.
(118) Pradhan, N.; Pal, A.; Pal, T. Catalytic reduction of aromatic nitro compounds by coinage metal nanoparticles. *Langmuir* **2001**, *17*, 1800-1802.
(119) Tegeder, P.; Freitag, M.; Chepiga, K. M.; Muratsugu, S.; Möller, N.; Lamping, S.; Tada, M.; Glorius, F.; Ravoo, B. J. N-Heterocyclic Carbene-Modified Au–Pd Alloy Nanoparticles and Their Application as Biomimetic and Heterogeneous Catalysts. *Chem. Eur. J.* **2018**, *24*, 18682-18688.
(120) Zheng, G.; Polavarapu, L.; Liz-Marzán, L. M.; Pastoriza-Santos, I.; Pérez-Juste, J. Gold nanoparticle-loaded filter paper: a recyclable dip-catalyst for real-time reaction monitoring by surface enhanced Raman scattering. *Chem. Commun.* **2015**, *51*, 4572-4575.
(121) Roy, S.; Adury, V. S. S.; Rao, A.; Roy, S.; Mukherjee, A.; Pillai, P. P. Electrostatically Directed Long-Range Self-Assembly of Nucleotides with Cationic Nanoparticles To Form Multifunctional Bioplasmonic Networks. *Angew. Chem. Int. Ed.* **2022**, *61*, e202203924.
(122) Zhang, Y.; Yuan, X.; Wang, Y.; Chen, Y. One-pot photochemical synthesis of graphene composites uniformly deposited with silver nanoparticles and their high catalytic activity towards the reduction of 2-nitroaniline. *J. Mater. Chem.* **2012**, *22*, 7245-7251.
(123) Abdelrahman, A.; Hermann, J. M.; Jacob, T.; Kibler, L. A. Adsorption of acetate on Au (111): an in-situ scanning tunnelling microscopy study and implications on formic acid electrooxidation. *ChemPhysChem* **2019**, *20*, 2989-2996.

(124) Avramov-Ivić, M.; Štrbac, S.; Mitrović, V. The electrocatalytic properties of the oxides of noble metals in the electrooxidation of methanol and formic acid. *Electrochim. Acta* **2001**, *46*, 3175-3180.
(125) Li, J.; Wang, L.; Liu, L.; Guo, L.; Han, X.; Zhang, Z. Synthesis of tetrahexahedral Au nanocrystals with exposed high-index surfaces. *Chem. Commun.* **2010**, *46*, 5109-5111.
(126) Yoo, J. K.; Choi, M.; Yang, S.; Shong, B.; Chung, H.-S.; Sohn, Y.; Rhee, C. K. Formic acid electrooxidation activity of Pt and Pt/Au catalysts: Effects of surface physical properties and irreversible adsorption of Bi. *Electrochim. Acta* **2018**, *273*, 307-317.
(127) Shan, C. K.; Yao, S. L.; Driess, M. Where silylene-silicon centres matter in the activation of small molecules. *Chem. Soc. Rev.* **2020**, *49*, 6733-6754.
(128) Blom, B.; Gallego, D.; Driess, M. N-heterocyclic silylene complexes in catalysis: new frontiers in an emerging field. *Inorg. Chem. Front.* **2014**, *1*, 134-148.
(129) Zhou, Y. P.; Driess, M. Isolable Silylene Ligands Can Boost Efficiencies and Selectivities in Metal-Mediated Catalysis. *Angew. Chem. Int. Ed.* **2019**, *58*, 3715-3728.
(130) Man, R. W.; Li, C.-H.; MacLean, M. W.; Zenkina, O. V.; Zamora, M. T.; Saunders, L. N.; Rousina-Webb, A.; Nambo, M.; Crudden, C. M. Ultrastable gold nanoparticles modified by bidentate N-heterocyclic carbene ligands. *J. Am. Chem. Soc.* **2018**, *140*, 1576-1579.
(131) Bridonneau, N.; Hippolyte, L.; Mercier, D.; Portehault, D.; Desage-El Murr, M.; Marcus, P.; Fensterbank, L.; Chanéac, C.; Ribot, F. N-Heterocyclic carbene-stabilized gold nanoparticles with tunable sizes. *Dalton Trans.* **2018**, *47*, 6850-6859.
(132) Lovat, G.; Doud, E. A.; Lu, D.; Kladnik, G.; Inkpen, M. S.; Steigerwald, M. L.; Cvetko, D.; Hybertsen, M. S.; Morgante, A.; Roy, X.; Venkataraman, L. Determination of the structure and geometry of N-heterocyclic carbenes on Au(111) using high-resolution spectroscopy. *Chem. Sci.* **2019**, *10*, 930-935.
(133) Creel, E. B.; McCloskey, B. D. Scalable CO_2-to-oxygenate production. *Nat. Catal.* **2018**, *1*, 6-7.
(134) Voiry, D.; Shin, H. S.; Loh, K. P.; Chhowalla, M. Low-dimensional catalysts for hydrogen evolution and CO_2 reduction. *Nat. Rev. Chem* **2018**, *2*, 0105.
(135) Schneider, J.; Jia, H.; Muckerman, J. T.; Fujita, E. Thermodynamics and kinetics of CO_2, CO, and H^+ binding to the metal centre of CO_2 reduction catalysts. *Chem. Soc. Rev.* **2012**, *41*, 2036-2051.
(136) Khan, M. N.; van Ingen, Y.; Boruah, T.; McLauchlan, A.; Wirth, T.; Melen, R. L. Advances in CO_2 activation by frustrated Lewis pairs: from stoichiometric to catalytic reactions. *Chem. Sci.* **2023**, *14*, 13661-13695.
(137) Dalena, F.; Senatore, A.; Marino, A.; Gordano, A.; Basile, M.; Basile, A. Methanol production and applications: an overview. *Methanol* **2018**, 3-28.
(138) Chakraborty, S.; Zhang, J.; Krause, J. A.; Guan, H. An efficient nickel catalyst for the reduction of carbon dioxide with a borane. *J. Am. Chem. Soc.* **2010**, *132*, 8872-8873.
(139) Lu, Z.; Williams, T. J. Di(carbene)-Supported Nickel Systems for CO_2 Reduction Under Ambient Conditions. *ACS Catal.* **2016**, *6*, 6670-6673.
(140) Courtemanche, M.-A.; Legare, M.-A.; Maron, L.; Fontaine, F.-G. A highly active phosphine–borane organocatalyst for the reduction of CO_2 to methanol using hydroboranes. *J. Am. Chem. Soc.* **2013**, *135*, 9326-9329.
(141) Kostera, S.; Weber, S.; Blaha, I.; Peruzzini, M.; Kirchner, K.; Gonsalvi, L. Base-and Additive-Free Carbon Dioxide Hydroboration to Methoxyboranes Catalyzed by Non-Pincer-Type Mn (I) Complexes. *ACS Catal.* **2023**, *13*, 5236-5244.
(142) Adhikary, A.; Saha, S.; Kumar, N. S.; Oliver, A. G.; Krause, J. A.; Guan, H. Pitfalls for POCOP-Type Palladium Pincer Complexes in Catalytic Reduction of CO_2 with Catecholborane. *Organometallics* **2023**, *42*, 1525-1537.

(143) Courtemanche, M.-A.; Légaré, M.-A.; Maron, L.; Fontaine, F.-G. Reducing CO_2 to methanol using frustrated Lewis pairs: on the mechanism of phosphine–borane-mediated hydroboration of CO_2. *J. Am. Chem. Soc.* **2014**, *136*, 10708-10717.

Chapter 5: Summary of the Thesis and Future Directions

5.1 Summary of the thesis

Transition metal complexes bearing isolable NHSi ligands have emerged as a fascinating area of research with profound implications across various branches of chemistry. NHSis have revolutionized small molecule activation and transition metal-mediated organic transformations. Their advent marks a significant milestone in the quest for efficient and versatile catalysts in synthetic chemistry.

5.1.1 Reactivity of bis-silylene ligands.

In the first section of the thesis, attention is directed towards the reactivity of bis-silylene ligands with chalcogens. The synthesis and characterization of Si=Ch compounds (where Ch represents sulfur, selenium, or tellurium) highlight the challenges associated with isolating higher homologs of ketones due to orbital misalignment and significant electronegativity disparities between silicon and chalcogen atoms. Moreover, the elucidation of C-H···Ch interactions add a new dimension to understanding intermolecular forces and chemical bonding. Furthermore, the ability of bis-silylene ligands to stabilize reactive group 13 Lewis acid cations underscores their pivotal role in small molecule activation and species stabilization. By exploring these reactivity patterns, the thesis aims to uncover fundamental insights into the intricate electronic properties governing the coordination fashion with Lewis acidic centers.

5.1.2 Coinage metal complexes with NHSi ligands and their photophysical properties.

The subsequent section deals with synthesizing and characterizing coinage metal complexes incorporating NHSi ligands, offering a glimpse into their unique reactivity and bonding pattern. These complexes exhibit intriguing photophysical properties, making them attractive candidates for applications in luminescent materials and optoelectronic devices. Through rational fine-tuning of their electronic and steric properties, this thesis endeavors to unlock the full potential of these complexes in homogeneous catalysis, optoelectronic applications, and beyond.

5.1.3 Utilization of NHTs as surface-capping ligands.

Building upon the foundation laid by previous sections, the thesis explores the utilization of N-heterocyclic tetrylene (NHTs) as surface-capping ligands for gold nanoparticles (AuNPs). The remarkable stability conferred by CAAC-capped NPs in solution opens up new avenues for

their application in various catalytic processes. The investigation extends to NHSi as alternative capping agents, focusing on their integration into gold nanoparticles (AuNPs). The synthesis, characterization, and catalytic evaluation of these NHSi-functionalized AuNPs represent a significant advancement in nanoparticle chemistry and electrocatalysis.

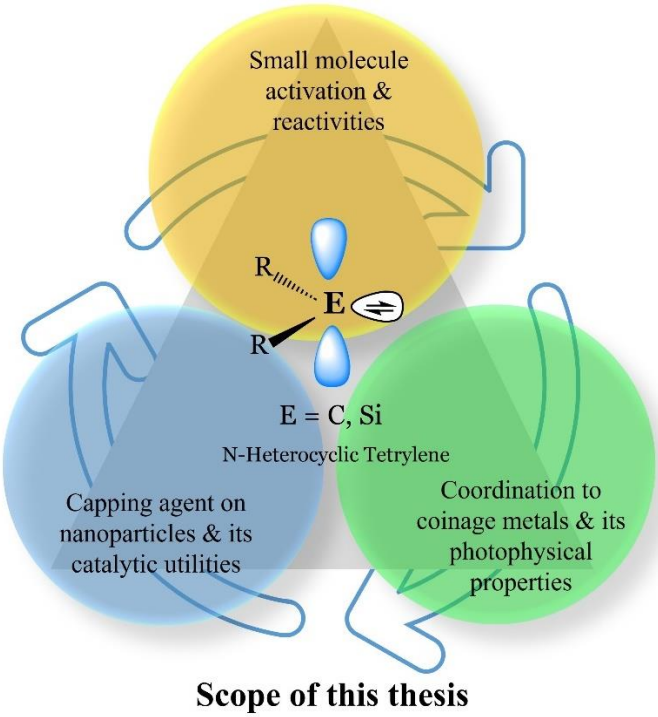

Figure 5.1. Overview of the work presented in this thesis.

5.2 Conclusion and future directions.

This thesis explores the pivotal role of low valent main group ligands, i.e., NHTs, particularly NHSis, in shaping the landscape of contemporary synthetic chemistry. The thesis aims to inspire further exploration in the field by shedding light on their diverse applications and properties. Future research directions may include the development of novel synthetic methodologies to introduce chiral NHSis, elucidating structure-property relationships, and the integration of NHSis into emerging technologies such as nanocomposites and sustainable energy systems. Overall, the thesis represents a comprehensive journey through the fascinating transition metal complexes bearing isolable NHSi ligands, offering insights into the road of nanocomposite functionalization, paving the way for future advancements in the field of chemistry. In conclusion, I am reminded,

"*It is like a voyage of discovery into unknown lands, seeking not for new territory but for new knowledge.*"

-Frederick Sanger, Noble Prize in Chemistry, 1980

2A.A.1 Crystallographic data for complexes 2A.2-2A.5.

	2A.2	**2A.3**
Chemical formula	C_{44} H_{66} N_4 O_2 Te_2 Si_2	C_{44} H_{66} N_4 O_2 S_2 Si_2
Formula weight	994.38 g/mol	803.30 g/mol
Temperature	100 K	100 K
Wavelength	0.71073 Å	0.71073 Å
Crystal system	Monoclinic	Monoclinic
Space group	*P* 21/c	*C* 2/c
Unit cell dimensions	a = 9.407(7) Å	a = 28.715(10) Å
	b = 20.525(19) Å	b = 9.00(3) Å
	c = 26.439(18) Å	c = 39.315(12) Å
	α = 90°	α = 90°
	β = 96.93(11)°	β = 101.117(5)°
	γ = 90°	γ = 90°
Volume	5068(7) $Å^3$	9935(11) $Å^3$
Z	4	8
Density (calculated)	1.303 g/cm^3	1.070 g/cm^3
Absorption coefficient	1.234 mm^{-1}	0.191 mm^{-1}
F(000)	2024.0	3472.00
Theta range for data collection	1.842 to 24.999°	2.112 to 24.995°
Reflections collected	85680	77576
Independent reflections	8931 [R(int) = 0.165]	8782 [R(int) = 0.173]
Coverage of independent reflections	100%	99.9%
Function minimized	Σ w(Fo^2 - Fc^2)^2	Σ w(Fo^2 - Fc^2)^2
Goodness-of-fit on F^2	1.015	1.013
Δ/σ max	0.002	0.000
Final R indices	5929 data[I>2σ(I)], R1 = 0.0464, wR2 = 0.0806	4913 data[I>2σ(I)], R1 = 0.0702, wR2 = 0.1548

	all data, R1 = 0.0909, wR2 = 0.0949	all data , R1 = 0.1407, wR2 = 0.1858
Largest diff. peak and hole	0.792 to -0.560 eÅ^{-3}	0.326 and -0.368 eÅ^{-3}
R.M.S. deviation from mean	0.112 eÅ^{-3}	0.069 eÅ^{-3}

	2A.4	**2A.5**
Chemical formula	C_{44} H_{66} N_4 O_2 Se_2 Si_2	C_{88} H_{132} N_8 O_8 Si_4
Formula weight	1794.21 g/mol	1542.37 g/mol
Temperature	100 K	150 K
Wavelength	0.71073 Å	0.71703 Å
Crystal system	Triclinic	Monoclinic
Space group	*P* -1	*C* 2/c
Unit cell dimensions	*a* = 8.995(4) Å	*a* = 24.793 Å
	b = 15.028(8) Å	*b* = 15.189 Å
	c = 39.77(2) Å	*c* = 28.556 Å
	α = 79.45(2)°	α = 90°
	β = 83.570(16)°	β = 96.29°
	γ = 72.59(2)°	γ = 90°
Volume	5033(5) Å^3	10689.3 Å^3
Z	2	4
Density (calculated)	1.184 g/cm^3	0.958 g/cm^3
Absorption coefficient	1.552 mm^{-1}	0.103 mm^{-1}
F(000)	1880.00	3344.00
Theta range for data collection	2.287 to 26.478°	2.59 to 25.49
Reflections collected	144535	76308
Independent reflections	20728 [R(int) = 0.1101]	9415 [R(int) = 0.1969]
Coverage of independent reflections	99.6%	99.9%
Function minimized	Σ w(Fo^2 - Fc^2)^2	Σ w(Fo^2 - Fc^2)^2

Goodness-of-fit on F^2	1.034	1.074
Δ/σ max	0.001	0.000
Final R indices	15244 data[I>2σ(I)], R1 = 0.0557, wR2 = 0.1140	5762 data[I>2σ(I)], R1 = 0.0714, wR2 = 0.1832
	all data, R1 = 0.0817, wR2 = 0.1227	all data , R1 = 0.1197, wR2 = 0.2055
Largest diff. peak and hole	0.652 and -0.766 eÅ^{-3}	0.328 and -0.359 eÅ^{-3}
R.M.S. deviation from mean	0.075 eÅ^{-3}	0.076 eÅ^{-3}

2A.A.2 NMR spectroscopic data for complexes 2A.2-2A.5.

***** = residual toluene (solvent)

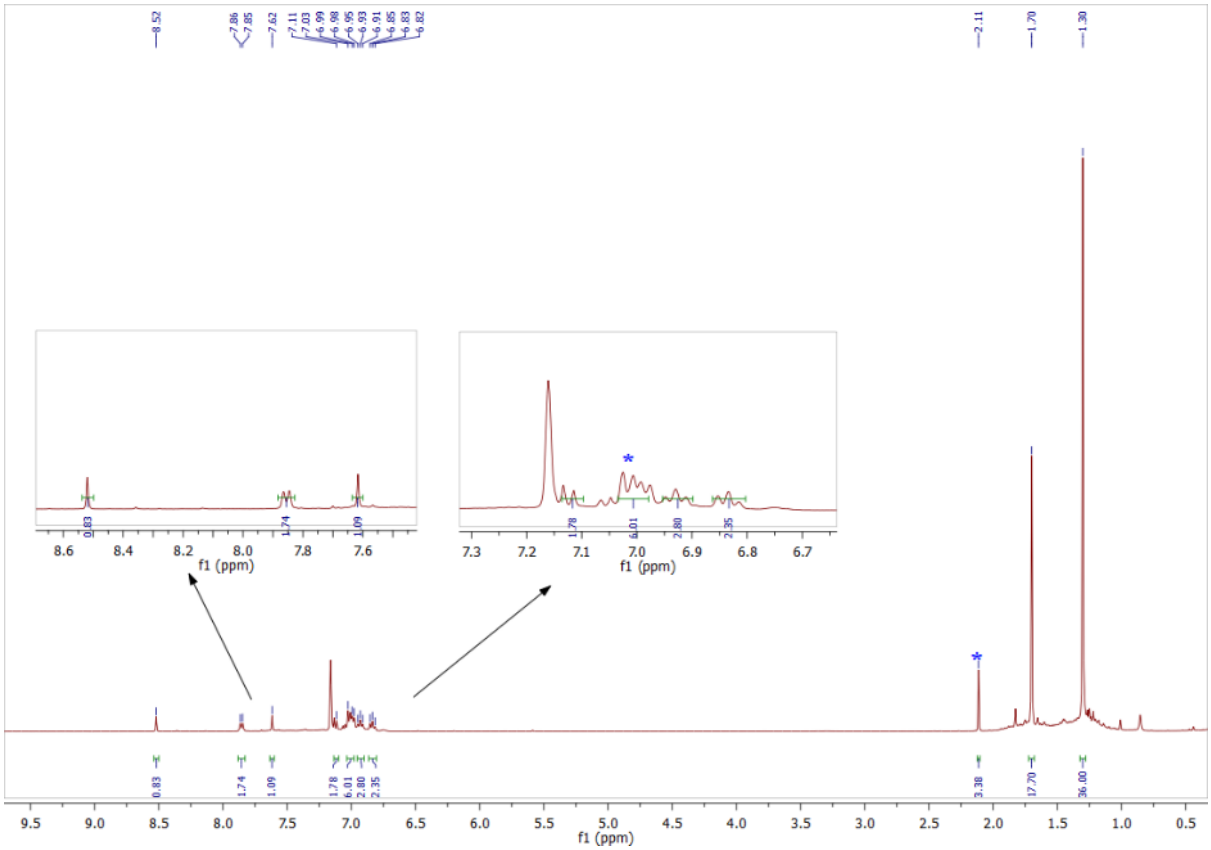

Figure 2A.A.1. ^{1}H NMR spectrum of complex **2A.2** in C_6D_6.

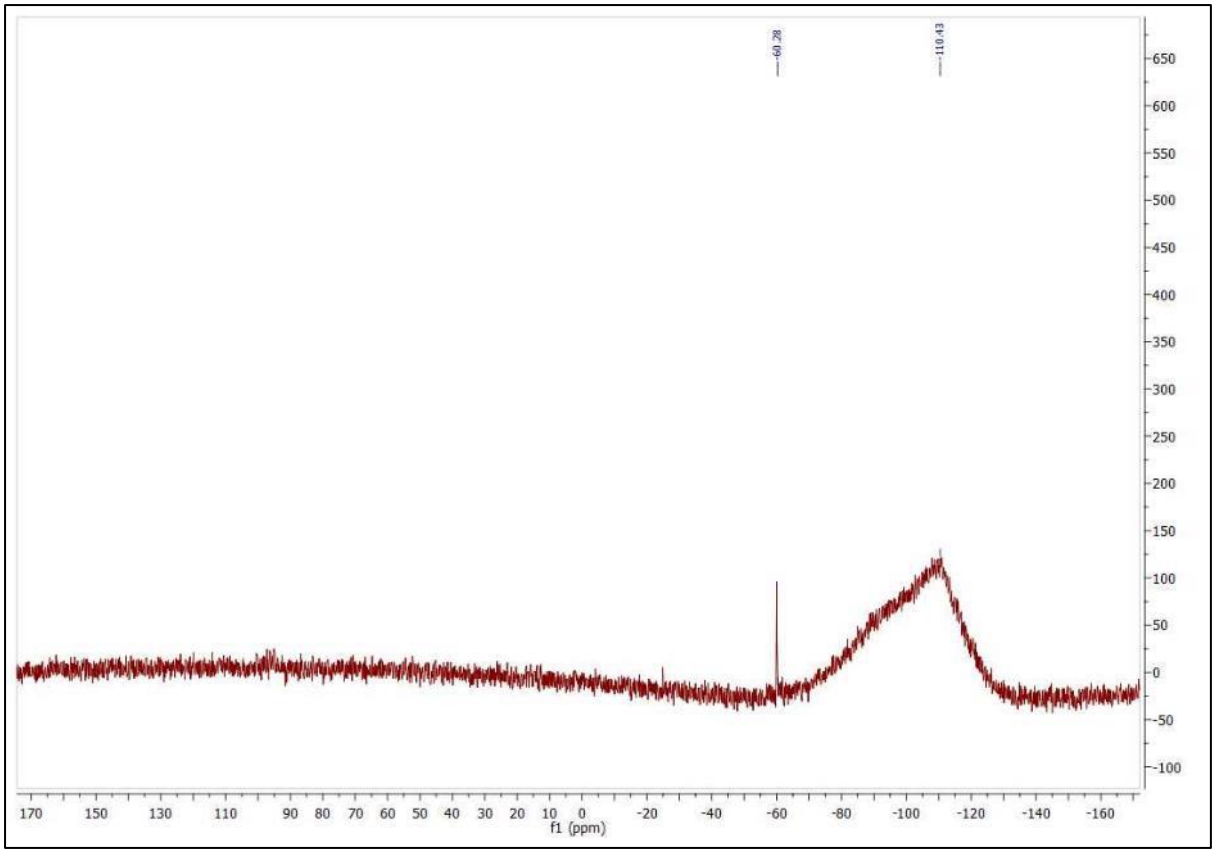

Figure 2A.A.2. ^{29}Si NMR spectrum of complex **2A.2** in C_6D_6.

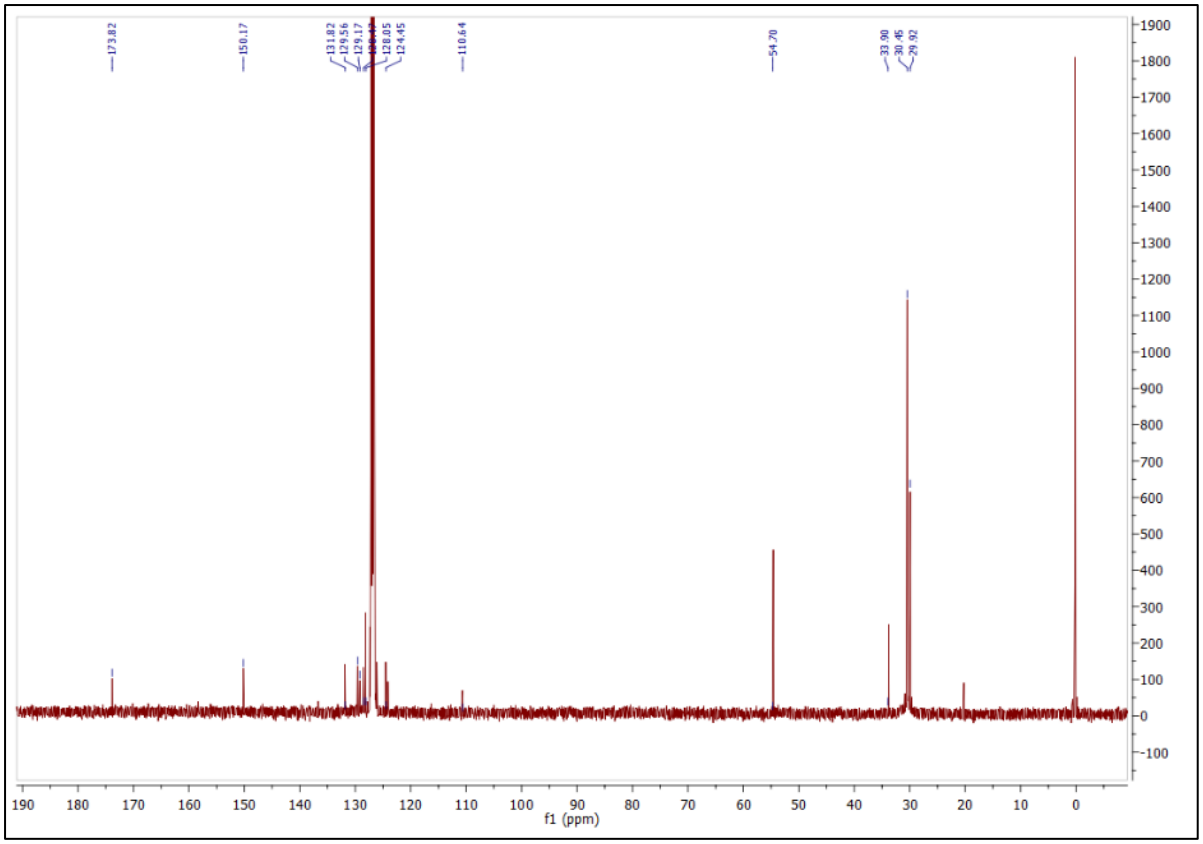

Figure 2A.A.3. ^{13}C NMR spectrum of complex **2A.2** in C_6D_6.

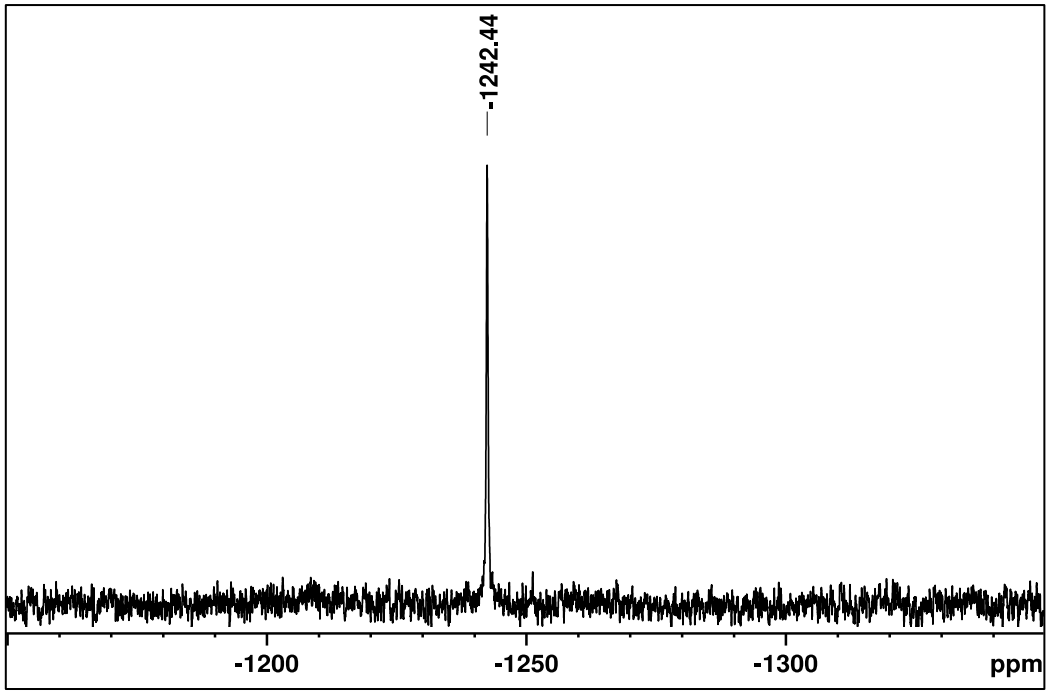

Figure 2A.A.4. $^{125}Te\{^{1}H\}$ NMR spectrum of complex **2A.2** at 298 K in C_6D_6.

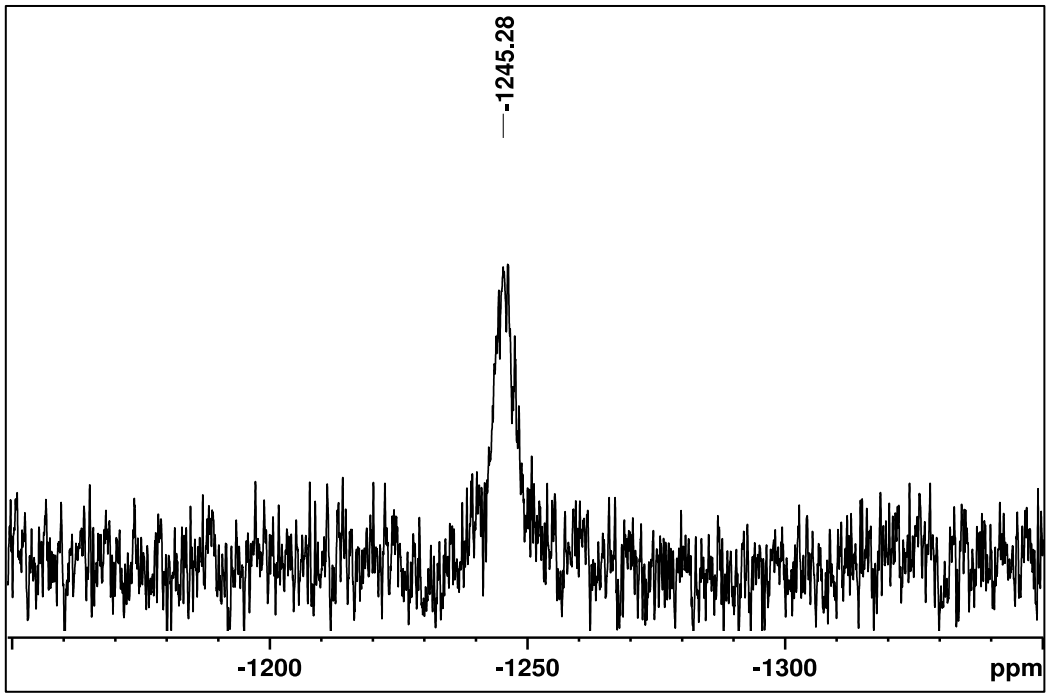

Figure 2A.A.5. ^{1}H coupled ^{125}Te NMR spectrum of complex **2A.2** at 220 K in C_6D_6.

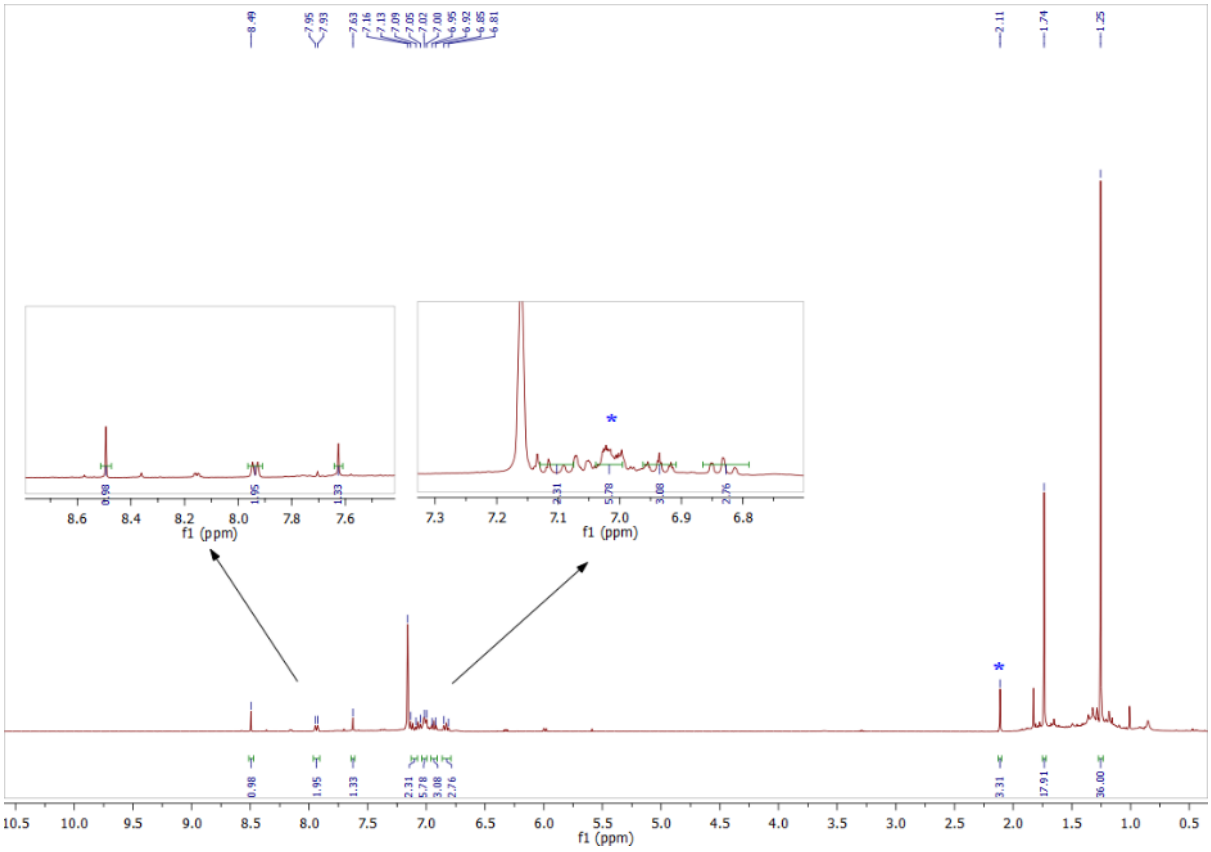

Figure 2A.A.6. ^{1}H NMR spectrum of complex **2A.3** in C_6D_6.

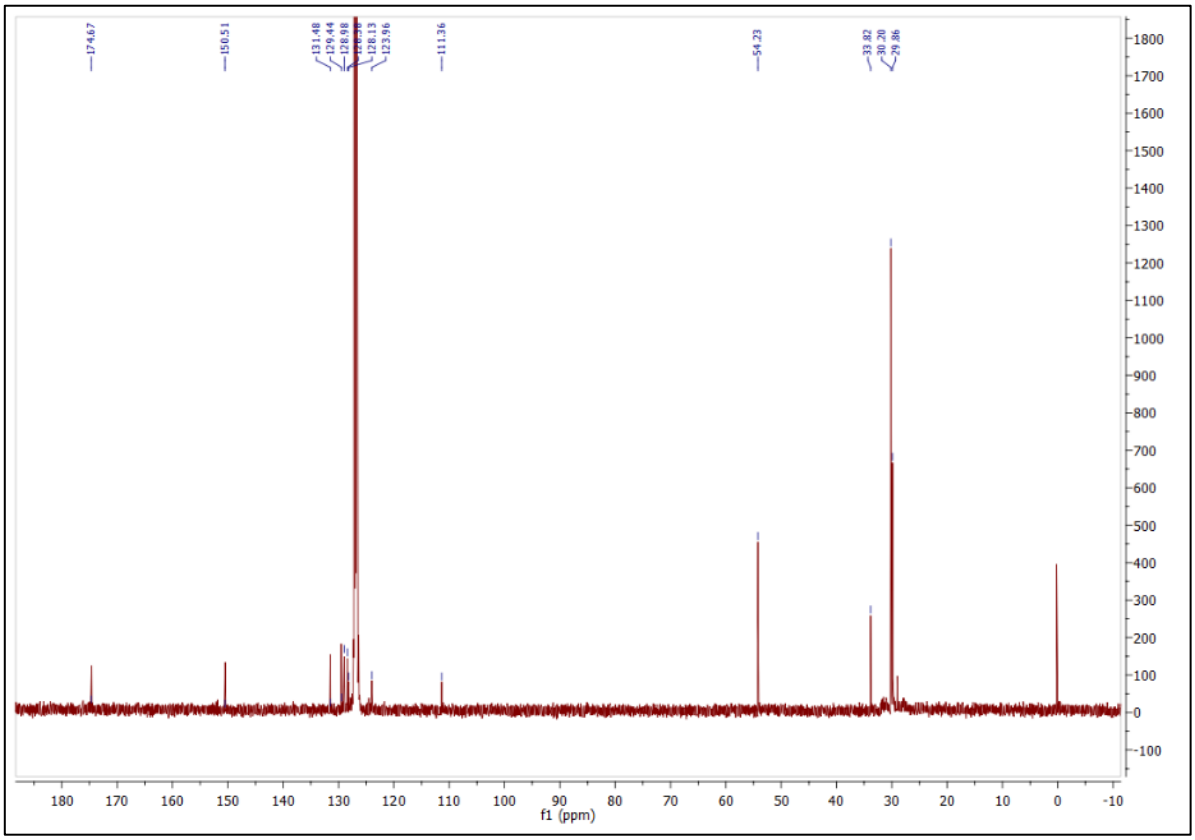

Figure 2A.A.7. ^{13}C NMR spectrum of complex **2A.3** in C_6D_6.

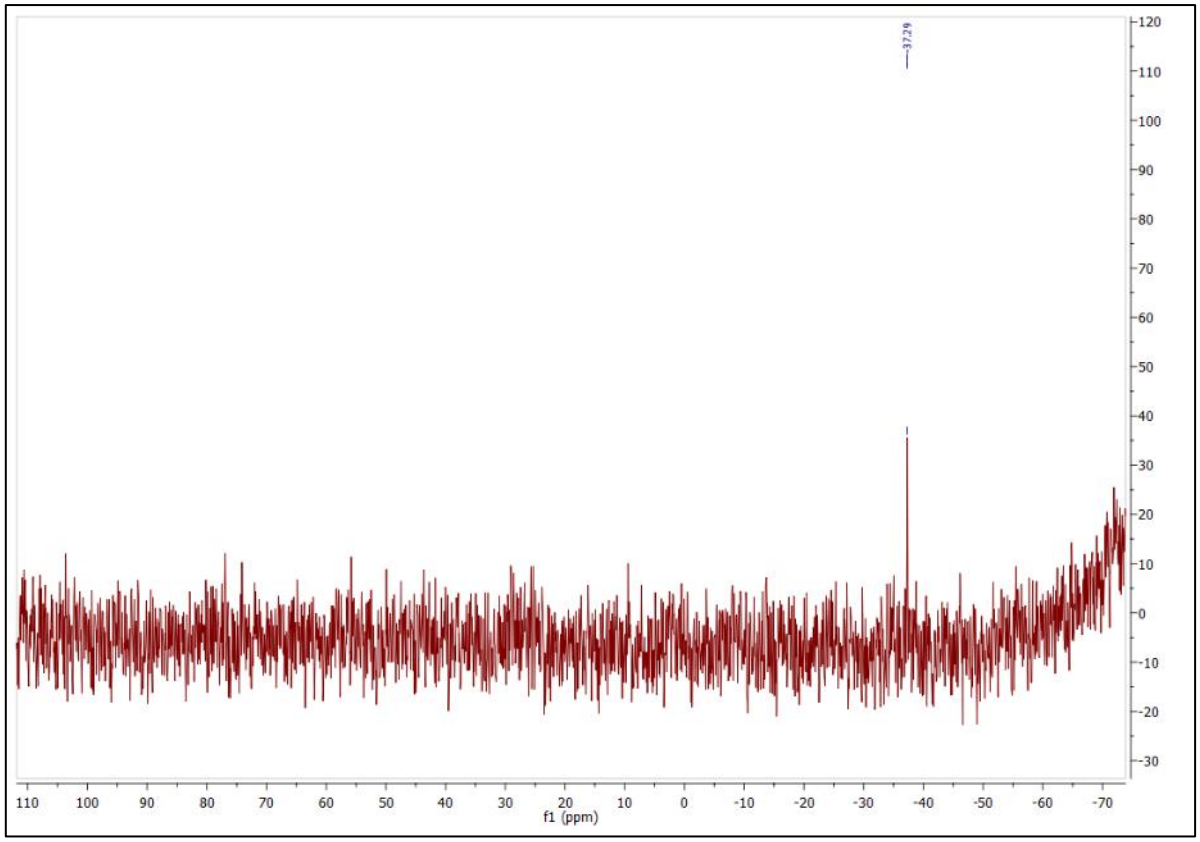

Figure 2A.A.8. ^{29}Si NMR spectrum of complex **2A.3** in C_6D_6.

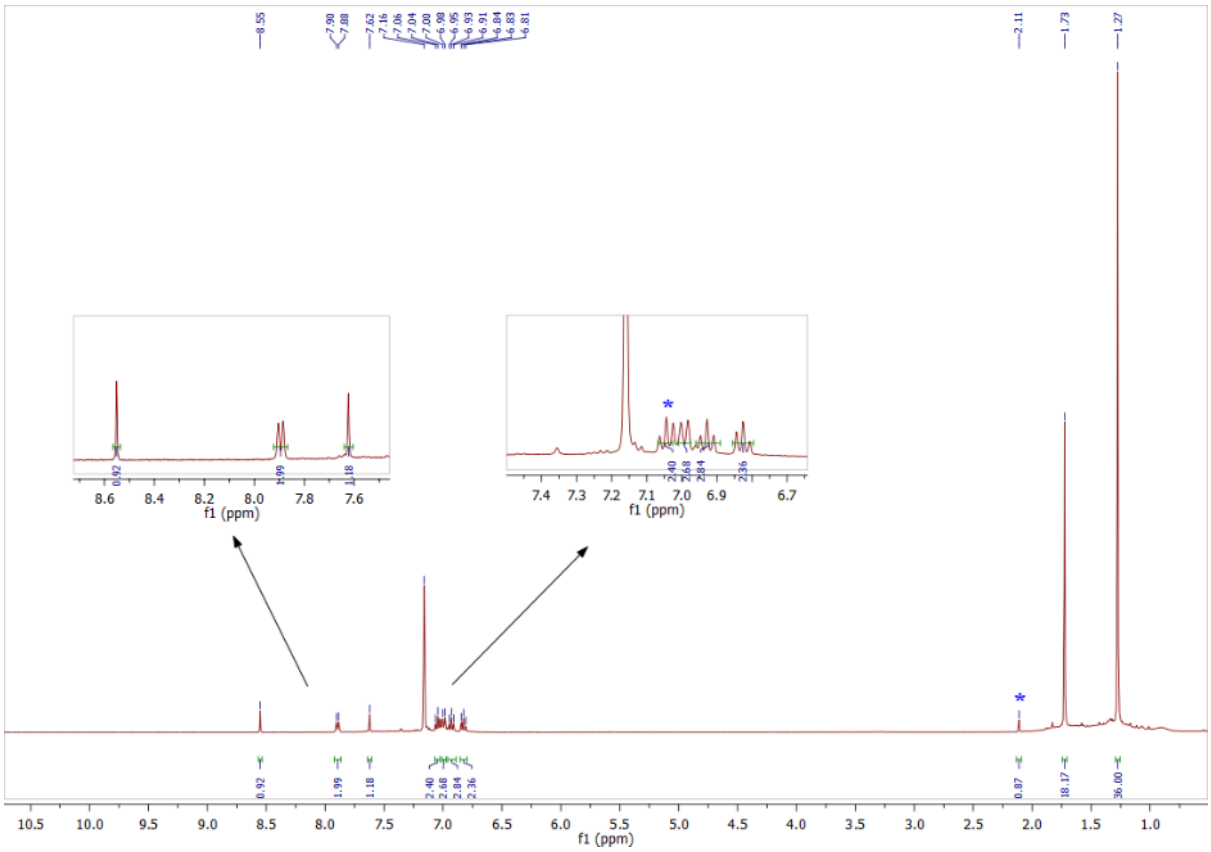

Figure 2A.A.9. ^{1}H NMR spectrum of complex **2A.4** in C_6D_6.

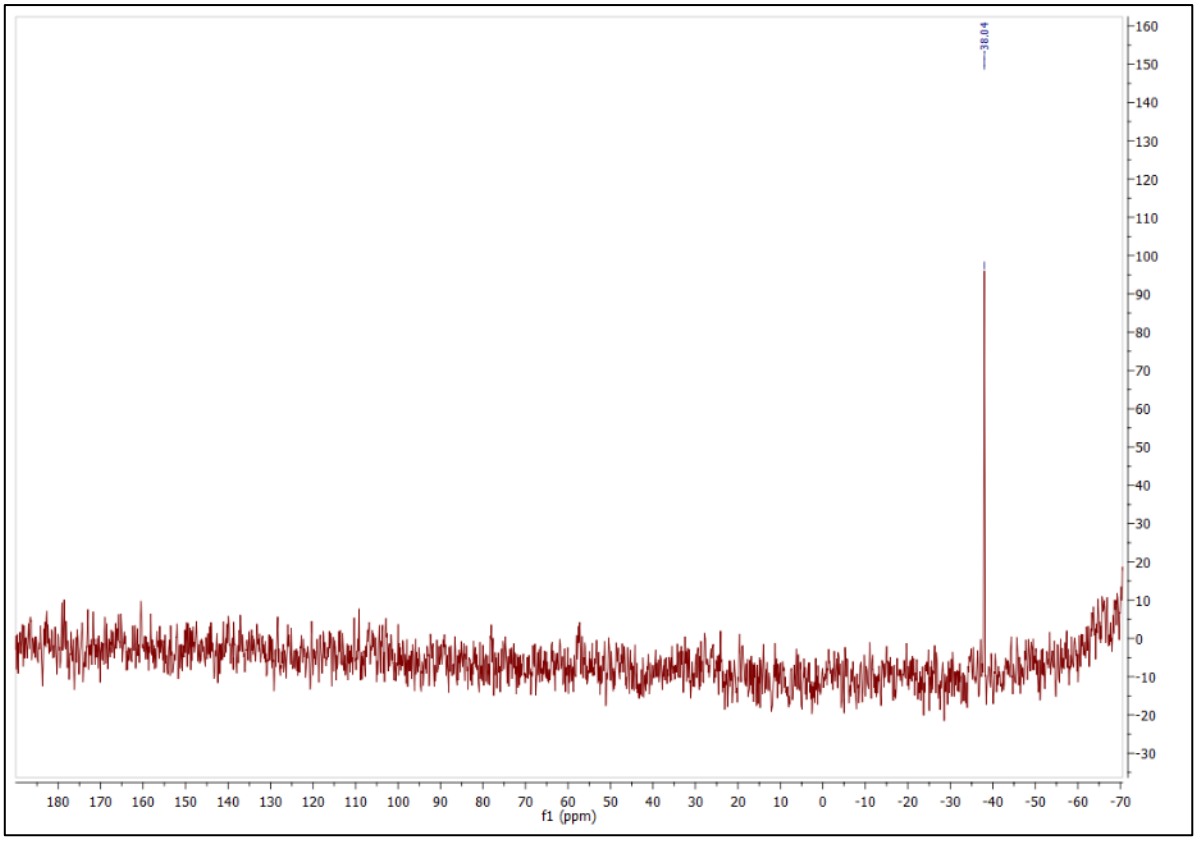

Figure 2A.A.10. ^{29}Si NMR spectrum of complex **2A.4** in C_6D_6.

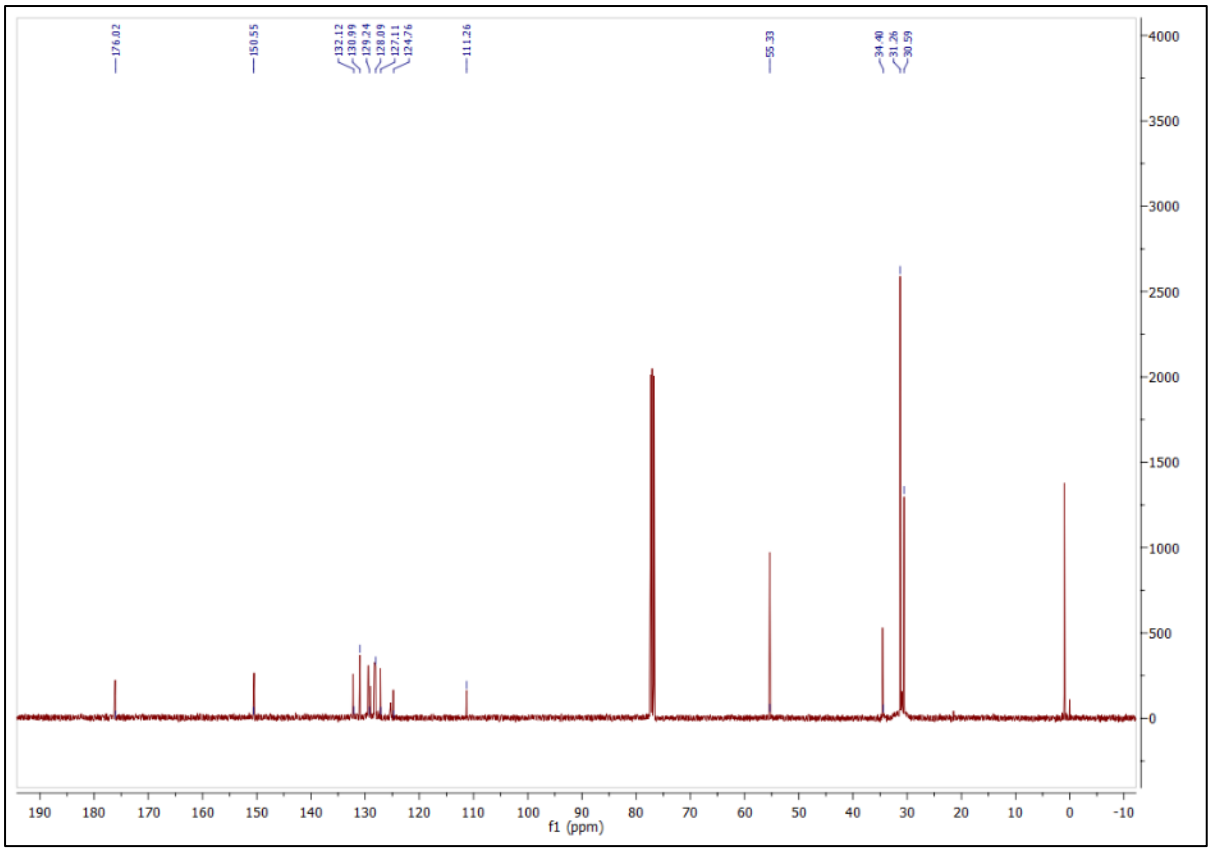

Figure 2A.A.11. ^{13}C NMR spectrum of complex **2A.4** in C_6D_6.

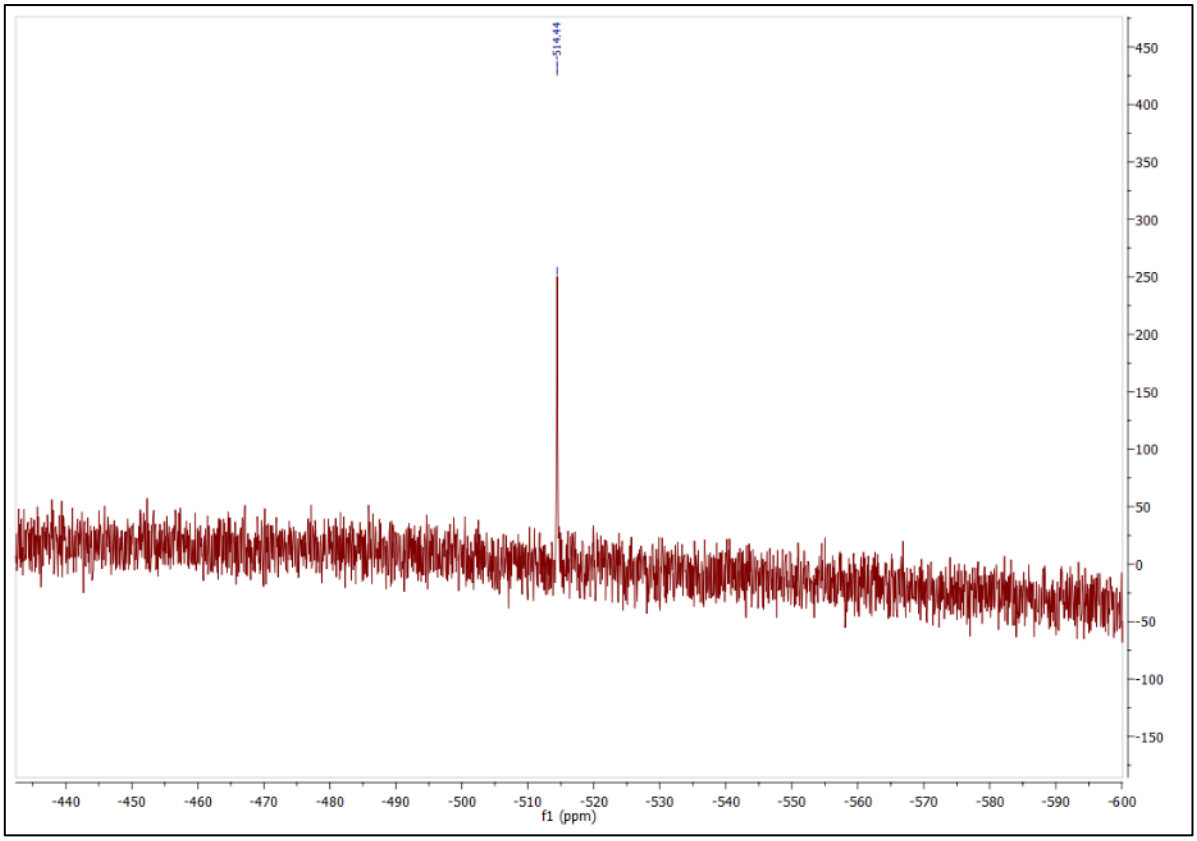

Figure 2A.A.12. $^{77}Se\{^{1}H\}$ NMR spectrum of complex **2A.4** at 298 K in C_6D_6.

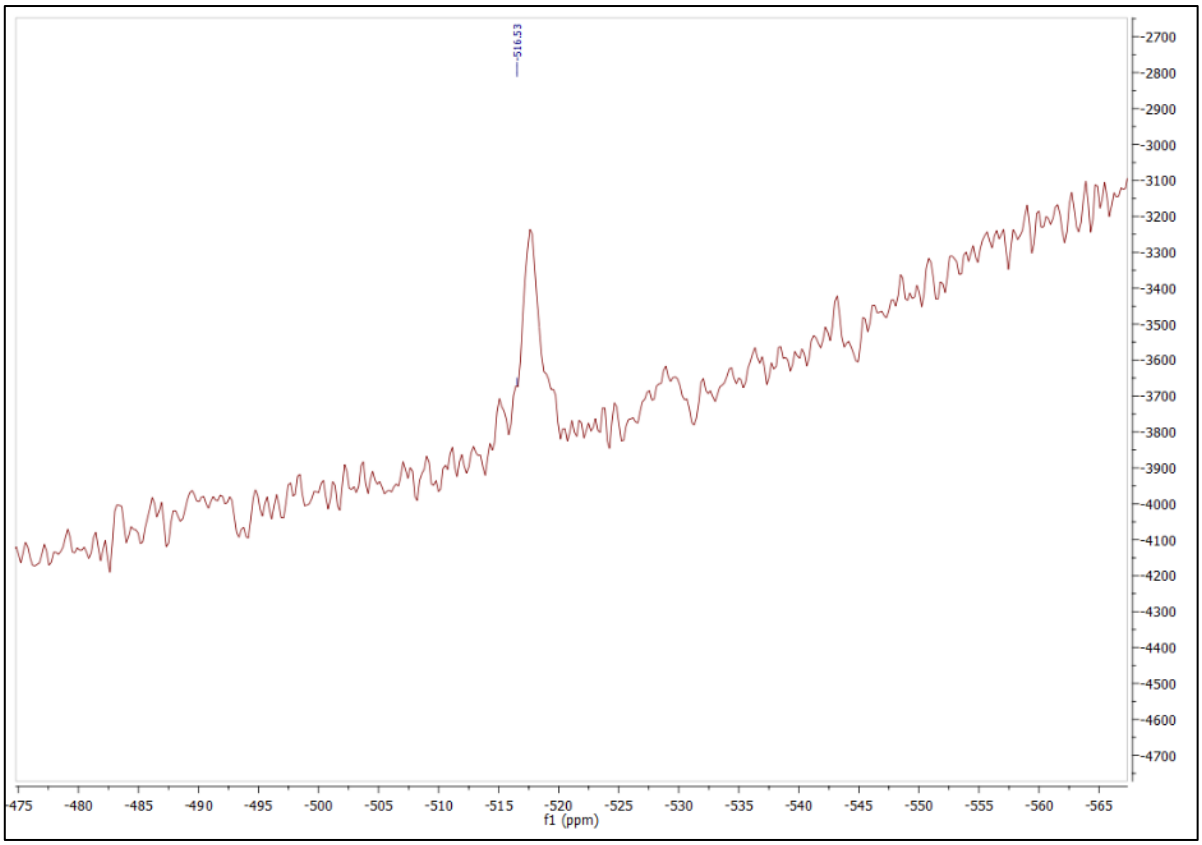

Figure 2A.A.13. ^{1}H coupled ^{77}Se NMR spectrum of complex **2A.4** at 223 K in C_6D_6.

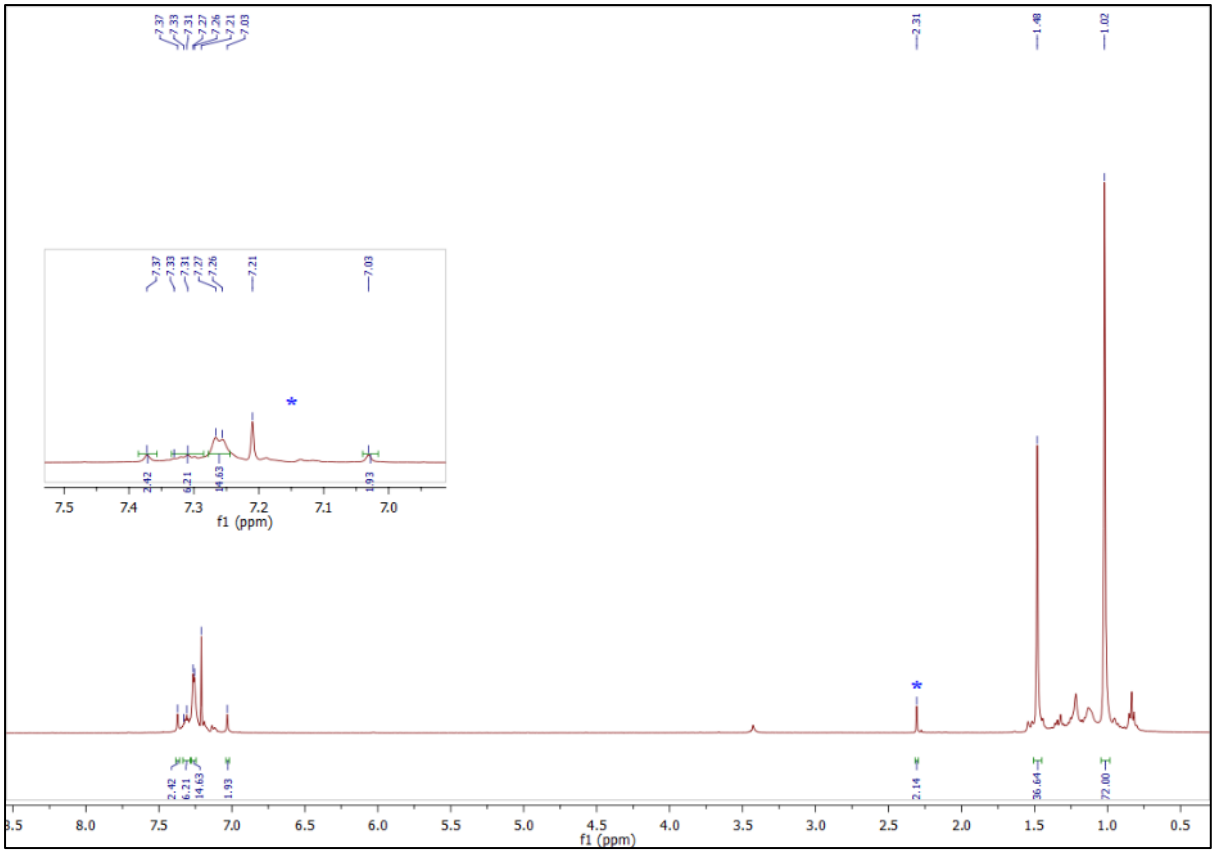

Figure 2A.A.14. ^{1}H NMR spectrum of complex **2A.5** in C_6D_6.

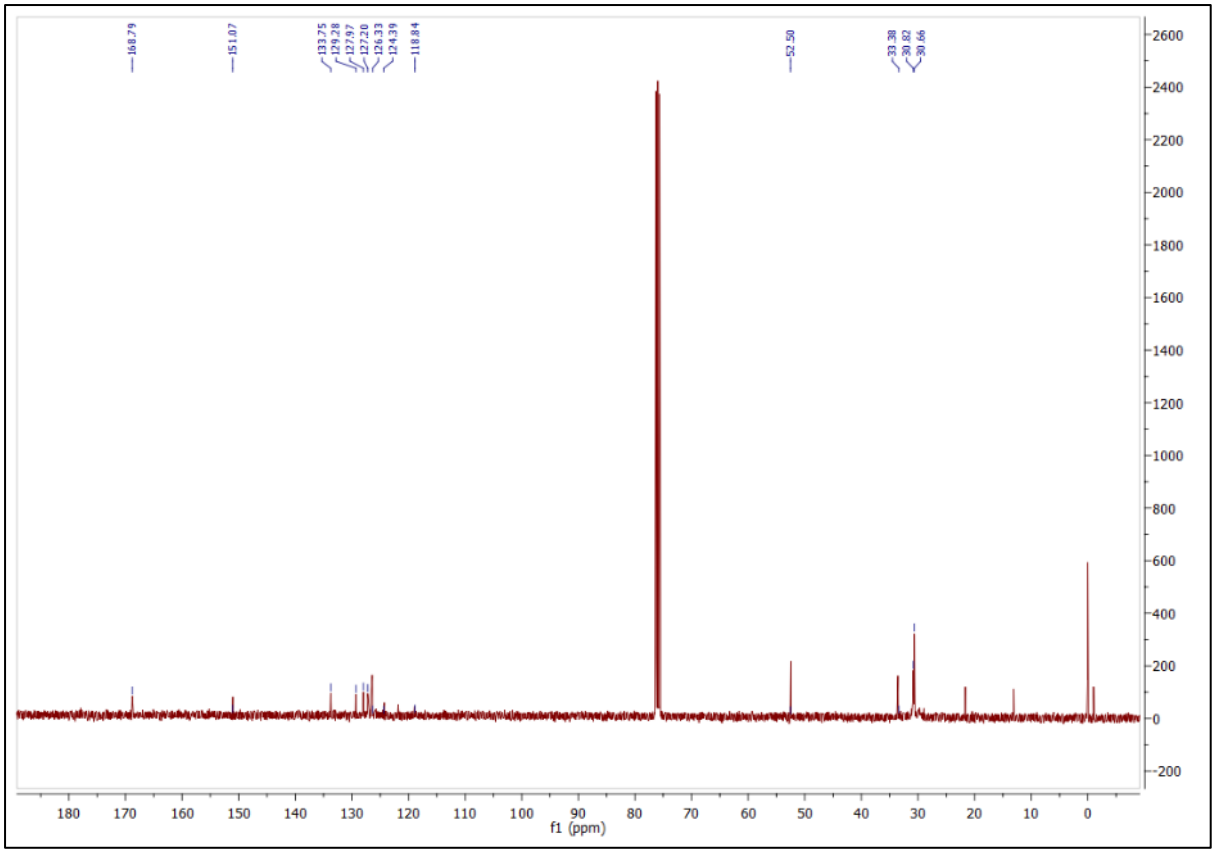

Figure 2A.A.15. ^{13}C NMR spectrum of complex **2A.5** in C_6D_6.

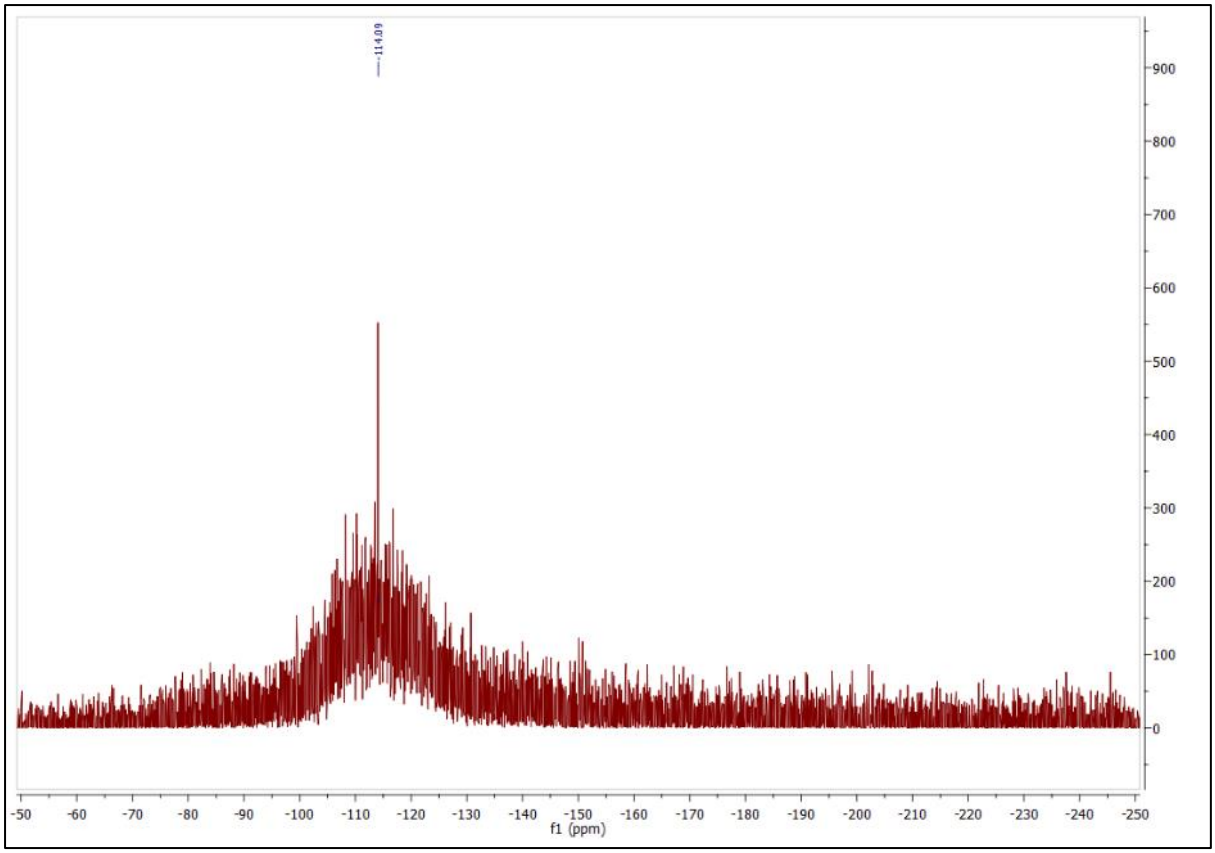

Figure 2A.A.16. ^{29}Si NMR spectrum of complex **2A.5** in C_6D_6.

2A.A.3 CSD analysis.

Analyzing the data in the crystal structures from the Cambridge Structural Database gives important information about non-covalent interactions. The CSD (ConQuest 1.21 version) analysis was done to establish the presence of C-H···Te interactions in the reported crystal structures satisfying the following criteria: (a) the crystallographic R factor <10%; (b) the H-atom positions normalized using the CSD default X–H bond lengths; (c) no polymer structures d) no powder structures e) no disordered structures. Our search includes intra as well as intermolecular C-H···Te interactions with H···Te (d) ≤ 3.26 Å (sum of the van der Waal radii) and $90^0 \leq \angle$C-H-Te (θ) $\leq 180^0$. This analysis was performed for the database where H and Te atoms are separated by more than three bonds (1, 5 type interaction) for intramolecular interactions. Most of the hits having the d in the range of 2.9-3.3 Å, and θ (angle) in the range of 110-150^0 highlight that C-H···Te interactions are weak in nature. A 3D-plot showing the frequency of the C-H···Te interactions as a function of the C-H···Te distance and angle is given in Figure 2A.A.17a, while the plot for d and θ is given in Figure 2A.A.17b. The analysis manifests that the number of C-H···Te interactions present in the CSD is quite significant.

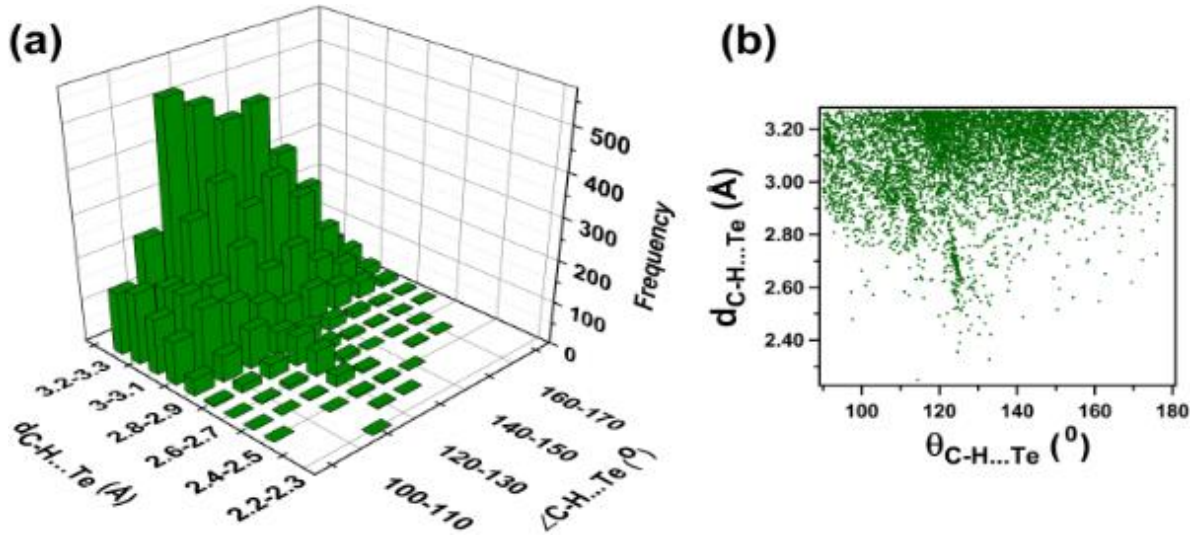

Figure 2A.A.17. CSD analysis: (a) Three-dimensional plot showing the frequency of the C-H···Te interaction as a function of $d_{C-H\cdots Te}$ (Å) and ∠ C-H···Te (°); (b) plot showing the distribution of $d_{C-H...Te}$ (Å) and ∠ C-H···Te (°).

2B.A.1 NMR spectra for 2B.1-2B.8.

* = untraced impurity , # = DCM , & = Toluene

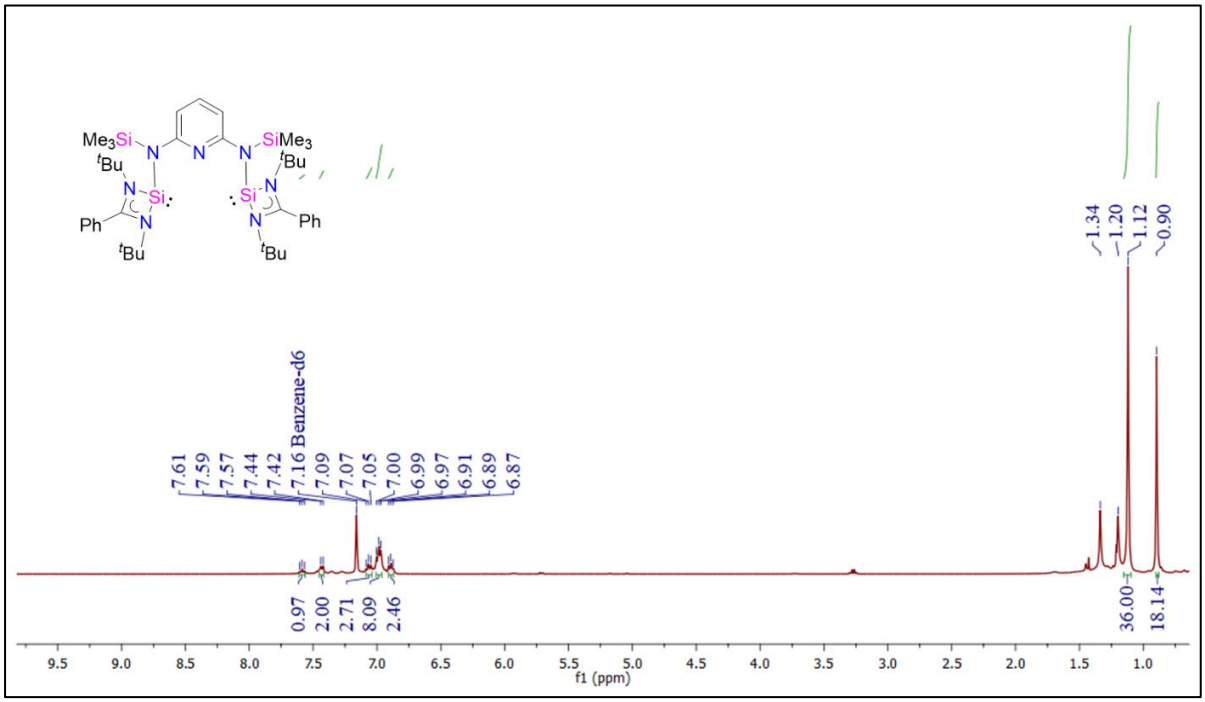

Figure 2B.A.1. ^{1}H NMR spectrum of complex **2B.1** in C_6D_6.

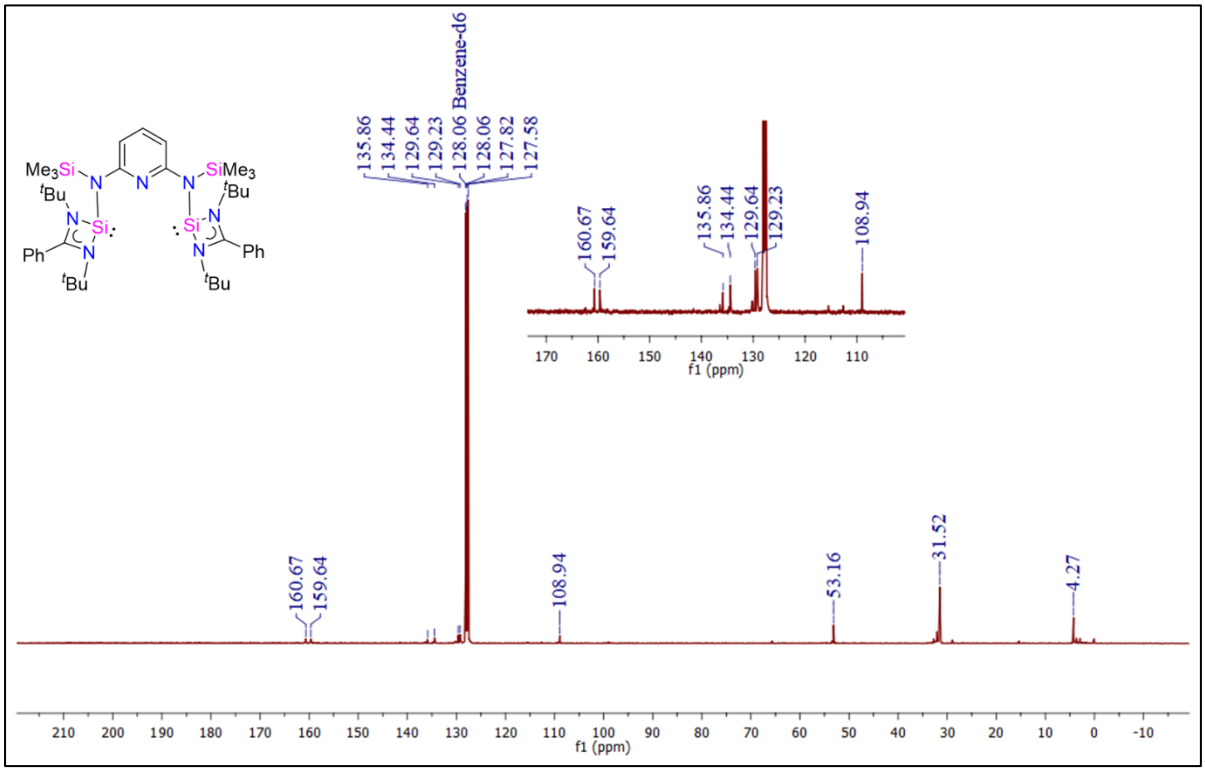

Figure 2B.A.2. $^{13}C\{^{1}H\}$ NMR spectrum of complex **2B.1** in C_6D_6.

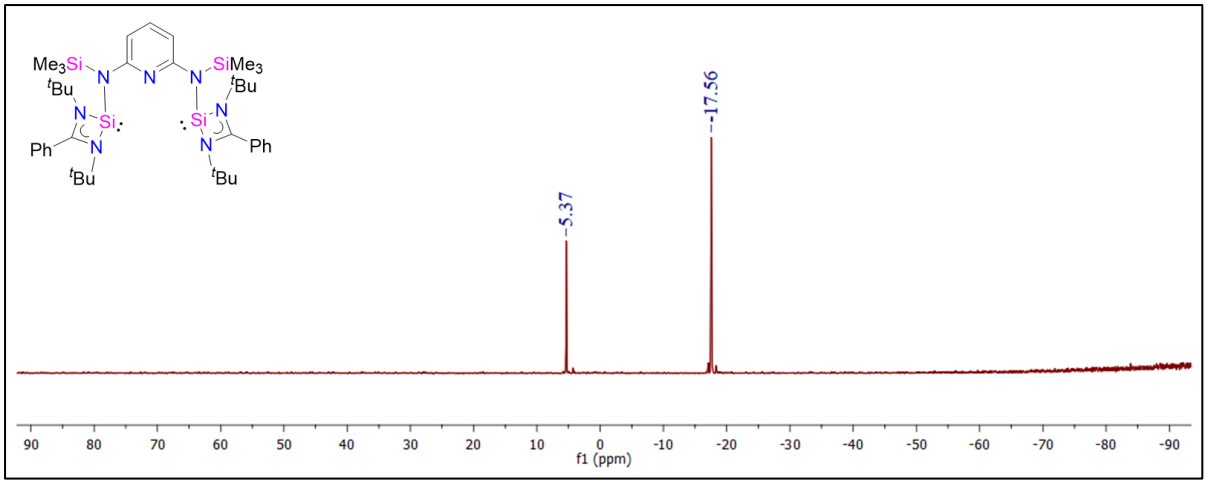

Figure 2B.A.3. $^{29}Si\{^{1}H\}$ NMR spectrum of complex **2B.1** in C_6D_6.

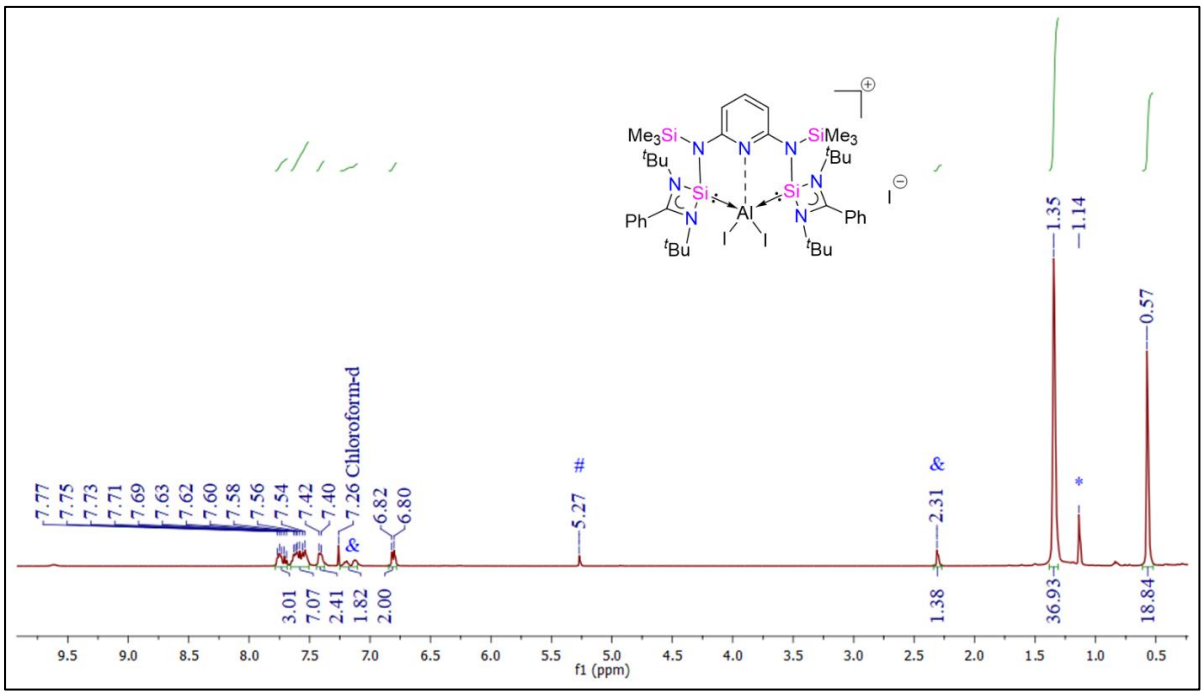

Figure 2B.A.4. ^{1}H NMR spectrum of complex **2B.2** in $CDCl_3$.

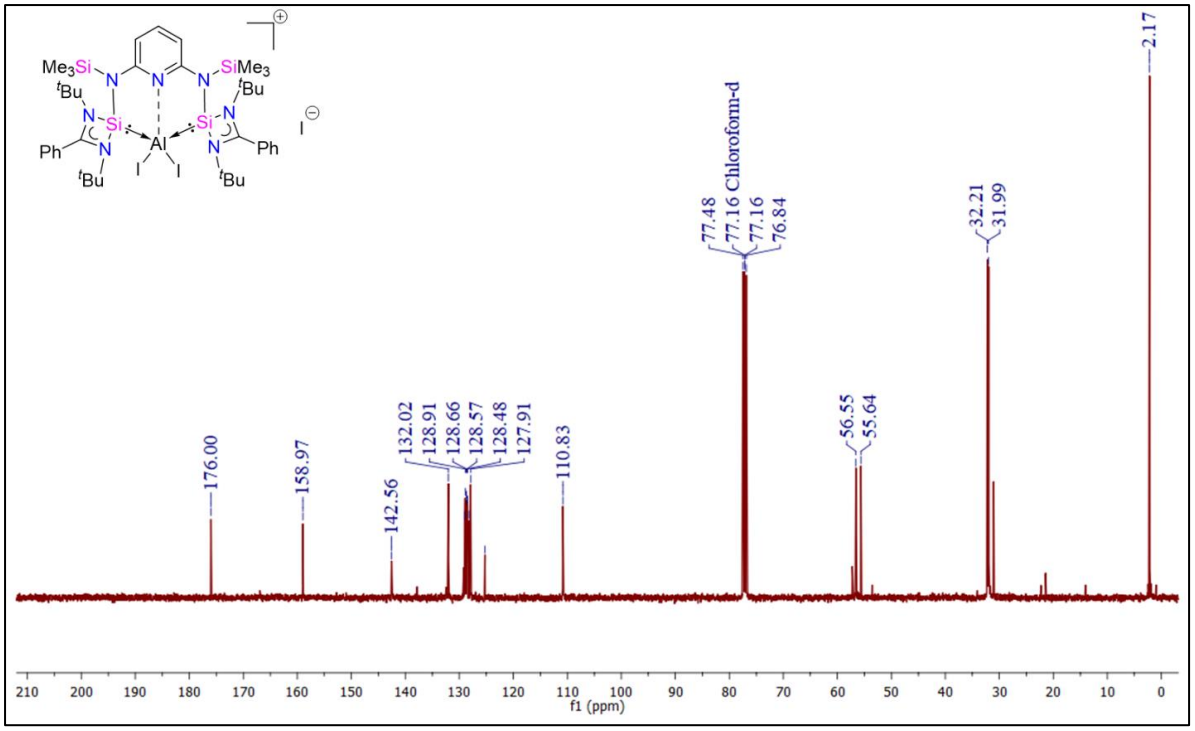

Figure 2B.A.5. $^{13}C\{^{1}H\}$ NMR spectrum of complex **2B.2** in $CDCl_3$.

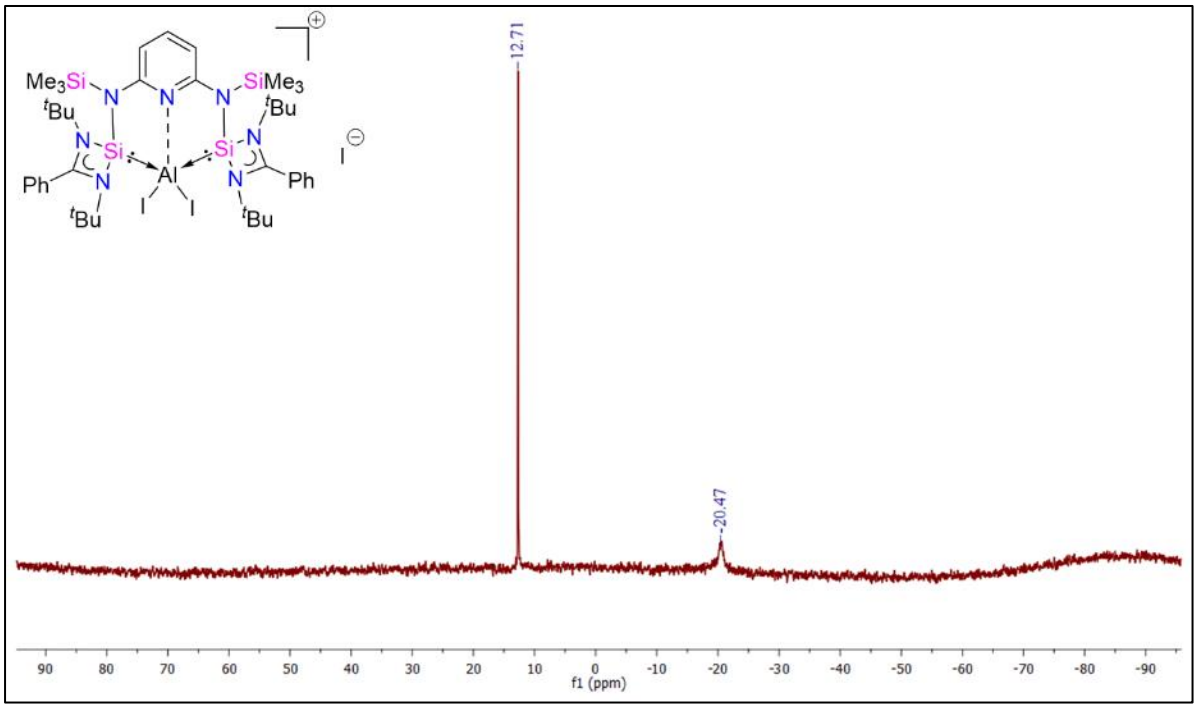

Figure 2B.A.6. $^{29}Si\{^{1}H\}$ NMR spectrum of complex **2B.2** in $CDCl_3$.

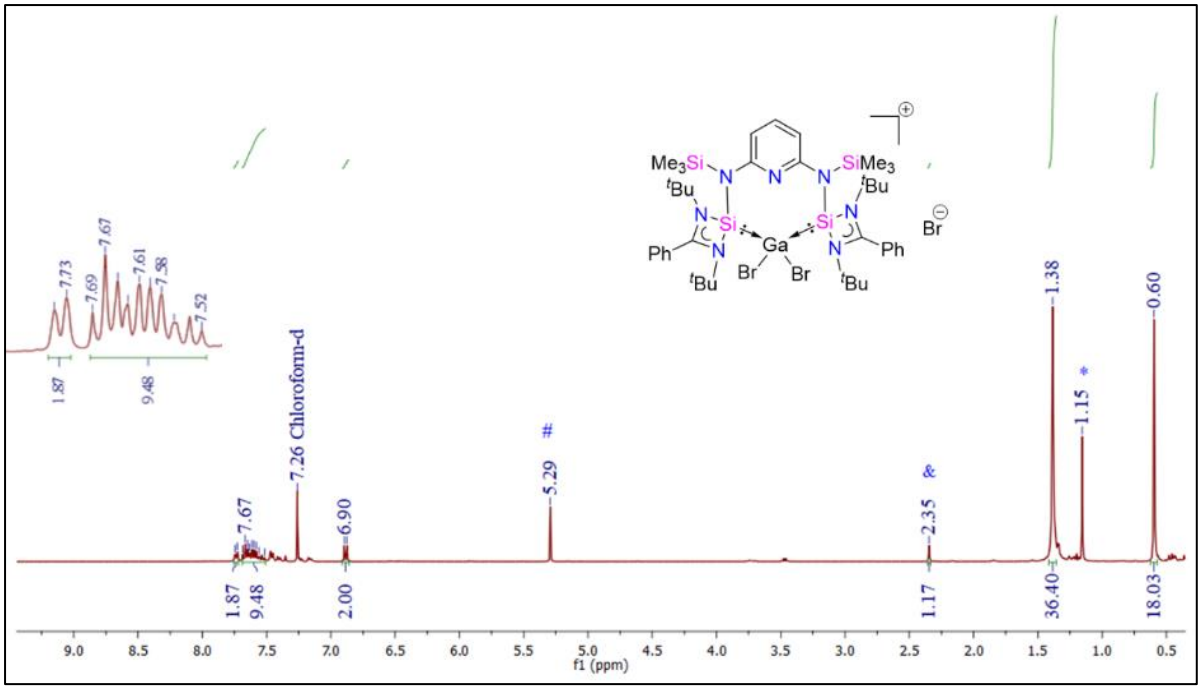

Figure 2B.A.7. ^{1}H NMR spectrum of complex **2B.3** in $CDCl_3$.

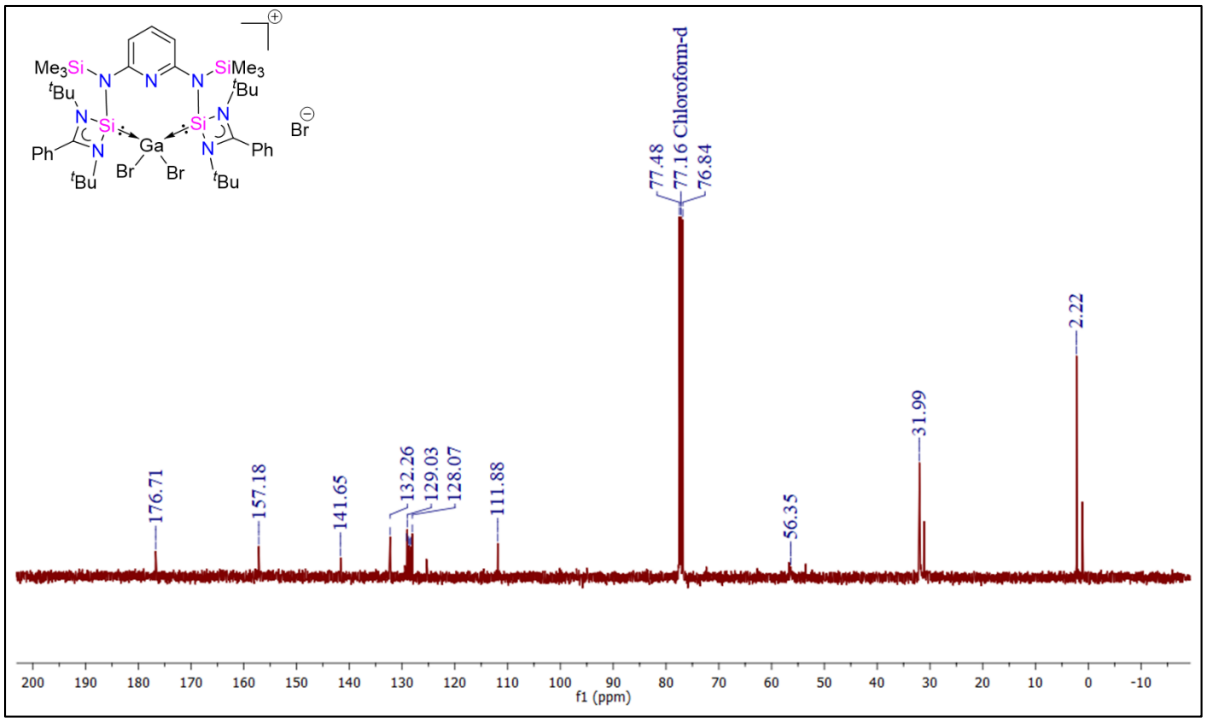

Figure 2B.A.8. $^{13}C\{^{1}H\}$ NMR spectrum of complex **2B.3** in $CDCl_3$.

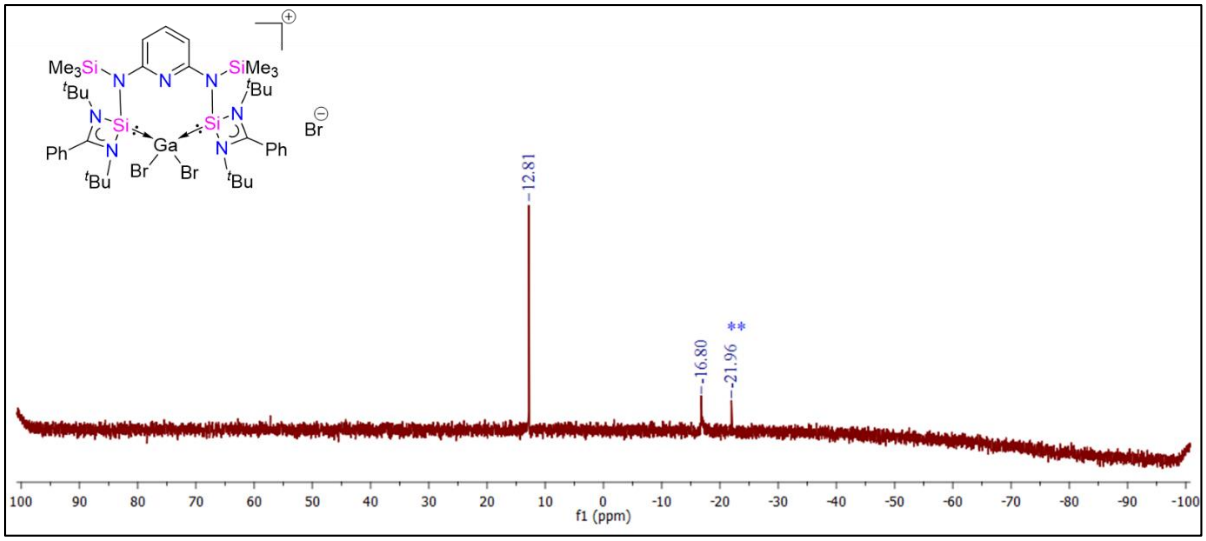

Figure 2B.A.9. $^{29}Si\{^{1}H\}$ NMR spectrum of complex **2B.3** in $CDCl_3$.

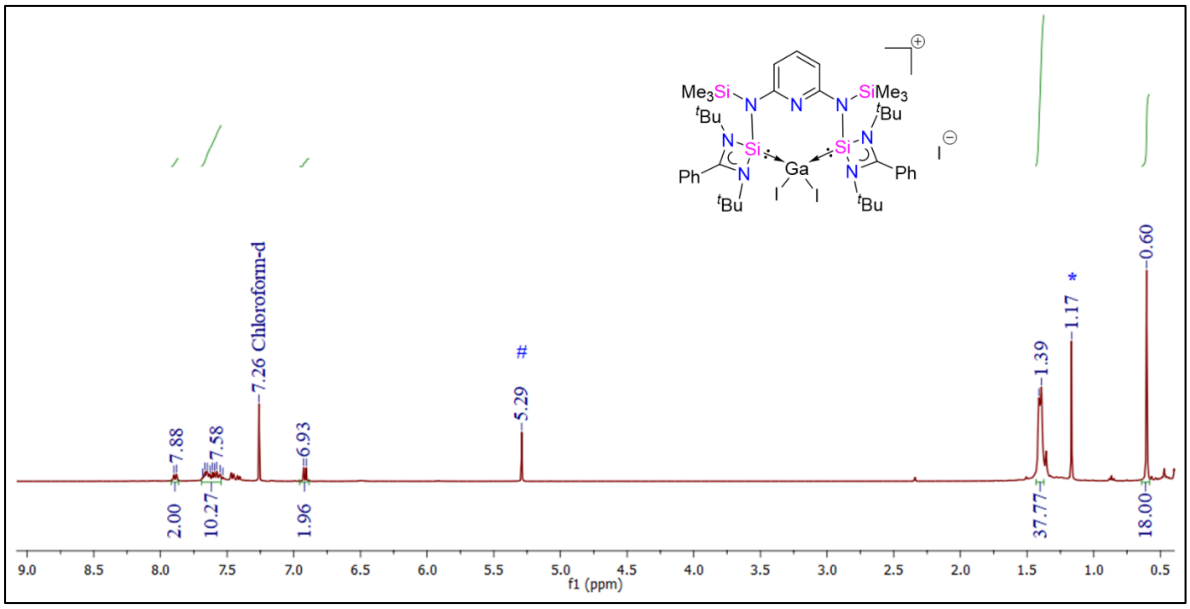

Figure 2B.A.10. ^{1}H NMR spectrum of complex **2B.4** in $CDCl_3$.

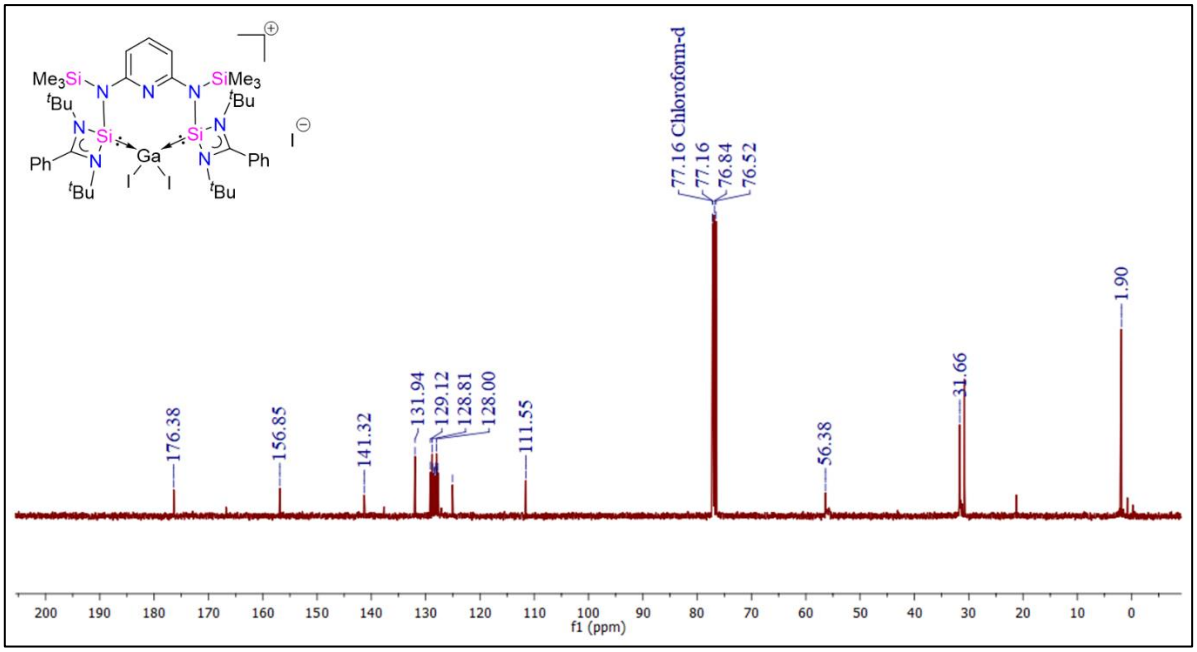

Figure 2B.A.11. $^{13}C\{^{1}H\}$ NMR spectrum of complex **2B.4** in $CDCl_3$.

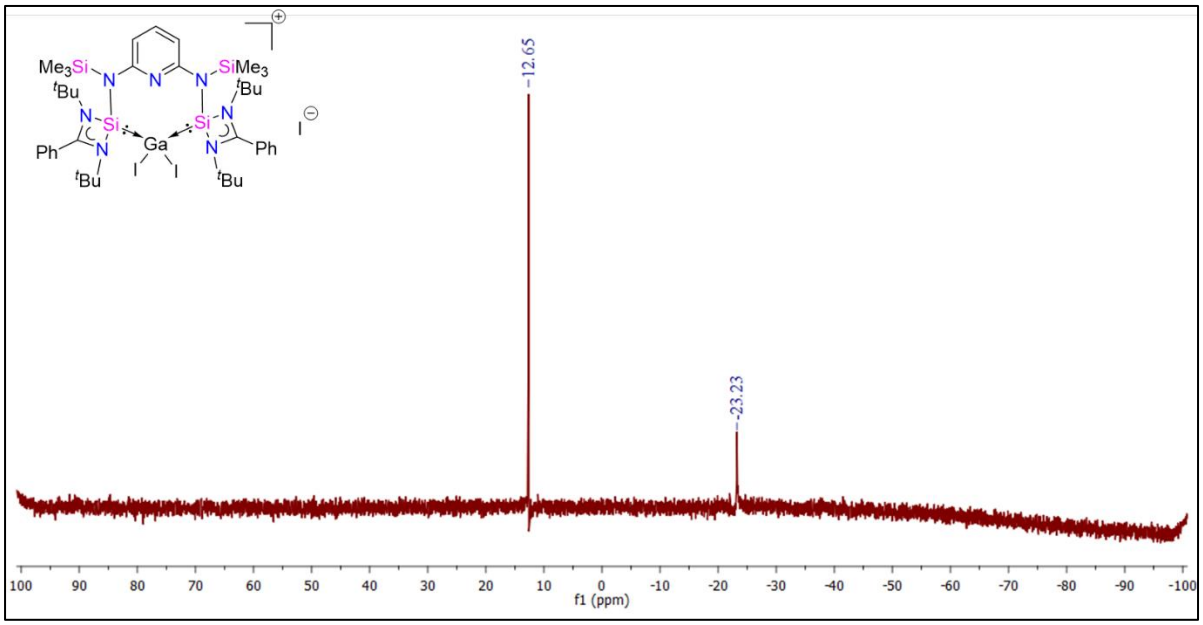

Figure 2B.A.12. $^{29}Si\{^{1}H\}$ NMR spectrum of complex **2B.4** in $CDCl_3$.

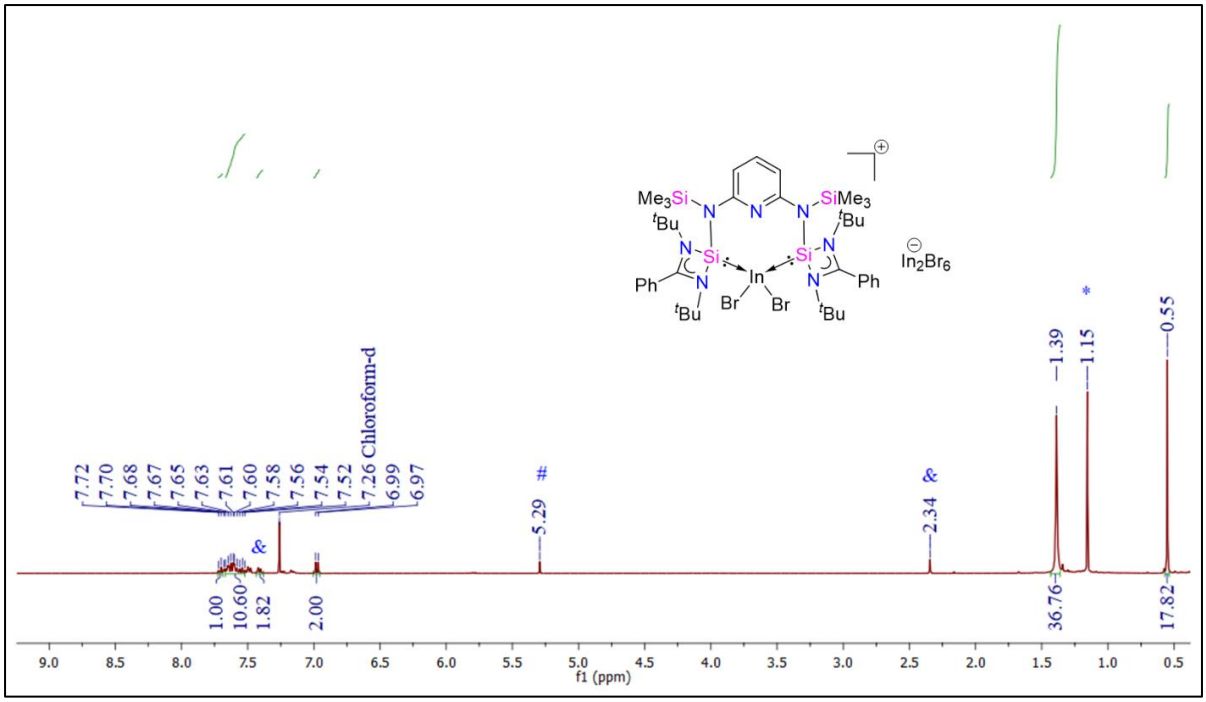

Figure 2B.A.13. ^{1}H NMR spectrum of complex **2B.6** in $CDCl_3$.

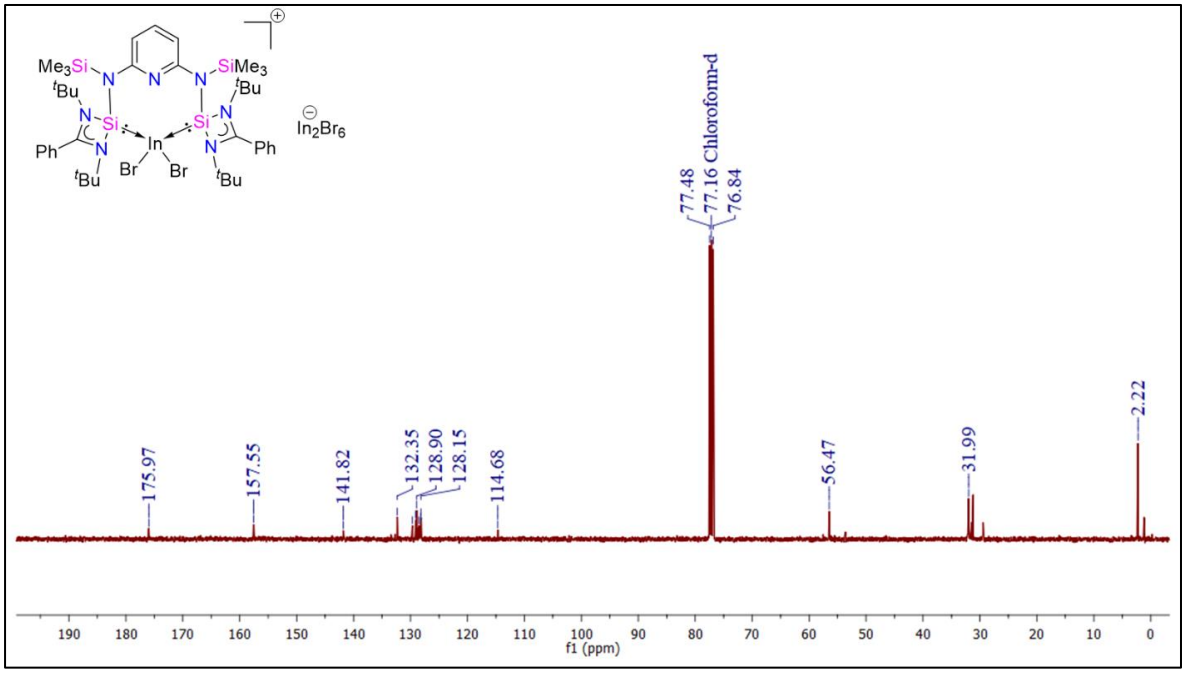

Figure 2B.A.14. $^{13}C\{^{1}H\}$ NMR spectrum of complex **2B.6** in $CDCl_3$.

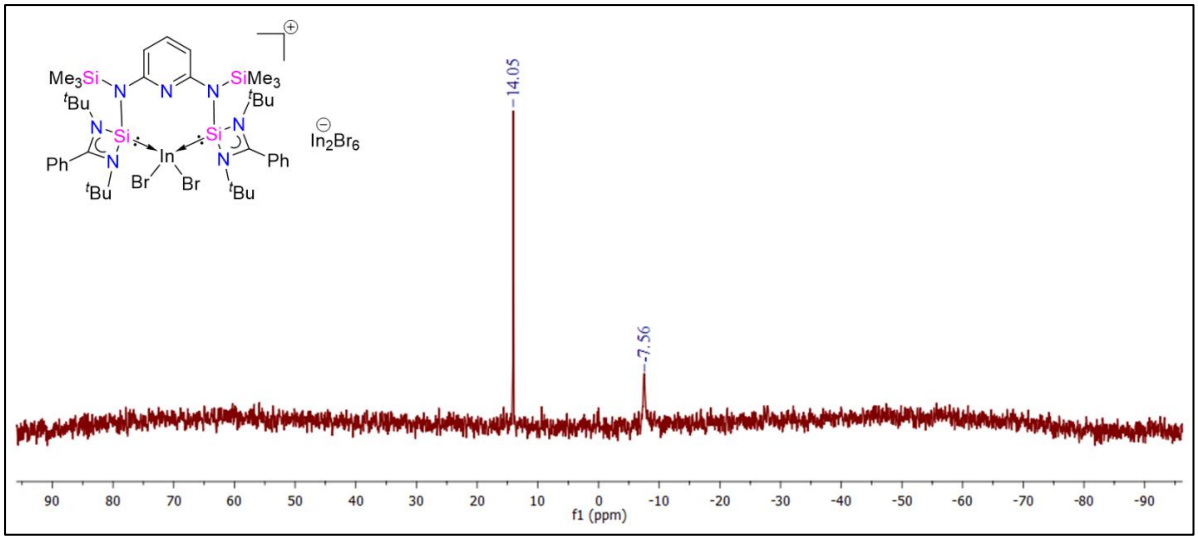

Figure 2B.A.15. $^{29}Si\{^{1}H\}$ NMR spectrum of complex **2B.6** in $CDCl_3$.

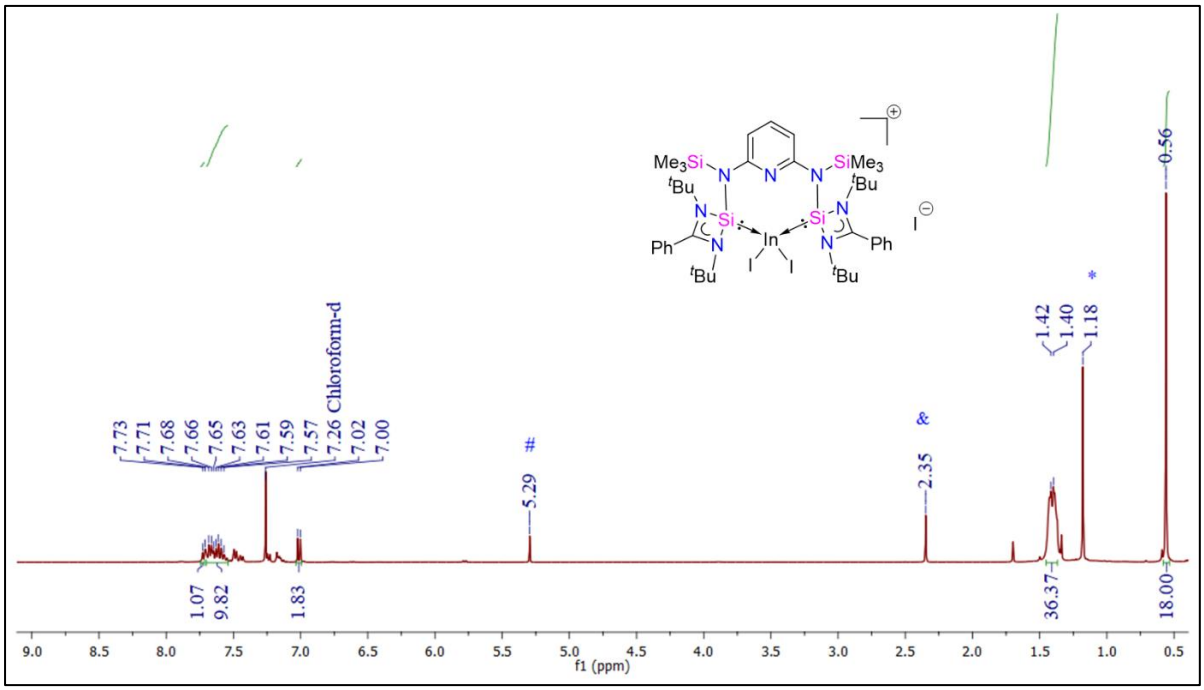

Figure 2B.A.16. ^{1}H NMR spectrum of complex **2B.7** in $CDCl_3$.

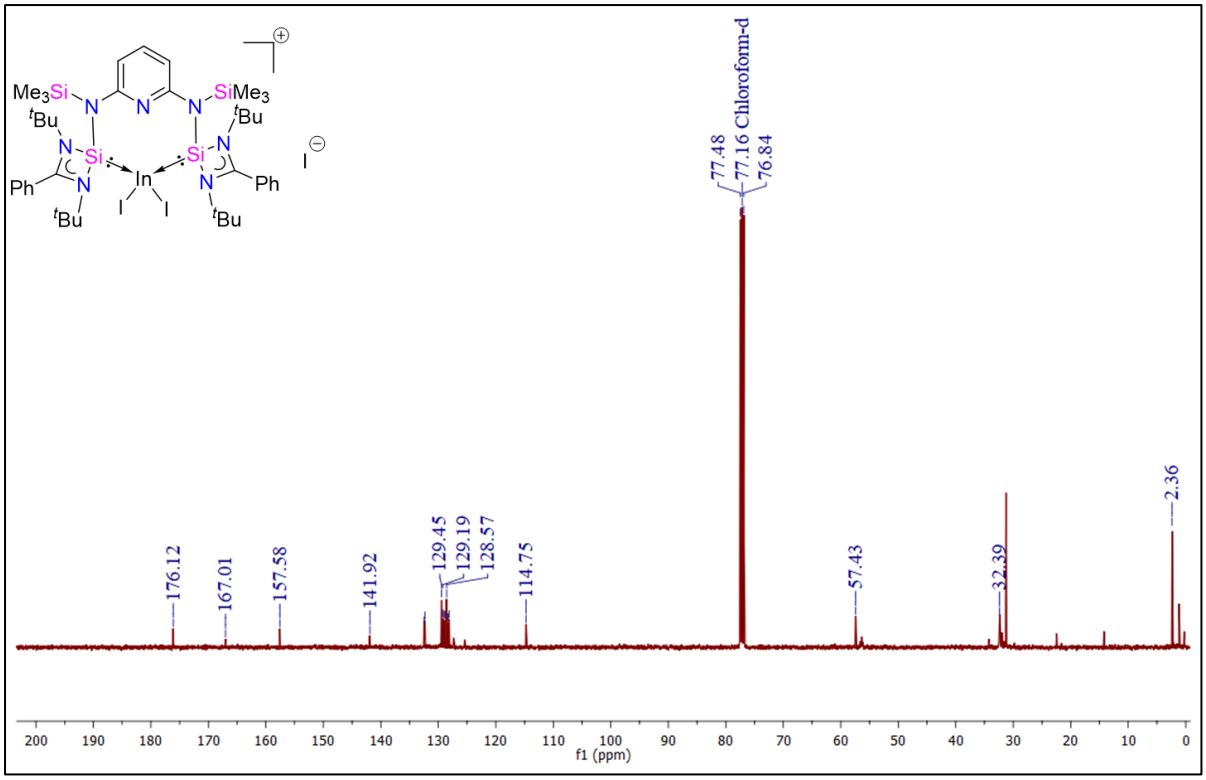

Figure 2B.A.17. $^{13}C\{^{1}H\}$ NMR spectrum of complex **2B.7** in $CDCl_3$.

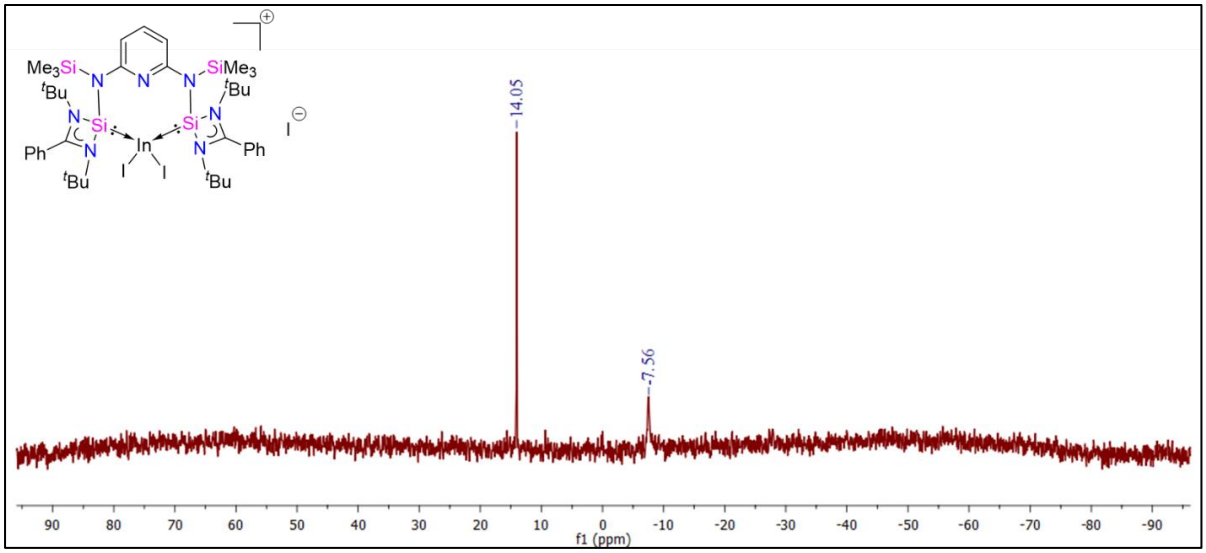

Figure 2B.A.18. $^{29}Si\{^{1}H\}$ NMR spectrum of complex **2B.7** in $CDCl_3$.

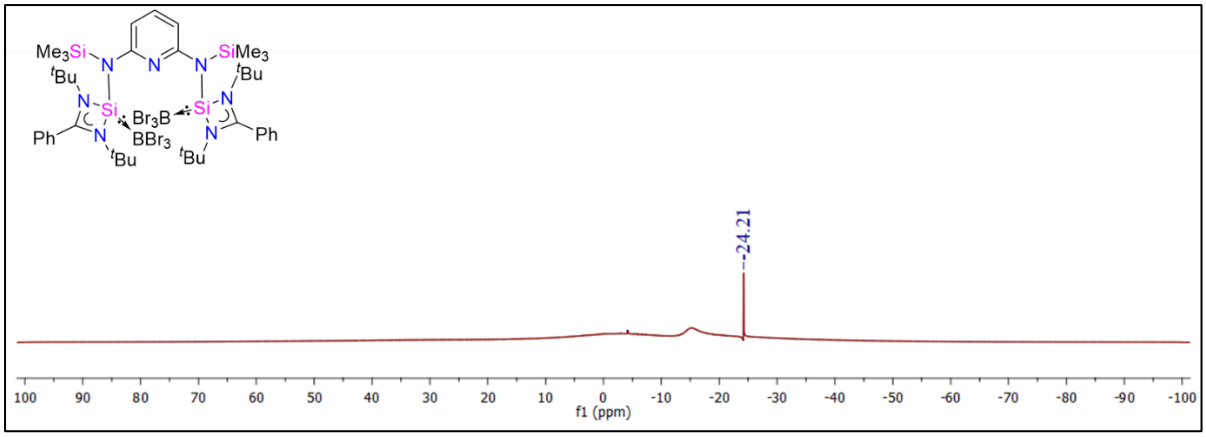

Figure 2B.A.19. $^{11}B\{^{1}H\}$ NMR spectrum of complex **2B.8** in $CDCl_3$.

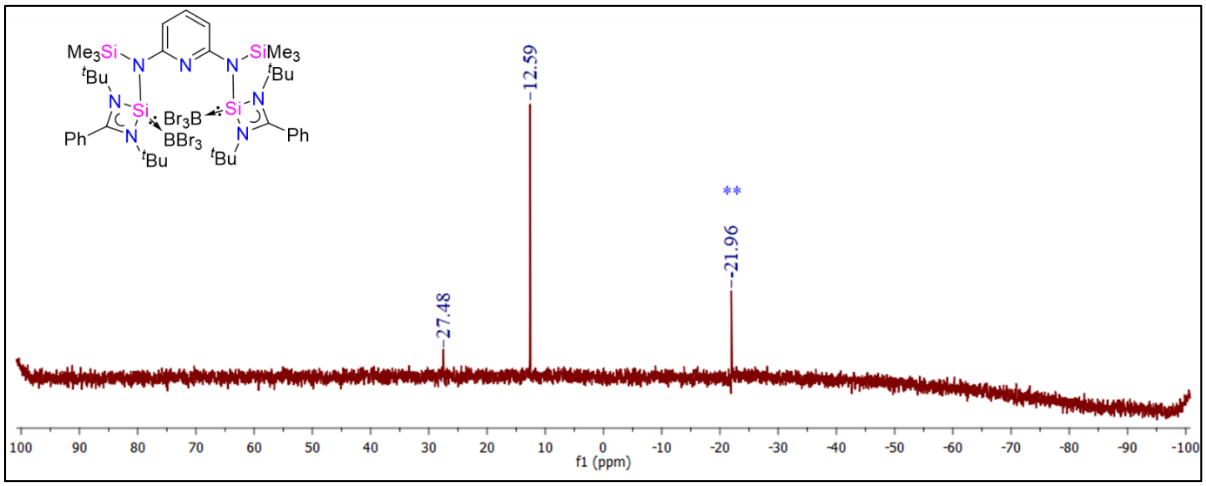

Figure 2B.A.20. $^{29}Si\{^{1}H\}$ NMR spectrum of complex **2B.8** in $CDCl_3$.

2B.A.2 Crystallographic data for 2B.2-2B.8.

Identification Code	**2B.2**	**2B.3**	**2B.5**
Chemical formula	$[C_{41}H_{67}AlI_2N_7Si_4, 3(CH_2Cl_2), I]$; $C_{44}H_{73}AlCl_6I_3N_7Si_4$	$C_{42}H_{69}Br_3Cl_2GaN_7Si_4$ [+ solvent]	$C_{41}H_{67}Br_3Ga_2I_3N_7Si_4$ [+ solvent]
Formula weight	1432.84	1164.72	1530.22
Temperature	150 K	150 K	100 K
Wavelength	0.71703 Å	0.71703 Å	0.71703 Å
Crystal system	Triclinic	Triclinic	Monoclinic
Space group	*P-1*	*P* -1	$P2_1/c$
Unit cell dimensions	a = 13.461(3) Å	a = 13.0927(16) Å	a = 16.703(2) Å
	b = 14.004(3) Å	b = 13.5817(16) Å	b = 32.333(5) Å

	c = 16.781(4) Å	c = 18.190(2) Å	c = 12.8383(19) Å
	α = 78.953(8)°	α = 103.413(3)°	α = 90°
	β = 81.573(7)°	β = 100.208(4)°	β = 108.339(4) °
	γ = 88.829(8)°	γ = 110.045(4)°	γ = 90°
Volume	3071.1(12) $Å^3$	2836.7(6) $Å^3$	6581.3(16) $Å^3$
Z	2	2	4
Density (calculated)	1.549 g/cm^3	1.364 g/cm^3	1.544 g/cm^3
Absorption coefficient	1.916 mm^{-1}	2.810 mm^{-1}	4.150 mm^{-1}
F(000)	1432.0	1192.0	2976.0
Theta range for data collection	2.21 to 28.32°	2.24 to 28.35°	2.28 to 27.82°
Index ranges	-16<=h<=16, -16<=k<=16, -20<=l<=20	-17<=h<= 17, -17<=k<=17, -23<=l<=23	-22<=h<=22, -43<=k<=43, -17<=l<=17
Reflections collected	110494	125611	222045
Independent reflections	11115 [R(int) = 0.0568]	13501 [R(int) = 0.0518]	16598 [R(int) = 0.1078]
Coverage of independent reflections	99.9%	99.9%	99.5%
Function minimized	Σ w $(Fo^2 - Fc^2)^2$	Σ w $(Fo^2 - Fc^2)^2$	Σ w $(Fo^2 - Fc^2)^2$
Data/restraints/parameters	11115 / 0 / 604	13501 / 0 / 550	16598 / 0 / 559
Goodness-of-fit on F^2	1.046	1.021	1.032
Δ/σ max	0.001	0.002	0.001
Final R indices	9595 data [I>2σ(I)], R1 = 0.0281, wR2 = 0.0584	11196 data [I>2σ(I)], R1 = 0.0311, wR2 = 0.0721	12103 data [I>2σ(I)], R1 =0.0862, wR2 = 0.2396
	all data, R1=0.0373, wR2 = 0.0619	all data, R1 =0.0436, wR2 = 0.0775	all data, R1 =0.1146, wR2 =0.2587
Largest diff. peak and hole	1.392 and -1.098 $eÅ^{-3}$	0.824 and -0.725 $eÅ^{-3}$	4.091 and -3.782$eÅ^{-3}$
R.M.S. deviation from mean	0.085 $eÅ^{-3}$	0.076 $eÅ^{-3}$	0.273 $eÅ^{-3}$

Identification Code	**2B.6**	**2B.7**	**2B.8**
Chemical formula	$C_{42}H_{69}Br_5Cl_2In_2N_7Si_4$	$C_{41}H_{67}I_5In_2N_7Si_4$	$C_{41}H_{67}B_2Br_6N_7Si_4$
Formula weight	1484.49	1634.51	1271.45
Temperature	150K	150 K	150 K
Wavelength	0.71703 Å	0.71703 Å	0.71703 Å
Crystal system	Triclinic	Triclinic	Monoclinic
Space group	*P-1*	*P-1*	*C2/c*
Unit cell dimensions	a = 13.512(3) Å	a = 13.9389(10) Å	a = 29.759(5) Å
	b = 13.601(2) Å	b = 13.9701(9) Å	b = 16.078(2) Å
	c = 18.754(3) Å	c = 18.2788(14) Å	c = 15.525(2) Å
	α = 104.830(5)°	α = 76.075(2) °	α = 90 °
	β = 98.135(5)°	β = 86.974(2) °	β = 100.928(9) °
	γ = 98.427(5)°	γ = 84.062(3)°	γ = 90 °
Volume	3237.5(10) $Å^3$	3434.8(4) $Å^3$	7293.5(18) $Å^3$
Z	2	2	4
Density (calculated)	1.523 g/cm^3	1.580 g/cm^3	1.158 g/cm^3
Absorption coefficient	3.986 mm^{-1}	3.016 mm^{-1}	3.395 mm^{-1}
F(000)	1466.0	1562.0	2552.0
Theta range for data collection	2.22 to 23.63°	2.43 to 28.16°	2.44 to 23.54°
Index ranges	-16<=h<=16, -16<=k<=16, -22<=l<=22	-16<=h<= 16, -16<=k<= 16, -21<=l<=21	-39<=h<=39, -20<=k<=20, -21<=l<=21
Reflections collected	65082	23218	30428
Independent reflections	11388 [R(int) = 0.3352]	11517 [R(int) = 0.0541]	9028 [R(int) =0.1583]
Coverage of independent reflections	100 %	95.1 %	98.7 %
Function minimized	Σ w $(Fo^2 - Fc^2)^2$	Σ w $(Fo^2 - Fc^2)^2$	Σ w $(Fo^2 - Fc^2)^2$

Data/restraints/parameters	11388 / 0 / 577	11517/ 0 / 569	9028 / 0 / 281
Goodness-of-fit on F^2	0.985	1.023	1.063
Δ/σ max	0.007	0.001	0.001
Final R indices	4737 data [I>2σ(I)], R1 = 0.0939, wR2 = 0.1857	8039 data [I>2σ(I)], R1 = 0.0670, wR2 =0.1248	3902 data [I>2σ(I)], R1 = 0.0831, wR2 = 0.1860
	all data, R1 =0.2249, wR2 = 0.2387	all data, R1 =0.1040, wR2 = 0.1444	all data, R1 =0.1929, wR2 = 0.2194
Largest diff. peak and hole	0.934 and -1.102eÅ^{-3}	4.348 and -1.733eÅ^{-3}	0.869 and -0.657 eÅ^{-3}
R.M.S. deviation from mean	0.182 eÅ^{-3}	0.184 eÅ^{-3}	0.162 eÅ^{-3}

2C.A.1 Crystallographic data for 2C.1-2C.8.

	2C.1	**2C.2**
Chemical formula	$C_{27}H_{31}N_3Si$	$C_{33}H_{36}CoN_3OSi$
Formula weight	425.64 g/mol	577.67 g/mol
Temperature	100 K	100 K
Wavelength	0.71703 Å	0.71073 Å
Crystal system	Triclinic	Monoclinic
Space group	*P* -1	$P2_1/n$
Unit cell dimensions	a = 9.7178(17) Å	a = 9.9383(4) Å
	b = 11.2040 (17) Å	b = 13.7155(5) Å
	c = 12.647 (2) Å	c = 20.9815(9) Å
	α = 107.961(5)°	α = 90°
	β = 107.208 (6)°	β = 94.859(2)°
	γ = 103.138(5)°	γ = 90°
Volume	1171.8 (3) $Å^3$	2849.7(2) $Å^3$
Z	2	4
Density (calculated)	1.206 g/cm^3	1.074 g/cm^3
Absorption coefficient	0.119 mm^{-1}	0.676 mm^{-1}
F(000)	456.00	1216.00
Theta range for data collection	2.34 to 28.10°	2.45 to 28.333°
Index ranges	-12<=h<=12, -13<=k<=14, -16<=l<=16	-13<=h<=13, -18<=k<=18, -28<=l<=28
Reflections collected	28909	100069
Independent reflections	5731 [R(int) = 0.0968]	7076 [R(int) = 0.1131]
Coverage of independent reflections	97.9%	99.6%
Function minimized	Σ w$(Fo^2 - Fc^2)^2$	Σ w$(Fo^2 - Fc^2)^2$
Data / restraints / parameters	5731/0/286	7076/ 0 / 358
Goodness-of-fit on F^2	1.050	1.067
Δ/σ max	0.000	0.000
Final R indices	3786 data[I>2σ(I)],	5000 data[I>2σ(I)],

	R1 = 0.0612, wR2 = 0.1111	R1 = 0.0523, wR2 = 0.0937
	all data , R1 = 0.1155, wR2 = 0.1272	all data , R1 = 0.0937, wR2 = 0.1064
Largest diff. peak and hole	0.551 and -0.318 eÅ^{-3}	0.94 and -0.57 eÅ^{-3}
R.M.S. deviation from mean	0.063 eÅ^{-3}	0.079 eÅ^{-3}

	2C.3	**2C.4**
Chemical formula	$C_{27}H_{31}N_3SiAuCl$	$C_{54}H_{62}N_6Si_2Cu_2Br_2$
Formula weight	658.06 g/mol	1322.4 g/mol
Temperature	100 K	100 K
Wavelength	0.71073 Å	0.71073 Å
Crystal system	Monoclinic	Triclinic
Space group	*C2/c*	*P* -1
Unit cell dimensions	*a* = 18.969(9) Å	*a* = 10.7857(19) Å
	b = 18.011(9) Å	*b* = 17.269(3) Å
	c = 18.047(11) Å	*c* = 18.185(3) Å
	α = 90°	*α* = 99.213(5)°
	β = 121.69(2)°	*β* = 98.840(5)°
	γ = 90°	*γ* = 106.744(5)°
Volume	5246(5) Å^3	3129.2(10) Å^3
Z	8	2
Density (calculated)	1.666 g/cm^3	1.403 g/cm^3
Absorption coefficient	5.775 mm^{-1}	2.041 mm^{-1}
F(000)	2592.00	1368.0
Theta range for data collection	2.52 to 26.547°	2.017 to 28.357°
Index ranges	-23<=h<=23, -22<=k<=22, -22<=l<=22	-14<=h<=14, -23<=k<=23, -24<=l<=24
Reflections collected	94570	83965
Independent reflections	5469 [R(int) =	15564 [R(int) =

	0.2074]	0.1690]
Coverage of independent reflections	99.7%	99.3%
Function minimized	Σ w(Fo^2 - Fc^2)^2	Σ w(Fo^2 - Fc^2)^2
Data / restraints / parameters	5469 / 0 / 299	15564/ 0 / 735
Goodness-of-fit on F^2	1.021	1.052
Δ/σ max	0.002	0.001
Final R indices	3961 data[I>2σ(I)], R1 = 0.0557, wR2 = 0.0808	7712 data[I>2σ(I)], R1 = 0.0867, wR2 = 0.1300
	all data, R1 = 0.0661, wR2 = 0.0877	all data, R1 = 0.2099, wR2 = 0.1628
Largest diff. peak and hole	1.921 and -0.985 eÅ^{-3}	0.94 to -0.84 eÅ^{-3}
R.M.S. deviation from mean	0.170 eÅ^{-3}	0.126 eÅ^{-3}

	2C.5	**2C.6**
Chemical formula	C_{54} $H_{61}N_6Si_2CuI$	$C_{56}H_{62}N_6O_2S_2Si_2F_6Cu_2$
Formula weight	1040.70 g/mol	1276.49 g/mol
Temperature	100 K	100 K
Wavelength	0.71703 Å	0.71073 Å
Crystal system	Monoclinic	Monoclinic
Space group	*P* 2_1/c	*P* 2_1/n
Unit cell dimensions	*a* = 15.0498(9) Å	*a* = 11.561(3) Å
	b = 44.112(3) Å	*b* = 18.692(4) Å
	c = 9.1050(5) Å	*c* = 14.271(4) Å
	α = 90°	α = 90°
	β = 103.835(2)°	β = 113.576(12)°
	γ = 90°	γ = 90°
Volume	5869.2(6) Å^3	2826.5(13) Å^3
Z	4	4

Density (calculated)	1.178 g/cm^3	1.500 g/cm^3
Absorption coefficient	0.975 mm^{-1}	0.945 mm^{-1}
F(000)	2148.00	1320.00
Theta range for data collection	2.31 to 26.407°	2.68 to 28.425°
Index ranges	-18<=h<=18, -55<=k<=55, -11<=l<=11	-15<=h<=15, -25<=k<=25, -19<=l<=19
Reflections collected	151515	77987
Independent reflections	12038 [R(int) = 0.1161]	7065 [R(int) = 0.1945]
Coverage of independent reflections	99.8%	100%
Function minimized	Σ w(Fo^2 - Fc^2)^2	Σ w(Fo^2 - Fc^2)^2
Data / restraints / parameters	12038/0/589	7065/ 0 / 367
Goodness-of-fit on F^2	1.099	1.091
Δ/σ max	0.001	0.000
Final R indices	9145 data[I>2σ(I)], R1 = 0.0715, wR2 = 0.1686	4249 data[I>2σ(I)], R1 = 0.0660, wR2 = 0.1143
	all data , R1 = 0.1006, wR2 = 0.1809	all data , R1 = 0.1486, wR2 = 0.1474
Largest diff. peak and hole	2.152 and -0.929 eÅ^{-3}	0.60 and -0.99 eÅ^{-3}

	2C.7	**2C.8**
Chemical formula	$C_{54}H_{62}N_6Si_2Br_2Ag_2$	$C_{57}H_{62}N_6Si_2Ag_2I_2$
Formula weight	1226.83 g/mol	1575.59 g/mol
Temperature	100 K	100 K
Wavelength	0.71073 Å	0.71073 Å
Crystal system	Monoclinic	Monoclinic
Space group	*P* 2$_1$/*n*	*P*-1
Unit cell dimensions	*a* = 10.699(4) Å	*a* = 14.8886(17)Å
	b = 15.525(4) Å	*b* = 15.2459(19)Å

	c = 17.296(5) Å	c = 16.403(2)Å
	α = 90°	α = 67.202(4)°
	β = 107.452(10)°	β = 89.316(4)°
	γ = 90°	γ = 67.948(4)°
Volume	2740.7(14) $Å^3$	3142.3(7) $Å^3$
Z	2	2
Density (calculated)	1.487 g/cm^3	1.940 g/cm^3
Absorption coefficient	2.256 mm^{-1}	1.665 mm^{-1}
F(000)	1240.00	1564.0
Theta range for data collection	2.40 to 34.315°	1.859 to 25.250°
Index ranges	-16<=h<=16, -24<=k<=24, -27<=l<=27	-17<=h<=17, -18<=k<=18, -19<=l<=19
Reflections collected	131405	160529
Independent reflections	11343 [R(int) = 0.0545]	11375 [R(int) = 0.0541]
Coverage of independent reflections	99.1%	100%
Function minimized	Σ w(Fo^2 - Fc^2)^2	Σ w(Fo^2 - Fc^2)^2
Data / restraints / parameters	11343 / 0 / 304	11375/ 0 / 689
Goodness-of-fit on F^2	1.058	1.104
Δ/σ max	0.002	0.001
Final R indices	7614 data[I>2σ(I)], R1 = 0.0463, wR2 = 0.0705	9826 data[I>2σ(I)], R1 = 0.0347, wR2 = 0.0963
	all data, R1 = 0.0964, wR2 = 0.0843	all data, R1 = 0.0439, wR2 = 0.1094
Largest diff. peak and hole	0.743 and -1.002 $eÅ^{-3}$	1.513 to -1.384 $eÅ^{-3}$

2C.A.2 NMR spectroscopic data for complexes 2C.1-2C.8.

* corresponds to Benzene-d_6, # corresponds to Chloroform-*d*

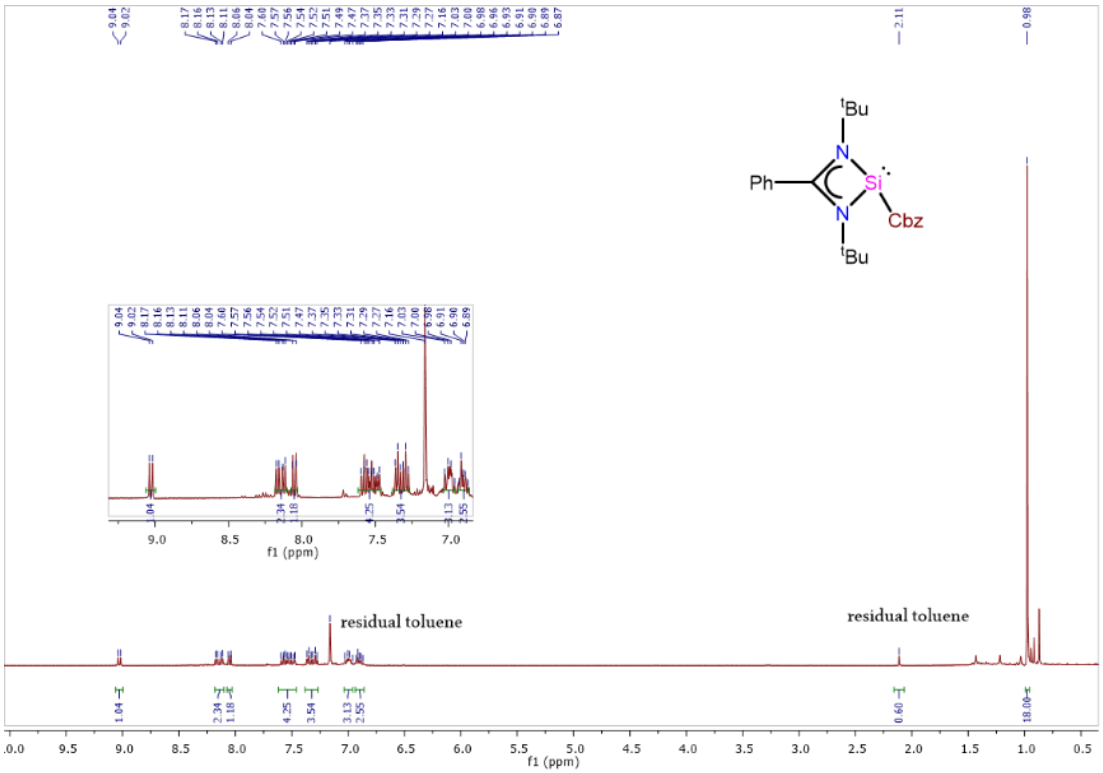

Figure 2C.A.1. ^{1}H NMR spectrum of **2C.1** in C_6D_6.

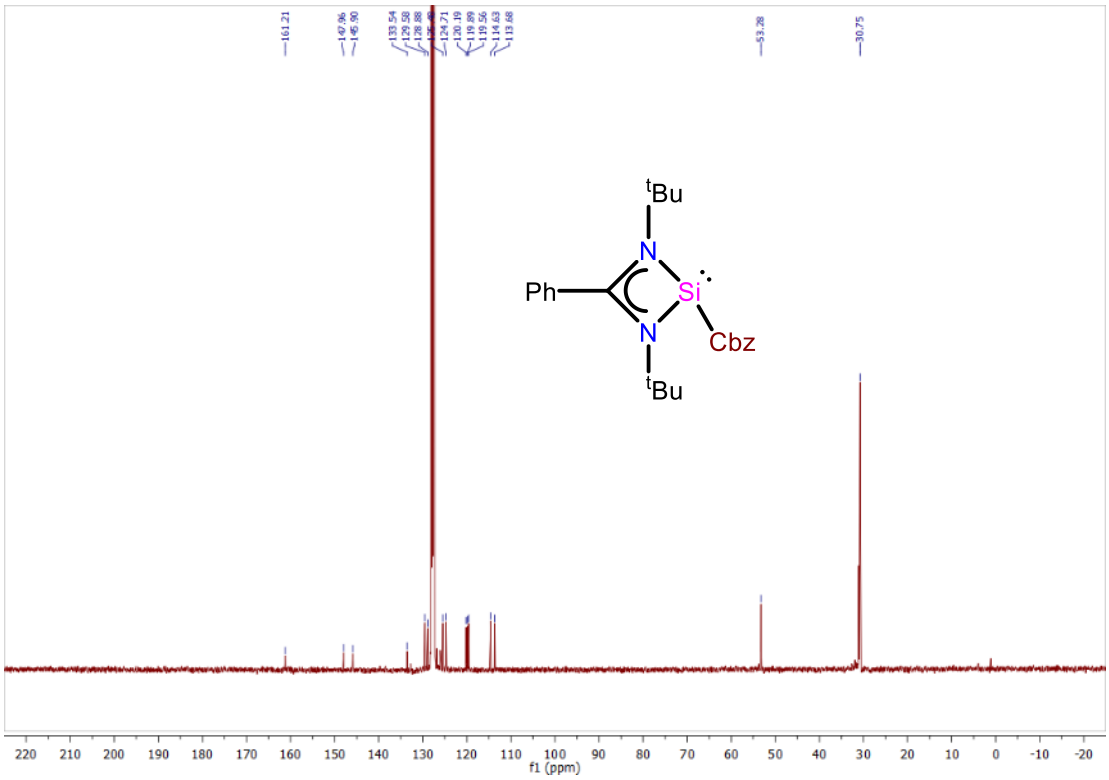

Figure 2C.A.2. ^{13}C NMR spectrum of **2C.1** in C_6D_6.

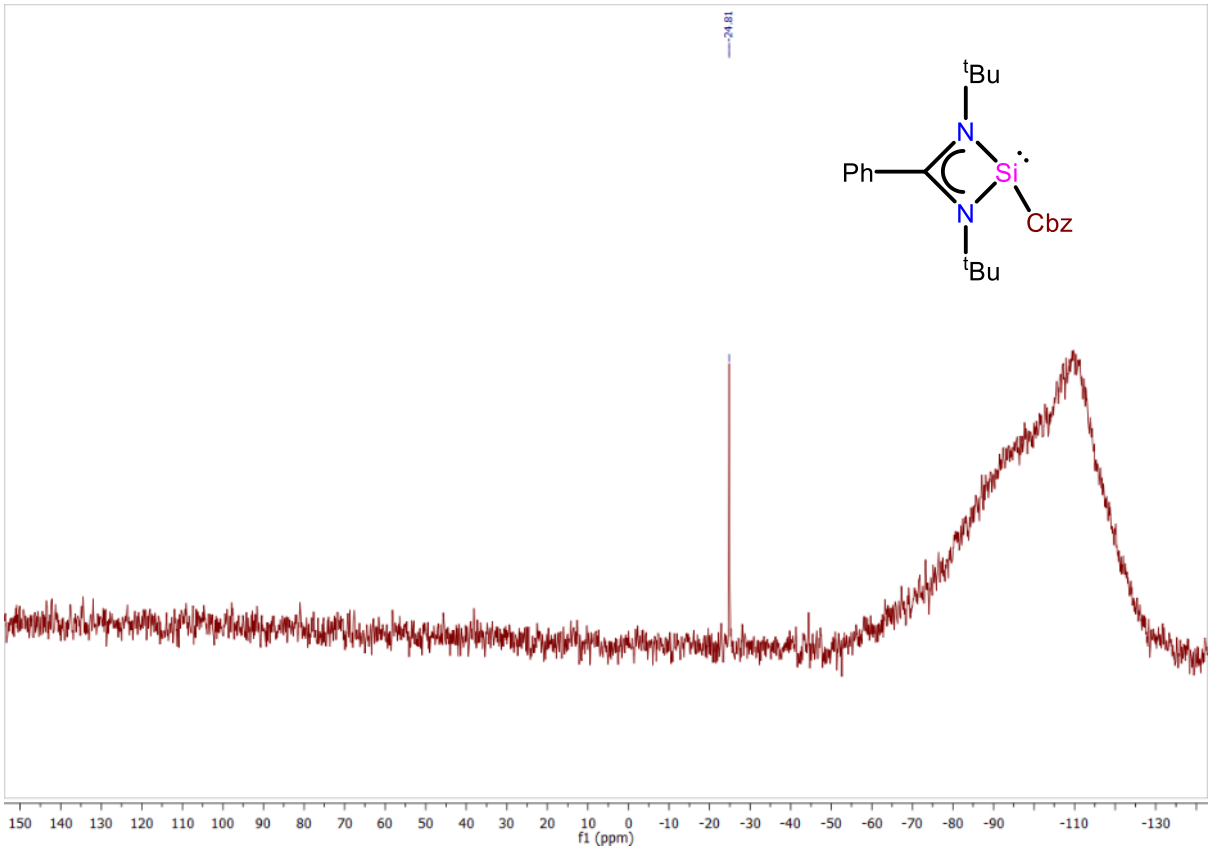

Figure 2C.A.3. ^{29}Si NMR spectrum of **2C.1** in C_6D_6.

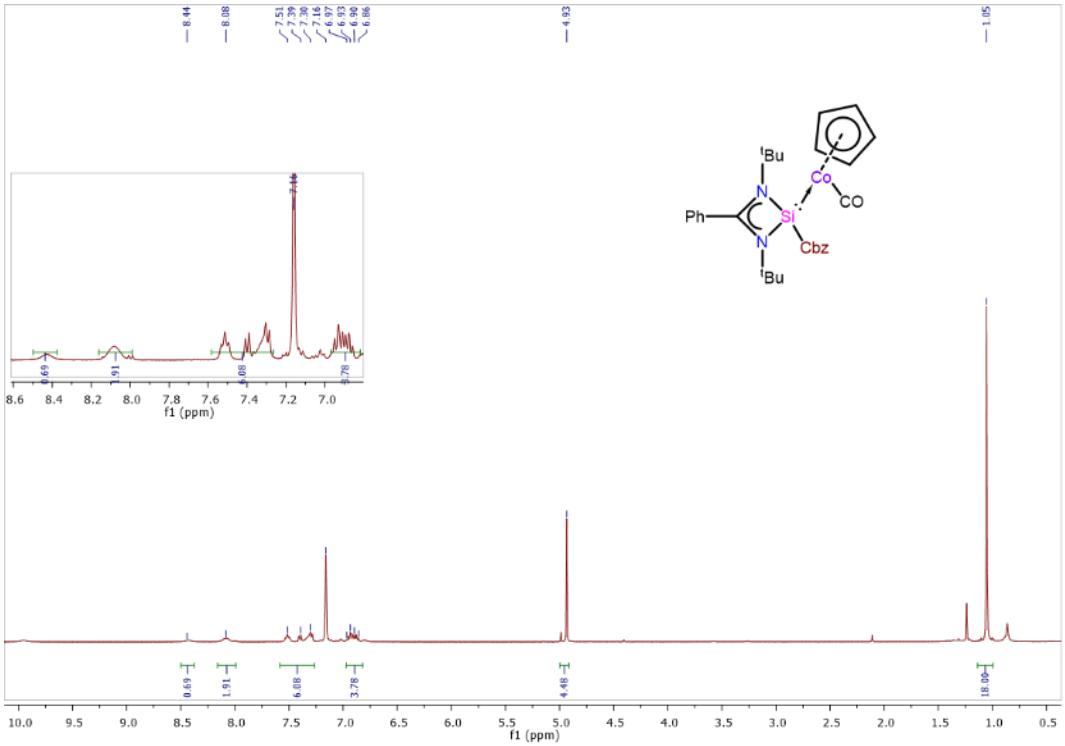

Figure 2C.A.4. ^{1}H NMR spectrum of complex **2C.2** in C_6D_6.

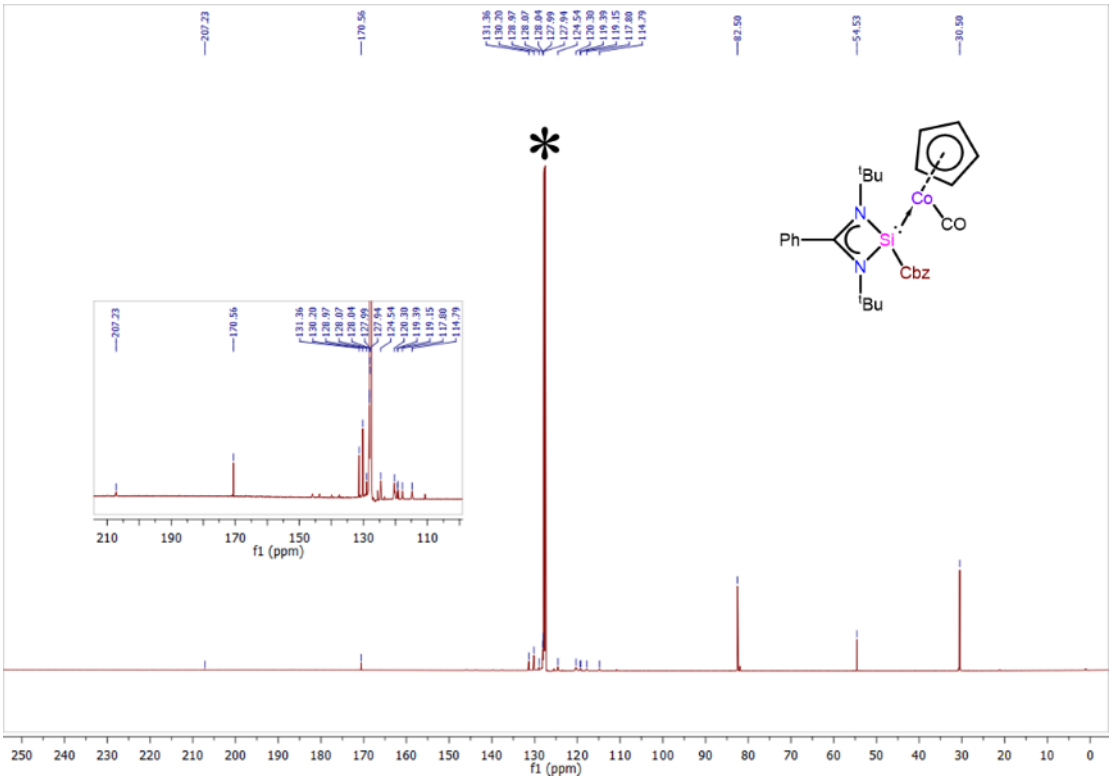

Figure 2C.A.5. ^{13}C NMR spectrum of complex **2C.2** in C_6D_6.

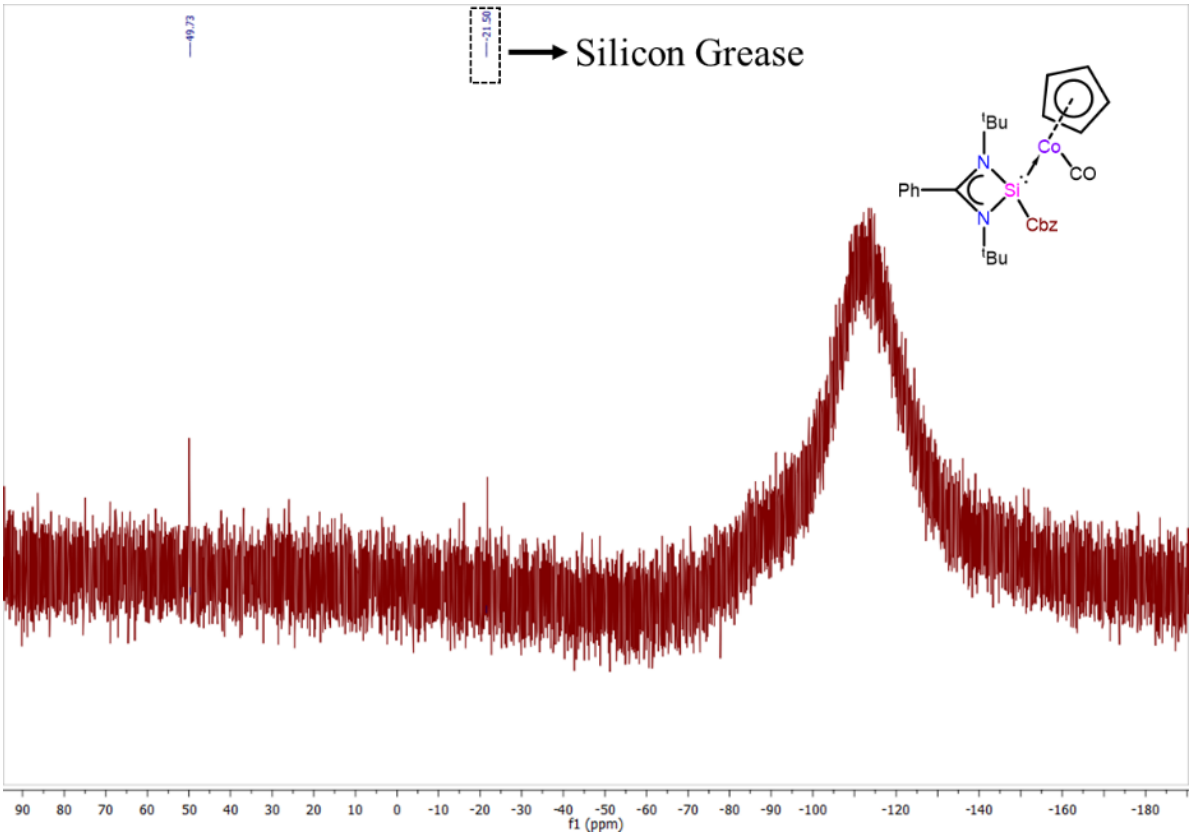

Figure 2C.A.6. ^{29}Si NMR spectrum of **2C.2** in C_6D_6.

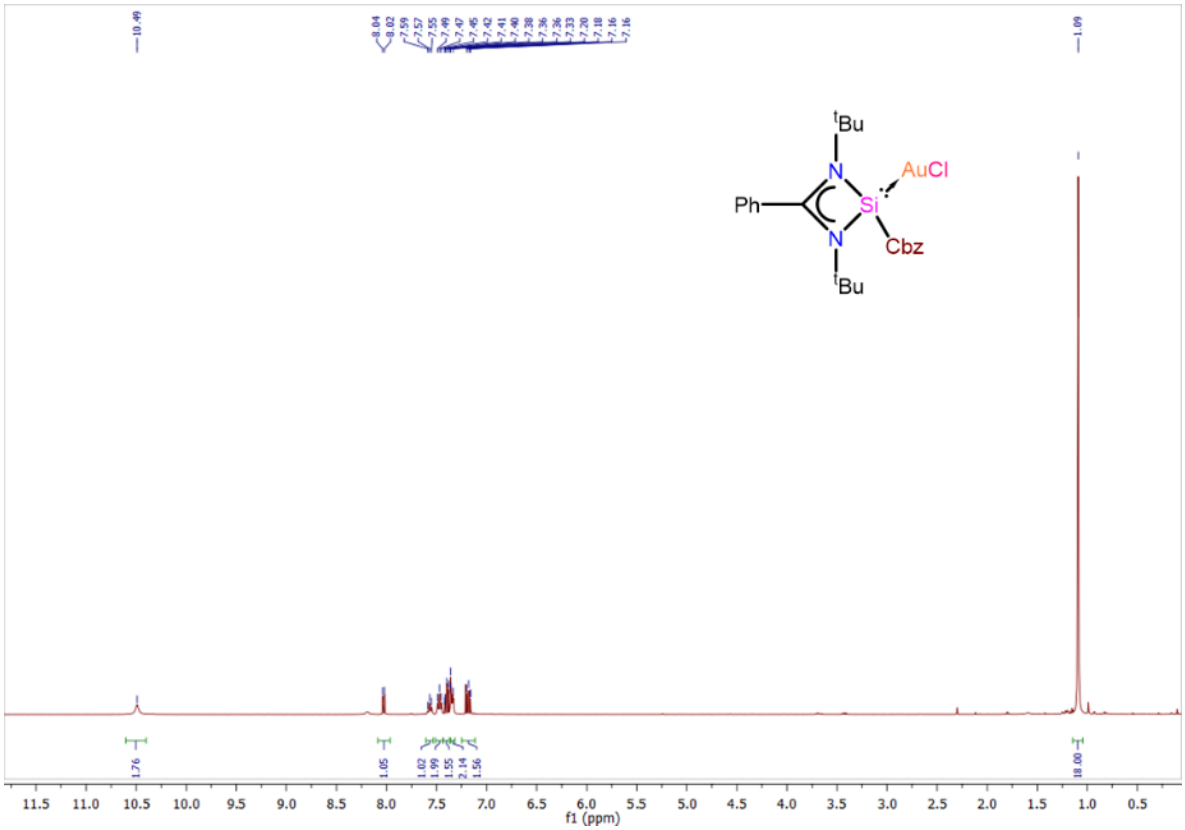

Figure 2C.A.7. ^{1}H NMR spectrum of **2C.3** in $CDCl_3$.

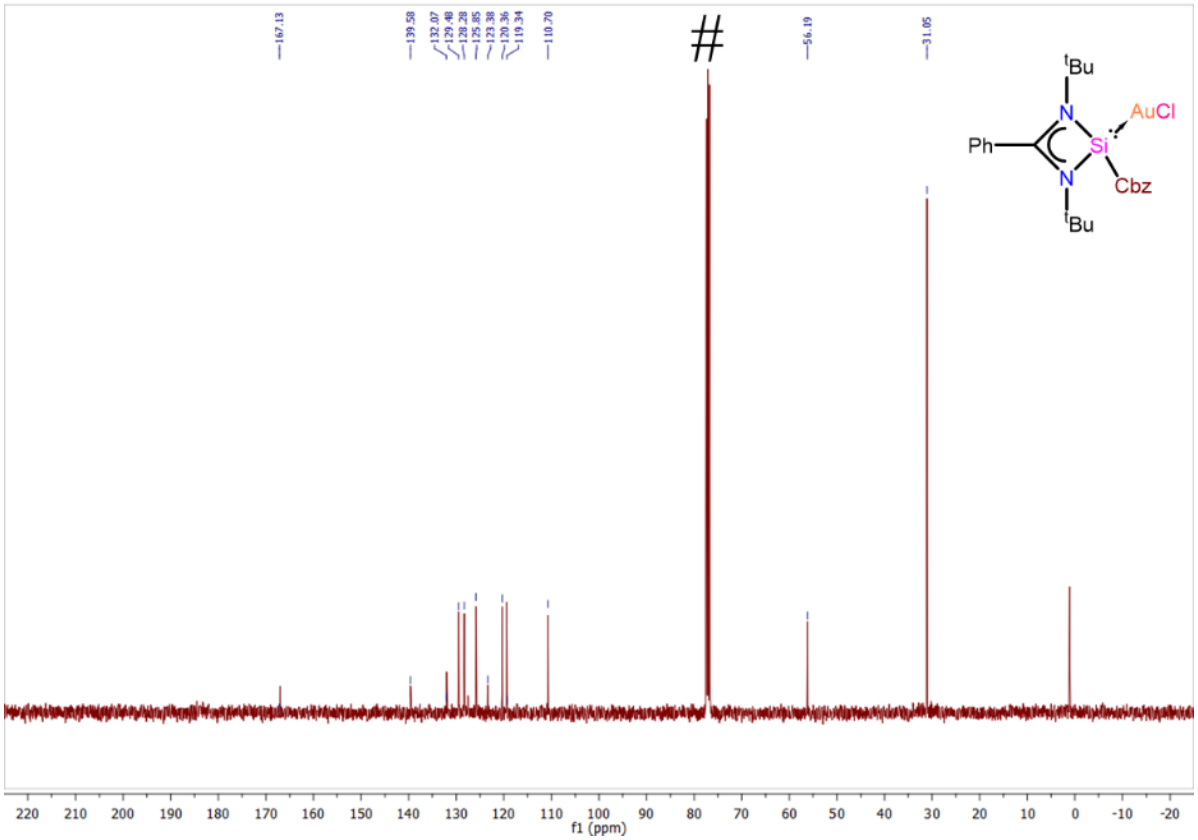

Figure 2C.A.8. ^{13}C NMR spectrum of **2C.3** in $CDCl_3$.

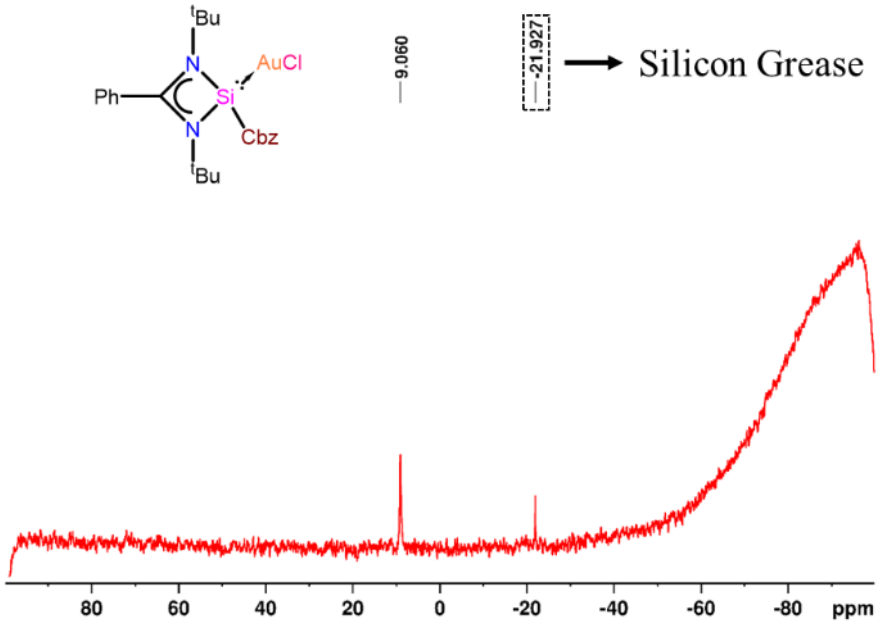

Figure 2C.A.9. ^{29}Si NMR spectrum of **2C.3** in $CDCl_3$.

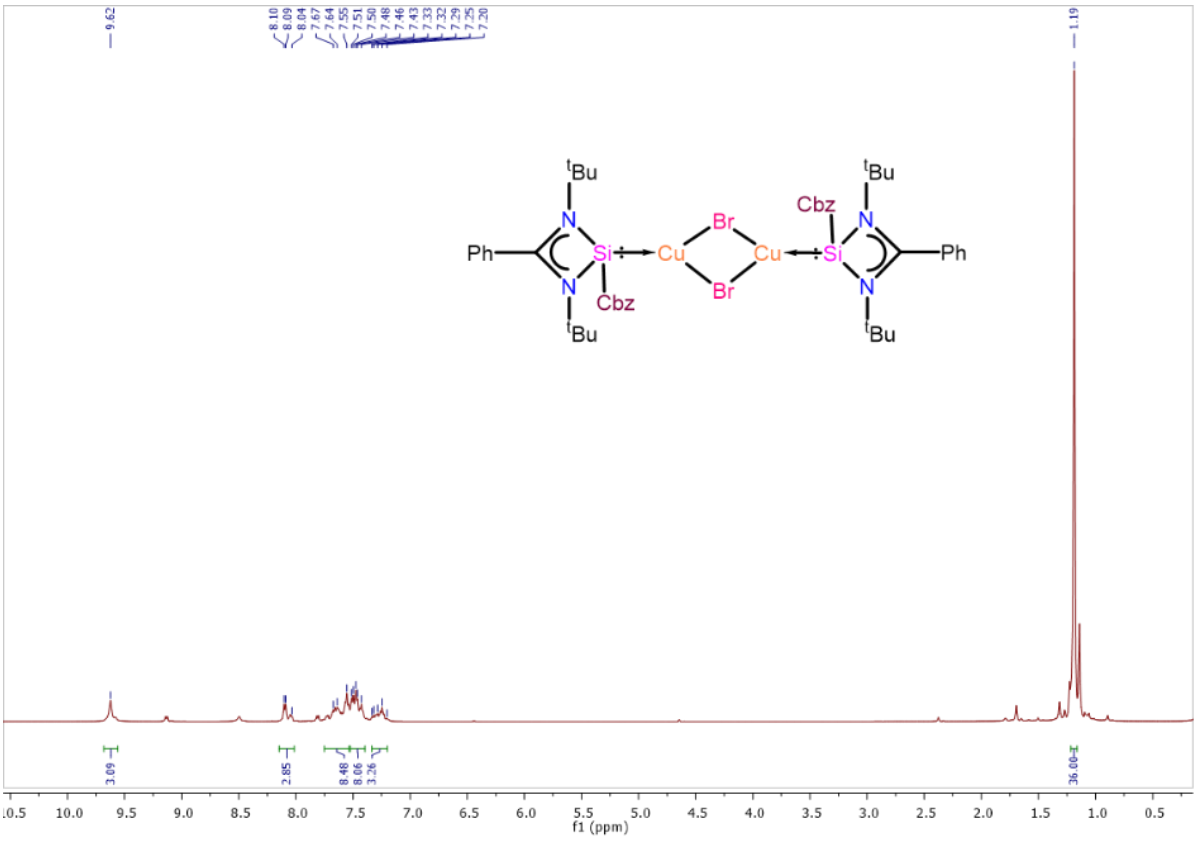

Figure 2C.A.10. ^{1}H NMR spectrum of **2C.4** in $CDCl_3$.

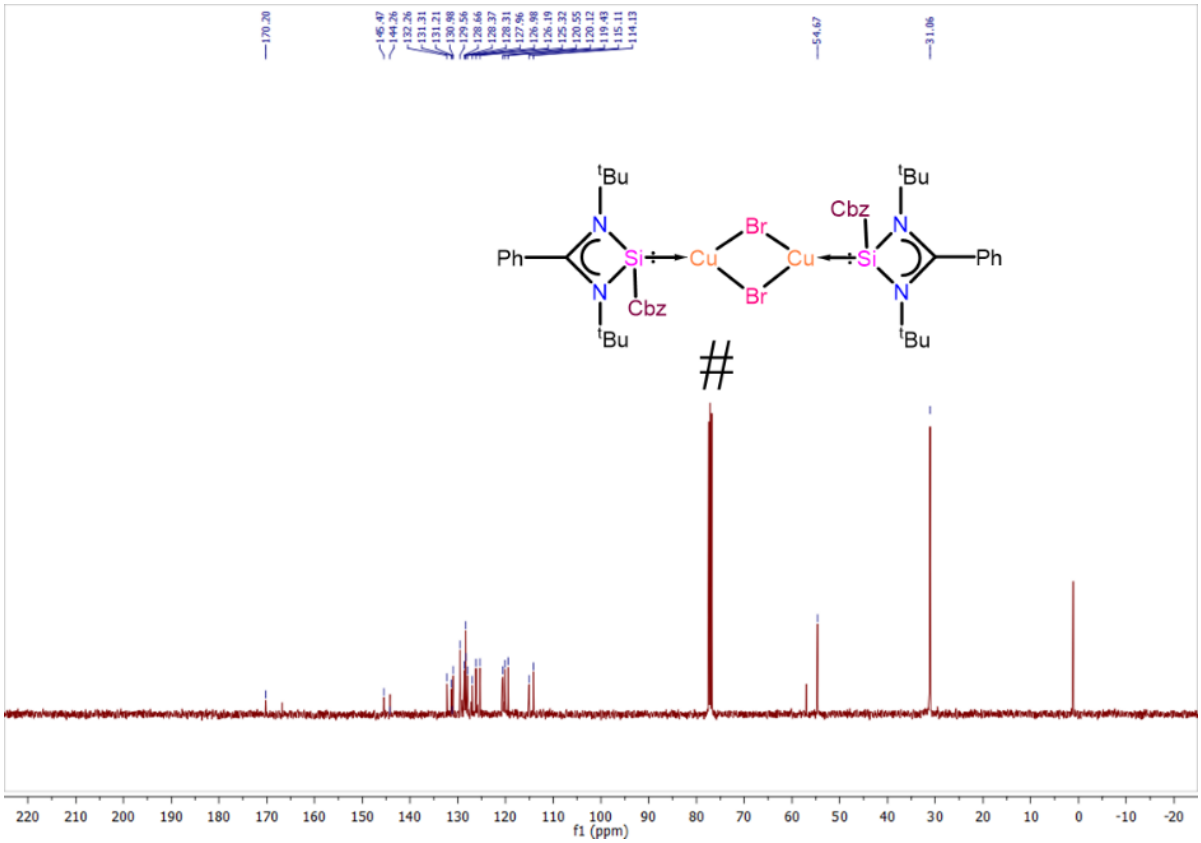

Figure 2C.A.11. ^{13}C NMR spectrum of **2C.4** in $CDCl_3$.

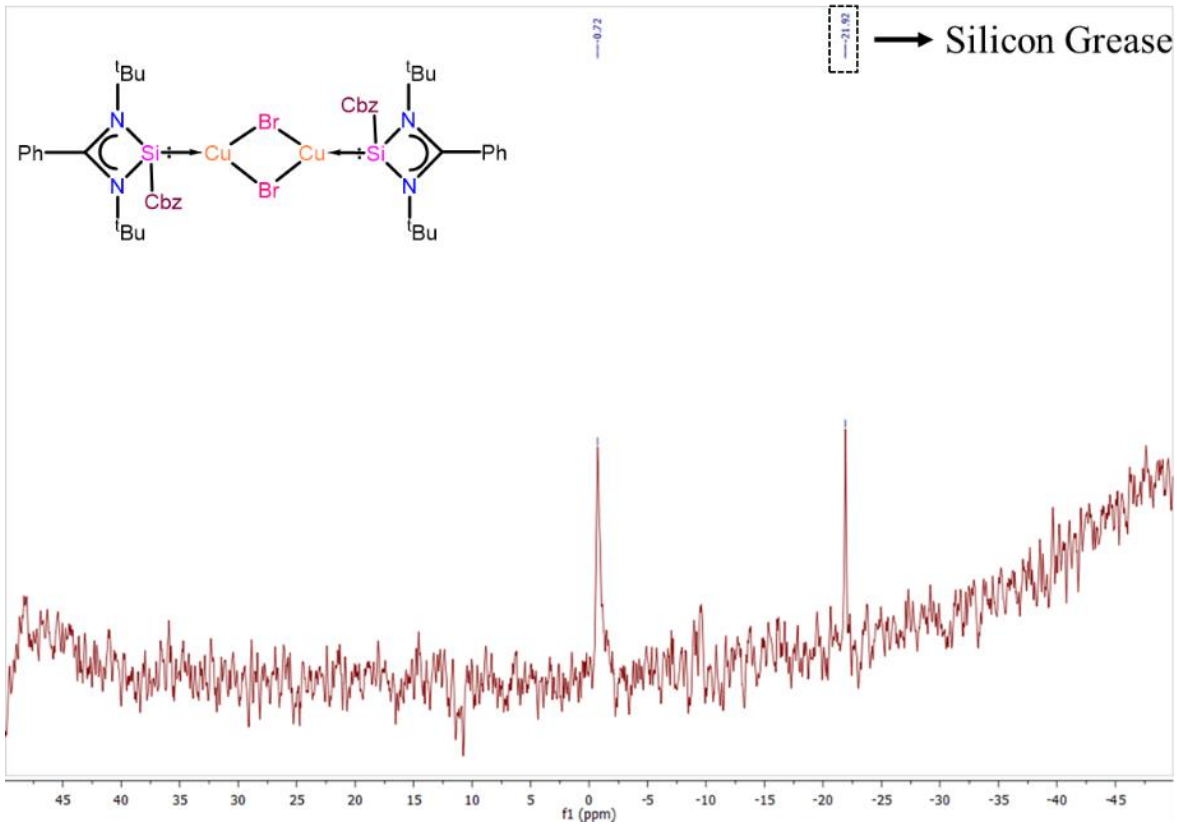

Figure 2C.A.12. ^{29}Si NMR spectrum of **2C.4** in $CDCl_3$.

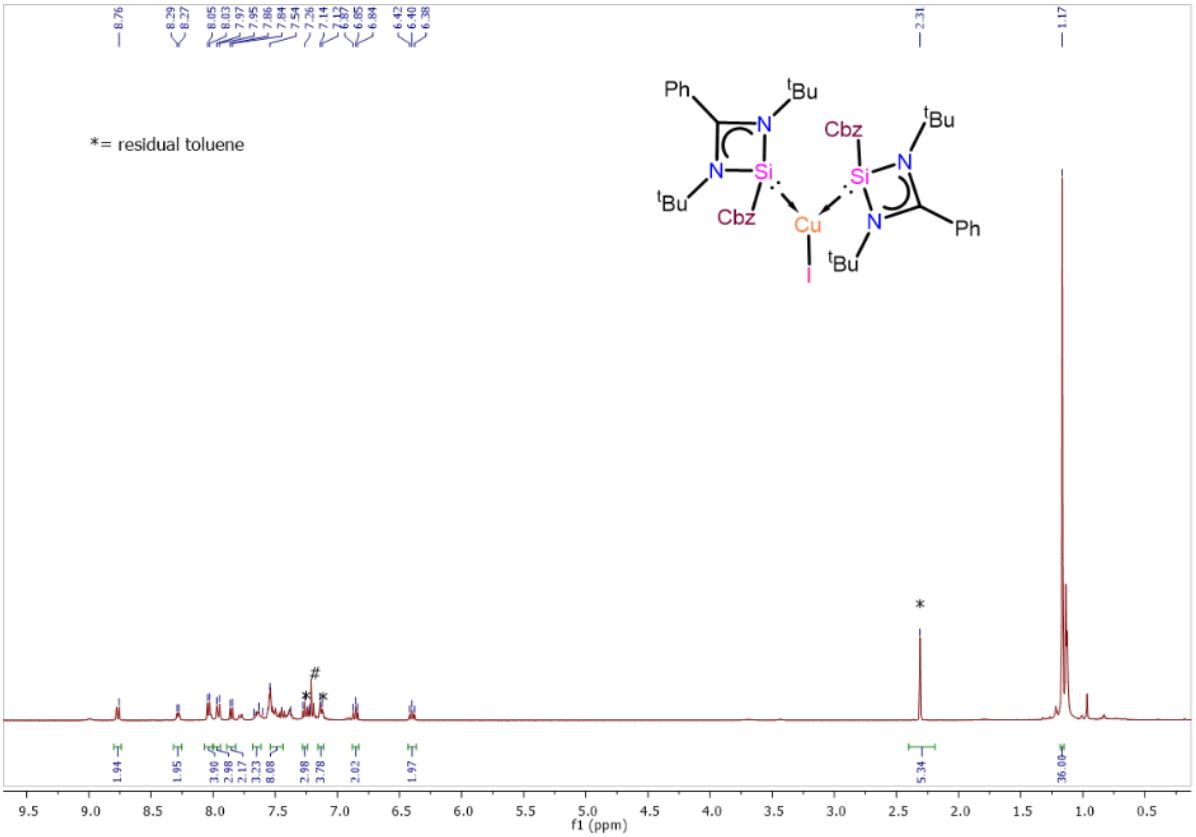

Figure 2C.A.13. ^{1}H NMR spectrum of **2C.5** in $CDCl_3$.

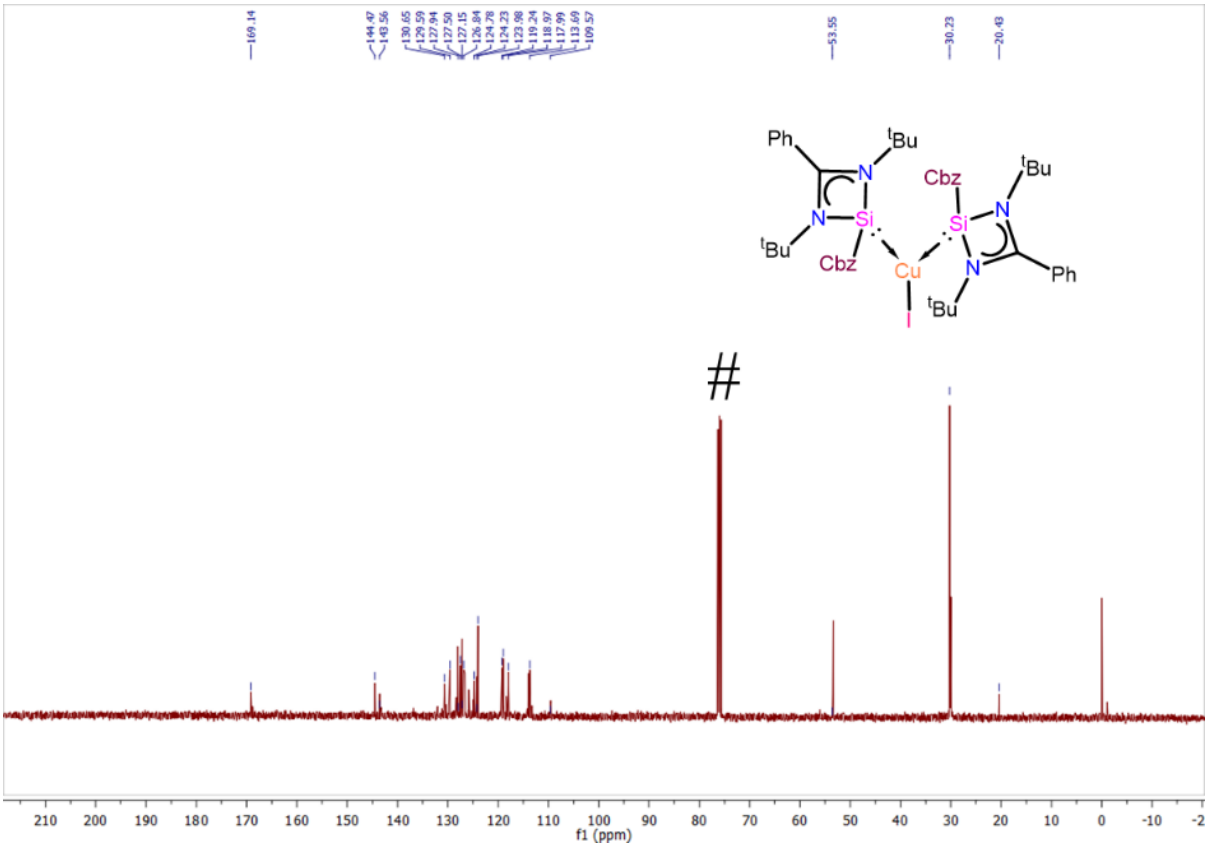

Figure 2C.A.14. ^{13}C NMR spectrum of **2C.5** in $CDCl_3$.

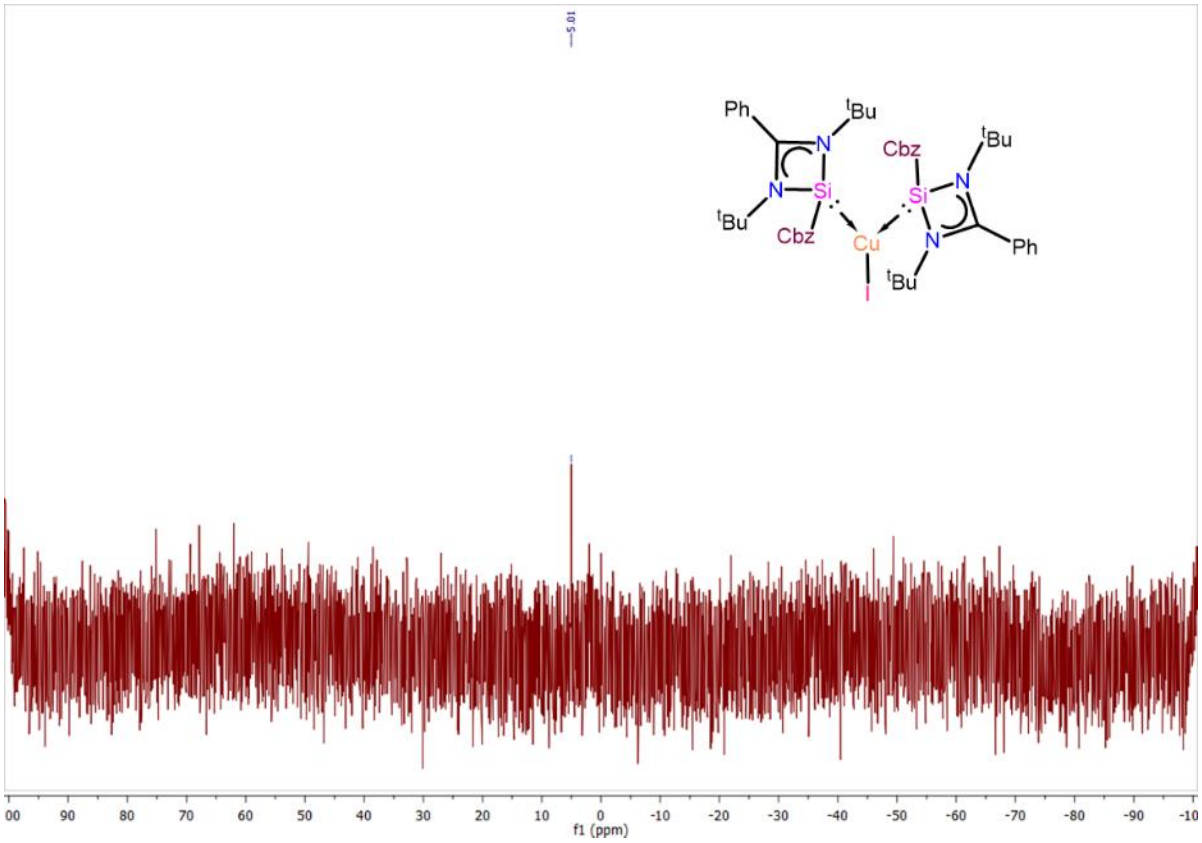

Figure 2C.A.15. ^{29}Si NMR spectrum of **2C.5** in $CDCl_3$.

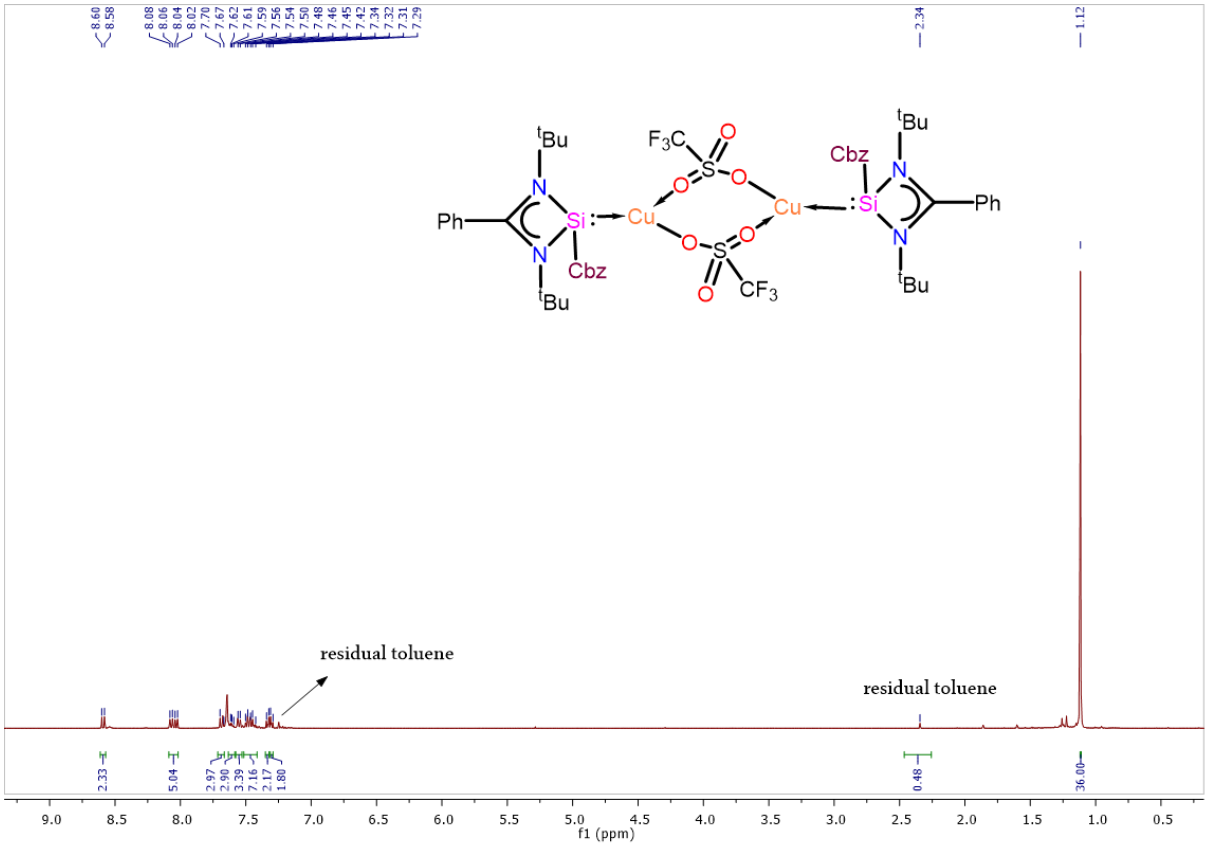

Figure 2C.A.16. ^{1}H NMR spectrum of **2C.6** in $CDCl_3$.

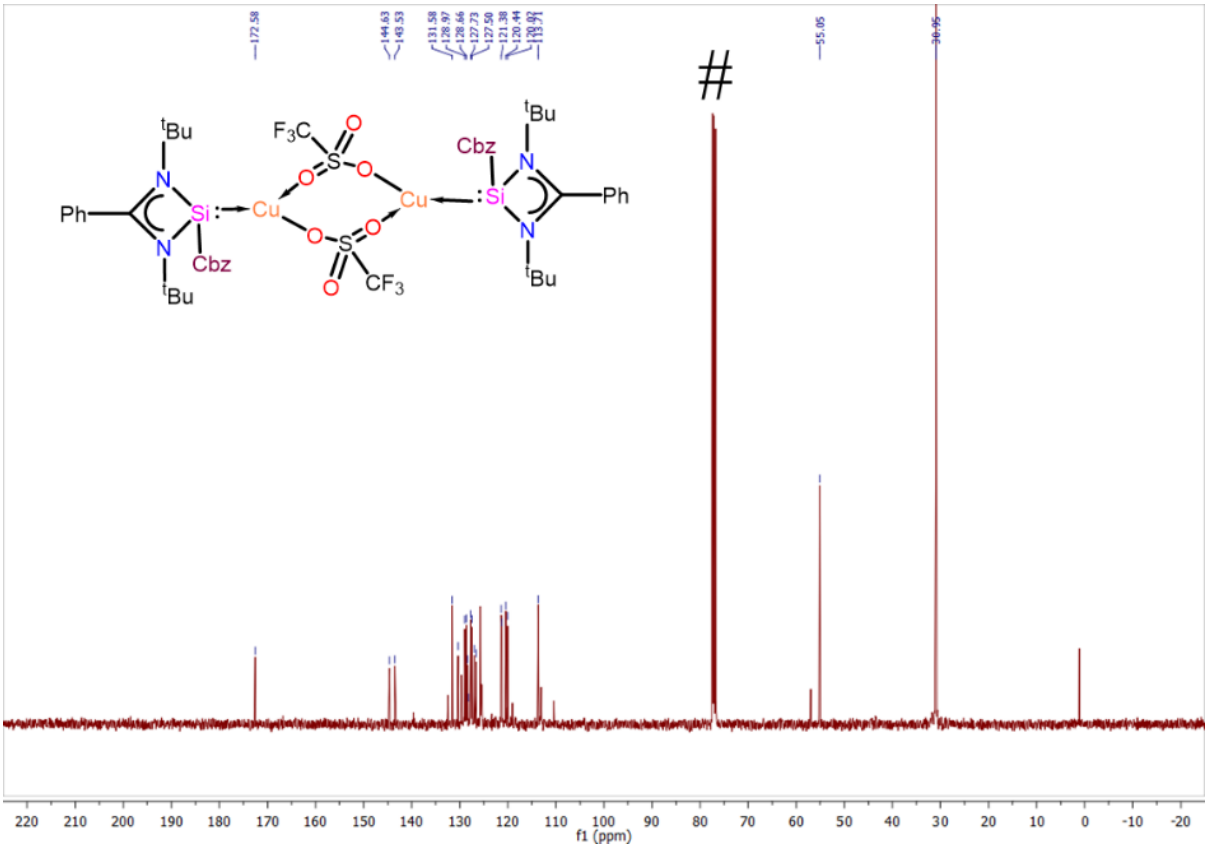

Figure 2C.A.17. ^{13}C NMR spectrum of **2C.6** in $CDCl_3$.

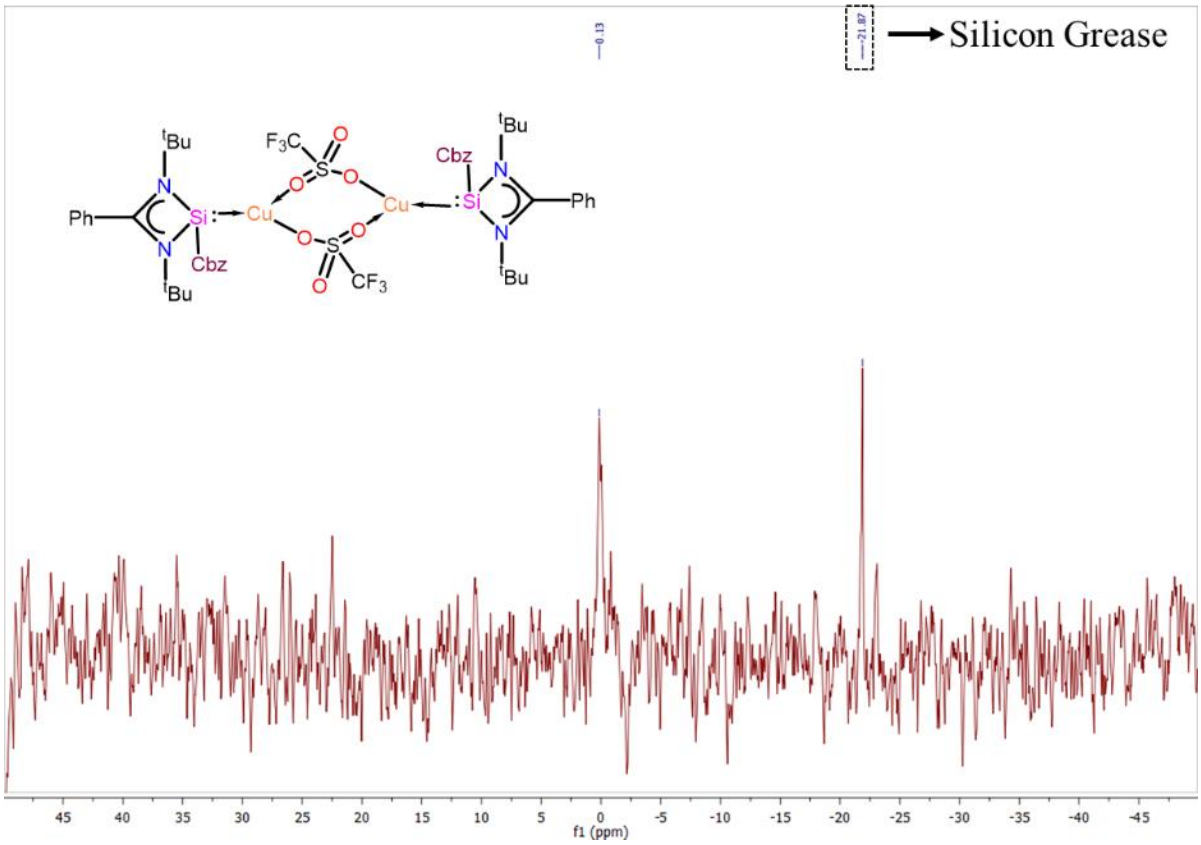

Figure 2C.A.18. ^{29}Si NMR spectrum of **2C.6** in $CDCl_3$.

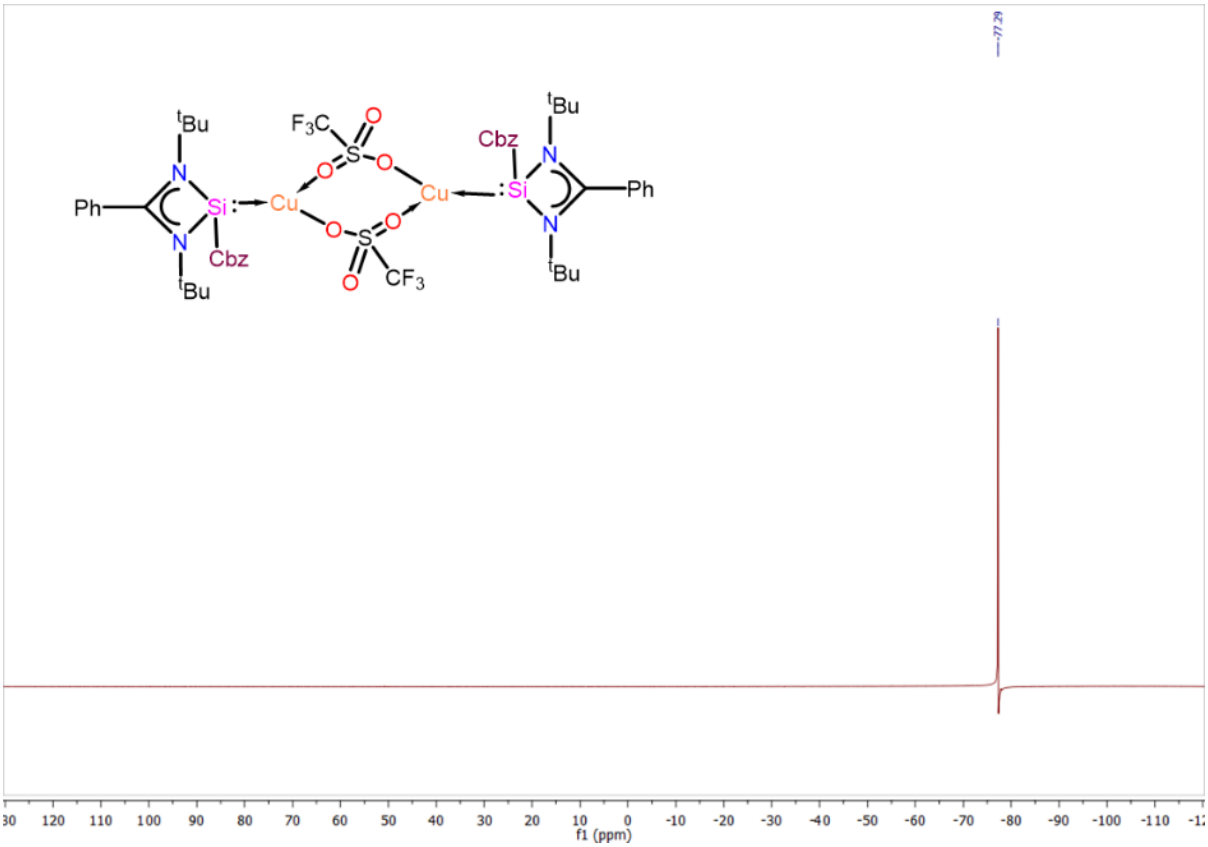

Figure 2C.A.19. ^{19}F NMR spectrum of **2C.6** in $CDCl_3$.

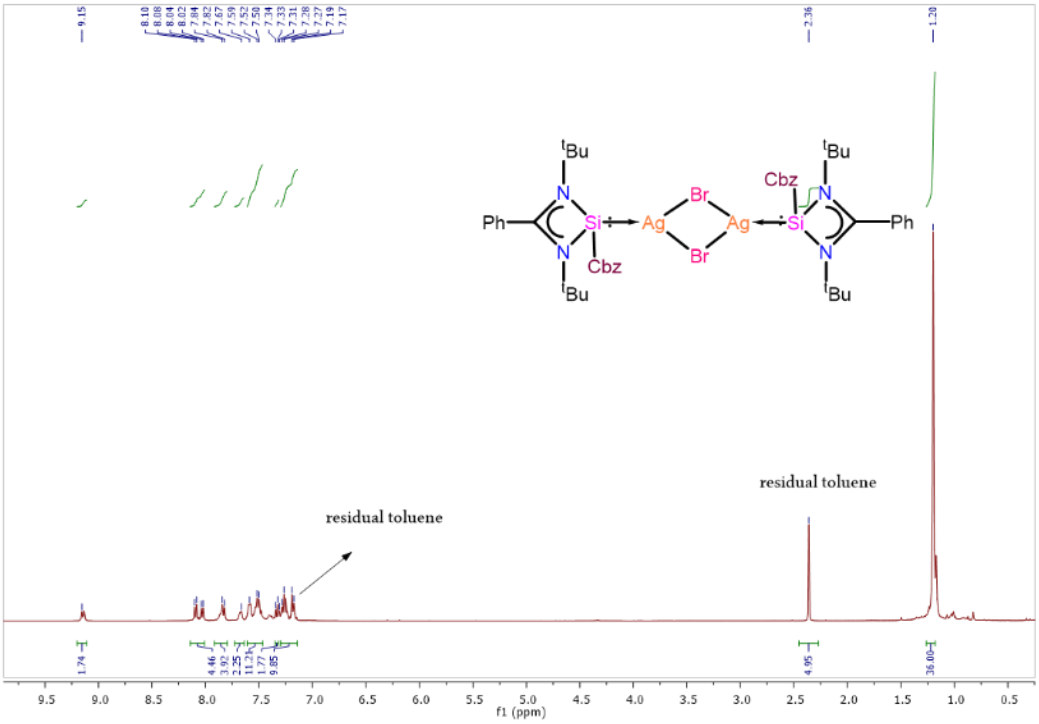

Figure 2C.A.20. ^{1}H NMR spectrum of **2C.7** in $CDCl_3$.

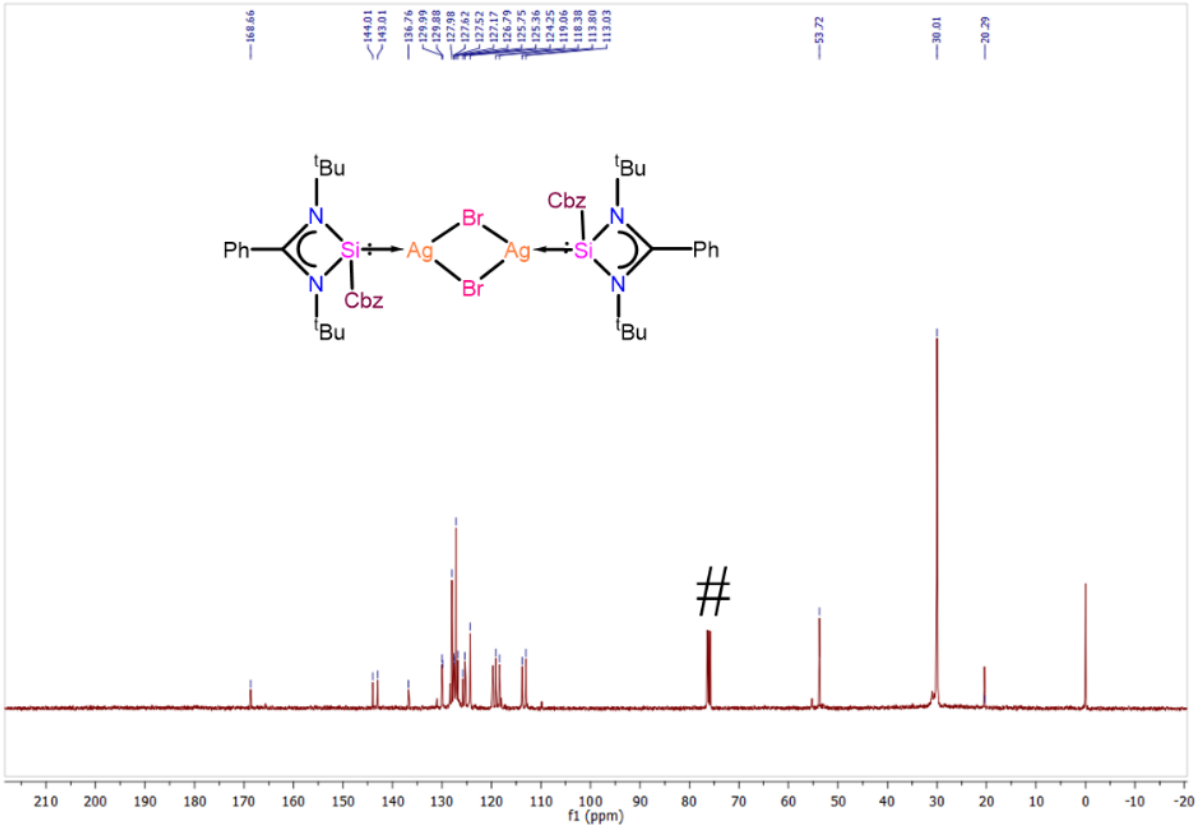

Figure 2C.A.21. ^{1}H NMR spectrum of **2C.7** in $CDCl_3$.

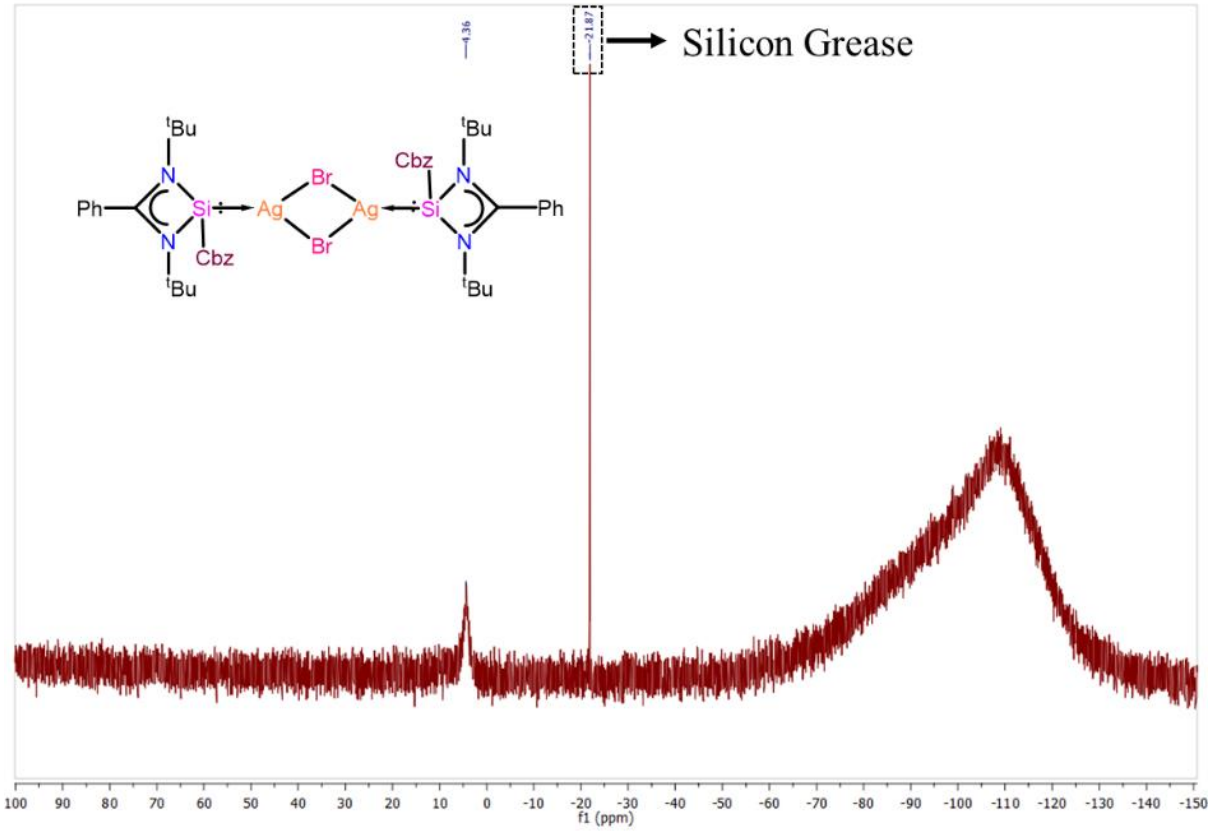

Figure 2C.A.22. ^{29}Si NMR spectrum of **2C.7** in $CDCl_3$.

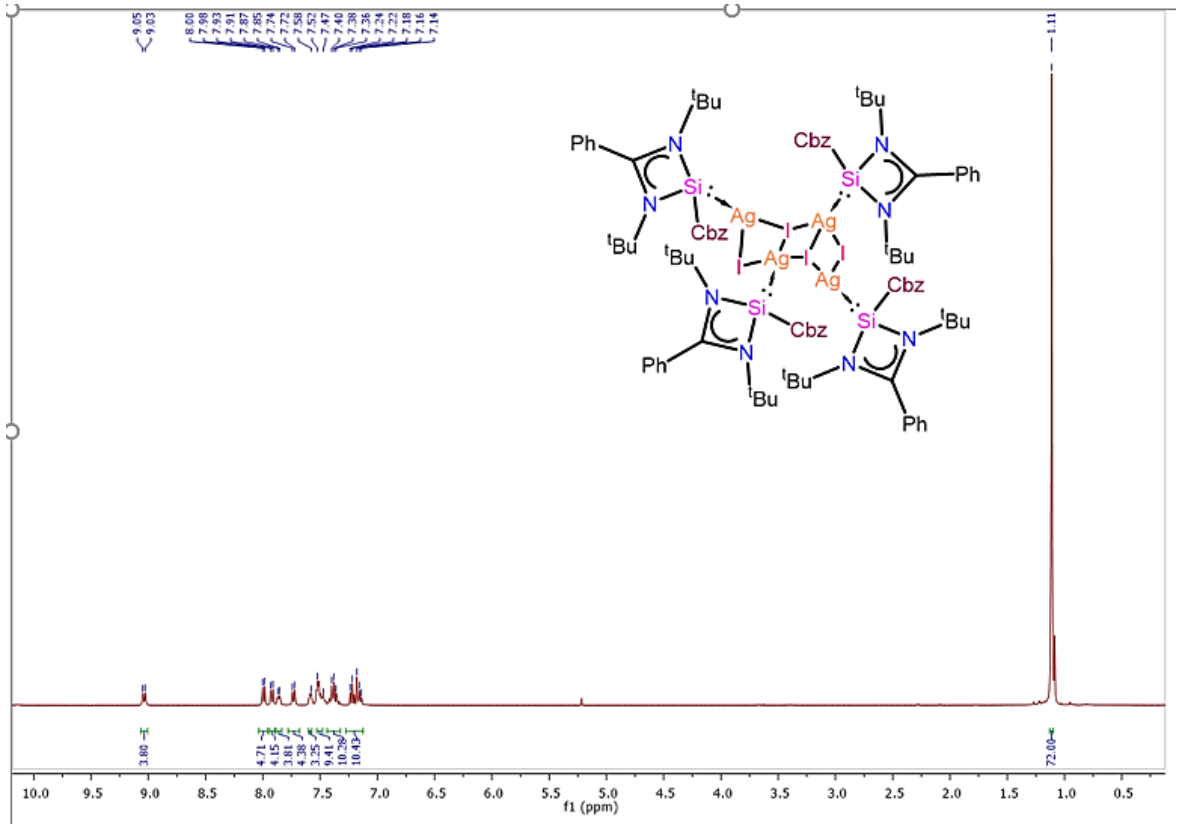

Figure 2C.A.23. ^{1}H NMR spectrum of **2C.8** in $CDCl_3$.

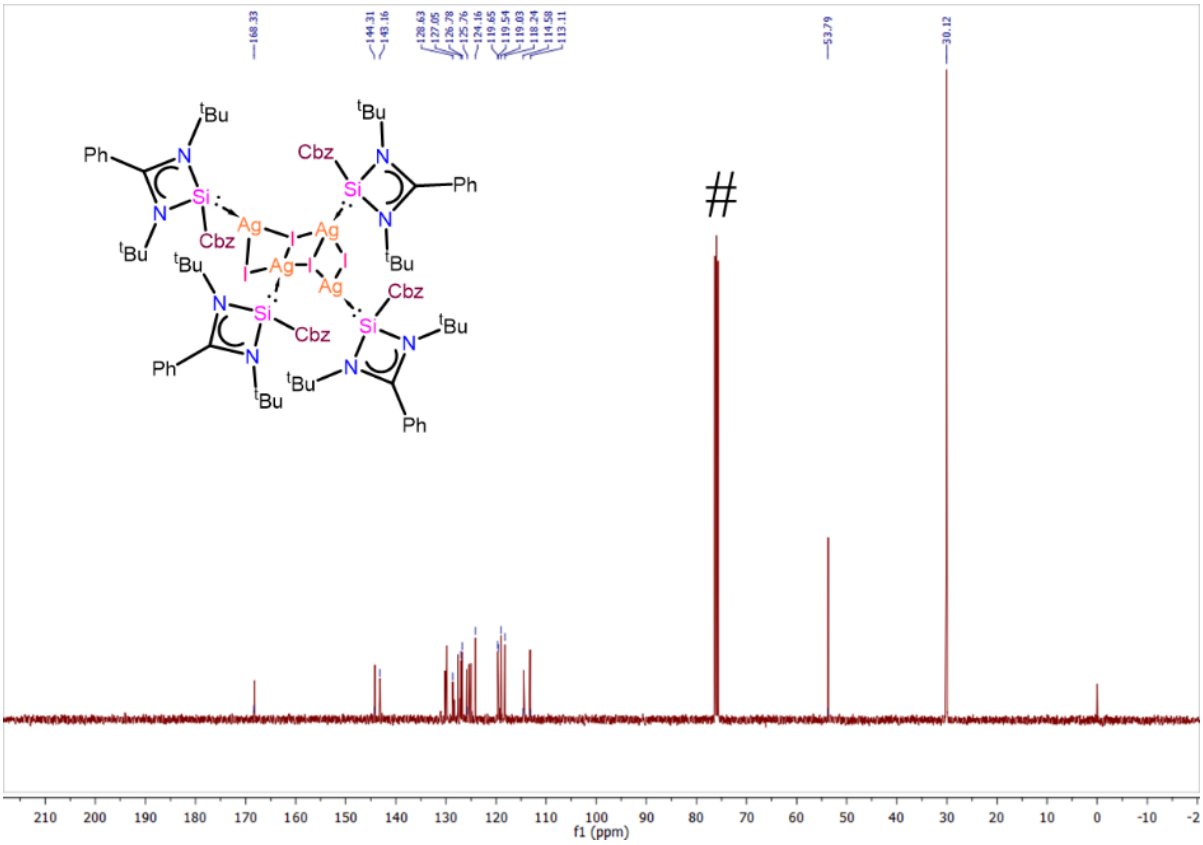

Figure 2C.A.24. ^{13}C NMR spectrum of **2C.8** in $CDCl_3$.

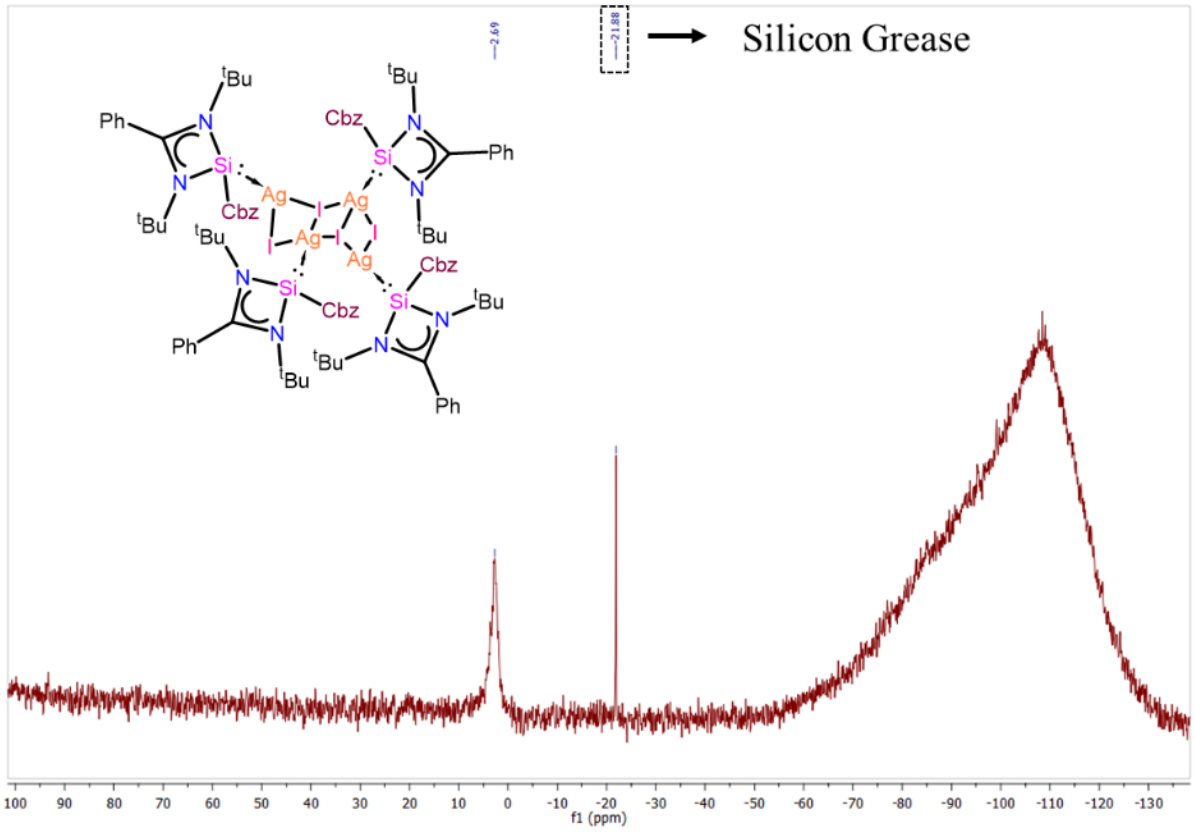

Figure 2C.A.25. ^{29}Si NMR spectrum of **2C.8** in $CDCl_3$.

2D.A.1 NMR spectra of complexes 2D.2-2D.16.

(*: residual solvent peak = Toluene)

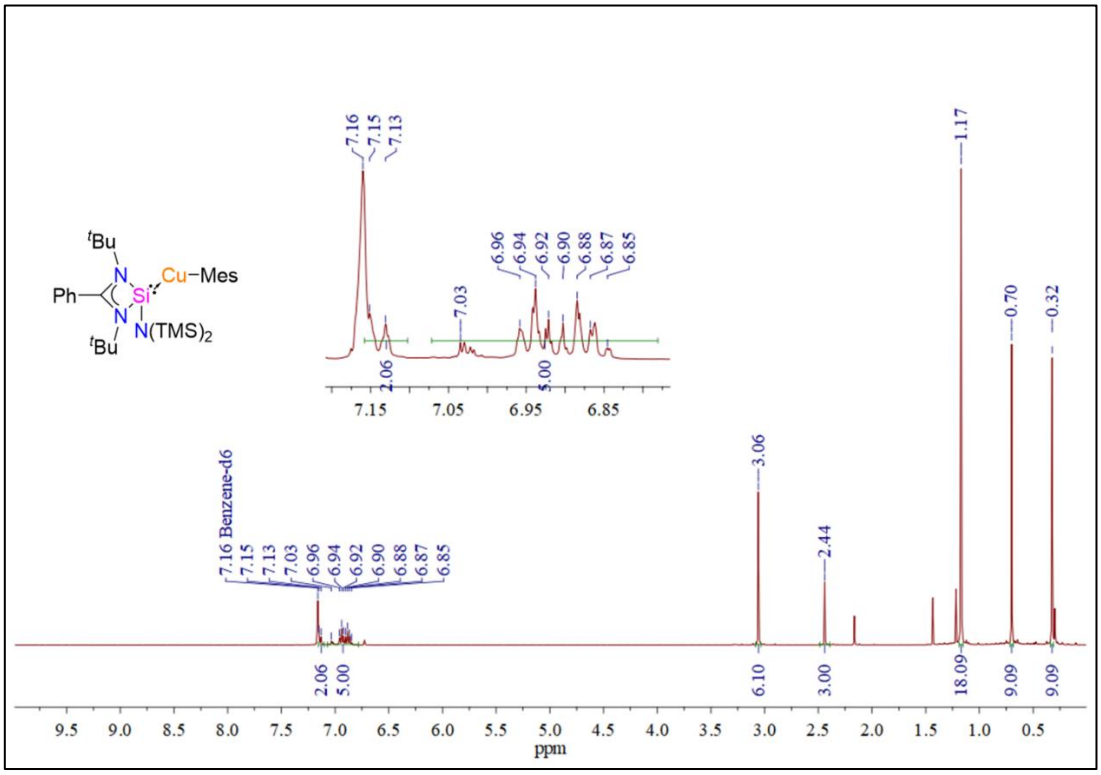

Figure 2D.A.1. ^{1}H NMR spectrum of complex **2D.2** in C_6D_6.

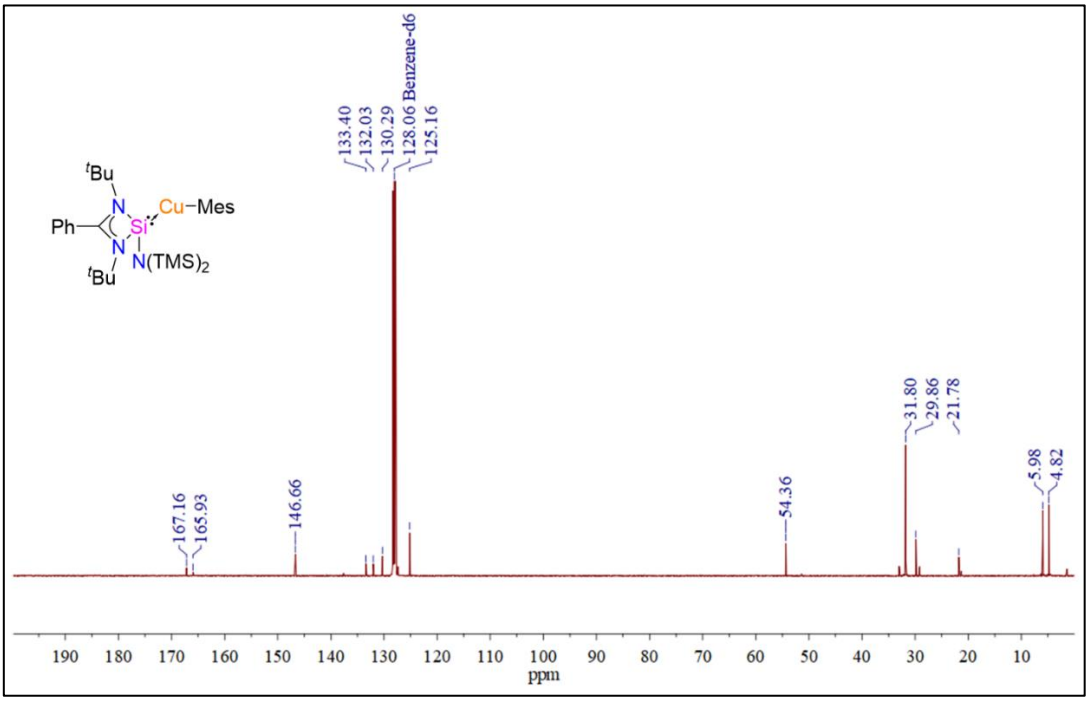

Figure 2D.A.2. $^{13}C\{^{1}H\}$ NMR spectrum of complex **2D.2** in C_6D_6.

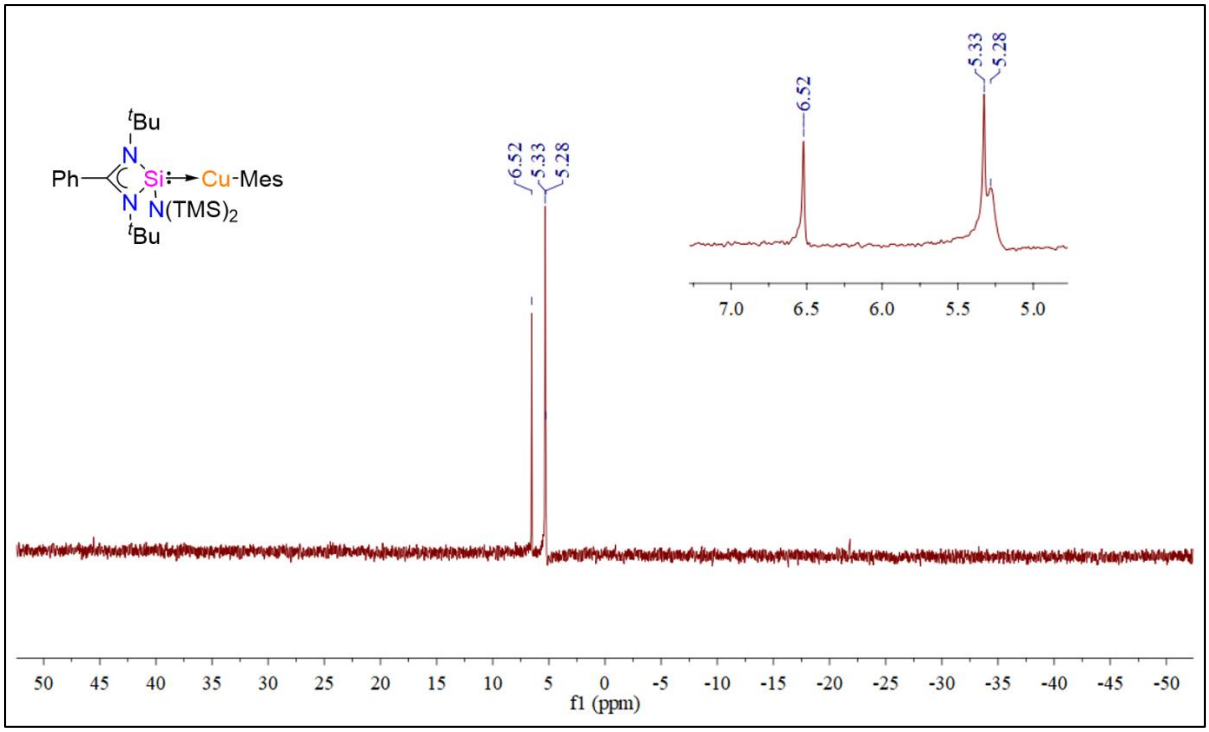

Figure 2D.A.3. $^{29}Si\{^{1}H\}$ NMR spectrum of complex **2D.2** in C_6D_6.

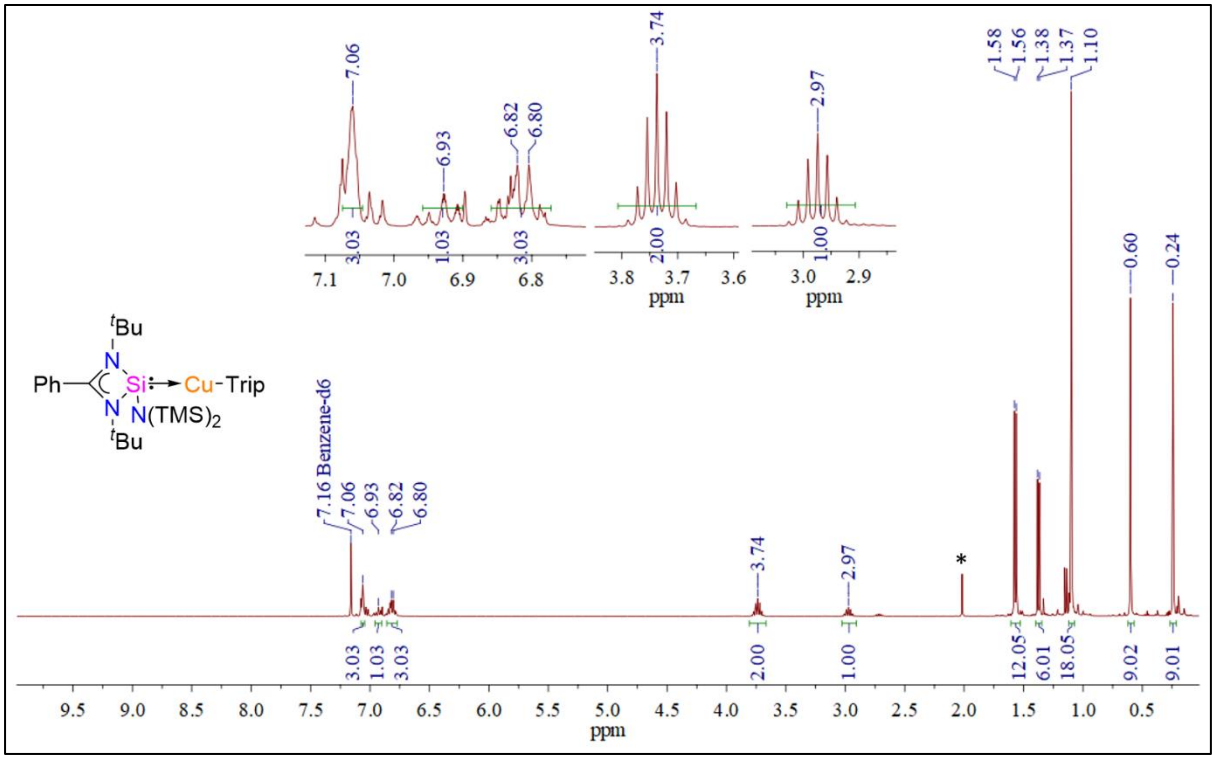

Figure 2D.A.4. ^{1}H NMR spectrum of complex **2D.3** in C_6D_6.

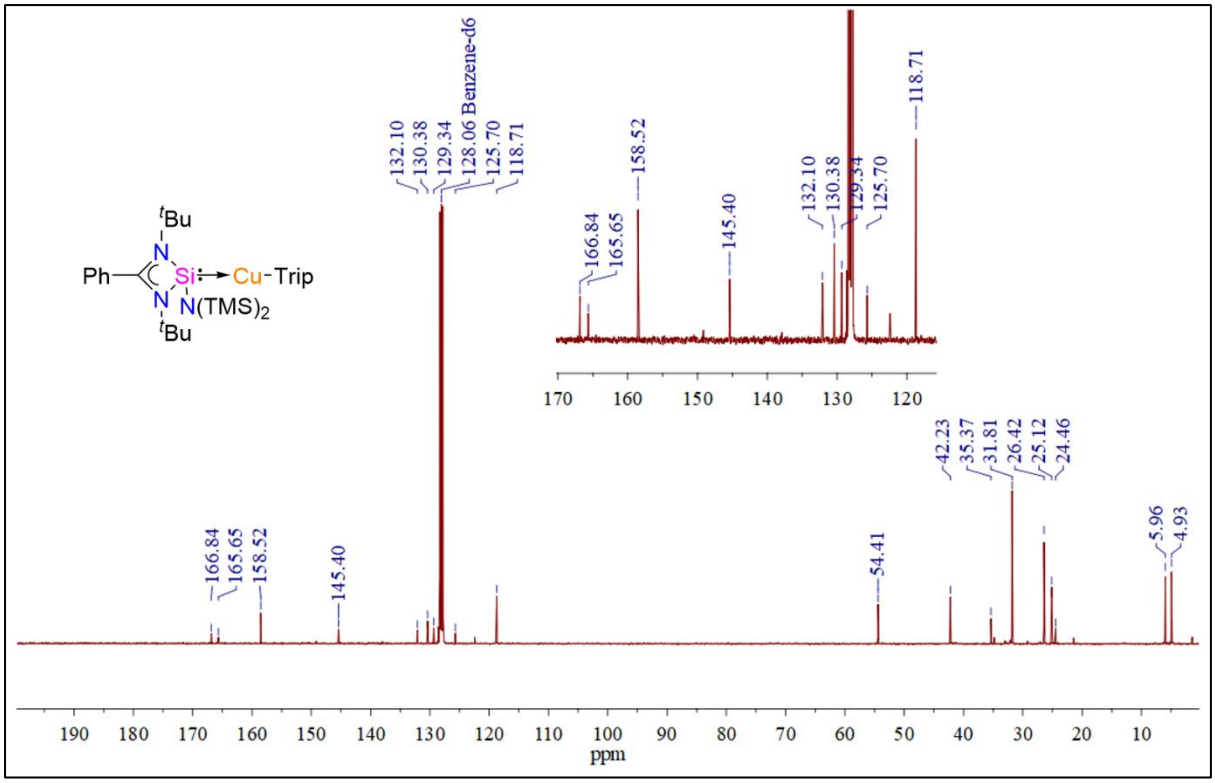

Figure 2D.A.5. $^{13}C\{^{1}H\}$ NMR spectrum of complex **2D.3** in C_6D_6.

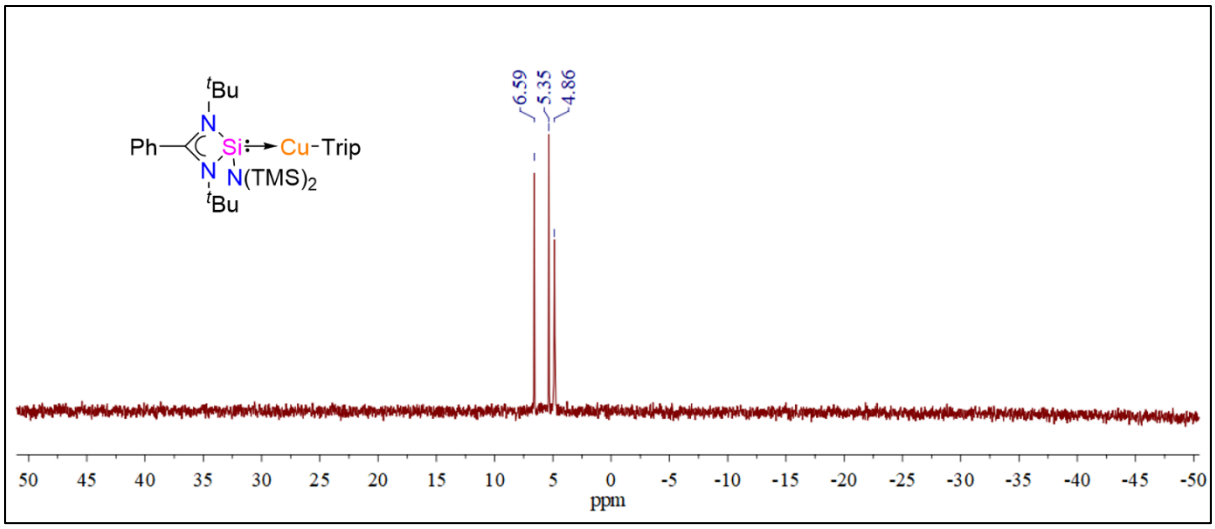

Figure 2D.A.6. $^{29}Si\{^{1}H\}$ NMR spectrum of complex **2D.3** in C_6D_6.

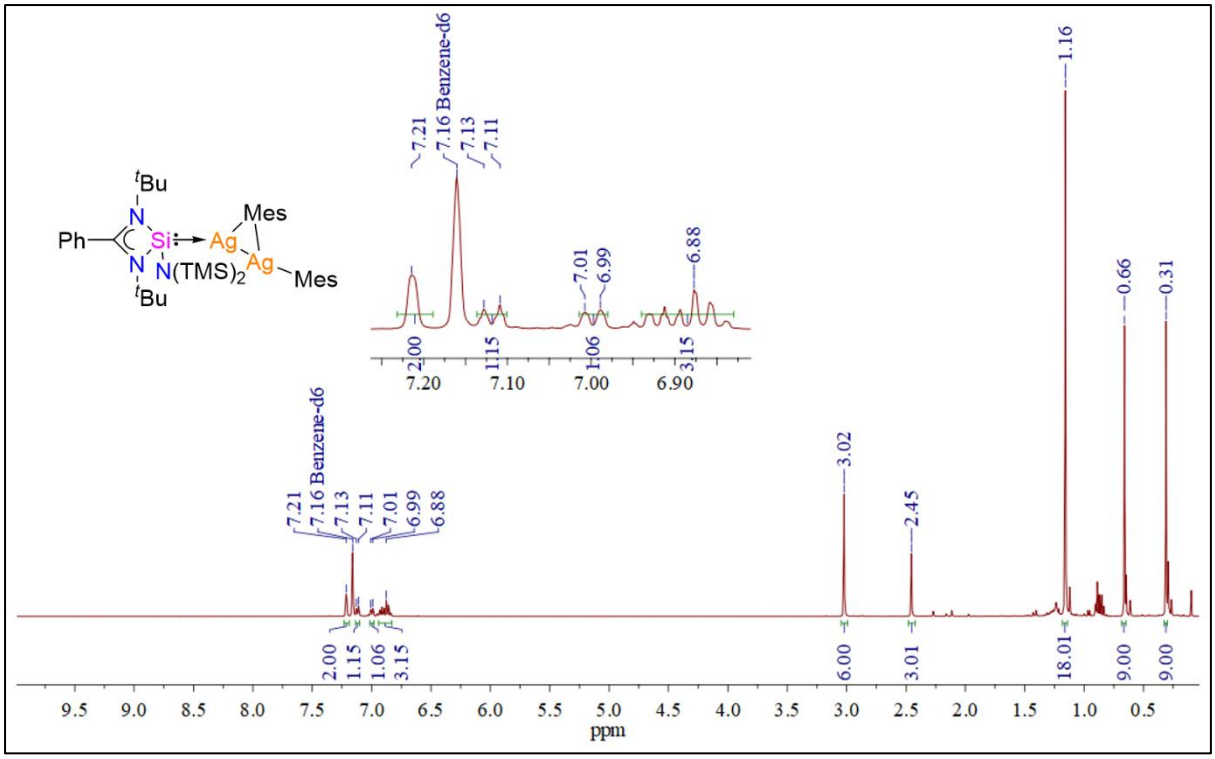

Figure 2D.A.7. ^{1}H NMR spectrum of complex **2D.4** in C_6D_6.

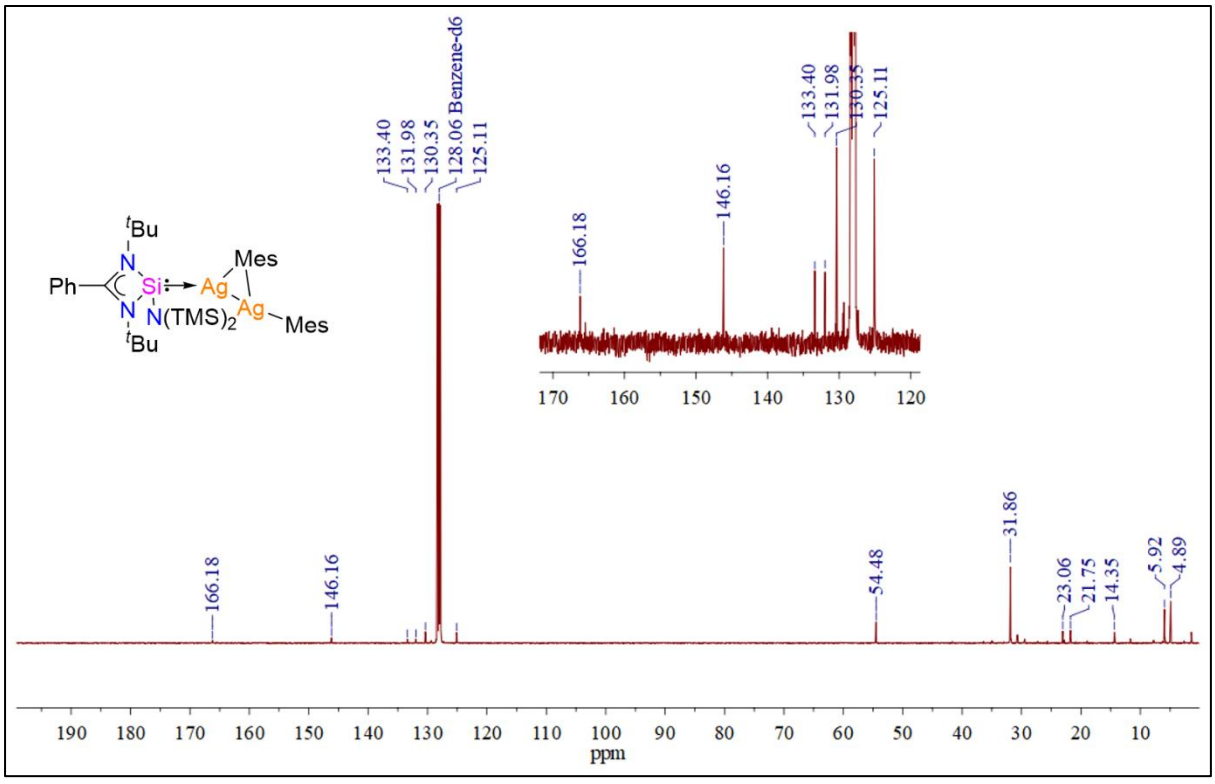

Figure 2D.A.8. ^{13}C{^{1}H} NMR spectrum of complex **2D.4** in C_6D_6.

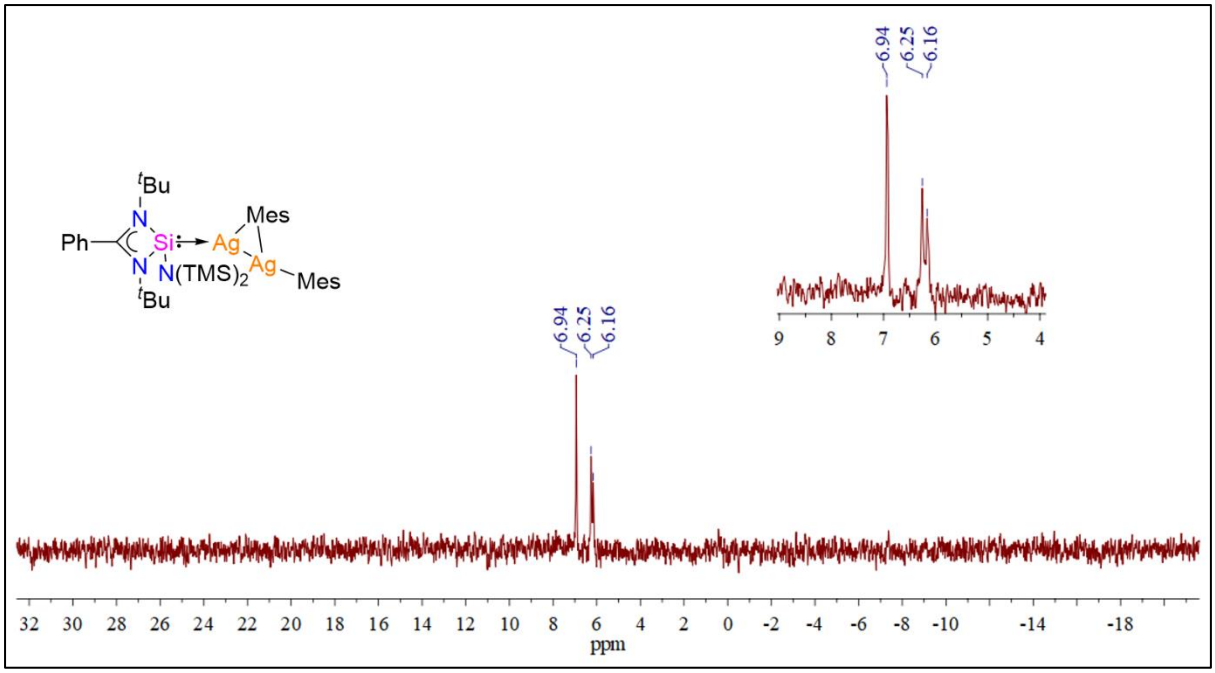

Figure 2D.A.9. $^{29}Si\{^{1}H\}$ NMR spectrum of complex **2D.4** in C_6D_6.

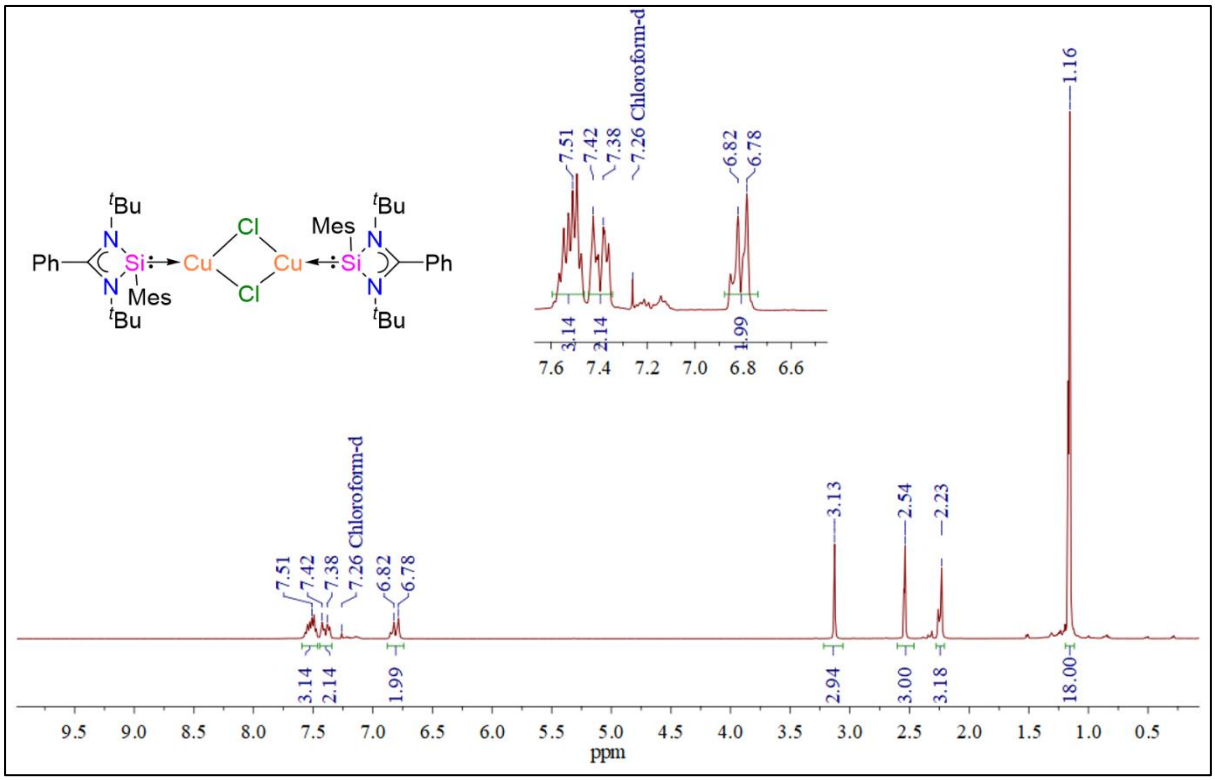

Figure 2D.A.10. ^{1}H NMR spectrum of complex **2D.5** in $CDCl_3$.

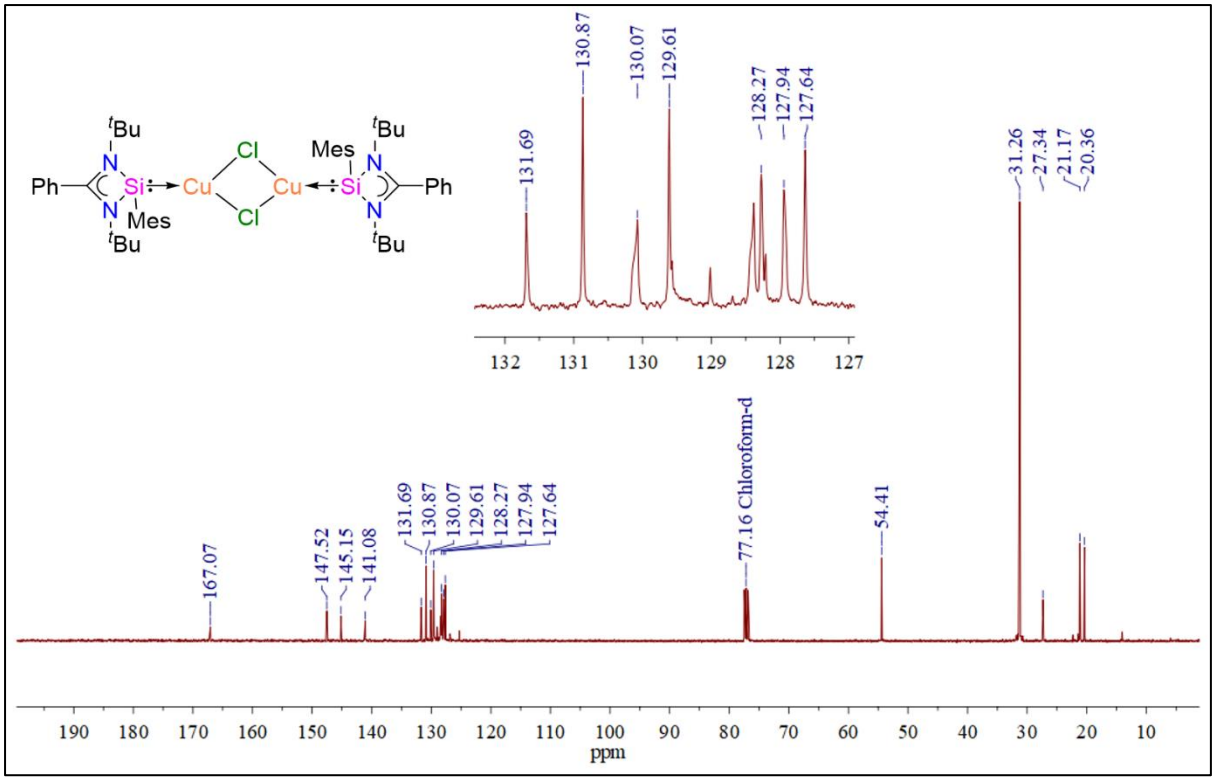

Figure 2D.A.11. $^{13}C\{^{1}H\}$ NMR spectrum of complex **2D.5** in $CDCl_3$.

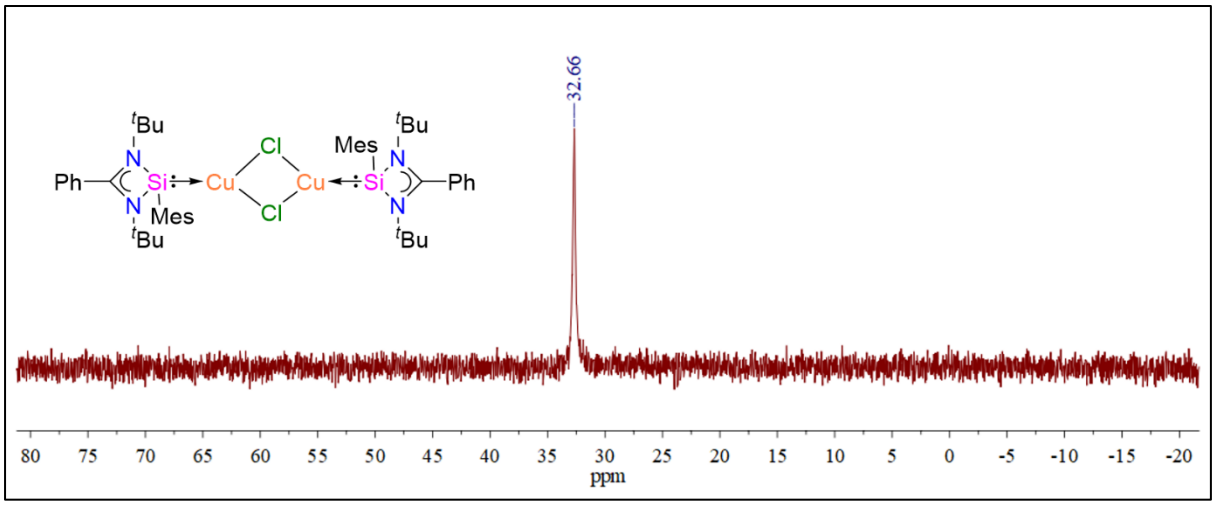

Figure 2D.A.12. $^{29}Si\{^{1}H\}$ NMR spectrum of complex **2D.5** in $CDCl_3$.

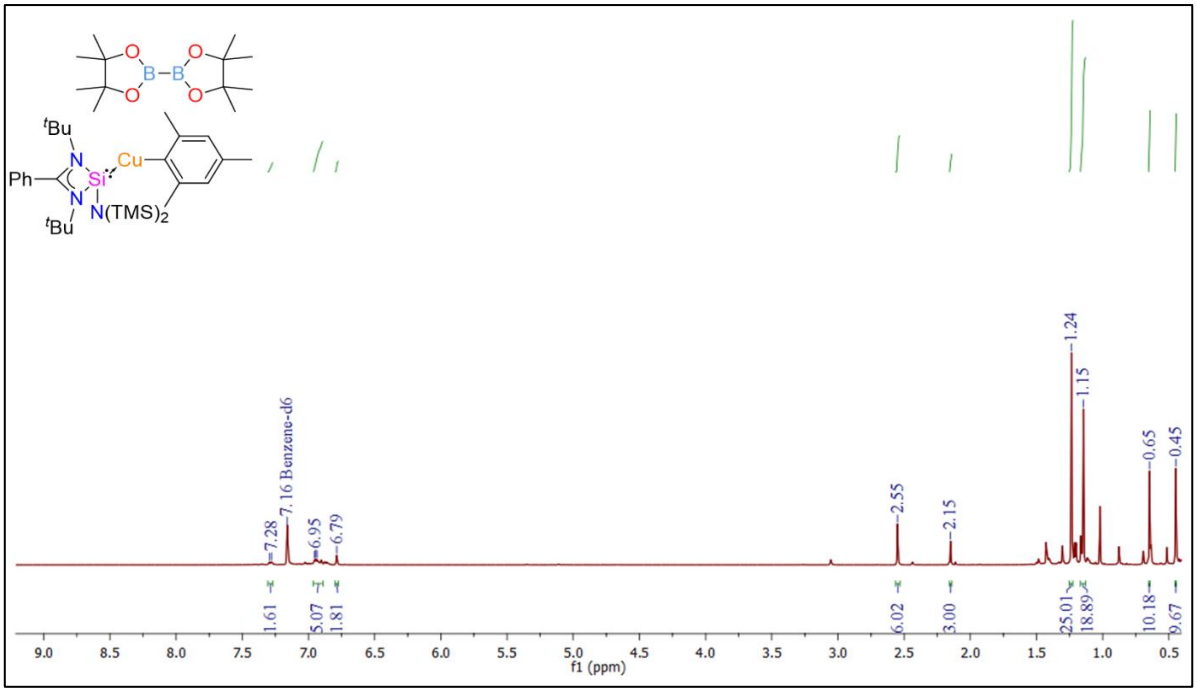

Figure 2D.A.13. ^{1}H NMR spectrum of complex **2D.7** in C_6D_6.

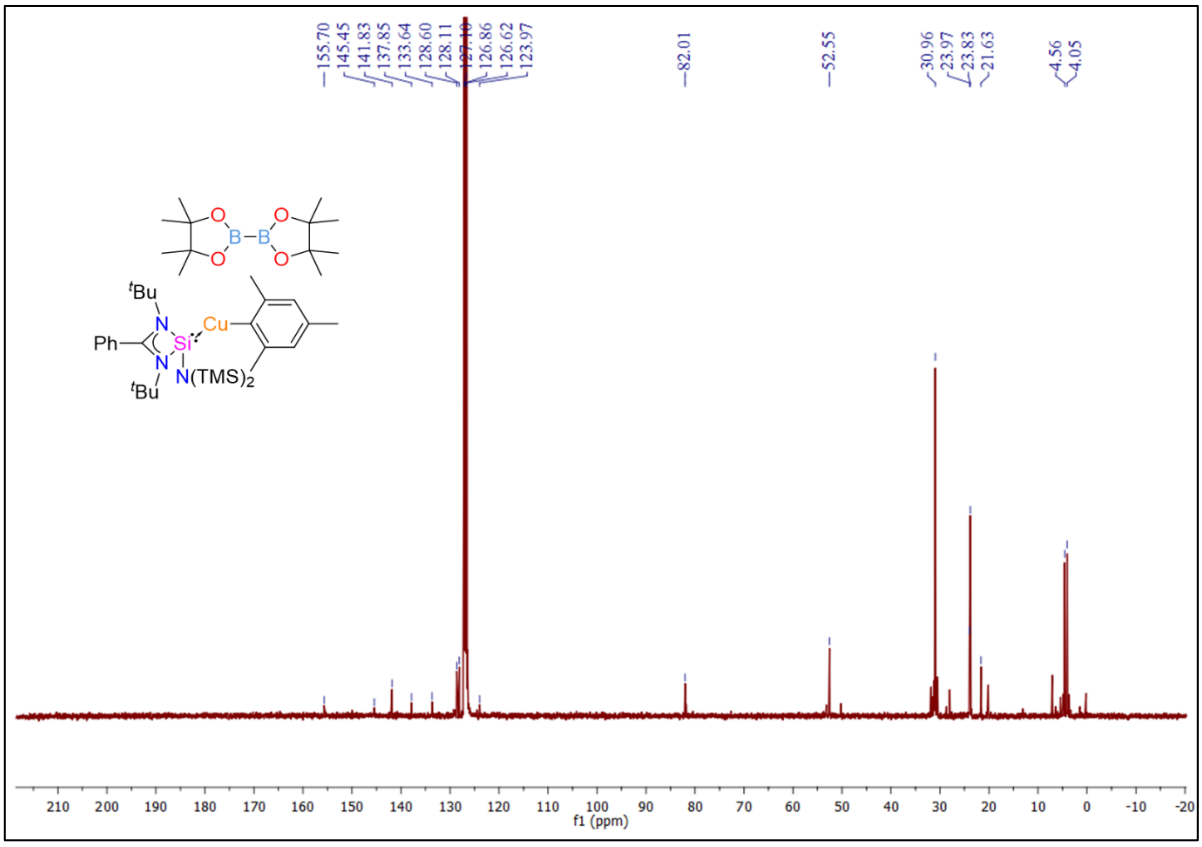

Figure 2D.A.14. ^{13}C{^{1}H} NMR spectrum of complex **2D.7** in C_6D_6.

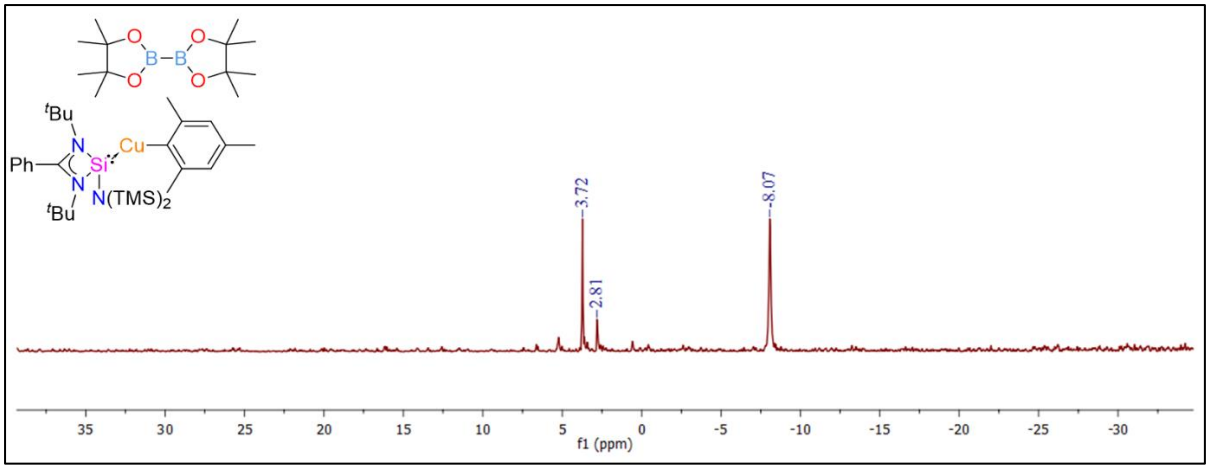

Figure 2D.A.15. $^{29}Si\{^{1}H\}$ NMR spectrum of complex **2D.7** in C_6D_6.

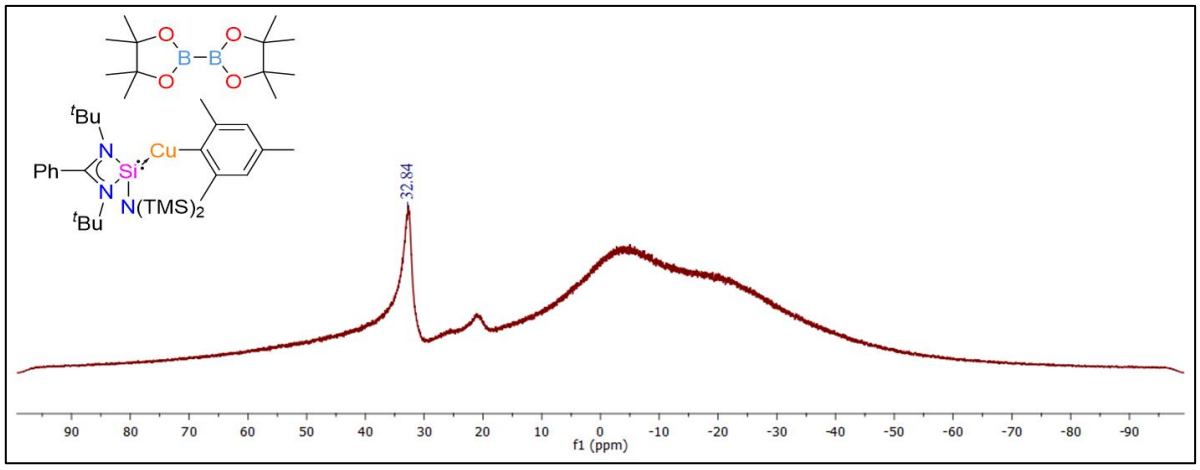

Figure 2D.A.16. $^{11}B\{^{1}H\}$ NMR spectrum of complex **2D.A.7** in C_6D_6.

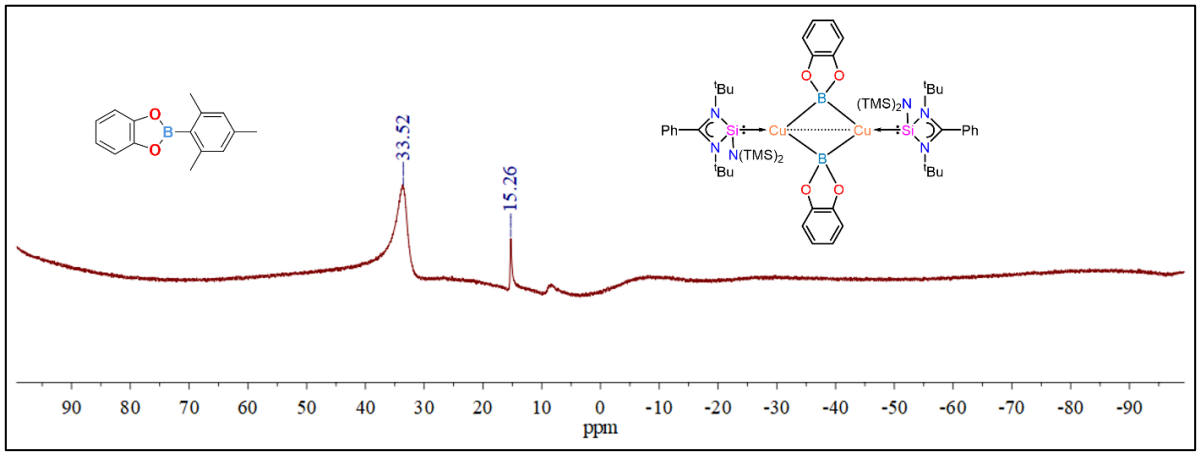

Figure 2D.A.17. $^{11}B\{^{1}H\}$ NMR spectrum of complexes **2D.8** and **2D.9** in C_6D_6.

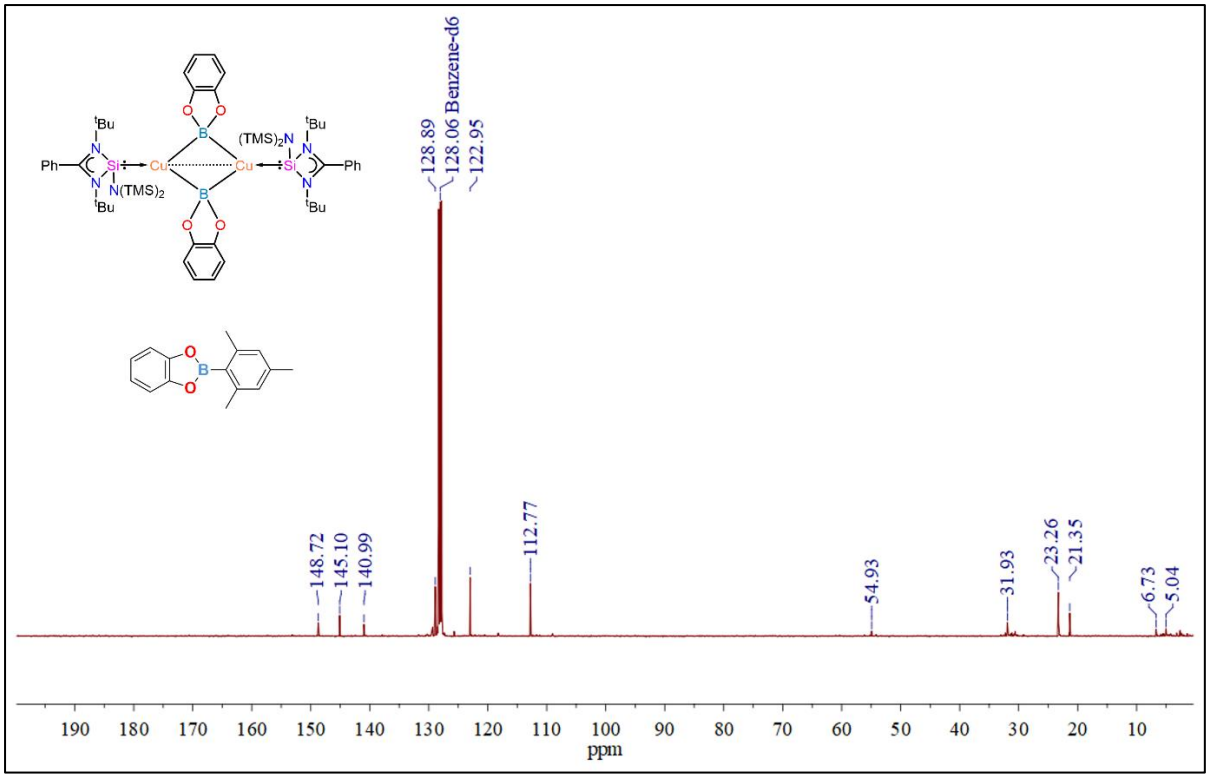

Figure 2D.A.18. $^{13}C\{^{1}H\}$ NMR spectrum of complexes **2D.8** and **2D.9** in C_6D_6.

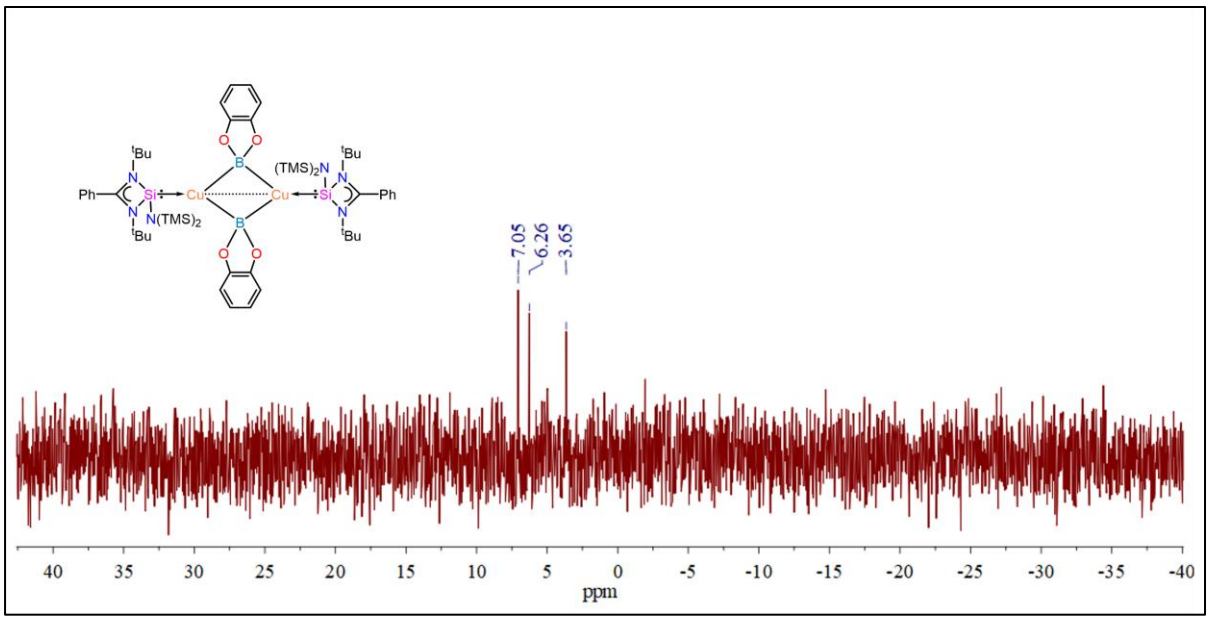

Figure 2D.A.19. $^{29}Si\{^{1}H\}$ NMR spectrum of complex **2D.8** in C_6D_6.

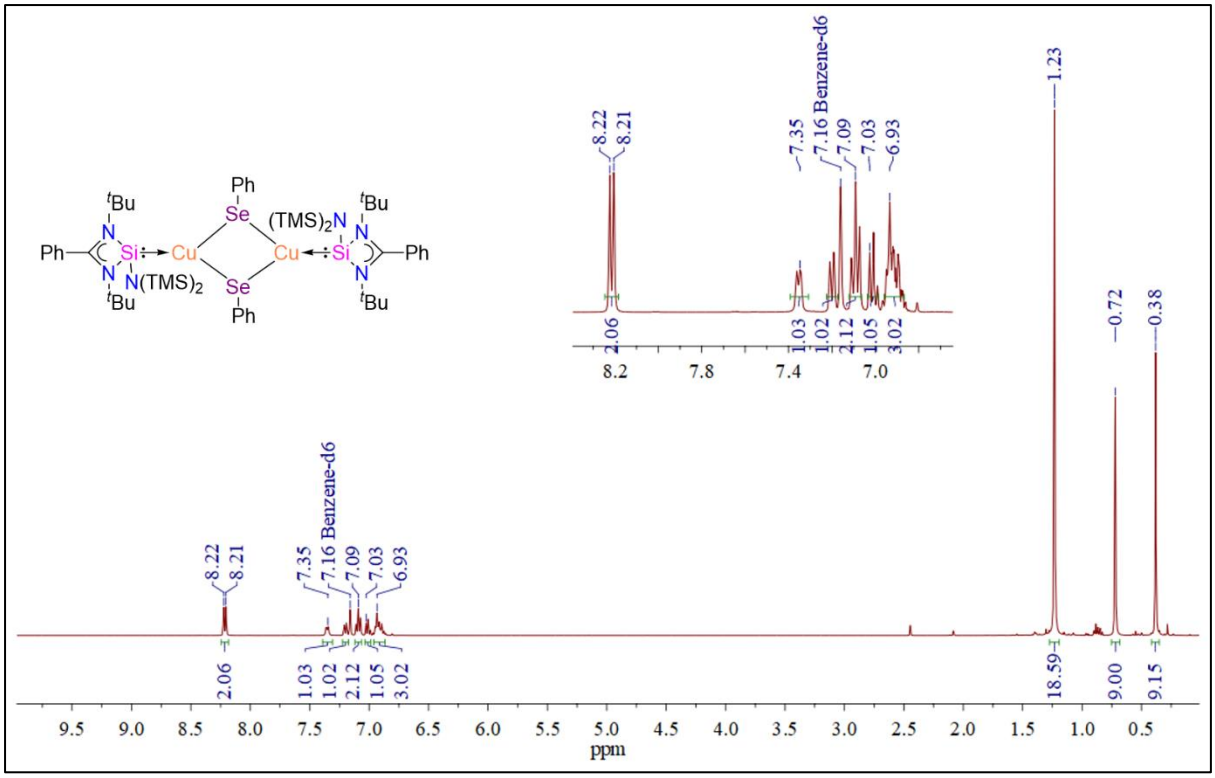

Figure 2D.A.20. ^{1}H NMR spectrum of complex **2D.10** in C_6D_6.

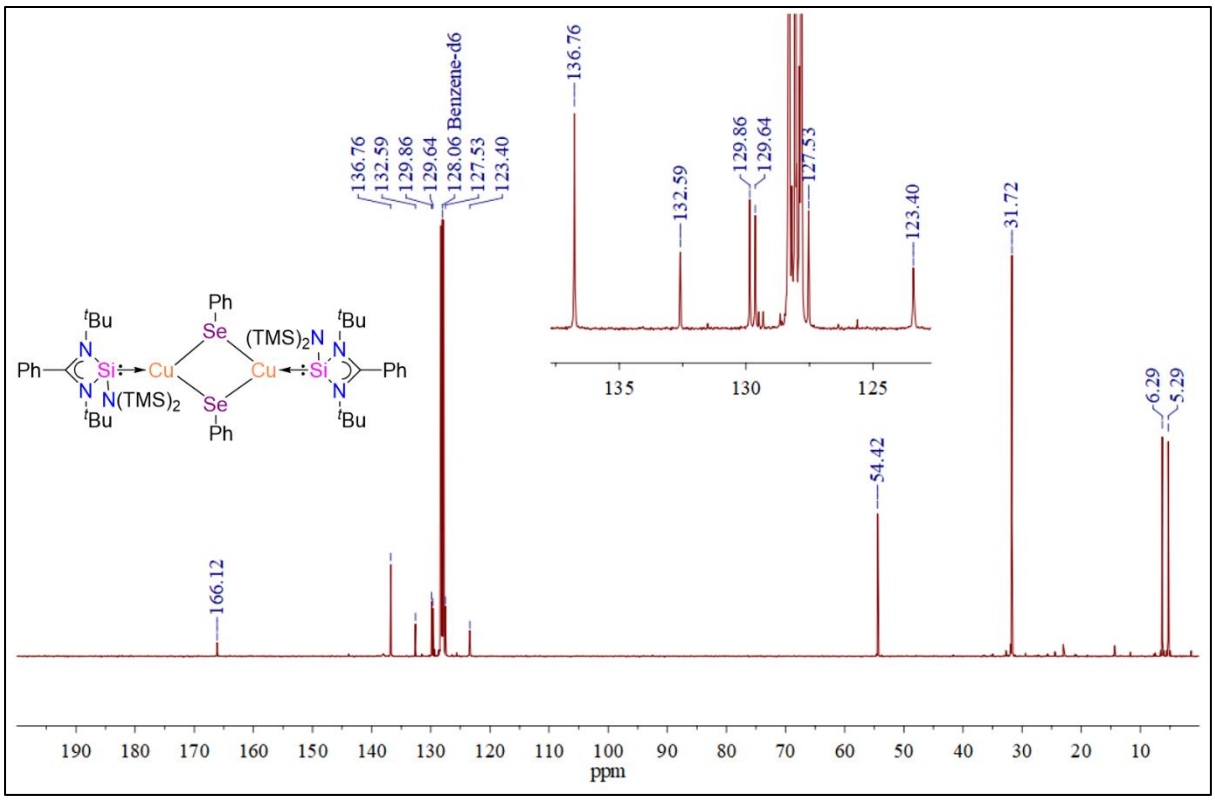

Figure 2D.A.21. ^{13}C{^{1}H} NMR spectrum of complex **2D.10** in C_6D_6.

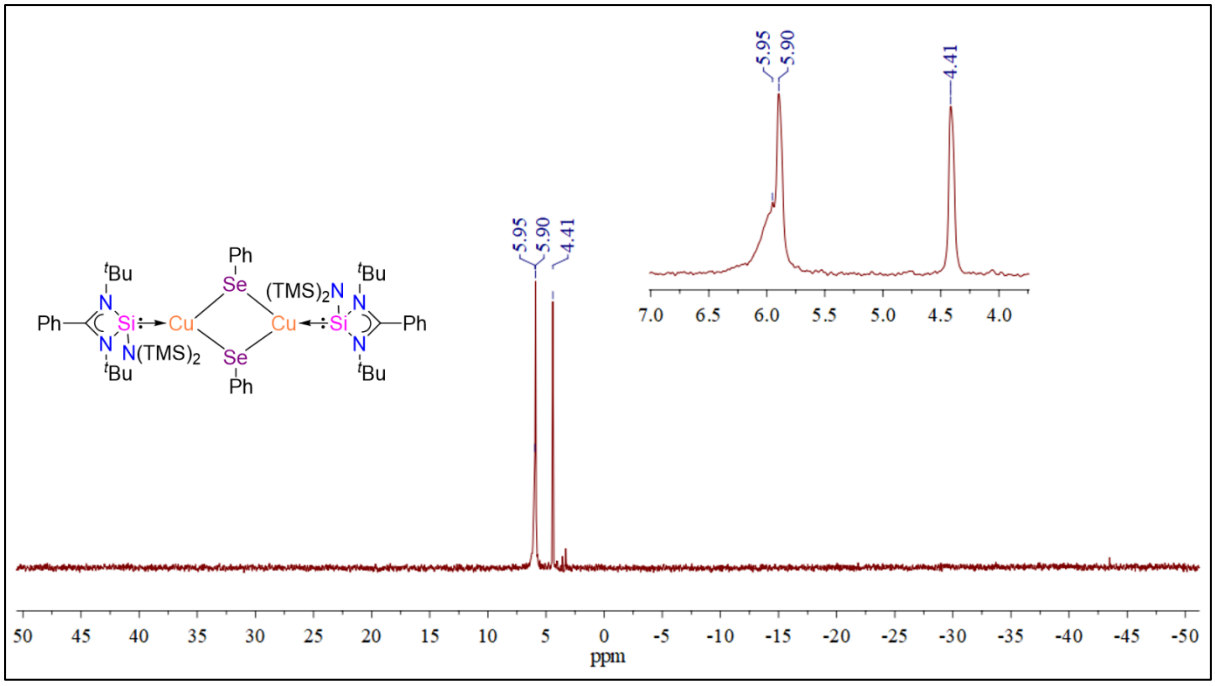

Figure 2D.A.22. $^{29}Si\{^{1}H\}$ NMR spectrum of complex **2D.10** in C_6D_6.

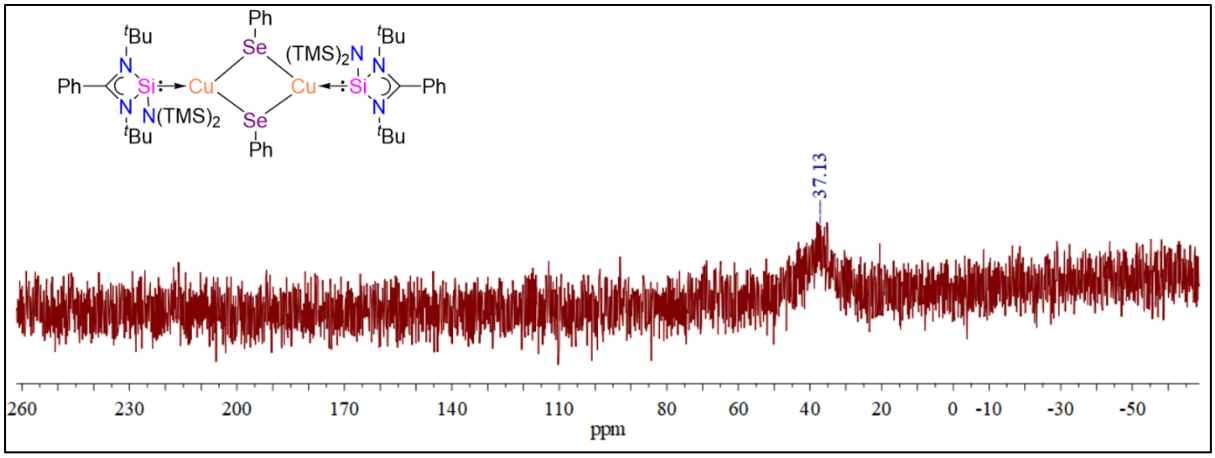

Figure 2D.A.23. $^{77}Se\{^{1}H\}$ NMR spectrum of complex **2D.10** in C_6D_6.

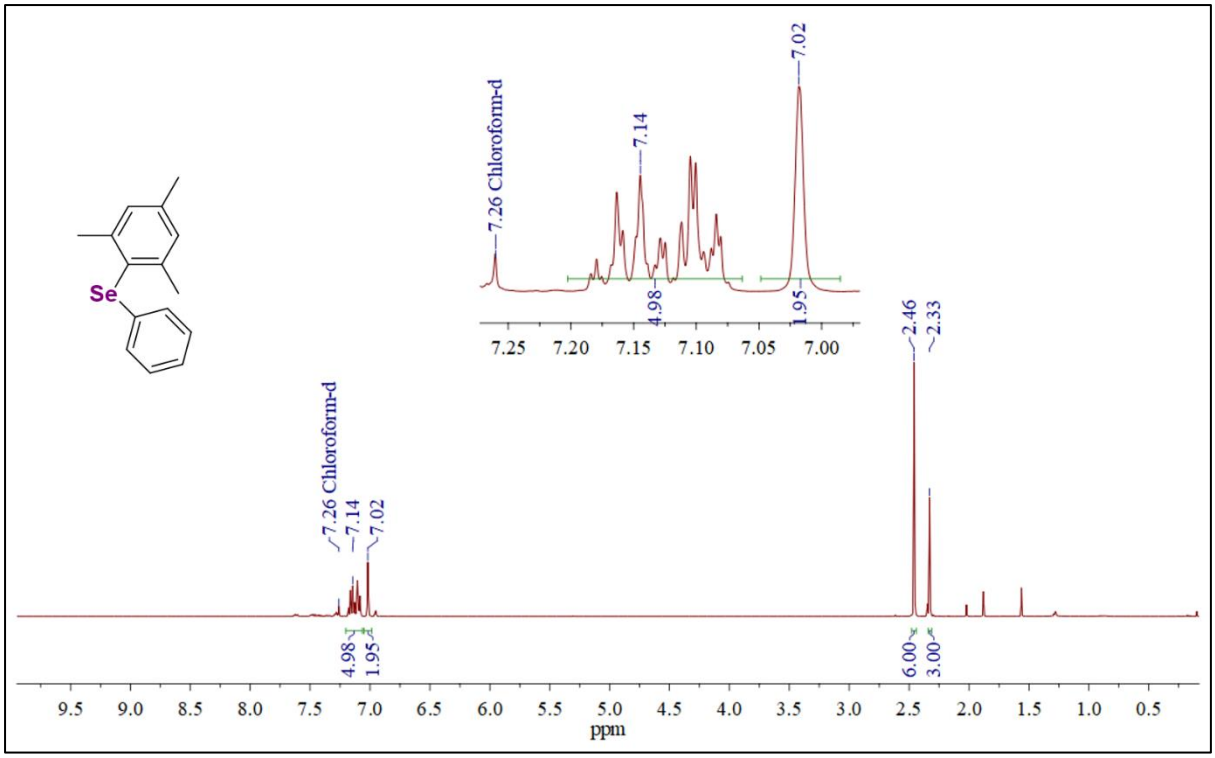

Figure 2D.A.24. ^{1}H NMR spectrum of complex Mesityl(phenyl)selane in $CDCl_3$.

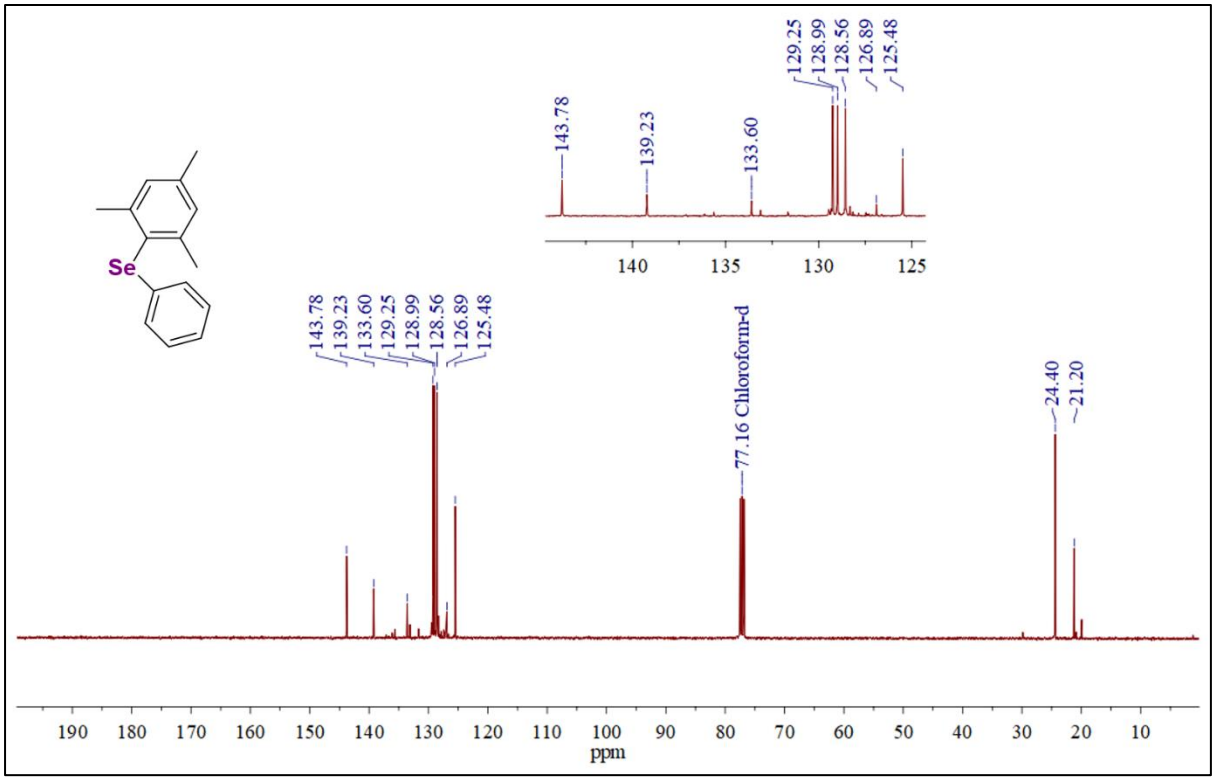

Figure 2D.A.25. ^{13}C{^{1}H} NMR spectrum of complex Mesityl(phenyl)selane in $CDCl_3$.

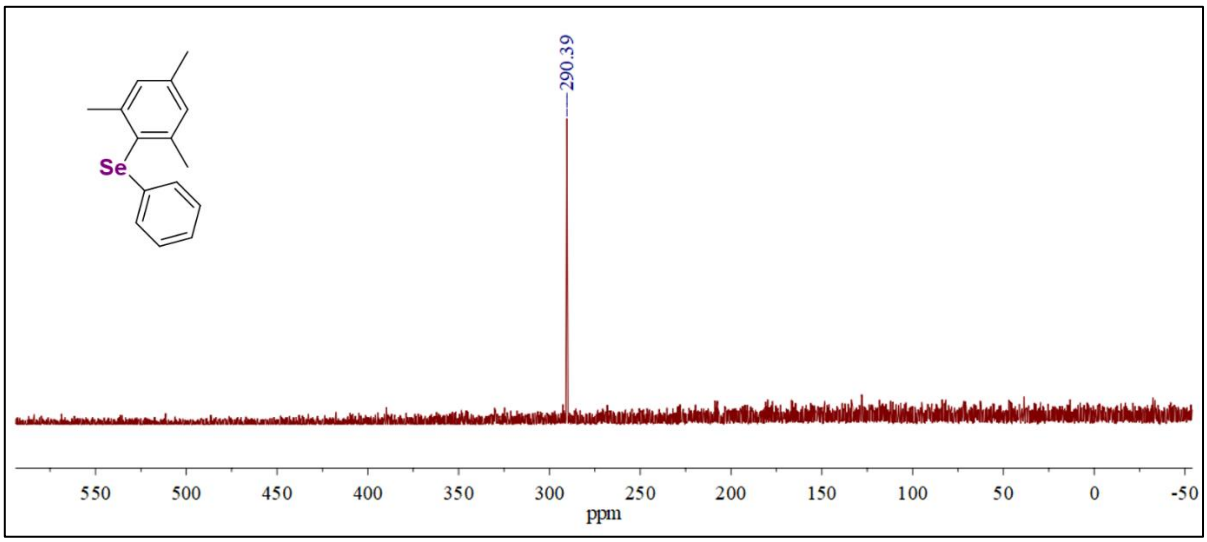

Figure 2D.A.26. $^{77}Se\{^{1}H\}$ NMR spectrum of complex Mesityl(phenyl)selane in $CDCl_3$.

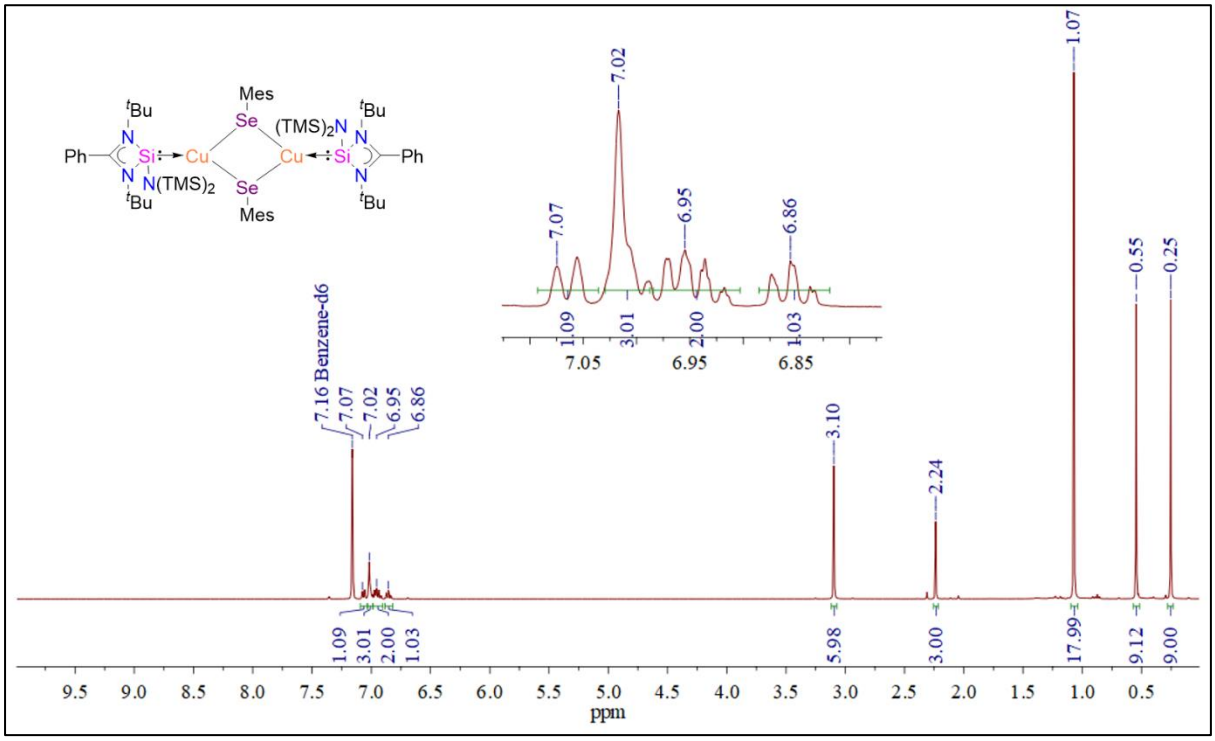

Figure 2D.A.27. ^{1}H NMR spectrum of complex **2D.11** in C_6D_6.

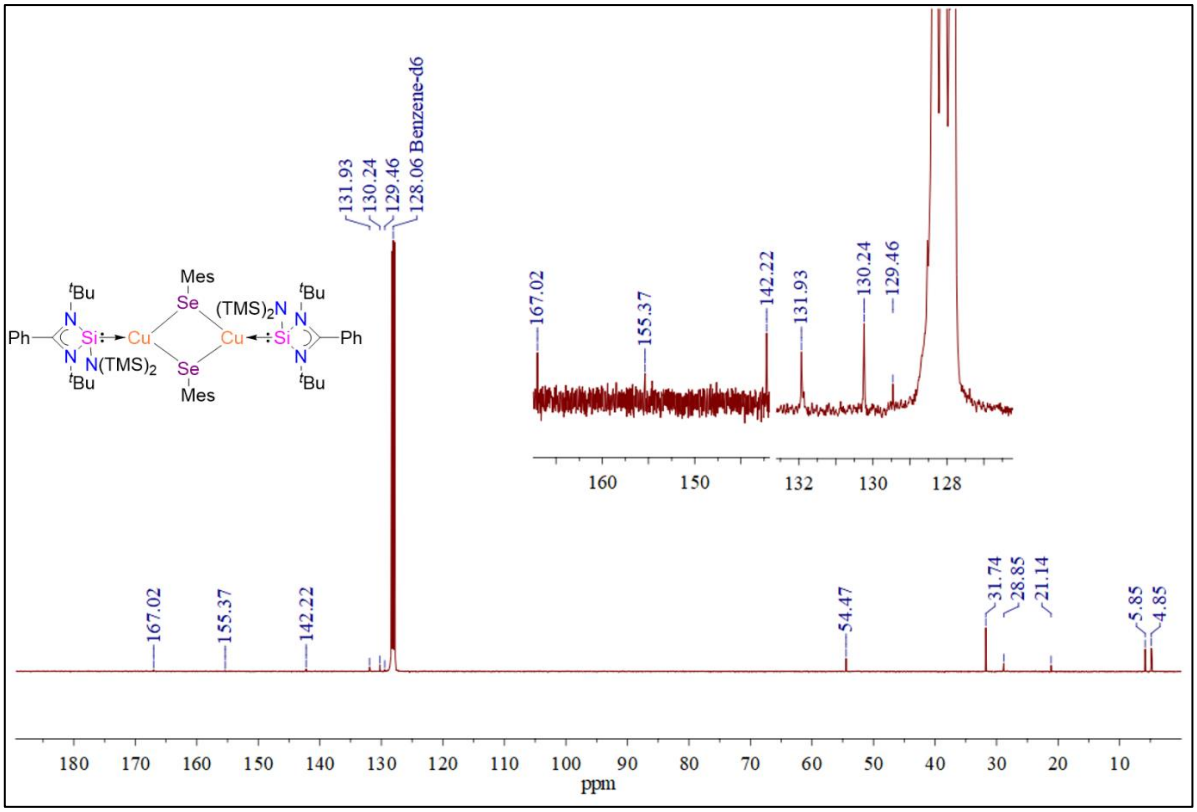

Figure 2D.A.28. $^{13}C\{^{1}H\}$ NMR spectrum of complex **2D.11** in C_6D_6.

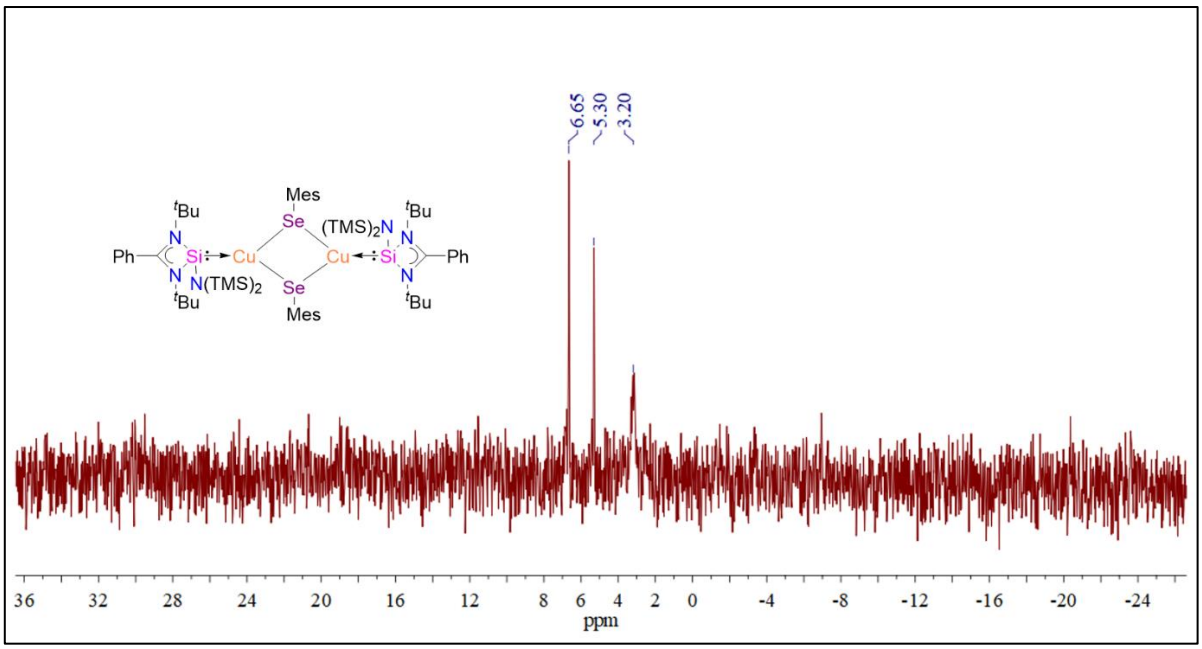

Figure 2D.A.29. $^{29}Si\{^{1}H\}$ NMR spectrum of complex **2D.11** in C_6D_6.

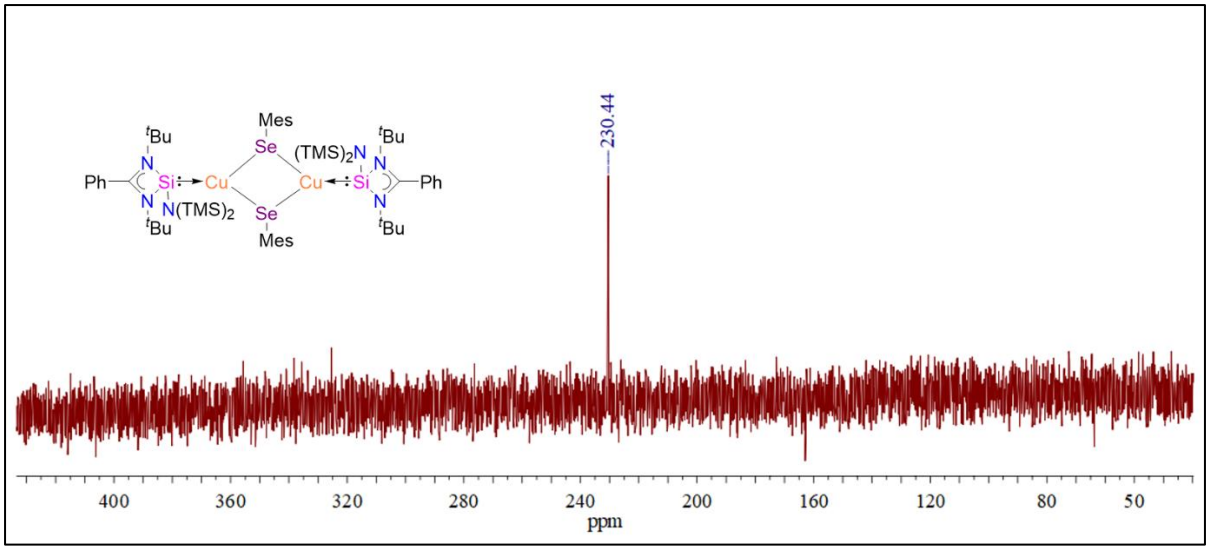

Figure 2D.A.30. $^{77}Se\{^{1}H\}$ NMR spectrum of complex **2D.11** in C_6D_6.

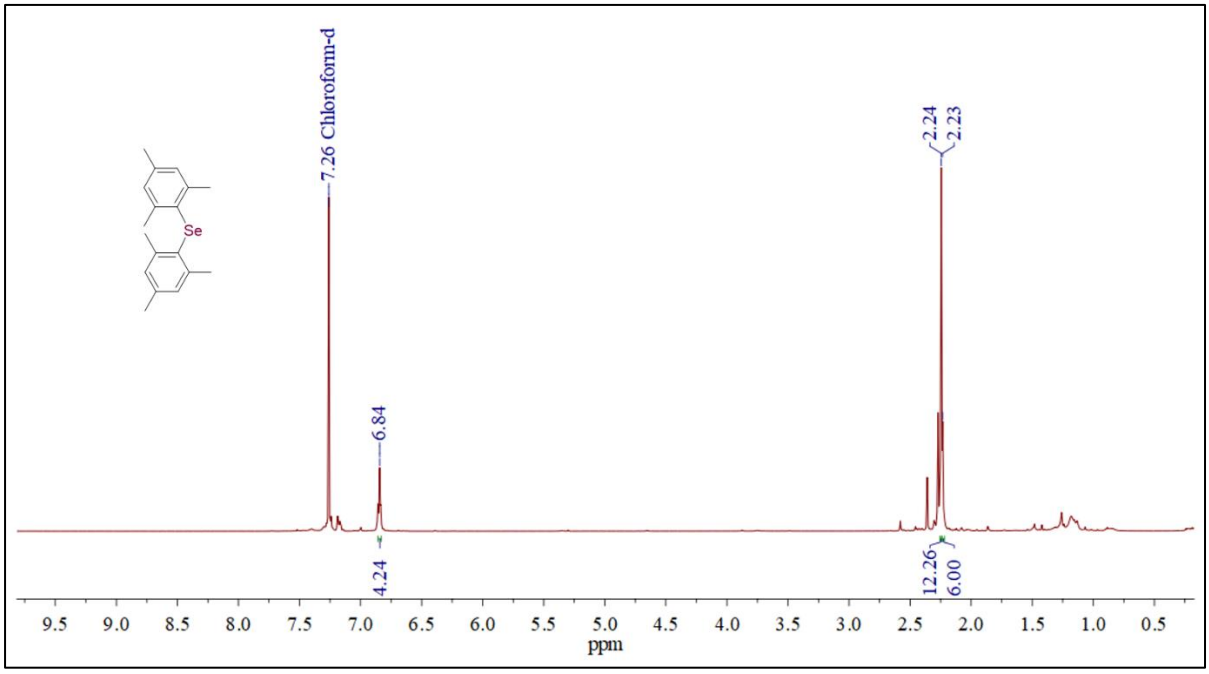

Figure 2D.A.31. ^{1}H NMR spectrum of complex Dimesityl selane in $CDCl_3$.

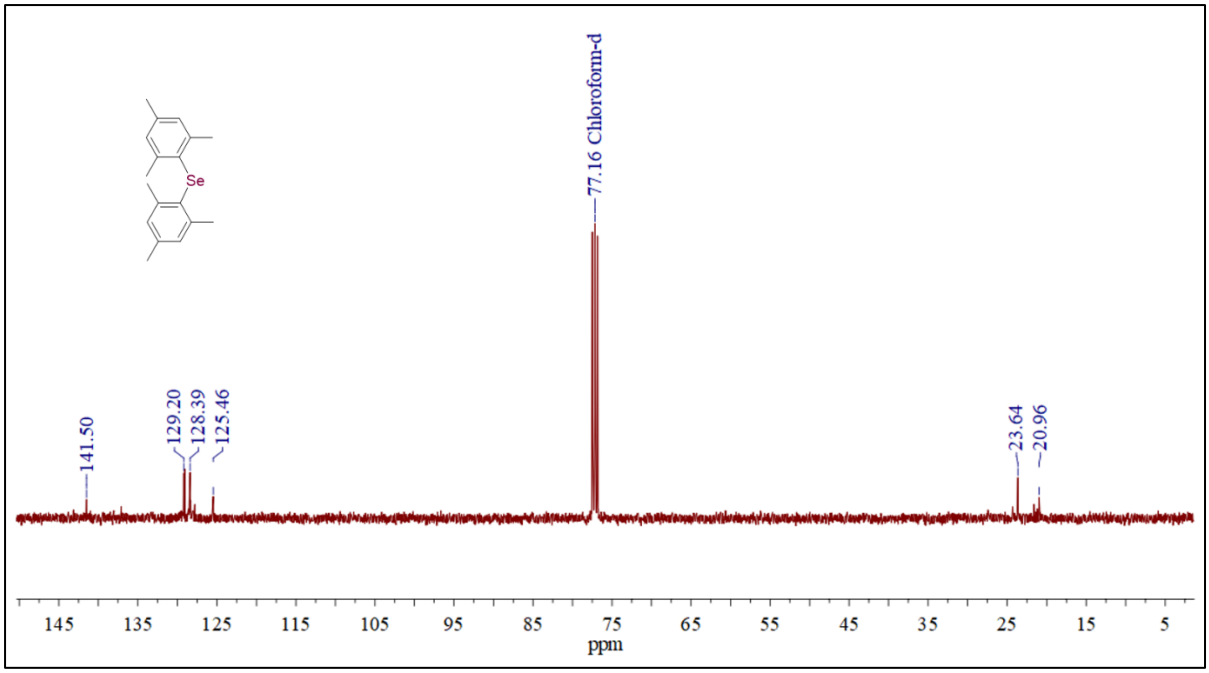

Figure 2D.A.32. $^{13}C\{^{1}H\}$ NMR spectrum of complex Dimesityl selane in $CDCl_3$.

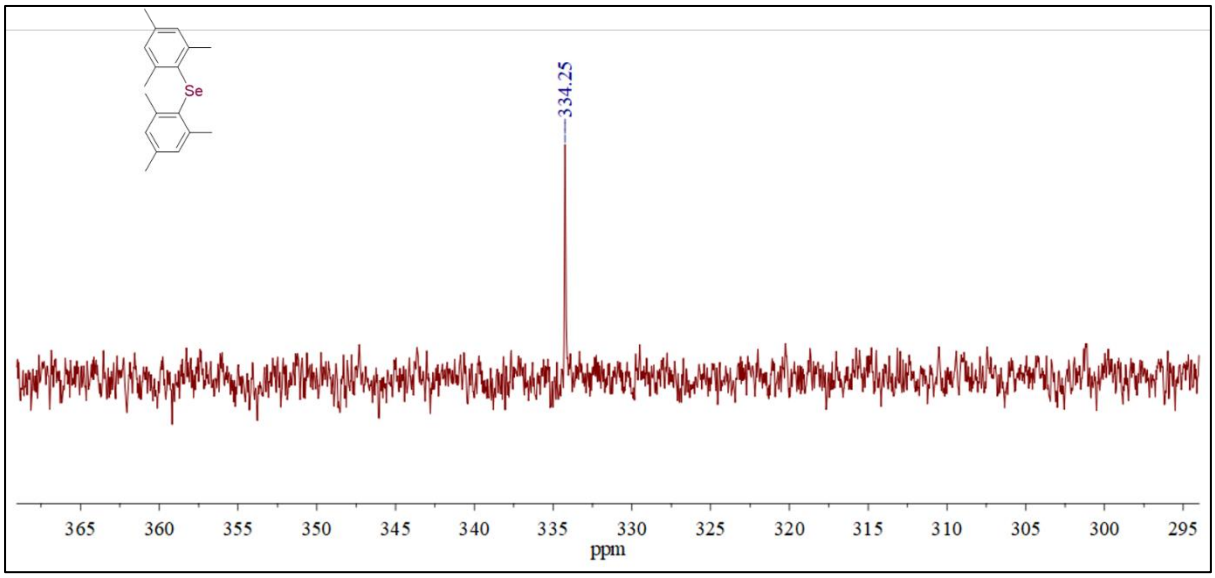

Figure 2D.A.33. $^{77}Se\{^{1}H\}$ NMR spectrum of complex Dimesityl selane in $CDCl_3$.

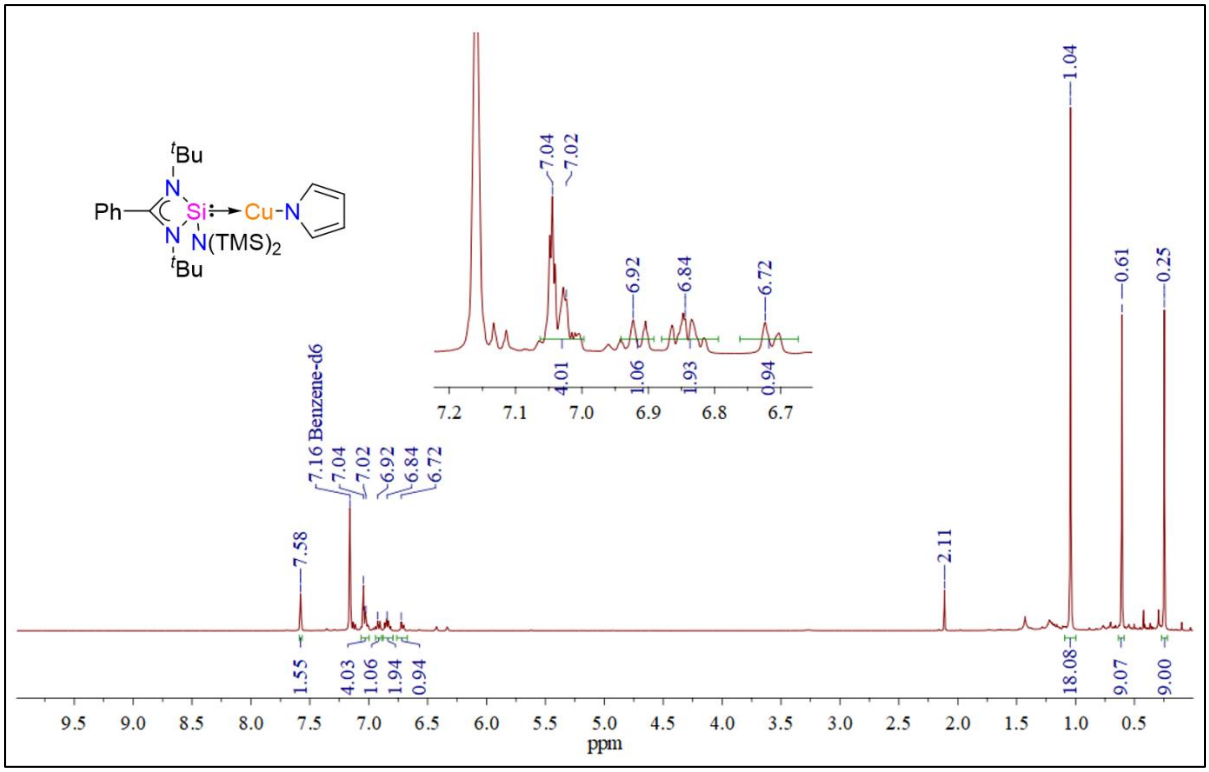

Figure 2D.A.34. ^{1}H NMR spectrum of complex **2D.12** in C_6D_6.

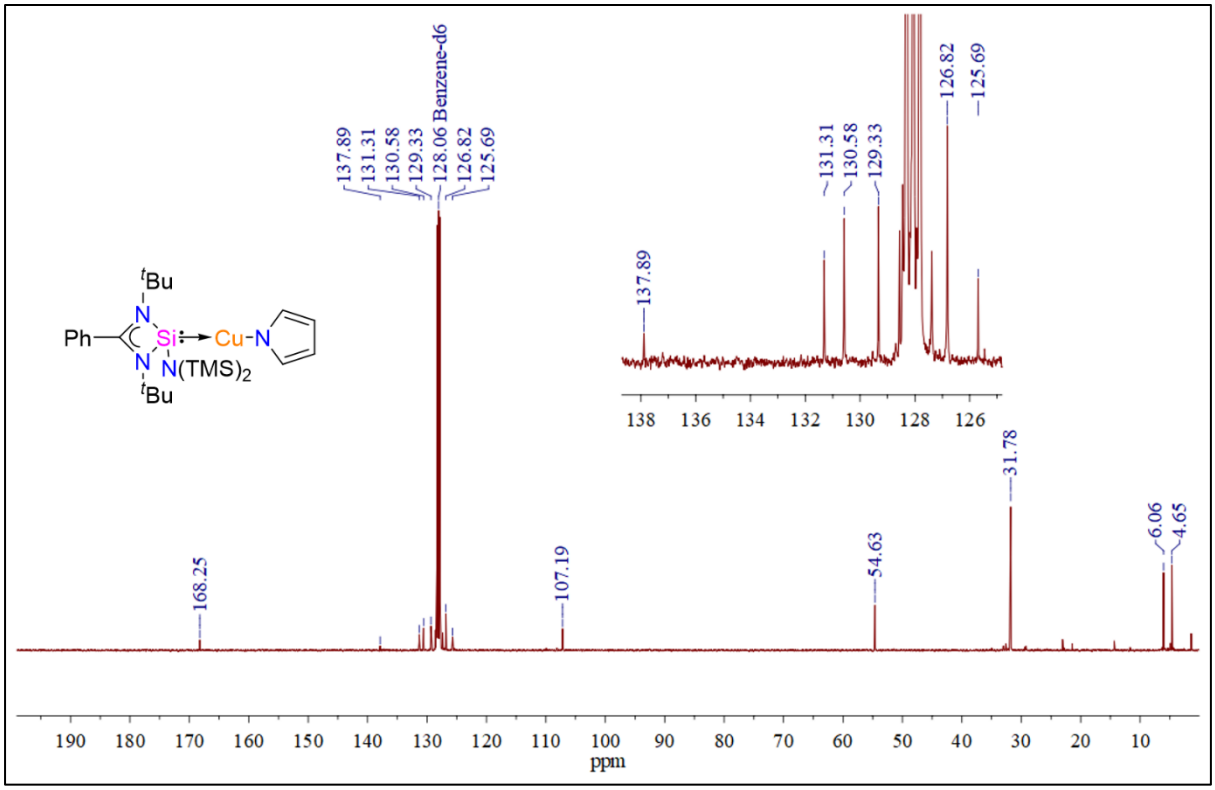

Figure 2D.A.35. ^{13}C{^{1}H} NMR spectrum of complex **2D.12** in C_6D_6.

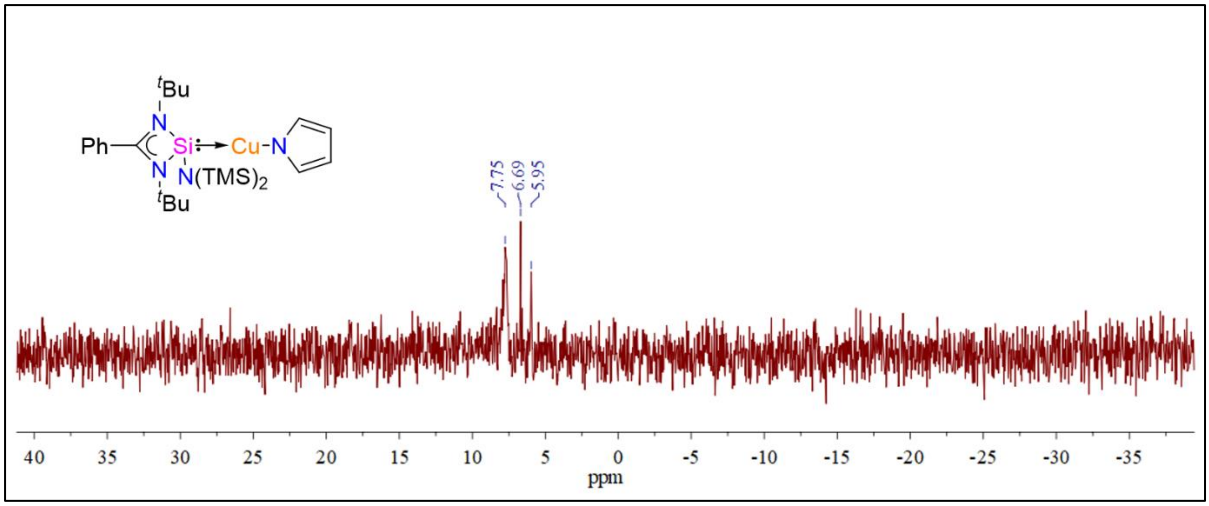

Figure 2D.A.36. $^{29}Si\{^{1}H\}$ NMR spectrum of complex **2D.12** in C_6D_6.

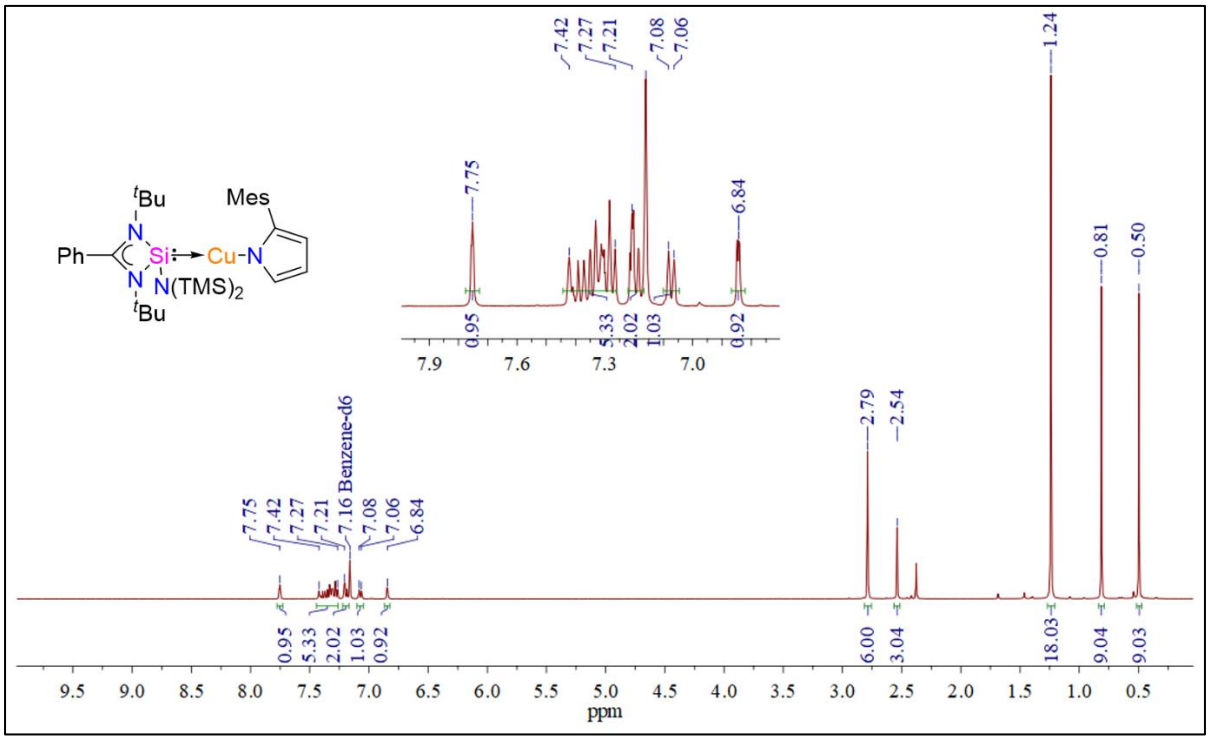

Figure 2D.A.37. ^{1}H NMR spectrum of complex **2D.13** in C_6D_6.

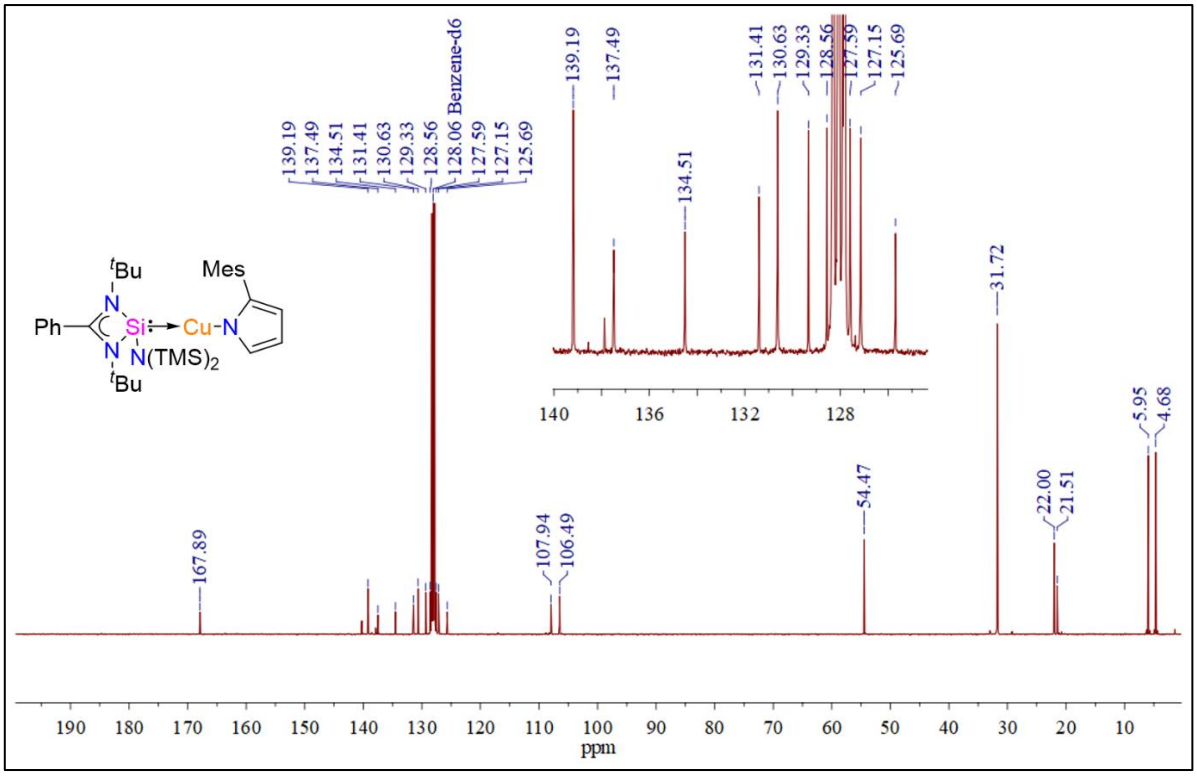

Figure 2D.A.38. $^{13}C\{^{1}H\}$ NMR spectrum of complex **2D.13** in C_6D_6.

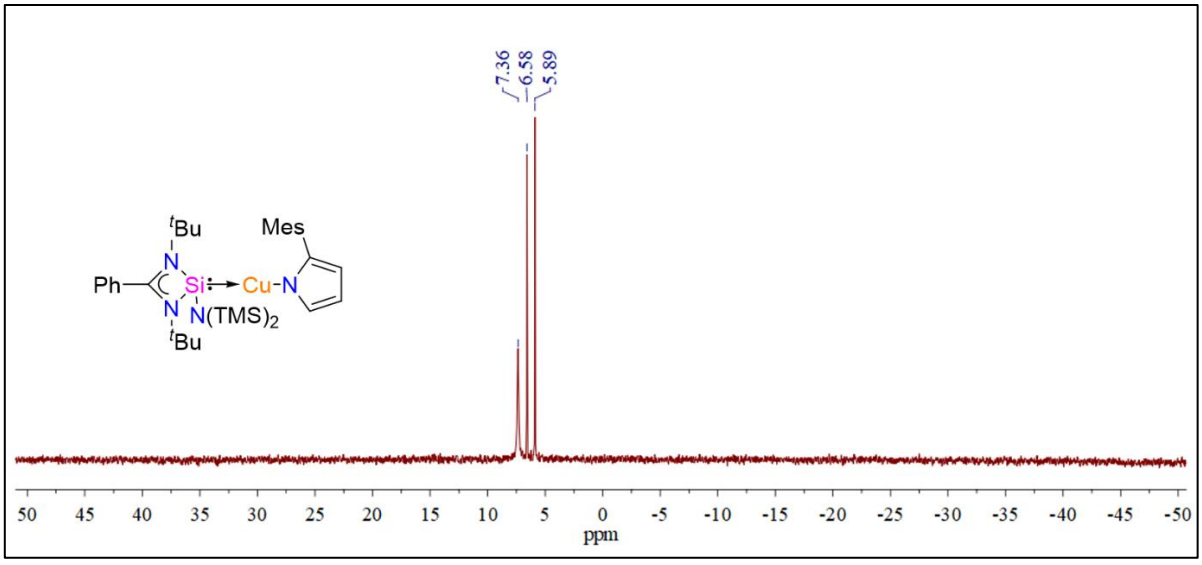

Figure 2D.A.39. $^{29}Si\{^{1}H\}$ NMR spectrum of complex **2D.13** in C_6D_6.

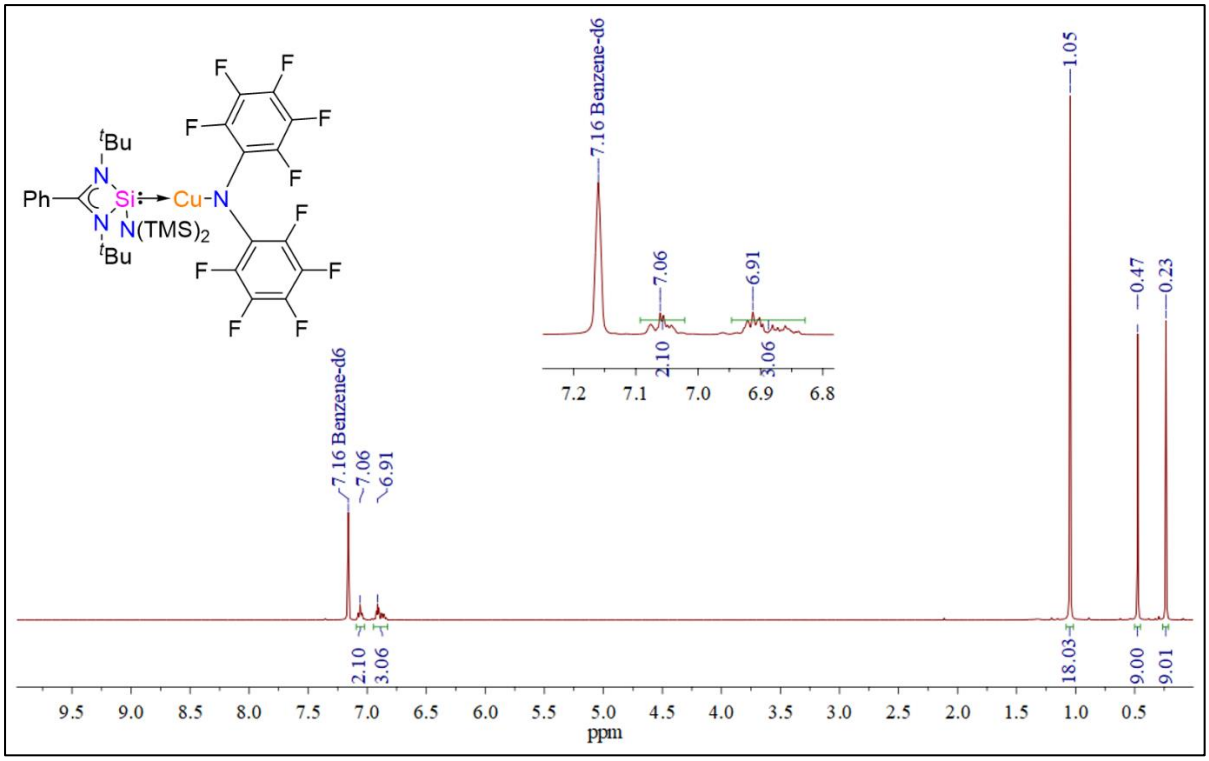

Figure 2D.A.40. ^{1}H NMR spectrum of complex **2D.14** in C_6D_6.

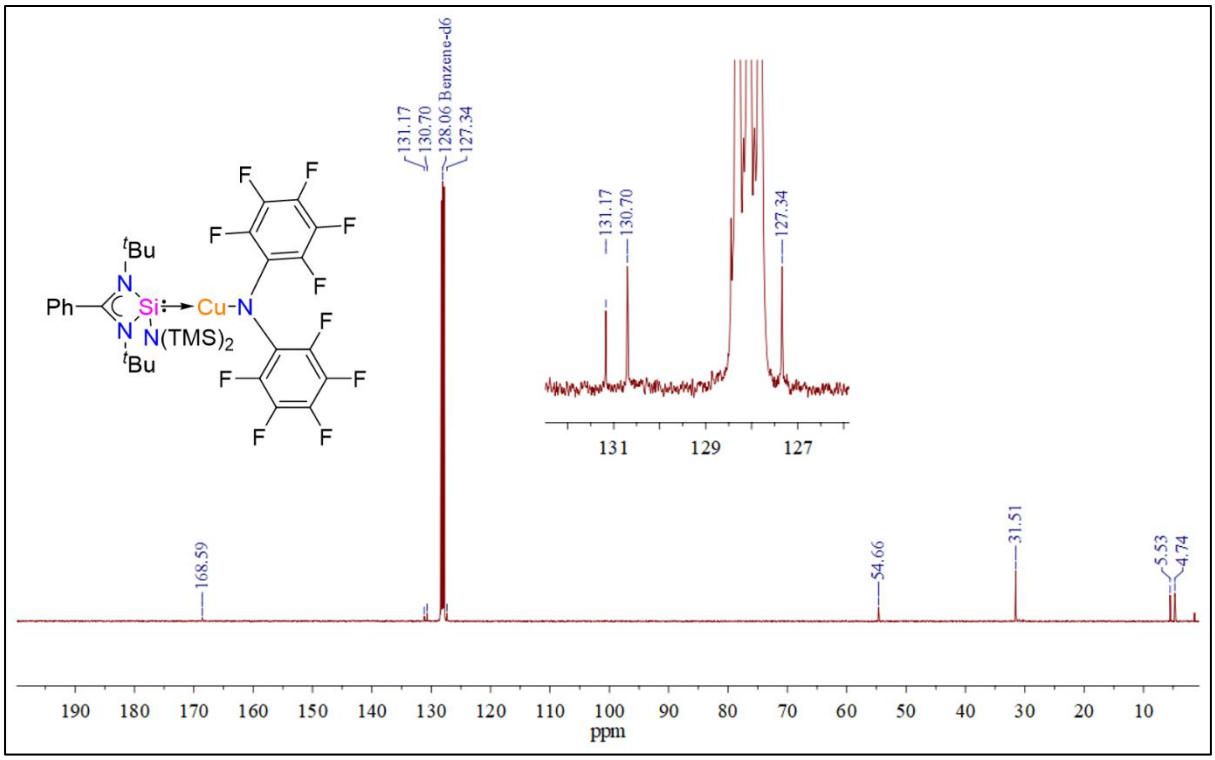

Figure 2D.A.41. $^{13}C\{^{1}H\}$ NMR spectrum of complex **2D.A.14** in C_6D_6.

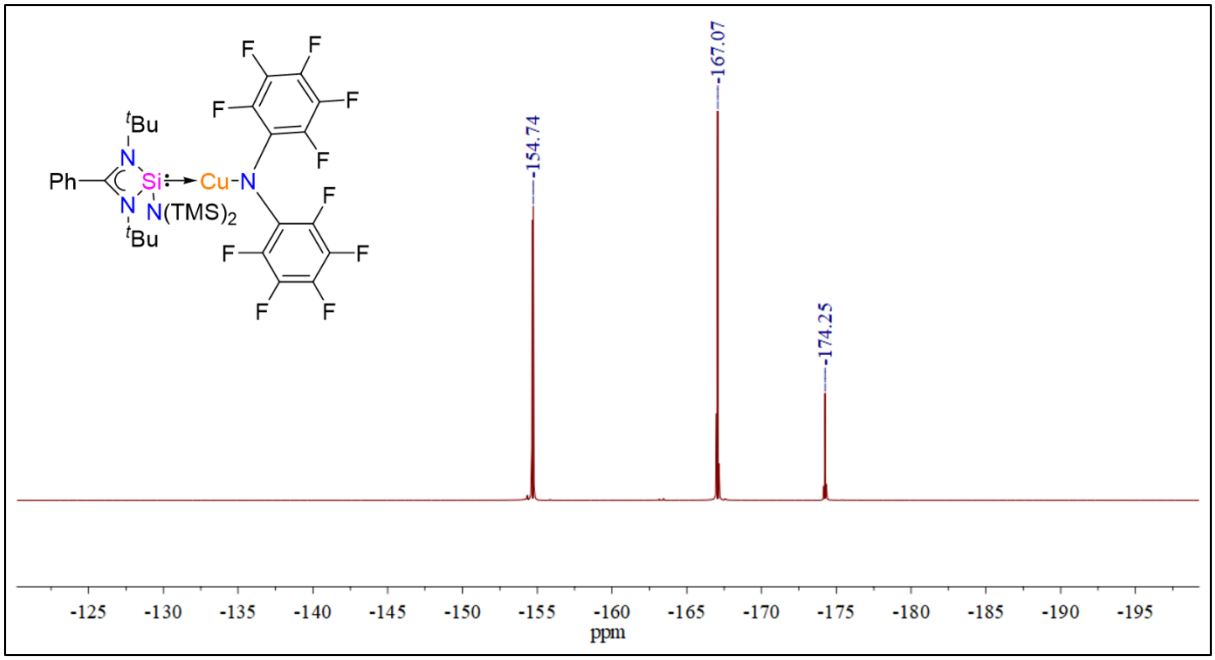

Figure 2D.A.42. ^{19}F NMR spectrum of complex **2D.14** in C_6D_6.

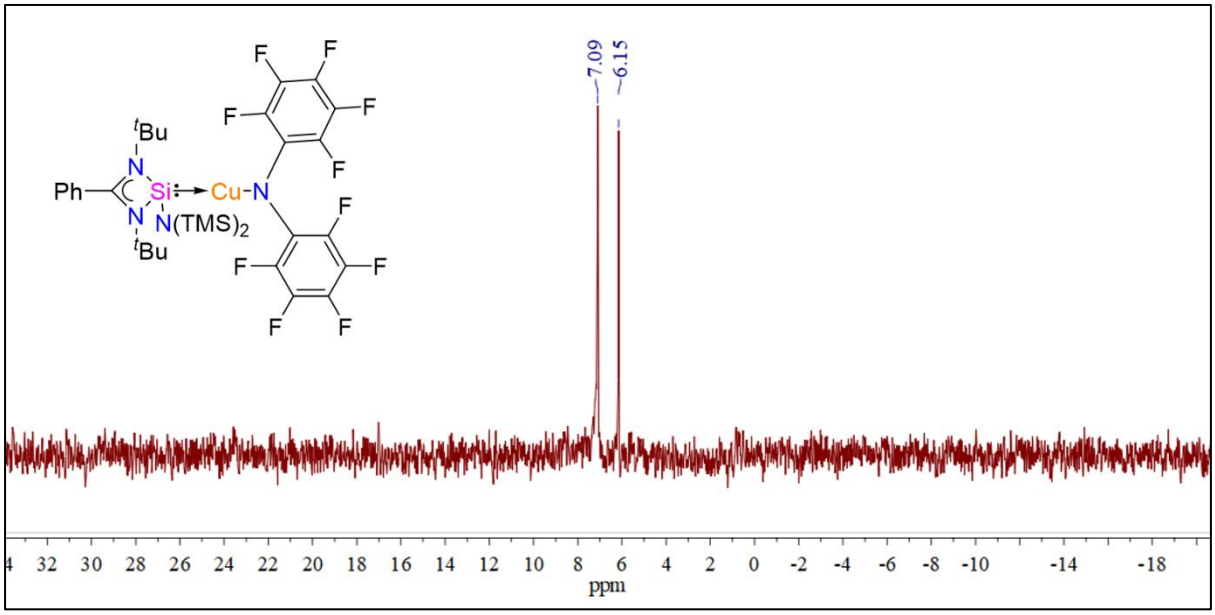

Figure 2D.A.43. $^{29}Si\{^1H\}$ NMR spectrum of complex **2D.14** in C_6D_6.

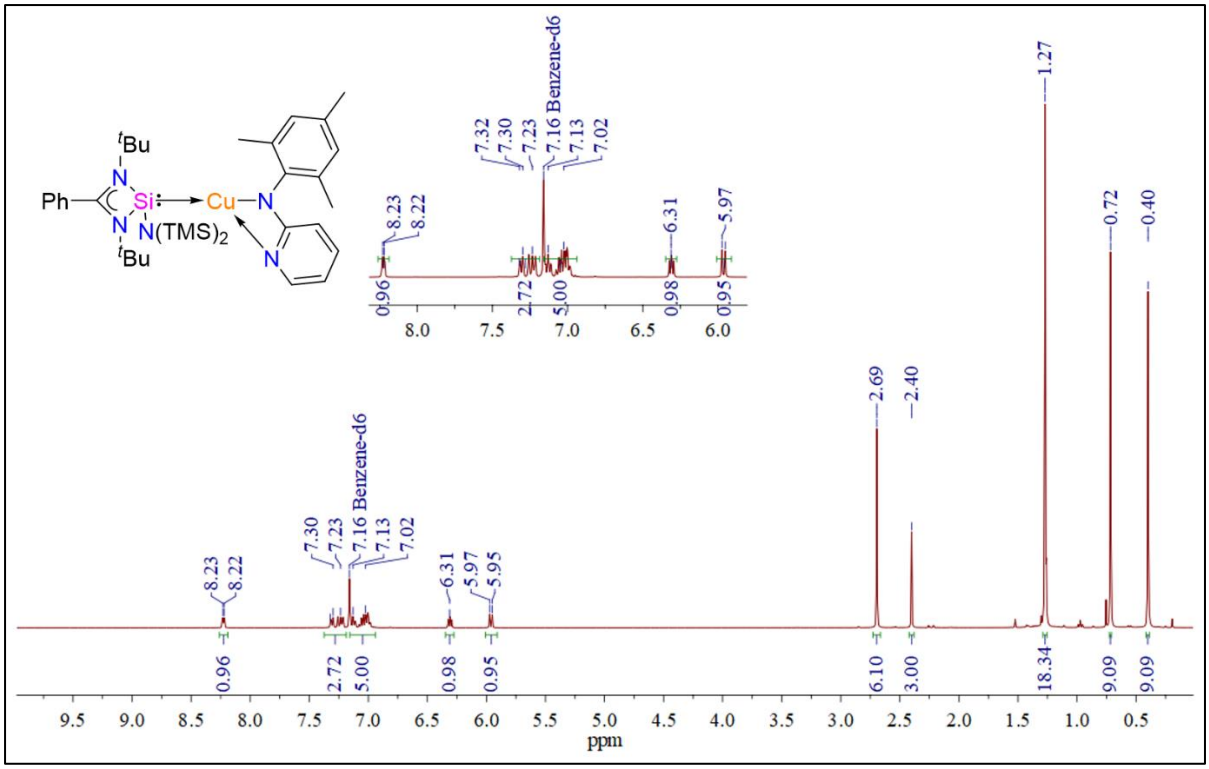

Figure 2D.A.44. ^{1}H NMR spectrum of complex **2D.15** in C_6D_6.

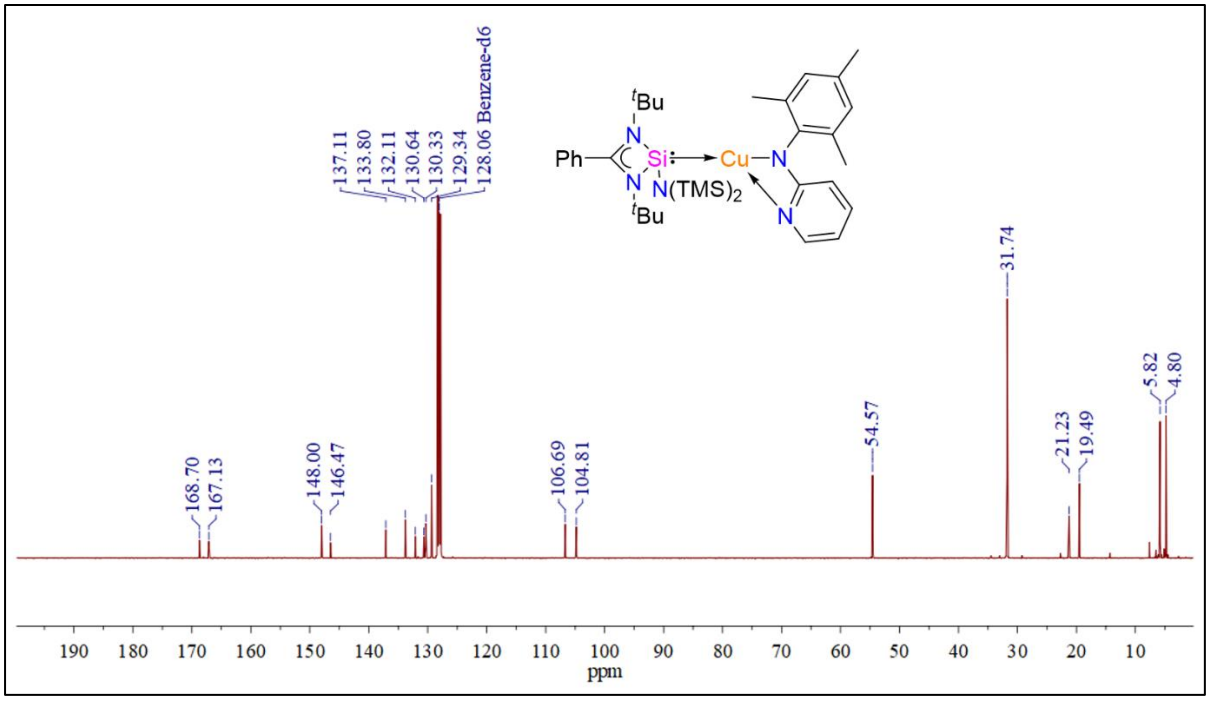

Figure 2D.A.45. ^{13}C{^{1}H} NMR spectrum of complex **2D.15** in C_6D_6.

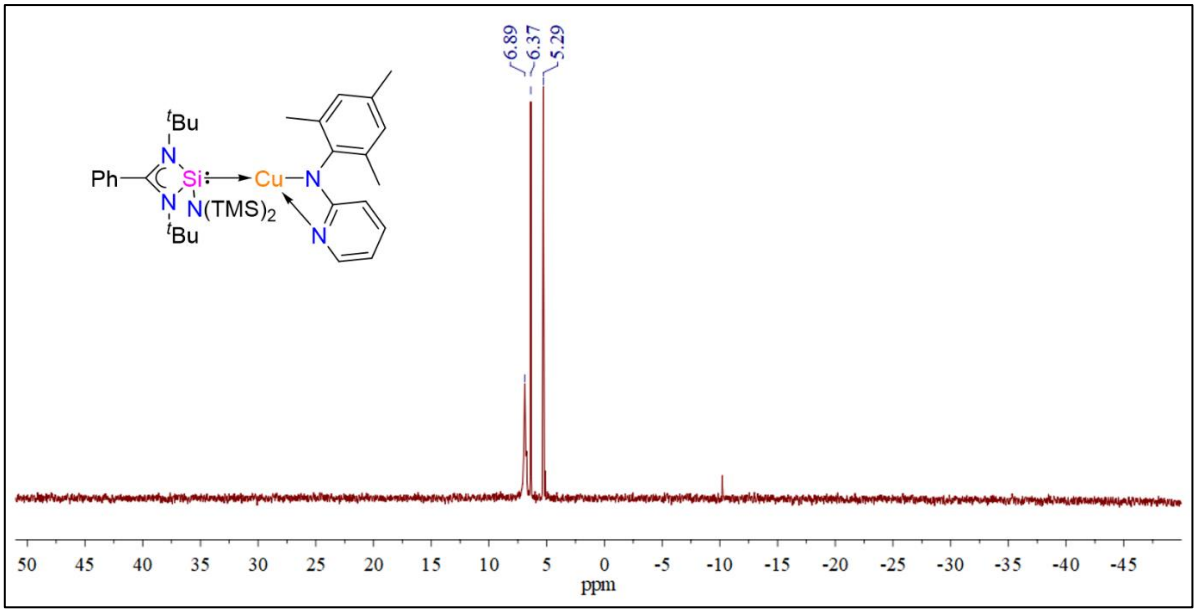

Figure 2D.A.46. $^{29}Si\{^{1}H\}$ NMR spectrum of complex **2D.15** in C_6D_6.

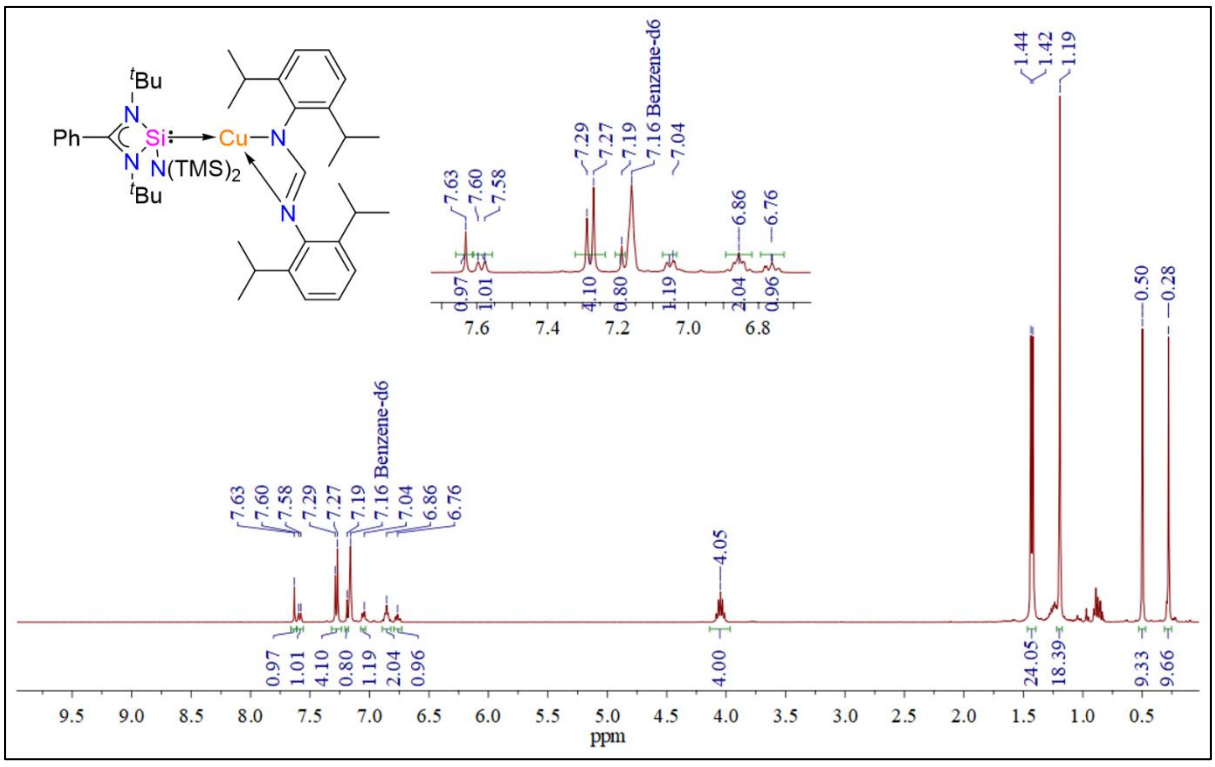

Figure 2D.A.47. ^{1}H NMR spectrum of complex **2D.16** in C_6D_6.

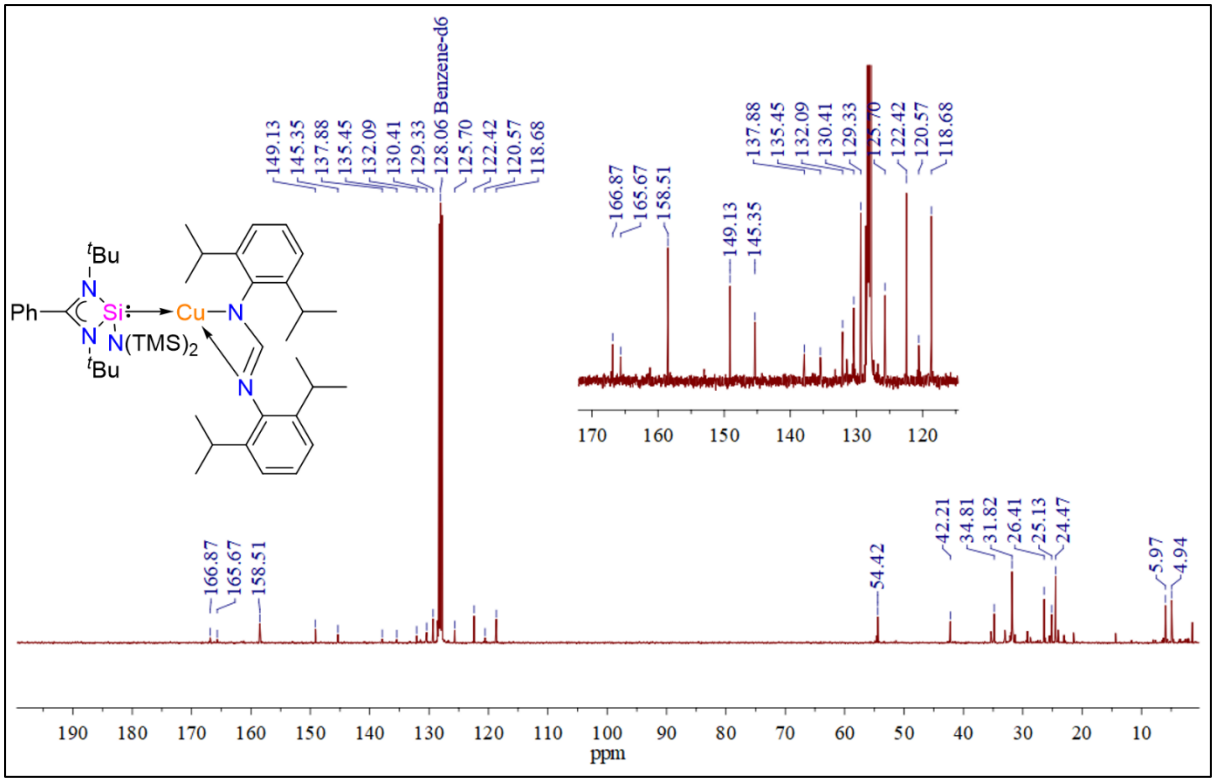

Figure 2D.A.48. $^{13}C\{^{1}H\}$ NMR spectrum of complex **2D.16** in C_6D_6.

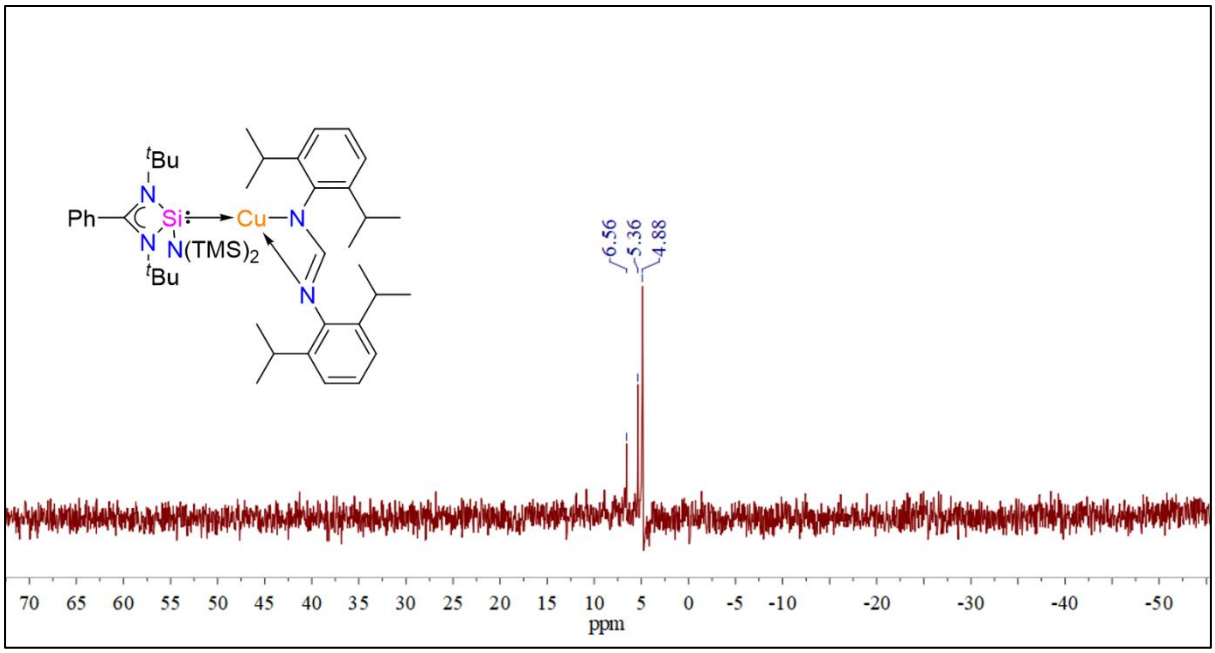

Figure 2D.A.49. $^{29}Si\{^{1}H\}$ NMR spectrum of complex **2D.16** in C_6D_6.

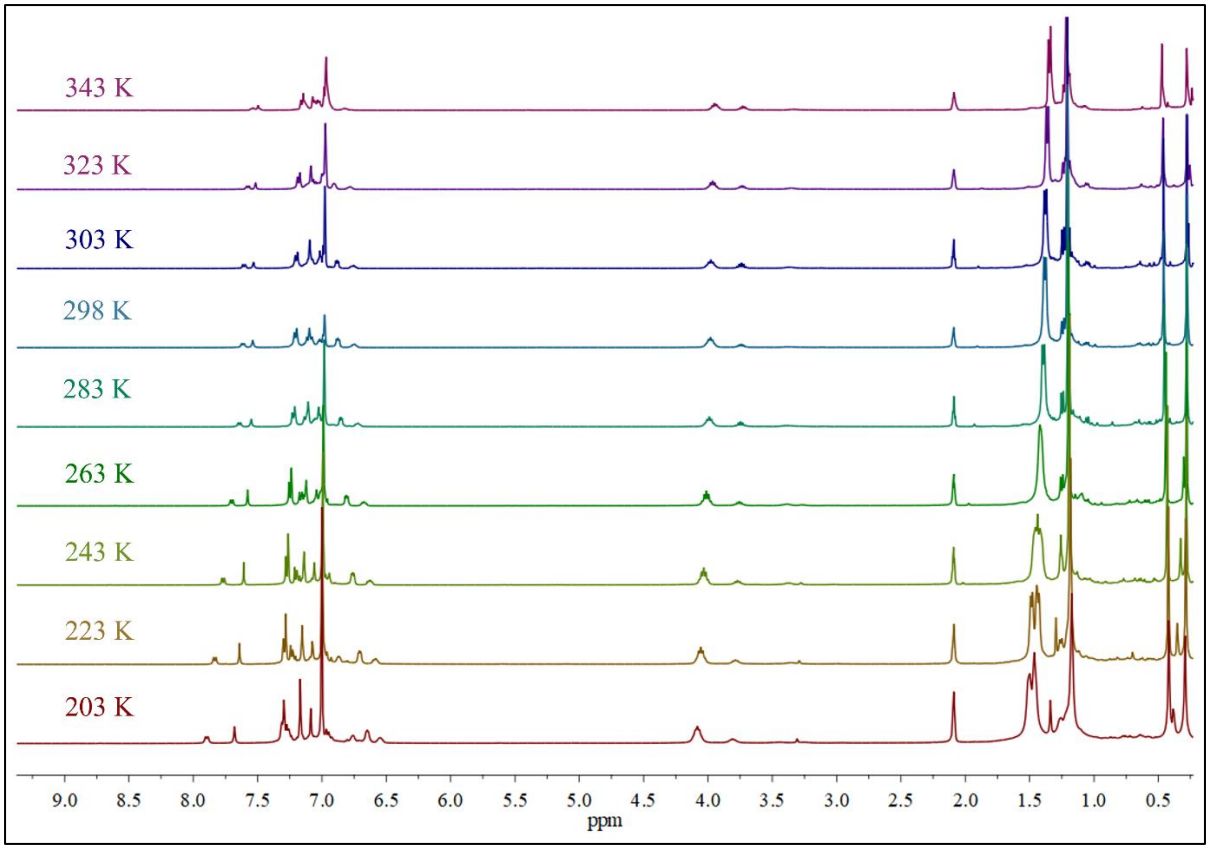

Figure 2D.A.50. Variable temperature ^{1}H NMR spectra of complex **2D.16** in toluene d_8.

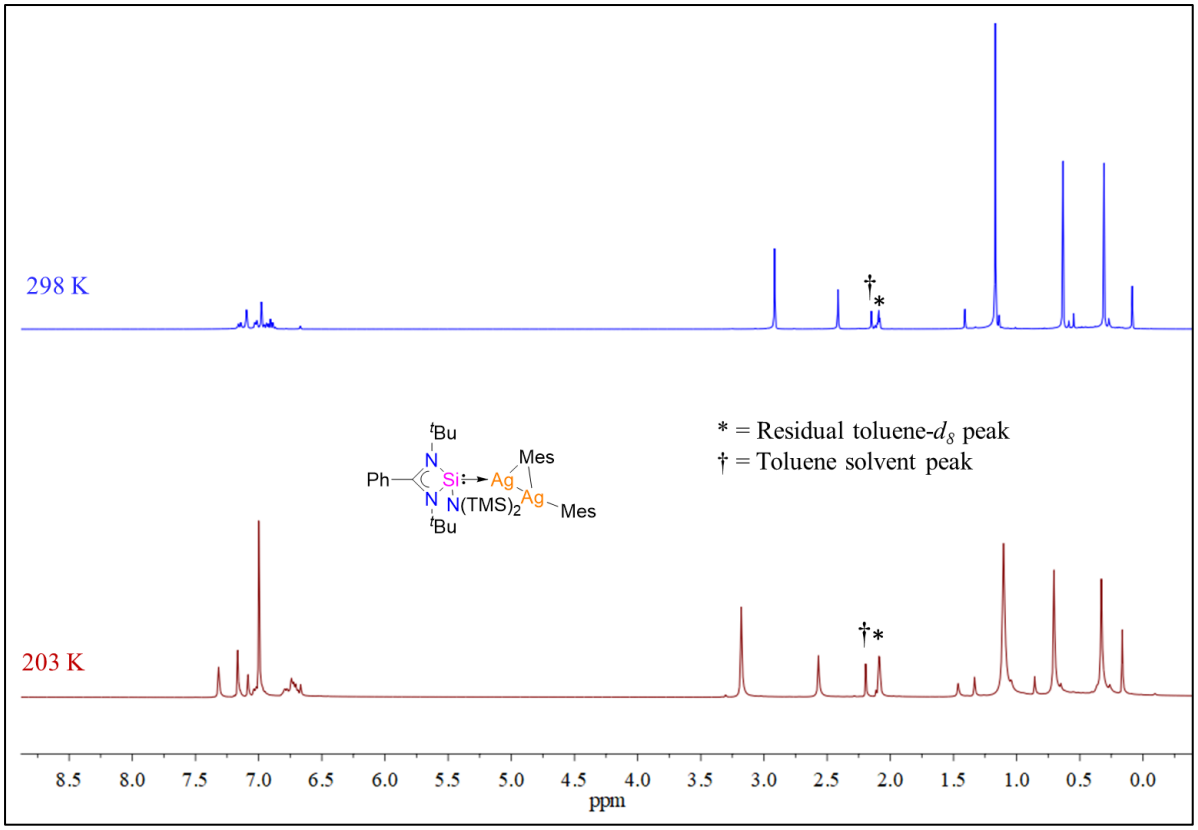

Figure 2D.A.51. Variable temperature ^{1}H NMR spectra of complex **2D.4** in toluene d_8.

2D.A.2 NMR spectra of C-C coupled products.

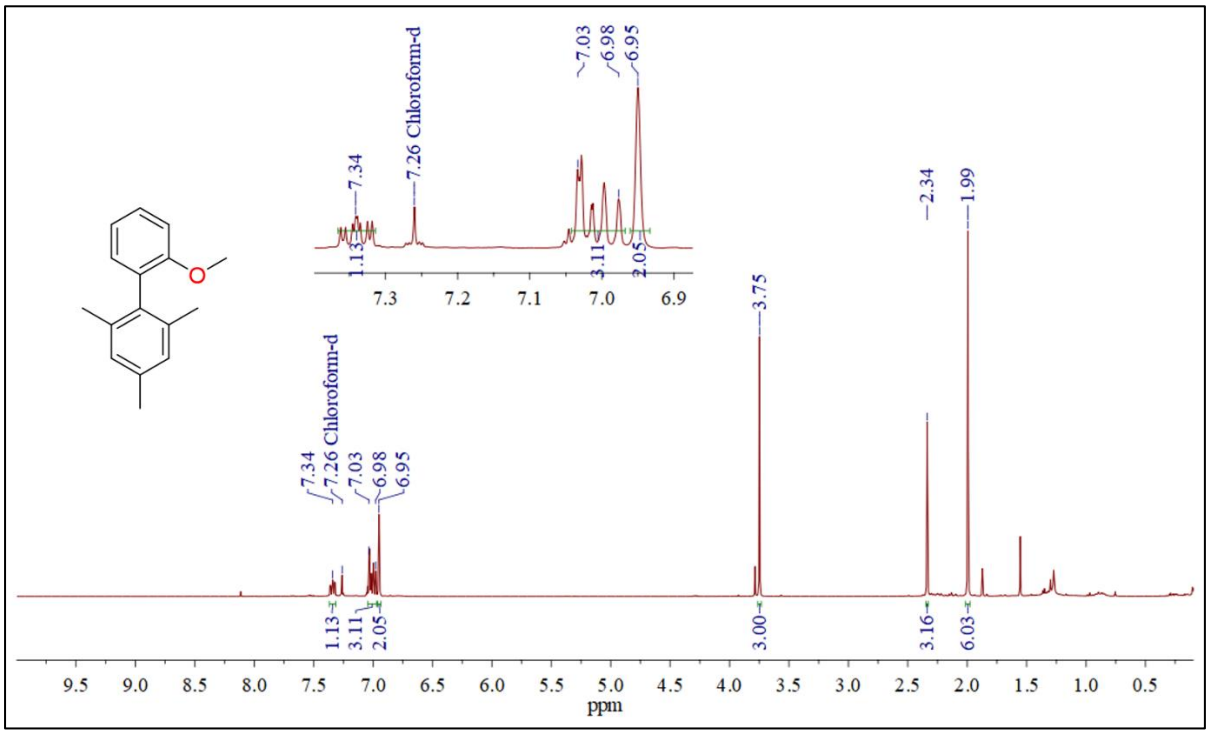

Figure 2D.A.52. ^{1}H NMR spectrum of complex **2D.I** in $CDCl_3$.

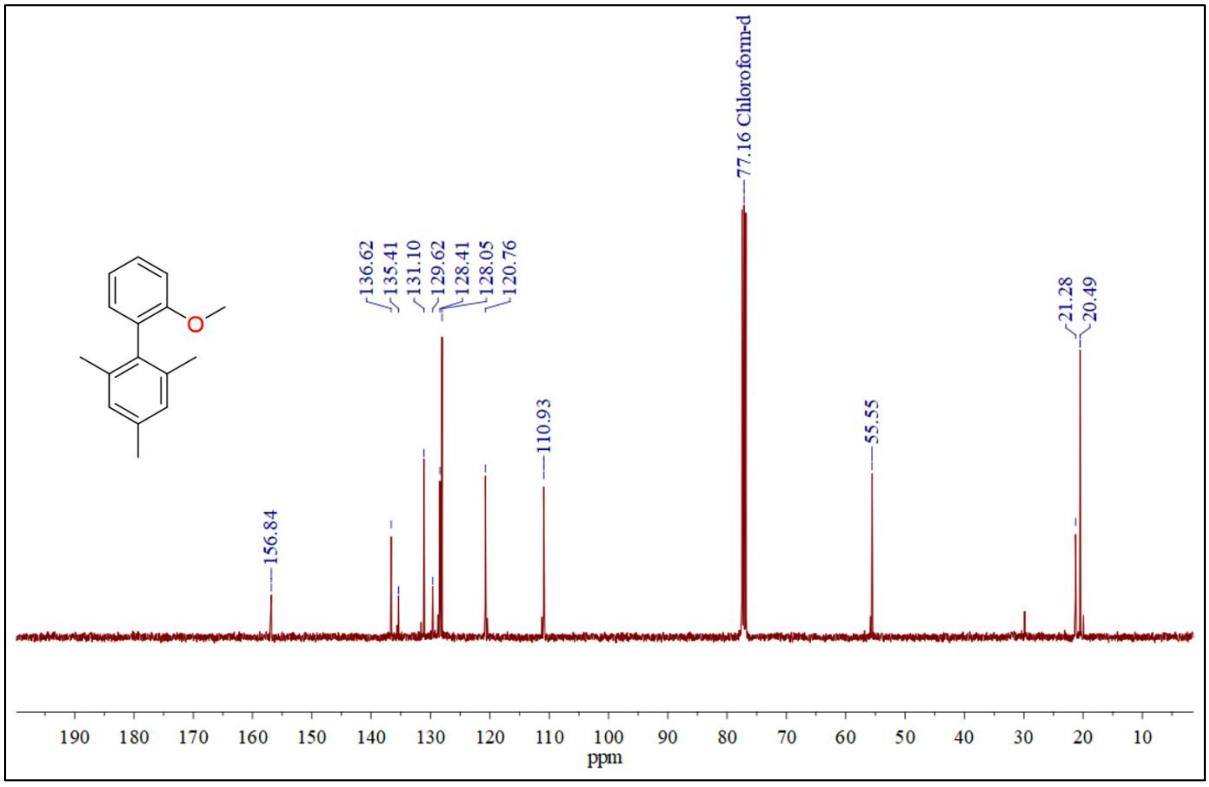

Figure 2D.A.53. $^{13}C\{^{1}H\}$ NMR spectrum of complex **2D.I** $CDCl_3$.

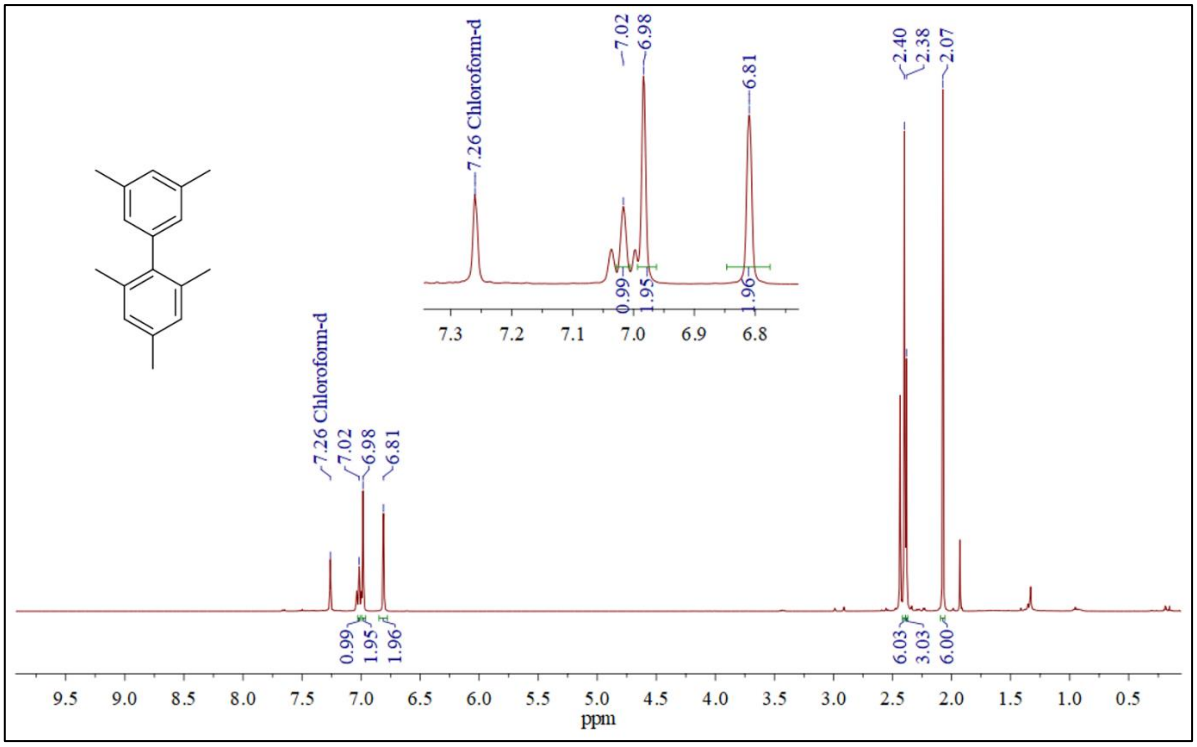

Figure 2D.A.54. ^{1}H NMR spectrum of complex **2D.II** $CDCl_3$.

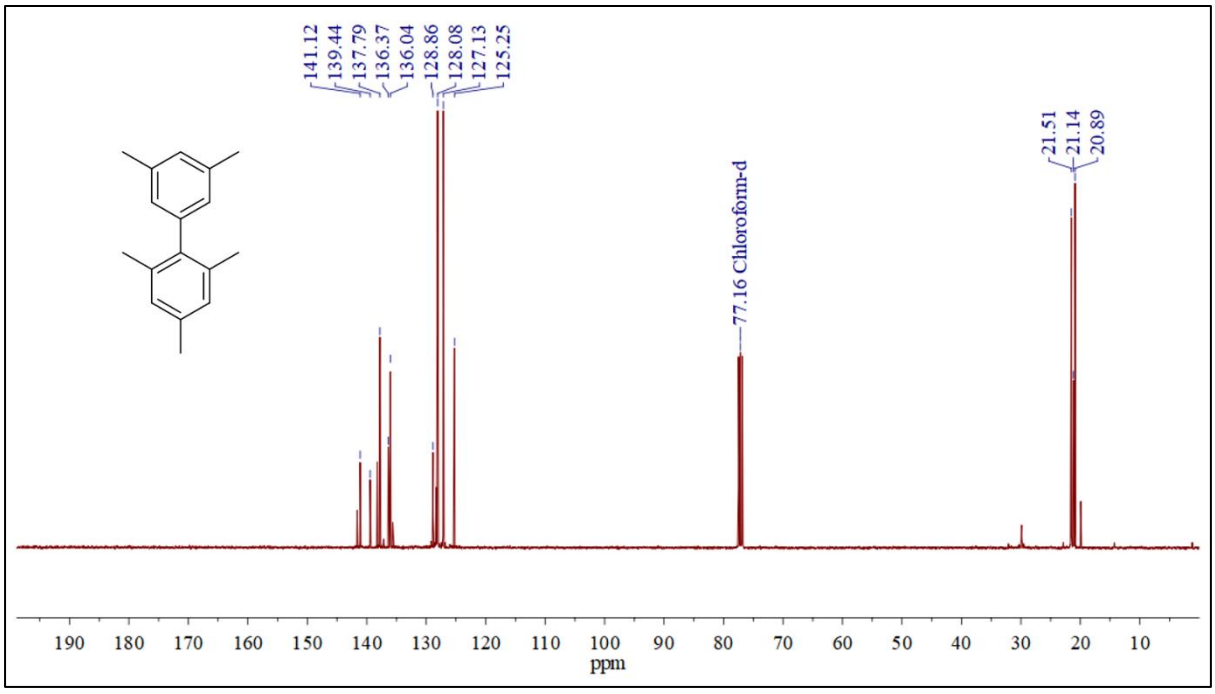

Figure 2D.A.55. ^{13}C{^{1}H} NMR spectrum of complex **2D.II** $CDCl_3$.

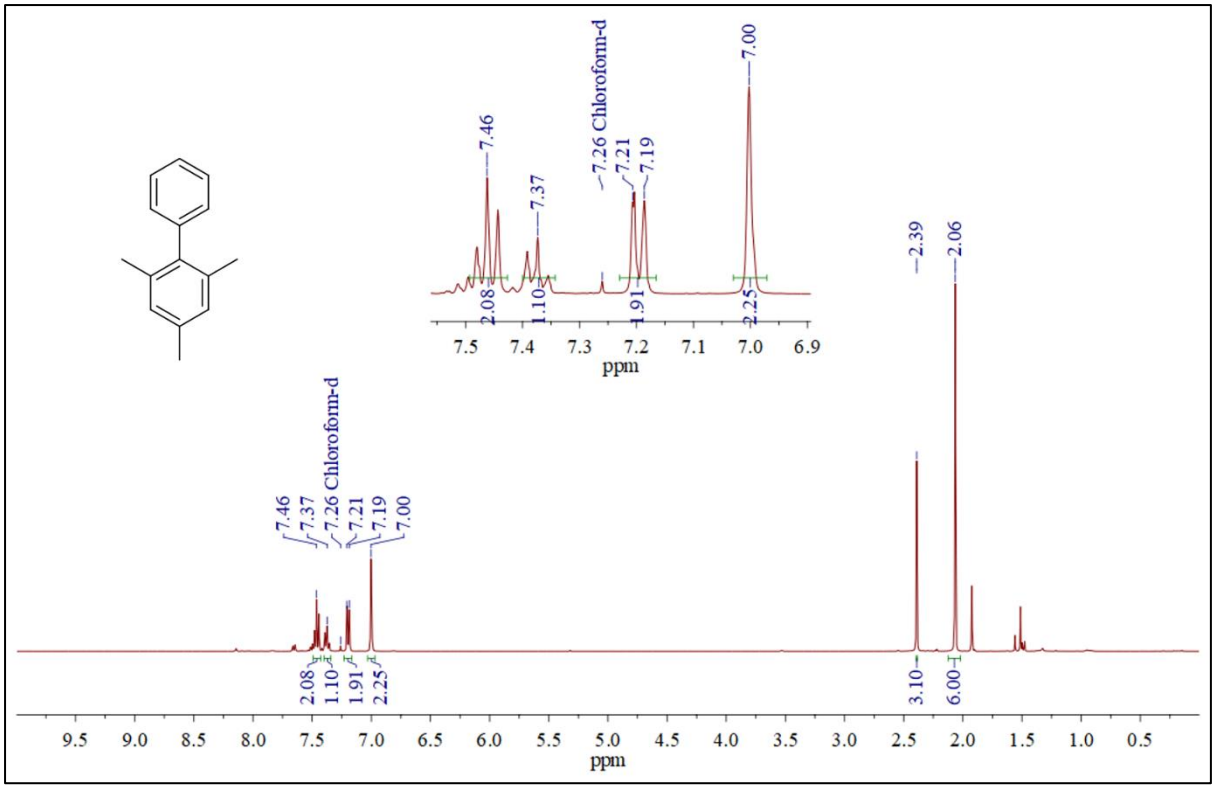

Figure 2D.A.56. ^{1}H NMR spectrum of complex **2D.III** $CDCl_3$.

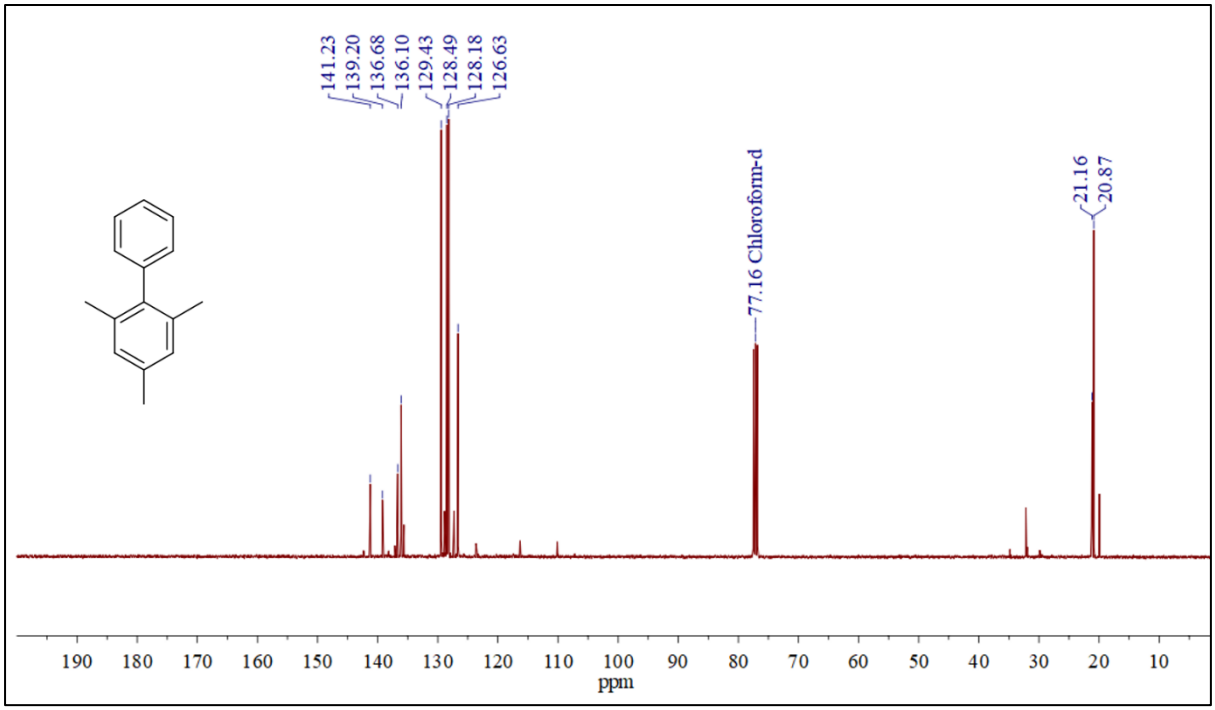

Figure 2D.A.57. ^{13}C{^{1}H} NMR spectrum of complex **2D.III** $CDCl_3$.

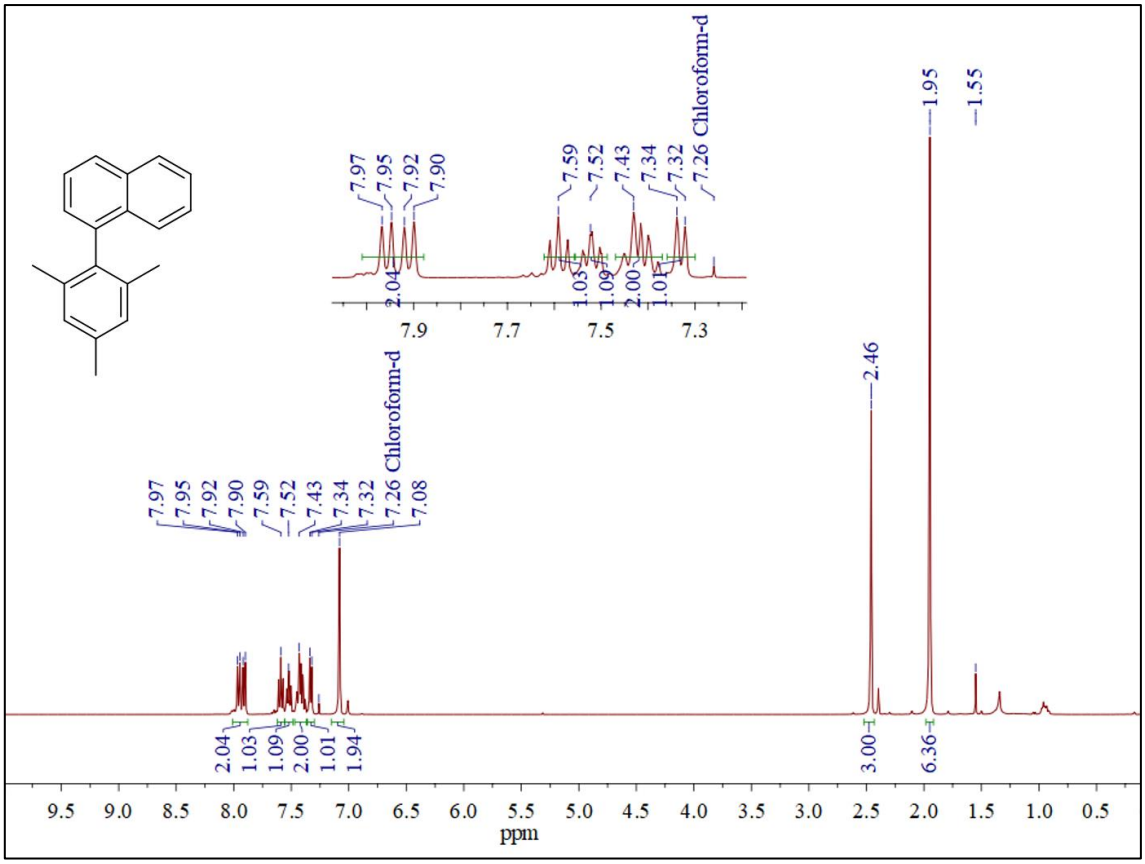

Figure 2D.A.58. ^{1}H NMR spectrum of complex **2D.IV** $CDCl_3$.

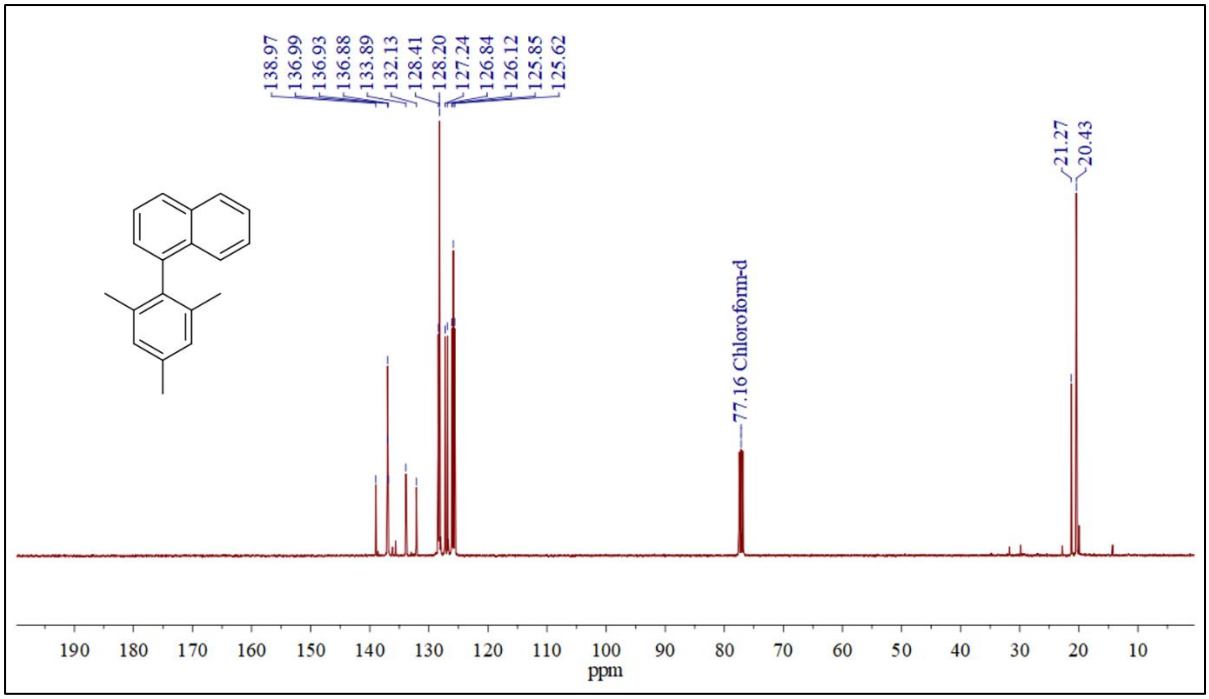

Figure 2D.A.59. $^{13}C\{^{1}H\}$ NMR spectrum of complex **2D.IV** $CDCl_3$.

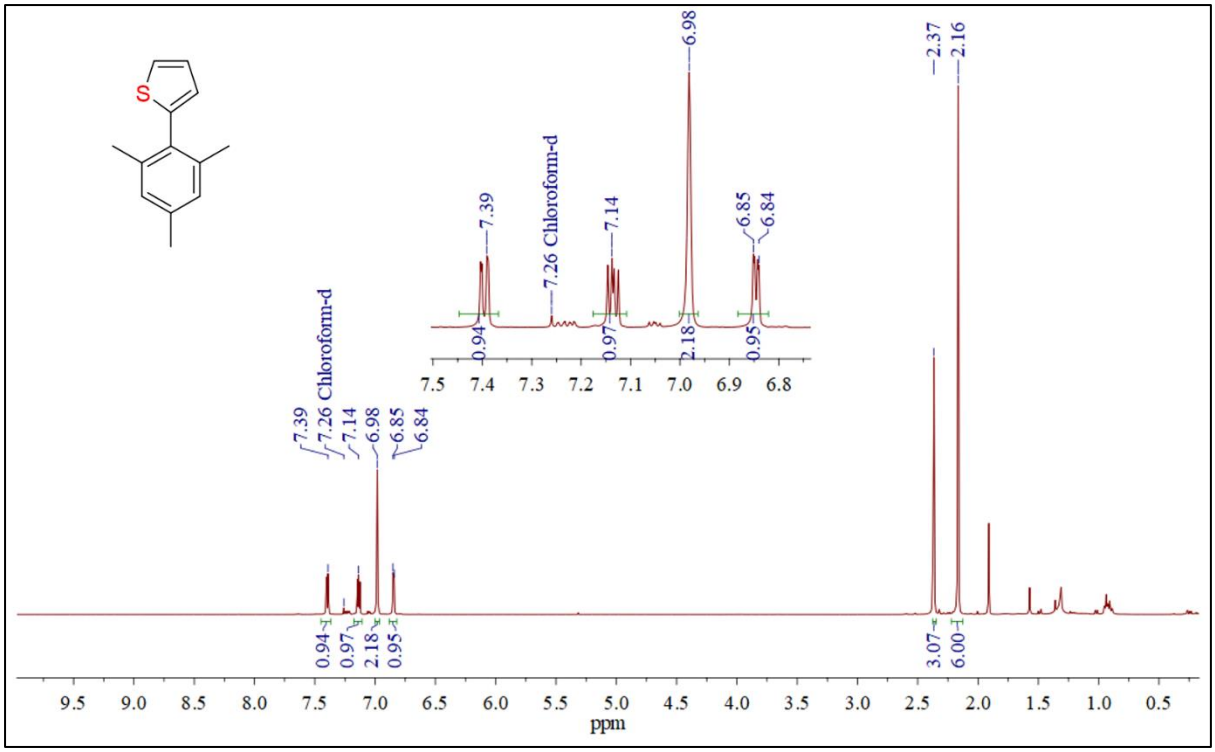

Figure 2D.A.60. ^{1}H NMR spectrum of complex **2D.V** in $CDCl_3$.

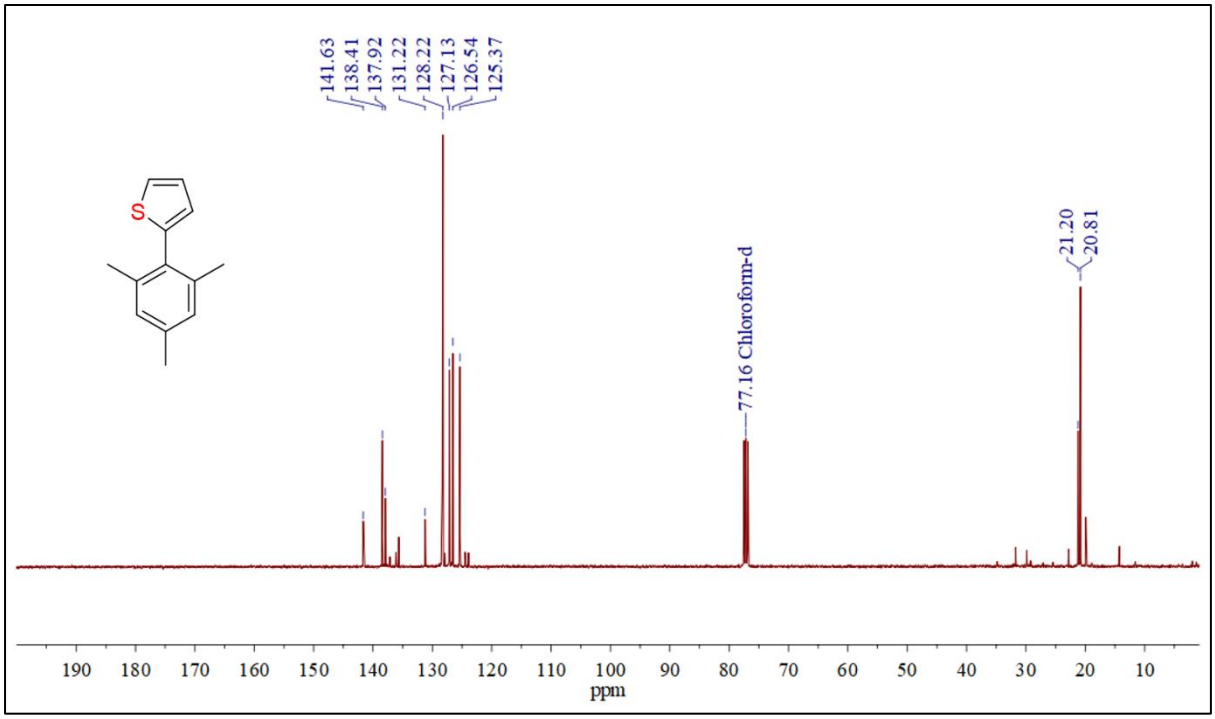

Figure 2D.A.61. $^{13}C\{^{1}H\}$ NMR spectrum of complex **2D.V** in $CDCl_3$.

2D.A.3 Crystallographic details of complexes 2D.2-2D.16.

Identification Code	**2D.2**	**2D.3**	**2D.4**	**2D.5**
Chemical formula	$C_{30}H_{52}CuN_3Si_3$	$C_{40}H_{64}CuN_3Si_3$	$C_{39}H_{63}Ag_2N_3Si_3$	$C_{48}H_{68}Cl_2Cu_2N_4Si_2$
Formula weight	602.55	734.75	873.93	955.22
Temperature	150 K	150 K	296 K	296 K
Wavelength	0.71703 Å	0.71703 Å	0.71703 Å	0.71703 Å
Crystal system	Monoclinic	Monoclinic	Triclinic	Monoclinic
Space group	*P* 1 2_1/c 1	*P* 1 2_1/c 1	*P* -1	*P* 1 2_1/n 1
Unit cell dimensions	*a*=8.7311(17) Å	*a*=21.7756(10) Å	*a*=10.0668(17) Å	*a*=10.1287(9) Å
	b=16.101(3) Å	*b*=9.2187(5) Å	*b*=12.265(2) Å	*b*=13.8838(14) Å
	c=24.398(4) Å	*c*=22.1281(12) Å	*c*=19.889(4) Å	*c*=17.7827(18) Å
	α=90°	*α*=90°	*α*=78.550(5)°	*α*=90°
	β=96.891 (6)°	*β*=102.979(2)°	*β*=77.056(5)°	*β*=94.649(3)°
	γ=90°	*γ*=90°	*γ*=65.830(4)°	*γ*=90°
Volume	3405.0(11)$Å^3$	4328.6(4)$Å^3$	2167.6(7) $Å^3$	2492.5(4) $Å^3$
Z	4	4	2	2
Density (calculated)	1.175 g/cm^3	1.127 g/cm^3	1.339 g/cm^3	1.273 g/cm^3
Absorption coefficient	0.769 mm^{-1}	0.616 mm^{-1}	1.015 mm^{-1}	1.044 mm^{-1}
F(000)	1296.0	1584.0	908.0	1008.0
Theta range for data collection	2.35 to 28.26°	2.40 to 28.23°	2.27 to 28.25°	2.30 to 25.80°
Index ranges	-11<=h<= 11, -21<=k<= 21, -32<=l<= 32	-29<=h<= 29, -12<=k<= 12, -29<=l<= 29	-13<=h<= 13, -16<=k<= 16, -26<=l<= 26	-12<=h<= 12, -16<=k<= 16, -21<=l<= 21
Reflections collected	139004	155660	110264	122744
Independent reflections	8516 [R(int) = 0.0965]	10866 [R(int) = 0.1030]	10769 [R(int) = 0.0590]	4387 [R(int) = 0.0786]

Coverage of independent reflections	99.9 %	99.5 %	99.7 %	100 %
Function minimized	Σ w $(Fo^2 - Fc^2)^2$	Σ w $(Fo^2 - Fc^2)^2$	Σ w $(Fo^2 - Fc^2)^2$	Σ w $(Fo^2 - Fc^2)^2$
Data/restraints/parameters	8516 / 0 / 350	10866 / 2 / 453	10769 / 0 / 443	4387 / 0 / 311
Goodness-of-fit on F^2	1.056	1.150	1.152	1.041
Δ/σ max	0.008	0.001	0.002	0.000
Final R indices	6835 data [I>2σ(I)], R1 = 0.0424, wR2 = 0.0811	7997 data [I>2σ(I)], R1 = 0.0537, wR2 = 0.1138	9118 data [I>2σ(I)], R1 = 0.0329, wR2 = 0.0738	3516 data [I>2σ(I)], R1 = 0.0572, wR2 = 0.1545
	all data, R1 = 0.0623, wR2 = 0.0885	all data, R1 = 0.0887, wR2 = 0.1332	all data, R1 =0.0457, wR2 = 0.0847	all data, R1 = 0.0746, wR2 = 0.1691
Largest diff. peak and hole	0.508 and -0.340 eÅ^{-3}	1.106 and -0.650 eÅ^{-3}	0.701 and -0.566 eÅ^{-3}	1.472 and -0.620 eÅ^{-3}
R.M.S. deviation from mean	0.071 eÅ^{-3}	0.147 eÅ^{-3}	0.158 eÅ^{-3}	0.104 eÅ^{-3}

Identification Code	**2D.6**	**2D.7**	**2D.9**	**2D.10**
Chemical formula	$C_{40}H_{73}BCuN_3O_4Si_3$	$C_{42}H_{76}B_2CuN_3O_4Si_3$	$C_{15}H_{15}BO_2$	$C_{31}H_{36}CuN_3SeSi_3$
Formula weight	818.63	856.50	238.08	677.40
Temperature	100 K	100 K	150 K	100 K
Wavelength	0.71703 Å	0.71703 Å	0.71703 Å	0.71703 Å
Crystal system	Monoclinic	Monoclinic	Orthorhombic	Monoclinic
Space group	*P* $12_1/c$ 1	*P*$2_1/n$	*Pnma*	*C* 12/c 1
Unit cell dimensions	*a*=14.128(5) Å	*a*=13.634(4) Å	*a*=23.369(4) Å	*a*=17.820(3) Å
	b=13.972(6) Å	*b*=27.708(9) Å	*b*=11.3535(19) Å	*b*=11.6656(17) Å

	c=24.447(10) Å	*c*=14.191(4) Å	*c*=4.5612(7) Å	*c*=31.588(5) Å
	α=90°	*α*=90°	*α*=90°	*α*=90°
	β=104.660(9)°	*β*=114.983(8)°	*β*=90°	*β*=97.787(4)°
	γ=90°	*γ*=90°	*γ*=90°	*γ*=90°
Volume	4669(3) $Å^3$	4859(3) $Å^3$	1210.2(3) $Å^3$	6506.2(16) $Å^3$
Z	4	4	4	8
Density (calculated)	1.165 g/cm^3	1.171 g/cm^3	1.307 g/cm^3	1.383 g/cm^3
Absorption coefficient	0.584 mm^{-1}	0.563 mm^{-1}	0.084 mm^{-1}	1.925 mm^{-1}
F(000)	1768.0	1848.0	504.0	2784.0
Theta range for data collection	2.45 to 16.93°	2.160 to 24.999°	2.50 to 28.27°	2.24 to 26.88°
Index ranges	-16<=h<= 16, -16<=k<= 16, -29<=l<= 29	-16<=h<= 16, -32<=k<= 32, -16<=l<= 16	-31<=h<= 31, -15<=k<= 15, -6<=l<= 6	-24<=h<= 24, -15<=k<= 15, -42<=l<= 42
Reflections collected	48933	103206	29948	139356
Independent reflections	8222 [R(int) = 0.6213]	8544 [R(int) = 0.3230]	1570 [R(int) = 0.0575]	8370 [R(int) = 0.1098]
Coverage of independent reflections	99.9 %	99.9 %	99.3 %	99 %
Function minimized	Σ w (Fo^2 - Fc^2)^2	Σ w (Fo^2 - Fc^2)^2	Σ w (Fo^2 - Fc^2)^2	Σ w (Fo^2 - Fc^2)^2
Data / restraints / parameters	8222 / 0 / 490	8544 / 0 / 520	1570/0/90	8370 / 0 / 364
Goodness-of-fit on F^2	0.988	1.009	1.101	1.030
Δ/σ max	0.000	0.001	0.000	0.001
Final R indices	2532 data [I>2σ(I)], R1 = 0.1109, wR2 = 0.1719	4644 data [I>2σ(I)], R1 = 0.0669, wR2 = 0.0880	1310 data [I>2σ(I)], R1 = 0.0439, wR2 =0.0975	5040 data [I>2σ(I)], R1 = 0.1030, wR2 = 0.2301

	all data, R1 =0.3484, wR2 = 0.2543	all data, R1 = 0.1662, wR2 = 0.1122	all data, R1 =0.0560, wR2 =0.1028	all data, R1 = 0.1720, wR2 = 0.2767
Largest diff. peak and hole	0.402 and -0.656 eÅ^{-3}	0.460 and -0.473 eÅ^{-3}	0.261 and -0.272 eÅ^{-3}	1.425 and -2.007 eÅ^{-3}
R.M.S. deviation from mean	0.098 eÅ^{-3}	0.098 eÅ^{-3}	0.050 eÅ^{-3}	0.156 eÅ^{-3}

Identification Code	**2D.11**	**2D.13**	**2D.14**	**2D.15**	**2D.16**
Chemical formula	$C_{60}H_{104}Cu_2N_6Se_2Si_6$	$C_{34}H_{55}CuN_4Si_3$	$C_{33}H_{41}CuF_{10}N_4Si_3$	$C_{35}H_{56}CuN_5Si_3$	$C_{46}H_{76}CuN_5Si_3$
Formula weight	1363.03	667.63	831.51	694.65	846.92
Temperature	150 K	100 K	150 K	150 K	150 K
Wavelength	0.71703 Å	0.71703 Å	0.71703 Å	0.71703 Å	0.71703 Å
Crystal system	Monoclinic	Triclinic	Monoclinic	Monoclinic	Monoclinic
Space group	*P*2$_1$/*n*	*P* -1	*P* 1 2$_1$/n 1	*P* 1 2$_1$/c 1	*C* 1 c 1
Unit cell dimensions	*a*=16.060(3) Å	*a*=12.8772(11) Å	*a*=14.938(3) Å	*a*=11.5755(12) Å	*a*=17.1666(19) Å
	b=9.6579(15) Å	*b*=13.0612(11) Å	*b*=13.376(2) Å	*b*=14.9774(16) Å	*b*=13.5100(15) Å
	c=22.092(4) Å	*c*=14.7699(13) Å	*c*=19.384(4) Å	*c*=22.191(2) Å	*c*=22.268(3) Å
	α=90°	*α*=70.646(3)°	*α*=90°	*α*=90°	*α*=90°

	β=91.670(5)°	β=75.242(3)°	β=105.935(5)°	β=90.984(3)°	β=102.071(3)°
	γ=90°	γ=60.717(2)°	γ=90°	γ=90°	γ=90°
Volume	3425.1(10) Å^3	2031.3(3) Å^3	3724.3(12) Å^3	3846.7(7) Å^3	5050.3(10) Å^3
Z	2	2	4	4	4
Density (calculated)	1.322 g/cm^3	1.092 g/cm^3	1.483 g/cm^3	1.199 g/cm^3	1.114 g/cm^3
Absorption coefficient	1.828 mm^{-1}	0.651 mm^{-1}	0.763 mm^{-1}	0.691 mm^{-1}	0.537 mm^{-1}
F(000)	1432.0	716.0	1712.0	1488.0	1832.0
Theta range for data collection	3.092 to 57.732°	2.47 to 28.31°	2.014 to 24.999°	2.39 to 28.26°	2.26 to 27.38°
Index ranges	-21<=h<= 21, -12<=k<= 12, -29<=l<= 29	-17<=h<= 17, -17<=k<= 17, -19<=l<= 19	-17<=h<= 17, -15<=k<= 15, -23<=l<= 23	-15<=h<= 15, -19<=k<= 19, -29<=l<= 29	-22<=h<= 22, -18<=k<= 18, -29<=l<= 29
Reflections collected	156003		108936	44646	116056
Independent reflections	8819 [R(int) = 0.0801, R(sigma)= 0.0320]	10170 [R(int) = 0.0652]	6551 [R(int) = 0.2102]	9290 [R(int) =0.0915]	12644 [R(int) = 0.1001]
Coverage of independent	98.2 %	99.6 %	100 %	96.8 %	100 %

reflections					
Function minimized	Σ w $(Fo^2 - Fc^2)^2$	Σ w $(Fo^2 - Fc^2)^2$	Σ w $(Fo^2 - Fc^2)^2$	Σ w $(Fo^2 - Fc^2)^2$	Σ w $(Fo^2 - Fc^2)^2$
Data / restraints / parameters	8819 / 0 / 551	10170 / 0 / 394	6551 / 0 / 472	9290 / 0 / 413	12644 / 2 / 517
Goodness-of-fit on F^2	1.068	1.025	1.043	1.067	1.030
Δ/σ max	0.001	0.001	0.000	0.001	0.001
Final R indices	7627 data [$I>2\sigma(I)$], R1 = 0.0285, wR2 = 0.0624	8019 data [$I>2\sigma(I)$], R1 = 0.0376, wR2 = 0.0868	4248 data [$I>2\sigma(I)$], R1 = 0.0606, wR2 = 0.0933	6711 data [$I>2\sigma(I)$], R1 =0.0584, wR2 = 0.1055	10448 data [$I>2\sigma(I)$], R1 = 0.0408, wR2 = 0.0846
	all data, R1 = 0.0386, wR2 = 0.0671	all data, R1 = 0.0554, wR2 = 0.0945	all data, R1 = 0.1140, wR2 = 0.1091	all data, R1 = 0.0966, wR2 = 0.1177	all data, R1 = 0.0598, wR2 = 0.0917
Largest diff. peak and hole	0.55 and -0.47 $eÅ^{-3}$	0.521 and -0.435 $eÅ^{-3}$	0.600 and -0.698 $eÅ^{-3}$	0.505 and -0.426 $eÅ^{-3}$	0.644 and -0.510 $eÅ^{-3}$
R.M.S. deviation from mean	0.071 $eÅ^{-3}$	0.056 $eÅ^{-3}$	0.090 $eÅ^{-3}$	0.084 $eÅ^{-3}$	0.054 $eÅ^{-3}$

Table 2D.A.1. Relevant geometrical parameters of various complexes

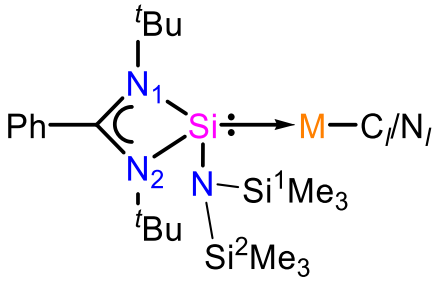

	2D.2	**2D.3**	**2D.4**	**2D.6**	**2D.13**	**2D.14**	**2D.15**	**2D.16**
Si-M	2.2583	2.2513	2.3838	2.2029	2.2217	2.2237	2.2073	2.2014
M-C_{ipso}/N_{amide}/$O_{ligand1}$	1.9578	1.9608	2.2220	2.0979	1.8951	1.9442	1.9187	1.9031
M- C_{ipso}/N_{amide}/$O_{ligand2}$	-	-	-	2.0798	-	-	-	-
Si-M-C_{ipso}/N_{amide}/$O_{ligand1}$	171.39	172.00	178.13	141.70	168.95	165.23	168.12	174.18
Si-M-C_{ipso}/N_{amide}/$O_{ligand2}$	-	-	-	147.30	-	-	-	-
Si-N1	1.8581	1.8597	1.8435	1.8677	1.8477	1.8483	1.8589	1.8521
Si-N2	1.8610	1.8575	1.8469	1.8596	1.8564	1.8520	1.8527	1.8533
N1-Si-N2	70.25	70.29	70.85	70.14	70.62	70.68	70.44	70.59
N1-Si-M	111.03	109.08	109.58	108.54	115.77	112.17	106.27	109.45
N2-Si-M	108.56	110.27	107.39	117.15	106.13	108.13	114.29	110.05
Si-N_{TMS}	1.7377	1.7366	1.7311	1.7372	1.7323	1.7278	1.7323	1.7279
N_{TMS}-Si-N1	112.24	113.38	113.77	114.47	112.93	113.08	113.57	114.64
N_{TMS}-Si-N2	113.03	112.73	114.16	110.29	114.03	113.92	112.87	114.11
N_{TMS}-Si-M	127.46	127.07	127.19	123.94	124.40	125.71	125.75	125.18
N_{TMS}-Si1	1.7808	1.7815	1.7814	1.7836	1.7827	1.7858	1.7851	1.7895
N_{TMS}-Si2	1.7598	1.7601	1.7666	1.7621	1.7636	1.7646	1.7606	1.7617

M-M	-	-	2.8195	-	-	-	-	-
F-M	-	-	-	-	-	2.6907	-	-
F-M	-	-	-	-	-	3.0693	-	-
N_{Py}-M	-	-	-	-	-	-	2.6706	-
$N_{formamidine}$-M	-	-	-	-	-	-	-	2.7123

	2D.5		**2D.10**	
	unit 1	**unit 2**	**unit 1**	**unit 2**
Si-M	2.2184	2.2233	2.2556	2.2556
M-Cl1/Se1	2.4129	2.2692	2.5297	2.5297
M-Cl2/Se2	2.3018	2.5804	2.4630	2.4630
Si-M-Cl1/Se1	126.99	154.09	130.02	130.02
Si-M-Cl2/Se2	131.65	108.78	137.06	137.06
Si-N1	1.8537	1.8575	1.8634	1.8634
Si-N2	1.8605	1.8571	1.8660	1.8660
N1-Si-N2	70.26	70.22	70.04	70.04
N1-Si-M	117.38	116.03	108.28	108.28
N2-Si-M	111.49	112.14	113.07	113.07
Si-N_{TMS}	-	-	1.7433	1.7433
N_{TMS}-Si-N1	-	-	111.53	111.53
N_{TMS}-Si-N2	-	-	111.27	111.27
N_{TMS}-Si-M	-	-	127.87	127.87
N_{TMS}-Si1	-	-	1.7774	1.7774
N_{TMS}-Si2	-	-	1.7587	1.7587
M-M	2.7424		2.8874	

3.A.1 NMR spectra of compounds 3.II, 3.III, 3.2-3.6, 3.8, and 3.9.

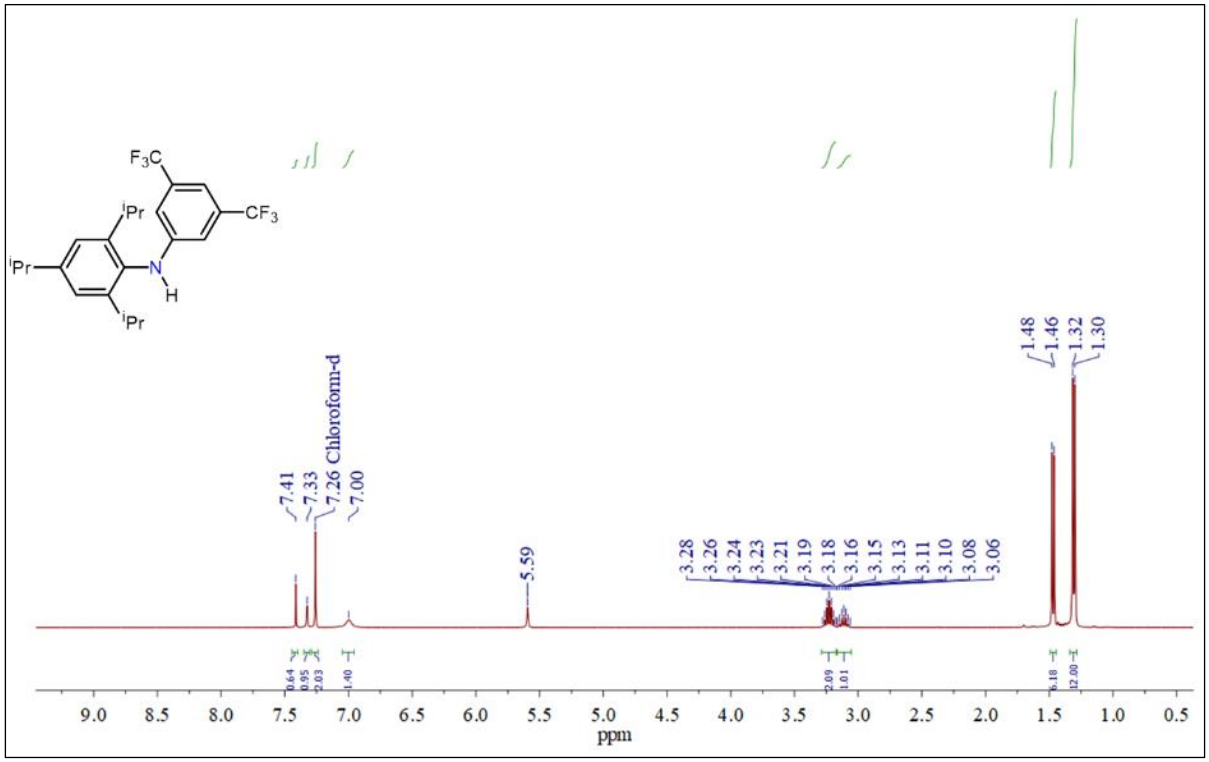

Figure 3.A.1. ^{1}H NMR spectrum of complex **3.II** in $CDCl_3$.

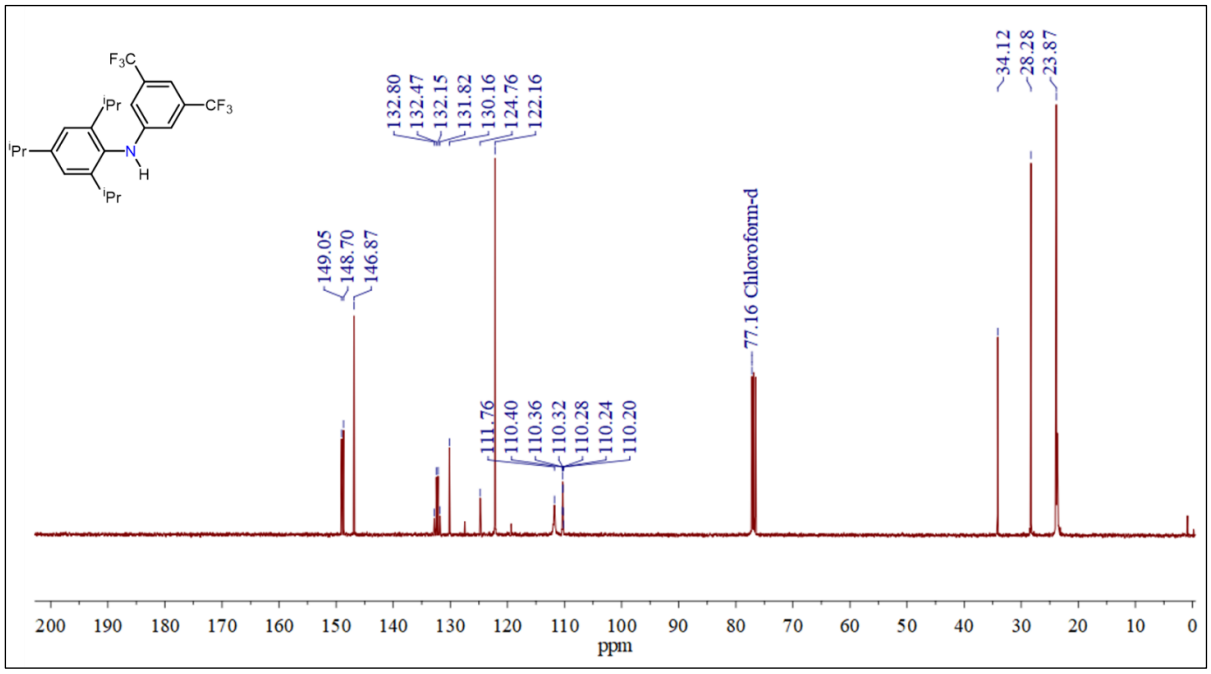

Figure 3.A.2. ^{13}C NMR spectrum of complex **3.II** in $CDCl_3$.

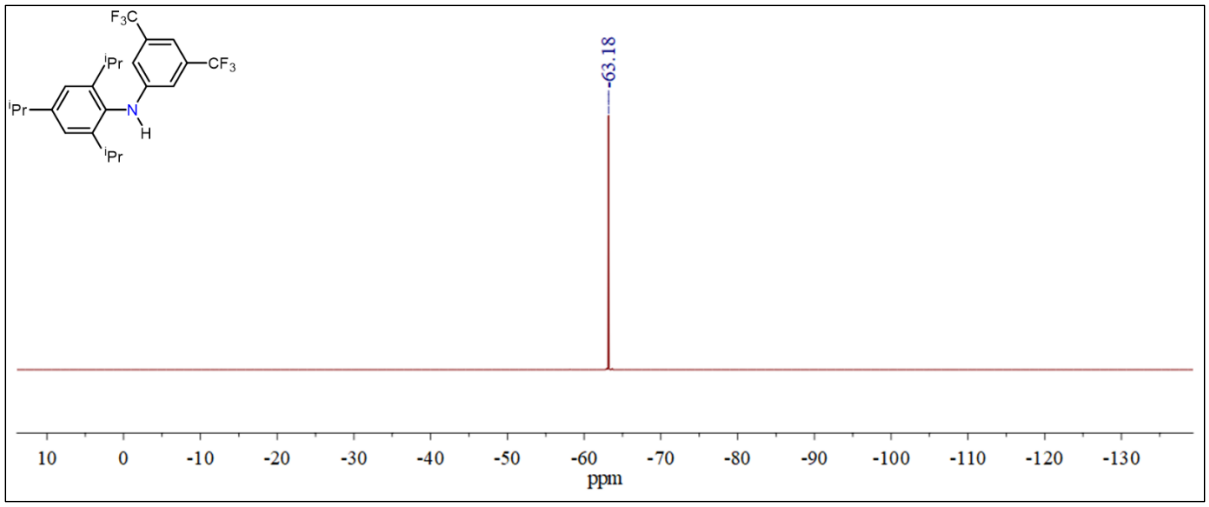

Figure 3.A.3. ^{19}F NMR spectrum of complex **3.II** in $CDCl_3$.

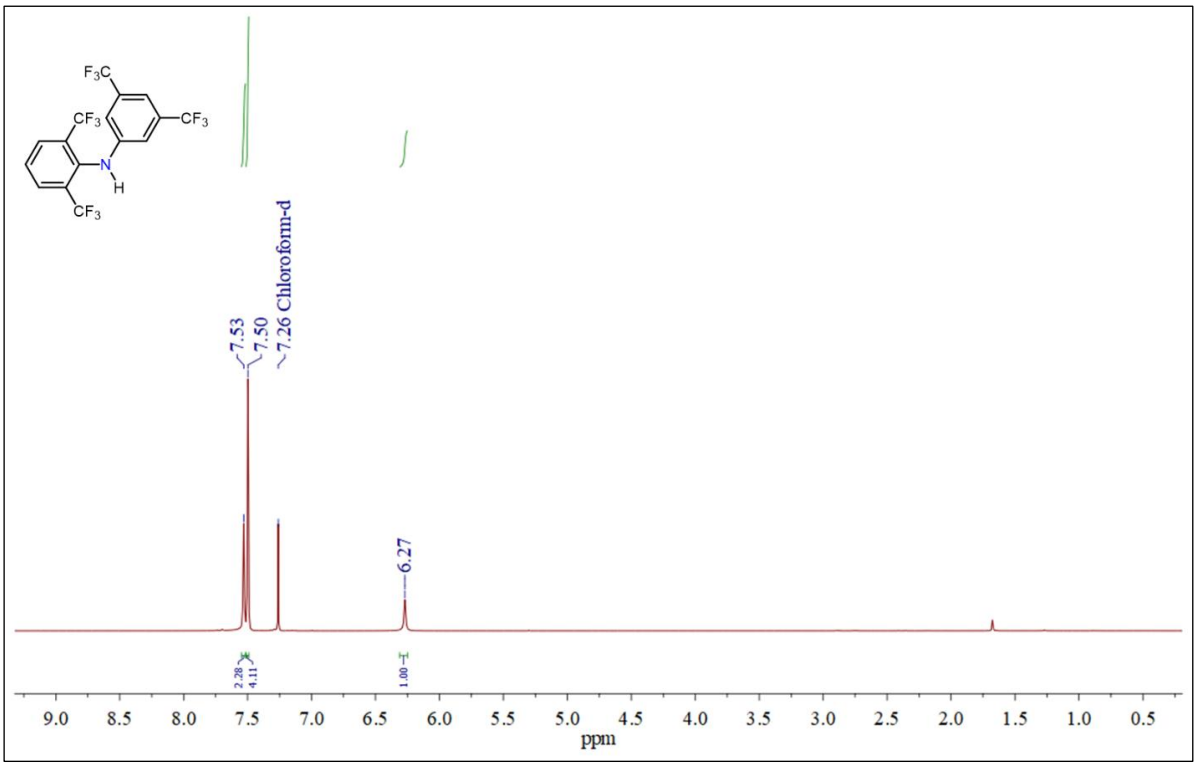

Figure 3.A.4. ^{1}H NMR spectrum of complex **3.III** in $CDCl_3$.

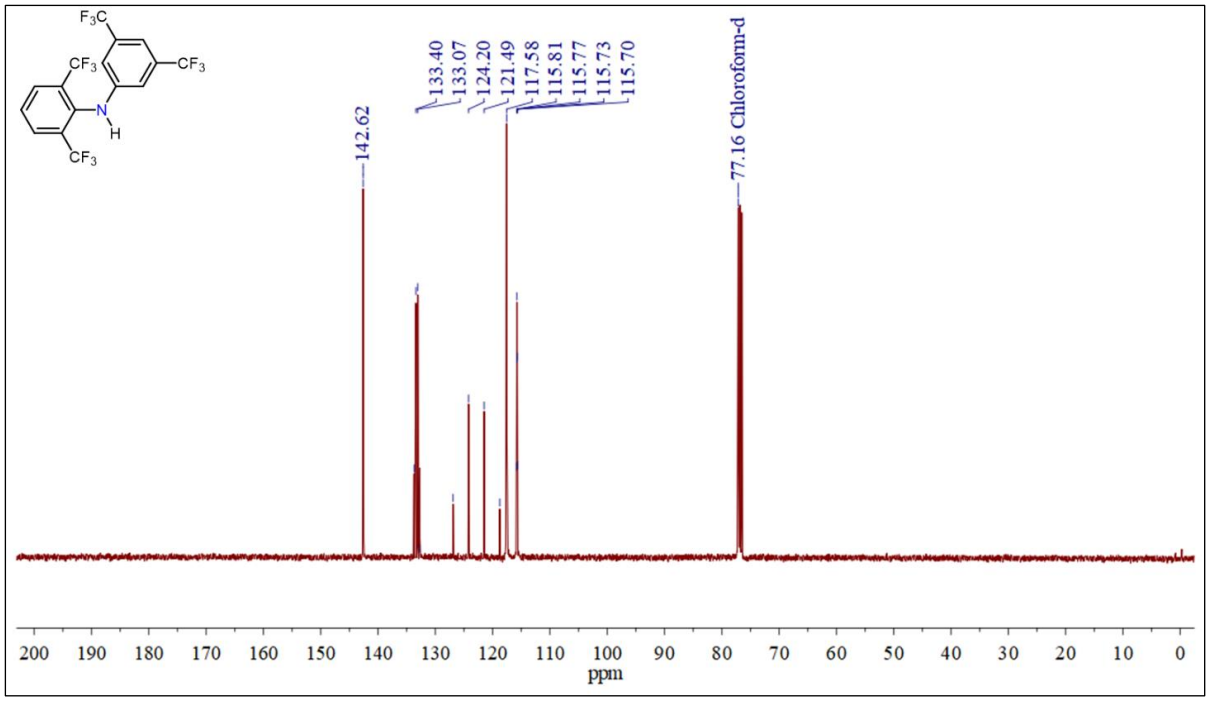

Figure 3.A.5. ^{13}C NMR spectrum of complex **3.III** in $CDCl_3$.

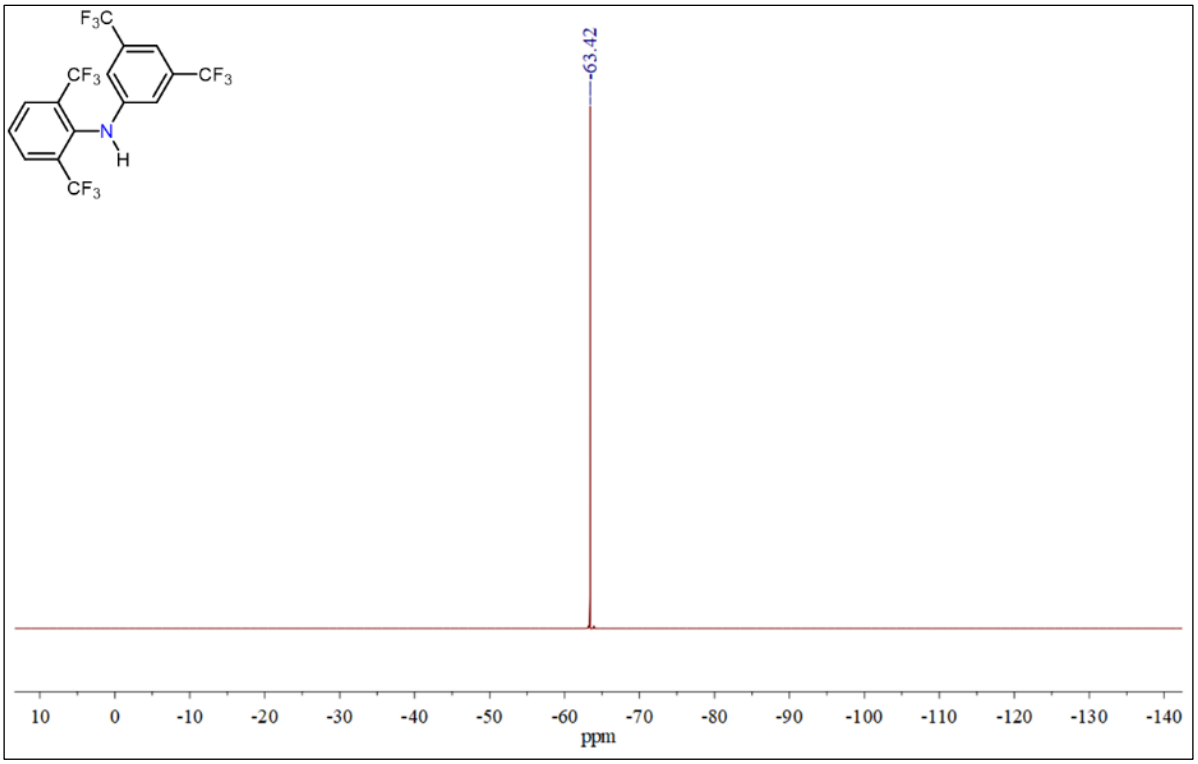

Figure 3.A.6. ^{19}F NMR spectrum of complex **3.III** in $CDCl_3$.

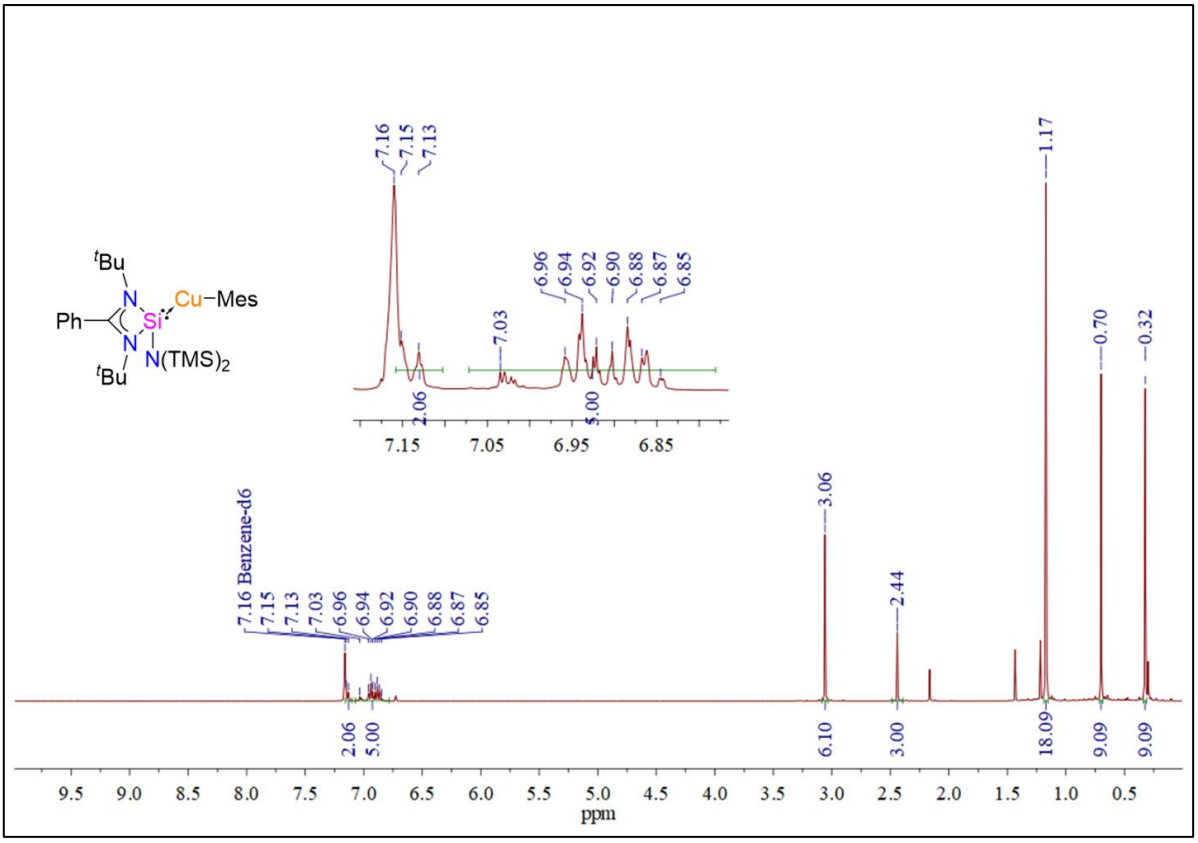

Figure 3.A.7. ^{1}H NMR spectrum of complex **3.1** in C_6D_6.

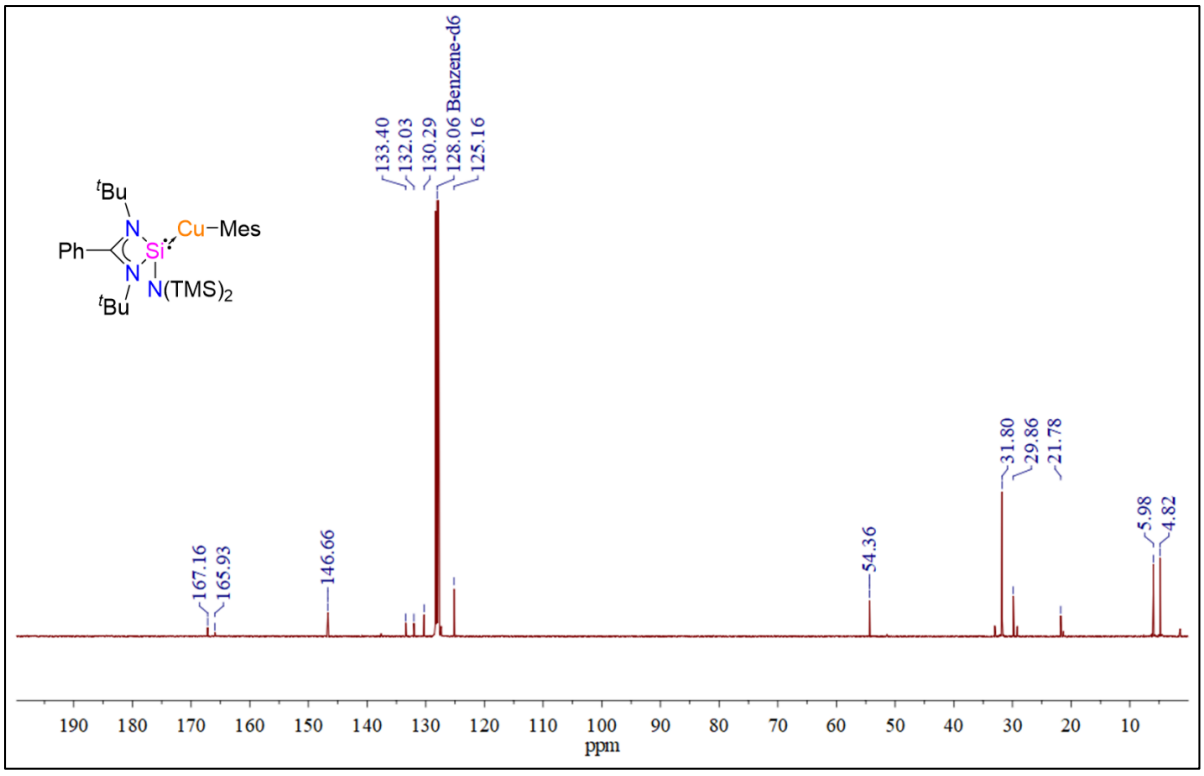

Figure 3.A.8. $^{13}C\{^{1}H\}$ NMR spectrum of complex **3.1** in C_6D_6.

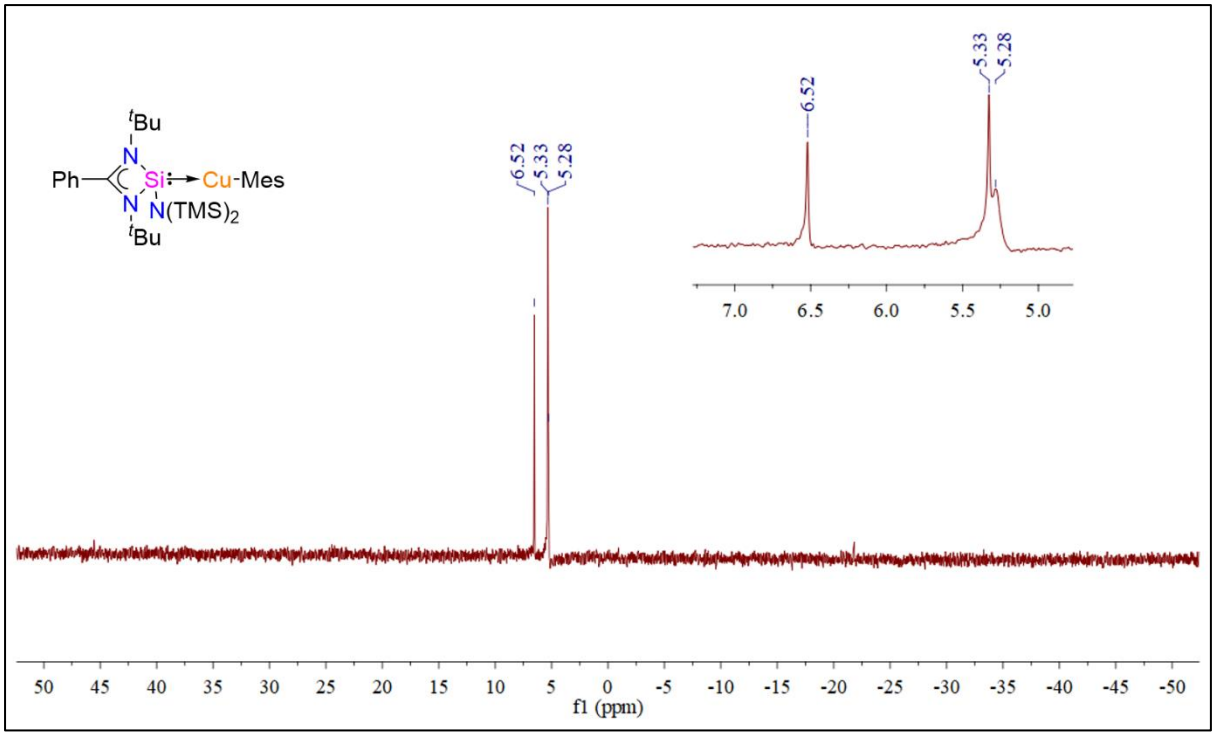

Figure 3.A.9. $^{29}Si\{^{1}H\}$ NMR spectrum of complex **3.1** in C_6D_6.

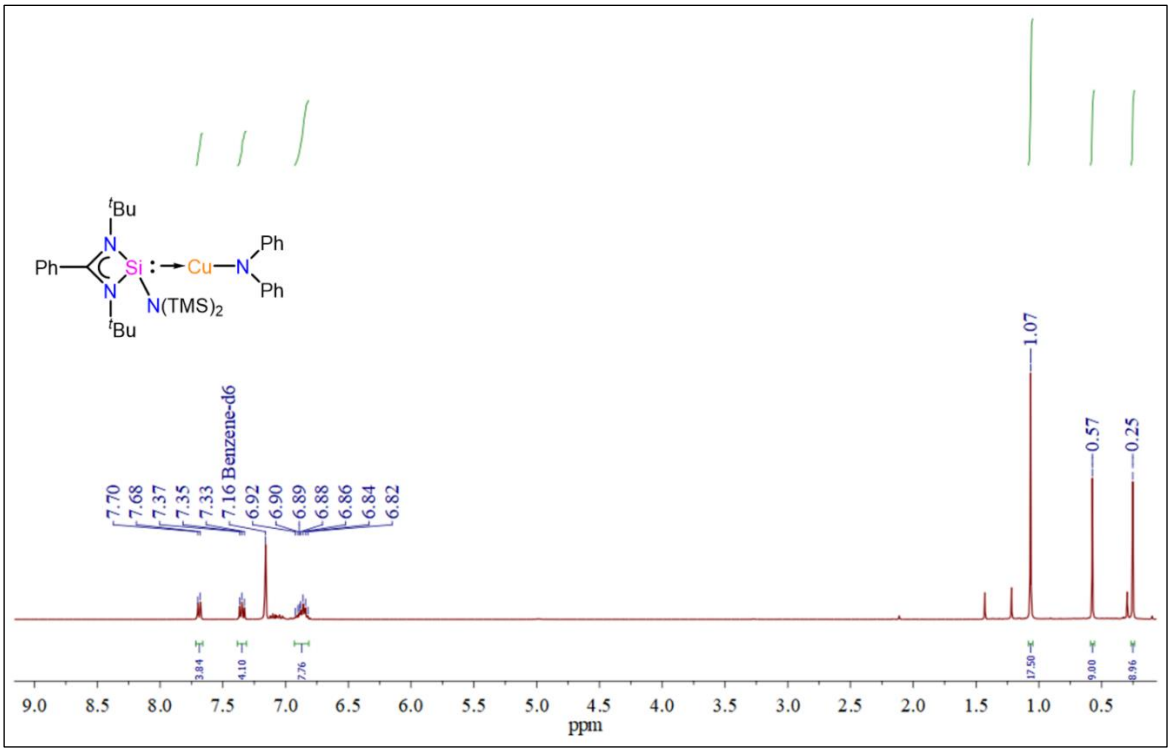

Figure 3.A.10. ^{1}H NMR spectrum of complex **3.2** in C_6D_6.

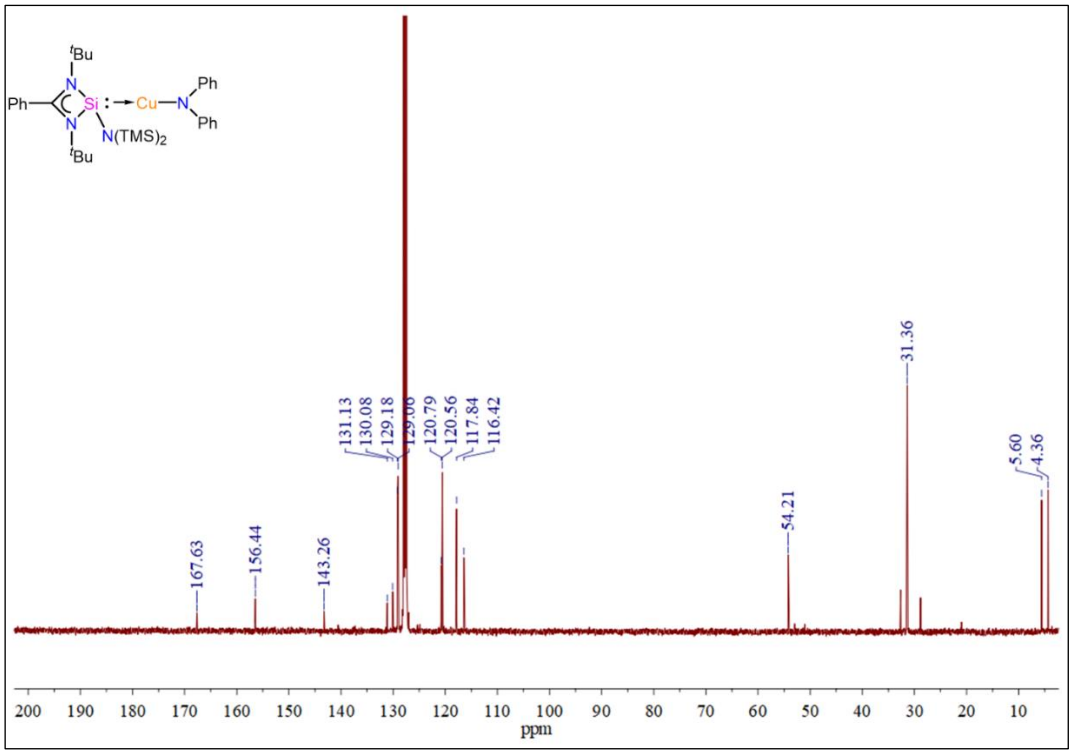

Figure 3.A.11. ^{13}C NMR spectrum of complex **3.2** in C_6D_6.

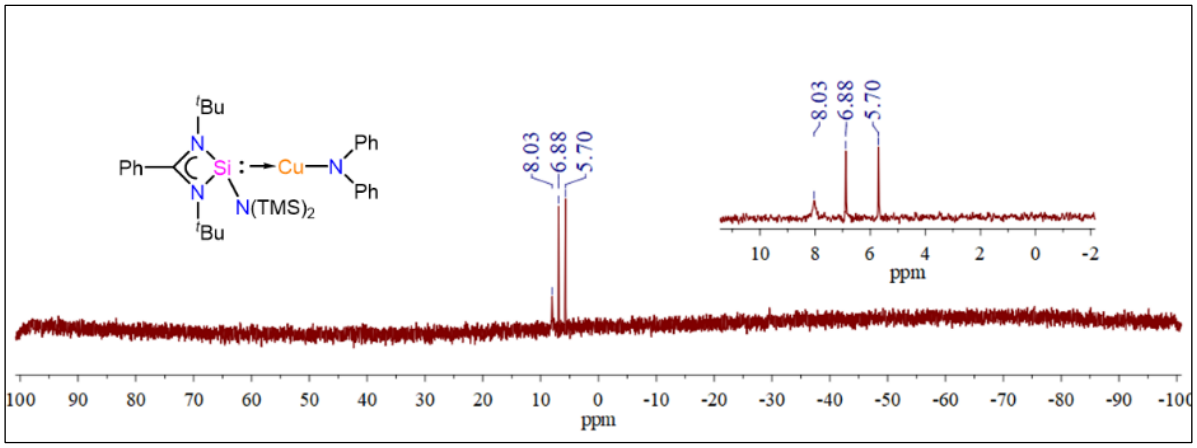

Figure 3.A.12. $^{29}Si\{^1H\}$ NMR spectrum of complex **3.2** in C_6D_6.

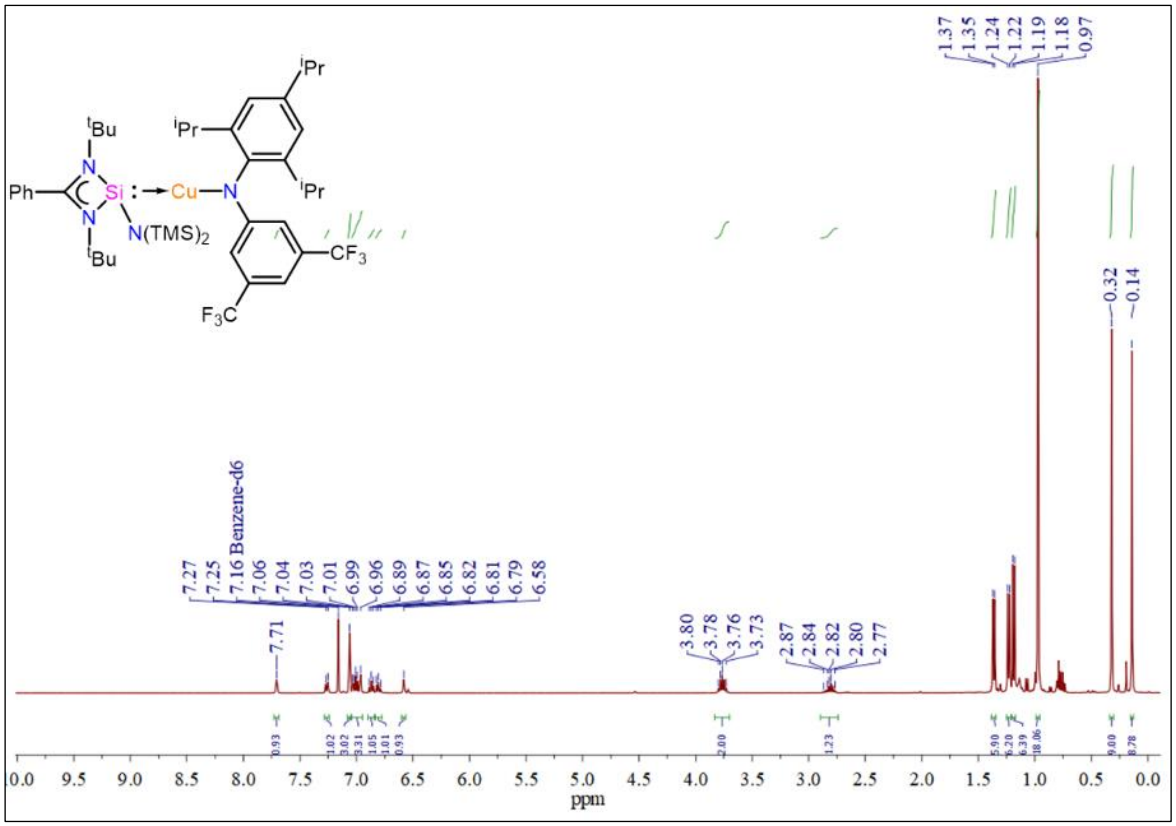

Figure 3.A.13. ^{1}H NMR spectrum of complex **3.3** in C_6D_6.

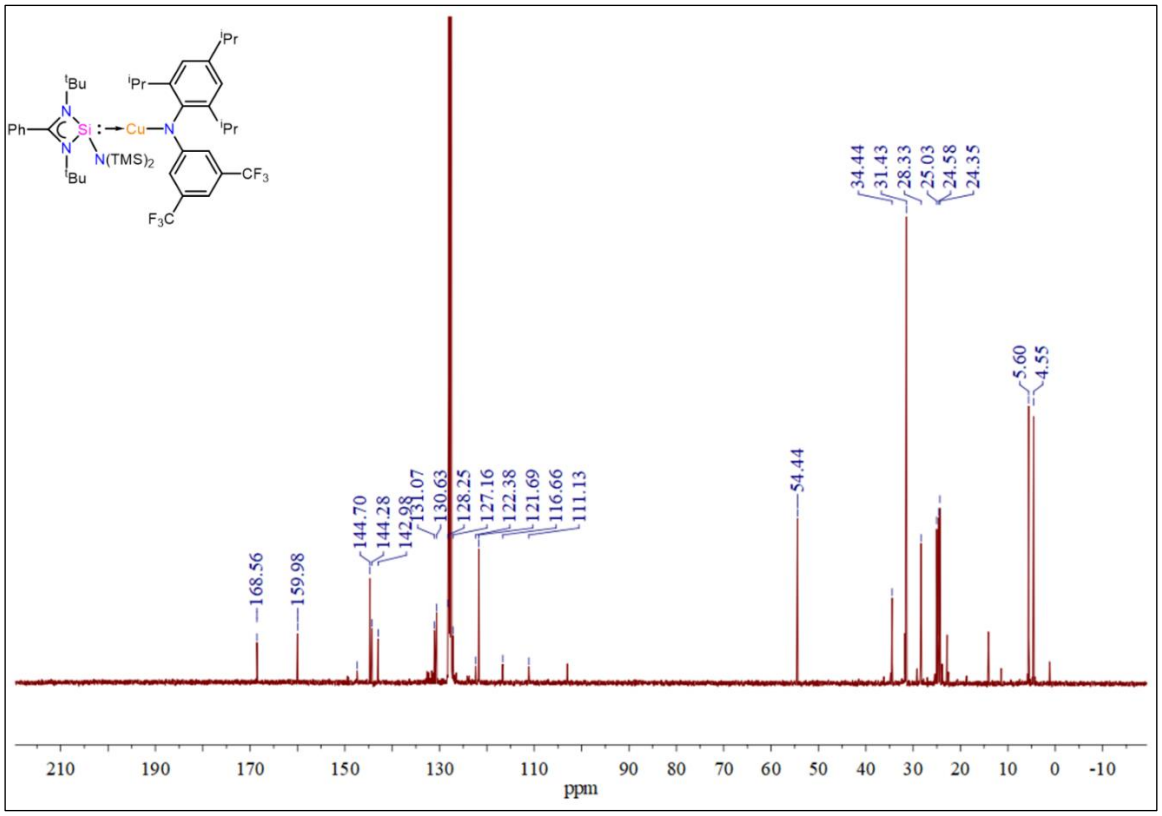

Figure 3.A.14. ^{13}C NMR spectrum of complex **3.3** in C_6D_6.

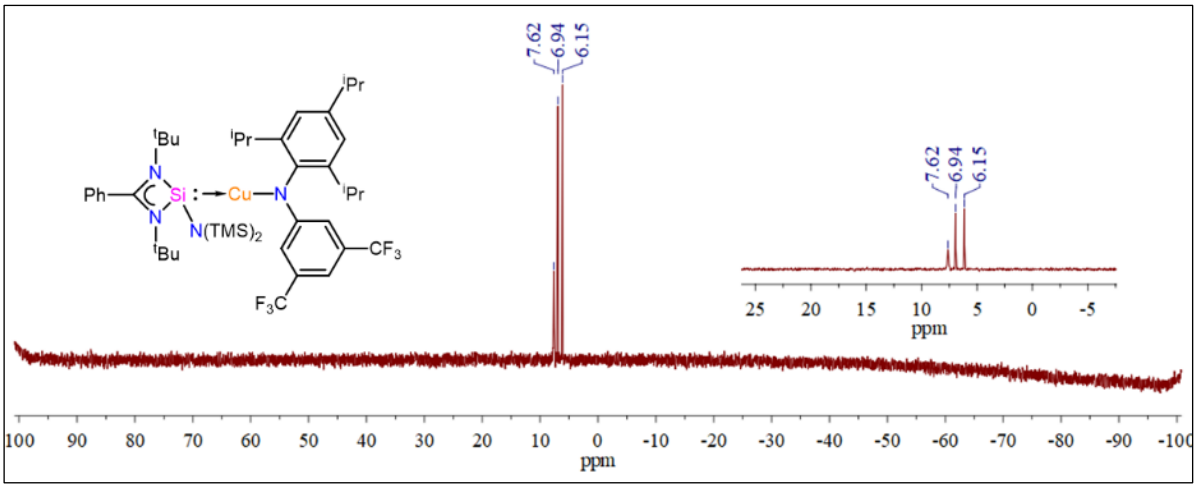

Figure 3.A.15. $^{29}Si\{^{1}H\}$ NMR spectrum of complex **3.3** in C_6D_6.

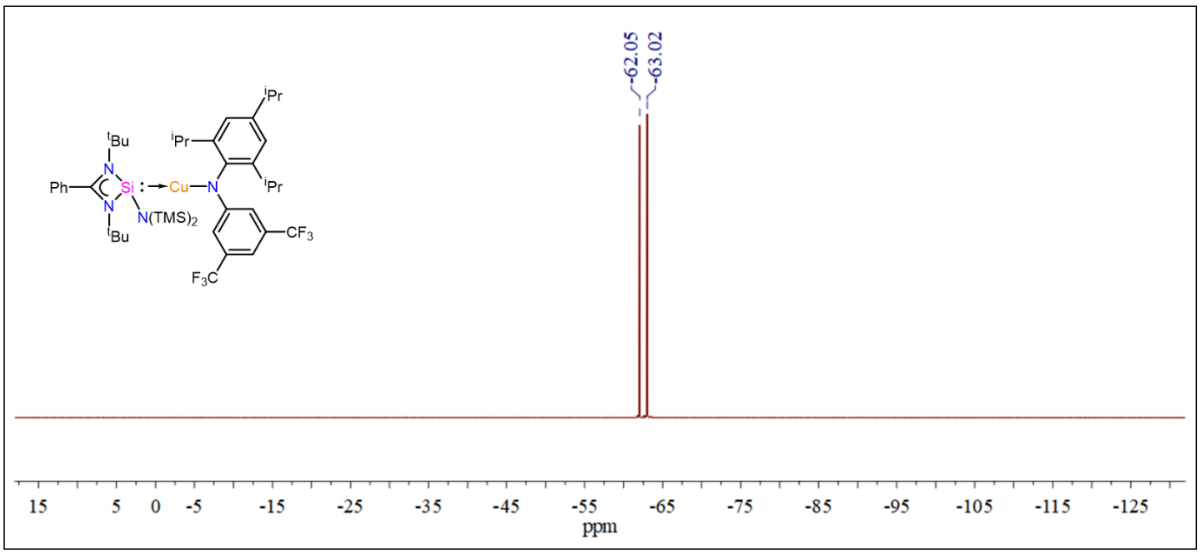

Figure 3.A.16. $^{19}F\{^{1}H\}$ NMR spectrum of complex **3.3** in C_6D_6.

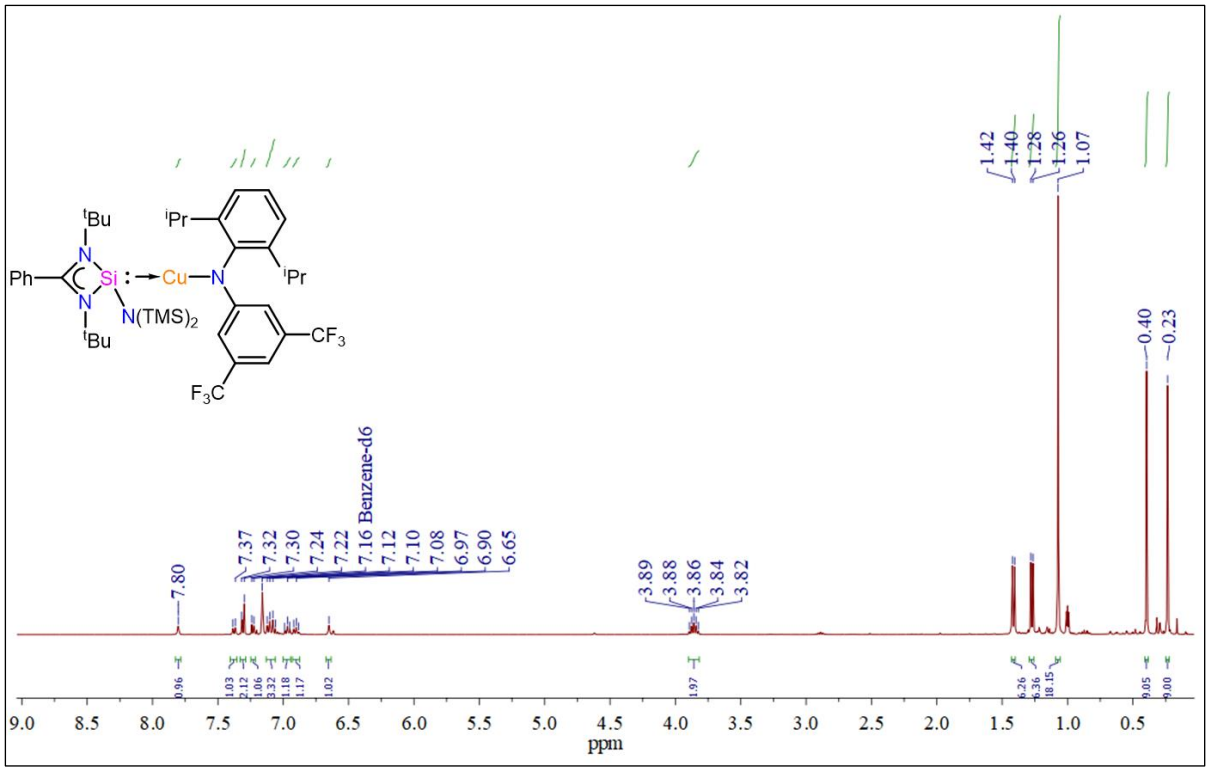

Figure 3.A.17. ^{1}H NMR spectrum of complex **3.4** in C_6D_6.

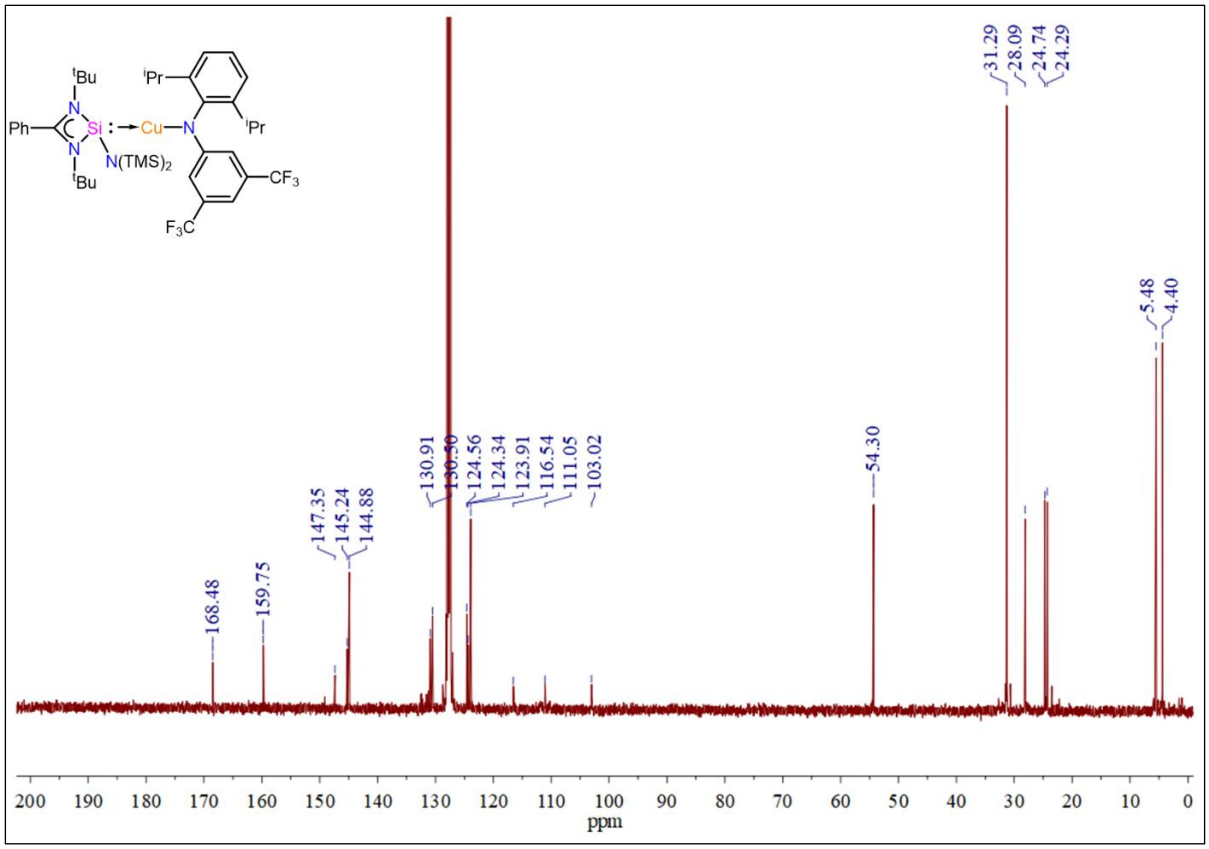

Figure 3.A.18. ^{13}C NMR spectrum of complex **3.4** in C_6D_6.

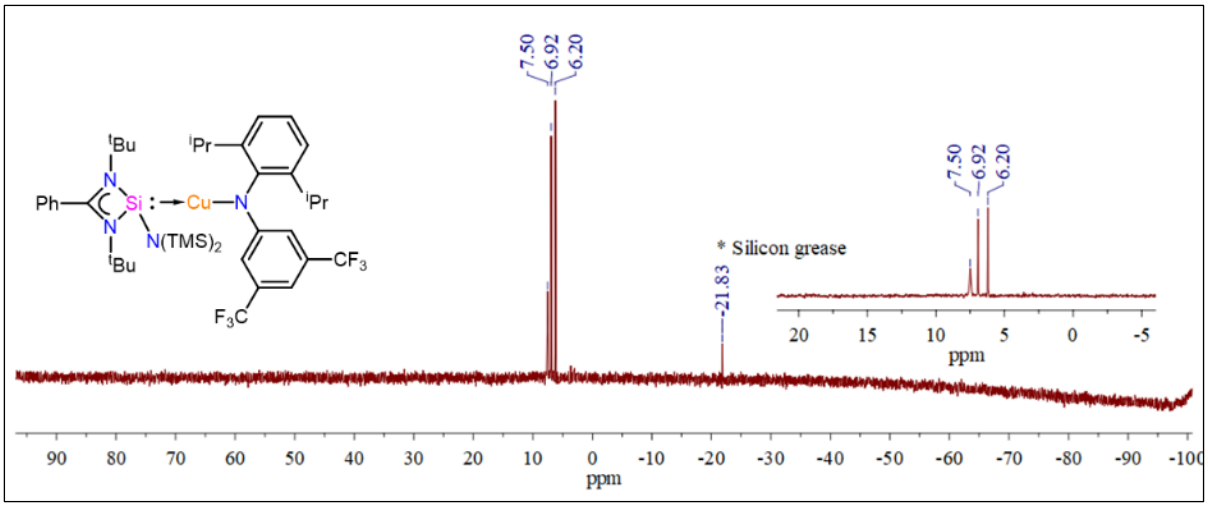

Figure 3.A.19. $^{29}Si\{^{1}H\}$ NMR spectrum of complex **3.4** in C_6D_6.

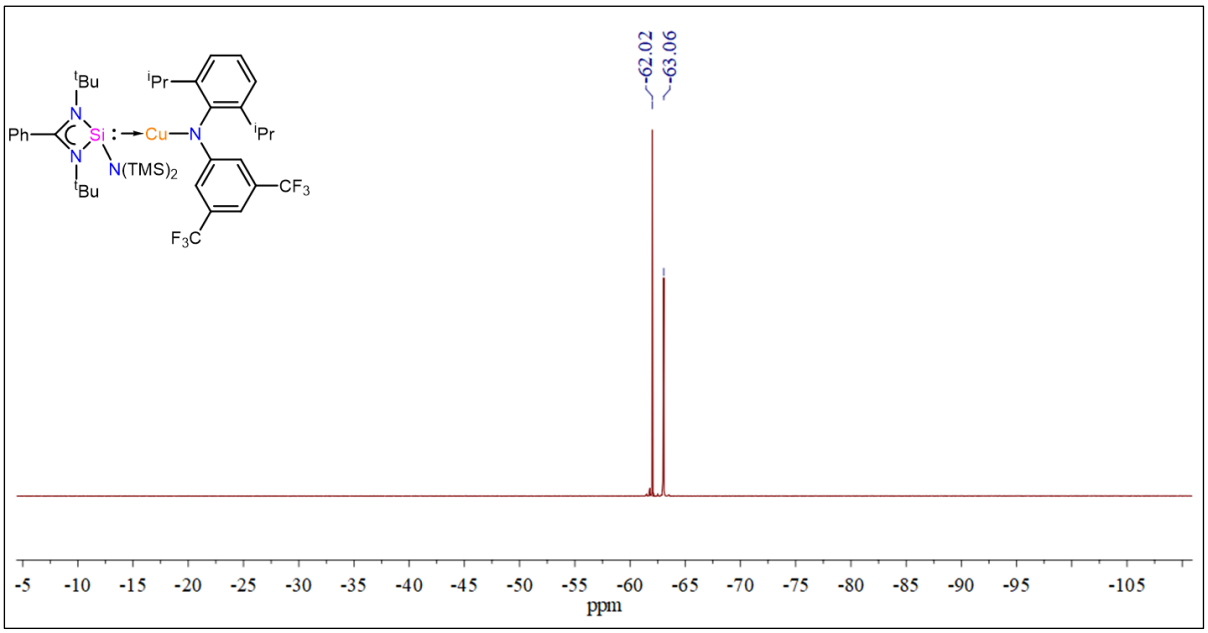

Figure 3.A.20. ^{19}F NMR spectrum of complex **3.4** in C_6D_6.

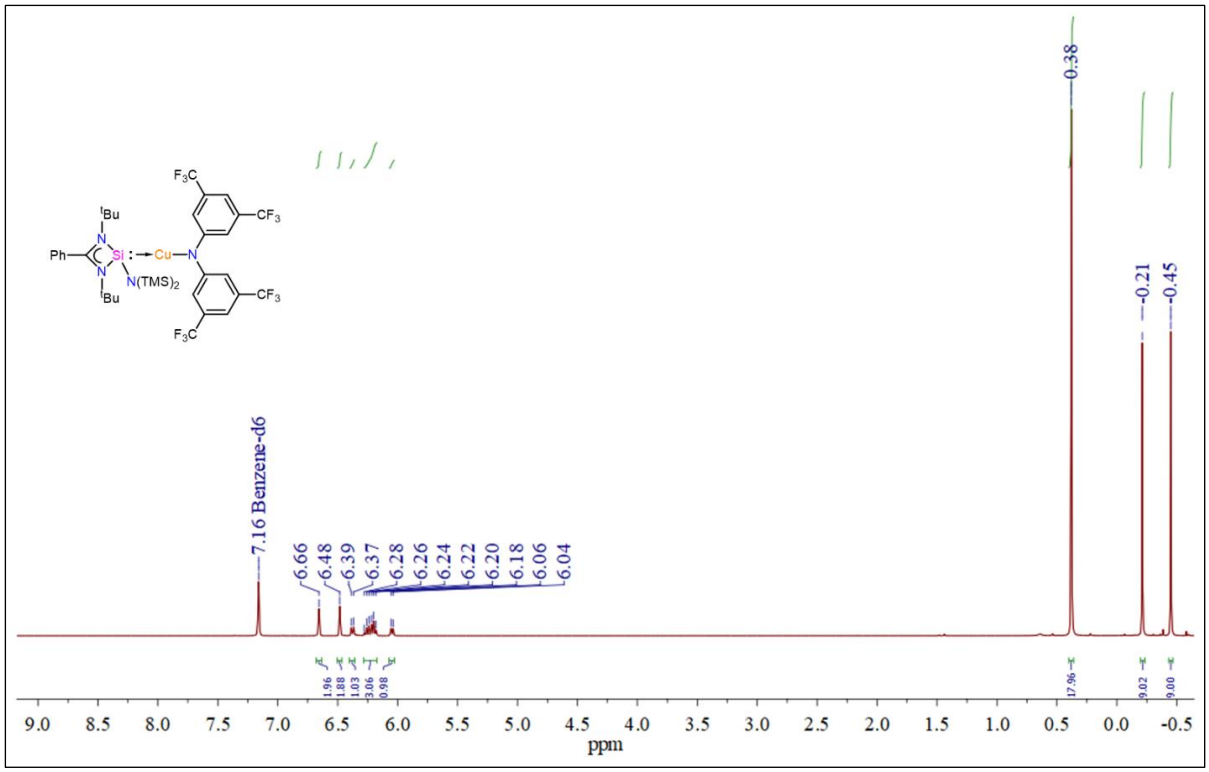

Figure 3.A.21. ^{1}H NMR spectrum of complex **3.5** in C_6D_6.

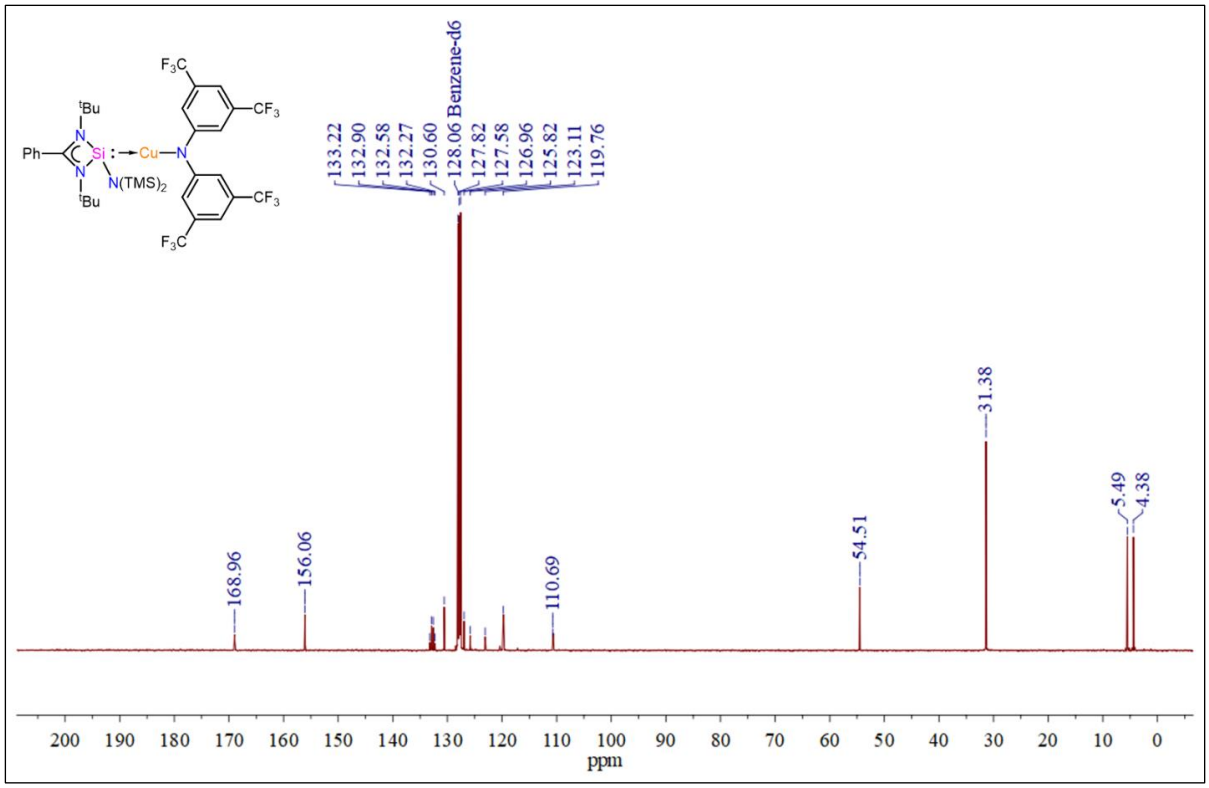

Figure 3.A.22. ^{13}C NMR spectrum of complex **3.5** in C_6D_6.

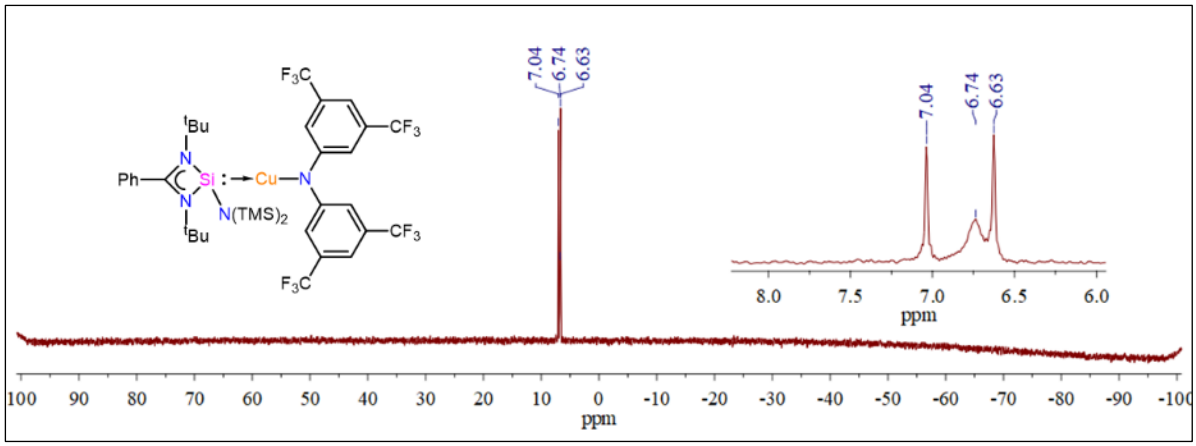

Figure 3.A.23. $^{29}Si\{^{1}H\}$ NMR spectrum of complex **3.5** in C_6D_6.

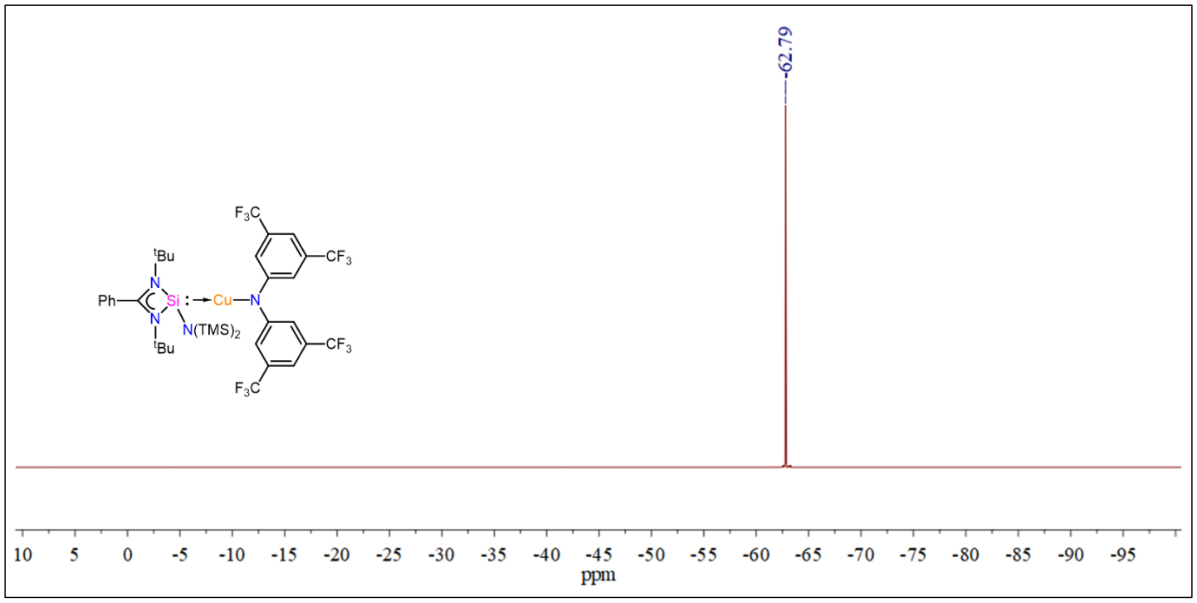

Figure 3.A.24. $^{19}F\{^{1}H\}$ NMR spectrum of complex **3.5** in C_6D_6.

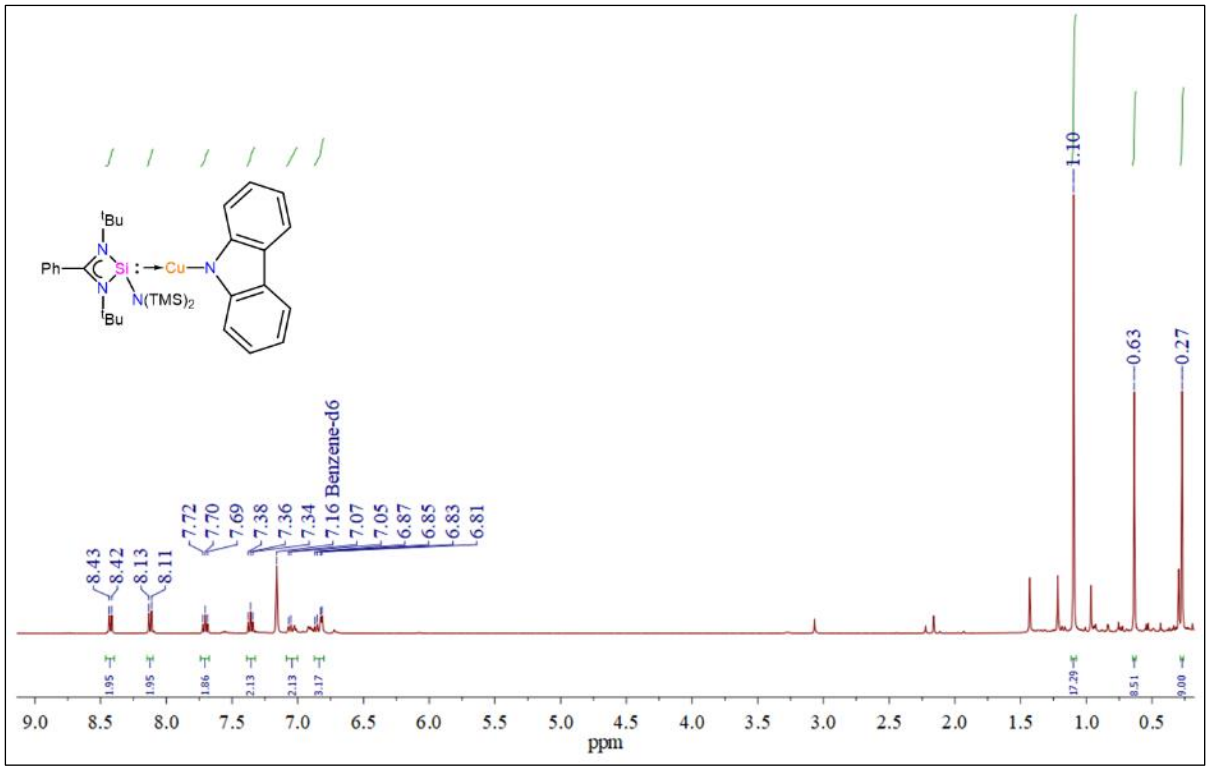

Figure 3.A.25. ^{1}H NMR spectrum of complex **3.6** in C_6D_6.

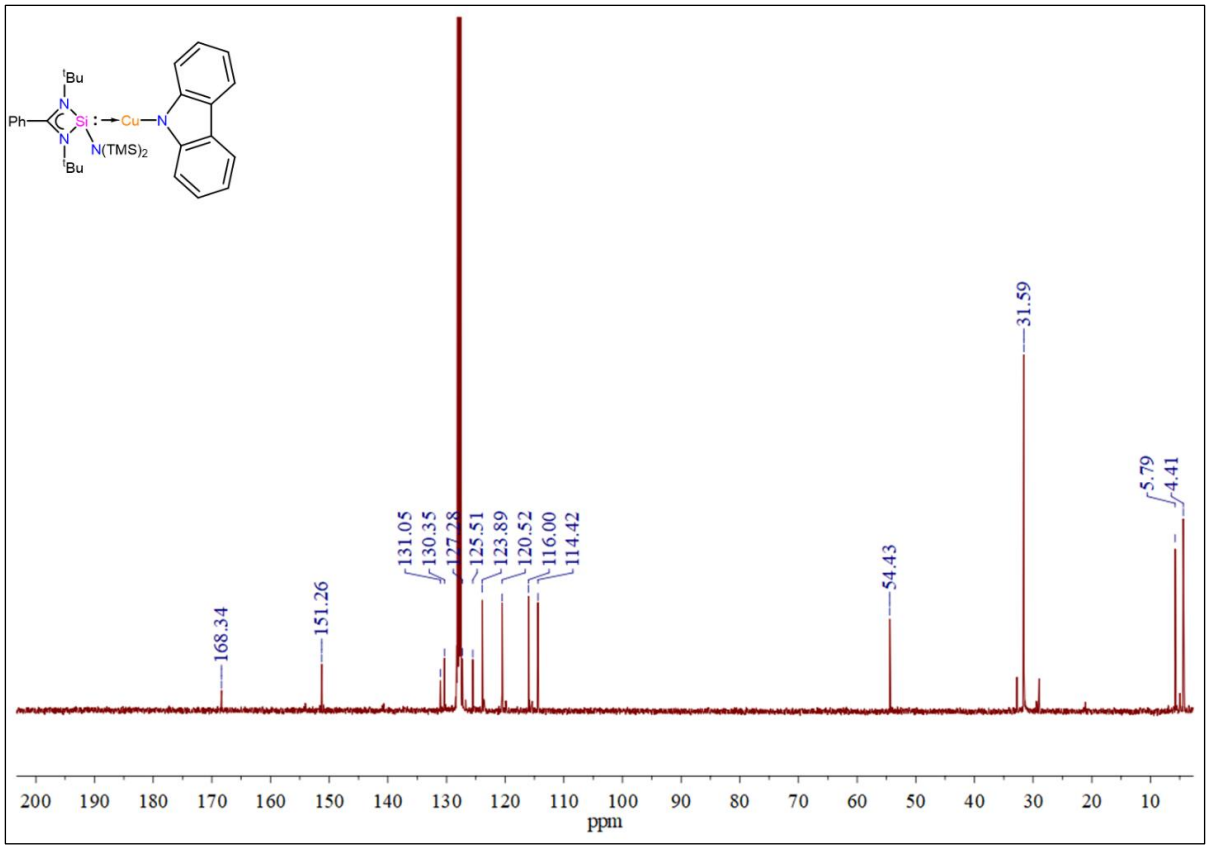

Figure 3.A.26. ^{13}C NMR spectrum of complex **3.6** in C_6D_6.

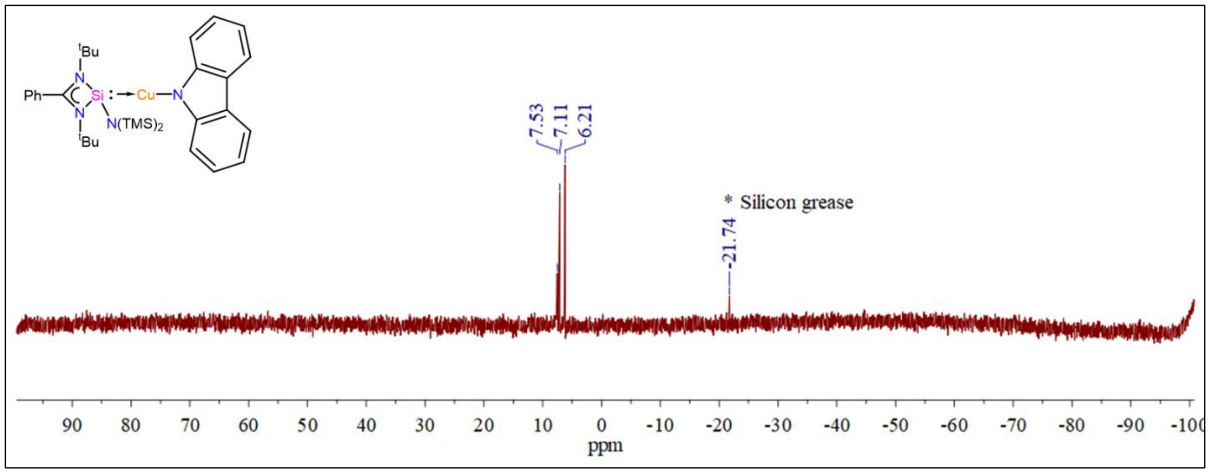

Figure 3.A.27. $^{29}Si\{^{1}H\}$ NMR spectrum of complex **3.6** in C_6D_6.

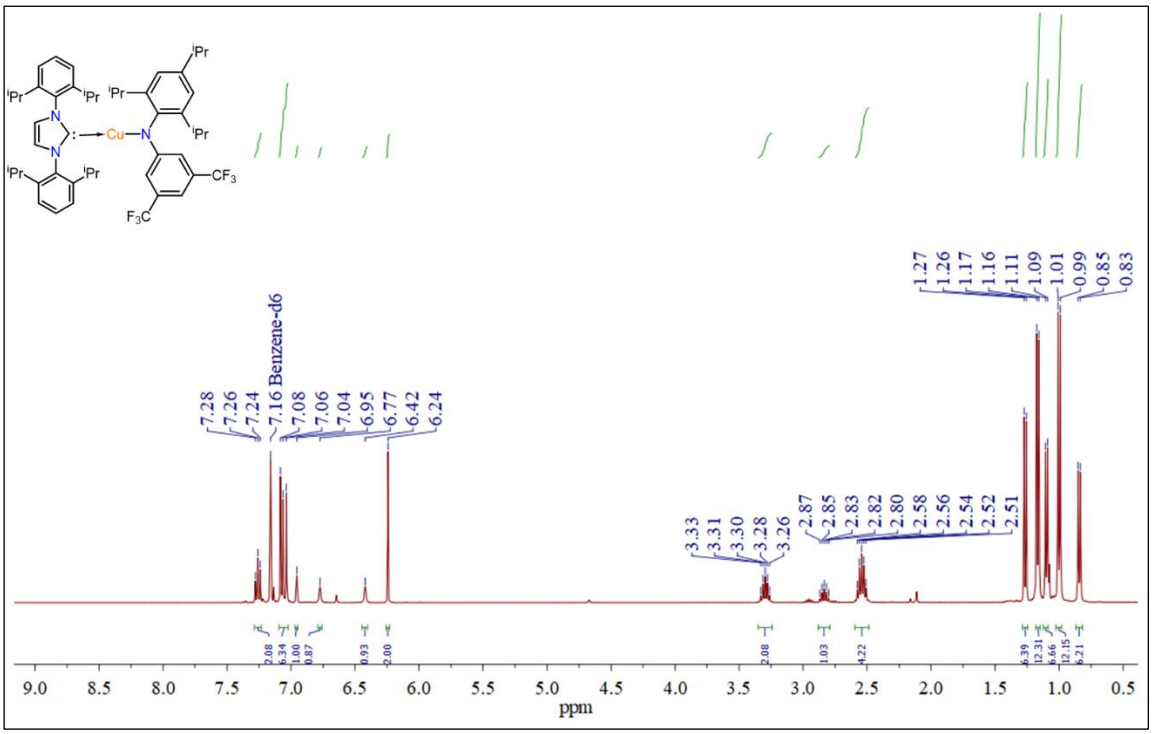

Figure 3.A.28. ^{1}H NMR spectrum of complex **3.8** in C_6D_6.

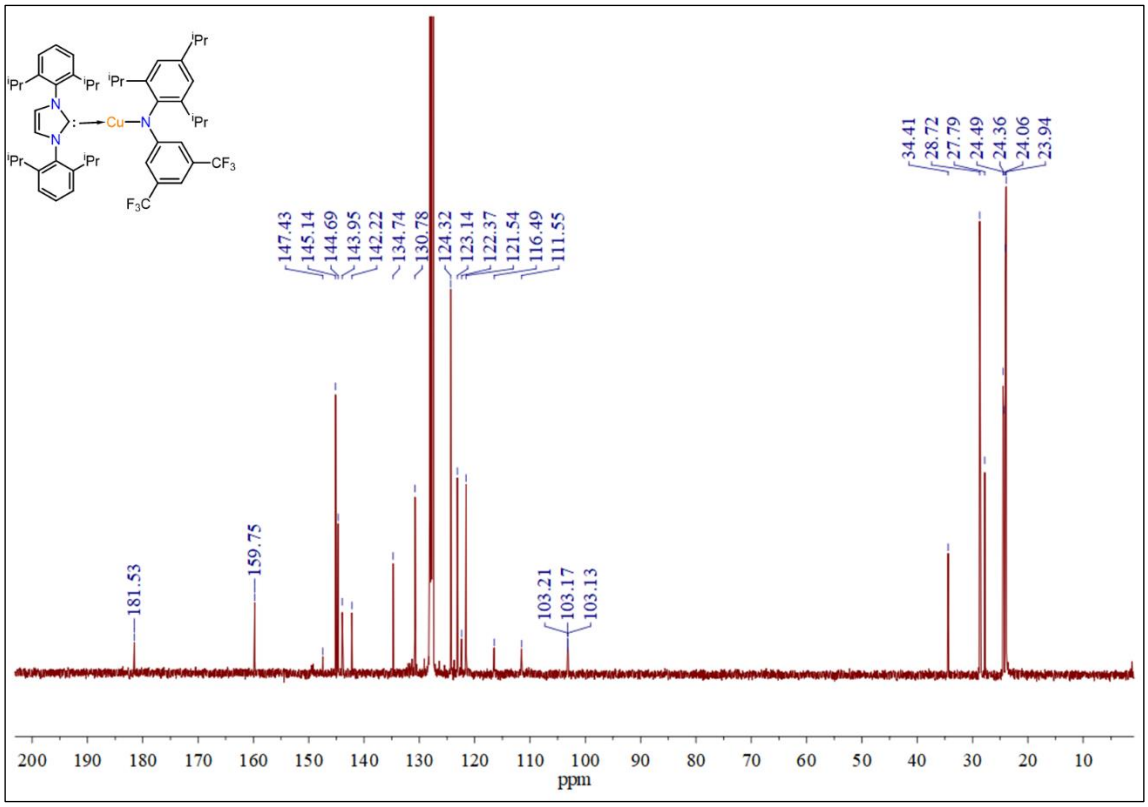

Figure 3.A.29. ^{13}C NMR spectrum of complex **3.8** in C_6D_6.

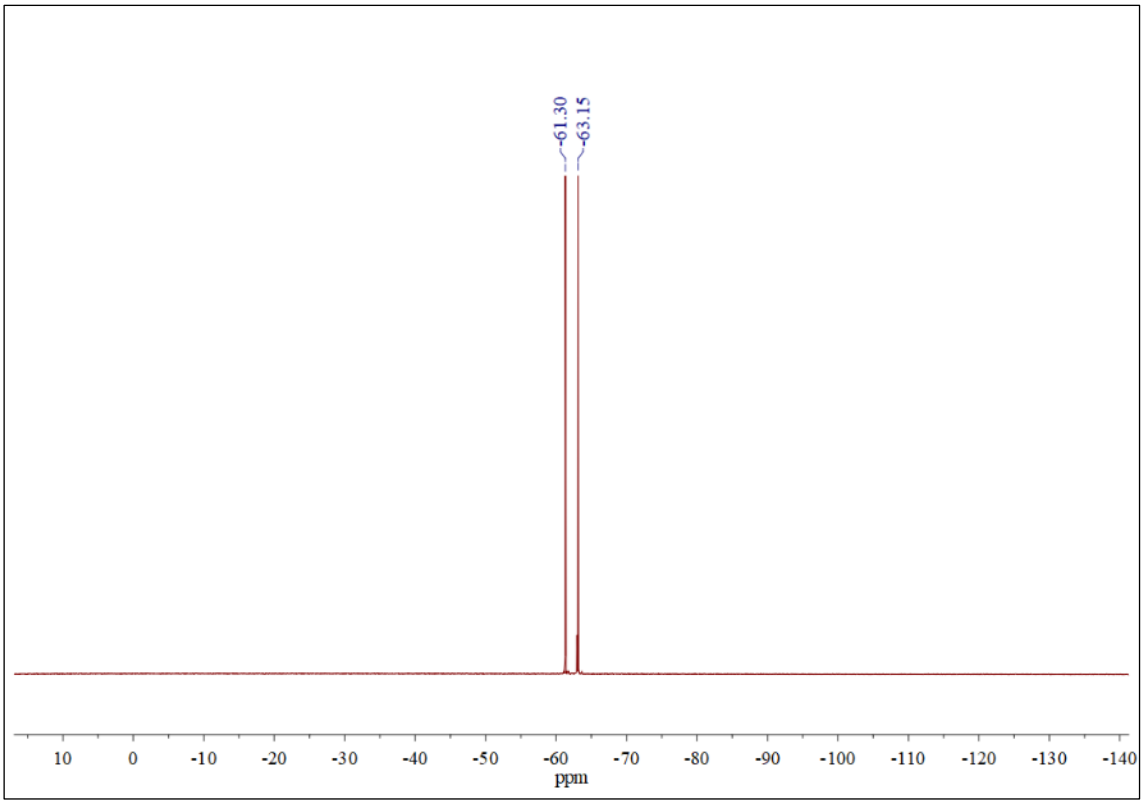

Figure 3.A.30. ^{19}F NMR spectrum of complex **3.8** in C_6D_6.

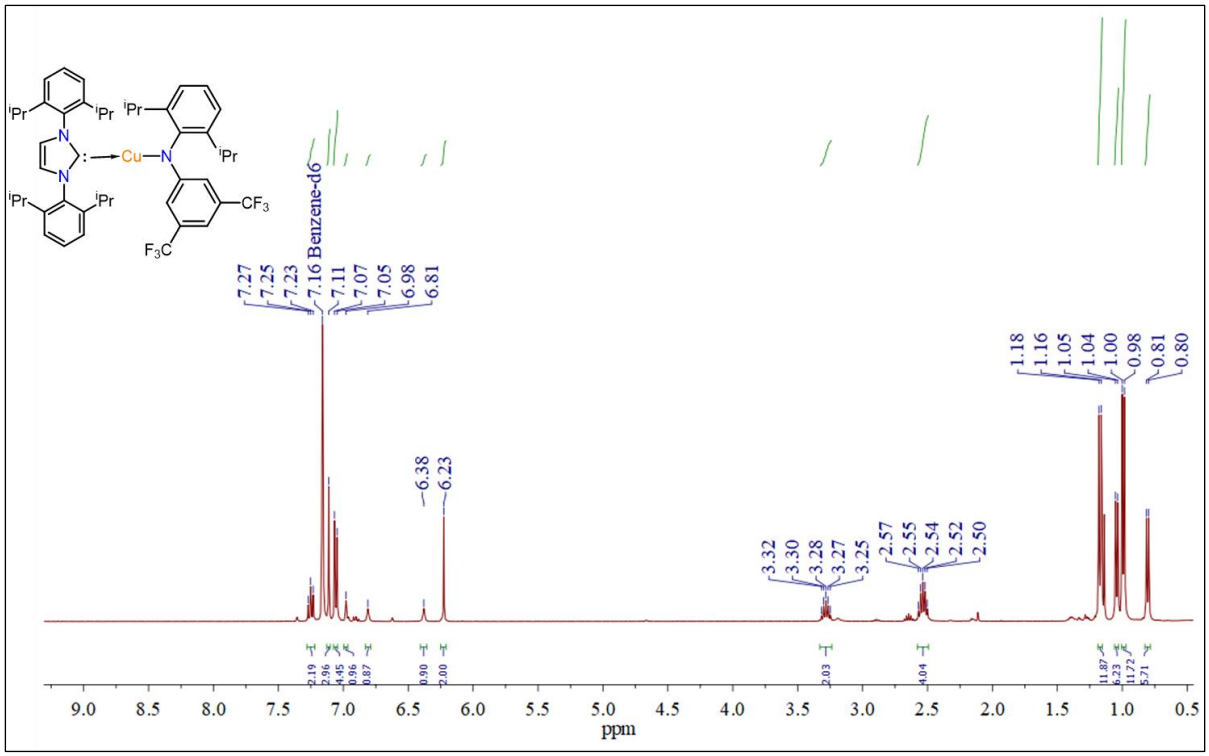

Figure 3.A.31. ^{1}H NMR spectrum of complex **3.9** in C_6D_6.

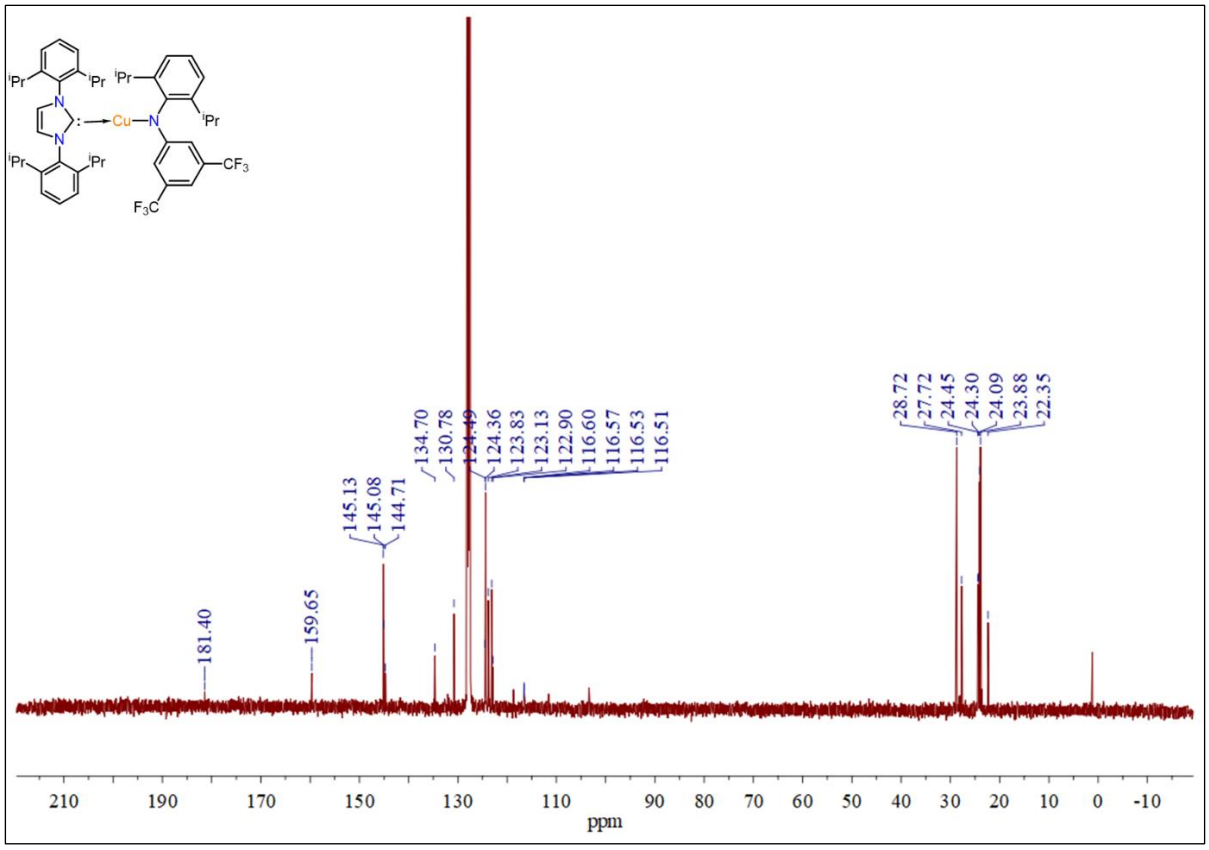

Figure 3.A.32. ^{13}C NMR spectrum of complex **3.9** in C_6D_6.

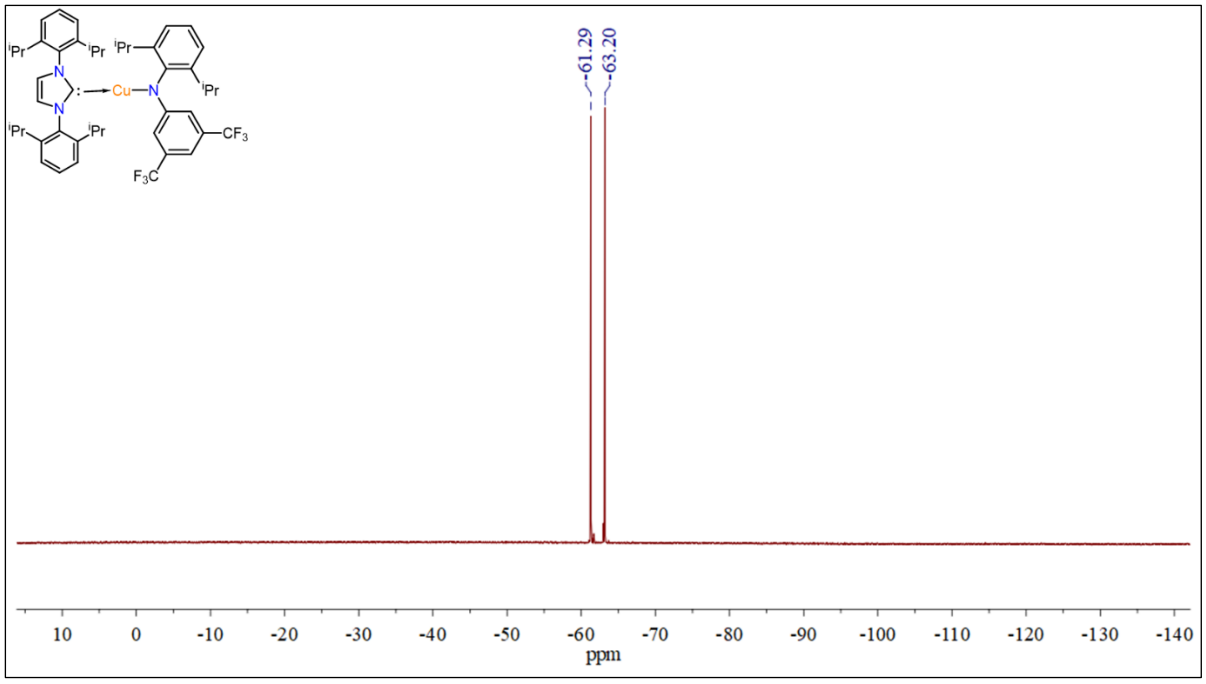

Figure 3.A.33. ^{19}F NMR spectrum of complex **3.9** in C_6D_6.

3.A.2 Crystallographic data of complexes 3.2-3.6 and 3.8-3.9.

Identification Code	**3.2**	**3.3**	**3.4**	**3.5**
Chemical formula	$C_{33}H_{51}CuN_4Si_3$	$C_{44}H_{67}CuF_6N_4Si_3$	$C_{41}H_{61}CuF_6N_4Si_3$	$C_{37}H_{47}CuF_{12}N_4Si_3$
Formula weight	651.58	913.82	871.74	923.59
Temperature	100 K	100 K	100 K	100 K
Wavelength	0.71703 Å	0.71703 Å	0.71703 Å	0.71703 Å
Crystal system	Monoclinic	Triclinic	Triclinic	Monoclinic
Space group	*P2₁/c*	*P-1*	*P-1*	*P2₁/c*
Unit cell dimensions	*a*=11.729(3) Å	*a*=13.416(5) Å	*a*=13.407(3) Å	*a*=11.432(2) Å
	b=14.702(4) Å	*b*=13.552(5) Å	*b*=13.983(3) Å	*b*=18.869(4) Å
	c=20.806(5) Å	*c*=14.189(6) Å	*c*=14.017(3) Å	*c*=20.984(4) Å
	α=90°	*α*=102.091(12)°	*α*=75.454(8)°	*α*=90°
	β=105.147(8)°	*β*=100.503(12)°	*β*=83.199(7)°	*β*=103.923(5)°

	γ=90°	γ=97.395(13)°	γ=65.393(7)°	γ=90 °
Volume	3462.9(15) $Å^3$	2442.6(16) $Å^3$	2312.3(9) $Å^3$	4393.5(14) $Å^3$
Z	4	2	2	4
Density (calculated)	1.250g/cm^3	1.242 g/cm^3	1.252 g/cm^3	1.396 g/cm^3
Absorption coefficient	0.762 mm^{-1}	0.577 mm^{-1}	0.606 mm^{-1}	0.661 mm^{-1}
F(000)	1392.0	968.0	920.0	1904.0
Theta range for data collection	4.542 to 56.788°	3.782 to 49.998°	3.924 to 49.994°	4 to 57.382 °
Index ranges	-15<=h<=15, -19<=k<= 19, -27<=l<=27	-15<=h<=15, -16<=k<=16, -16<=l<=16	-15<=h<=15, -16<=k<=16, -16<=l<=16	-15<=h<= 15, -25<=k<= 25, -28<=l<=28
Reflections collected	86886	36924	57955	214449
Independent reflections	8640 [Rint = 0.0794, Rsigma = 0.0451]	8575 [Rint = 0.2339, Rsigma = 0.2327]	8159 [Rint = 0.0609, Rsigma = 0.0395]	11280 [Rint = 0.0910, Rsigma = 0.0379]
Coverage of independent reflections	99.4 %	99.9 %	99.9 %	99.4 %
Function minimized	Σ w (Fo^2 - Fc^2)^2	Σ w (Fo^2 - Fc^2)^2	Σ w (Fo^2 - Fc^2)^2	Σ w (Fo^2 - Fc^2)^2
Data/restraints/parameters	8640/0/382	8575/0/541	8159/0/512	11280/ 0 / 565
Goodness-of-fit on F^2	1.112	1.012	1.024	1.114
Δ/σ max	0.001	0.001	0.000	0.003
Final R indices	data [I>2σ(I)], R1 = 0.0489, wR2 = 0.0900	data [I>2σ(I)], R1 = 0.0900, wR2 = 0.1506	data [I>2σ(I)], R1 = 0.0720, wR2 = 0.1724	data [I>2σ(I)], R1 = 0.0631, wR2 = 0.1427

	all data, R1 = 0.0746, wR2 = 0.1002	all data, R1 = 0.2140, wR2 =0.1943	all data, R1 = 0.0911, wR2 = 0.1865	all data, R1 = 0.0906, wR2 =0.1596
Largest diff. peak and hole	0.42 and -0.42 eÅ^{-3}	0.96 and -0.63 eÅ^{-3}	1.76 and -0.77 eÅ^{-3}	1.30 and -0.64 eÅ^{-3}
R.M.S. deviation from mean	0.085 eÅ^{-3}	0.070 eÅ^{-3}	0.101 eÅ^{-3}	0.145 eÅ^{-3}

Identification Code	**3.6**	**3.8**	**3.9**
Chemical formula	$C_{33}H_{49}CuN_4Si_3$	$C_{50}H_{62}CuF_6N_3$	$C_{47}H_{56}CuF_6N_3$
Formula weight	649.57	882.56	840.48
Temperature	100 K	100 K	100 K
Wavelength	0.71703 Å	0.71703 Å	0.71703 Å
Crystal system	Triclinic	Monoclinic	Monoclinic
Space group	*P-1*	$P2_1/n$	$P2_1/n$
Unit cell dimensions	a = 10.271(5) Å	a = 13.464(2) Å	a =10.23(5) Å
	b = 13.644(5) Å	b = 24.225(5)Å	b = 24.73(6) Å
	c =13.731(6) Å	c = 14.903(3) Å	c = 21.09(5) Å
	α = 79.505(10)°	α = 90°	α =90°
	β =76.434(13) °	β = 108.096(4) °	β = 91.87(18) °
	γ = 71.282(10) °	γ = 90°	γ = 90°
Volume	1759.6(13) Å^3	4620.3(14) Å^3	5331(34) Å^3
Z	2	4	4
Density (calculated)	1.226 g/cm^3	1.269 g/cm^3	1.047 g/cm^3
Absorption coefficient	0.750 mm^{-1}	0.533 mm^{-1}	0.459 mm^{-1}
F(000)	692.0	1864	1768.0
Theta range for data collection	4.264 to 57.012°	3.942 to 50°	3.82 to 50 °
Index ranges	-13<=h<=13, -17<=k<=17, -18<=l<=18	-16<=h<=16, -28<=k<=28, -17<=l<=17	-12<=h<=12, -29<=k<=29, -25<=l<=25
Reflections collected	42593	160567	136453

Independent reflections	8785 [Rint = 0.1111, Rsigma = 0.1226]	8112 [Rint = 0.1529, Rsigma = 0.0517]	9384 [Rint = 0.2364, Rsigma = 0.0911]
Coverage of independent reflections	98.4 %	100 %	99.9 %
Function minimized	Σ w $(Fo^2 - Fc^2)^2$	Σ w $(Fo^2 - Fc^2)^2$	Σ w $(Fo^2 - Fc^2)^2$
Data/restraints/parameters	8785/0/382	9384 / 0 /534	9384 / 0 / 554
Goodness-of-fit on F^2	1.010	1.139	1.110
Δ/σ max	0.001	0.001	0.000
Final R indices	data [I>2σ(I)], R1 = 0.0559, wR2 =0.0936	data [I>2σ(I)], R1 = 0.0597, wR2 = 0.1137	data [I>2σ(I)], R1 = 0.0784, wR2 =0.1978
	all data, R1 = 0.1261, wR2 =0.1105	all data, R1 = 0.0819, wR2 = 0.1218	all data, R1 = 0.1100, wR2 =0.2111
Largest diff. peak and hole	0.45 and -0.37 $eÅ^{-3}$	0.83 and -0.46 $eÅ^{-3}$	0.55 and -0.57 $eÅ^{-3}$
R.M.S. deviation from mean	0.084 $eÅ^{-3}$	0.070 $eÅ^{-3}$	0.098 $eÅ^{-3}$

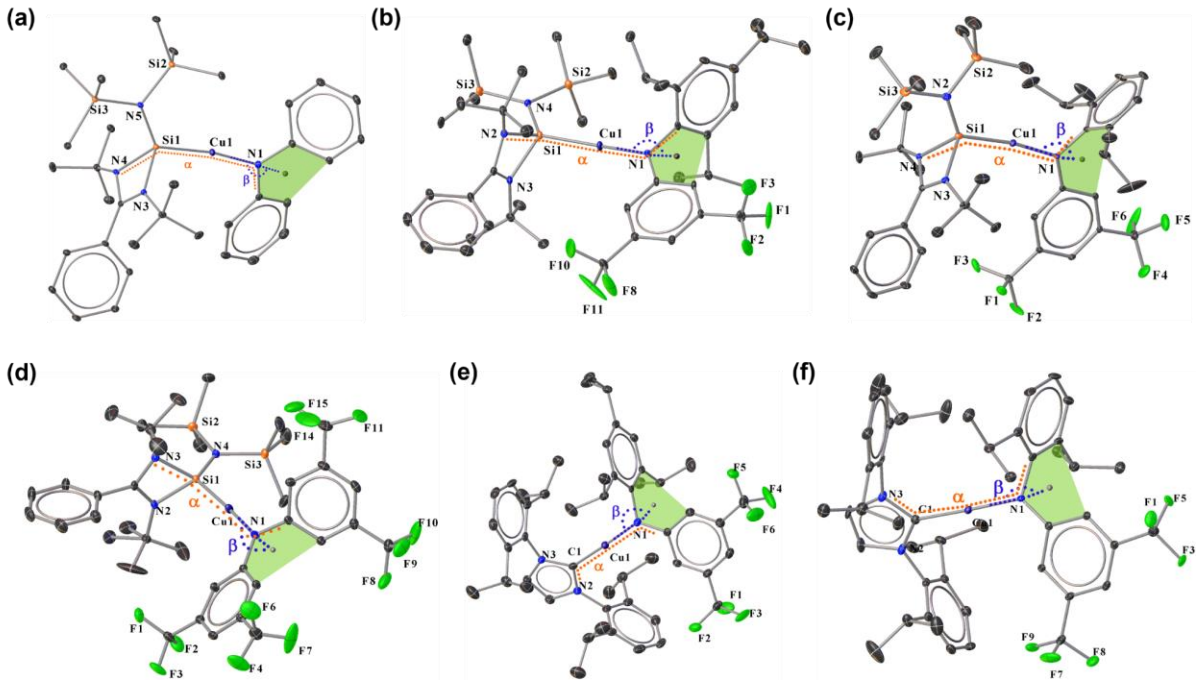

Figure 3.A.34. Planes of carbene str.

3.A.3 Instrumentation details used for performing photophysical studies. Steady-state solution-based absorption spectra were recorded on UV-2600 UV spectrophotometer (Shimadzu). Steady-state emission spectra and time-gated emission spectra of all the samples in solution and solid state were recorded by using a Fluorolog-3 (HORIBA) instrument. Absolute quantum yields were measured in the Fluoromax-4C (HORIBA) instrument by using an integrating sphere. For complex **3.2**, temperature-dependent PL and PL decay profiles were recorded in an Edinburgh FLS980 Instrument coupled with a cryostat. The solid samples were placed between two sapphire plates and fixed in a gold-coated copper sample holder. The sample holder is fixed in a closed cycle He cryostat (Advanced Research Systems) attached with a Lake Shore 335 temperature controller. For **3.3**, **3.4**, **3.5**, **3.8**, and **3.9**, steady-state PL spectra were recorded on a JASCO FP-8500 spectrofluorometer instrument. The lifetime, low-temperature PLwere measured in an Edinburgh FLS1000 photoluminescence spectrometer, attached with an Optistat DN cryostat. The temperature was controlled using a Mercury iTC temperature controller (Oxford Instruments). The sample was excited using a xenon lamp, and emission was collected from 320 to 800 nm.

3.A.4 Computational section. Crystal structures are used as initial coordinates for obtaining the ground state (S_0) geometries of these complexes. The *Gaussian 09* program package was used to perform these calculations at the Grimme's dispersion corrected B3LYP functional (B3LYP-D3) using a def2-SVP basis set.[1] Optimized geometries were further used to perform

the Franck-Condon TD-DFT calculations (FC-TD-DFT) to obtain further insights into the various singlet/triplet excited states, such as energies of excited states, oscillator strengths, and optical excitations. Spin-orbit coupling matrix elements (SOCME) between various electronic states are calculated using the pySOC program.[2]

Table 3.A.1. Various contributing components in lifetime data of complex **3.2**

Temperature (K)	α_1	τ_1	α_2	τ_2	α_3	τ_3	$\langle\tau\rangle$
20	70%	5.95 µs	30%	195 µs	-	-	182.35 µs
8	79%	4.22 µs	15.6%	21.24 µs	5.4%	342.30 µs	248.71 µs

Table 3.A.2. SOCME values for complexes **3.8** and **3.9**

In cm^{-1}	3A.8	3A.9
S_0-T_1	0.67477	1.40608
S_0-T_2	15.68406	7.06788
S_0-T_3	8.8587	6.79439
S_1-T_1	2.07867	1.94265
S_1-T_2	2.65351	1.29996
S_1-T_3	7.3533	5.7328

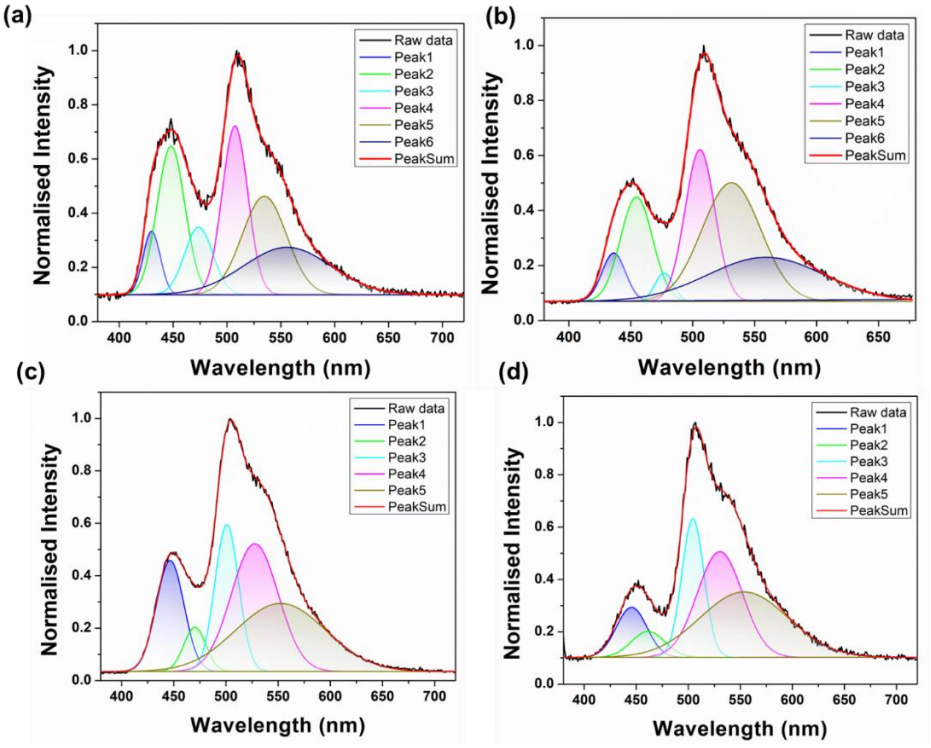

Figure 3.A.35. Deconvoluted emission bands for (a) complex **3.3**, (b) complex **3.4**, (c) complex **3.8**, and (d) complex **3.9**.

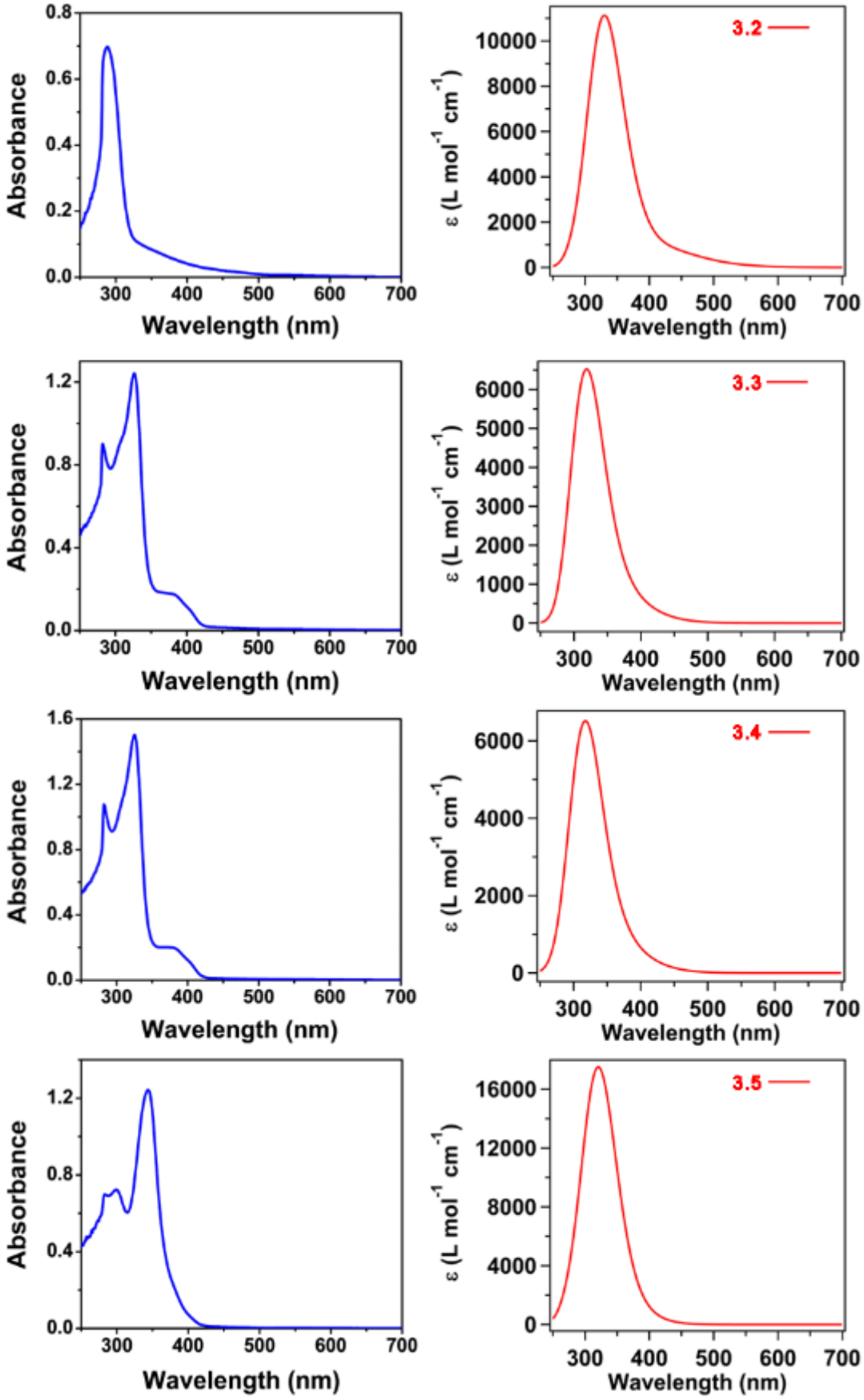

Figure 3.A.36. Experimental (in toluene) and simulated UV-Vis spectra of complexes **3.2**-**3.5**.

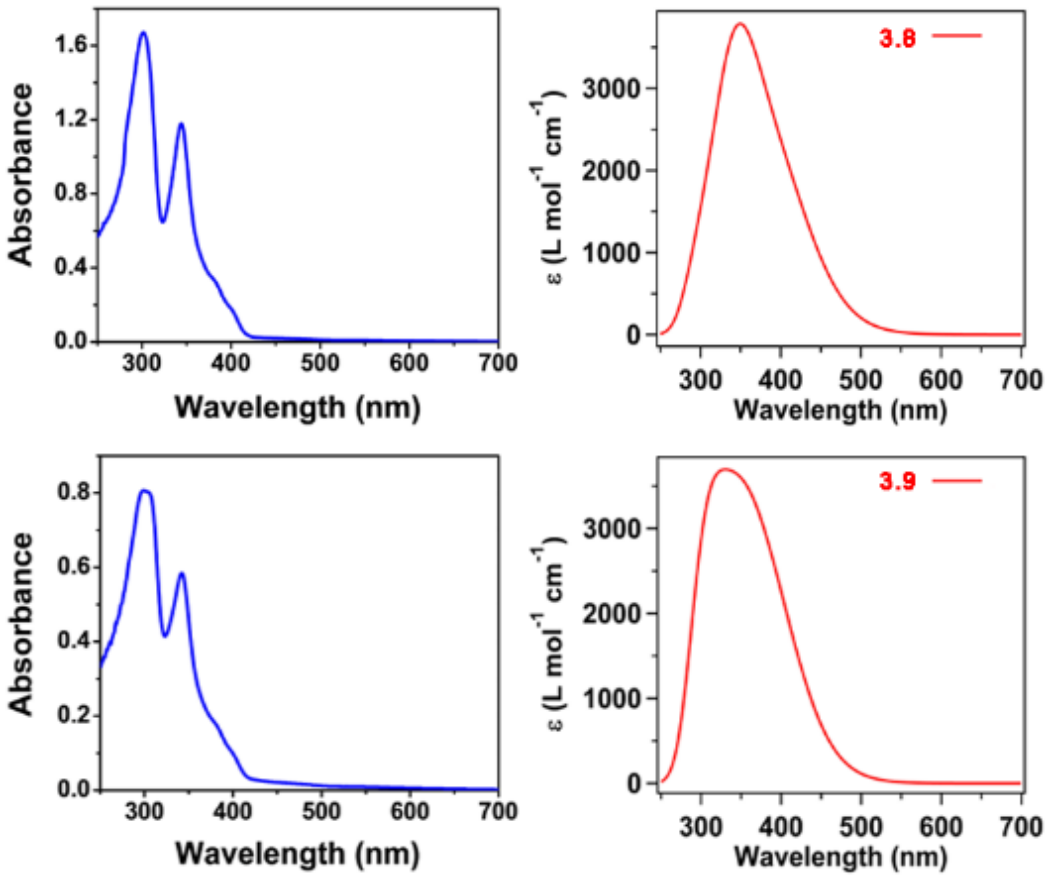

Figure 3.A.37. Experimental (in toluene) and simulated UV-Vis spectra of complexes **3.8** and **3.9**.

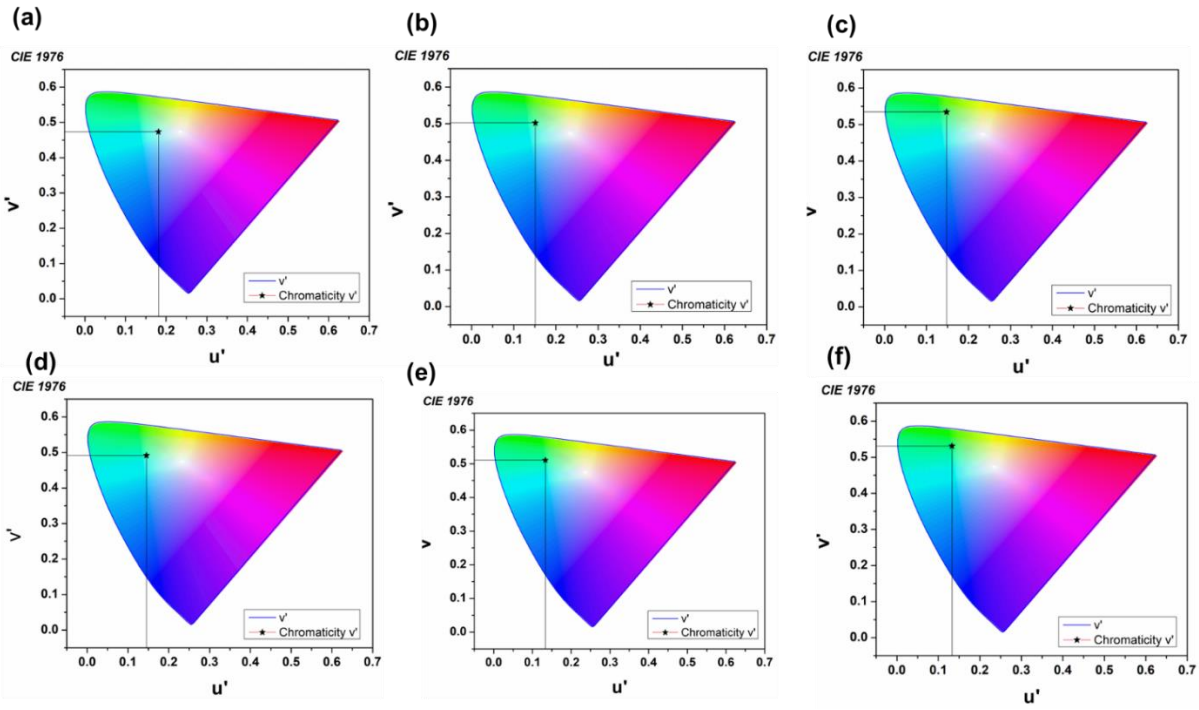

Figure 3.A.38. CIE 1976 diagrams for (a) complex **3.2**, (b) complex **3.3**, (c) complex **3.4**, (d) complex **3.5**, (e) complex **3.8**, and (f) complex **3.9**.

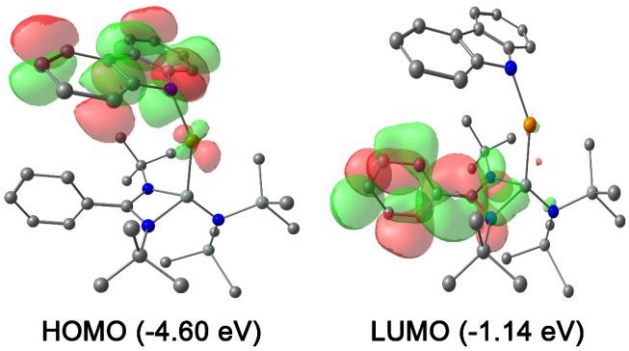

Figure 3.A.39. HOMO and LUMO of complex **3.6**.

Table 3.A.3. Photophysical parameters of complexes

Sample	τ_{PF}	τ_{Phos}	k_{ISC}	Φ
3.3	5.77 ns	0.41 ms	$1.61 \times 10^8\ s^{-1}$	20%
3.4	5.23 ns	3.37 ms	$1.82 \times 10^8\ s^{-1}$	19.23%
3.5	5.49 ns	0.63 ms	$1.82 \times 10^8\ s^{-1}$	5.03%
3.8	4.54 ns	1.44 ms	$2.15 \times 10^8\ s^{-1}$	10.17%
3.9	4.30 ns	2.10 ms	$2.26 \times 10^8\ s^{-1}$	20.07%

Calculation of k_{ISC}

$$k_{ISC} = \frac{1 - \Phi_{PF}}{\tau_{PF}}$$

$$\Phi_{PF} = \Phi$$

4A.A.1 Synthesis of DiMeCAAC and IMES according to the literature procedure.[3, 4]

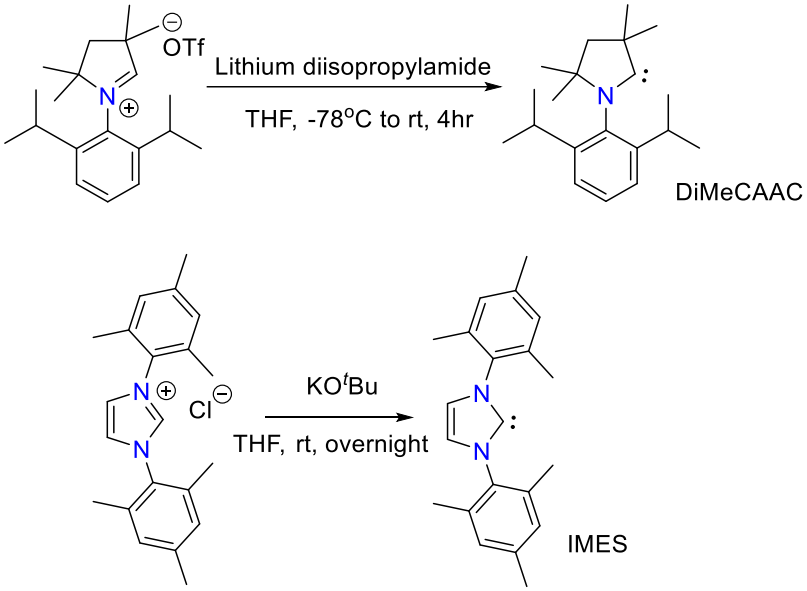

4A.A.2 Synthesis of OA@AuNPs.

Oleylamine capped AuNPs (OA@AuNPs) was synthesized, followed by a modified reported procedure.[5] 5 mL oleylamine (OA) was taken in a three-neck 100 ml round bottom flask. Then, the solution was refluxed at 150 °C under an inert atmosphere for 15-20 mins. After that, a solution containing 0.3 mmol of $HAuCl_4 \cdot 3H_2O$ and 1 mL OA was rapidly injected into the first solution at 150 ^{0}C. Then, the heating was continued for 1.5 hours for the complete growth of OA@AuNPs. After the reaction, the flask was allowed to come to room temperature, and 1 mL toluene was added to quench the reaction. The NP solution was purified through centrifugation at 5000 rpm for 6 min. Ethanol was added to the NP solution in a 1:2 (v/v) ratio to precipitate the OA@AuNPs, and the excess OA was removed through centrifugation. Finally, the OA@AuNPs was redispersed in dry toluene to synthesize DiMeCAAC@AuNPs.

4A.A.3 Synthesis of DiMeCAAC@AuNPs (Ligand exchange reaction).

The DiMeCAAC@AuNPs was synthesized *via* a ligand exchange method from OA@AuNPs. At first, OA@AuNPs was synthesized as written previously. Next, OA@AuNPs was first taken in anhydrous toluene under an inert condition, and it was treated with a THF solution with ~50-fold excess of DiMeCAAC. Instantaneous precipitation of NP was observed, and the solution was kept undisturbed overnight for the complete ligand exchange to occur. Then, the purification was performed *via* centrifugation at 5000 rpm (5 minutes) for 2 times and washed with toluene to remove the free excess ligands. Finally, the DiMeCAAC@AuNPs was dispersed in DMSO after sonication for ~5 mins to use further.

4A.A.4 Synthesis of IMES@AuNPs (Ligand exchange reaction).

The IMES@AuNPs was synthesized *via* a ligand exchange method from OA@AuNPs. At first, OA@AuNPs was synthesized as written previously. Next, OA@AuNPs was first taken in anhydrous toluene under an inert condition, and it was treated with ~100-fold excess of IMES. Instantaneous precipitation of NP was observed, and the solution was kept undisturbed overnight for the complete ligand exchange to occur. Then, the purification was performed *via* centrifugation at 5000 rpm (5 minutes) for 2 times and washed with toluene to remove the free excess ligands. Finally, the IMES@AuNPs was dispersed in DMSO after sonication for ~5 mins to use further.

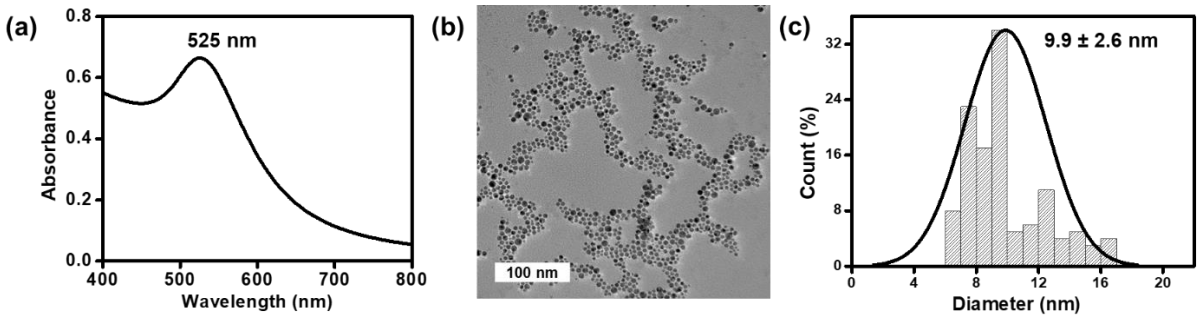

Figure 4A.A.1. (a) UV-vis spectra of IMES@AuNPs in DMSO showing the characteristic LSPR band at ~525 nm (b) A representative TEM image of IMES@AuNPs. (c) The corresponding size distribution histogram.

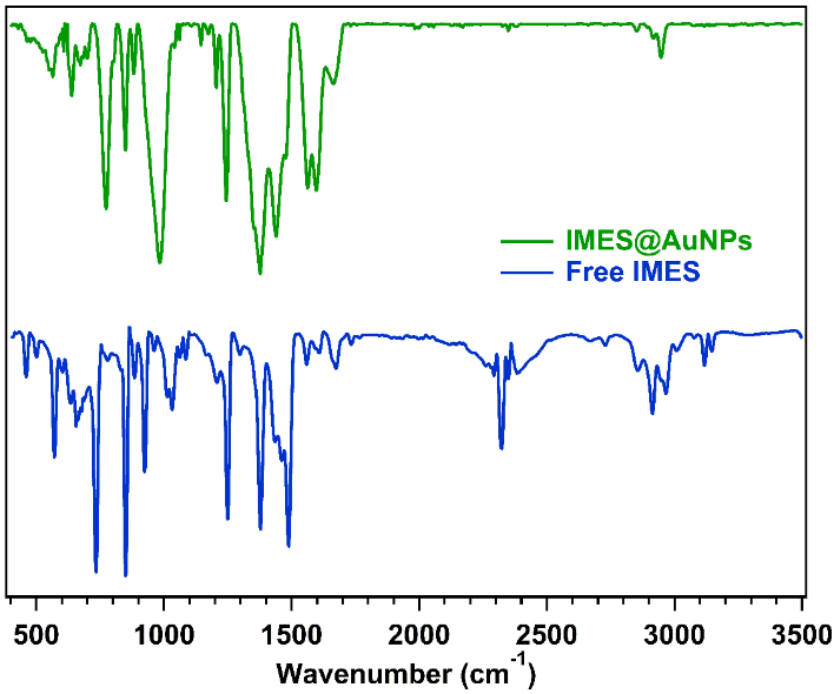

Figure 4A.A.2. IR spectra for IMES@AuNPs and IMES. This correlates well with the report by Chang and co-workers.[6]

4A.A.5 Raman spectroscopic data of DiMeCAAC@AuNPs.

The Raman spectra (Figure 4A.A.3) also show strong bands at 1588, 1448, 1383, and 1248 cm^{-1}. The bands between 1248-1448 cm^{-1} can be assigned to the coupling of the hydrogens of the isopropyl group to the hydrogens of the ring, where the resulting normal modes are affected by the orientation of the side groups.[7, 8] The strong band at 1588 cm^{-1} can be assigned to the imidazole ring N-H bending modes.[9]

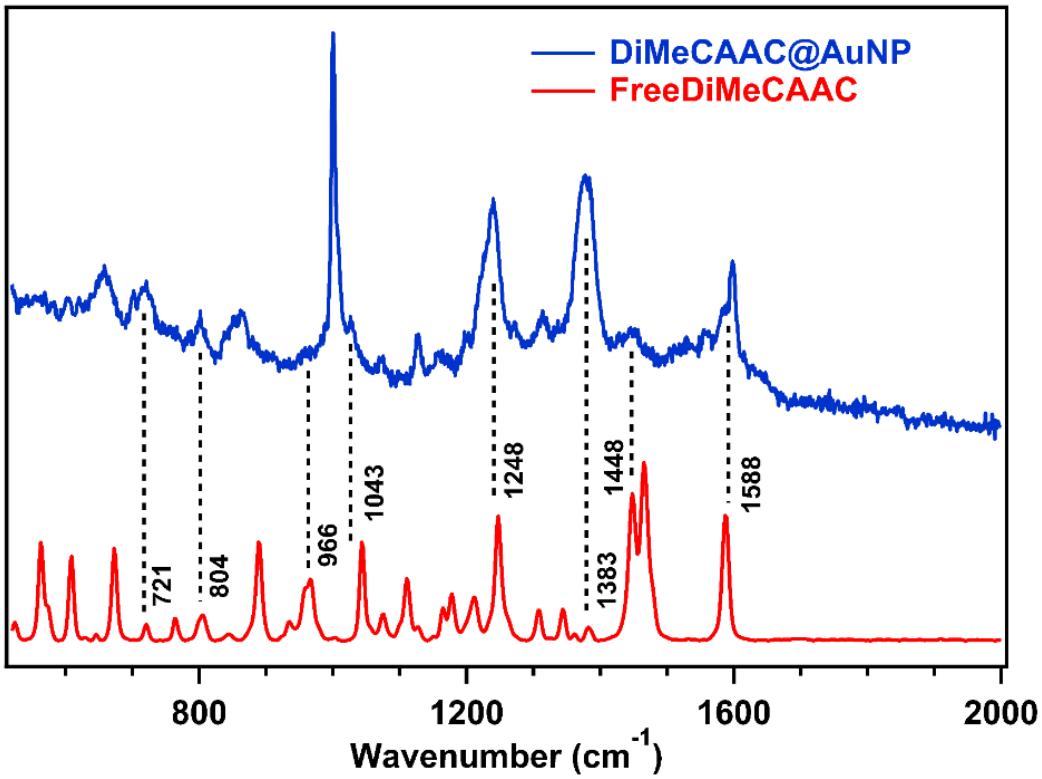

Figure 4A.A.3. Raman spectra for DiMeCAAC@AuNPs and DiMeCAAC. The findings are listed in Table 4A.A.1.

Table 4A.A.1. Peak assignments from Figure 4A.A.3

Peak Position (cm^{-1})	Assignments
1588	Deformation of CH_3
1448	Coupling of the hydrogens of isopropyl group
1383	Ring Stretching
1248	Coupling of the hydrogens of isopropyl group
1043	C-H of phenyl
966	Interaction of ring stretching modes
804	C-H out of the plane
721	C-H out of the plane

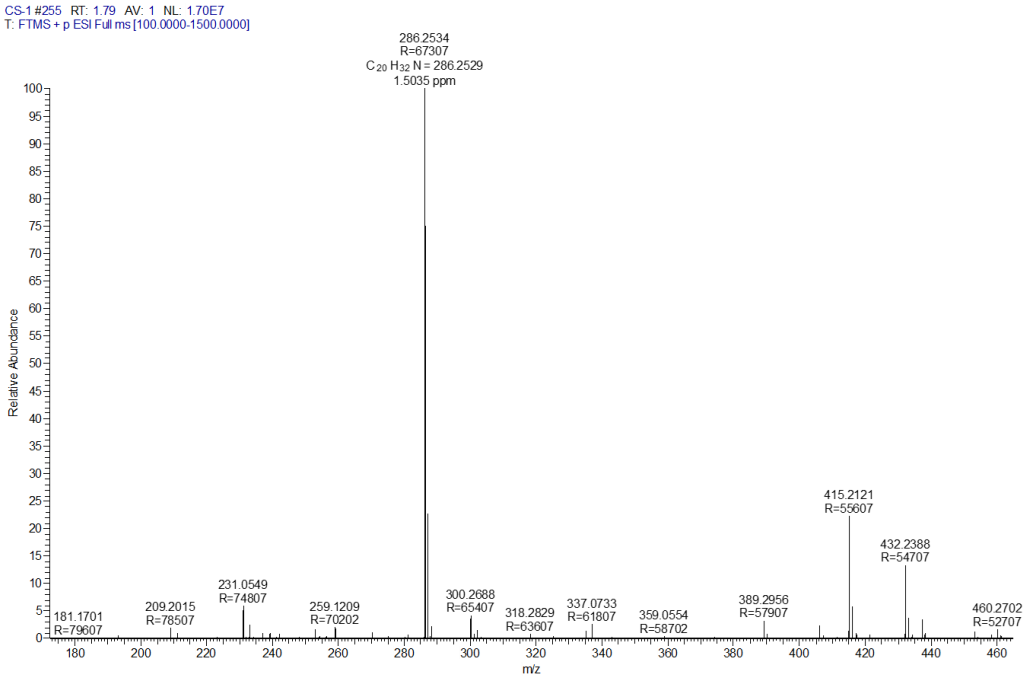

Figure 4A.A.4. Mass spectroscopic data of DiMeCAAC@AuNPs showing the peak of $[M+H]^+$ ion (observed *m/z* 286.2584) of DiMeCAAC.

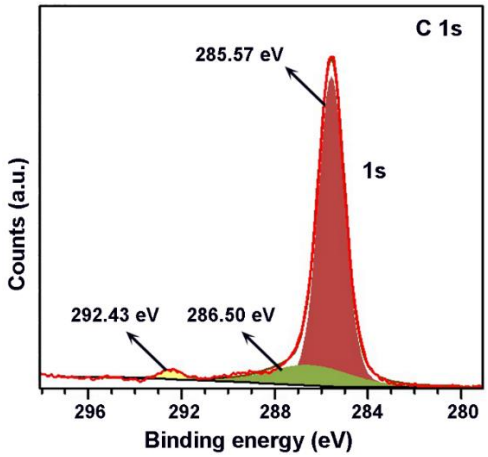

Figure 4A.A.5. X-ray photoelectron spectra for DiMeCAAC@AuNPs showing C 1s.

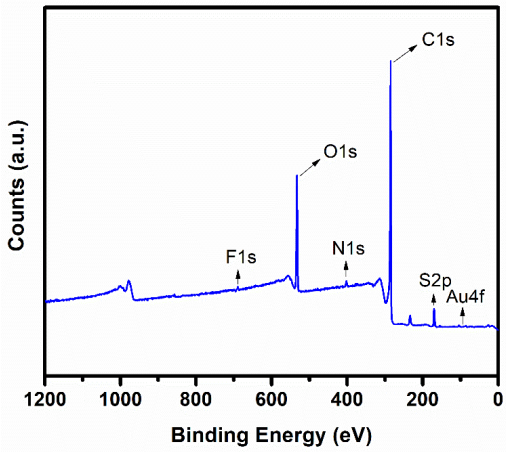

Figure 4A.A.6. XPS survey spectra of DiMeCAAC@AuNPs. The characteristics peak corresponding to all the major elements are properly assigned: Au4f, N1s, C1s.

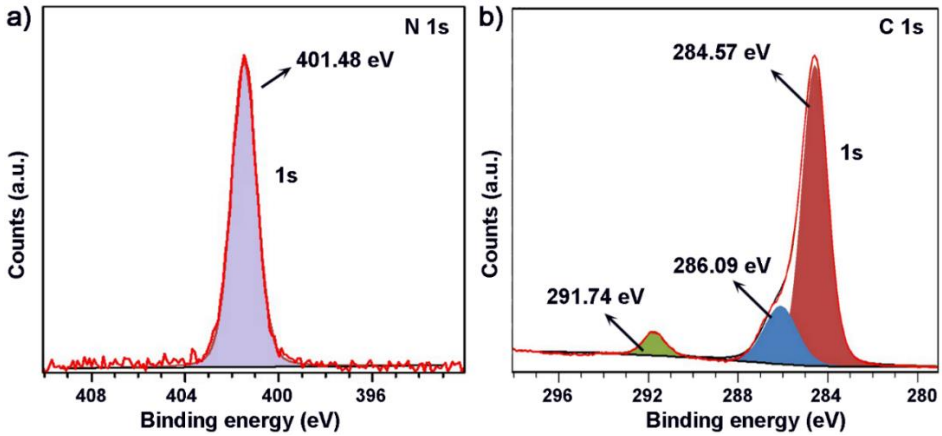

Figure 4A.A.7. X-ray photoelectron spectra for DiMeCAAC.OTf precursor (a) N 1s spectra showing a peak at 401.48 eV, indicative of pyrrolidine N peak according to the literature[10] (b) C 1s showing a peak at 291.74 eV is denoting C peak of $–CF_3$ moiety. Other assignments are enlisted in Table 4A.A.2.

Table 4A.A.2. XPS peak assignments of DiMeCAAC.OTf

Binding Energy (eV)	Assignments
401.48 for N 1s	Pyrrolidine N of DiMeCAAC.OTf
291.74 for C 1s	-CF_3 of DiMeCAAC.OTf
286.09 for C 1s	C-N moiety of pyrrolidine backbone of DiMeCAAC.OTf
284.57 for C 1s	Aromatic C-C of benzene backbone

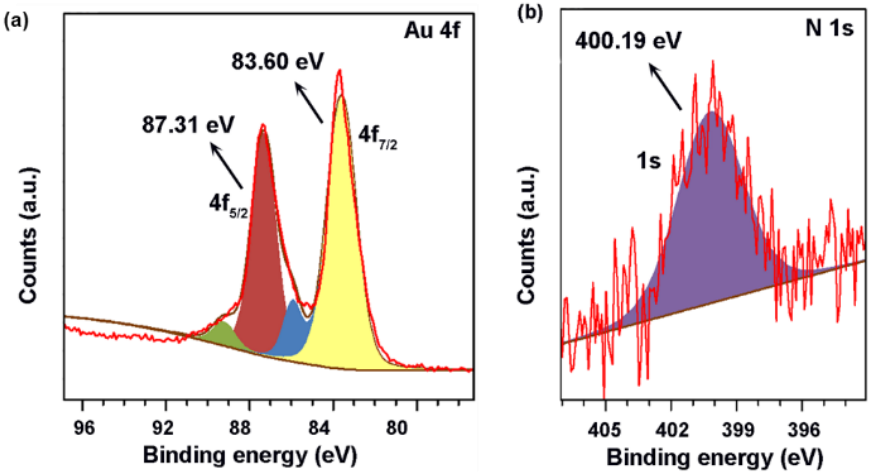

Figure 4A.A.8. X-ray Photoelectron Spectra for IMES@AuNPs showing (a) Au 4f showing spin-pair doublets at 83.61 and 87.23 eV for $4f_{7/2}$ and $4f_{5/2}$, respectively; (b) N 1s spectra showing peak at 400.19 eV.

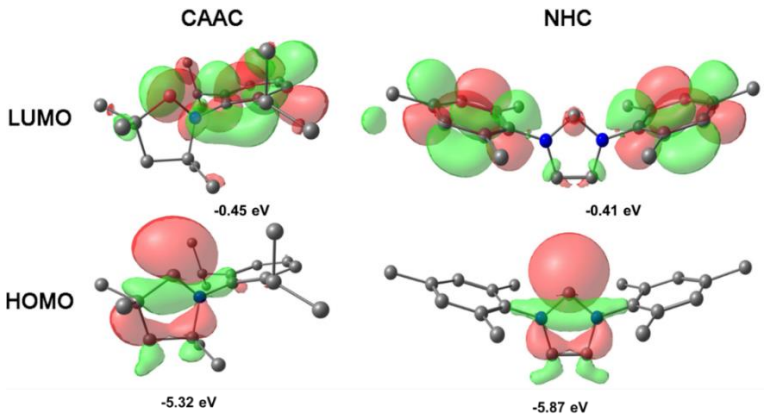

Figure 4A.A.9. HOMO and LUMO energy levels of DiMeCAAC and IMES using B3LYP-D3/def2TZVPP level of theory.

4A.A.6 Electrocatalytic CO_2 reduction.

4A.A.6.1 Preparation of the working electrode.

Toray carbon paper purchased from Global Nanotech were used as purchased. Carbon papers were cut into desired dimensions (1 cm^2 for CPE experiments), and then these were immersed in sample AuNPs solutions and dried using a heat gun to evaporate the solvent. After drying, the surface was washed thoroughly with distilled water to remove any loosely bound catalyst on the surface and dried under N_2 flow before use in electrolysis experiments for CO_2 reduction. To record the electrochemical data, a three-electrode-containing sealed electrochemical setup (AuNPs-coated carbon paper as the working electrode) was taken with the Pt-wire as the counter electrode separated from the working solution using a glass chamber containing a vycor frit. Standard double junction silver/silver chloride (Ag/AgCl) was used as the reference electrode, and 0.5 M $KHCO_3$ buffer solution as the electrolyte (pH 8.2 air saturated; pH 6.8 CO_2 saturated).

4A.A.6.2 Cyclic voltammetry.

Cyclic voltammograms were recorded on a potentiostat (CHI700E electrochemical analyzer) using a three-electrode containing sealed electrochemical setup with the sample deposited carbon paper electrodes as the working electrode in 0.5M aqueous potassium bicarbonate buffer solution as electrolyte (pH 8.2 air saturated; pH 6.8 CO_2 saturated). A spiral platinum wire having a large surface area was used as the counter electrode, which was separated from the working solution using a glass chamber containing a vycor frit. Standard double junction silver/silver chloride was used as the reference electrode, and 0.5 M $KHCO_3$ buffer. The platinum counter electrode and reference electrodes (standard double-junction silver/silver chloride filled with 4 M KNO_3 solution) were purchased from Pine Instruments. The working

buffer solution was deaerated by bubbling N_2 or CO_2 prior to recording the CV as appropriate. All the electrochemical experiments were performed at room temperature.

4A.A.6.3 Controlled potential electrolysis (CPE) and gas collection.

After saturating the working buffer solution with CO_2, the controlled potential electrolysis was performed on a potentiostat (CHI700E electrochemical analyzer) using the prepared working electrodes at different potentials (-0.4 to -0.9 V vs. Ag/AgCl) in a well-sealed two-compartment electrochemical cell for 2-3 hours. Agilent GC instrument (model no. 7890B (G3440B), serial no. CN14333203) fitted with a TCD detector was used to detect any gases that evolved during CPE. Any formation of formate was determined using an ion chromatography instrument equipped with an anion column 6.1006.530 Metrosep A Supp 5-250 with serial no. 0022.2486. ATR-FTIR data of the carbon paper working electrodes were obtained at room temperature in UATR (Universal Attenuated Total Reflection) set up of Perkin-Elmer FTIR Frontier instrument using Lithium Tantalate ($LiTaO_3$) detector. During each experiment, an average of 1000 scans was taken.

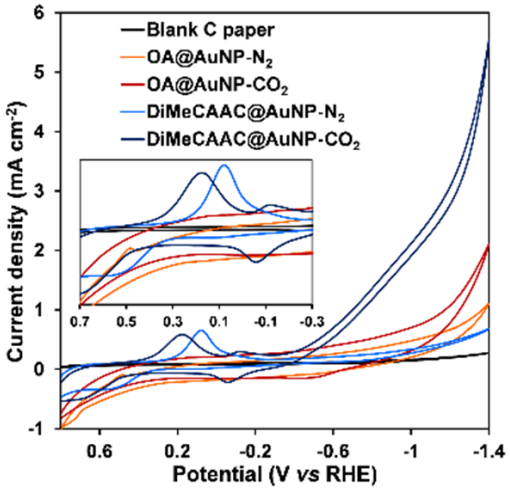

Figure 4A.A.10. Overlay of cyclic voltammograms of blank carbon paper, DiMeCAAC@AuNPs, OA@AuNPs, and IMES@AuNPs under N_2 and CO_2 saturation. Voltammograms were recorded at 0.1 Vs^{-1} in 0.5 M $KHCO_3$ buffer.

4A.A.6.4 Figures of merit to describe electrochemical CO_2R.[11]

1. We have achieved an FE for CO formation of up to 94% at a very low overpotential.

2. Current density (j) = I/A: Since we have used 1cm^2 carbon paper as the working electrode, the maximum current density we obtain in the presence of CO_2 is in the mA scale. This is comparable to other reports of functionalized gold nanoparticles. Utilizing other engineered electrodes or gas diffusion electrodes may improve this.

3. Energy efficiency (EE) = $\frac{E^0 * FE\ product}{E^0 + \eta}$, where E^0 is the equilibrium cell potential for the desired product (E^0 cathode-E^0 anode), and η is the sum of overpotentials on the cathode and anode.

Under CO_2 saturated conditions (0.5M $KHCO_3$ buffer, pH=6.8), DiMeCAAC@AuNP physisorbed on carbon paper, for conversion of CO_2 to CO, E°= -700 mV, FE_{CO} = 94%, η = -590mV (equilibrium potential (*vs.* RHE) for CO_2/CO couple at pH 6.8 = -110 mV); energy efficiency (%) = $\frac{-700 \times 94}{-700-590} = 51\%$; For our catalyst, the conversion of CO_2 to CO energy efficiency is calculated to be 51%. These figures may be improved with the same catalyst in an improved engineered electrochemical setup.

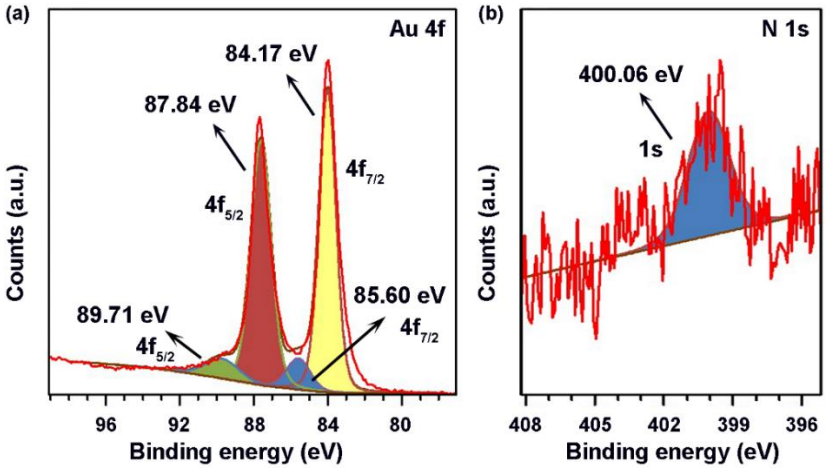

Figure 4A.A.11. X-ray Photoelectron Spectra for DiMeCAAC@AuNPs coated Carbon paper showing (a) Au 4f showing spin-pair doublets at 84.17 and 87.84 eV for $4f_{7/2}$ and $4f_{5/2}$, respectively, after electrocatalysis; (b) N 1s spectra showing peak at 400.06 eV, after electrolysis.

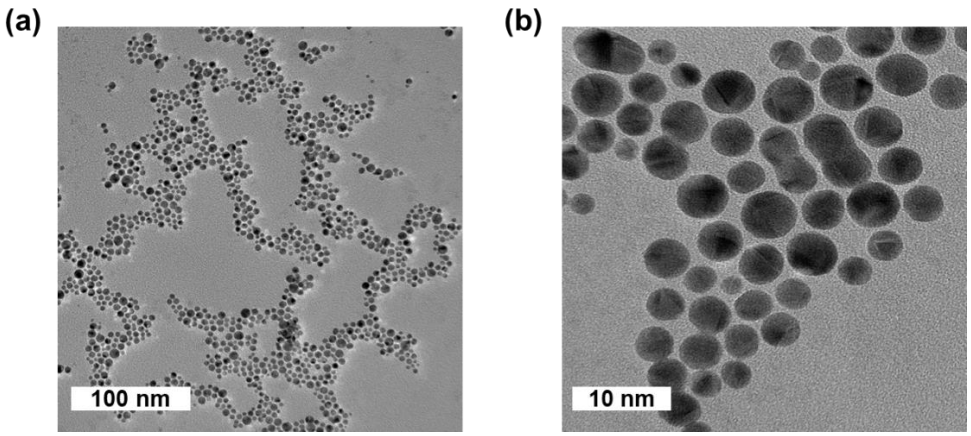

Figure 4A.A.12. TEM images of IMES@AuNPs (a) before and (b) after the electrocatalysis show negligible change in the morphology of AuNPs.

4B.A.1 Magnetic studies of DiMeCAAC@AuNPs.

Magnetic measurements of the samples were carried out using a Quantum Design make magnetic property measurement system (MPMS). The following complex magnetic measurements were carried out on the samples using the SQUID and VSM modes of the instrument.

1. Magnetization versus magnetic field at variable temperature different temperatures (5 K and 300 K) up to a maximum magnetic field of 6 Tesla (60 kOe). [kOe= kilo oersted]
2. The Magnetization of the samples was recorded as a function of temperature in the range 5-300 K under a) Magnetic field of 100 Oe; b) Zero field cooled (ZFC) and field cooled (FC) conditions

The samples were cooled in zero field to 5 K for ZFC measurements, and magnetization was measured while warming in a field of 100 Oe. For FC measurement, the samples were cooled from 300 K to 5 K in a magnetic field of 100 Oe, and the magnetization was measured while warming in a field of 100 Oe. Before the measurement, the instrument was calibrated using a standard sample of high-purity Palladium metal.

4B.A.2 Catalytic reduction of nitro-arene compounds.

We monitored the catalytic reduction of nitroarene compounds in a 3 ml quartz cuvette using SHIMADZU UV-3600 plus UV-Vis-NIR spectrophotometer. In a typical absorption experiment, DiMeCAAC@AuNP loaded filter paper dipped in the working solution, and $NaBH_4$ in a 3 ml quartz cuvette, and the absorption spectra were collected with a time interval of 10 and 20 min for 4-nitrophenol, 2-nitroaniline, 4-nitroacetophenone and a 30 sec interval for potassium ferricyanide. The kinetic experiments were monitored by observing the decrease in the absorbance of the reactant at its λ_{max} value with time.

4B.A.2.1 PNP reduction.

Reduction of 4-nitrophenol was carried out by taking 60 µL of 4-nitrophenol (50 mM), 300 µL of $NaBH_4$ (0.1 M), and 2.694 mL of milliQ water in a 3 mL quartz cuvette. Absorbance at 400 nm was monitored for the time-dependent absorption measurements.

4B.A.2.2 2-nitroaniline reduction.

Reduction of 2-nitroaniline was carried out by taking 60 µL of 4-nitrophenol (50 mM), 300 µL of $NaBH_4$ (0.1 M), and 2.694 mL of milli-Q water in a 3 mL quartz cuvette. Absorbance was monitored for the time-dependent absorption measurements.

4B.A.2.3 4-nitroacetophenone reduction.

Reduction of 4-nitroacetophenone was carried out by taking 60 µL of 4-nitrophenol (50 mM), 300 µL of $NaBH_4$ (0.1 M), and 2.694 mL of milliQ water in a 3 mL quartz cuvette. Absorbance at 400 nm was monitored for the time-dependent absorption measurements.

4B.A.2.4 Potassium ferricyanide reduction.

Reduction of potassium ferricyanide was carried out by taking 60 µL of 4-nitrophenol (50 mM), 300 µL of $NaBH_4$ (0.1 M), and 2.694 mL of milliQ water in a 3 mL quartz cuvette. Absorbance at ~420 nm was monitored for the time-dependent absorption measurements.

Table 4B.A.1. Versatility of $K_3[Fe(CN)_6]$ and nitroarene reactions, catalyzed by DiMeCAAC@AuNP

Substrate Scope	Product	Substrate Concentration		Catalyst loading (nM)	Time (min)	Yield (%)
		Nitroarene (mM)	**$NaBH_4$ (M)**			
$K_3[Fe(CN)_6]$	$K_2[Fe(CN)_6]$	50	0.1	18	1.5	96
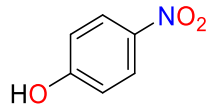	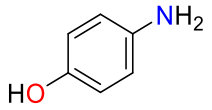	50	0.1	18	160	90
	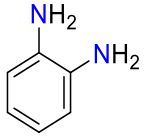	50	0.1	18	140	94
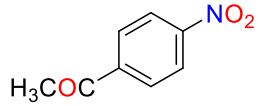	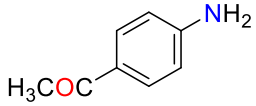	50	0.1	18	130	79

4B.A.3 Electrochemical studies.

The electrochemical measurements were carried out in a three-electrode setup using catalyst slurry coated Toray carbon paper (CP) (Global Nanotech) of area 1 cm^2 as the working electrode, graphite rod as the counter electrode, and $Hg/HgSO_4$ as a reference electrode in a BioLogic electrochemical workstation (VMP-300). The applied potentials were normalized with respect to a reversible hydrogen electrode (RHE). The catalyst solution (50 µL) in DMSO (Thomas Baker) was drop-cast on the CP and dried under an IR lamp. Subsequently, 5 µL of 0.01 wt % Nafion (DuPont) solution in ethanol was dropped to the catalyst-coated CP, which acts as an ionomer as well as a binder.

Bibliography of appendices.

(1) Frisch, M. J.; Trucks, G. W.; Schlegel, H. B.; Scuseria, G. E.; Robb, M. A.; Cheeseman, J. R.; Scalmani, G.; Barone, V.; Mennucci, B.; Petersson, G. A.; Nakatsuji, H.; Caricato, M.; Li, X.; Hratchian, H. P.; Izmaylov, A. F.; Bloino, J.; Zheng, G.; Sonnenberg, J. L.; Hada, M.; Ehara, M.; Toyota, K.; Fukuda, R.; Hasegawa, J.; Ishida, M.; Nakajima, T.; Honda, Y.; Kitao, O.; Nakai, H.; Vreven, T.; Montgomery, J., J. A.; Peralta, J. E.; Ogliaro, F.; Bearpark, M.; Heyd, J. J.; Brothers, E.; Kudin, K. N.; Staroverov, V. N.; Kobayashi, R.; Normand, J.; Raghavachari, K.; Rendell, A.; Burant, J. C.; Iyengar, S. S.; Tomasi, J.; Cossi, M.; Rega, N.; Millam, N. J.; Klene, M.; Knox, J. E.; Cross, J. B.; Bakken, V.; Adamo, C.; Jaramillo, J.; Gomperts, R.; Stratmann, R. E.; Yazyev, O.; Austin, A. J.; Cammi, R.; Pomelli, C.; Ochterski, J. W.; Martin, R. L.; Morokuma, K.; Zakrzewski, V. G.; Voth, G. A.; Salvador, P.; Dannenberg, J. J.; Dapprich, S.; Daniels, A. D.; Farkas, Ö.; Foresman, J. B.; Ortiz, J. V.; Cioslowski, J.; Fox, D. J. *GAUSSIAN 09, Revision D.01, Gaussian, Inc., Wallingford CT (**2009**).*

(2) Gao, X.; Bai, S.; Fazzi, D.; Niehaus, T.; Barbatti, M.; Thiel, W. Evaluation of spin-orbit couplings with linear-response time-dependent density functional methods. *J. Chem. Theory Comput.* **2017**, *13*, 515-524.

(3) Lavallo, V.; Canac, Y.; Präsang, C.; Donnadieu, B.; Bertrand, G. Stable Cyclic (Alkyl)(Amino)Carbenes as Rigid or Flexible, Bulky, Electron-Rich Ligands for Transition-Metal Catalysts: A Quaternary Carbon Atom Makes the Difference. *Angew. Chem. Int. Ed.* **2005**, *44*, 5705-5709.

(4) Hintermann, L. Expedient syntheses of the N-heterocyclic carbene precursor imidazolium salts IPr· HCl, IMes· HCl and IXy· HCl. *Beilstein J. Org. Chem.* **2007**, *3*, 22.

(5) Liu, S.; Chen, G.; Prasad, P. N.; Swihart, M. T. Synthesis of monodisperse Au, Ag, and Au–Ag alloy nanoparticles with tunable size and surface plasmon resonance frequency. *Chem. Mater.* **2011**, *23*, 4098-4101.

(6) Cao, Z.; Kim, D.; Hong, D.; Yu, Y.; Xu, J.; Lin, S.; Wen, X.; Nichols, E. M.; Jeong, K.; Reimer, J. A.; Peidong, Y.; J., C. C. A molecular surface functionalization approach to tuning nanoparticle electrocatalysts for carbon dioxide reduction. *J. Am. Chem. Soc.* **2016**, *138*, 8120-8125.

(7) Sherman, L. M.; Strausser, S. L.; Borsari, R. K.; Jenkins, D. M.; Camden, J. P. Imidazolinium N-Heterocyclic Carbene Ligands for Enhanced Stability on Gold Surfaces. *Langmuir* **2021**, *37*, 5864-5871.

(8) Trujillo, M. J.; Strausser, S. L.; Becca, J. C.; DeJesus, J. F.; Jensen, L.; Jenkins, D. M.; Camden, J. P. Using SERS to understand the binding of N-heterocyclic carbenes to gold surfaces. *J. Phys. Chem. Lett.* **2018**, *9*, 6779-6785.

(9) Suwaiyan, A.; Zwarich, R.; Baig, N. Infrared and Raman spectra of benzimidazole. *J. Raman Spectrosc.* **1990**, *21*, 243-249.

(10) Moock, D.; Wiesenfeldt, M. P.; Freitag, M.; Muratsugu, S.; Ikemoto, S.; Knitsch, R.; Schneidewind, J.; Baumann, W.; Schäfer, A. H.; Timmer, A. Mechanistic understanding of the heterogeneous, rhodium-cyclic (alkyl)(amino) carbene-catalyzed (fluoro-) arene hydrogenation. *ACS Catal.* **2020**, *10*, 6309-6317.

(11) Garg, S.; Li, M.; Weber, A. Z.; Ge, L.; Li, L.; Rudolph, V.; Wang, G.; Rufford, T. E. Advances and challenges in electrochemical CO_2 reduction processes: an engineering and design perspective looking beyond new catalyst materials. *J. Mater. Chem. A* **2020**, *8*, 1511-1544.

1. Chapter 1 is partially adapted from: **a)** M. Ghosh and S. Khan*, N-Heterocyclic Silylenes in Coinage Metal Chemistry: An Account of Recent Advances. *Dalton Trans.* 2021, *50*, 10674-10688 and **b)** M. Ghosh and S. Khan*, N-Heterocyclic Carbenes Capped Metal Nanoparticles: An Overview of Their Catalytic Scope. *ACS Catal.* 2023, *13*, 9313-9325

Copyright 2021: Royal Society of Chemistry

N-Heterocyclic silylenes in coinage metal chemistry: an account of recent advances

M. Ghosh and S. Khan, *Dalton Trans.*, 2021, **50**, 10674 **DOI:** 10.1039/D1DT01955D

To request permission to reproduce material from this article, please go to the Copyright Clearance Center request page.

If you are **an author contributing to an RSC publication, you do not need to request permission** provided correct acknowledgement is given.

If you are **the author of this article, you do not need to request permission to reproduce figures and diagrams** provided correct acknowledgement is given. If you want to reproduce the whole article in a third-party publication (excluding your thesis/dissertation for which permission is not required) please go to the Copyright Clearance Center request page.

Read more about how to correctly acknowledge RSC content.

The dissertation author is the main author of this article.

Copyright 2023: American Chemical Society

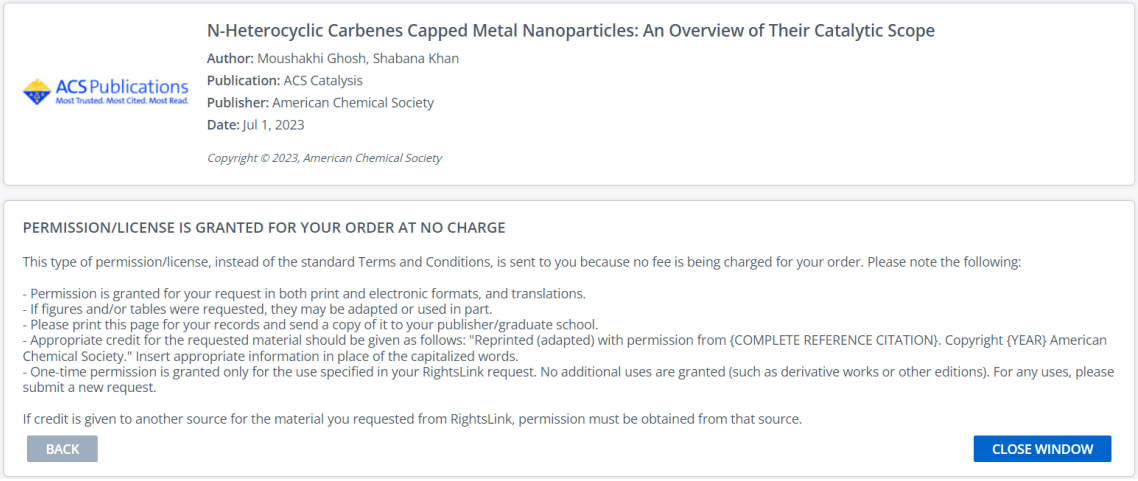

ACS Publications
Most Trusted. Most Cited. Most Read.

N-Heterocyclic Carbenes Capped Metal Nanoparticles: An Overview of Their Catalytic Scope

Author: Moushakhi Ghosh, Shabana Khan
Publication: ACS Catalysis
Publisher: American Chemical Society
Date: Jul 1, 2023

Copyright © 2023, American Chemical Society

PERMISSION/LICENSE IS GRANTED FOR YOUR ORDER AT NO CHARGE

This type of permission/license, instead of the standard Terms and Conditions, is sent to you because no fee is being charged for your order. Please note the following:

- Permission is granted for your request in both print and electronic formats, and translations.
- If figures and/or tables were requested, they may be adapted or used in part.
- Please print this page for your records and send a copy of it to your publisher/graduate school.
- Appropriate credit for the requested material should be given as follows: "Reprinted (adapted) with permission from {COMPLETE REFERENCE CITATION}. Copyright {YEAR} American Chemical Society." Insert appropriate information in place of the capitalized words.
- One-time permission is granted only for the use specified in your RightsLink request. No additional uses are granted (such as derivative works or other editions). For any uses, please submit a new request.

If credit is given to another source for the material you requested from RightsLink, permission must be obtained from that source.

BACK CLOSE WINDOW

The dissertation author is the main author of this article.

2. Chapter 2A and **Chapter 2C** are adapted from **a)** M. Ghosh, P. Panwaria, S. Tothadi, A. Das* and S. Khan*, Bis (silanetellurone) with C–H···Te interaction. *Inorg. Chem.* 2020, *59*, 17811-17821 and **b)** M. Ghosh, S. Tothadi, and S. Khan*, Carbazole Substituted Amidinato Silylene: Synthesis, Bonding, and Coordination Behavior with Coinage Metals. *Organometallics* 2021, *40*, 3201-3210, respectively.

Copyright 2020: American Chemical Society

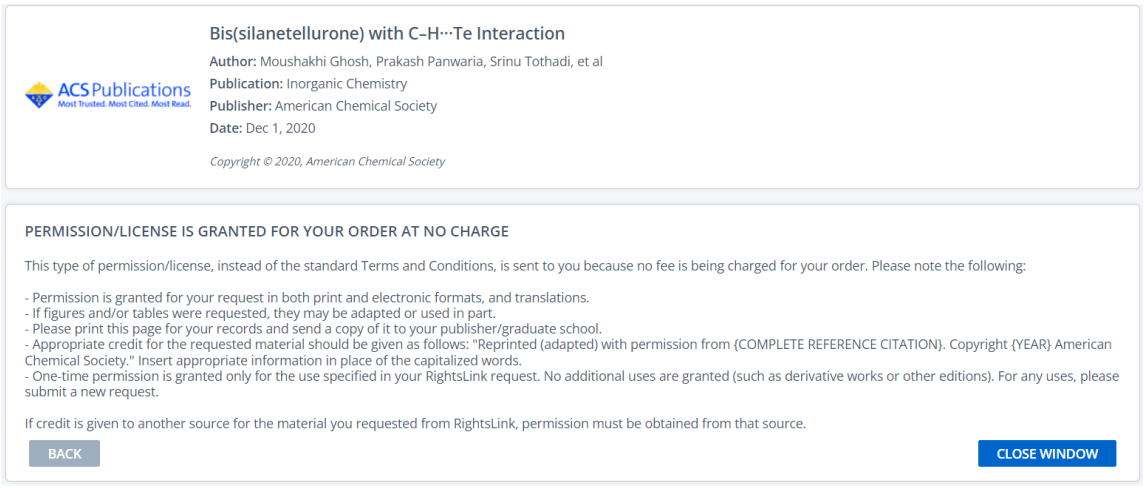

Bis(silanetellurone) with C–H···Te Interaction

Author: Moushakhi Ghosh, Prakash Panwaria, Srinu Tothadi, et al
Publication: Inorganic Chemistry
Publisher: American Chemical Society
Date: Dec 1, 2020

Copyright © 2020, American Chemical Society

PERMISSION/LICENSE IS GRANTED FOR YOUR ORDER AT NO CHARGE

This type of permission/license, instead of the standard Terms and Conditions, is sent to you because no fee is being charged for your order. Please note the following:

- Permission is granted for your request in both print and electronic formats, and translations.
- If figures and/or tables were requested, they may be adapted or used in part.
- Please print this page for your records and send a copy of it to your publisher/graduate school.
- Appropriate credit for the requested material should be given as follows: "Reprinted (adapted) with permission from {COMPLETE REFERENCE CITATION}. Copyright {YEAR} American Chemical Society." Insert appropriate information in place of the capitalized words.
- One-time permission is granted only for the use specified in your RightsLink request. No additional uses are granted (such as derivative works or other editions). For any uses, please submit a new request.

If credit is given to another source for the material you requested from RightsLink, permission must be obtained from that source.

BACK CLOSE WINDOW

The dissertation author is the main author of this article.

Copyright 2021: American Chemical Society

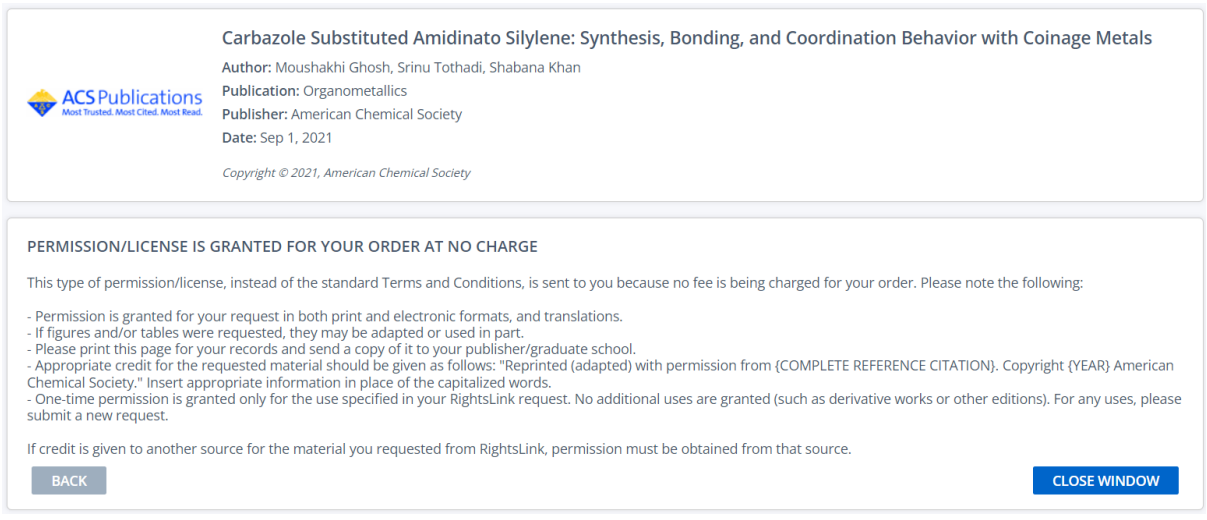

Carbazole Substituted Amidinato Silylene: Synthesis, Bonding, and Coordination Behavior with Coinage Metals

Author: Moushakhi Ghosh, Srinu Tothadi, Shabana Khan
Publication: Organometallics
Publisher: American Chemical Society
Date: Sep 1, 2021

Copyright © 2021, American Chemical Society

PERMISSION/LICENSE IS GRANTED FOR YOUR ORDER AT NO CHARGE

This type of permission/license, instead of the standard Terms and Conditions, is sent to you because no fee is being charged for your order. Please note the following:

- Permission is granted for your request in both print and electronic formats, and translations.
- If figures and/or tables were requested, they may be adapted or used in part.
- Please print this page for your records and send a copy of it to your publisher/graduate school.
- Appropriate credit for the requested material should be given as follows: "Reprinted (adapted) with permission from {COMPLETE REFERENCE CITATION}. Copyright {YEAR} American Chemical Society." Insert appropriate information in place of the capitalized words.
- One-time permission is granted only for the use specified in your RightsLink request. No additional uses are granted (such as derivative works or other editions). For any uses, please submit a new request.

If credit is given to another source for the material you requested from RightsLink, permission must be obtained from that source.

BACK CLOSE WINDOW

The dissertation author is the main author of this article.

3. Chapter 3 is adapted from M. Ghosh, J. Chatterjee, P. Panwaria, A. Kudlu, S. Tothadi, and S. Khan*, Silylene-Copper-Amide Emitters: From Thermally Activated Delayed Fluorescence to Dual Emission. *Angew. Chem. Int. Ed.* **2024**, e202410792.

Copyright 2024: Wiley VCH

License Details

This Agreement between Moushakhi Ghosh ("You") and John Wiley and Sons ("John Wiley and Sons") consists of your license details and the terms and conditions provided by John Wiley and Sons and Copyright Clearance Center.

Print Copy

License Number	5894150211001
License date	Oct 22, 2024
Licensed Content Publisher	John Wiley and Sons
Licensed Content Publication	Angewandte Chemie International Edition
Licensed Content Title	Silylene-Copper-Amide Emitters: From Thermally Activated Delayed Fluorescence to Dual Emission
Licensed Content Author	Shabana Khan, Srinu Tothadi, Ashwath Kudlu, et al
Licensed Content Date	Oct 16, 2024
Licensed Content Volume	0
Licensed Content Issue	0
Licensed Content Pages	11
Type of Use	Dissertation/Thesis
Requestor type	Author of this Wiley article
Format	Print and electronic
Portion	Full article
Will you be translating?	No
Title of new work	N-Heterocyclic Tetrylenes: Potential Platforms for Multidimensional Applications
Institution name	Indian Institute of Science Education and Research (IISER) Pune
Expected presentation date	Dec 2024
The Requesting Person / Organization to Appear on the License	Moushakhi Ghosh
Requestor Location	Indian Institute of Science Education and Research (IISER) Pune Department of Chemistry Main Building IISER Dr. Homi Bhbha Road, Pashan, Pune Pune, Maharashtra 411008 India Attn: Indian Institute of Science Education and Research (IISER) Pune
Publisher Tax ID	EU826007151
Total	**0.00 USD**

The dissertation author is the main author of this article.

4. Chapter 4A is adapted from M. Ghosh, P. Saha, S. Roy, S. Barman, P. P. Pillai*, A. Dey*, and S. Khan*, Cyclic(Alkyl)(Amino)Carbene Stabilized Gold Nanoparticles for Selective CO_2 Reduction. *ACS Catal.* 2024, *14*, 7011-7019 (*Published at Front Cover*); also available at ChemRxiv 2023

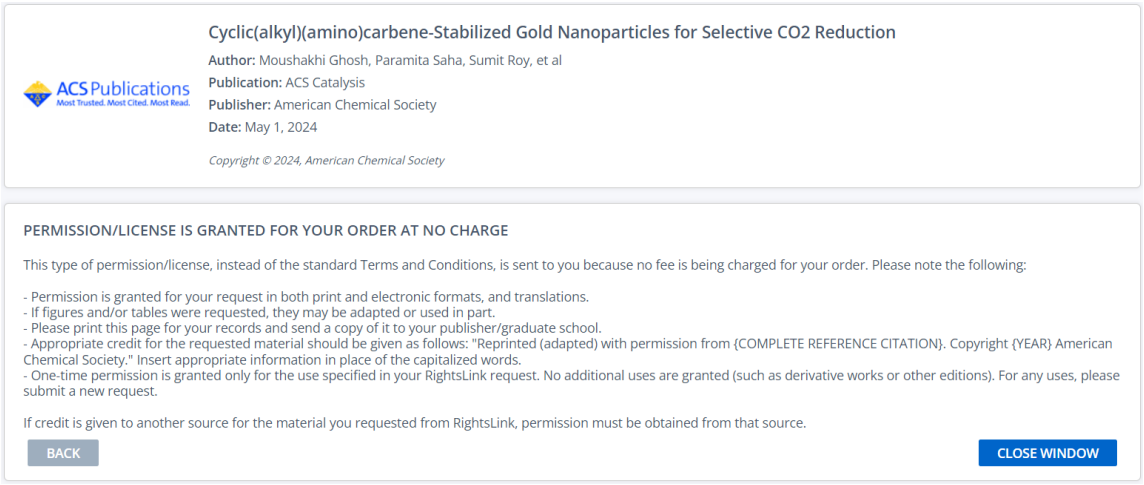

Cyclic(alkyl)(amino)carbene-Stabilized Gold Nanoparticles for Selective CO2 Reduction

Author: Moushakhi Ghosh, Paramita Saha, Sumit Roy, et al
Publication: ACS Catalysis
Publisher: American Chemical Society
Date: May 1, 2024

Copyright © 2024, American Chemical Society

PERMISSION/LICENSE IS GRANTED FOR YOUR ORDER AT NO CHARGE

This type of permission/license, instead of the standard Terms and Conditions, is sent to you because no fee is being charged for your order. Please note the following:

- Permission is granted for your request in both print and electronic formats, and translations.
- If figures and/or tables were requested, they may be adapted or used in part.
- Please print this page for your records and send a copy of it to your publisher/graduate school.
- Appropriate credit for the requested material should be given as follows: "Reprinted (adapted) with permission from {COMPLETE REFERENCE CITATION}. Copyright {YEAR} American Chemical Society." Insert appropriate information in place of the capitalized words.
- One-time permission is granted only for the use specified in your RightsLink request. No additional uses are granted (such as derivative works or other editions). For any uses, please submit a new request.

If credit is given to another source for the material you requested from RightsLink, permission must be obtained from that source.

BACK CLOSE WINDOW

The dissertation author is the main author of this article.